AFRL-VA-WP-TR-2005-3034

CONSISTENT STRUCTURAL INTEGRITY AND EFFICIENT CERTIFICATION WITH ANALYSIS

Volume 2: Detailed Report on Innovative Research Developed, Applied, and Commercially Available

Craig Collier

Collier Research Corporation
2 Eaton Street, Suite 504
Hampton, VA 23669

MAY 2005

Final Report for 27 June 2002 – 27 June 2004

THIS IS A SMALL BUSINESS INNOVATION RESEARCH (SBIR) PHASE II REPORT.

Approved for public release; distribution is unlimited.

STINFO FINAL REPORT

AIR VEHICLES DIRECTORATE
AIR FORCE RESEARCH LABORATORY
AIR FORCE MATERIEL COMMAND
WRIGHT-PATTERSON AIR FORCE BASE, OH 45433-7542

NOTICE

Using Government drawings, specifications, or other data included in this document for any purpose other than Government procurement does not in any way obligate the U.S. Government. The fact that the Government formulated or supplied the drawings, specifications, or other data does not license the holder or any other person or corporation; or convey any rights or permission to manufacture, use, or sell any patented invention that may relate to them.

This report was cleared for public release by the Air Force Research Laboratory Wright Site (AFRL/WS) Public Affairs Office (PAO) and is releasable to the National Technical Information Service (NTIS). It will be available to the general public, including foreign nationals.

PAO Case Number: AFRL-WS 05-2760, 12 Dec 2005

THIS TECHNICAL REPORT IS APPROVED FOR PUBLICATION.

/ / S / /

DUANE E. VELEY
Aerospace Engineer
Structural Design & Development Branch

/ / S / /

MICHAEL L. ZEIGLER
Branch Chief
Structural Design & Development Branch

/ / S / /

MICHAEL D. PILKENTON, Lt Col, USAF
Deputy Chief
Structures Division

This report is published in the interest of scientific and technical information exchange and its publication does not constitute the Government's approval or disapproval of its ideas or findings.

REPORT DOCUMENTATION PAGE	*Form Approved* *OMB No. 0704-0188*

The public reporting burden for this collection of information is estimated to average 1 hour per response, including the time for reviewing instructions, searching existing data sources, searching existing data sources, gathering and maintaining the data needed, and completing and reviewing the collection of information. Send comments regarding this burden estimate or any other aspect of this collection of information, including suggestions for reducing this burden, to Department of Defense, Washington Headquarters Services, Directorate for Information Operations and Reports (0704-0188), 1215 Jefferson Davis Highway, Suite 1204, Arlington, VA 22202-4302. Respondents should be aware that notwithstanding any other provision of law, no person shall be subject to any penalty for failing to comply with a collection of information if it does not display a currently valid OMB control number. **PLEASE DO NOT RETURN YOUR FORM TO THE ABOVE ADDRESS**.

1. REPORT DATE *(DD-MM-YY)* May 2005	**2. REPORT TYPE** Final	**3. DATES COVERED *(From - To)*** 06/27/2002 – 06/27/2004

4. TITLE AND SUBTITLE

CONSISTENT STRUCTURAL INTEGRITY AND EFFICIENT CERTIFICATION WITH ANALYSIS

Volume 2: Detailed Report on Innovative Research Developed, Applied, and Commercially Available

5a. CONTRACT NUMBER
F33615-02-C-3216

5b. GRANT NUMBER

5c. PROGRAM ELEMENT NUMBER
0605502

6. AUTHOR(S)

Craig Collier

5d. PROJECT NUMBER
A01V

5e. TASK NUMBER

5f. WORK UNIT NUMBER
0A

7. PERFORMING ORGANIZATION NAME(S) AND ADDRESS(ES)

Collier Research Corporation
2 Eaton Street, Suite 504
Hampton, VA 23669

8. PERFORMING ORGANIZATION REPORT NUMBER

9. SPONSORING/MONITORING AGENCY NAME(S) AND ADDRESS(ES)

Air Vehicles Directorate
Air Force Research Laboratory
Air Force Materiel Command
Wright-Patterson AFB, OH 45433-7542

10. SPONSORING/MONITORING AGENCY ACRONYM(S)
AFRL/VASD

11. SPONSORING/MONITORING AGENCY REPORT NUMBER(S)
AFRL-VA-WP-TR-2005-3034

12. DISTRIBUTION/AVAILABILITY STATEMENT

Approved for public release; distribution is unlimited.

13. SUPPLEMENTARY NOTES

This is a Small Business Innovation Research (SBIR) Phase II report. Report contains color.

This is Volume 2 of a three-volume work. See also Volume 1 (AFRL-VA-WP-TR-2005-3033) and Volume 3 (AFRL-VA-WP-TR-2005-3035).

14. ABSTRACT

Report developed under SBIR contract for topic AF01-239.

This SBIR report maintains that reliable pretest predictions and efficient certification are suffering from inconsistent structural integrity that is prevalent throughout a project's design maturity. Eight primary inconsistencies practiced in aerospace structural analysis are identified. This SBIR proposes solutions for these inconsistencies and documents software implementation and real world examples. Volume 2 looks at four example failure analysis correlations to test and describes new analysis methods developed for composite bonded joint stress analysis and failure and composite material stress analysis and failure.

15. SUBJECT TERMS

SBIR Report, HyperSizer, certification, analysis, structures, aerospace, bonded joints, composite materials

16. SECURITY CLASSIFICATION OF:			**17. LIMITATION OF ABSTRACT:**	**18. NUMBER OF PAGES**	**19a. NAME OF RESPONSIBLE PERSON** (Monitor)
a. REPORT	**b. ABSTRACT**	**c. THIS PAGE**			Duane E. Veley
Unclassified	Unclassified	Unclassified	SAR	256	**19b. TELEPHONE NUMBER** *(Include Area Code)* (937) 255-8286

Standard Form 298 (Rev. 8-98)
Prescribed by ANSI Std. Z39-18

Table of Contents

Section Page

PART A: PHASE II PROPOSAL SOW

LIST OF FIGURES 7

LIST OF TABLES 11

ACKNOWLEDGMENTS 12

1 PHASE II SOW 1

1.1 TASK 1. Demonstrate the certification process using HyperSizer for Air Force projects 1
1.2 TASK 2. Calibrate State-of-the-Art Analyses to Experimental Tests 1
1.3 TASK 3. Incorporate Probabilistic Methods in HyperSizer 2
1.4 TASK 4. Develop Analytical Methods for Airframe Structural Analyses 2
1.5 TASK 5. Document Methods and Equations and Provide in Electronic Format 3

2 CORRELATION TO TEST: HONEYCOMB SANDWICH FACESHEET WRINKLING 6

2.1 Theory 6
2.2 Test Data Description 7
  2.2.1 Sample Theoretical Calculation *8*
2.3 Test Data Correlation for Honeycomb Sets A and B 9
2.4 HyperSizer Setup 12
2.5 The μ_3 Correlation Factor 13
2.6 Simple Verification of HyperSizer Statistics 14
  2.6.1 Honeycomb Wrinkling Correlation with $\mu_1 = 0.59$; $\mu_3 = 1{,}000{,}000$ *14*
  2.6.2 Foam Sandwich Wrinkling Correlation with $\mu_1 = 0.88$; $\mu_3 = 1{,}000{,}000$ *15*
2.7 References 16

3 CORRELATION TO TEST: BONDED JOINT FAILURE; DELAMINATION, FIBER FRACTURE 17

3.1 Theory 17
3.2 Test Data Description 18
  3.2.1 NASA Stepped Bonded Doubler Tests *18*
  3.2.2 Cheuk and Tong Bonded Doubler Joint Tests *19*
  3.2.3 Cheuk and Tong Bonded Single Lap Joint Tests *19*
  3.2.4 Sample Theoretical Calculation *20*
3.3 Test Data Correlation 22
  3.3.1 Correlation Category: Joint, Bonded, Adherend Delamination (Linear) *22*
  3.3.2 Correlation Category: Joint, Bonded, Adherend Fracture (Linear) *24*
3.4 References 26

4 CORRELATION TO TEST: COMPOSITE LAMINATE STRENGTH 27

4.1 Validation Test Data 27
  4.1.1 Source of Test Data *27*
  4.1.2 Failure Envelopes *28*
4.2 The HyperSizer Correlation Factor (CF) Approach 29
  4.2.1 Choice of correlation: Individual ply properties vs. Failure criteria/material system *29*
4.3 A simple introductory example: WWFE Case 1 with 19 test data 31
  4.3.1 Test data entered, and histograms and PDFs generated *32*
  4.3.2 Failure theories compared for case 1 .... *32*
  4.3.3 Two step process for defining correlations factors *32*
4.4 Tsai-Hahn and LaRC03 best overall failure criteria for the 130 tests 36
  4.4.1 Theoretical background Larc03 .... *36*
  4.4.2 Theoretical background Tsai-Hahn *36*
  4.4.3 Tsai-Hahn correlation to the 130 tests *37*
  4.4.4 LarC03 correlation to the 130 tests *39*

4.5 SUMMARY OF EACH FAILURE THEORY'S CFS 40
4.6 IN-SITU EFFECTS OF A ± θ LAYUP OF A SPECIFIC MATERIAL SYSTEM 41
4.7 HOW THE EFFECT OF M&P CAN BE CAPTURED WITH CFS 42
4.7.1 AS4/3502 Properties 43
4.7.2 IM7/8552 Properties 46
4.8 REFERENCES 47

5 CORRELATION TO TEST: CYLINDRICAL PANEL BUCKLING 48

5.1 THEORY 48
5.2 TEST SETUP, DIMENSIONS AND MATERIAL PROPERTIES 48
5.3 SUMMARY OF PHASE I RESULTS 49
5.3.1 Phase I Test Data Comparison 49
5.3.2 Correlation Factors based on Two Parameters 51
5.4 PHASE II UPDATED CORRELATION FACTORS 55
5.5 INDEPENDENT VERIFICATION OF NASA SP-8007 RELIABILITY 57
5.6 HYPERSIZER CFS AND GENERATED HISTOGRAM 58
5.7 EXAMPLE: APPLICATION OF γ_μ AND η TO BUCKLING OF [02/±45]S CURVED LAMINATES 59
5.7.1 Cylindrical Buckling of Beer Cans 62
5.7.1.1 Theoretical Failure Loads 62
5.7.1.2 Computed Buckling Knockdown Factors and Allowable Loads 63
5.7.1.3 Prediction Summary 65
5.7.1.4 Test Data Failure Loads 66
5.7.1.5 Correlation Summary 67
5.7.1.6 Final comments 68
5.8 REFERENCES 69

6 COMPOSITE BONDED JOINT STRESS ANALYSIS AND FAILURE 70

6.1 RAPID, ACCURATE AND RELIABLE FAILURE PREDICTION 71
6.1.1 References 72
6.2 ACCURATE INTERLAMINAR STRESS PREDICTIONS 73
6.2.1 In-Service Structural Panels vs. Standalone Test Articles 74
6.2.2 In-Service Panel Deformations 76
6.2.3 In-Plane and Through Thickness Stress Distributions 77
6.2.4 Non-linear Adhesives 80
6.2.4.1 Bonded Joint Example with Non-Linear Adhesive 81
6.2.5 Scarfed and Stepped Joints 83
6.2.5.1 Bonded Joint Example with Stepped Adherend 85
6.2.6 Spew Fillets 87
6.3 WHY A NEW CAPABILITY WAS DEVELOPED 88
6.3.1 Contrasting HyperSizer with Hart-Smith (A4EI) 88
6.3.2 Contrasting HyperSizer with FEA 92
6.3.2.1 When is 2D FEA Inadequate and 3D Solid Model FEA required 95
6.3.2.2 Observations from HyperSizer – FEA comparisons 96
6.3.3 References 97
6.4 THEORETICAL DEVELOPMENT OF BONDED JOINT STRESS ANALYSIS 98
6.4.1 Summary 98
6.4.2 Symbols 98
6.4.3 Bonded Joint Concepts Analyzed By BondJo 100
6.4.4 Basic assumptions for the structural modeling of bonded joints 102
6.4.5 Adherends as Plates in Generalized Cylindrical Bending 102
6.4.6 Constitutive Relations for the Adhesive Layer 104
6.4.6.1 Linear spring adhesive model 104
6.4.6.2 Non-linear adhesive model 104
6.4.6.3 Equilibrium equations 104
6.4.6.4 The complete set of system equations 107
6.4.6.5 The boundary conditions 108
6.4.6.6 Multi-segment method of integration 108
6.4.7 In-plane Stresses in the Adherends 108
6.4.8 Out-of-plane (Interlaminar) Stresses in the Adherends 110
6.4.9 Nonlinear Analysis of Adhesive 113

6.4.9.1 Non-linear Material Model of the Adhesive 113
6.4.9.1.1 Elastic-plastic model 113
6.4.9.1.2 Bi-linear model 113
6.4.9.1.3 Power law material model 114
6.4.9.1.4 Ramberg-Osgood model 114
6.4.9.1.5 Multilinear (Polynomial) model 114
6.4.9.2 Yielding of the Adhesive 115
6.4.9.3 Stresses of Elastic Adhesive Layer 115
6.4.9.4 Non-linear Solution Procedure 116
6.4.9.5 Conclusions 119
6.4.10 References 119
6.5 STRENGTH FAILURE THEORIES 120
6.5.1 Summary of Failure Modes and Equations 120
6.5.2 Adherend Failure 120
6.5.2.1 Interlaminar delamination 120
6.5.2.2 Matrix cracking 122
6.5.3 Adhesive Failure (cohesive and adhesive/adherend interface failure) 123
6.5.4 Fracture Mechanics Based Failure Criteria 124
6.5.5 References 125
6.6 ISSUES WITH PREDICTING PEAK BONDED JOINT INTERLAMINAR STRESSES 127
6.6.1 Disparity in Stress Results from Different Analysis Methods 127
6.6.2 Uncertainty in Predicting Failure at the Reentrant Corner 129
6.7 HYPERSIZER EXAMPLE: COMPOSITE BONDED JOINT 131
6.7.1 Software Operation 131
6.7.2 Analysis Result Screenshots 134
6.7.3 Limitations of Capability 142
6.8 FUTURE DEVELOPMENT 143
6.8.1 Inclusion of deformable shear theory in the adherend 143
6.8.2 Inclusion of geometric non-linearity in joint analysis. 145
6.8.3 Replace Spring Model with Higher Order Theory Continuum Model 148
6.8.4 Micromechanics Analysis of Bonded Joints 149
6.8.5 References 150
6.9 VERIFICATION EXAMPLES 151
6.9.1 Bonded Doubler Verification – Delale and Erdogan, monolithic 151
6.9.2 Bonded Doubler Verification – StressCheck FEA, [0/±45/90] Laminate 155
6.9.3 Bonded Doubler Verification – Mortensen [0/30/60] Laminate 158
6.9.4 Single Lap Verification – Mortenson, [0/30/60] Laminate 161
6.9.5 References 164
6.10 VALIDATION EXAMPLES 165
6.10.1 Approach Summary 165
6.10.2 Bonded Doubler Validation – Tong Example 166
6.10.3 Bonded Doubler Validation – NASA Example 168
6.10.4 Single Lap Validation – Tong Example 173
6.10.5 References 175
6.11 SIGN CONVENTIONS AND REFERENCE PLANES 176
6.11.1 Sign Convention 176
6.11.2 Reference Planes 178
6.11.2.1 Reference Planes for Reporting of Results 178
6.11.2.2 Reference Planes for Introduction of Loads 179

7 COMPOSITE MATERIAL STRESS ANALYSIS AND FAILURE 181

7.1 BACKGROUND 182
7.1.1 The Physics of Composite Failure 182
7.1.2 V&V of Failure Criteria 183
7.1.3 Uncertainty at the Ply Level 184
7.2 DESIGN CRITERIA 185
7.2.1 Typical material properties vs. Design-to allowables 185
7.2.2 Design-to allowables 185
7.2.3 Ply vs. laminate allowables 186
7.2.4 1st ply damage initiation vs. progressive failure 186

7.2.4.1 Macro ply level progressive failure 187
7.2.4.2 Micro fiber/matrix level progressive failure 187
7.3 CHARACTERISTIC DIMENSION 188
7.4 FAILURE ANALYSES FOR PRELIMINARY AND FINAL DESIGN 189
7.5 REVIEW OF BEST FAILURE THEORIES TO DATE 190
7.5.1 Max Strain, Max Stress, Tsai-Hill, Tsai-Wu, and Tsai-Hahn failure theories 190
7.5.1.1 Maximum Stress Criterion 190
7.5.1.2 Maximum Strain Criterion 191
7.5.1.3 Tsai-Hill Criterion 192
7.5.1.4 Tsai-Wu Criterion 194
7.5.1.5 Tsai-Hahn Criterion 195
7.5.1.6 Summary of Tsai Theories 196
7.5.2 Zinoviev failure theory 196
7.5.3 Hashin failure theory (2D and 3D) 196
7.5.4 Sun failure theory 199
7.5.5 Puck failure theory 200
7.5.5.1 Fiber failure (FF) 200
7.5.5.2 Inter-Fiber Failure (matrix cracking) 202
7.5.5.3 Parameters in Puck's failure criteria 205
7.5.5.4 Overall performance of Puck failure criteria and its adaptability to industry 206
7.5.6 LaRC03 failure theory 206
7.5.6.1 Matrix failure 207
7.5.6.1.1 Criterion for matrix failure under transverse compression ($\sigma_{22} < 0$) 207
7.5.6.1.2 Criterion for matrix failure under transverse tension ($\sigma_{22} > 0$) 209
7.5.6.2 Fiber failure 212
7.5.6.2.1 Criterion for fiber tension failure 212
7.5.6.2.2 Criterion for fiber compression failure 212
7.5.6.3 Matrix Damage in Biaxial compression 214
7.5.7 Strain Invariant Failure Theory (SIFT) 214
7.5.8 Summary Conclusions 216
7.6 BLANK SECTION 216
7.7 IMPLEMENTATION OF LARC03 FAILURE THEORY 217
7.7.1 Input parameters for LaRC03 failure criterion 217
7.7.2 Methods of generation of LaRC03 failure envelops 219
7.7.2.1 Newton-Raphson method 219
7.7.2.2 Equations for generation of failure envelopes 220
7.8 IMPLEMENTATION OF HASHIN FAILURE THEORY 222
7.8.1 Input parameters for Hashin failure criterion 222
7.8.2 Generation of failure envelopes and calculation of margin of safety 222
7.9 IMPLEMENTATION OF STRAIN INVARIANT FAILURE THEORY (SIFT) 224
7.9.1 Conditions of using SIFT for matrix failure 224
7.9.2 Critical values of the strain invariants 225
7.9.3 Margin of Safety 225
7.9.4 Multi-scale analysis exploring the fields in fiber and matrix phases 225
7.9.5 Verification 226
7.9.6 Discussion 233
7.10 REFERENCES 235

List of Figures

FIGURE		PAGE
1.0	HyperSizer Plug-Ins	3
2.2a	Wrinkling failure test article	7
2.2b	Test results for a) Set A “0 ° core”, and b) Set B “90 °core”	7
2.2c	Test results for c) Set E “Isotropic (Foam) Core”	8
2.3	P = T because test data not yet reanalyzed with established CFs	9
2.4	P and T are now different values because test data has been reanalyzed	10
2.5	Test results for a) Set A “0° core”, and b) Set B “90° core”	11
2.6	Histogram showing eight honeycomb sandwich data points	14
2.7	Histogram from HyperSizer showing seven foam sandwich data points	15
3.1	Delamination failure in the NASA stepped bonded doubler example	18
3.2	Schematics of a skin/flange specimen (bonded doubler)	18
3.3	Schematic of bonded doubler test specimens	19
3.4	Schematic of bonded single lap joint test specimens	19
3.5	Stress in the facesheet outer ply (adjacent to the adhesive)	21
3.6	P = T because test data not yet reanalyzed with established CFs	22
3.7	P and T now different values because test data has been reanalyzed	23
3.8	P = T because test data not yet reanalyzed with established CFs	24
3.9	P and T now different values because test data has been reanalyzed	25
4.1	Failure envelopes plotted with superimposed WWFE test data	28
4.2	Data sheet from Mil-Hdbk-17	29
4.3	HyperSizer generated failure envelopes for WWFE Case 1	31
4.4	For WWFE Case 1, biaxial σy-σxy failure envelopes *0°* ***E-glass***	34
4.5	For WWFE Case 1, biaxial σy-σxy failure envelopes. Max Strain	34
4.6	After applying correlation factors for WWFE Case 1 *of 0°* ***E-glass***	35
4.7	After applying correlation factors for WWFE Case 1, Max Strain	35
4.8	LaRC03 failure criteria distinguishes between 6 possible failures	36
4.9	A HyperSizer Composite Strength, Tsai-Hahn histogram,130 test data pts	38
4.10	Composite Strength, LaRC03 Fiber Failure after correlation.	39
4.11	Composite Strength, LaRC03 Matrix Cracking after correlation.	39
4.12	Compressive strength of [+/-θ]s AS4/3502 predicted by failure theories	41
4.13	Compressive strength of [+/-θ]s AS4/3502 predicted by LaRC03	42
4.14	AS4/3502 using a-prior Mil-Hdbk-17-2E material properties	44
4.15	AS4/3502 using in-situ test data material properties	45
5.1	The ratio of experimental buckling load divided by theoretical	51
5.2	Linear regression of the analysis correlation factor, γ_μ, for two parameters	52
5.3	Bar chart comparing γ_μ values from Table 14	53
5.4	NASA SP8007 knockdown &(D13+D23)/(D11+D22) bending stiffness	54
5.5	Overall knockdown factor is now less reliant on the off-diagonal D ratio	55
5.6	Bar chart itemized by test specimen groups comparing γ_μ from Table 17	56
5.7	Panel Buckling, Curved, Simple, Fixed, or Free BC, Biaxial stiffness	58
5.8	HyperSizer Raleigh Ritz buckling solutions for the beer can, compression	62
5.9	PDF for 32 beer can buckling test articles	65
5.10	Histogram of the 32 beer can buckling failure loads	66
5.11	Traditional one knockdown approach to cylindrical panel buckling	68
6.1	HyperSizer predicts bonded joint failure to avoid failure such as this	70
6.1.1	Composite failure mode at the reentrant corner of a bonded flange	71

FIGURE		PAGE
6.1.2	Failure modes in adhesively bonded joints	72
6.1.3	Failure prediction require accurate out-of-plane interlaminar shear peel	72
6.2.1	Panel loads into interlaminar stresses of adhesive and laminate adherends	73
6.2.2	BCs on an “in-service panel” enforced uniform edge deformation	74
6.2.3	Free BCs on standalone test article permit non-uniform edge deformation	75
6.2.4	The five deformations of in-service panels are handled by BondJo	76
6.2.5	Interlaminar stress calculations throughout depth of bonded joint	77
6.2.6	Stress calculations performed by HyperSizer through the depth of the joint	78
6.2.7	In-plane stresses through the laminate and adhesive depth	79
6.2.8	Non-linear adhesive effects can reduce peak interlaminar shear ,peel stress	80
6.2.9	Composite bonded doubler joint example configuration	81
6.2.10	Stress-strain curves of epoxy AY103 adhesive	81
6.2.11	Linear versus non-linear results for a bonded doubler	82
6.2.12	Scarfed or stepped effects can reduce peak interlaminar shear, peel stress	83
6.2.13	HyperSizer BondJo computes stresses through the thickness of each ply	84
6.2.14	Composite stepped bonded doubler joint example configuration	85
6.2.15	Linear versus non-linear results for a stepped bonded doubler	86
6.2.16	Spew fillets can reduce peak interlaminar shear and peel stress	87
6.3.1	Hart-Smith (A4EI) permitted loads in contrast to HyperSizer-BondJo	88
6.3.4	Meshes of 3D finite element model for the bonded doubler	95
6.4.1a	Single-lap joint with straight adherend	100
6.4.1b	Single-lap joint with scarfed adherend	100
6.4.1c	Double-lap joint with straight adherend	100
6.4.1d	Bonded doubler joint with straight, scarfed, or stepped adherend	100
6.4.1e	Single sided stepped joint	101
6.4.1f	Single sided scarfed joint	101
6.4.1g	Double sided stepped joint	101
6.4.1h	Double sided scarfed joint	101
6.4.2	Schematic illustration of adhesive single lap joint with straight adherends	105
6.4.3	Equilibrium elements of adherend outside the overlap zone	106
6.4.4	Equilibrium element of adherends inside the overlap zone for joints	106
6.4.5	Lay-up of a laminate and the coordinate system	109
6.4.6	Models for nonlinear adhesive stress-strain curves	114
6.4.7	Illustration of the nonlinear solution procedure for adhesive joints	117
6.4.8	Points on the adhesive layer in nonlinear analysis	117
6.4.9	Flow chart for the nonlinear analysis for the adhesively bonded joints	118
6.5.1	Failure modes in adhesively bonded joints by Heslehurst and Hart-Smith	120
6.6.1	Differences in peak interlaminar stress predictions at the reentrant corner	127
6.6.2	Stresscheck verification example, small area around the reentrant corner	127
6.6.3	With more points, shape of curve same, peak stress increases	128
6.6.4	Four methods for predicting failure in bonded joints, reentrant corner	129
6.7.1	Configuration for bonded joint example	131
6.7.2	Adherend 1 (top facesheet) laminate specification	131
6.7.3	Flange laminate (Adherend 2) and adhesive specification	132
6.7.4	Bonded joint geometry shown in HyperSizer graphics	132
6.7.5	Joint loads entered on HyperSizer’s FBD tab	133
6.7.6	Joint parameters entered as “backdoor data”	133
6.7.7	Composite Joint Margins of safety reported on the failure tab	142

FIGURE		PAGE
6.8.1	Introducing first-order shear deformable theory into bonded joint analysis	144
6.8.2	Typical linear deformation of a bonded doubler joint	145
6.8.3	Schematic of bonded doubler test specimens examined by Cheuk and Tong	145
6.8.4	Vertical deflection, w, of the Cheuk and Tong validation problem	146
6.8.5	Comparison of FEA results to the experimental of axial strain vs. load	146
6.8.6	Modeling geometric nonlinearity in a single lap joint	147
6.8.7	Normalized adhesive layer peel & interlaminar shear stress, using SMA	148
6.8.8	Forces on the stiffened panel	149
6.9.1	Configuration of bonded doubler joint example	151
6.9.2	Comparisons for the applied tensile load case	152
6.9.3	Comparisons for the applied moment case	153
6.9.4	Through-the-thickness distribution of out-of-plane stresses (Nxx)	154
6.9.5	Through-the-thickness distribution of out-of-plane stresses (Mxx)	154
6.9.6	HyperSizer-BondJo to Stresscheck verification problem	155
6.9.7	Adhesive stress validation for panel applied axial force	156
6.9.8	Adhesive stress validation for panel applied axial moment	156
6.9.9	Through-thickness stress result comparison between HyperSizer-BondJo and Stresscheck for panel applied axial force	157
6.9.10	Through-thickness stress result comparison between HyperSizer-BondJo and Stresscheck for panel applied moment	157
6.9.11	Configuration of Mortenson’s composite bonded doubler joint example	158
6.9.12	Adherend transverse displacement HyperSizer-BondJo and Mortensen	159
6.9.13	Adherend bending moment between HyperSizer-BondJo and Mortensen	159
6.9.14	Out-of-plane adhesive stress between HyperSizer-BondJo and Mortensen	159
6.9.15	Mortensen’s example for single lap joints.	160
6.9.16	Single-lap joint comparison between HyperSizer-BondJo and Mortensen	162
6.9.16	Single-lap joint comparison between HyperSizer-BondJo and Mortensen	163
6.10.1	Schematic of bonded doubler test specimens by Cheuk and Tong.	166
6.10.2	Through-the-thickness distribution of margin of safety of adherend 1 at point a with linear adhesive under P =13 kN.	167
6.10.3	Through-the-thickness distribution of margin of safety of adherend 1 at point a with nonlinear adhesive under P =14 kN.	167
6.10.4	Schematics of a skin/flange specimen	168
6.10.5	Modeling of the flange scarf	169
6.10.6	Quasi-static and fatigue failure loads for the NASA tested skin/flange specimens. HyperSizer-BondJo results compared only to quasi-static data	170
6.10.7	Adhesive peel and interlaminar shear stresses along the bond line of the NASA skin/flange specimens.	171
6.10.8	Through-the-thickness distribution of interlaminar stresses at 1 and 2	171
6.10.9	Through-the-thickness distribution of interlaminar stresses at 3 and 4	172
6.10.11	Through-the-thickness distribution of interlaminar stresses at 5	172
6.10.12	Through-the-thickness distribution of the margin of safety of skin at the bond line corner (position 1), under longitudinal tension of 24.4 kN.	172
6.10.13	Single lap joint configuration in Tong’s problem.	173
6.10.14	All of the load-displacement curves from experimental results deviate	174
6.10.15	Through-the-thickness margin of safety of adherend 1 with linear	174
6.10.16	Through-the-thickness margin of safety of adherend 1 with nonlinear	174
6.11.1	The “HyperSizer panel” sign convention	176

FIGURE		**PAGE**
6.11.2	The “typical academic” sign convention follows standalone test article.	177
6.11.3	Reference plane HyperSizer panel coordinate system.	178
6.11.4	Reference plane in the typical academic sign convention.	178
6.11.4	Reference plane in the typical academic sign convention single lap joints	179
6.11.4	Loads are always introduced at the same reference	179
6.11.5	In the BondJo, each adherend of the joint is treated as a separate piece	180
7.1.1	LaRC03 distinguishes between six different possible physical failures	183
7.1.2	Compressive strength of [+/-θ]s AS4/3502 predicted	183
7.2.1	An example table from Mil Hnbk 17 showing typical (mean)	185
7.2.2	An example “carpet pot” laminate based strain allowable	186
7.2.3	Failure envelope of progressive failure	187
7.3.1	Illustration of different radial distances used	188
7.5.1	Maximum Stress Failure Envelope	190
7.5.2	Comparison, max stress to max strain	192
7.5.3	Tsai Hill	194
7.5.4	Tsai-Hill with different compression/tension allowables	194
7.5.5	Tsai Wu Failure Envelope	195
7.5.6	Lamina subjected to longitudinal stress	201
7.5.7	The concept of fracture plane in UD lamina	202
7.5.8	Matrix failure envelopes for a typical unidirectional E-glass/epoxy	209
7.5.9	A crack embedded in a constrained UD ply (Dvorak’s model)	210
7.5.10	Misaligned fibers under compression	213
7.7.1	Compressive strength of [+/-θ]s AS4/3502 predicted by LaRC03	218
7.7.2	Polar coordinates of a point in the failure envelope	220
7.9.1	Measurement of critical strain invariants in the matrix of IM7/epoxy	224
7.9.2	Multi-scale analysis from laminates to constituents.	226
7.9.3	Experimental stress-strain curves for IM7/977-3 lamina under tension.	227
7.9.4	Configurations of unit cells a) 2 by 2 subcells b) 7 by 7 subcells	228
7.9.5	Comparison of matrix phase J1 predicted by Gosse and HyperSizer	229
7.9.6	J1 in the matrix phase predicted by HyperSizer under failure	232
7.9.7	J1 in the matrix phase predicted by HyperSizer under failure	233
7.9.8	Dealing with nonlinearity when implantation of SIFT.	235

List of Tables

TABLE		PAGE
2.1	Test Data Summary for Sets A, B and E	7
2.2	Test failure loads, theoretical & predicted allowables for Data Sets A& B	14
2.3	Test failure loads, theoretical & predicted allowables for Data Set E	15
3.1	Summary of theoretical failure load vs. experimental result	18
3.2	Individual test data summary for bonded doubler specimens	19
3.3	Individual test data summary for single lap joint specimens	20
4.1	HyperSizer Failure Test Data Summary	27
4.2	Summary of HyperSizer CFs for Composite Failure Theories	40
4.3	Properties of UD AS4/3502 from MIL-HBK-17 & NASA LaRC03 report	43
4.4	Properties of UD IM7/8552 from MIL-HBK-17 NASA, Boeing/Collier	46
5.1	Experimental load divided by the Phase I theoretical buckling load	49
5.2	Experimental and theoretical buckling loads for HyperSizer & SS8 code	50
5.3	Coefficients of Eq. 5.1.4 resulting from a linear regression	52
5.4	Test specimen groups, correlation factors, and NASA knockdown factors	53
5.5	Changed buckling results for Phase II correlation factor calculation	55
5.6	Coefficients of Equation 5.3.4 resulting from a linear regression	55
5.7	Summary of test groups, correlation factors, NASA knockdown factors	56
5.8	HyperSizer theoretical, predicted and actual failure loads for 5 test articles	60
5.9	Beer Can Data	63
5.10	Beer Can Failure Allowables (crushing load)	65
5.11	32 beer can buckling failure loads	66
5.12	Beer Can Test Summary Failure Results	66
6.3.1	Comparison of HyperSizer-BondJo to Hart-Smith A4EI	89
6.3.2	Comparison of HyperSizer-BondJo with Stresscheck FEA	92
6.4.1	Symbols used in BondJo theoretical development	98
6.10.1	Summary of bonded doubler validation examples	165
6.10.1	Comparison of HyperSizer-BondJo predicted to average test failure load	166
6.10.2	Individual test data summary for bonded doubler specimens	166
6.10.3	Comparison of HyperSizer-BondJo predicted to average test failure load	169
6.10.3	Comparison of HyperSizer-BondJo predicted to average test failure load	173
7.5.1	Summary of Puck IFF criteria for plane stress case	204
7.5.2	Summary of Puck IFF criteria for 3D stress case	205
7.5.3	Strength values and inclination parameters for typical FRP in Puck	206
7.5.4	Comparison of up-to-date best failure theories for FRP	216
7.7.1	Required UD material properties for LaRC03	217
7.7.2	Optional UD material parameters for LaRC03	217
7.8.1	Required UD material properties for Hashin failure criteria	222
7.9.1	Failure loads for matrix dominated lamina (IM7/977-3 tape)	226
7.9.2	Material properties of IM7 fiber and 977-3 resin	227
7.9.3	Maximum point, phase average, and homogenized lamina effective strain invariants within the matrix phase of the matrix dominated UNT data	227
7.9.4	Comparison of predicted effective properties of IM7/977-3 (Vf = 0.60)	228
7.9.5	MOS (J1critical = 2.34e-2) and predicted J1 in the matrix phase under failure loads	228

TABLE		PAGE
7.9.6	local strain fields (26 by 26 subcells) in the angle-ply lamina using J1critical = 2.34e-2	230
7.9.7	MOS (J1critical = 0.798 e-2) and predicted J1 in the matrix phase under failure loads	231
7.9.8	MOS (J1critical = 0.9548e-2) and predicted J1 in the matrix phase under failure loads	232

Acknowledgments

This material is based upon work supported by the United States Air Force under Contract

1. AFRL VA SBIR Phase I contract # F33615-01-M-3125
2. AFRL VA SBIR Phase II contract # F33615-02-C-3216
3. LM Aero LRSA Contract/PO # 7067581

PART A: PHASE II PROPOSAL SOW

1 Phase II SOW

The SBIR approach to certification is based squarely on the building-block approach. The process is to establish the capability of each individual failure mode to be predicted in a robust, general, and reliable manner on a well controlled experimental test before moving to the next level of built-up hardware complexity. This process is much like the practice of commercial software development where individual modules (software components) are extensively tested individually before integrating into a larger system.

1.1 TASK 1. Demonstrate the certification process using HyperSizer for Air Force projects

The plan is for LM Aero engineers at Fort Worth, TX and Marietta, GA, with extensive support and interaction with the PI, to use HyperSizer's existing capabilities and those developed during Phase II for design and analysis of on-going Air Force projects. The demonstration of the process is proposed for all areas of interest to the Air Vehicles Directorate. A structural component/assembly based approach for demonstrating certification will be used. The emphasis is on reliable robust design that lends itself to dependable certification by analysis and test.

The objective is to work a wide array of problems that will both acquaint LM Aero with HyperSizer and act to gain confidence in the analytic solutions. Successful demonstration of the certification by analysis process and the newly developed correlation test data defined in the other tasks of Phase II will provide a direct transition of the results to the private sector. A higher level of "certification by analysis" can only be incorporated in industry production practice by repeatedly demonstrating good correlation with verification test results. To this end, LM Aero will conduct conceptual design trades using HyperSizer to compare with results from prior design and test results. Structural designs are planned to be evaluated for applications ranging from fighter and transport aircraft, to emerging air vehicle designs for unmanned and future strike air platforms.

1.2 TASK 2. Calibrate State-of-the-Art Analyses to Experimental Tests

This task is to be performed in two parts. The first part is collection of test data and will be performed by LM Aero for LM owned data and by the PI for all other non-LM data. The second part, performed by the PI, is the statistical processing of the data into two distinct correlation factors, γ_{μ} and $\gamma_{\eta,}$ for use with a probabilistic method implementation as described in Task 3. Furthermore the collection of test data can be identified as new or existing. The new data will primarily be from on-going LM Aero projects that involve HyperSizer. This data will more likely be one or only a few test samples and not statistically relevant. To achieve large enough test samples to be statistically relevant for a given configuration and investigated failure mode, it is expected that existing experimental test data will need to be collected for developing trends and identifying repeatable stochastic failure behavior.

By collecting existing data, prior investment could be taken advantage of for meeting the technical objectives of this SBIR. The data then would be evaluated for completeness before attempting to perform an analysis for correlation purposes. Once proven to be complete data and useful for developing trends and identifying repeatable stochastic failure behavior, it will then be made available for appropriate transition to the private sector (separating if necessary based on existing proprietary ownership) and included in the HyperSizer commercial product.

The two distinct correlation factors, γ_μ and γ_η, for each failure analysis were demonstrated in Phase I to provide advantages over current analysis practices. This is summarized in Appendix A of this proposal. The first advantage is an ability to confidently predict average failure load and expected stochastic behavior. The second advantage is to be able to achieve uniform reliability for all failure modes and associated analysis method inaccuracies using the PM implementation defined in task 3.

1.3 TASK 3. Incorporate Probabilistic Methods in HyperSizer

This work will be carried out by Collier Research Corp by the PI. The intent is to be able to achieve uniform reliability for each potential failure mode and associated analysis method by implementing the two distinct statistical correlation factors, γ_μ and γ_η quantified in task 2. γ_μ represents test average failure loads, and γ_η represents test coefficient of variation of test scatter.

Value of Existing Test Data for Certification by Analysis

The value of test data for meeting certification by analysis technical objectives has been demonstrated in Phase I. Therefore, at the very least, for Phase II plans are in place to modify HyperSizer to handle the statistical correlation factors, γ_μ and γ_η defined from Task 2.

As an example of the benefit, correlation factors for two different failure analyses have been calculated and shown in the table below. Thin shell cylindrical buckling is a widely known extreme case of analysis inaccuracy. This was chosen as a Phase I example to evaluate the limit of the proposed certification by analysis process. Based on test data, we now are able to predict the average cylindrical compression buckling load and a buckling load design-to allowable using the correlation factors, γ_μ and $\gamma_{\eta,}$ respectively.

1.4 TASK 4. Develop Analytical Methods for Airframe Structural Analyses

The focus of Task 4 is to fill holes in missing analysis capability needed for certification. This is to be accomplished three ways: 1) Implementing legacy and/or Lockheed Martin Aero (LM Aero) analysis methods into the HyperSizer ***framework*** through the plug-in capability; 2) Implementing HyperSizer into LM Aero's design system using its Object Model; and 3) Develop new analysis failure methods in HyperSizer.

Automating the software input process

Collier Research is continuously developing two capabilities that open up an opportunity for using HyperSizer as a certification by analysis tool. The first of these, which is available in the current version of the software, is the ability of HyperSizer to act ***as a framework*** for incorporating higher fidelity, specialty analyses codes through software 'plug-ins.' The plug-in concept is illustrated in Figure 1. These specialty codes, which can be found throughout the government and industry, are currently interfaced through manual ASCII file input and output which is generally inefficient. HyperSizer automates the I/O by connecting them into the data flow stream of the software. This 'plug-in' framework, which is designed for efficiency, tight thermo-structural analysis method coupling, and project data integrity, can live inside of larger general-purpose frameworks. The ability to integrate ***into a framework*** is the second HyperSizer capability proposed to enhance the certification by analysis process. Over the last year, an "Object Model" for HyperSizer has been developed as part of the High Performance Computing and Communications Program (HPCCP) at NASA Langley. This Object Model allows HyperSizer to be interfaced to any number of framework environments, such as Advanced Modeling Language (AML) from Technosoft, Inc. or ModelCenter from Phoenix Integration.

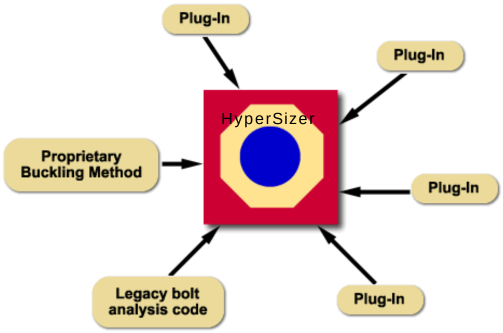

Figure 1, HyperSizer Plug-Ins

Inclusion of additional analysis method types into HyperSizer

Other structural failure methods that are identified as being necessary for structural certification by the Air Force, Lockheed Martin and/or Collier Research will be developed and implemented natively in HyperSizer. This goes along with the "design-by-analysis" idea where the more analyses methods that are included early in the design process, the farther toward certification a structural design will be. Our intention is not only to include intrinsic HyperSizer capabilities for these additional analysis types, but also to provide software integration protocols that would provide plug-in capabilities for these additional analysis types.

1.5 TASK 5. Document Methods and Equations and Provide in Electronic Format

This work will be carried out by the PI and other research engineers from Collier Research Corp., with some limited support from both LM Aero facilities. The intent is to provide documentation in both typical report format and in electronic format that records the results of the SBIR research.

The electronic format is planned to be in the most commonly used format for web based distribution and for integration with engineering software applications. The electronic version will be searchable and store all types of documentation such as text, equations, and graphics. In addition to Word format, another proposed format is PDF. The PDF documents will be stored in a data tree structure with HTML hyperlinks to different sections.

The electronic format may also include a software facility, such as a database, for storing raw experimental test data and the resulting statistical reductions. This will aid in preserving and keeping the link to the specific test article data source intact over time as the software implements the derived correlation factors for a specific failure analysis. The raw data would include the article shape and dimensions, material properties, loadings, boundary conditions, and resulting failure load and strain gage readings.

The need for the documentation has been expressed repeatedly by LM Aero and other companies over the years. Bob Olliffe interviewed many stress analysts in Marietta about analysis certification and engineering documentation. Bob says that

> No formal process appears to exist for the "certification" of software for use in performing detailed stress analysis on production aircraft programs. Most computerized methods currently used are encoded hand analysis methods derived from the Lockheed Martin Stress Memo Manual (SMM), other in-house generated methods and practices, or generally accepted textbook physics-based solutions. The impression that I received from the stress groups was that new analysis software should contain detailed documentation including examples for various types of analysis, applied loads, and geometry. Some number of solutions would be generated using the software on applicable problems, and compared to solutions generated using current methods. Obviously, any improved correlation with actual test data compared to that generated using existing methods would be of great benefit.

The documentation could also include ***use cases*** that address issues such as how to model stiffened panels and ringframes and their associated offsets. An important issue which always comes up is how FEMs with equivalent 2-D planar meshes compare to discrete 3-D modeling. A case in point is using CROD elements representing longerons vs. HyperSizer equivalent stiffness approach. Another example is the number of elements required in a panel bay to capture out-of-plane pressure and bending moments.

In summary, the bulk of this work will be directed to the actual generation of the documentation and not the development of the electronic facilities to retrieve and view it.

The general categories of items to document in Phase II are

- Test data
- Analysis methods and equations
- Modeling issues including the FEM mesh
- Correlation to analysis predictions, and resulting correlation factors

PART B: FOUR EXAMPLE FAILURE ANALYSIS CORRELATIONS TO TESTS

The Validation Examples in Chapters 2-5 are provided to show the derivation of the appropriate correlation factors (CFs) used for the failure analyses in the Long Range Strike Aircraft (LRSA) demonstration example of Volume I, Chapters 10 and 11. The CFs are necessary pieces for the newly developed reliability analysis approach. For the airframe example, three primary failure modes are investigated: cylindrical panel buckling, composite material strength, and honeycomb sandwich facesheet wrinkling [2.4]. Each of these potential failures is briefly discussed in this section in terms of their theoretical background and test data correlation. It will be shown that some of these failures have larger observed scatter in test response and in analytical predictive accuracy. For these failure modes and associated analyses that provide less confidence, the proper assignment of correlation factors (CFs) will allow them all to be used with the same reliability to achieve consistent structural integrity during preliminary design sizing.

The process starts with collecting test data for unique failure modes (e.g. honeycomb facesheet wrinkling) and identifying a Probability Density Function (PDF) signature that is repeatable and unique to that mode's nature. The PDF signature represents expected test data scatter for a given material type (metallic vs. composite) and loading. Included with the formulation of the PDF is identification of intrinsic parameters used to scale the analytical prediction to cause a better statistical fit of test data. At this time, normal distributions are assumed as probability density functions. This process can rely on existing "building block" test data to form the basis of analytical prediction confidence. We start with a simplistic correlation of honeycomb facesheet wrinkling test data, then to laminate strength, and end with a fairly complex cylindrical panel buckling correlation.

The discussed analysis methods in order of increasing complexity and insight:

- Honeycomb
- Bonded joint
- Composite material strength
- Panel buckling

2 Correlation to Test: Honeycomb Sandwich Facesheet Wrinkling

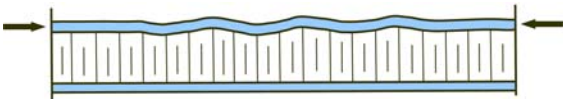

Sandwich structures with thin facesheets and lightweight cores are prone to a type of local failure known as facesheet wrinkling. The term wrinkling refers to local, short wavelength buckling phenomenon of the facesheet, with mode shapes having wavelengths up to the thickness of the core. The small buckling wavelength of the wrinkling mode results in the allowable load being insensitive to structural boundary conditions and curvature. Sandwich structures exhibit little or no post-wrinkling load carrying capability, therefore wrinkling failure is typically catastrophic. As a consequence, accurate prediction of wrinkling is important for quantifying structural integrity.

2.1 Theory

The equation for sandwich wrinkling with isotropic (e.g. foam) cores is

$$\sigma_{wr} = k_1 \left(E_f \ E_c \ G_c\right)^{\frac{1}{3}} \tag{2.1.1}$$

and for honeycomb cores the recommended equation is

$$\sigma_{wr} = k_2 \, E_f \sqrt{\frac{E_c \ t_f}{E_f \ t_c}} \tag{2.1.2}$$

References [2.1] and [2.2] provide the suggested factors to use with the wrinkling allowable stress equations, which are:

$$k_1 = 0.63 \qquad k_2 = 0.82$$

These k1 and k_2 values are based on theory and are not based on empirical correlations.

2.2 Test Data Description

The following series of compressive panel tests performed in 2004 for sandwich wrinkling, Fig. 2.1, are used for correlation. The test articles were composed of either two or three ply composite facesheets with either 3 pcf Nomex honeycomb or Divynicell H45 Foam Cores. The facesheet and core properties and test conditions for each set of data are summarized in Table 2.1. Sets A and B contain identical panel designs but with different loading (0° in Set A, and 90° in Set B).

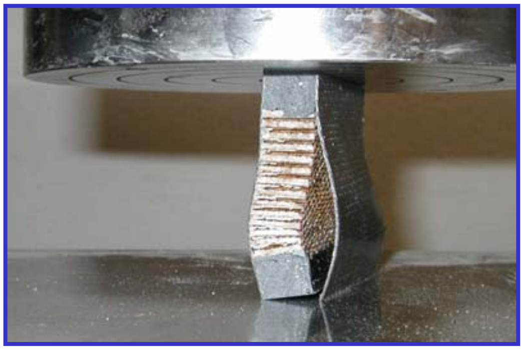

Fig. 2.1, Wrinkling failure test article

Table 2.1, Test data summary for sets A, B and E. The panel designs for Sets A and B are identical but the loadings are different

Validation Set	Specimen Description	Facesheet Thickness (in)	Facesheet Ex (psi)	Facesheet Ey (psi)	Facesheet nuxy	Core Thickness (in)	Core Gxz (psi)	Core Ez (psi)	Avg Test Strength (lbs/in)	Failure Mode	Comment
A	2 Ply Facesheets, 3.0 lb Nomex 0° direction	0.015	9.20E+06	9.20E+06	0.06	0.5	5200	20000	1032	Wrinkling	4 (of 6) Bad tests - (premature failures)
B	2 Ply Facesheets, 3.0 lb Nomex 90° direction	0.015	9.20E+06	9.20E+06	0.06	0.5	2500	20000	1025	Wrinkling	* Good data
E	2 Ply Facesheets, H45 Divynicell Foam	0.015	9.20E+06	9.20E+06	0.06	0.5	2610	NA	862	Wrinkling	* Good data

Fig. 2.2 a), b) and c) shows the summary of test results compared to theoretical predictions. The first four test points failed prematurely (concluded to be due to manufacturing defects) and were not included as part of the correlation procedure.

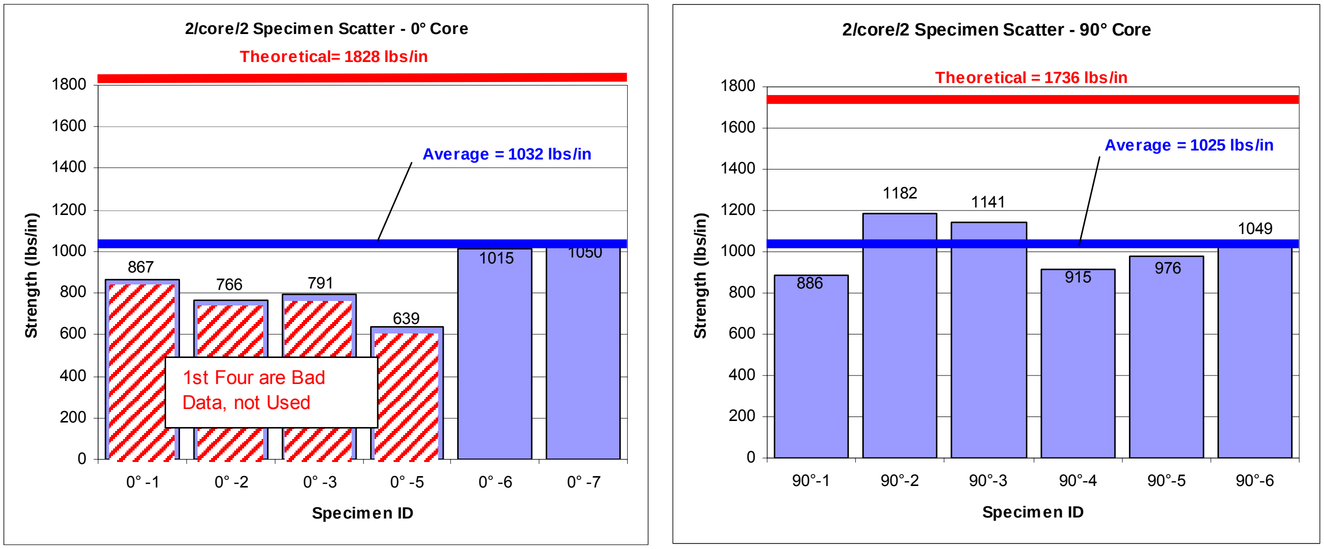

a)

b)

Fig. 2.2, Test results for a) Set A "0° core", and b) Set B "90° core". The red line indicates the theoretical allowable, and the blue line indicates the average test failure load. The average test failure load for Set A does not include the four premature failure test data points.

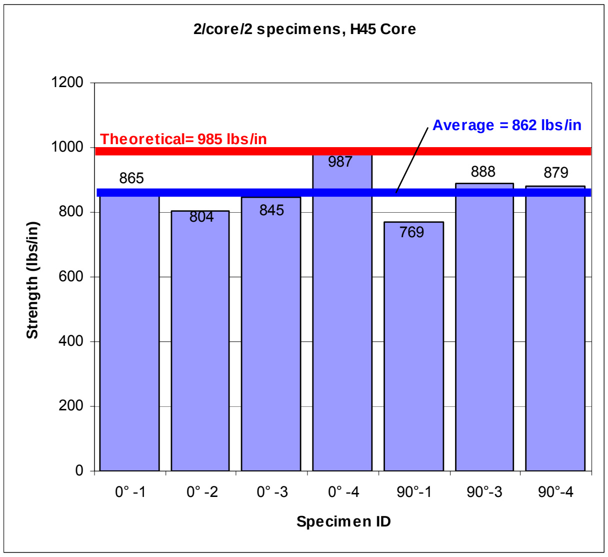

c)

Fig. 2.2c, Test results for c) Set E "Isotropic (Foam) Core" The red line indicates the theoretical allowable, and the blue line indicates the average test failure load. The theoretical and test values are much closer for the isotropic core wrinkling predictions than for the honeycomb core.

2.2.1 Sample Theoretical Calculation

Using the material properties given in Table 2.1 for Sets A and B, and noting that the core is honeycomb, the theoretical wrinkling stress is calculated from Equation 2.1.2,

$$\sigma_{wr} = .82\,(9200\ ksi)\sqrt{\frac{(20\ ksi)\ 0.015}{(9200\ ksi)\,0.5}} = 60.9 ksi$$

The theoretical wrinkling allowable load is the wrinkling stress times the facesheet thickness. For the wrinkling stress in the 90° direction, a 0.95 factor, suggested by Bruhn [2.3], is used to account for the reduction in strength in the perpendicular core direction.

$$Nx_{wr} = (60.9 ksi)(.015 in)(2\text{ faces}) = 1828\ (lb/in) \quad \textit{Theoretical Wrinkling Allowable in X direction}$$

$$Ny_{wr} = (0.95)(1828\ lb/in) = 1737\ (lb/in) \quad \textit{Theoretical Wrinkling Allowable in Y direction}$$

2.3 Test Data Correlation for Honeycomb Sets A and B

The eight 'good' test points from sets A and B are not enough data to be statistically relevant. However, these series of tests were specific to a particular fabrication process and as such do provide useful correlation to a particular design that will be made with these honeycomb panels. For such a use, the following correlation then becomes valuable for assessing reliability.

The correlation equation for sandwich wrinkling (Equation 1.1.3 from Volume 3, shown below in Fig. 2.3) allows for an overall γ_μ that depends on the actual sandwich design by including the *R* term. This parameter depends on the relative ratio of stiffness and core strength with facesheet and core combinations. However, because all of the test points in Sets A and B use the same honeycomb design, there were no variations in *R* that allow us to determine proper correlation factors to make use of this relation. Therefore, we will use a simpler correlation that does not try to account for different sandwich designs, but instead treats all sandwich panels with the same effective ***knockdown***. In this case, μ_3 is set to an arbitrarily high number, say 1,000,000, and μ_1 is determined from the test data.

By averaging the Test Failure Loads from Figs. 2.2a and 2.2b, we calculate the average failure load of the eight tests as 1027 (lb/in). The theoretical average prediction is (2*1828+6*1736)/8 = 1759 (lb/in). The proper knockdown is then the average failure load divided by the average theoretical allowable, or 1027/1759 = .5839. First, if we were to plot the histogram of uncorrelated analysis to test comparisons, we indeed see in Fig. 2.3 both the theoretical ***T*** and predicted ***P*** = 0.5839.

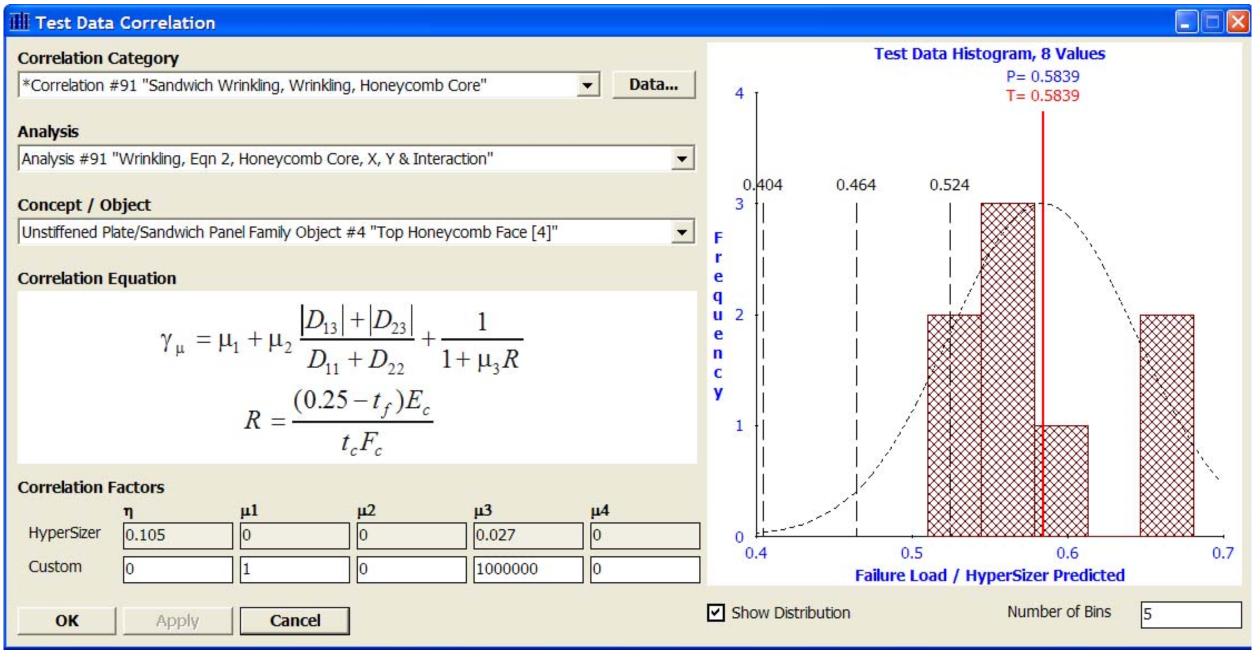

Correlation Category

*Correlation #91 "Sandwich Wrinkling, Wrinkling, Honeycomb Core"

Analysis

Analysis #91 "Wrinkling, Eqn 2, Honeycomb Core, X, Y & Interaction"

Concept / Object

Unstiffened Plate/Sandwich Panel Family Object #4 "Top Honeycomb Face [4]"

Correlation Equation

$$\gamma_\mu = \mu_1 + \mu_2 \frac{|D_{13}| + |D_{23}|}{D_{11} + D_{22}} + \frac{1}{1 + \mu_3 R}$$

$$R = \frac{(0.25 - t_f)E_c}{t_c F_c}$$

Correlation Factors

	η	µ1	µ2	µ3	µ4
HyperSizer	0.105	0	0	0.027	0
Custom	0	1	0	1000000	0

☑ Show Distribution

Number of Bins 5

*Fig. 2.3, **P** and **T** equal the same value because the test data hasn't yet been reanalyzed with the established CFs. Note the dashed curve is the mathematical plot of a normal PDF using the standard deviation of this test data.*

To make use of this correlation, we then would set μ_1 = 0.5839, however, instead of using 0.5839, let's use a value of μ_1 = **0.59** to prevent some of the ratios from becoming unity, which will better illustrate the histogram process with numbers. After doing so, and then rerunning the software, a new histogram is generated that quantifies how well the correlated predicted analysis matches test data.

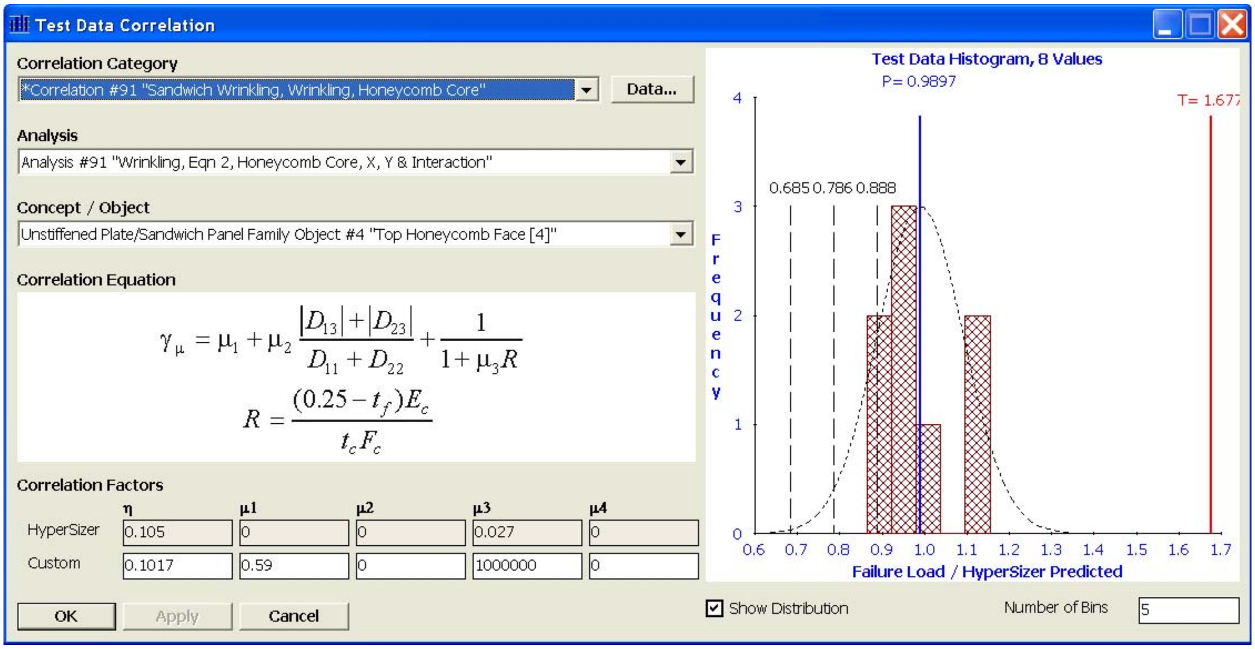

Correlation Category
*Correlation #91 "Sandwich Wrinkling, Wrinkling, Honeycomb Core"

Analysis
Analysis #91 "Wrinkling, Eqn 2, Honeycomb Core, X, Y & Interaction"

Concept / Object
Unstiffened Plate/Sandwich Panel Family Object #4 "Top Honeycomb Face [4]"

Correlation Equation

$$\gamma_{\mu} = \mu_1 + \mu_2 \frac{|D_{13}| + |D_{23}|}{D_{11} + D_{22}} + \frac{1}{1 + \mu_3 R}$$

$$R = \frac{(0.25 - t_f)E_c}{t_c F_c}$$

Correlation Factors

	η	µ1	µ2	µ3	µ4
HyperSizer	0.105	0	0	0.027	0
Custom	0.1017	0.59	0	1000000	0

☑ Show Distribution

Number of Bins 5

Fig. 2.4, ***P*** *and* ***T*** *are now different values because the test data has been reanalyzed with the established CFs displayed in the bottom left boxes.*

μ_1*=(P=0.9897 / T=1.677)=0.59.*

η*=0.9897-0.888 = 0.1017*

Referring to Fig. 2.4 we see at the top of the histogram that **P=0.9897**. This value is a result of the CFs shown in the bottom left. Therefore the predicted average is (1/0.9897) higher than the test failure load average as indicated by the title failure load/HyperSizer predicted on the horizontal axis. Since the average of the eight tests = 1027 (lb/in), the predicted failure load average is equal to 1027/0.9897 = 1037.7 (lb/in). On the histogram graph, the definition of μ_1 = (predicted/theoretical) = **(P=0.9897 / T=1.677) = 0.59**, and as a check with the actual allowables: (predicted/theoretical) = (1037.7/1759) =**0.59**✓.

Again referring to Fig. 2.4, the dashed vertical black lines (moving from left to right) represent 3σ, 2σ, and 1σ. Using these lines, we calculate standard deviation value, σ = 0.9897-0.888 = **0.1017**, and assign this value to η. To determine the allowable for 99.865% reliability, K=3.00 (see the Master Table at the beginning of the document), the resulting average strength allowable is 1037.7*(0.9897 - 3.0*0.1017) = 710.4 (lb/in). As a final check, using the 99.865% reliability numbers from Fig. 2.5, (701.3*6 + 738.2*2)/8= 710.5. So in summary, the **average allowables** are: theoretical 1759 (lb/in), predicted 1038 (lb/in), and for 99.865% reliability 710 (lb/in).

To determine the theoretical, predicted and 99.865% (3σ) allowables for sets A and B individually, 1025 (lb/in) was entered on the HyperSizer FBD load entry tab for each component and the analysis was performed. The allowables are then determined from the following calculations where the underlined numbers are margins-of-safety (MS) computed by HyperSizer.

Set A
Theoretical = 1025*(1 + $\underline{.7831}$) = **1827.7**, a check see above
Predicted = 1025*(1 + $\underline{.05204}$)= **1078.34**, a check 1827.7*.59 = **1078.34**
Reliability 3σ = 1025*(1 $\underline{- .2798}$) = **738.2**, a check 1078.34(0.9897-3*.1017) =**738.2**
Set B
Theoretical = 1025*(1 + $\underline{.694}$) = **1736.3**, a check see above
Predicted = 1025*(1 $\underline{- .00056}$) = **1024.4**, a check 1736.3*.59 = **1024.4**
Reliability 3σ = 1025*(1 $\underline{- .3158}$) = **701.3**, a check 1024.4(0.9897-3*.1017) =**701.3**

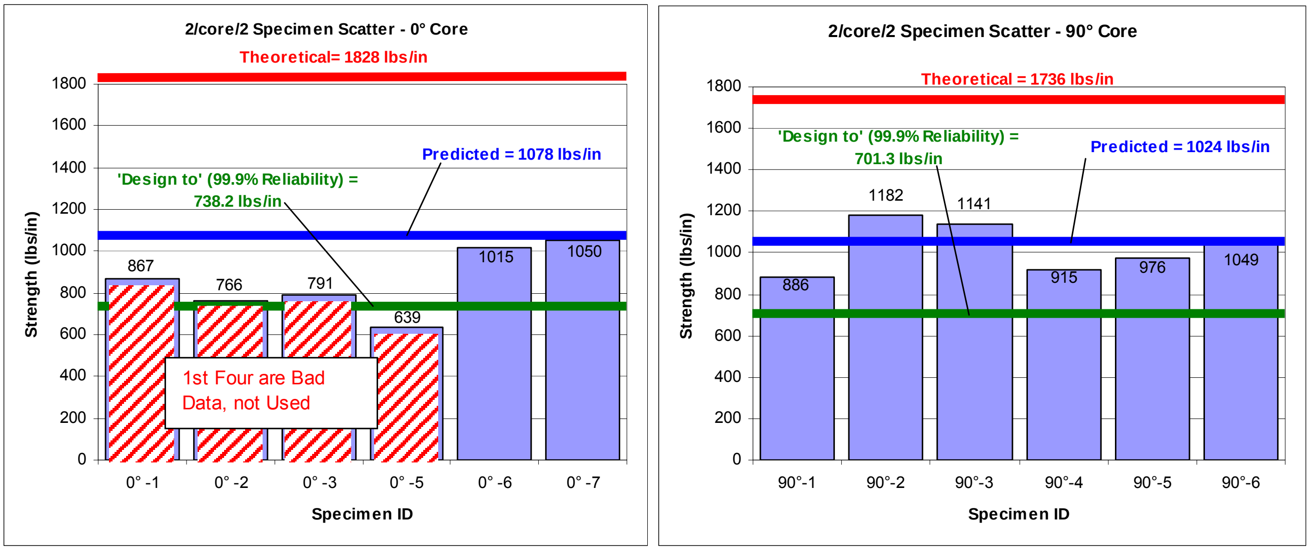

a) b)

Fig. 2.5, Test results for a)Set A "0° core", and b) Set B "90° core". The red line indicates the theoretical allowable. The blue line now indicates the predicted allowable, and the green line the allowable to achieve 99.9% reliability. The distance between the red and green lines give a visual cue for the amount of knockdown required to obtain necessary reliability.

2.4 HyperSizer Setup

Data sets A, B and E were added to the HyperSizer V&V database into the “Honeycomb and Foam Sandwich Wrinkling Test Validation” workspace. The two unique layup/core combinations (Sets A&B, and Set E) were placed into two HyperSizer groups. Within those groups, the cases were divided between two components for 0 degree and 90 degree loading. Therefore, each component represents a single layup/core/loading combination.

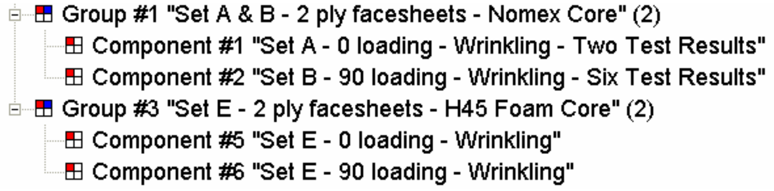

Group #1 "Set A & B - 2 ply facesheets - Nomex Core" (2)
  Component #1 "Set A - 0 loading - Wrinkling - Two Test Results"
  Component #2 "Set B - 90 loading - Wrinkling - Six Test Results"
Group #3 "Set E - 2 ply facesheets - H45 Foam Core" (2)
  Component #5 "Set E - 0 loading - Wrinkling"
  Component #6 "Set E - 90 loading - Wrinkling"

For each component, the average test failure load was entered on the FBD tab as listed in Table 2.1 under the column, “Test Strength”.

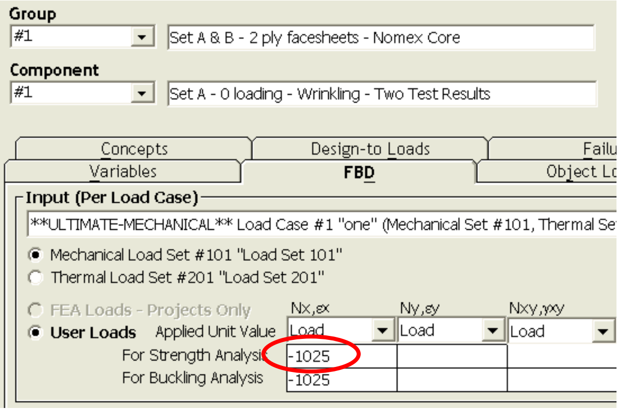

Group: #1 Set A & B - 2 ply facesheets - Nomex Core
Component: #1 Set A - 0 loading - Wrinkling - Two Test Results

Concepts
Design-to Loads
Failu
Variables
FBD
Object Lo

Input (Per Load Case)
ULTIMATE-MECHANICAL Load Case #1 "one" (Mechanical Set #101, Thermal Se

● Mechanical Load Set #101 "Load Set 101"
○ Thermal Load Set #201 "Load Set 201"

○ FEA Loads - Projects Only
● User Loads

	Nx,εx	Ny,εy	Nxy,γxy
Applied Unit Value	Load	Load	Load
For Strength Analysis	-1025		
For Buckling Analysis	-1025		

The individual test points were entered into the HyperSizer database by computing a margin of safety for each test data point,

$$MS = \frac{Test\ Failure\ Load}{Applied\ Load} - 1$$

and entering these margins into HyperSizer’s Project Test Data form. For example, the first 'good' data point in Fig. 2.2a failed at 1015 lb/in. The margin of safety for an applied load of 1025 lb/in. is

$$MS = \frac{1015}{1025} - 1 = -0.00976$$

The test data points are listed as the vertical blue bars in Fig. 2.2 and are also listed in Tables 2.2 and 2.3 under the column, “Test”.

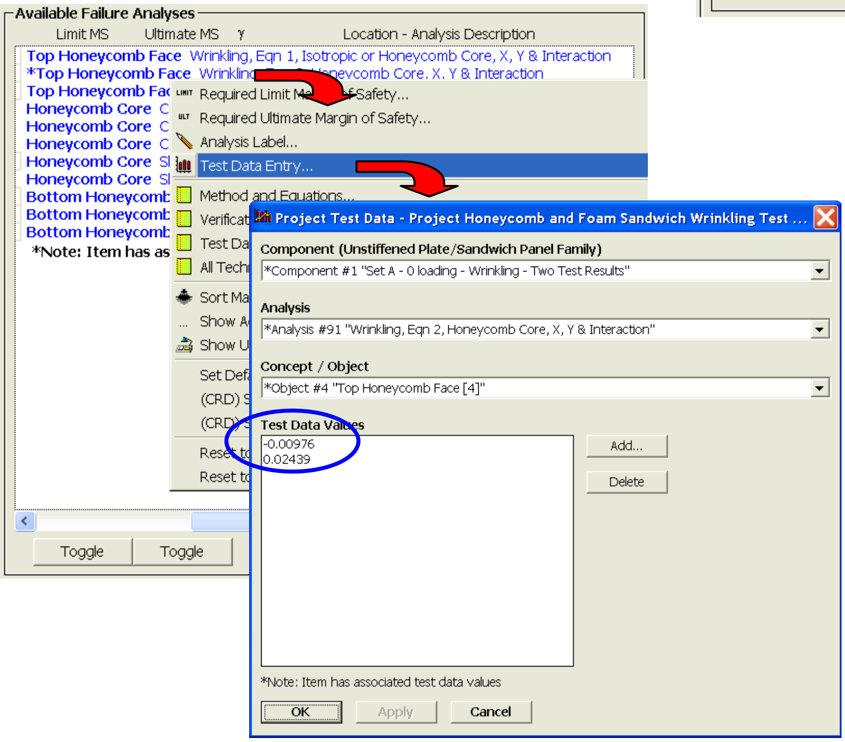

Available Failure Analyses

Limit MS
Ultimate MS
Location - Analysis Description

Top Honeycomb Face Wrinkling, Eqn 1, Isotropic or Honeycomb Core, X, Y & Interaction
*Top Honeycomb Face Wrinkling, Eqn 2, Honeycomb Core, X, Y & Interaction
Top Honeycomb Fac
Honeycomb Core C
Honeycomb Core C
Honeycomb Core C
Honeycomb Core S
Honeycomb Core S
Bottom Honeycomb
Bottom Honeycomb
Bottom Honeycomb
*Note: Item has as

Required Limit Margin of Safety...
Required Ultimate Margin of Safety...
Analysis Label...
Test Data Entry...
Method and Equations...
Verificat
Test Da
All Tech
Sort Ma
Show A
Show U
Set Def
(CRD) S
(CRD) S
Reset to
Reset to
Toggle
Toggle

Project Test Data - Project Honeycomb and Foam Sandwich Wrinkling Test ...

Component (Unstiffened Plate/Sandwich Panel Family): *Component #1 "Set A - 0 loading - Wrinkling - Two Test Results"

Analysis: *Analysis #91 "Wrinkling, Eqn 2, Honeycomb Core, X, Y & Interaction"

Concept / Object: *Object #4 "Top Honeycomb Face [4]"

Test Data Values:
-0.00976
0.02439

*Note: Item has associated test data values

Add...
Delete
OK
Apply
Cancel

2.5 The μ_3 Correlation Factor

As mentioned earlier, the overall correlation factor, γ_μ, allows for a knockdown that depends on the actual design being analyzed. This is accomplished with the R and μ_3 parameters in Equation 1.1.3 from Volume 3 (repeated here).

$$\gamma_\mu = \mu_1 + \mu_2 \frac{|D_{13}| + |D_{23}|}{D_{11} + D_{22}} + \frac{1}{1 + \mu_3 R}$$

$$R = \frac{(0.25 - t_f)E_c}{t_c F_c}$$

Because all of the test panels for which we have failure data are of the same design, the R value is the same for each panel. Therefore not enough information is available for determining appropriate correlation factors for a general honeycomb design. A μ_3 value can be specified that makes this correlation work well for this specific set of test data. However, because R is constant for this data set, this is really the same as specifying a constant value for μ_1.

$$R = \frac{(0.25 - 0.015in)(20000psi)}{(0.5in)(325psi)} = 28.923 \tag{2.5.1}$$

Using this constant value of R, we can find an equivalent μ_3 so that the *third term* in Equation 1.1.3 has the same effect as entering a constant μ_1=0.59.

$$\begin{aligned} \mu_1 &= \frac{1}{1 + \mu_3 R} \\ 0.59 &= \frac{1}{1 + \mu_3 (28.923)} \end{aligned} \tag{2.5.2}$$

Solving Equation (2.5.2) gives $\boldsymbol{\mu_3 = 0.024}$.

Using this value is dangerous, however, because we have no idea how this relation will work for any other designs. In other words, if we tried to use this same CF for other honeycomb designs, we would be ***extrapolating*** the relation outside the bounds from which it was derived.

This was actually mistakenly tested and the consequences of the extrapolation were seen. Equation 1.1.3 with μ_1=0 and μ_3=0.024 was applied to a typical titanium honeycomb panel, and the knockdown that resulted for wrinkling was on the order of 0.1 (that is, the predicted wrinkling load was 10 times less than the theoretical). This is clearly not correct because the correlation was not interpolating within the bounds of the composite honeycomb test data.

If comprehensive test data is available for a particular honeycomb material/fabrication process, then a value of μ_3 can be derived to fit that set of data. **If only limited test data is available, we recommend using a constant value for γ_μ by specifying a value for μ_1 and removing the effect of *R* by setting μ_3 to a very large number.**

2.6Simple Verification of HyperSizer Statistics

2.6.1 Honeycomb Wrinkling Correlation with μ_1 = 0.59; μ_3 = 1,000,000

Table 2.2 lists the test data as entered into an Excel Spreadsheet. Simple statistical analysis is performed to verify the HyperSizer correlations. The Avg and StdDev values are Excel statistically processed values derived from the last column, "Test/Pred". The three black vertical lines in the HyperSizer histogram (Fig. 2.6) represent 1, 2, and 3 standard deviations from the mean value, therefore the HyperSizer calculated value for η = 0.9897–0.888 = 0.1017. The average and standard deviation from the spreadsheet and the HyperSizer histogram agree, verifying the statistical implementation of HyperSizer for this case.

Table 2.2, Test failure loads, theoretical and predicted allowables for Data Sets A and B. The first four test articles in Set A failed prematurely and were not used.

Test Data Points	Case	Test	Test MS	HS Theo	HS Pred	Test / Pred	
Component 1	0°-1	867	-0.1541	1828	1078	0.8040	
2/Nomex/2; 0°	0°-2	766	-0.2527	1828	1078	0.7103	<-- Not included - "bad data - premature failures
	0°-3	791	-0.2283	1828	1078	0.7335	
	0°-5	639	-0.3766	1828	1078	0.5926	
	0°-6	1015	-0.0098	1828	1078	0.9413	
	0°-7	1050	0.0244	1828	1078	0.9737	
Component 2	90°-1	886	-0.1356	1736	1024	0.8649	
2/Nomex/2; 90°	90°-2	1182	0.1532	1736	1024	1.1538	
	90°-3	1141	0.1132	1736	1024	1.1138	
	90°-4	915	-0.1073	1736	1024	0.8932	
	90°-5	976	-0.0478	1736	1024	0.9527	
	90°-6	1049	0.0234	1736	1024	1.0240	
					Avg	0.9897	
					StdDev	0.1017	<-- Eta for honeycomb core

At K=1, Reliability = 84% (≈5/6), therefore we expect one failure out of every six specimens. Out of these 8 specimens, one does fail below the K=1 threshold as shown in yellow.

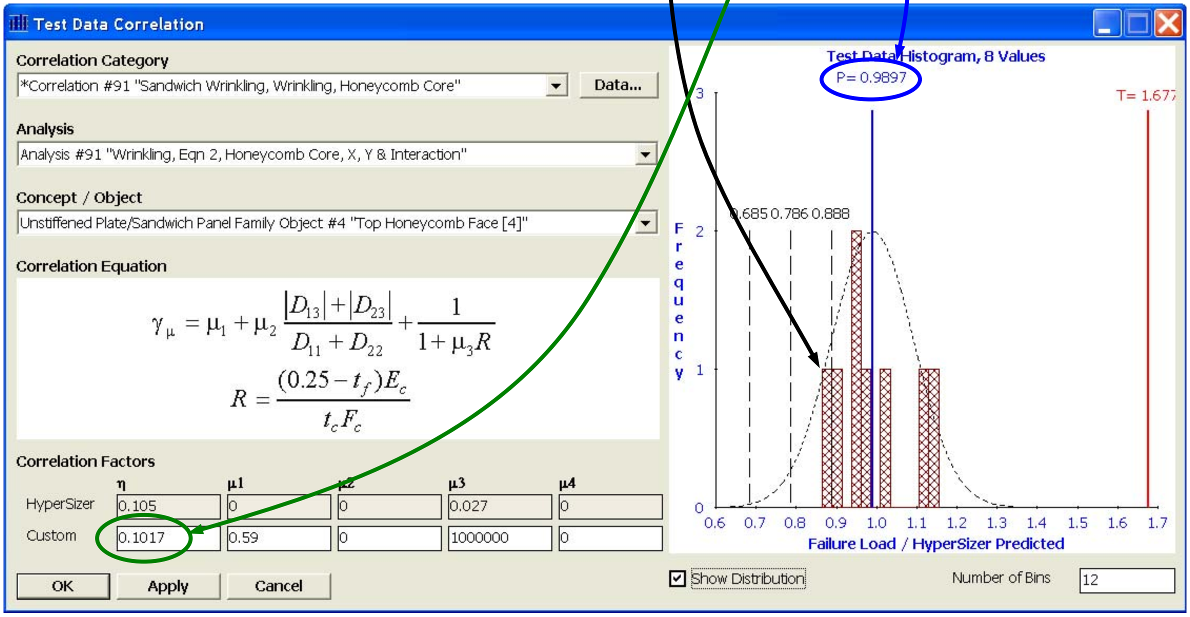

Correlation Category: *Correlation #91 "Sandwich Wrinkling, Wrinkling, Honeycomb Core"

Analysis: Analysis #91 "Wrinkling, Eqn 2, Honeycomb Core, X, Y & Interaction"

Concept / Object: Unstiffened Plate/Sandwich Panel Family Object #4 "Top Honeycomb Face [4]"

Correlation Equation

$$\gamma_{\mu} = \mu_1 + \mu_2 \frac{|D_{13}| + |D_{23}|}{D_{11} + D_{22}} + \frac{1}{1 + \mu_3 R}$$

$$R = \frac{(0.25 - t_f)E_c}{t_c F_c}$$

Correlation Factors

	η	µ1	µ2	µ3	µ4
HyperSizer	0.105	0	0	0.027	0
Custom	0.1017	0.59	0	1000000	0

☑ Show Distribution

Number of Bins: 12

Fig. 2.6, Histogram from the HyperSizer interface showing the eight honeycomb sandwich data points in Sets A and B. One fails below the 1σ (84%) threshold.

2.6.2 Foam Sandwich Wrinkling Correlation with μ_1 = 0.88; μ_3 = 1,000,000

The theoretical predictions for the isotropic (foam) core wrinkling analysis were substantially closer than those for the honeycomb core. Therefore the required correlation knock down was not as severe.

Once again, not enough variation in test data was available to derive a proper value for μ_3, therefore γ_μ is assumed to be constant by setting μ_1=0.88 and μ_3=1,000,000.

As with the spreadsheet and histogram from the honeycomb case, the values calculated from this spreadsheet and HyperSizer histogram once again agree, verifying the HyperSizer calculation.

Table 2.3, Test failure loads, theoretical and predicted allowables for Data Set E.

Test Data Points	Case	Test	Test MS	HS Theo	HS Pred	Test / Pred	
Component 5	0°-1	865	0.0058	985	867	0.9976	
2/H45/2; 0°	0°-2	804	-0.0651	985	867	0.9273	
	0°-3	845	-0.0174	985	867	0.9746	
	0°-4	987	0.1477	985	867	1.1384	
Component 6	90°-1	769	-0.1058	985	867	0.8869	
2/H45/2; 90°	90°-3	888	0.0326	985	867	1.0242	
	90°-4	879	0.0221	985	867	1.0138	
					Avg	0.9947	
					StdDev	0.0800	<- Eta for isotropic core

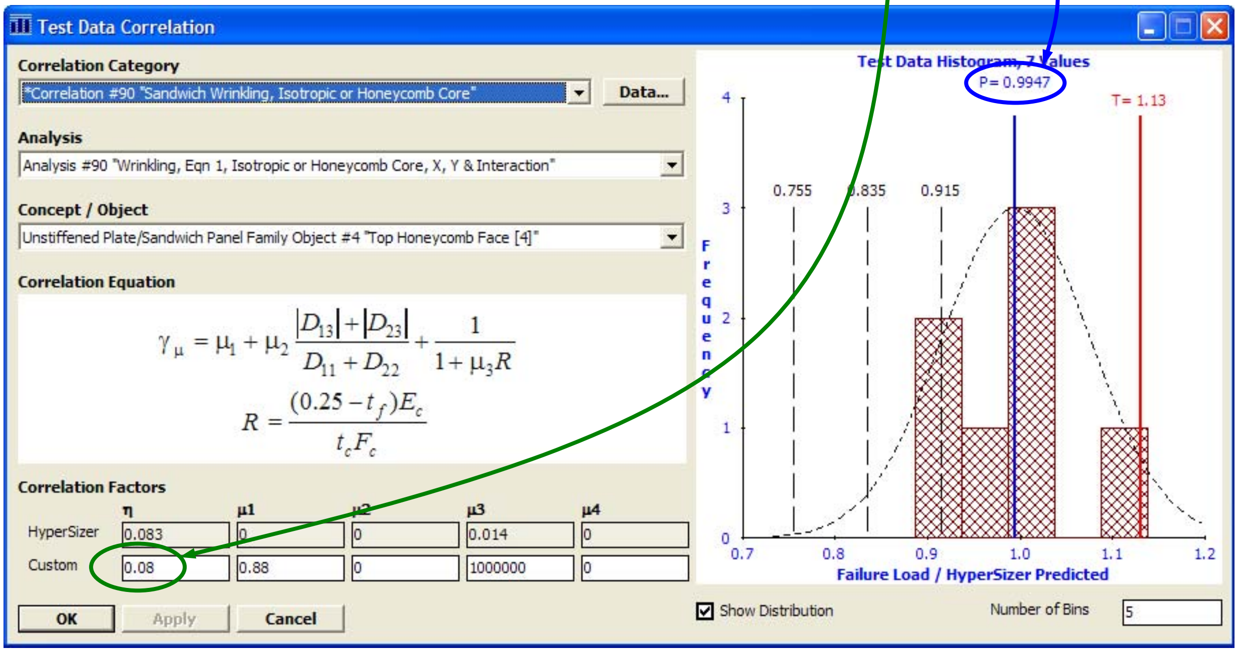

Test Data Correlation

Correlation Category

*Correlation #90 "Sandwich Wrinkling, Isotropic or Honeycomb Core"

Analysis

Analysis #90 "Wrinkling, Eqn 1, Isotropic or Honeycomb Core, X, Y & Interaction"

Concept / Object

Unstiffened Plate/Sandwich Panel Family Object #4 "Top Honeycomb Face [4]"

Correlation Equation

$$\gamma_\mu = \mu_1 + \mu_2 \frac{|D_{13}| + |D_{23}|}{D_{11} + D_{22}} + \frac{1}{1 + \mu_3 R}$$

$$R = \frac{(0.25 - t_f)E_c}{t_c F_c}$$

Correlation Factors

	η	µ1	µ2	µ3	µ4
HyperSizer	0.083	0	0	0.014	0
Custom	0.08	0.88	0	1000000	0

☑ Show Distribution

Number of Bins: 5

Fig. 2.7, Histogram from the HyperSizer interface showing the seven foam sandwich data points in Set E.

2.7References

2.1 Ley, R. P., Lin, W., Mbanefo, U., “Facesheet Wrinkling in Sandwich Structures”, NASA CR-1999-208994, 1999.

2.2 Gutierrez, A.J. and Webber, J.P.H., “Flexural Wrinkling of Honeycomb Sandwich Beams with Laminated Faces,” International Journal of Solids and Structures, Vol. 16, 1980, pp. 645-651.

2.3 Bruhn, E.F., “Analysis & Design of Flight Vehicle Structures”, January 1965, C12.5.3.

2.4 Collier Research Corporation, "Consistent Structural Integrity and Efficient Certification with Analysis", SBIR Final Report, Volumes 1, 2, and 3, August 2004

3 Correlation to Test: Bonded Joint Failure; Delamination, Fiber Fracture

The validations included here involve three different test programs that are used to validate and determine CFs for two of the bonded joint failure methods implemented in HyperSizer. The two failures that are considered are:

a) “Joint, Bonded, **Delamination**, Peel, Longitudinal & Transverse Shear, Axial and Transverse”
b) “Joint, Bonded, **Fracture**, Max Stress 1 direction”

The three test cases used to validate these methods and determine CFs are:

1) Five **stepped bonded doubler joint** specimens built and tested by NASA [3.1] (used for the bonded joint delamination failure mode, a)
2) Six **bonded doubler joint** specimens tested by Cheuk and Tong [3.2] (used for the bonded joint fracture failure mode, b).
3) Three **bonded single lap joint** specimens also tested by Cheuk and Tong [3.3] (used for the bonded joint fracture failure mode, b).

3.1 Theory

For both correlations, the first step is to calculate the stresses throughout the joint using the HyperSizer joint analysis program, which is described in Chapter 6.

For the NASA stepped bonded doubler example, the failure mode chosen for correlation is the one chosen as the controlling failure mode, “Joint, Bonded, Delamination, Peel, Longitudinal & Transverse Shear, Axial and Transverse” (see Equation 6.5.2.9, Section 6.5 for a description of the joint failure methods). This method is a 3D extension of an equation presented by Tong [6.5.10] and predicts delamination failure in the joint when the following interaction relation becomes true,

$$\left(\frac{\sigma_1^2-\sigma_1\sigma_3}{X_tX_c}\right)+\left(\frac{\sigma_2^2-\sigma_2\sigma_3}{Y_tY_c}\right)+\left(\frac{\sigma_3}{Z}\right)^2+\left(\frac{\tau_{23}}{Q}\right)^2+\left(\frac{\tau_{13}}{R_{13}}\right)^2+\left(\frac{\tau_{12}}{R_{12}}\right)^2\geq 1 \tag{3.1.1}$$

where X_t, X_c, are the ply allowables in the fiber direction for tension and compression, Y_t, Y_c are the allowables in the transverse direction, and Q, R_{13}, and R_{12} are allowable shear strengths. In HyperSizer the material labels are: (Q = interlaminar Fsu23, R_{13} = interlaminar Fsu13, and R_{12} = In-plane Fsu12)

For the Cheuk and Tong bonded doubler and single lap joint problems, the failure mode chosen for correlation is “Joint, Bonded, Fracture, Max Stress 1 direction” (See Equation 6.5.2.13) as recommended by Cheuk and Tong [3.2]. Note that no other failure analyses could be performed for this specific test data because no material strength data other than X_t was provided. This method predicts fracture failure when,

$$\frac{\sigma_1}{X_t}\geq 1 \tag{3.1.2}$$

3.2 Test Data Description

Three test validations are used to derive CFs for bonded joint methods. The first test, performed by NASA [3.1] on stepped bonded doubler joints, is used to derive correlation factors for Delamination failure modes. The second and third tests, both by Cheuk and Tong involve test programs featuring a bonded doubler joint [3.2] and a single lap joint [3.3]. Each of these tests is modeled using HyperSizer considering both linear and non-linear models for the joint adhesive layer. These test validations are discussed in detail in Volume 3, Chapters 9, 10, and 11.

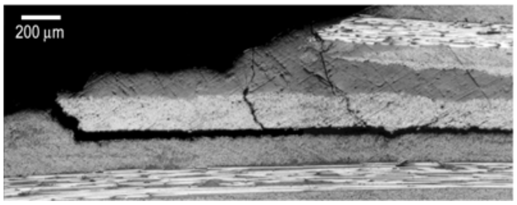

Fig. 3.1, Delamination failure in the NASA stepped bonded doubler example

3.2.1 NASA Stepped Bonded Doubler Tests

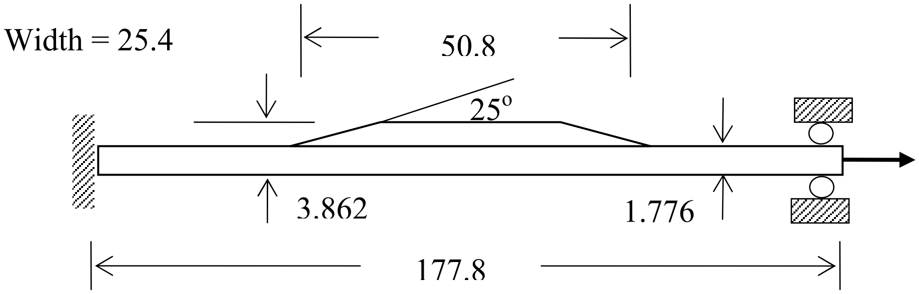

All dimensions in mm

Skin: [45/-45/0/-45/45/90/90/-45/45/0/45/-45] IM7/8552 tape, $t_{ply} = 0.148$
Stiffener: [45/0/45/0/45/0/45/0/45] IM7/8552 plain woven fabric, $t_{ply} = 0.212$
Adhesive: Grade 5 FM300, thickness = 0. 178 mm

Fig. 3.2, Schematics of a skin/flange specimen (bonded doubler) studied by Krueger et al. [3.1]. The specific material stiffnesses and strengths are listed in Volume3, Chapter 10.

Table 3.1, Summary of theoretical failure load vs. experimental result [3.1]

Experiment		HyperSizer Theoretical			
		Linear Adhesive		Nonlinear Adhesive	
Number	Initial Failure Load^2 (kN)	Theoretical Failure Load (kN)	$\frac{Theoretical}{Test}$	Theoretical Failure Load (kN)	$\frac{Theoretical}{Test}$
1	16.2	13.5	0.83	≈ 15.4	0.95
2	16.5	13.5	0.82	≈ 15.4	0.93
3	18.1	13.5	0.75	≈ 15.4	0.85
4	18.3	13.5	0.74	≈ 15.4	0.84
5	19.8	13.5	0.68	≈ 15.4	0.78
Average	17.8	13.5	0.76	≈ 15.4	0.87

3.2.2 Cheuk and Tong Bonded Doubler Joint Tests

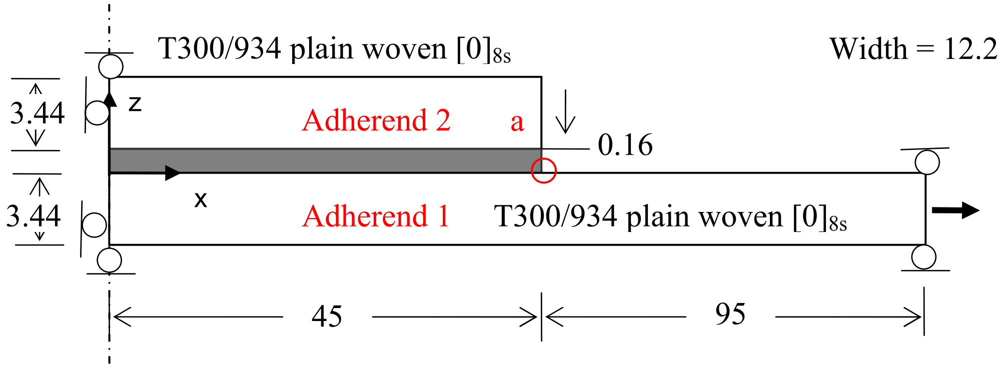
T300/934 plain woven $[0]_{8s}$
Width = 12.2
3.44
z
Adherend 2
a
0.16
3.44
x
Adherend 1
T300/934 plain woven $[0]_{8s}$
45
95

All dimensions in mm.

Fig. 3.3, Schematic of bonded doubler test specimens studied by Cheuk and Tong. The specific material stiffnesses and strengths are listed in Volume 3, Chapter 9 [3.2].

Table 3.2, Individual test data summary for bonded doubler specimens [3.2]**.**

Experiment		HyperSizer Theoretical			
		Linear Adhesive		Nonlinear Adhesive	
Number	Final Failure Load (kN)	Theoretical Failure Load (kN)	*Theoretical* / *Test*	Theoretical Failure Load (kN)	*Theoretical* / *Test*
1	19.162	13.5	0.70	14.4	0.75
2	18.272	13.5	0.74	14.4	0.79
3	17.502	13.5	0.77	14.4	0.83
4	18.987	13.5	0.71	14.4	0.76
5	18.765	13.5	0.72	14.4	0.77
6	19.048	13.5	0.71	14.4	0.76
Average	18.623	13.5	0.73	14.4	0.77

3.2.3 Cheuk and Tong Bonded Single Lap Joint Tests

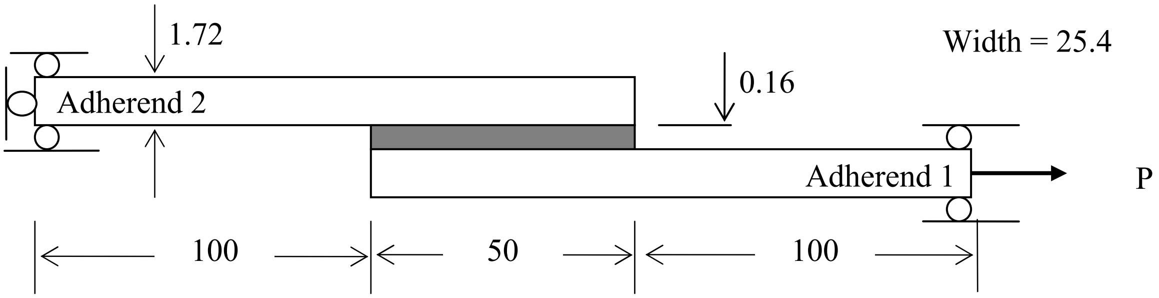
1.72
Width = 25.4
0.16
Adherend 2
Adherend 1
P
100
50
100

All dimensions in mm

Fig. 3.4, Schematic of bonded single lap joint test specimens studied by Cheuk and Tong. The specific material stiffnesses and strengths are listed in Volume 3, Chapter 11.

Table 3.3, Individual test data summary for single lap joint specimens [3.3]

Experiment			HyperSizer Theoretical			
			Linear Adhesive		Nonlinear Adhesive	
Number	Final Failure Load (kN)	Initial Failure Load (kN)	Theoretical Failure Load (kN)	$\frac{Theoretical}{Test}$	Theoretical Failure Load (kN)	$\frac{Theoretical}{Test}$
1	14.374	7.2	6.85	0.95	6.82	0.95
2	14.064	7.2	6.85	0.95	6.82	0.95
3	14.076	7.2	6.85	0.95	6.82	0.95
Average	14.171	7.2	6.85	0.95	6.82	0.95

3.2.4 Sample Theoretical Calculation

This calculation shows the failure load for the Cheuk and Tong bonded doubler joint using the failure mode, "Joint, Bonded, Fracture, Max Stress 1 direction". The authors report the adherend ply strength in the 1 direction as X_t = 518 MPa, and failure is indicated when:

$$\frac{\sigma_1}{X_t} > 1 \tag{3.2.1}$$

To determine the failure load, an arbitrary load of 10 kN (unit load = 819.6 N/mm) was applied to the joint and HyperSizer was executed. The stress calculated in the fiber direction for the surface ply of the facesheet (adjacent to the adhesive) is shown in Fig. 3.5. The peak σ_y stress from that plot is 383.9 MPa. The margin of safety is then calculated as:

$$\begin{aligned} MS &= \frac{X_t}{\sigma_1} - 1.0 \\ &= \frac{518}{383.9} - 1.0 = 0.3493 \end{aligned} \tag{3.2.2}$$

Using this margin of safety, the theoretical failure load is calculated by multiplying the applied load by (1.0 + *MS*).

$P_{failure} = (1.0 + 0.3493)(10kN) = 13.493kN$ *Theoretical Failure Load for Adherend Fracture*

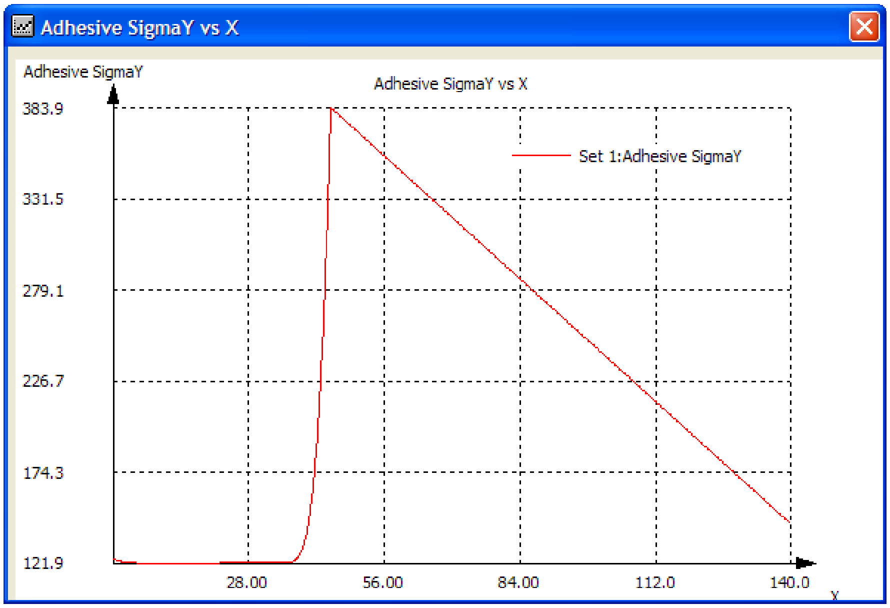

Fig. 3.5, Stress in the facesheet outer ply (adjacent to the adhesive) for the Cheuk and Tong bonded doubler joint example. This stress results from an applied load of 10 kN.

3.3 Test Data Correlation

3.3.1 Correlation Category: Joint, Bonded, Adherend Delamination (Linear)

We calculate the average experimental failure load of the five tests as 17.78 kN (700 N/mm). Because there is only one test configuration, the theoretical average prediction is simply the single theoretical calculated value of 533.4 N/mm. The proper knockdown is then the average failure load divided by the average theoretical allowable, or 700/533.4 = 1.312.

The value of knockdown being greater than 1.0 indicates that instead of knocking down, we will instead be scaling up the theoretical calculation to match test data.

This discussion presents theoretical, predicted and reliability allowable loads for the entire data set and uses these values to illustrate the correlation process. This procedure only works, however, if the theoretical values for all test articles are equal or nearly equal. In the next section, some of the test articles have very different theoretical values and presenting one value for theoretical, predicted, and reliability does not make sense.

If we were to plot the histogram of uncorrelated analysis to test comparisons, we indeed see in Fig. 3.6 both the theoretical ***T*** and predicted ***P*** = 1.312.

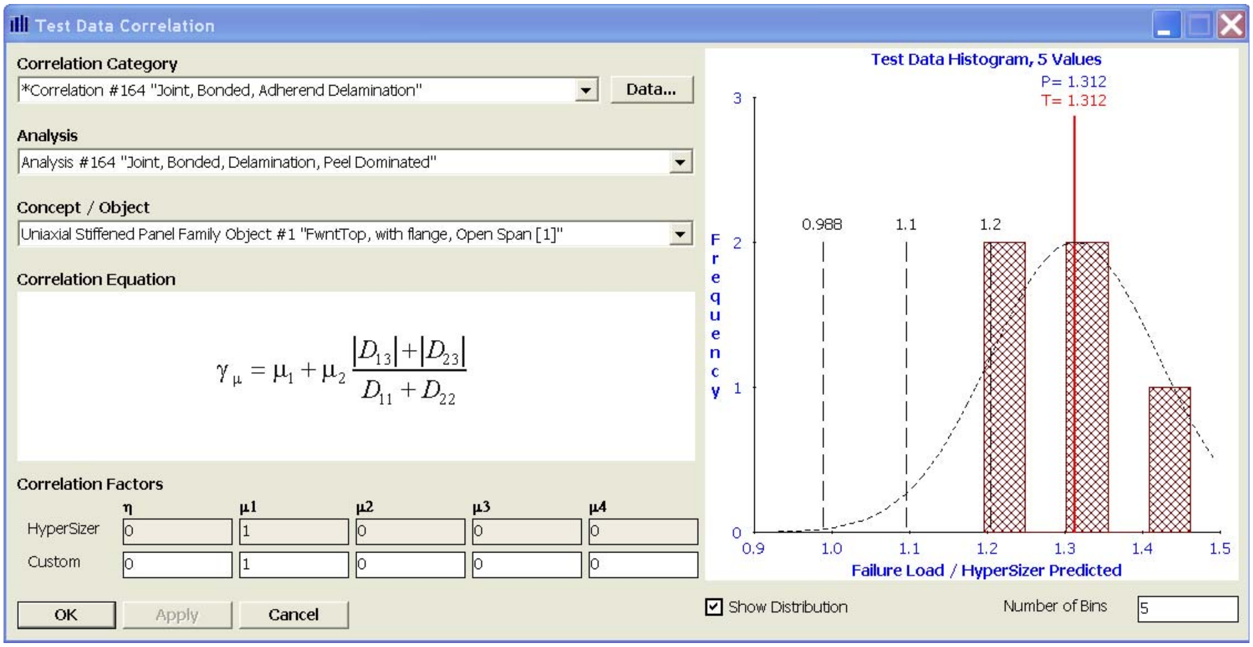

Correlation Category: *Correlation #164 "Joint, Bonded, Adherend Delamination"

Analysis: Analysis #164 "Joint, Bonded, Delamination, Peel Dominated"

Concept / Object: Uniaxial Stiffened Panel Family Object #1 "FwntTop, with flange, Open Span [1]"

Correlation Equation

$$\gamma_{\mu} = \mu_1 + \mu_2 \frac{|D_{13}| + |D_{23}|}{D_{11} + D_{22}}$$

Correlation Factors

	η	µ1	µ2	µ3	µ4
HyperSizer	0	1	0	0	0
Custom	0	1	0	0	0

☑ Show Distribution

Number of Bins: 5

*Fig. 3.6, **P** and **T** equal the same value because the test data hasn't yet been reanalyzed with the established CFs. Note the dashed curve is the mathematical plot of a normal PDF using the standard deviation of this test data.*

To make use of this correlation, we then would set μ_1 = 1.312, however, instead of using 1.312, let's use a value of μ_1 = **1.32** to prevent some of the ratios from becoming unity, which will better illustrate the histogram process with numbers. After doing so, and then rerunning the software, a new histogram is generated, shown in Fig. 3.7, which quantifies how well the correlated predicted analysis matches test data.

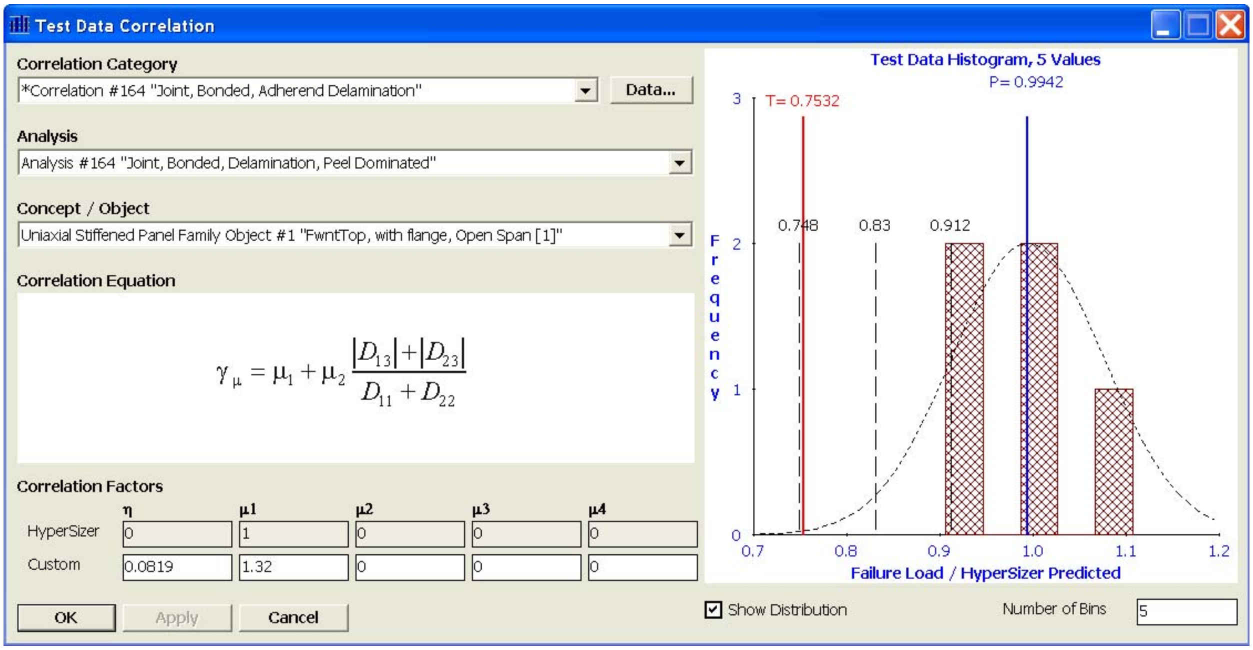

Correlation Category
*Correlation #164 "Joint, Bonded, Adherend Delamination"

Analysis
Analysis #164 "Joint, Bonded, Delamination, Peel Dominated"

Concept / Object
Uniaxial Stiffened Panel Family Object #1 "FwntTop, with flange, Open Span [1]"

Correlation Equation

$$\gamma_{\mu} = \mu_1 + \mu_2 \frac{|D_{13}|+|D_{23}|}{D_{11}+D_{22}}$$

Correlation Factors

	η	μ1	μ2	μ3	μ4
HyperSizer	0	1	0	0	0
Custom	0.0819	1.32	0	0	0

☑ Show Distribution

Number of Bins 5

*Fig. 3.7, **P** and **T** are now different values because the test data has been reanalyzed with the established CFs displayed in the bottom left boxes.*
μ_1=*(P=0.9942 / T=0.7532)=1.32.*
η=*0.9942-0.912 = 0.0822*

Referring to Fig. 3.7 we see at the top of the histogram that **P=0.9942**. This value is a result of the CFs shown in the bottom left. Therefore the predicted average is (1/0.9942) higher than the test failure load average as indicated by the title *failure load/HyperSizer predicted* on the horizontal axis. Since the average of the eight tests = 700 (N/mm), the predicted failure load average is equal to 700/0.9942 = 704.1 (N/mm). On the histogram graph, the definition of μ_1 = (predicted/theoretical) = **(P=0.9942 / T=0.7532) = 1.32**, and as a check with the actual allowables: (predicted/theoretical) = (704.1/533.4) =**1.32**✓.

Again referring to Fig. 3.7, the dashed vertical black lines (moving from left to right) represent 3σ, 2σ, and 1σ. Using these lines, we calculate standard deviation value, σ = 0.9942-0.912 = **0.0822**, and assign this value to η. (By carrying more significant digits, the value of η is actually **0.0819**). To determine the allowable for 99.865% reliability, K=3.00 (see the K vs Reliability Table at the beginning of the Volume 3), the resulting average strength allowable is 704.1*(0.9942 - 3.0*0.0819) = 527 (N/mm).

To determine the theoretical, predicted and 99.865% (3σ) allowables from HyperSizer for this data set, an arbitrary load of 10 kN (=393.7 N/mm) was entered on the HyperSizer FBD load entry tab and the analysis was performed. The allowables were then determined from the following calculations where the underlined numbers are margins-of-safety (MS) computed by HyperSizer.

Theoretical = 393.7 *(1 + .3548) = **533.4**, a check see above
Predicted = 393.7 *(1 + .7883) = **704.1**, a check 533.4*1.32 = **704.1**
Reliability 3σ = 393.7 *(1 + .3386) = **527.0**, a check 704.1*(0.9942 - 3.0*0.0819)=**527**

So in summary, the **average allowables** are: theoretical 533.4 (N/mm), predicted 704.1 (N/mm), and for 99.865% reliability 527 (N/mm).

3.3.2 Correlation Category: Joint, Bonded, Adherend Fracture (Linear)

This second set of test data comes from two completely different test cases with different materials, geometry and loadings. Therefore the explanations made in section 3.3.1 where we compared average failure loads for the entire data set will not make sense in this case. Here we can only work with the failure loads after they have been normalized by either the theoretical or the predicted values. To determine the knockdown, we start with the average of the test divided by theoretical ratio, which is **1.2705**. This is the proper "knockdown" used to arrive at the HyperSizer predicted value. If we plot the histogram of uncorrelated analysis to test comparisons, we see in Fig. 3.8 both the theoretical ***T*** and predicted ***P*** = 1.271 (Note, this value has been truncated to three decimal places, the actual value is 1.2705).

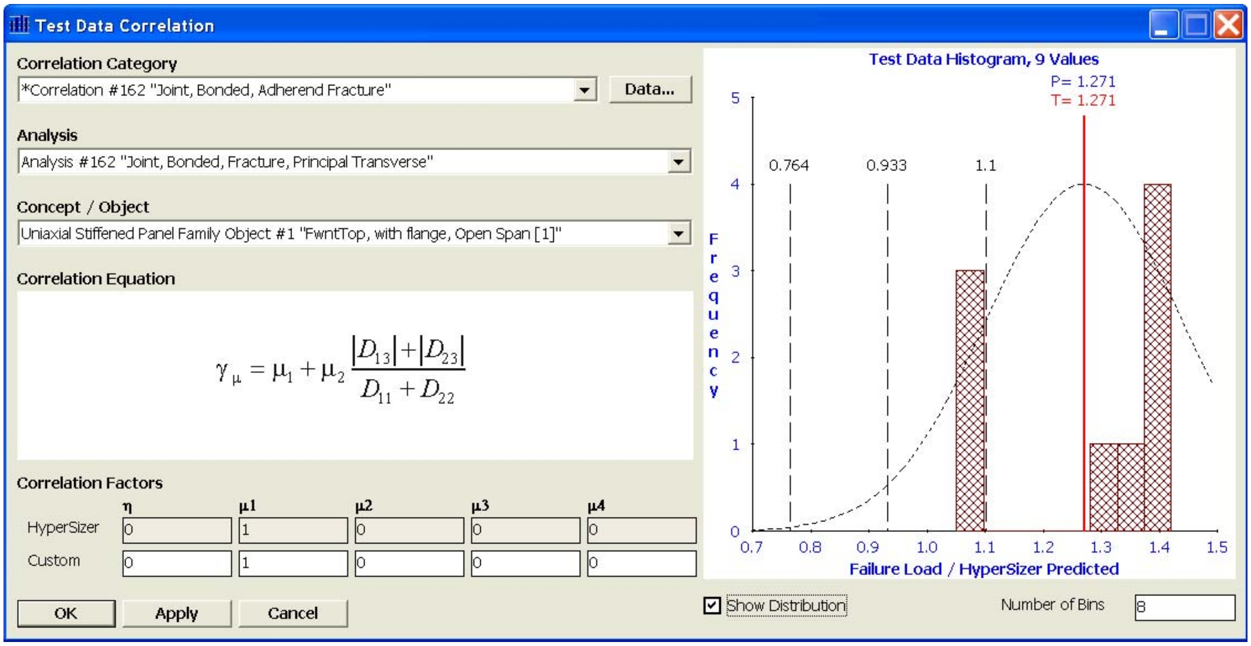

Correlation Category: *Correlation #162 "Joint, Bonded, Adherend Fracture"

Analysis: Analysis #162 "Joint, Bonded, Fracture, Principal Transverse"

Concept / Object: Uniaxial Stiffened Panel Family Object #1 "FwntTop, with flange, Open Span [1]"

Correlation Equation

$$\gamma_{\mu} = \mu_1 + \mu_2 \frac{|D_{13}| + |D_{23}|}{D_{11} + D_{22}}$$

Correlation Factors

	η	μ1	μ2	μ3	μ4
HyperSizer	0	1	0	0	0
Custom	0	1	0	0	0

☑ Show Distribution

Number of Bins: 8

*Fig. 3.8, **P** and **T** equal the same value because the test data hasn't yet been reanalyzed with the established CFs. Note the dashed curve is the mathematical plot of a normal PDF using the standard deviation of this test data.*

To make use of this correlation, we would set μ_1 = 1.2705, however, instead of using 1.2705, let's use a value of μ_1 = **1.28** to prevent some of the ratios from becoming unity, which will better illustrate the histogram process with numbers. After doing so, and then rerunning the software, a new histogram is generated, shown in Fig. 3.9, which quantifies how well the correlated predicted analysis matches test data.

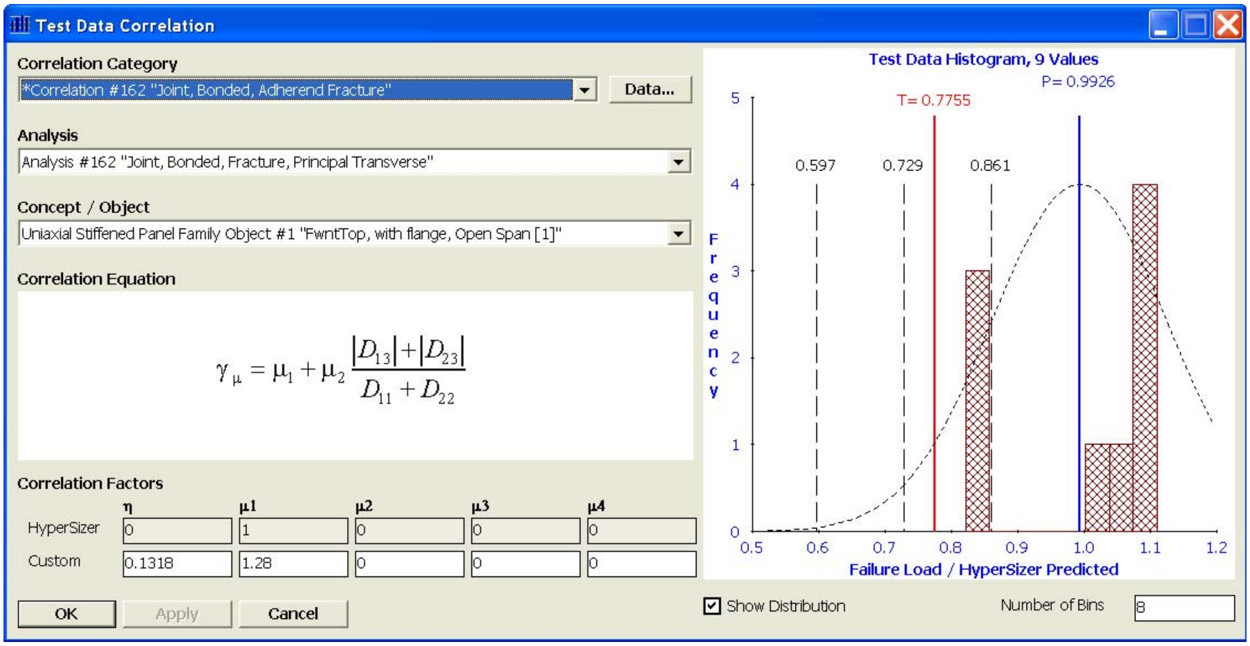

Correlation Category: *Correlation #162 "Joint, Bonded, Adherend Fracture"

Analysis: Analysis #162 "Joint, Bonded, Fracture, Principal Transverse"

Concept / Object: Uniaxial Stiffened Panel Family Object #1 "FwntTop, with flange, Open Span [1]"

Correlation Equation

$$\gamma_{\mu} = \mu_1 + \mu_2 \frac{|D_{13}|+|D_{23}|}{D_{11}+D_{22}}$$

Correlation Factors

	η	μ1	μ2	μ3	μ4
HyperSizer	0	1	0	0	0
Custom	0.1318	1.28	0	0	0

☑ Show Distribution

Number of Bins: 8

Fig. 3.9, ***P*** *and* ***T*** *are now different values because the test data has been reanalyzed with the established CFs displayed in the bottom left boxes.*

μ_1=(P=0.9926 / T=.7755)=1.28.

η=0.9926-0.861 = 0.1316

The predicted failure loads are determined by multiplying the theoretical failure loads by the established knockdown factor of 1.28. The theoretical values are 1106 N/mm and 270 N/mm for the bonded doubler joint and single lap joint tests respectively. This gives predicted values of (1.28)(1106) = 1416 N/mm and (1.28)(270) = 345 N/mm for the two test panels. These values are confirmed by allowing HyperSizer to calculate margins of safety and using these to back out the same predicted failure loads as shown on the following page.

Again referring to Fig. 3.9, the dashed vertical black lines (moving from left to right) represent 3σ, 2σ, and 1σ. Using these lines, we calculate the standard deviation value, σ = 0.9926-0.861 = **0.1316**, and assign this value to η. (By carrying more significant digits, the value of η is actually **0.1318**). To determine the allowable for 99.865% reliability, K=3.00 (see the K vs Reliability Table at the beginning of the Volume 3), the resulting allowable strengths are calculated from, (*predicted*) * ($P - 3\eta$) = 1416*(0.9926 - 3.0*0.1318) = 845 (N/mm) for the bonded doubler joint and 345*(0.9926 - 3.0*0.1318) = 206 (N/mm) for the single lap joint. These numbers also match those calculated by HyperSizer as shown on the following page.

To determine the theoretical, predicted and 99.865% (3σ) allowables from HyperSizer for these two data sets, arbitrary loads of 10 kN (819.7 N/mm) and 5 kN (196.9 N/mm) were entered for the bonded doubler and single lap joint respectively on the HyperSizer FBD load entry tab. The allowables are determined from the following calculations where the underlined numbers are margins-of-safety (MS) computed by HyperSizer.

Bonded Doubler

Theoretical = 819.7 *(1 + .3492) = **1106**,
Predicted = 819.7 *(1 + .7270) = **1416**, a check 1106*1.28 = **1416**✓
Reliability 3σ = 819.7 *(1 + .03137) = **845**, a check 1416*(0.9926 - 3.0*0.1318)=**845**✓

In summary, the **average allowables** are: theoretical 1106 (N/mm), predicted 1416 (N/mm), and for 99.865% reliability 845 (N/mm).

Single Lap

Theoretical = 196.9 *(1 + .3701) = **270**,
Predicted = 196.9 *(1 + .7538) = **345**, a check 270*1.28 = **345**✓
Reliability 3σ = 196.9 *(1 + .04736) = **206**, a check 345*(0.9926 - 3.0*0.1318)=**206**✓

In summary, the **average allowables** are: theoretical 270 (N/mm), predicted 345 (N/mm), and for 99.865% reliability 206 (N/mm).

3.4 References

3.1 Krueger, R., Paris, I. L., O'Brien T. K., and Minguet, P. J., 2001, "Fatigue Life Methodology for Bonded Composite Skin/Stringer Configurations," NASA/TM-2001-210842, ARL-TR-2432.

3.2 Cheuk, P. T. and Tong L., (2002), "Failure of adhesive bonded composite lap shear joints with embedded precrack," *Composites Science and Technology*, 62, 1079-1095.

3.3 Tong, L., (1998), "Failure of adhesive-Bonded Composite Single Lap Joints with Embedded Cracks," AIAA journal, Vol.36, No.3, pp.448.

4 Correlation to Test: Composite Laminate Strength

This chapter will show how validation to test data can be visually inspected using failure envelopes and histograms, and can also be quantified with the HyperSizer Correlation Factors.

4.1 Validation Test Data

Established correlation factors (CFs) for the Tsai-Hahn and LaRC03 failure criteria are reported in this section. For all other failure criteria, refer to Vol 3, Chapters 3 and 4. The data was collected, CF's were quantified, and figures are provided of the resulting histograms to visually see performance of each failure theory. The presented CFs are based on 130 tests of either unidirectional ply or [±θ] laminates.

4.1.1 Source of Test Data

The validation cases included in this chapter are from the World Wide Failure Exercises (WWFE), [4.1], referred to as cases 1 through 7, two additional failure envelope unidirectional cases (cases 8 and 9) from [4.10], and a ± θ layup of AS4/3502 material (case 10) reported by [4.2, 4.3] and described in detail in this section. Table 4.1 summarizes the test cases.

Table 4.1, HyperSizer Failure Test Data Summary. Refer to the contents of Vol 3, Ch 3 & 4

Case	WWFE	Layup	Loading Interaction	Prog. Failure	Material	HyperSizer Workspace
1	✓	Unidirectional [0°]	σ_y-τ_{xy}		E-glass/LY556/HT907	A
2	✓	Unidirectional [0°]	σ_x-τ_{xy}		Gr/Ep T300/BSL914C	A
3	✓	[±85°]	σ_x-σ_y		E-glass/MY750	A
4	✓	[-30/+30/90]s	σ_x-σ_y	✓	E-glass/LY556/HT907	A
5	✓	[-30/+30/90]s	σ_x-τ_{xy}	✓	E-glass/LY556/HT907	A
6	✓	[+55/-55]s	σ_x-σ_y		E-glass/MY750	A
7	✓	[0/-45/+45/90]s	σ_x-σ_y	✓	Gr/Ep AS4/3501-6	A
8		Unidirectional [0°]	σ_y-τ_{xy}		Gr/Ep AS4_55A	B
9		Unidirectional [0°]	σ_y-τ_{xy}		Gr/Ep T800_3900-2	B
10		[±θ]	Loading on [±θ]		Gr/Ep AS4/3502	B

A= WWFE test data, HyperSizer Workspace: World Failure Exercise Composite Failure
B= Non-WWFE test data, HyperSizer Workspace: LaRC03 Workspace

Laminate failure strengths are calculated using ply strengths and ply based failure criteria. The published test data are for final failure instead of initial failure. Initial failure is also referred to as damage initiation and as first-ply-failure. For unidirectional laminates and for [±θ] layups where all plies fail at the same time the first ply fails, initial failure is final failure, as in cases 1, 2, 3, 8, 9, and 10. Some of the invited WWFE contributors developed degradation models or revised their models post test (Part B) to account for progressive failure. HyperSizer will include macro (ply level) and micro (fiber/matrix level) progressive failure in the near future. Shown in Section 7.2.4 are preliminary HyperSizer micromechanics progressive failure predictions that illustrate close comparison to test final failures. For now though, the emphasis is initial first ply failure. As a final point, the composite strengths are for pristine laminates, that is without damage. For an airframe design, damage tolerance and survivability allowables would be established and used as additional limiting strength requirements.

4.1.2 Failure Envelopes

A traditional way of visualizing the strength of a composite laminate is to generate a failure envelope that defines the combination of loadings that cause failure. Fig. 4.1 is a failure envelope of HyperSizer generated allowables. Uni-Directional (UD) material allowable strengths provided by the WWFE are "a given" and provided for uniaxial tension, uniaxial compression, or pure shear. As such, they serve as anchor points that all failure theory pass through, as depicted on the four axes of Fig. 4.1. Differences in failure theories will be observed for biaxial and shear loading interactions. The included failure envelopes are: Max Strain, Max Stress, Tsai-Hill, Tsai-Wu, Tsai-Hahn, Hoffman, Hashin Matrix Cracking, Hashin Fiber Failure, LaRC03 Matrix Cracking, and LaRC03 Fiber Failure. Refer to Chapter 7 for detail on these failure criteria.

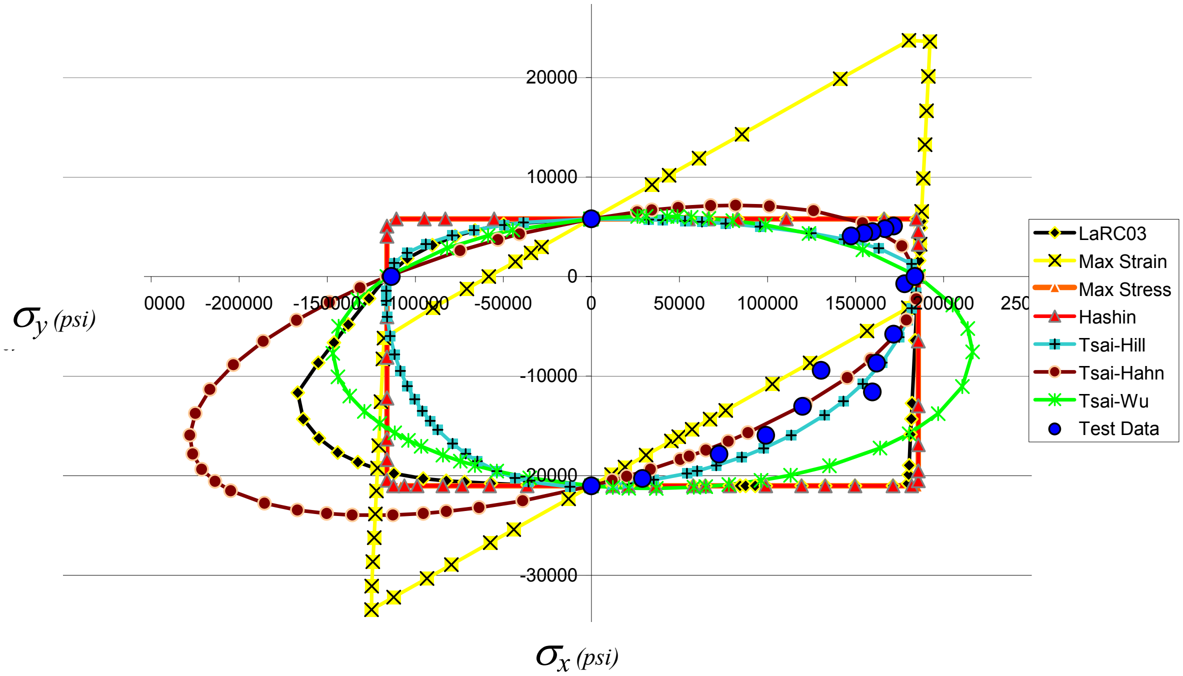

Fig. 4.1, Failure envelopes generated by HyperSizer plotted with superimposed WWFE test data (blue circles) for the case 3 [±85°] *layup from Table 4.1*

As observed in Fig. 4.1, the test data for the loading interactions for this particular laminate only compares well with the Tsai-Hahn failure theory. Other test data may prove to match other failure theories better. The next section describes how to account for failure analysis inaccuracy and to more confidently predict laminate failure for different layups.

4.2 The HyperSizer Correlation Factor (CF) Approach

Each of the failure theories implemented in HyperSizer have been correlated to 130 tests. Before doing the correlation, a fundamental decision was made as to how to correlate.

4.2.1 Choice of correlation: Individual ply properties vs. Failure criteria/material system

The choice of correlating tests to the ply level or laminate level is as fundamental as the choice to perform composite stress analysis on the ply or laminate level. Though HyperSizer can perform the stress analysis on the laminate, ply, and fiber/matrix constituent levels, its primary composite strength predictions are performed on the ply level. Because of this, the choice of correlating analysis inaccuracies and test scatter to individual material ply properties at first seemed like the proper choice. In fact, Mil-Hdbk-17 characterizes the variability of ply data this way and publishes the mean, minimum, maximum, coefficient of variation, and either **A** or **B** basis design values, as described in section 7.2, and shown in Fig. 4.2. Establishing this type of statistical data for composite materials, where each distinct material property has experimentally measured uncertainty established, is likely due to the way metallic materials have historically been characterized in Mil-Hdbk-5.

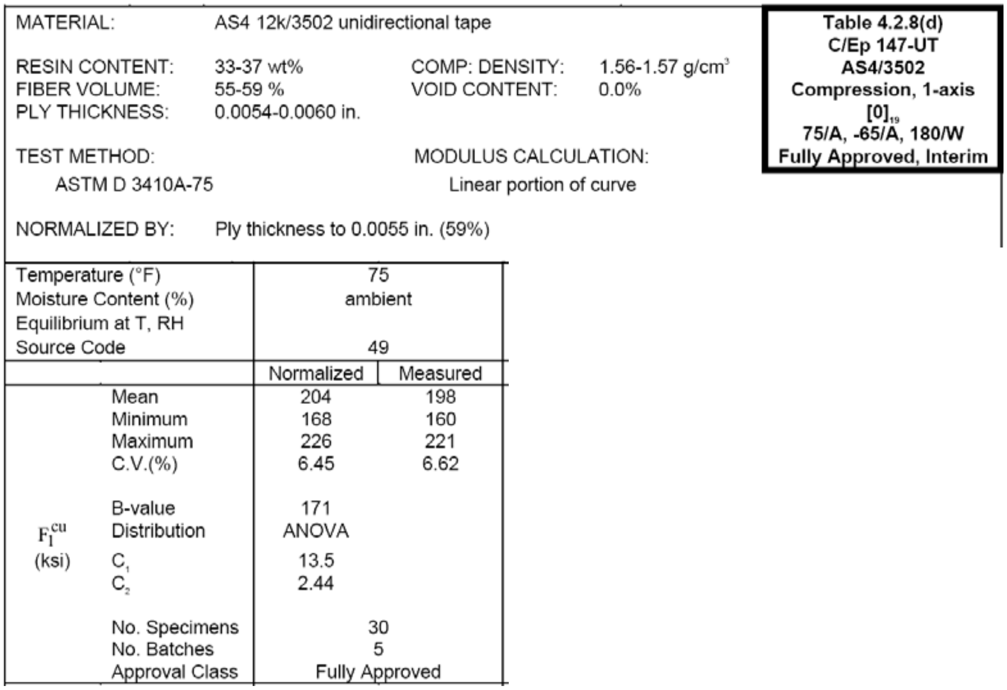

MATERIAL: AS4 12k/3502 unidirectional tape

RESIN CONTENT: 33-37 wt%
FIBER VOLUME: 55-59 %
PLY THICKNESS: 0.0054-0.0060 in.
COMP: DENSITY: 1.56-1.57 g/cm^3
VOID CONTENT: 0.0%

TEST METHOD:
ASTM D 3410A-75

MODULUS CALCULATION:
Linear portion of curve

NORMALIZED BY: Ply thickness to 0.0055 in. (59%)

Table 4.2.8(d)
C/Ep 147-UT
AS4/3502
Compression, 1-axis
$[0]_{19}$
75/A, -65/A, 180/W
Fully Approved, Interim

Temperature (°F)		75	
Moisture Content (%)		ambient	
Equilibrium at T, RH			
Source Code		49	
		Normalized	Measured
F_1^{cu} (ksi)	Mean	204	198
	Minimum	168	160
	Maximum	226	221
	C.V.(%)	6.45	6.62
	B-value	171	
	Distribution	ANOVA	
	C_1	13.5	
	C_2	2.44	
	No. Specimens	30	
	No. Batches	5	
	Approval Class	Fully Approved	

Fig. 4.2, Data sheet from Mil-Hdbk-17.

For isotropic metallic materials, this approach worked well when used with a dependable failure theory, such as von-Mises interaction. Unfortunately, the use of statistically defined allowables on each individual ply property type may not work as well for composites. First, they are at least twice as many unique properties used to characterize composites than metallics. So approaches like running Monte Carlo where each ply property as a data input that has its own probability density function (PDF) would likely get computational expensive. Second, with so many unique properties that are likely coupled in the physical behavior sense, there would be many more interactions to consider such that their individual uncertainties become less significant, and their combined uncertainty more of an impact. Third, there are many failure theories currently used and each one has its own analysis uncertainty. So it doesn't really mean much for composites to use **A** or **B** basis statistical individual properties at the ply level, when where it matters is at the laminate level. Combined with so much variability of so many variables at the ply level, defining uncertainty of laminate strength based on individual ply property uncertainty was decided not appropriate. Instead, **HyperSizer, composite laminate strength uncertainty is defined as a pair: failure theory & ply material system**. In this way, HyperSizer includes the combined effect of the statistical variation of each distinct material property identified in Mil Hndbk 17 such as Ft1, Ft2, Fc1, Fc2, Fsu, etc., and loading and layup variability.

However, establishing each distinct ply level material property scatter is useful in quantifying an expected minimum amount of scatter to expect at the laminate level.

In contrast to composite strength, uncertainty in composite elastic response (stiffness) of the laminate does seem feasible to compute from the individual, statistically characterized ply modulus properties. This is because there are fewer variables and the relative accuracy of calculating laminate stiffness from ply data is well established and consistent using classical lamination theory (CLT).

The next section describes the process for defining correlation factors.

4.3 A simple introductory example: WWFE Case 1 with 19 test data

The World Wide Failure Exercises (WWFE) case 1 of HyperSizer implementation of correlation factors is repeated here from Vol. 1, Ch 9.2.5.

This is an example only. Refer to Vol 3, Chapter 4 for actual CFs defined based on all available test data.

A typical failure envelope for a composite material has four quadrants representing the four possibilities of compression-tension biaxial loading, as illustrated in Fig. 4.1. As a way of introduction, however, we start with Case 1 of the WWFE that only shows two quadrants of the failure envelope - meaning no distinction between positive/negative shear. The calculated failure envelopes generated for that material system and loading is illustrated in Fig. 4.3, along with test data shown as blue circles.

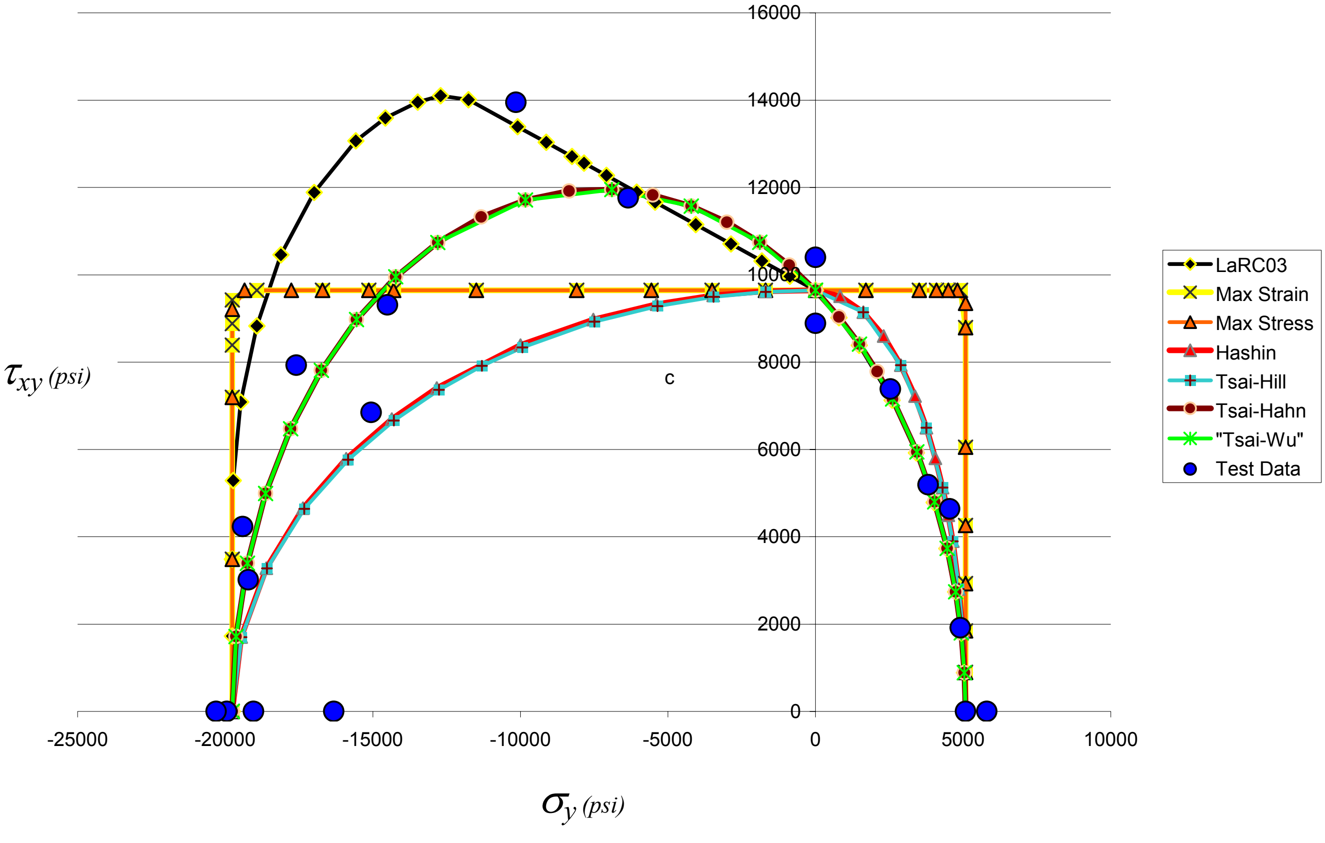

Fig. 4.3, HyperSizer generated failure envelopes for WWFE Case 1, biaxial σ_y-τ_{xy} of 0° ***E-glass/LY556*** *lamina. 19 Test data shown as filled blue circles. These plots use unidirectional strengths based on test results. Units of (psi).*

The discrepancy between the test data and the failure envelopes shows the analysis inaccuracies of many leading composite failure theories. We see that the Max Strain and Max Stress failure theories do not appear to be capturing the measured biaxial loading strength behavior. Both Tsai-Hahn and LaRC03 appear to do quite well, particularly in the first quadrant of tension transverse stress combined with in-plane shear stress. LaRC03 failure theory seems to be tracking well an apparent linear relationship in the compressive/in-plane shear quadrant. However, by doing so, it appears to be overshooting failures that are best captured with Tsai-Hahn interaction criteria. However the one data point not being predicted by Tsai-Hahn is captured by LaRC03.

While some criteria match test data better than others, all failure theories exhibit inaccuracies, as illustrated by their calculated failure envelopes. Even if there was a perfect criterion, there always exists natural scatter in observed strengths. Referring back to Vol 1, Fig. 5.1, as indicated with the blue filled circles, there exists large variations in test measured strengths for pristine laminates. All of the reported test cases of WWFE and those collected by the authors show a great amount of test data scatter in measured strengths. It is for this reason that the CF approach provides significant value to establishing consistent structural integrity and the means to move toward more efficient certification with analysis.

4.3.1 Test data entered, and histograms and PDFs generated

Fig. 4.4 and Fig. 4.5 show histograms for the 19 test values of WWFE Case 1. Three different failure theories are included: Tsai-Hahn, LaRC03, and Max Strain since it is the most frequently used in industry. Tsai-Hahn and LaRC03 show the 19 values in one histogram, where as for Max Strain, two histograms are shown: one for the condition where strain 2 (transverse to the fiber) controls and one for the condition where max strain 12 (in-plane shear) controls. For these combinations of stresses, a matrix cracking criteria controls for LaRC03 in all 19 tests.

4.3.2 Failure theories compared for case 1

The four histograms, displayed side-by-side, give a statistical indication of the relative accuracy of the different failure theories. In general we see that Tsai-Hahn and LaRC03 do considerably better than Max Strain. Also note that **Tsai-Hahn** does exceptionally well for Case 1, as it also did for the entire collection of test data as presented in Vol 3, Ch 3 & 4. Again, its histogram illustrates the ratio of failure load to failure prediction =**1.012** which is very close to 1.0 and its standard deviation is small (1.012-0.933 = **0.079**) meaning the test data is relatively tight without much scatter. Each dashed vertical bar, starting from left to right represents 3σ, 2σ, and 1σ standard deviations. In contrast to the accuracy of Tsai-Hahn, Max Strain is less accurate. For instance, **Max Strain 12** shows a ratio of failure load to failure prediction =**1.072** which is not that bad, however more importantly, its standard deviation is quite large (1.072-0.829 = **0.243**). This will cause this failure theory's theoretical prediction to be heavily knocked down to achieve equal reliability as other failure theories. Finally, since the ratio of failure load to failure prediction, and standard deviation are slightly smaller for Tsai-Hahn, the histograms quantify what is observed in the graphical failure envelopes of Fig. 4.11, and that is it matches test data slightly better than LaRC03.

4.3.3 Two step process for defining correlations factors

After statistically quantifying analysis inaccuracy and scatter in measured tests, the next step is to establish proper CFs for a particular correlation category. The entire process is performed in two steps. The first step is to collect test data and make comparisons directly between theoretical and test data. In-fact, Figs. 4.4 and 4.5 are histograms of this first step. They are untouched theoretical failure predictions against experimentally measured failure loads.

The second step is to define the CFs and then rerun HyperSizer (using the new reliability analysis) for all the components that comprise the 19 test data points. The CFs are established by using the inaccuracy of the theoretical and standard deviation of the test scatter. Using max strain 2 as an example, from Fig. 4.5 we see that T=P=0.9422. The horizontal axis (failure load/HyperSizer predicted) means that HyperSizer is theoretically over predicting failure. We need to knockdown the theoretical by 0.9422. This value is placed into the user input box for μ, Fig. 4.7. The CF η is entered into the user input box as well. η is calculated as:

$$\eta = \frac{\sigma}{\mu} = \frac{(0.9422 - 0.616)}{3}\left(\frac{1}{0.9422}\right) = 0.115$$

Figs. 4.6 and 4.7 are histograms made after the second step. They show us how well HyperSizer is now predicting average failure. After running HyperSizer with the CFs for the 19 tests, the histograms of Figs. 4.6 and 4.7 should show P=1.0, or very close due to round off. A P=1.0 means that we can now predict average failure load. Fig. 4.7 for Max Strain 2 now shows theoretical to be 1.061 higher than the calibrated predicted failure load (T=1.061=1/0.942). Vol 1, Section 9.2.7 shows how HyperSizer makes use of the μ and η CFs.

Since this is one material system, the material characterization and calibration of correlation factors is based on in-situ properties from the tests. One of the more important in-situ data is for the shear allowable, Fsu. These issues are covered in detail in this chapter.

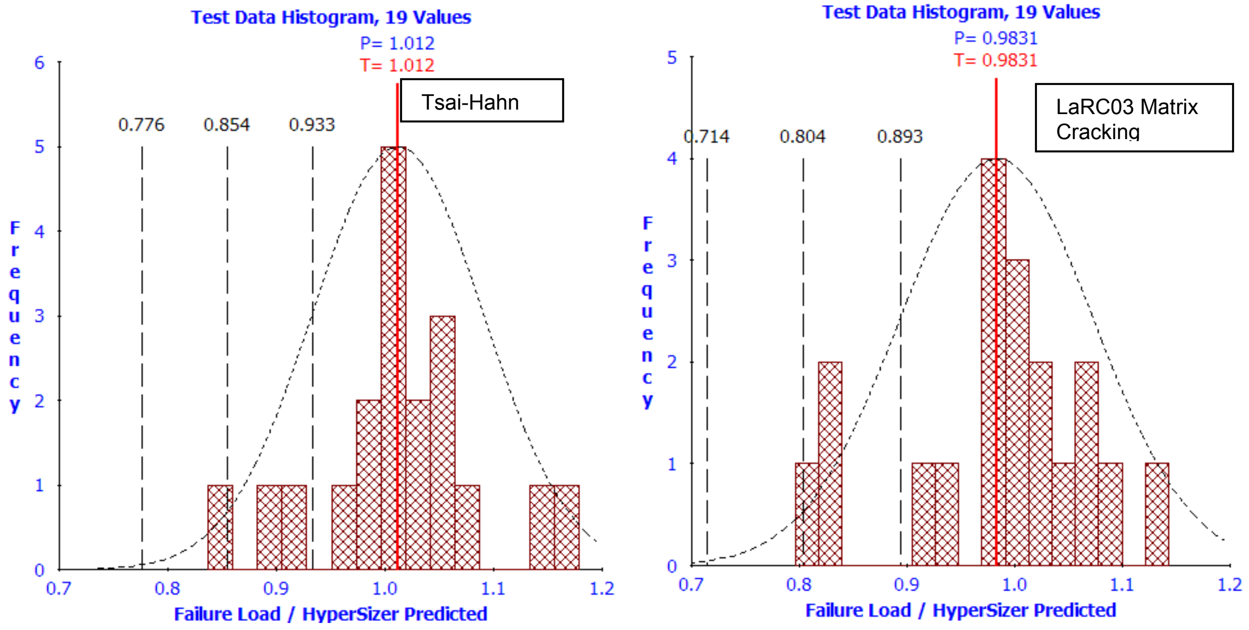

Fig. 4.4, For WWFE Case 1, biaxial σ_y- τ_{xy} failure envelopes of 0° ***E-glass/LY556*** *lamina. Composite Failure Theories: Tsai-Hahn on the left, LaRC03 Matrix Cracking on the right.*

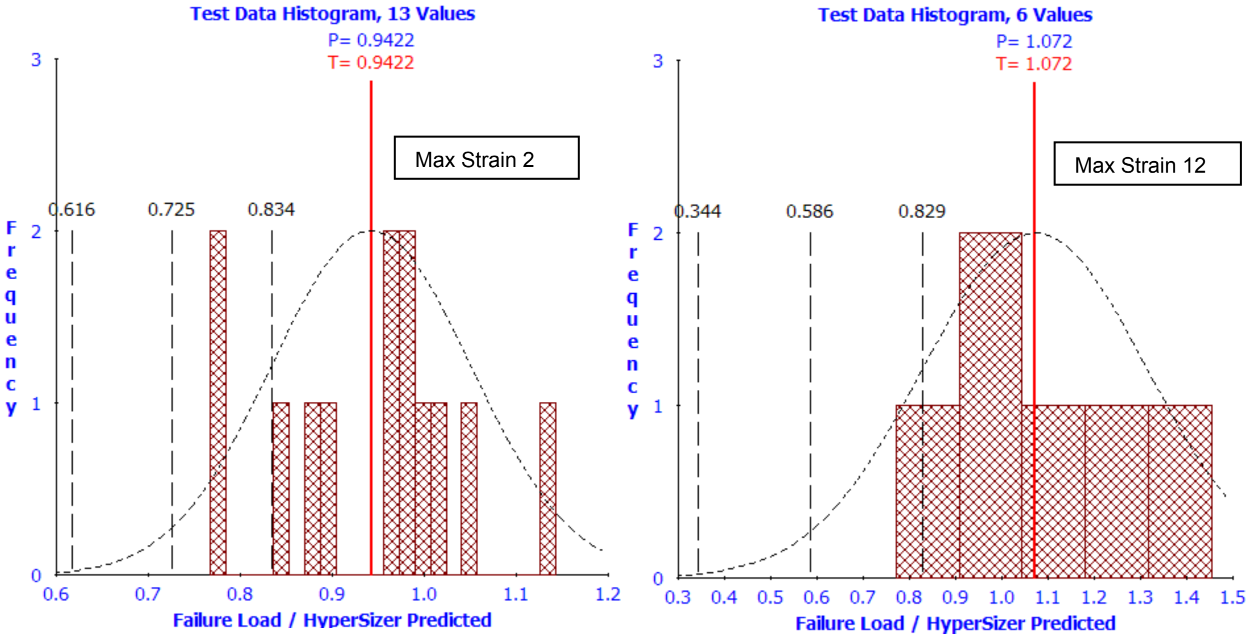

Fig. 4.5, For WWFE Case 1, biaxial σ_y- τ_{xy} failure envelopes.
Max Strain Failure Theory: Max strain 2 direction on the left, Max strain 12 direction on the right.

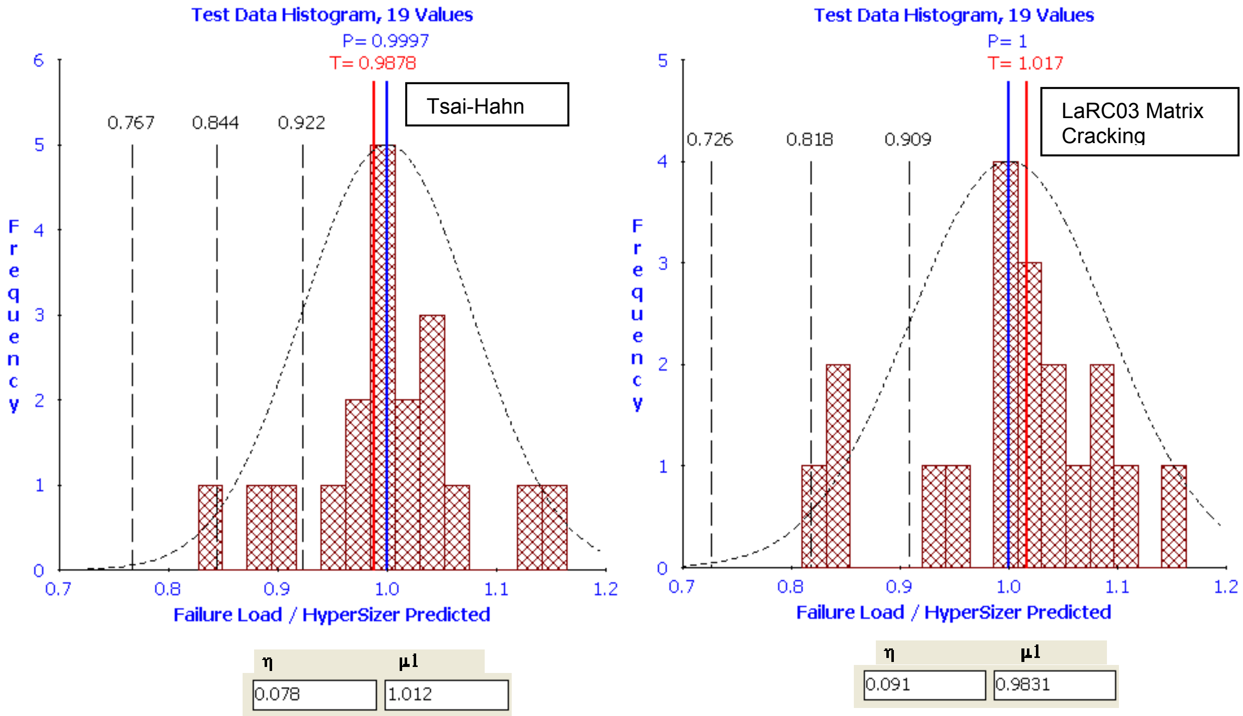

Fig. 4.6, After applying correlation factors for WWFE Case 1, biaxial σ_y-τ_{xy} failure envelopes of 0° ***E-glass/LY556*** *lamina. Tsai-Hahn on the left, LaRC03 Matrix Cracking on the right.*

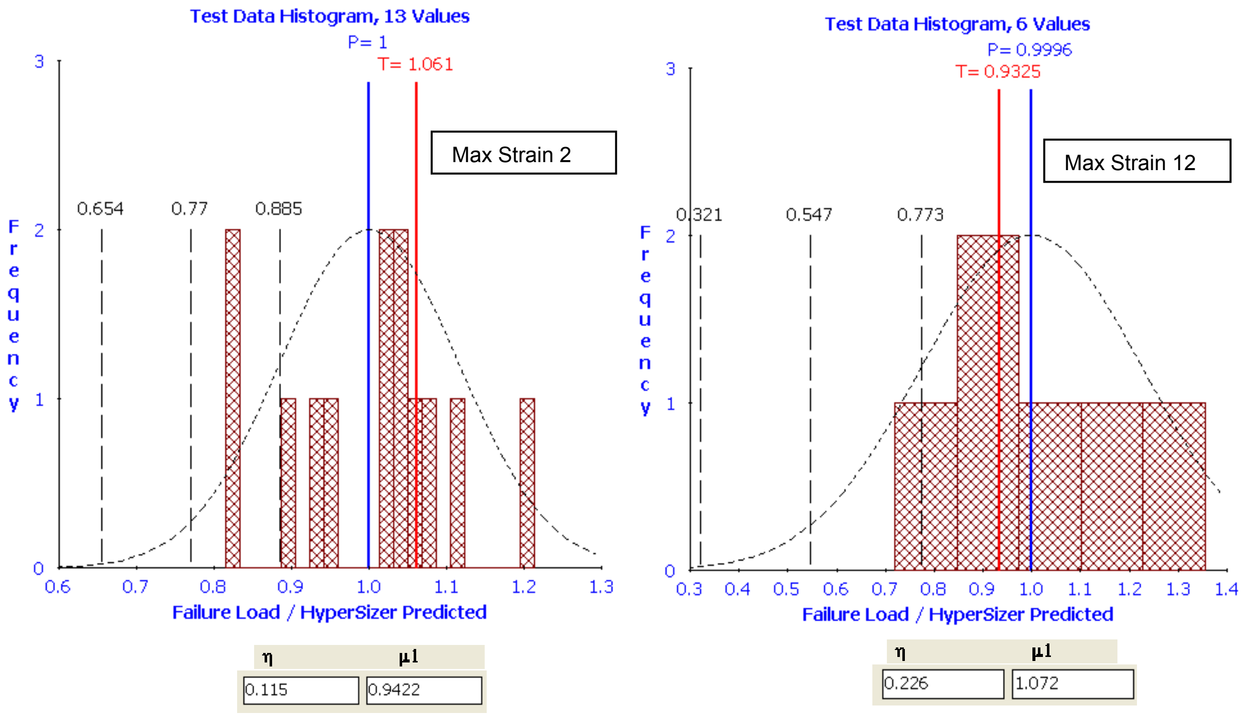

Fig. 4.7, After applying correlation factors for WWFE Case 1, biaxial σ_y-τ_{xy} failure envelopes. Max Strain Failure Theory: Max strain 2 direction on the left, Max strain 12 direction on the right.

4.4 Tsai-Hahn and LaRC03 best overall failure criteria for the 130 tests

For this composite material strength correlation, the Tsai Hahn and LaRC03 failure criteria are chosen to be used as they were deemed most accurate based on comparison to the WWFE and other test data. For both criteria, 130 different tests were collected and made part of the correlation, many from the WWFE.

4.4.1 Theoretical background Larc03

LaRC03 and Hashin criterion are phenomenological based, in that they identify failure as being in the matrix or fiber, which lends itself well to progressive failure techniques. An interaction type failure like Tsai-Wu or Tsai-Hahn, seems not appropriate for progressive failure. For this reason, LaRC03 may prove to be the better failure criteria for a typical laminate that will undergo progressive failure to achieve ultimate loading. LaRC03 has the unique ability to capture the response of an increasing compressive transverse stress which will increase the in-plane shear strength, almost in a straight line, Fig. 4.3, which is observed in some, but not all data. The LaRC03 failure criterion is too voluminous to be repeated here, but is documented in Vol 2, Ch 7.

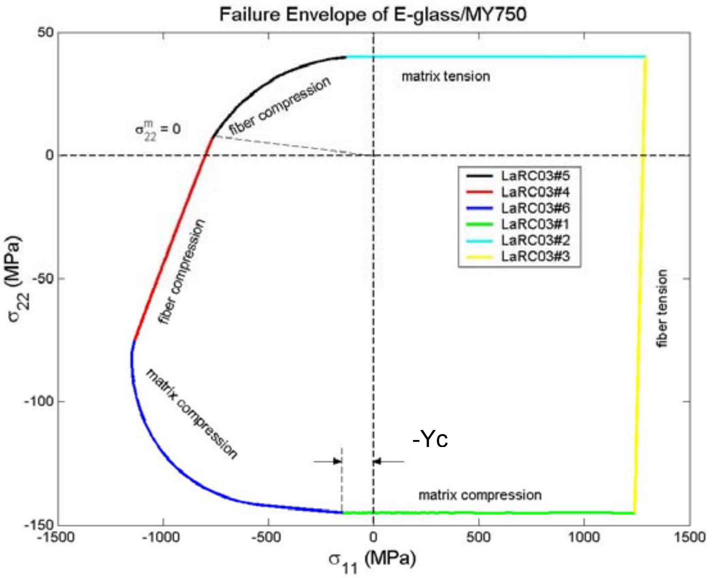

Fig. 4.8, LaRC03 failure criteria distinguishes between six different possible physical failures, and so, unlike interaction criterion such as Tsai-Wu or Tsai-Hahn, is deemed more promising in the long term, especially for progressive failure.

4.4.2 Theoretical background Tsai-Hahn

To describe Tsai-Hahn, we first start with Tsai-Wu. The Tsai-Wu criterion [4.4], unlike directional criteria like max stress or max strain, is based on a single relationship for a biaxial stress field. This criterion predicts failure when,

$$\left(\frac{1}{X_t}-\frac{1}{X_c}\right)\sigma_{11}+\left(\frac{1}{Y_t}-\frac{1}{Y_c}\right)\sigma_{22}+\frac{\sigma_{11}^2}{X_tX_c}+\frac{\sigma_{22}^2}{Y_tY_c}+\frac{\tau_{12}^2}{S^2}+2F_{12}\sigma_{11}\sigma_{22}\geq 1.0 \qquad (4.4.1)$$

where X_t and X_c are the tensile and compressive strengths in the fiber direction, Y_t and Y_c are the tensile and compressive strengths in the transverse direction, and S is the in-plane shear strength. The interaction term, F_{12}, that involves σ_{11} and σ_{22} cannot be determined via a uniaxial ply level test as can the other strengths and typically has relatively a minor effect on the criterion's prediction, for most laminates. Therefore, F_{12} it is often set to zero, as is in done in HyperSizer. A modification to the Tsai-Wu theory was proposed by Tsai and Hahn [4.5], which estimates the F_{12} coefficient as,

$$F_{12} \approx -\frac{1}{2\sqrt{X_t\, X_c\, Y_t\, Y_c}} \tag{4.4.2}$$

The addition of equation (4.4.2) to equation (4.4.1) is referred to as the **Tsai-Hahn** criterion.

4.4.3 Tsai-Hahn correlation to the 130 tests

In Vol. 1, Chapter 8.2 we described the process for inputting test data and displaying it as a histogram using the Tsai-Hahn failure analysis. Here we continue discussion of that process by giving more detail into the source of the data and by showing the final histogram generated after running HyperSizer on all 130 applicable tests with the Tsai-Hahn specific CFs.

Shown in Fig. 4.9 is a histogram generated by HyperSizer that plots the statistical distribution of the 130 test failures normalized by predicted failures. The histogram is used to determine the proper correlation factors (CFs) for a given correlation category: in this case "Composite Strength, Tsai-Hahn." The height of the vertical bars indicates frequency of occurrence and to some degree a normal distribution. More importantly, the histogram illustrates the ratio of failure load to failure prediction is very close to 1.0 for the Tsai-Hahn failure theory. More importantly, the standard deviation is small meaning the data is relatively tight without much scatter.

For the correlation category "Composite Strength, Tsai-Hahn" the correlation factors: η=0.10 and μ_1 = 0.9872 and μ_2 = 0 have been established to best fit the data. From the histogram of Fig. 4.8, the standard deviation, σ = 1.013 - 0.913 ≈ **0.10**. If we were to establish a 99.865% reliability, K=3.00, and the resulting average strength allowable knockdown would equal 1.013(1 - 3.0*0.10) = 0.709 (which due to round-off, is also equal to the left most vertical dashed line which represents the position on the PDF of 3σ. In summary, the theoretical is 1.013, the predicted is 1.000, and a 99.9 % reliability is ≈0.71.

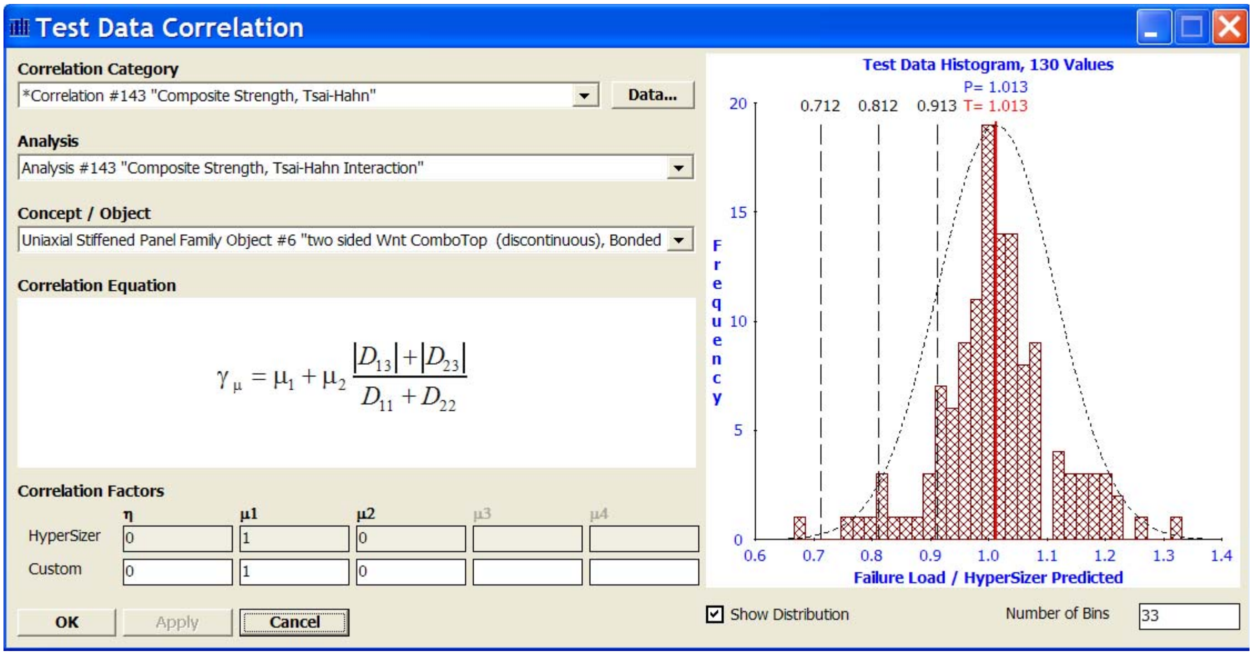
Test Data Correlation
Data...
Test Data Histogram, 130 Values
P= 1.013
T= 1.013
0.712
0.812
0.913
Frequency
0
5
10
15
20
0.6
0.7
0.8
0.9
1.0
1.1
1.2
1.3
1.4
Failure Load / HyperSizer Predicted
OK
Apply
Cancel

Correlation Category
*Correlation #143 "Composite Strength, Tsai-Hahn"

Analysis
Analysis #143 "Composite Strength, Tsai-Hahn Interaction"

Concept / Object
Uniaxial Stiffened Panel Family Object #6 "two sided Wnt ComboTop (discontinuous), Bonded

Correlation Equation

$$\gamma_{\mu} = \mu_1 + \mu_2 \frac{|D_{13}| + |D_{23}|}{D_{11} + D_{22}}$$

Correlation Factors

	η	μ1	μ2	μ3	μ4
HyperSizer	0	1	0		
Custom	0	1	0		

☑ Show Distribution

Number of Bins 33

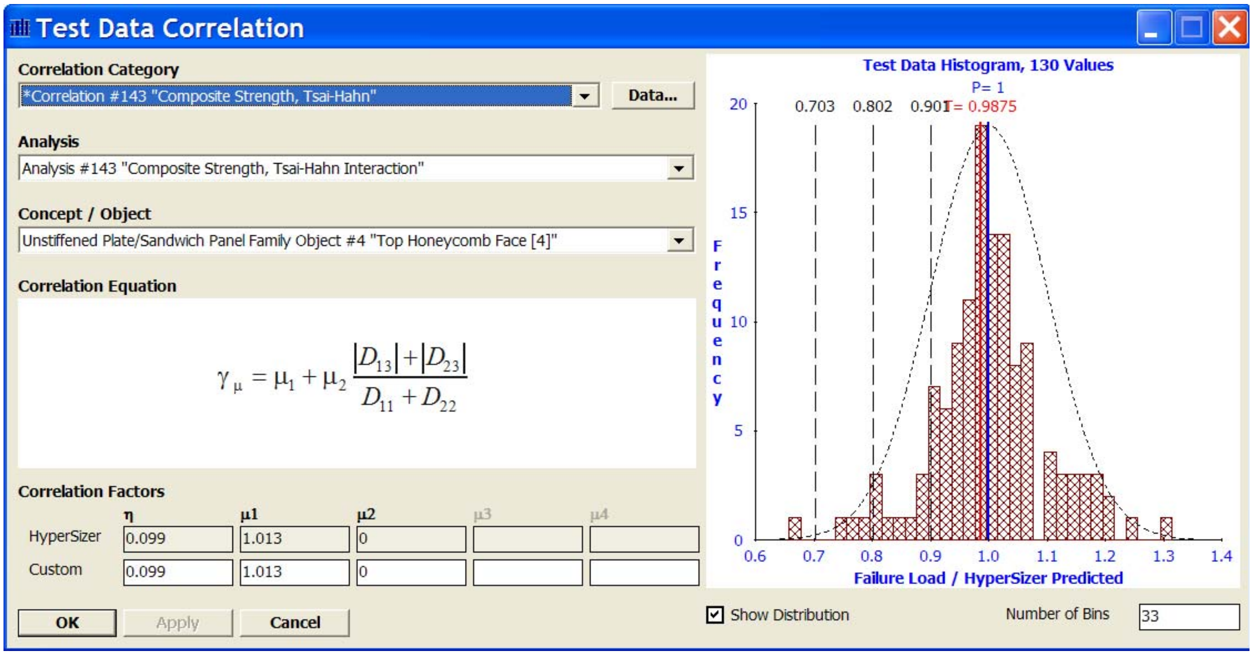
Test Data Correlation
Data...
Test Data Histogram, 130 Values
P= 1
T= 0.9875
0.703
0.802
0.901
Frequency
0
5
10
15
20
0.6
0.7
0.8
0.9
1.0
1.1
1.2
1.3
1.4
Failure Load / HyperSizer Predicted
OK
Apply
Cancel

Correlation Category
*Correlation #143 "Composite Strength, Tsai-Hahn"

Analysis
Analysis #143 "Composite Strength, Tsai-Hahn Interaction"

Concept / Object
Unstiffened Plate/Sandwich Panel Family Object #4 "Top Honeycomb Face [4]"

Correlation Equation

$$\gamma_{\mu} = \mu_1 + \mu_2 \frac{|D_{13}| + |D_{23}|}{D_{11} + D_{22}}$$

Correlation Factors

	η	μ1	μ2	μ3	μ4
HyperSizer	0.099	1.013	0		
Custom	0.099	1.013	0		

☑ Show Distribution

Number of Bins 33

Fig. 4.9, A HyperSizer Composite Strength, Tsai-Hahn histogram plot of 130 test data points. Top image before correlation. These are untouched, theoretical comparisons to tests. Tsai-Hahn theory matches test very well Bottom image after correlation factors applied.

4.4.4 LarC03 correlation to the 130 tests

For the LaRC03 criteria there are two correlation categories: – fiber failure (49 tests) and matrix cracking (81 tests) for a total of 130 test data. To best fit test data, the “Composite Strength, LaRC03 Fiber Failure” has correlation factors: **η=0.1107 and μ_1 = 0.9388**. “Composite Strength, LaRC03 Matrix Cracking” has CFs: **η=0.157 and μ_1 = 1.001.** These values and the resulting histograms are shown in Fig. 4.10 and 4.11. Even though the theoretical values for matrix cracking are nearly equal to average test values (which is good), the shortcoming is the relatively large scatter noted with η=0.157. This will cause the matrix cracking failure mode to be heavily penalized to reach the same reliability as the other failure criteria.

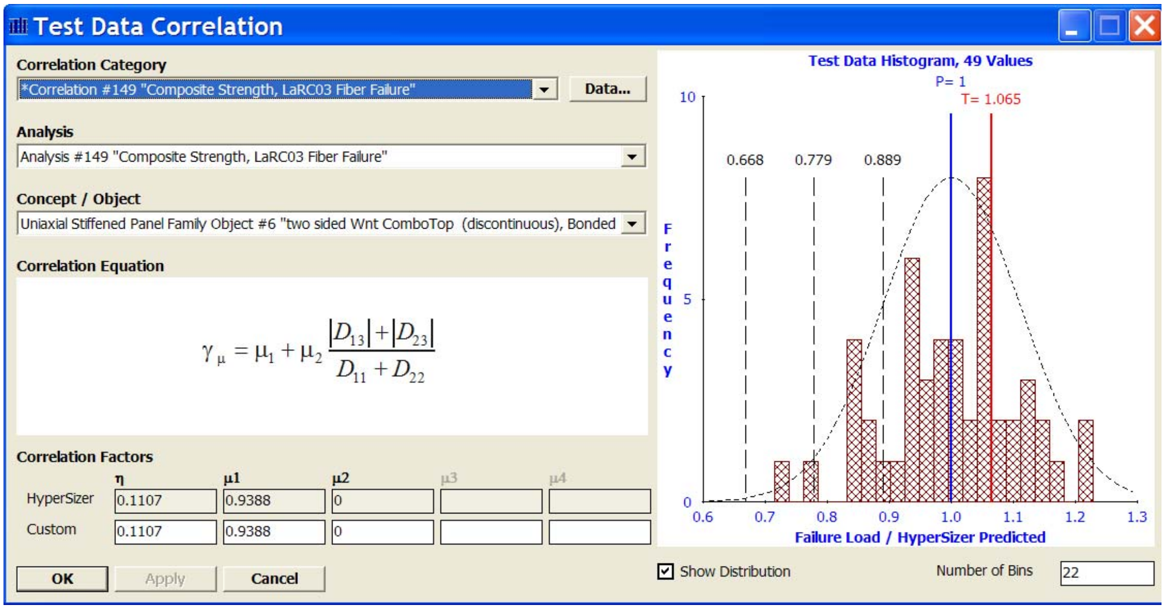
Test Data Correlation
Data...
OK
Apply
Cancel
Test Data Histogram, 49 Values
P= 1
T= 1.065
0.668
0.779
0.889
Frequency
0
5
10
0.6
0.7
0.8
0.9
1.0
1.1
1.2
1.3
Failure Load / HyperSizer Predicted

Correlation Category: *Correlation #149 "Composite Strength, LaRC03 Fiber Failure"

Analysis: Analysis #149 "Composite Strength, LaRC03 Fiber Failure"

Concept / Object: Uniaxial Stiffened Panel Family Object #6 "two sided Wnt ComboTop (discontinuous), Bonded

Correlation Equation

$$\gamma_\mu = \mu_1 + \mu_2 \frac{|D_{13}| + |D_{23}|}{D_{11} + D_{22}}$$

Correlation Factors

	η	µ1	µ2	µ3	µ4
HyperSizer	0.1107	0.9388	0		
Custom	0.1107	0.9388	0		

☑ Show Distribution

Number of Bins: 22

Fig. 4.10, Composite Strength, LaRC03 Fiber Failure after correlation.

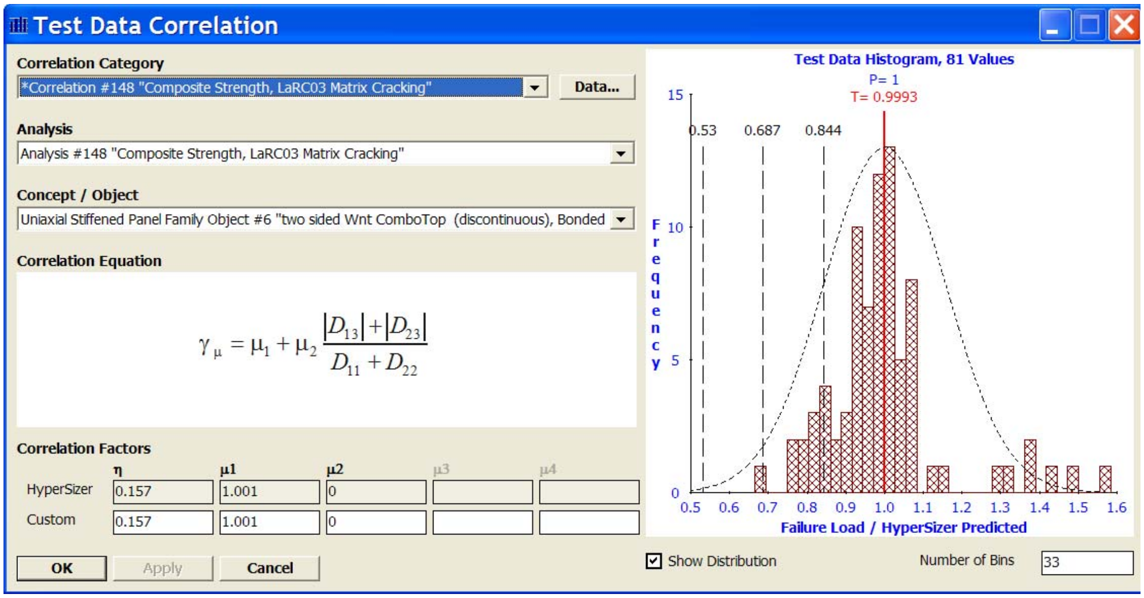
Test Data Correlation
Data...
OK
Apply
Cancel
Test Data Histogram, 81 Values
P= 1
T= 0.9993
0.53
0.687
0.844
Frequency
0
5
10
15
0.5
0.6
0.7
0.8
0.9
1.0
1.1
1.2
1.3
1.4
1.5
1.6
Failure Load / HyperSizer Predicted

Correlation Category: *Correlation #148 "Composite Strength, LaRC03 Matrix Cracking"

Analysis: Analysis #148 "Composite Strength, LaRC03 Matrix Cracking"

Concept / Object: Uniaxial Stiffened Panel Family Object #6 "two sided Wnt ComboTop (discontinuous), Bonded

Correlation Equation

$$\gamma_\mu = \mu_1 + \mu_2 \frac{|D_{13}| + |D_{23}|}{D_{11} + D_{22}}$$

Correlation Factors

	η	µ1	µ2	µ3	µ4
HyperSizer	0.157	1.001	0		
Custom	0.157	1.001	0		

☑ Show Distribution

Number of Bins: 33

Fig. 4.11, Composite Strength, LaRC03 Matrix Cracking after correlation.

4.5 Summary of each failure theory's CFs

Table 4.2 lists CFs for all composite laminate failure criteria. By inspection of the table, and each individual histogram of Vol 3, Ch 4, there are a few observations that can be made.

- Tsai-Hahn failure theory best predicts failure of the 130 measured tests. It has the lowest η correlation factor and one of the closest μ_1 to 1.0
- Of the two physically based failure theories, LaRC03 did substantially better than Hashin. For LARC03, all results are within 2 sigma for fiber failure, and within 3 sigma for matrix failure
- Max strain and Max stress did quite poorly. Hashin fiber failure and Max Strain 2 direction did very poorly.

Table 4.2, Summary of HyperSizer CFs for Composite Failure Theories Based on 130 Different Tests.

(*Note: The closer μ_1 is to 1.0 the more accurate the theory. The lower η is, the more reliable the theory.)*

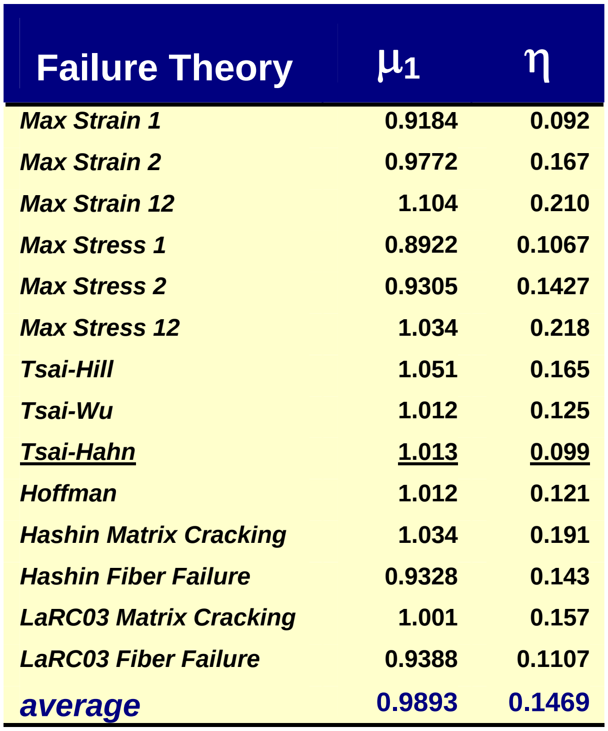

Failure Theory	μ_1	η
Max Strain 1	0.9184	0.092
Max Strain 2	0.9772	0.167
Max Strain 12	1.104	0.210
Max Stress 1	0.8922	0.1067
Max Stress 2	0.9305	0.1427
Max Stress 12	1.034	0.218
Tsai-Hill	1.051	0.165
Tsai-Wu	1.012	0.125
Tsai-Hahn	1.013	0.099
Hoffman	1.012	0.121
Hashin Matrix Cracking	1.034	0.191
Hashin Fiber Failure	0.9328	0.143
LaRC03 Matrix Cracking	1.001	0.157
LaRC03 Fiber Failure	0.9388	0.1107
average	0.9893	0.1469

At first it is surprising to see the relative inaccuracy of the fiber strength prediction for Max strain, Max stress, Hashin, and LaRC03 is on average 10% over predicting measured strengths. However, part of the data included in the correlation category for fiber strength includes those loads that are not pure axial. For instance some loads that are primarily axial with a small component of transverse or in-plane shear load could still cause this failure mode to be flagged as critical, and yet large enough to diminish its accuracy as pure axial criteria.

4.6 In-situ effects of a ± *θ* layup of a specific material system

This section describes case 10 and provides a detailed study of a specific Gr/Ep material system (AS4/3502) and its ± θ layup in-situ effects on correlation. In the previous sections, correlation factors were identified for the complete set of 130 test data that includes many different material systems. In this section we look in detail at in-situ material data properties and their effect on derived correlation factors of a specific material system, and resulting refinement to CFs.

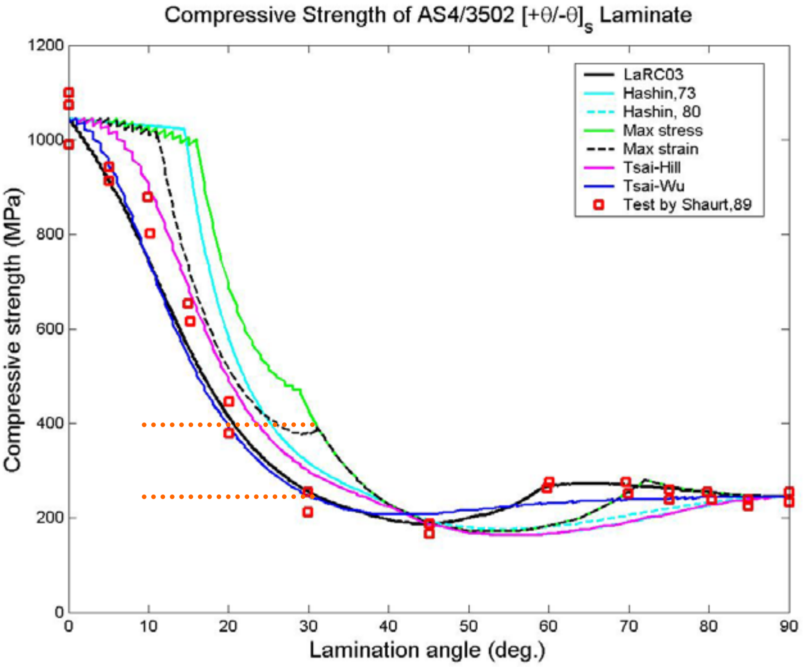

Fig. 4.12, Compressive strength of [+/-θ]s AS4/3502 predicted by different failure theories. For the 0, 90, and 45 angles, the criteria pass through the test data since these angles are test data given anchor points. At different angles the predictions vary. As an example of error, the orange horizontal lines indicate the large difference in test and prediction at 30° for max strain. In this plot LaRC03 matches best.

Fig. 4.12 plots the comparison of failure loads for a cross-ply laminate generated by max strain, max stress, Hashin’73, Hashin’80, Tsai-Hill, Tsai-Wu and LaRC03 failure criteria for AS4/3502 as a function of ± θ layup. It shows that Tsai-Wu and Tsai-Hill match experimental data well for ply angles below 45° and that LaRC03 matches experimental data well for all angle degrees because it is using in-situ material properties. During the maturing stages of a design, as discussed in section 7.1, if the cost is acceptable based on criticality of a part and the volume of an end product, then the recommendation is to define specific CF’s for a material system, that includes a customer’s fabrication and processing (material and processing MP) in-situ effects.

Fig. 4.12 is shown again as Fig. 4.13 with only LaRC03 failure theory that uses different in-situ Fsu allowables. In essence, the effects of off axis loading on a unidirectional tape material of single ply, or [±θ] laminate are correlated. Note, that the anchor points for failure criteria are the 0, 90, and 45 ply orientations. So at these angles the material allowable strengths are “a given”, hence a specific M&P starting point, and all failure criteria pass through these points as seen in both Fig. 4.12 and 4.13, except the LaRC03 that uses an analytical expression for the in-situ strength (green color).

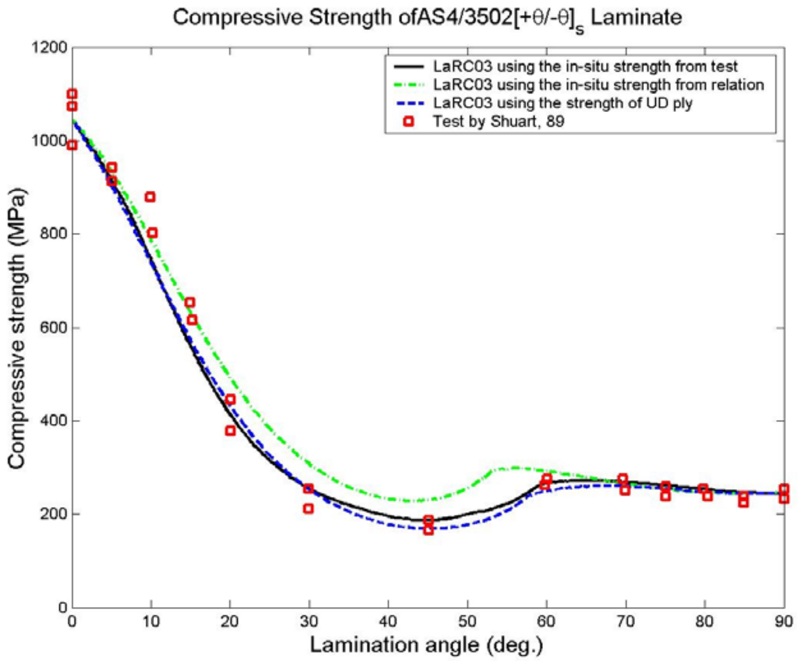

Fig. 4.13, Compressive strength of [+/-θ]s AS4/3502 predicted by LaRC03 using different values of in-situ strength. 27 test data points.

The 'in-situ' strength from experiment is 95.1 MPa. The reported ply strength in MIL-HDBK-17, is 102 MPa, and the 'in-situ' strength derived from the analytical relation is S_{is} = 114.8 MPa (G_{Ic}= 82 J/m^2, G_{IIc} = 120.5 J/m^2). Material properties are listed in Table 4.3. The LaRC03 angle α_0 was obtained by searching numerically for the angle that maximizes the failure criterion. See Section 7.7.1 for more detail.

Fig. 4.13 purpose is to quantify how in-situ data provides more accurate failure prediction for a known material and a specific M&P. This poses the question of how specific M&P data can improve CF's. In the next section we show the in-situ material data effects on derived correlation factors. However a broader perspective will be taken, in that more than just F_{su} in-situ material data will be considered.

4.7 How the effect of M&P can be captured with CFs

If economically possible, statistically relevant tests of a material should be done that accounts for a full range of loading interactions/ply angles. This section quantifies the possible inaccuracy in laminate load prediction when specific M&P testing is not performed. The comparison is based on using **MIL-HBK-17** handbook data vs. characterized composite material properties that include specific vendor M&P effects. The important issue is how well we would have predicted failure ***a-priori*** with preexisting handbook data. Unfortunately, as shown below, the answer is quite poorly.

The test is a compressive load, Fig. 4.12, and as such, F_{1c} is a relevant property to compare as well as F_{su}. As documented in Table 4.3, Mil-Hdbk-17-2E data shows a values for $F_{1c} = 204$ ksi / 1406 MPa (mean) and 171 ksi / 1179 MPa (B-basis). The measured in-situ value of 1045 MPa should be nearly equal to the handbook typical value, but the Mil-Hdbk-17-2E typical value of 1406 MPa is 40% higher. Such a variation in this strength property is not expected since it is based on fiber failure, a relatively easy and consistent data property to characterize. This is one suspected reason for the poor a-priori failure strength prediction.

As seen in Table 4.3, the “B” basis properties are closer to the in-situ properties measured by NASA, and if performing a traditional analysis and sizing these properties would be used for achieving required safety. However, the close match between the in-situ and “B” basis properties should be considered a fluke and not to be expected. Typical material properties should be used for test prediction and for reliability sizing where the CF’s provide appropriate statistical values.

4.7.1 AS4/3502 Properties

Table 4.3, Properties of UD AS4/3502 from MIL-HBK-17 (75 °F) and NASA LaRC03 report [4.2, 4.3]. Note big discrepancies in data.

	MIL-HBK-17 Typical	MIL-HBK-17 Design-“B” Basis	LaRC03 report (Shuart)
E_{1t}/E_{1c} (MPa)	133073	124106	127600
E_{2t}/E_{2c} (MPa)	9722	9308	11300
G_{12} (MPa)	3744	--	6000
ν_{12}	0.30	0.30	0.278
F_{1t} (MPa)	1779	--	N/A
F_{1c} (MPa)	1406	1179	1045
F_{2t} (MPa)	53.5	--	N/A
F_{2c} (MPa)	238.6	183	244
$F_6/F_{12}/F_{su}$(MPa)	102.0	92.4	95.1 (in-situ)

Suggestion: Use all test data if a specific M&P is not known. Do this for PD to get more consistent reliability. Then once the specific material and process is known, then use that available test data to generate specific CFs and use for the remainder of the project design.

Fig. 4.14 and 4.15 illustrate via histograms the large difference between reliability and accuracy of failure prediction caused by variation in material properties. Fig. 4.14 represents substantial inaccuracy and Fig. 4.15 quality failure predictions with measured in-situ properties, with the largest error between test average and prediction being 3%. However, even when in-situ properties are used, a reliability analysis based on test correlation factors is necessary to account for test scatter as noted with some of the histogram bars being outside 2 standard deviations.

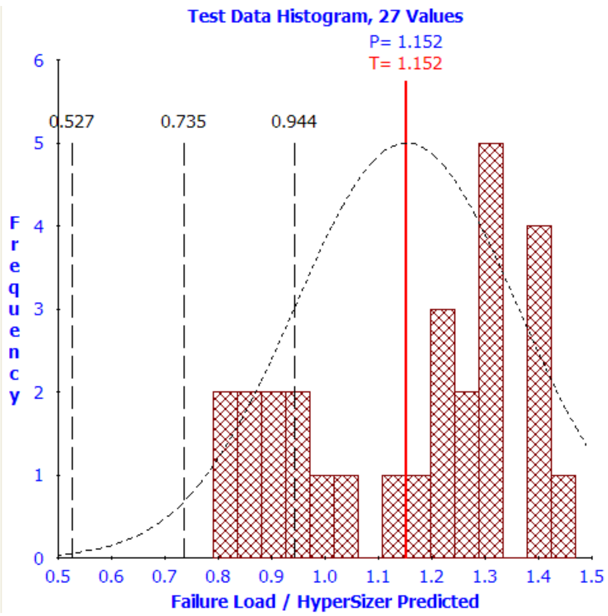

Fig. 4.14(a), AS4/3502, Mil-Hdbk-17-2E Tsai-Wu

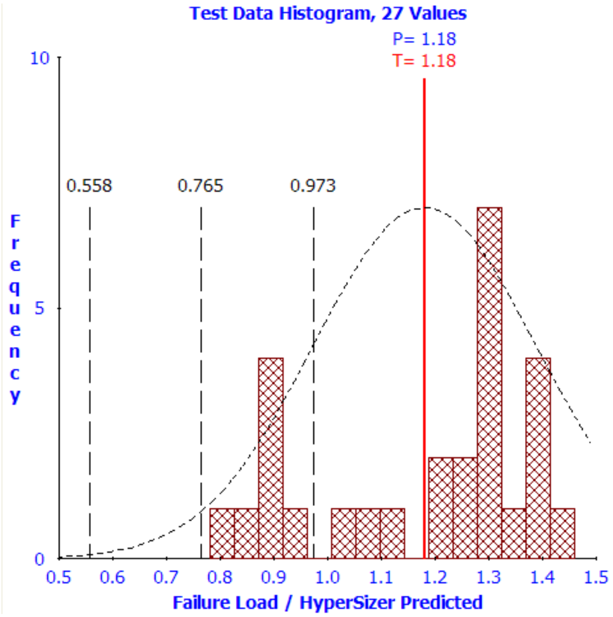

Fig. 4.14(b), AS4/3502, Mil-Hdbk-17-2E Tsai-Hahn

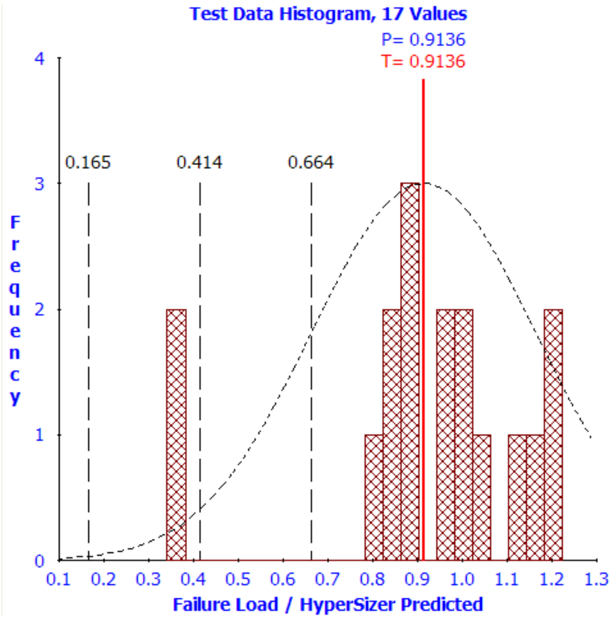

Fig. 4.14(c), AS4/3502, Mil-Hdbk-17-2E LaRC03 Fiber Failure

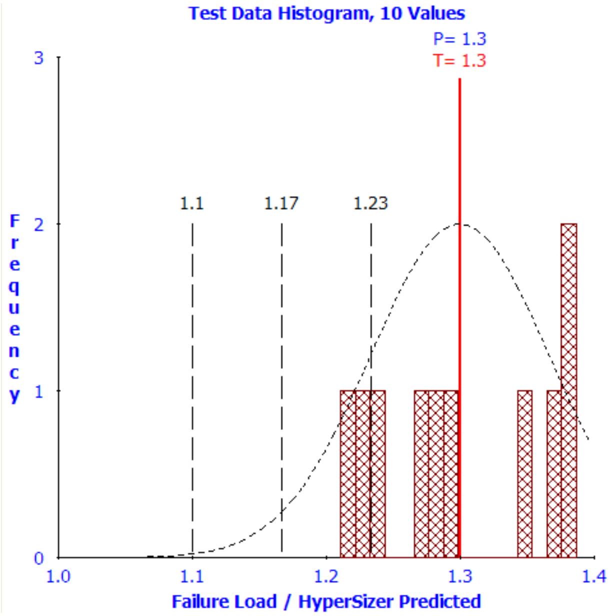

Fig. 4.14(d), AS4/3502 , Mil-Hdbk-17-2E LaRC03 Matrix Cracking

AS4/3502 ***using a-prior Mil-Hdbk-17-2E material properties****.*

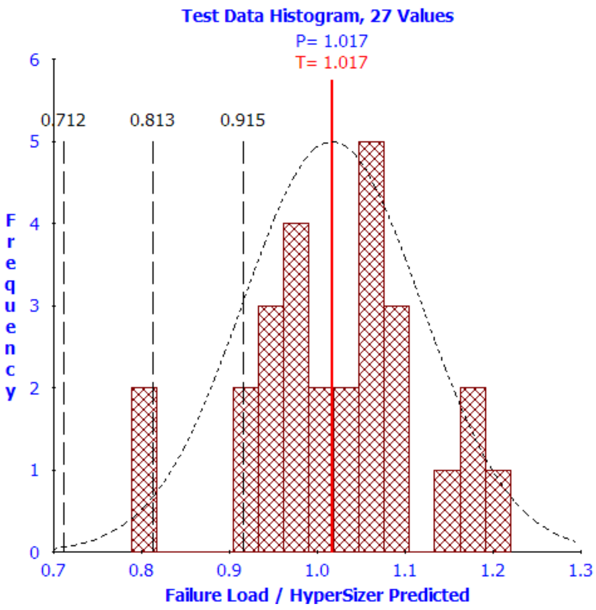

Fig. 4.15(a), AS4/3502 ,Fsu=95 MPa
Tsia-Wu (η=.1012)

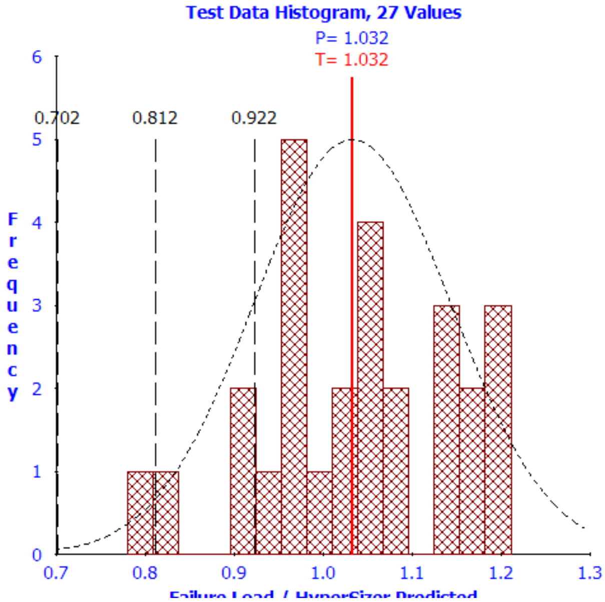

Fig. 4.15(b), AS4/3502 ,Fsu=95 MPa
Tsia-Hahn (η=.11)

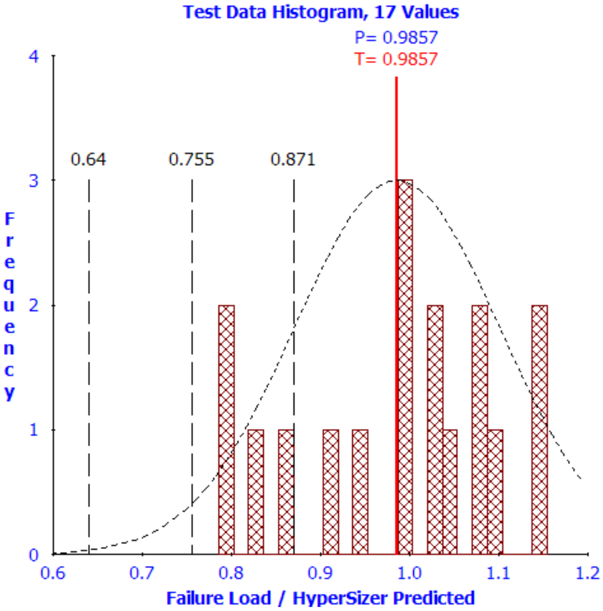

Fig. 4.15(c), AS4/3502 ,Fsu=95 MPa
LaRC03 Fiber Failure (η=.1152)

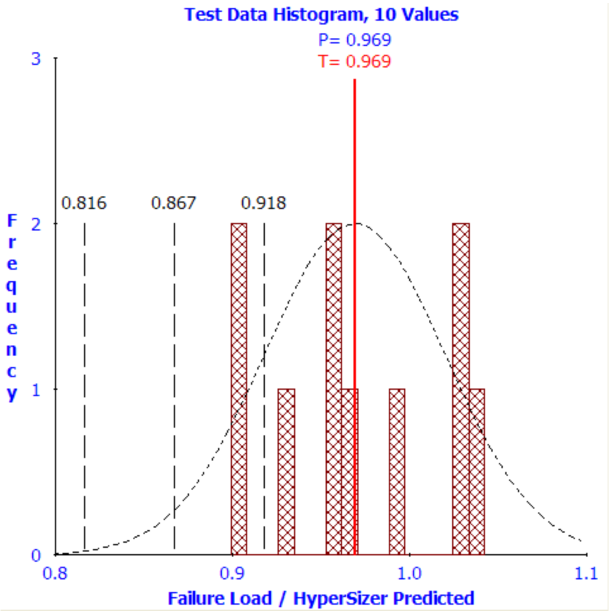

Fig. 4.15(d), AS4/3502 ,Fsu=95 MPa
LaRC03 Matrix Cracking(η=.051)

*AS4/3502 using **in-situ test data material properties**.*
Weighted Average of the LaRC03:Fiber Failure and Matrix Cracking (μ_l=.9795 = 1/1.021) (η=.0914)

4.7.2 IM7/8552 Properties

Often it is difficult obtaining proper material properties. Described is a process frequently performed by the engineer in identifying material data for PD material screening trade studies. An ideal situation is to fund a characterization effort. However, a complete test program is usually not available early in design, and many preliminary designs are based on gathering required material properties from various sources. For instance, the analysis performed for the NASA stepped bonded joint used five different sources. As such, the need for a reliability approach which takes uncertainty into account is very much needed. From the table we see the large variation of material properties. All properties from MIL-HDBK-17 are assumed to be pristine, dry, ambient 72°F data.

Table 4.4, Properties of UD IM7/8552 from MIL-HBK-17 (75 °F), NASA, Boeing/Collier, and industry consultant. Many sources are required to identify all necessary properties.

Property	NASA [4.6]	MIL-17 (a) [4.7]	MIL-17 (b) [4.7]	Hoyt [4.8]	Collier-Van West [4.9]
E1t	23.35	23.5	-	20.7	20.8
E2t	1.65	-	1.35 (assume =E3t)	1.65	1.43
E1c	-	-	-	-	18.28
E2c	-	-	-	-	1.56
ν12	0.32	0.3111	-	0.34	0.31
E3t	1.65	-	1.35	1.65	-
G12	0.75	0.73	-	0.65	0.66
F1t	-	384	-	-	338
F2t	18.42	-	-	-	13.82
F1c	-	-	-	-	224.83
F2c	-	-	-	-	37.76
F12	-	17.4	-	-	15.8
F3t	-	-	8.16	3	-
F13	-	-	14.8	5	-
F23	-	-	5.32	5	-

The yellow and pink color properties are those included in the HyperSizer database for the NASA stepped bonded doubler validation problem. Pink properties are projected.

- **E1t** varies by **12%**
    - (comparing values between [4.6] and [4.8 & 4.9] for E1t, (23.35 – 20.8) / 20.8 = 12%).
- **F2t** varies by **33%**
    - (comparing values between [4.6] and [4.9] for F2t, (18.4-13.8)/13.8 = 33%).

4.8References

4.1 Soden P. D., Hinton, M. J., and Kaddour, A. S., (2002) "Biaxial test results for strength and deformation of a range of E-glass and carbon fibre reinforced composite laminates: failure exercise benchmark data," *Composite Science and Technology*, 62, pp.1489-1514.

4.2 Shuart, M. J., "Failure of Compression-Loaded Multidirectional Composite Laminates," AIAA Journal, Vol. 27, 1989, pp.1274-1279.

4.3 Davila, C. G. and Camanho, P. P., "Failure criteria for FRP laminates in plane stress," NASA/TM-2003-212663.

4.4 Tsai, S.W. and Wu, E.M. (1971) "A General Theory of Strength for Anisotropic Materials" Journal of Composite Materials, 58-80.

4.5 Tsai, S.W. and Hahn, H.T. (1980) Introduction to Composite Materials, Technomic Pub. Co., 1980.

4.6 Krueger, R., Paris, I. L., O'Brien T. K., and Minguet, P. J., 2001, "Fatigue Life Methodology for Bonded Composite Skin/Stringer Configurations," NASA/TM-2001-210842, ARL-TR-2432.

4.7 MIL-HDBK-17-E3, 1997.

4.8 Hoyt, D. M., Ward, S. H., Minguet, P. J., "Strength and Fatigue Life Modeling of Bonded Joints in Composite Structure," *American Society for Composites (ASC) 15th Technical Conference*, September 2000.

4.9 Collier, C., Yarrington, P., Van West, B., "Composite, Grid-Stiffened Panel Design for Post Buckling Using HyperSizer" AIAA-2002-1222, AIAA SDM Conference, April 2002.

4.10 Swanson,S.R., Tian,Z., Messick,M.J., Failure of carbon/epoxy lamina under combined stress, Journal of Composite Materials. Vol. 21, pp. 619-630. July 1987.

5 Correlation to Test: Cylindrical Panel Buckling

5.1 Theory

The phenomenon of panel buckling is highly dependent on panel cross sectional shape, bending moment of inertia, material stiffness, and relative span lengths. Additionally, if a panel is curved, the cylindrical geometry causes a beneficial stabilizing effect. However, in contrast with the stabilizing benefit are additional theoretical inaccuracies which must be accounted. All theoretical analysis methods over-predict critical buckling loads for unstiffened shells with curvature. Typically, the higher the radius/thickness ratio, the more substantial the over prediction. Shells composed of composite layups complicate the problem further.

These inaccuracies, which are well known to occur in both close form analytical methods as well as in high-powered, detailed FEA, have been traditionally handled by use of “knockdown factors.” Likely the most prominent publication on this topic used in industry is the NASA SP-8007 report [5.1]. This report, written in the mid 1960’s, is primarily intended for unstiffened metallic sheet and sandwich panels. The research described herein has extended the concept of the knockdown factors to account for composite laminates and reliability.

To derive correlation factors for curved panel buckling methods, 74 curved, composite buckling test articles from reference [5.3] were analyzed with HyperSizer and the results used to derive correlation factors. The use of the NASA SP8007 buckling knockdown factor was quantified and compared to results using a more consistently applied reliability approach.

The HyperSizer buckling is based on Raleigh Ritz [5.3] and has proven to provide nearly the same theoretical values as does linear FEA (MSC/NASTRAN eigenvalue buckling) .

5.2Test Setup, Dimensions and Material Properties

The 74 test panels are in the HyperSizer V&V database in the following location:
Workspace: CCCVal – Composite Curved Compression Panel Buckling RR3 Test Validation
Components: 100-173; Groups 100-173

Dimensions [5.3, p.36];
r= 12"
L= 13"
b= 9"
t_{ply}=0.0064" [derived]

Material properties [5.3, p.37]:
$E_1 = 20$ Msi
$E_2 = 2.1$ Msi
$\nu_{12} = 0.21$
$G_{12} = 0.85$ Msi

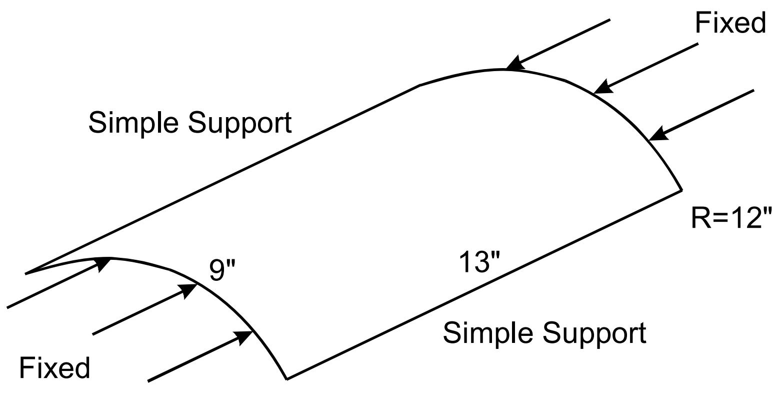

Boundary Conditions [5.3, p.56]
loaded ends – fixed; straight
unloaded edges – simple

5.3Summary of Phase I Results

5.3.1 Phase I Test Data Comparison

Since the test data reported in the 1973 reference [5.3] used the SS8 legacy code for analysis predictions, its results are included in Tables 5.1 and 5.2. Table 5.1 summarizes the comparisons of the SS8 and HyperSizer Raleigh Ritz's theoretical solutions to test results. While this table summarizes results for only the SS8 legacy code and the HyperSizer Raleigh Ritz code, it is important to recognize that linear eigenvalue FEA solutions would be expected to achieve similar accuracy. As such, the discussion of correlation factors presented here for HyperSizer solutions would be equally applicable to FEA. This is illustrated in a verification example in Section 5.7.1.

Table 5.1, Summary comparison of experimental load divided by the Phase I theoretical buckling load

Analysis Code	Average	Standard deviation	Max	Min
SS8 legacy code	0.64	0.17	0.92	0.16
HyperSizer Raleigh Ritz	0.71	0.13	0.97	0.38

The accuracy of each theoretical tool is defined as the experimental failure load divided by the theoretical prediction. SS8, with an average of 0.64, over predicts the experimental value more than HyperSizer, which has an average of 0.71. The standard deviation of HyperSizer's prediction accuracy is also smaller than SS8's meaning there is less variation between prediction average and test average. Finally, note the relatively wide variation in the extreme experimental vs. theoretical buckling load ratios indicated as Max and Min. This indicates a wide variation in theoretical solution accuracy for different panel configurations.

Table 5.2 provides detailed information for every test specimen. The 74 individual test articles were grouped into sets of 25 different unique laminates with each laminate's measured thickness used in the analysis predictions. The Snap, Moire, and Southwell columns represent different techniques to establish experimental buckling load. The first two SS8 and HyperSizer columns under "Failure Loads" represent the theoretical buckling loads, whereas the second set of columns under "knockdown" represent the ratio of experimental divided by theoretical. The last two columns with the headings γ_μ and η, are the average and standard deviation of the HyperSizer knockdown (test failure load / theoretical load) for each unique laminate. In columns where there is no value for η listed, there was only one specimen of this unique laminate, and therefore no standard deviation was calculated.

The knockdown for all 74 laminates is plotted as a histogram in Fig. 5.1. Note that this histogram is relatively flat, i.e. it does not have a bell shape curve as might be expected from random test data.

Table 5.2, Detailed listing of experimental and theoretical buckling loads for HyperSizer and the SS8 legacy code.

				Vertical Edges Simply Supported, Curved Edges Clamped											
				Failure Loads						Knockdown					
Panel	Laminate	Thickness, Inches	Variation, Inches	Snap	Moire	Southwell	Min. Experiment	SS8	HyperSizer	SS8	HyperSizer	Test Count	Test Average	γμ	γη
17A	[0/90]2s	0.0592	0.0021		6680	7323	6680	7200	7251.30	0.93	0.921				
17B	[0/90]2s	0.0528	0.0036		4865		4865	5900	5592.60	0.82	0.870	2.00	6421.95	0.90	0.22
19A	[±45]2s	0.0696	0.0030		8660	8750	8660	12400	10746.00	0.70	0.806				
19B	[±45]2s	0.0707	0.0030	9000		9050	9000	12700	11106.00	0.71	0.810	2.00	10926.00		
19C	[±45]2s	0.0713	0.0025		8820		8820	13000	11304.00	0.68	0.780				
19D	[±45]2s	0.0719	0.0019		8760		8760	13200	11502.00	0.66	0.762				
19E	[±45]2s	0.0598	0.0026		5740		5740	9500	7902.00	0.60	0.726	5.00	10512.00	0.78	0.17
21A	[0/90]s	0.0289	0.0015		985	1125	985	1530	1506.24	0.64	0.654				
21B	[0/90]s	0.0282	0.0013		925		925	1470	1429.74	0.63	0.647	2.00	1467.99	0.65	0.04
23A	[±45]s	0.0354	0.0025	1870	1870	1914	1870	4000	3109.50	0.47	0.601				
23B	[±45]s	0.0362	0.0033	1610		1695	1610	4180	3218.40	0.39	0.500				
23C	[±45]s	0.0340	0.0018		1590	1624	1590	3780	2925.90	0.42	0.543				
23D	[±45]s	0.0359	0.0025	1850			1850	4130	3177.00	0.45	0.582				
23E	[±45]s	0.0307	0.0013		1280	1314	1280	2950	2519.10	0.43	0.508	5.00	2989.98	0.55	0.15
27	(Alum)	0.0630		17000			17000	23500	19512.00	0.72	0.871	1.00	19512.00	0.87	
29C	[±45] 3s	0.1045	0.0027		17760	23125	17760	27700	25875.00	0.64	0.686				
29D	[±45] 3s	0.1066	0.0037			21889	21889	29200	27018.00	0.75	0.810				
29E	[±45] 3s	0.0892	0.0040		10780		10780	19700	18405.00	0.55	0.586	3.00	23766.00	0.71	0.33
31A	[+45]2s	0.0343	0.0024	1550	1550	1759	1550	2800	2799.00	0.55	0.554				
31B	[+45]2s	0.0356	0.0038		1505	1704	1505	2900	3034.80	0.52	0.496				
31C	[+45]2s	0.0353	0.0017		1520		1520	2900	2979.00	0.52	0.510				
31D	[+45]2s	0.0347	0.0021	1500			1500	2800	2870.10	0.54	0.523				
31E	[+45]2s	0.0289	0.0015	975			975	2000	1932.30	0.49	0.505	5.00	2723.04	0.52	0.17
33A	[+45] 4s	0.0692	0.0031	7050			7050	11700	9867.60	0.60	0.714				
33B	[+45] 4s	0.0679	0.0024	6340	6300	7000	6300	11300	9529.20	0.56	0.661				
33C	[+45] 4s	0.0622	0.0030		5700	5750	5700	9300	8116.20	0.61	0.702				
33D	[+45] 4s	0.0709	0.0035		6620		6620	12200	10323.00	0.54	0.641				
33E	[+45] 4s	0.0591	0.0024	4000	4000	4021	4000	8300	7398.00	0.48	0.541	5.00	9046.80	0.66	0.20
35A	[+45]6s	0.0902	0.0049		9180	10270	9180	20000	16182.00	0.46	0.567	1.00	16182.00	0.57	
37A	[-30]2s	0.0282	0.0071	725	715		715	2200	1872.00	0.33	0.382	1.00	1872.00	0.38	
39A	[-30]4s	0.0580	0.0022		4730		4730	8000	6144.30	0.59	0.770	1.00	6144.30	0.77	
41A	[-30]6s	0.0900	0.0018		10460	10435	10435	17800	14490.00	0.59	0.720	1.00	14490.00	0.72	
43A	[0]2s	0.0364	0.0020		1315	1575	1315	2100	2142.90	0.63	0.614				
43C	[0]2s	0.0368	0.0032	1540			1540	2100	2196.90	0.73	0.701				
43D	[0]2s	0.0362	0.0024	1315	1290	1418	1290	2100	2115.90	0.61	0.610				
43E	[0]2s	0.0294	0.0020	945			945	1800	1348.20	0.53	0.701	4.00	1950.97	0.65	0.19
45A	[0]4s	0.0701	0.0018		5580	6468	5580	8700	8573.40	0.64	0.651				
45B	[0]4s	0.0699	0.0028	5735			5735	8700	8515.80	0.66	0.673				
45C	[0]4s	0.0696	0.0014		5300	5553	5300	8700	8430.30	0.61	0.629				
45D	[0]4s	0.0695	0.0014		5080	5610	5080	8700	8401.50	0.58	0.605				
45E	[0]4s	0.0582	0.0029		5105	5122	5105	5800	5605.20	0.88	0.911	5.00	7905.24	0.68	0.05
47A	[0]6s	0.1064	0.0030		16500	18362	16500	21600	20385.00	0.76	0.809				
47B	[0]6s	0.1039	0.0027		18000	19598	18000	20600	19386.00	0.87	0.929				
47C	[0]6s	0.1013	0.0035		16760	17812	16760	19600	18387.00	0.86	0.912	3.00	19386.00	0.88	0.05
49A	[0/90]3s	0.0880	0.0026		14680	16625	14680	16200	16101.00	0.91	0.912				
49B	[0/90]3s	0.0781	0.0034		12460	14118	12460	12500	12825.00	1.00	0.972	2.00	14463.00	0.94	0.12
51A	[±30]s	0.0296	0.0019		1150		1150	2630	2083.50	0.44	0.552	1.00	2083.50	0.55	
53A	[±30]2s	0.0557	0.0023		5405	5818	5405	7750	7335.00	0.70	0.737	1.00	7335.00	0.74	
55A	[±30]3s	0.0807	0.0026		12900	13860	12900	17000	16281.00	0.76	0.792	1.00	16281.00	0.79	
57A	[0/-45/90/+45] s	0.0574	0.0018		8240	8966	8240	10000	9891.00	0.82	0.833				
57B	[0/-45/90/+45] s	0.0499	0.0028		6640	6691	6640	7500	7380.90	0.89	0.900				
57C	[0/-45/90/+45] s	0.0516	0.0023		6460	6897	6460	7900	7918.20	0.82	0.816				
57D	[0/-45/90/+45] s	0.0499	0.0028		5820	6416	5820	7500	7380.90	0.78	0.789				
57E	[0/-45/90/+45] s	0.0524	0.0032		6960	7194	6960	8250	8177.40	0.84	0.851	5.00	8149.68	0.84	0.13
59A	[0/±60]s	0.0422	0.0010		3355	3595	3355	5200	5053.50	0.65	0.664				
59B	[0/±60]s	0.0392	0.0018		3390	3626	3390	4450	4322.70	0.76	0.784				
59C	[0/±60]s	0.0382	0.0026		3400	3582	3400	4200	4093.20	0.81	0.831				
59D	[0/±60]s	0.0397	0.0020		3000	3170	3000	4600	4439.70	0.65	0.676				
59E	[0/±60]s	0.0390	0.0028		3460	3846	3460	4420	4275.90	0.78	0.809	5.00	4437.00	0.75	0.06
61A	[0/±60]2s	0.0870	0.0026		22950	23871	22950	27400	27423.00	0.84	0.837				
61B	[0/±60]2s	0.0794	0.0041		18080	18571	18080	22800	22383.00	0.79	0.808				
61C	[0/±60]2s	0.0785	0.0034		16920	18136	16920	22300	21825.00	0.76	0.775				
61D	[0/±60]2s	0.0782	0.0029		18800	19000	18800	22300	21645.00	0.84	0.869	4.00	23319.00	0.82	0.14
67	Alum	0.0320		3825	3645		3645	8500	5019.30	0.43	0.726	1.00	5019.30	0.73	
69A	[02/±45]s	0.0512	0.0026		5500	5663	5500	8150	7249.50	0.67	0.759				
69B	[02/±45]s	0.0521	0.0019	5410	5410	5114	5114	8150	7526.70	0.63	0.679				
69C	[02/±45]s	0.0488	0.0028		5385	5604	5385	7400	6541.20	0.73	0.823				
69D	[02/±45]s	0.0504	0.0025		5310	5581	5310	7900	7009.20	0.67	0.758				
69E	[02/±45]s	0.0506	0.0034	5870	5700	5882	5700	8000	7068.60	0.71	0.806	5.00	7079.04	0.76	0.04
71A	[0/±45]s	0.0408	0.0021		2930	3187	2930	4870	4880.70	0.60	0.600				

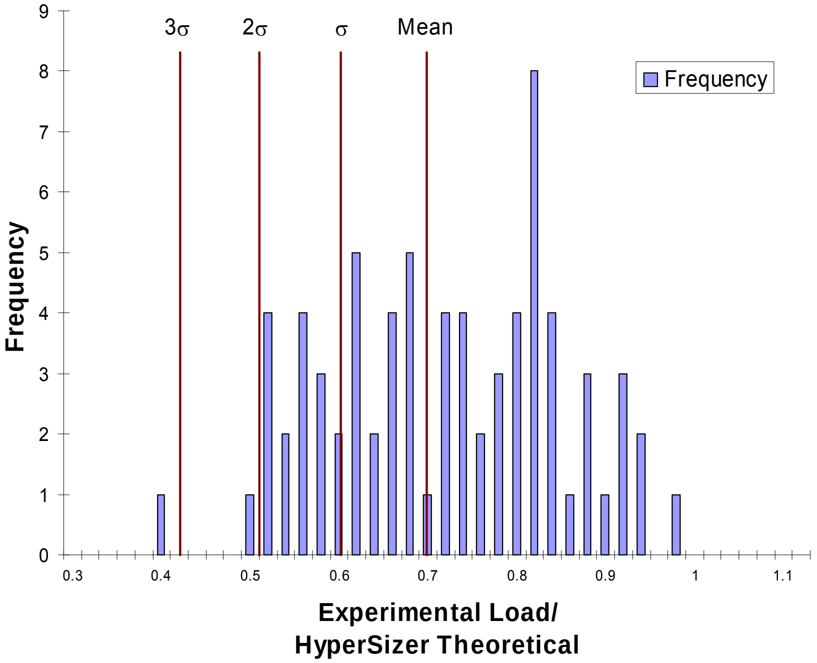

Fig. 5.1, The ratio of experimental buckling load divided by theoretical (HyperSizer Raleigh-Ritz) buckling load as a histogram chart, where the vertical bars of the Y-axis represent the frequency of occurrence for the 74 buckling experiments.

5.3.2 Correlation Factors based on Two Parameters

The uncorrelated histogram of Fig. 5.1 is flat because it does not take into account the affect of the individual panel designs on the theoretical accuracy. Upon analyzing trends in the theoretical to test data comparison, two parameters appeared to have the most influence over this accuracy. These were the panel radius to thickness ratio and the relative magnitude of the off-diagonal D bending stiffness terms. The dependence on r/t ratio is included by using the historical knockdown factor from NASA SP8007 [5.1] which is

$$NASA\,\gamma = 1 - 0.901(1 - e^{-\phi}) \qquad (5.3.1)$$

where

$$\phi = \frac{1}{16}\sqrt{\frac{r}{t}}, \quad for\,\frac{r}{t} \le 1500 \qquad \text{(for isotropic plates)} \qquad (5.3.2a)$$

$$\phi = \frac{1}{29.8}\left[\frac{r}{\sqrt[4]{\dfrac{\overline{D}x\overline{D}y}{\overline{E}x\overline{E}y}}}\right]^{\frac{1}{2}} \qquad \text{(for anisotropic plates)} \qquad (5.3.2b)$$

D_x, D_y and E_x, E_y are the longitudinal and transverse bending stiffnesses and membrane stiffnesses respectively.

The dependence on the off-diagonal bending stiffness terms is also included by,

$$\gamma_{Dratio} = \frac{|D_{13}| + |D_{23}|}{|D_{11}| + |D_{22}|} \tag{5.3.3}$$

Fig. 5.2 Highlights the relationship between these two parameters and the overall knockdown factor. As shown, the knockdown is a function of both the NASA SP8007 knockdown and the off-diagonal D terms. As such, the overall knockdown factor was determined by performing a linear regression of the test data, fitting the overall knockdown factor to equation 5.3.4. The resulting coefficients for this equation are shown in Table 5.3.

$$\gamma_{\mu} = \gamma_{\mu 1} + \gamma_{\mu 2} \frac{|D_{13}| + |D_{23}|}{|D_{11}| + |D_{22}|} + \gamma_{\mu 3}\left(NASA\,\gamma\right) \tag{5.3.4}$$

Table 5.3, Coefficients of Eq. 5.1.4 resulting from a linear regression of the test data to theoretical value comparison.

η	$\gamma_{\mu 1}$	$\gamma_{\mu 2}$	$\gamma_{\mu 3}$
0.12	0.4411	-0.2615	0.7723

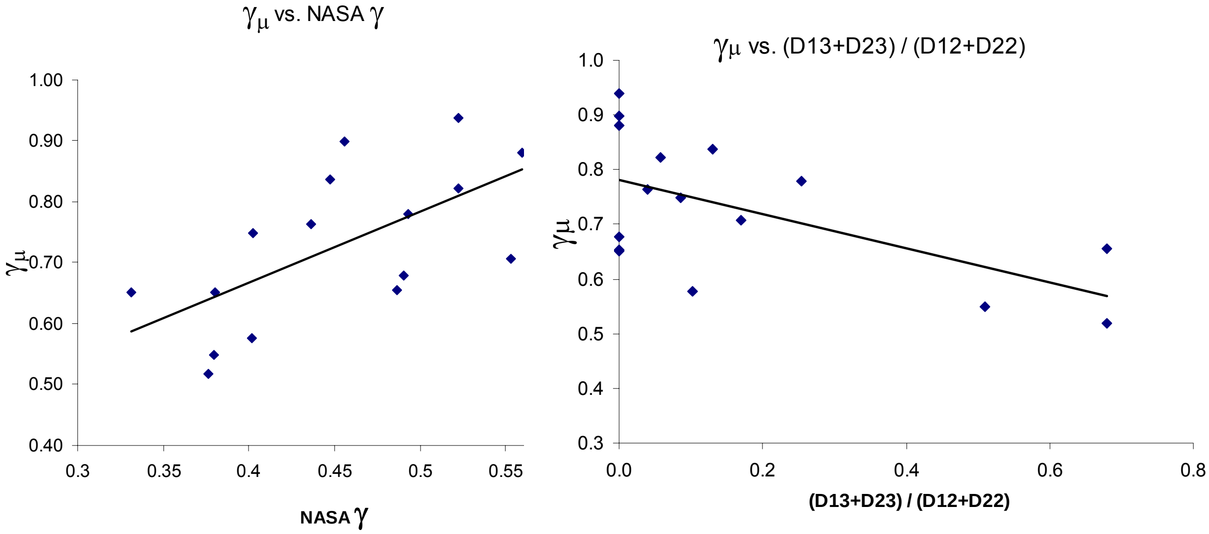

Fig. 5.2, Linear regression of the analysis correlation factor, γ_{μ}, for two parameters.

Table 5.4, Rolled up summary of test specimen groups, correlation factors, and NASA knockdown factors.

Specimen Number	Test Count	Repeats	Laminate	(D13+D23)/ (D11+D22)	$\gamma\eta$ test data	$\gamma\mu$ test data	$\gamma\mu$ predicted	NASA Knockdown Factor
19	5	1	[±45]2s	0.255	0.17	0.78	0.755	0.493
23	5	1	[±45]s	0.509	0.15	0.55	0.601	0.38
29	3	1	[±45] 3s	0.17	0.33	0.71	0.824	0.553
31	5	1	[+45]2s	0.679	0.17	0.52	0.554	0.376
33	5	1	[+45] 4s	0.679	0.20	0.66	0.639	0.486
43	4	1	[0]2s	0	0.19	0.65	0.735	0.38
45	5	1	[0]4s	0	0.05	0.68	0.820	0.49
47	3	1	[0]6s	0	0.05	0.88	0.873	0.559
57	5	6	[0/-45/90/+45] s	0.13	0.13	0.84	0.752	0.447
59	5	2	[0/±60]s	0.086	0.06	0.75	0.729	0.402
61	4	2	[0/±60]2s	0.057	0.14	0.82	0.829	0.522
69	5	2	[02/±45]s	0.04	0.04	0.76	0.767	0.436
71	5	1	[0/±45]s	0.102	0.09	0.58	0.725	0.402
Weighted Average						0.747	0.747	

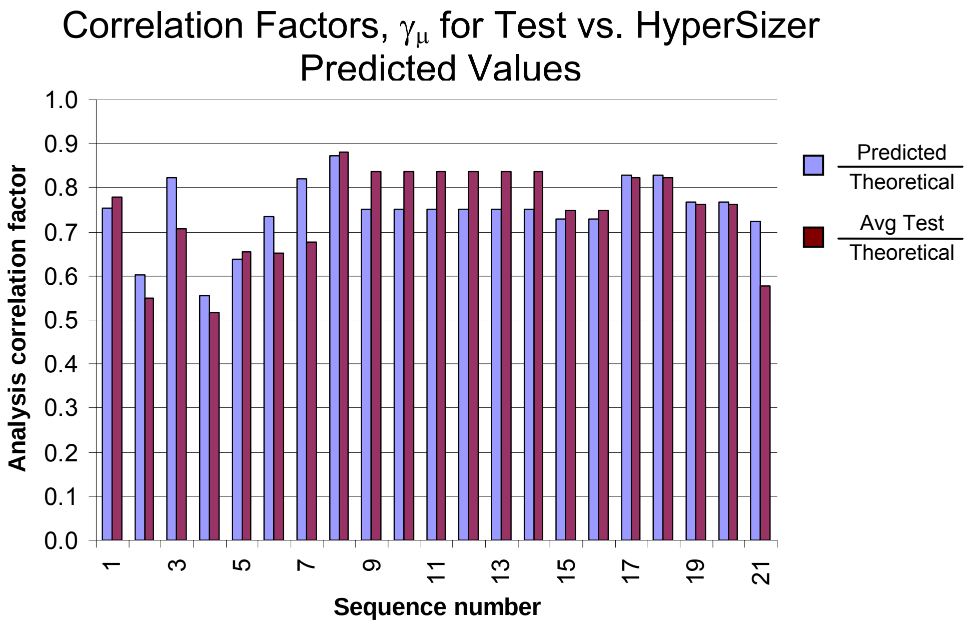

Fig. 5.3, Bar chart comparing γ_μ values from Table 5.4. The blue bars represent the ratio of HyperSizer predicted buckling load over theoretical, where γ_μ is computed with Equation (5.3.4). The dark red bars represent the ratio of average test buckling load over theoretical. These are test values that are found in the γ_μ column of Table 5.2.

The summary results using these correlation factors is shown in Table 5.4 and Fig. 5.3. Note that the original 74 test laminates have an undue influence toward non-typical layup stackings. It appears the test program of [5.3] emphasized extreme bounds of possible layups. Before performing regression analysis and establishing general use correlation factors, the more commonly used layup orientations (e.g. [0/-45/45/90]) were duplicated, and several non-standard layups were removed (such as the non-balanced [-30]$_{2s}$,). These duplicated layups are indicated in Table 5.4 as the number of “repeats”. This brings the total number of data points from 74 to 94 and the resulting average knockdown factor is 0.747.

The reliability knockdown factor, η, is determined from the standard deviation of the experimental failure divided by predicted failure. In this case, the final value was $\eta = 0.12$. These values for γ_μ and η lead to the final histogram shown in Fig. 5.4.

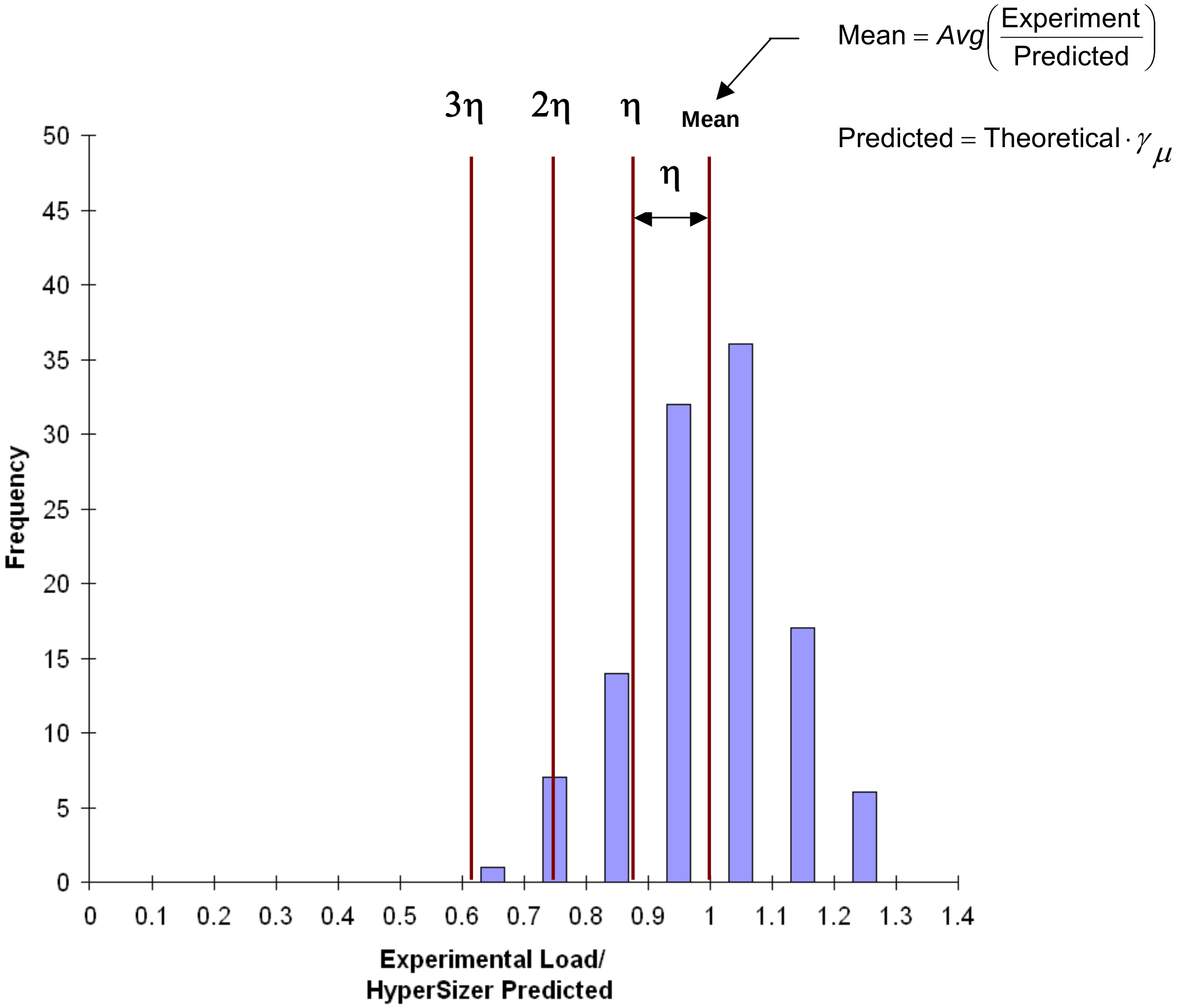

Fig. 5.4 Final histogram that includes the NASA SP8007 knockdown and the (D13+D23) / (D11+D22) bending stiffness ratio with duplicated more commonly used layups. Note how, compared to Fig. 5.1, this histogram more closely resembles a normal distribution with a definitive peak and less variance. It was generated using equation (5.3.4), the regression terms from Table 5.3, and an η value of 0.12.

5.4Phase II Updated Correlation Factors

Since the completion of Phase I, the implementation of Raleigh Ritz within HyperSizer has been improved which changed several of the layup results presented in phase I. The changed results are summarized in Table 5.5. In addition to the changed results, several additional layup families were added to the regression that were intentionally omitted from the Phase I data.

Table 5.5, Summary of changed buckling results for Phase II correlation factor calculation. Compare HyperSizer results (purple) to those shown in Table 5.2.

Panel	Laminate	Vertical Edges Simply Supported, Curved Edges Clamped					Test Count	Phase II $\gamma\mu$	Phase I $\gamma\mu$
		Failure Loads							
		Min. Experiment	Min Exp.Unit	Min Exp. MS	Average Experiment	HyperSizer			
19A	**[±45]2s**	**8660**	**962.22**	**8.6222**	**8705.00**	10278.00			
19B	**[±45]2s**	**9000**	**1000.00**	**9.0000**	**9025.00**	10620.00			
19C	**[±45]2s**	**8820**	**980.00**	**8.8000**	**8820.00**	10809.00			
19D	**[±45]2s**	**8760**	**973.33**	**8.7333**	**8760.00**	11007.00			
19E	**[±45]2s**	**5740**	**637.78**	**5.3778**	**5740.00**	7446.60	5.00	0.82	0.78
23A	**[±45]s**	**1870**	**207.78**	**1.0778**	**1884.67**	2290.50			
23B	**[±45]s**	**1610**	**178.89**	**0.7889**	**1652.50**	2397.60			
23C	**[±45]s**	**1590**	**176.67**	**0.7667**	**1607.00**	2108.70			
23D	**[±45]s**	**1850**	**205.56**	**1.0556**	**1850.00**	2357.10			
23E	**[±45]s**	**1280**	**142.22**	**0.4222**	**1297.00**	1709.19	5.00	0.75	0.55
33A	**[+45] 4s**	**7050**	**783.33**	**6.8333**	**7050.00**	8146.80			
33B	**[+45] 4s**	**6300**	**700.00**	**6.0000**	**6546.67**	7824.60			
33C	**[+45] 4s**	**5700**	**633.33**	**5.3333**	**5725.00**	6500.70			
33D	**[+45] 4s**	**6620**	**735.56**	**6.3556**	**6620.00**	8581.50			
33E	**[+45] 4s**	**4000**	**444.44**	**3.4444**	**4007.00**	5839.20	5.00	0.80	0.66

Once again, using the test data to theoretical value comparison, correlation factors were derived by linear regression using Equation (5.3.4). The resulting CFs are shown in Table 5.6.

Table 5.6, Coefficients of Equation 5.3.4 resulting from a linear regression of the Phase II test data to theoretical value comparison.

η	$\gamma_{\mu 1}$	$\gamma_{\mu 2}$	$\gamma_{\mu 3}$
0.136	0.3956	-0.1144	0.8751

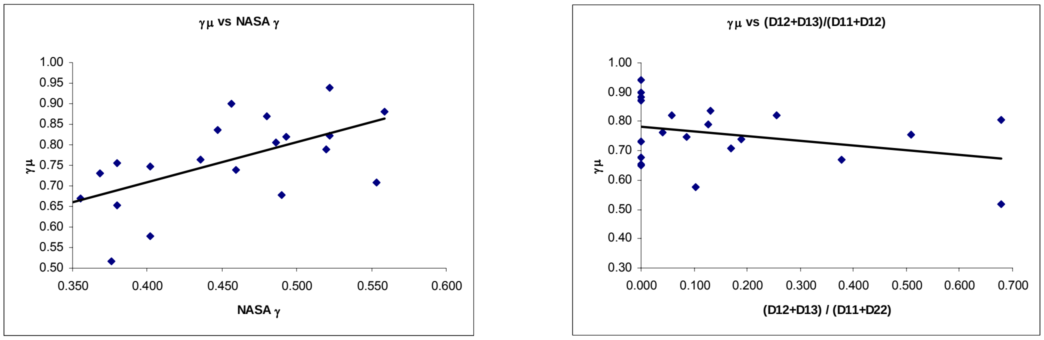

Fig 5.5, Using the test-to-theoretical regression for Phase II, the overall knockdown factor is now less reliant on the off-diagonal D ratio and more reliant on the NASA SP-8007 knockdown. This is also seen by the fact that the magnitude of $\gamma_{\mu 2}$ is lower and $\gamma_{\mu 3}$ is higher for Phase II than it was in Phase I.

The summary results with the improved Raleigh-Ritz analysis are shown in Table 5.7 and Fig. 5.6. The average knockdown for this data is 0.768 compared to the prior 0.747. This means that on average, the theoretical prediction is closer to the experimental data than in Phase I.

Table 5.7, Rolled up summary of test specimen groups, correlation factors, and NASA knockdown factors.

Specimen Number	Test Count	Repeats	Laminate	(D13+D23)/ (D11+D22)	η test data	γ_μ test data	γ_μ computed	Computed 99% Reliability	NASA Knockdown Factor	Computed Reliability for NASA Knockdown
17	2	1	[0/90]2s	0.000	0.22	0.90	0.795	0.478	0.456	99.36
19	5	1	[±45]2s	0.255	0.17	0.82	0.798	0.481	0.493	98.75
21	2	1	[0/90]s	0.000	0.04	0.65	0.685	0.369	0.331	99.54
23	5	1	[±45]s	0.509	0.15	0.75	0.670	0.354	0.380	98.35
27	1	1	(Alum)	0.000	-	0.87	0.816	0.499	0.480	99.32
29	3	1	[±45] 3s	0.170	0.33	0.71	0.860	0.544	0.553	98.80
31	5	1	[+45]2s	0.679	0.17	0.52	0.647	0.331	0.376	97.68
33	5	1	[+45] 4s	0.679	0.20	0.80	0.743	0.427	0.486	97.07
43	4	1	[0]2s	0.000	0.19	0.65	0.728	0.412	0.380	99.48
45	5	1	[0]4s	0.000	0.05	0.68	0.824	0.508	0.490	99.30
47	3	1	[0]6s	0.000	0.05	0.88	0.885	0.568	0.559	99.17
49	2	1	[0/90]3s	0.000	0.12	0.94	0.852	0.536	0.522	99.24
51	1	1	[±30]s	0.377	-	0.67	0.663	0.347	0.355	98.83
53	1	1	[±30]2s	0.189	-	0.74	0.776	0.459	0.459	99.01
55	1	1	[±30]3s	0.126	-	0.79	0.836	0.520	0.520	99.00
57	5	6	[0/-45/90/+45] s	0.130	0.13	0.84	0.772	0.456	0.447	99.16
59	5	2	[0/±60]s	0.086	0.06	0.75	0.738	0.421	0.402	99.32
61	4	2	[0/±60]2s	0.057	0.14	0.82	0.846	0.530	0.522	99.14
67	1	1	(Alum)	0.000	-	0.73	0.718	0.401	0.368	99.49
69	5	2	[02/±45]s	0.040	0.04	0.76	0.773	0.456	0.436	99.33
71	5	1	[0/±45]s	0.102	0.09	0.58	0.736	0.419	0.402	99.29
Weighted Average*						*0.768*	*0.768*	*0.452*	*0.447*	*99.09*

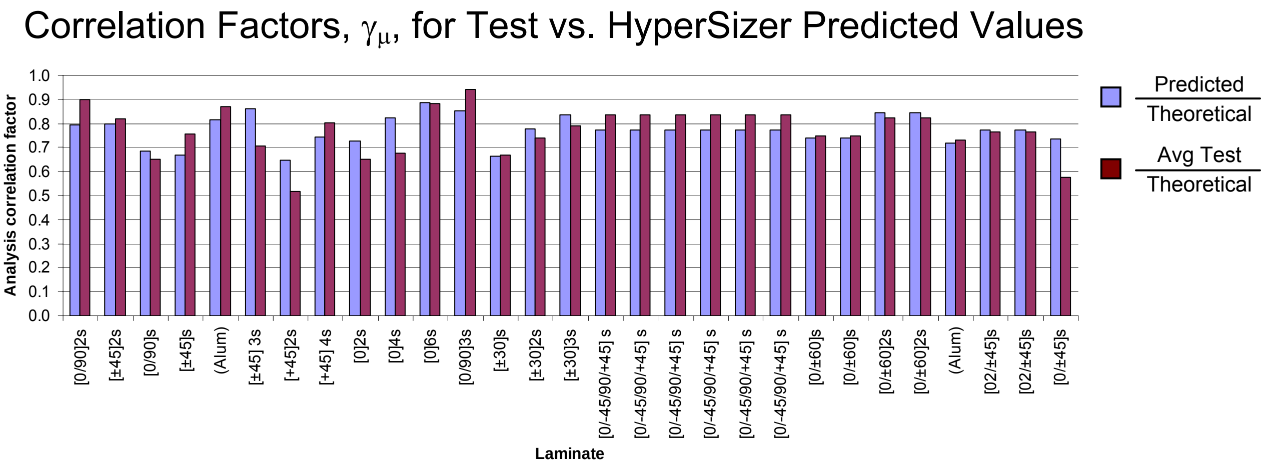

Fig. 5.6, Rolled up summary bar chart itemized by test specimen groups comparing γ_μ from Table 5.7. Many different layup combinations tested. The blue bars represent the ratio of HyperSizer predicted buckling load over theoretical, where γ_μ is computed with Equation (5.3.4). The dark red bars represent the ratio of average test buckling load over theoretical. These are test values that are found in the γ_μ column of Tables 5.2 and 5.5. Included with the newly defined CF data are the calculated NASA knockdown factors and their resulting reliabilities. The average of these 109 individually backed out reliabilities is 99.04%, which gives independent verification to NASA's larger collection of test data and the intended buckling knockdown safety of 99%.

5.5Independent Verification of NASA SP-8007 Reliability

In Table 5.7, not only are the values of γ_μ shown for each laminate stacking, but also the computed knockdown for a 99% reliability. Comparing this value to the NASA SP8007 knockdown factor, we can back out a reliability for the NASA knockdown. This is done by calculating the '*K*' value of the NASA knockdown factor and calculating a reliability from that *K* value. For example, for Specimen Number 55,

$$K = \frac{\gamma_\mu - NASA\ \gamma}{\eta} = \frac{0.836 - 0.52}{0.136} = 2.33$$

This K value of 2.33 corresponds to a reliability of 99% as shown in the right most column of Table 5.7. The relationship between K and reliability is found in the K vs. reliability table in the beginning of Volume 3.

The weighted averages of the each item is summarized at the bottom of each column in Table 5.7, these are calculated by:

$$Weighted\ Average = \frac{\sum\left[(Test\ Count)(Repeats)(Value)\right]}{\sum\left[(Test\ Count)(Repeats)\right]} \tag{5.5.1}$$

This value for the right-most column is the average reliability of the SP-8007 knockdown factors applied to the 109 individual test results, which is 99.09%. This gives a sanity check that the newly developed correlation factor capability is operating as intended. This second source of test data also provides independent verification against NASA's larger, original collection of test data where the intended buckling knockdown reliability target was 99%. A third source of test data provides yet another independent verification against NASA's larger, original collection of test data. Section 5.7.1 shows that for 32 steel beer cans tested for cylindrical buckling by Arbocz [5.4], the backed out NASA knockdown factor reliability ~99.2%.

At first glance it might appear that the correlations described in this document are merely a re-hashing of the work done in SP-8007 and therefore not really needed. However, in the present work we are taking the NASA original test data into account (by including the $NASA\ \gamma$ knockdown factor), adding dependence on the off-diagonal D_{13} and D_{23} terms, accounting for partial cylinders (width to radius ratios), and adding 74 composite test panels to the correlations. By doing this, we believe that the γ_μ correlations give slightly more accurate results, especially for composites. In addition, by using two separate knockdown factors, γ_μ and η, desired reliability can be specified by the user instead of being locked in, as with the SP-8007 knockdown factor.

5.6HyperSizer CFs and Generated Histogram

In the correlation category "Panel Buckling, Curved" the correlation factors: η=0.136 and μ_1 = 0.3956, μ_2 = -0.1144, and μ_3 = 0.8751 have been established to best fit the test data for the 109 data points. As shown in Fig. 5.7 the difference between the average failure load and average predicted allowable load is quite small (P=0.9847 *failure load/HyperSizer predicted*). Note that the average theoretical failure load is 1.287/0.985 = 131% of the predicted failure load.

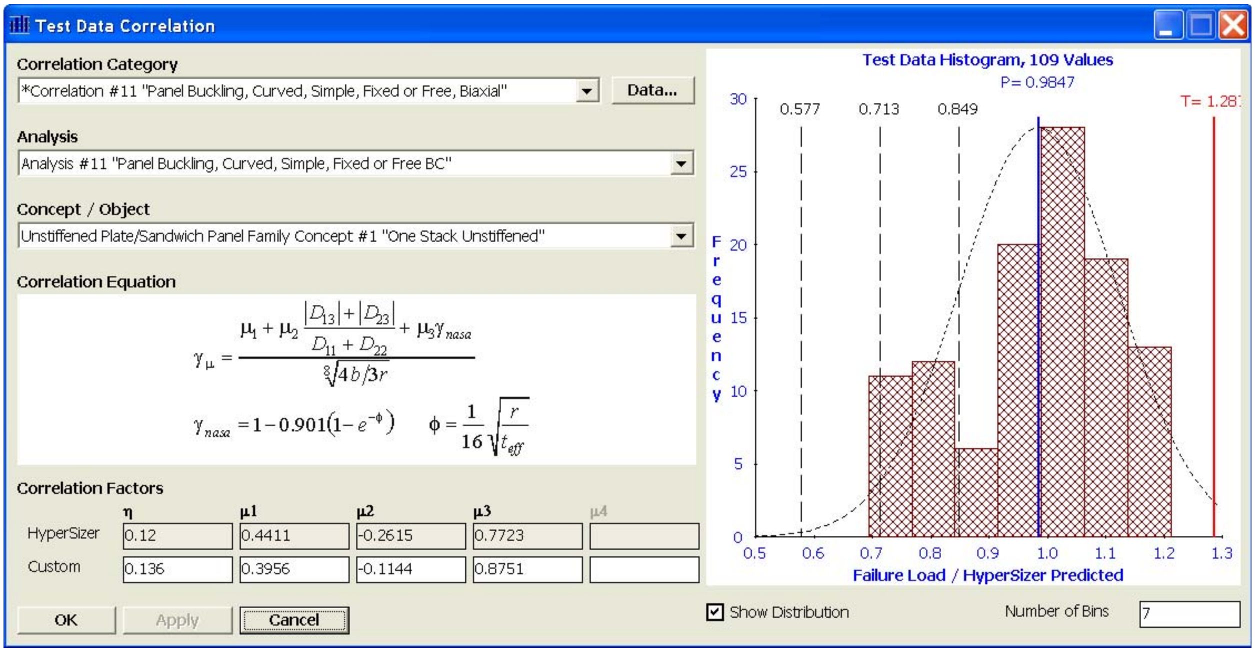

Test Data Correlation

Correlation Category: *Correlation #11 "Panel Buckling, Curved, Simple, Fixed or Free, Biaxial"

Analysis: Analysis #11 "Panel Buckling, Curved, Simple, Fixed or Free BC"

Concept / Object: Unstiffened Plate/Sandwich Panel Family Concept #1 "One Stack Unstiffened"

Correlation Equation

$$\gamma_{\mu} = \frac{\mu_1 + \mu_2 \dfrac{|D_{13}| + |D_{23}|}{D_{11} + D_{22}} + \mu_3 \gamma_{nasa}}{\sqrt[8]{4b/3r}}$$

$$\gamma_{nasa} = 1 - 0.901(1 - e^{-\phi}) \qquad \phi = \frac{1}{16}\sqrt{\frac{r}{t_{eff}}}$$

Correlation Factors

	η	μ1	μ2	μ3	μ4
HyperSizer	0.12	0.4411	-0.2615	0.7723	
Custom	0.136	0.3956	-0.1144	0.8751	

☑ Show Distribution

Number of Bins: 7

Fig. 5.7, Panel Buckling, Curved, Simple, Fixed, or Free BC, Biaxial stiffness panel correlation category.

From Fig. 5.7 note the normalized standard deviation value, η = 0.985 – 0.849 = **0.136**. If we were to establish a 99.865% reliability, K would be 3.0, and the resulting buckling allowable would equal 0.9847 - 3.0*0.136 = 0.577. So in summary, theoretical is 1.287, predicted is 0.985, and a 99.9 % reliability is 0.577, meaning that on average, the theoretically derived failure load is 1.287/0.577 = 223% of the design allowable. Said in another way, the knockdown is 0.577/1.287 = 0.4483.

5.7Example: Application of γ_μ and η to buckling of [02/±45]s curved laminates

In this example the correlation factors derived from the 74 composite curved shell test articles are applied to only five of the curved test laminates, all with the layup, [02/±45]s. We start the example by showing the math for just the 1st laminate of the five, noted as 69A (see Table 5.2). The remaining four laminates of the set are summarized in tables.

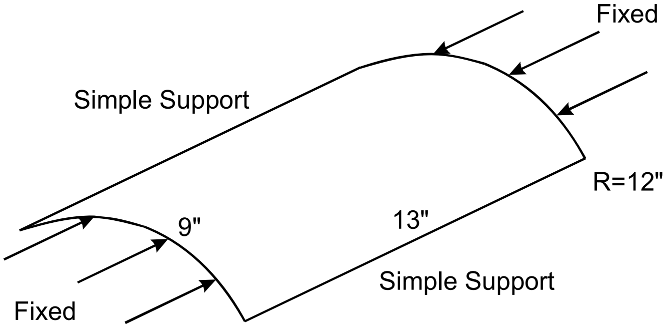

Dimensions :
R= 12", L= 13", b= 9"
t = 0.0512", r/t ratio = 12/0.0512 = 234.4
t_{ply} = 0.0064"

Material properties:
E_1=20 Msi, E_2=2.1 Msi, ν_{12}=0.21,
G_{12}=0.85 Msi

Boundary conditions:
loaded ends fixed,
straight unloaded edges simple

Step 1: Calculate the laminate stiffness terms

Using classical lamination theory, the relevant terms are:
$A_{11} = 683{,}911$ $E_x = A_{11}$
$A_{22} = 223{,}539$ $E_y = A_{22}$
$D_{11} = 205.9$ $D_x = D_{11}$
$D_{12} = 11.22$ $D_y = D_{22}$
$D_{22} = 29.91$ $D_y = D_{22}$
$D_{13} = -4.71$
$D_{23} = -4.71$ $\dfrac{|D_{13}|+|D_{23}|}{|D_{11}|+|D_{22}|} = 0.04$
$D_{33} = 15.77$

Step 2: Calculate the NASA buckling knockdown factor, NASA γ, using eqns (5.3.1) and (5.3.2), repeated here,

$$\phi = \frac{1}{29.8}\left[\frac{r}{\sqrt[4]{\dfrac{\overline{D}x\overline{D}y}{\overline{E}x\overline{E}y}}}\right]^{\frac{1}{2}} = 0.977 \qquad (5.3.2b)$$

$$NASA\,\gamma = 1 - 0.901(1 - e^{-\phi}) = 0.438 \qquad (5.3.1)$$

Step 3: Calculate the curved-cylindrical buckling analysis correlation factor, γ_μ, using eqn. (5.3.4), repeated here, and correlation factors from Table 5.6,

$$\gamma_\mu = \gamma_{\mu K} + \gamma_{\mu C1}\frac{|D_{13}|+|D_{23}|}{|D_{11}|+|D_{22}|} + \gamma_{\mu C2}(NASA\,\gamma) \tag{5.3.4}$$

$$\gamma_\mu = 0.3956 - 0.1144(0.04) + 0.8751(0.438) = 0.7743$$

Step 4: Calculate the theoretical buckling load ($N_{x,theoretical}$)

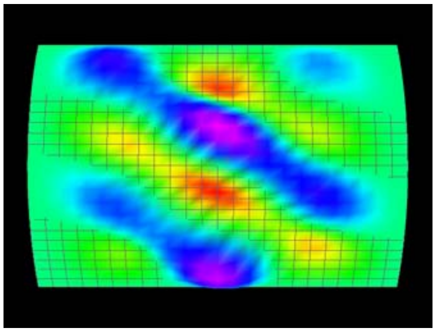

HyperSizer Raleigh Ritz
Buckling = 805.4 (lb/in)

The HyperSizer Raleigh Ritz solution is used to compute the theoretical buckling load, see figure to the right. For the given dimensions, boundary conditions, radius of curvature and unsymmetric B_{ij} stiffness terms if they exist:

$$N_{x,theoretical} = 805.4\ (lb/in)$$

Step 5: Calculate the predicted buckling load ($N_{x,pred}$)

$$N_{x,pred} = (N_{x,theo})(\gamma_\mu) = (805.4)(0.7743) = 623.7\ (lb/in)$$

Step 6: Compare the predicted buckling load to the experimental buckling failure load ($N_{x,experimental}$)

From Table 5.2, we find that the experimental buckling failure load for Specimen 69A is 5500 lb. For the 9" wide panel this gives a unit load of $N_{x,experimental}$ = 611.1 lb/in. The ratio of experimental buckling load / predicted buckling load = 611.1/623.7 = 0.980. The following summary table for all five [02/±45]s curved laminates shows HyperSizer predicted (mean) buckling load compared to the test failure load. No safety or reliability is included in this table.

Table 5.8, HyperSizer theoretical, predicted and actual failure loads for 5 test articles.

Experimental Test Group	r/t ratio	NASA γ knockdown	γ_μ	HyperSizer Theoretical (lb/in)	HyperSizer Predicted (lb/in)	Experimental Failure Load (lb/in)	Ratio: Experimental / Predicted
69A	234	0.438	0.774	805.4	623.7	611.1	0.980
69B	230	0.441	0.777	836.3	649.7	568.2	0.875
69C	246	0.430	0.767	726.8	557.8	598.3	1.073
69D	238	0.436	0.772	778.8	601.3	590.0	0.981
69E	237	0.436	0.773	785.3	606.9	633.3	1.044
Average		0.436	0.773	786.6	607.9	600.2	0.9906

Note that as expected and desired, some of the predicted buckling loads are higher and some are lower than the experiment failure load, but not by much. At this point we are fairly accurately computing the average buckling failure load. The next step is to apply a reliability.

Step 7: Compute the allowable buckling load (Pc,allow)

In order to find the reliability based allowable, we must first determine the relative accuracy of the predicted solution, which is expressed as:

$$P = Average\left(\frac{\text{Experimental}}{\text{Predicted}}\right)_i = 0.9906 \tag{5.7.1}$$

The allowable buckling load is then determined based on the desired level of reliability. The equation for determining the reliability allowable is:

$$N_{x,allowable} = \left(N_{x,theoretical}\right)\left(\gamma_\mu\right)\left(P - K\eta\right) \tag{5.7.2}$$

The value of η is determined by taking the standard deviation of the five test data values for Group 69, normalized by the predicted values.

$$\eta = STDEV\left(\frac{\text{Experimental}_{\text{i}}}{\text{Predicted}_{\text{i}}}\right) = 0.0762 \tag{5.7.3}$$

The value of *K* is determined by the desired reliability. For this example, we will consider 84% reliability or about 1 in 6 probability of failure. As shown in the *K* vs. Reliability Table at the beginning of Volume 3, for 84% reliability, *K* = 1.0, therefore the allowable load is:

$$\begin{aligned} N_{x,allowable} &= \left(N_{x,theoretical}\right)\left(\gamma_\mu\right)\left(P - K\eta\right) \\ &= (805.4)(0.774)\left(0.9906 - 1.0(.0762)\right) = 570\ (lb/in) \quad (84\%\ reliability) \end{aligned}$$

For this set of test data, we expect 84% (or 5 out of 6) of the panels to fail at or above 570 lb/in. Indeed as seen in Table 5.8, out of these five tests, only Panel 69B (Failure Load = 568 lb/in) failed below this allowable of 570 lb/in. Increasing the reliability to 90% (1 in 10 chance of failure) gives an allowable load of 558.6 lb/in. In this case none of the 5 panels in our samples would be expected to fail and indeed none of them do.

5.7.1 Cylindrical Buckling of Beer Cans

The HyperSizer Raleigh-Ritz buckling analysis and the correlation factor analysis methods were recently applied to 32 steel beer cans that were tested for cylindrical buckling by Arbocz [5.4]. The beer cans were stainless steel and tested in a special purpose testing machine at the University of Delft in 1987 [5.5]. Professor Arbocz of presented results from this set of 32 can crush tests at the AIAA SDM 2001 conference.

5.7.1.1 Theoretical Failure Loads

The theoretical and allowable buckling loads for these cans, as calculated with three different analysis methods, are presented in Table 5.10. **The three independent analyses, using substantially different methods, all compute nearly the same theoretical buckling loads and therefore the HyperSizer correlation factors presented herein are equally applicable to any of these methods.**

STAGS Theory = 1778 lbs.

The first, and most advanced of the three methods is the **STAGS** non-linear FEA program, which was applied to this problem by Professor Arbocz [5.4]. In the STAGS analysis, imperfections and non-linear collapse behavior was studied in detail.

HyperSizer Theory = 1764 lbs.

HyperSizer Raleigh Ritz solutions were performed for two different boundary conditions as shown in Fig. 5.8, with little difference in allowable buckling load predicted between them.

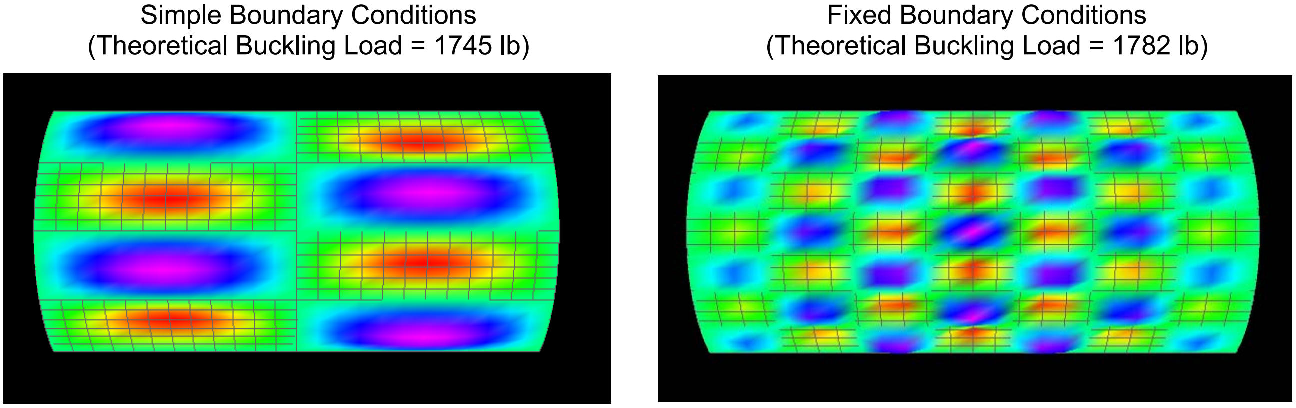

Simple Boundary Conditions
(Theoretical Buckling Load = 1745 lb)

Fixed Boundary Conditions
(Theoretical Buckling Load = 1782 lb)

Fig. 5.8, HyperSizer Raleigh Ritz buckling solutions for the beer can under compression. The average value of 1764 (lb) is used.

NASA closed form theory = 1763 lbs.

The NASA SP-8007 [5.1] closed form solutions were performed as follows. The equations shown are for buckling of thin-walled circular cylinders and are to be used in conjunction with empirical knockdown factors. The critical buckling stress, $\sigma_{x,cr}$, is calculated from,

$$\sigma_{x,cr} = \frac{\lambda E}{\sqrt{3(1-\nu^2)}} \frac{t}{r} \tag{5.7.4}$$

where E is the elastic modulus, t is the wall thickness, ν is poisons ratio, and r is the radius. For the special case where $\nu = 0.3$,

$$\sigma_{x,cr} = 0.6\ E\frac{t}{r} \tag{5.7.5}$$

Table 5.9, Beer Can Data

Variable	Metric Units	English Units
r	33 mm	1.2992 in
t	0.1 mm	0.003937 in
E	2.08x105 N/mm2	30.17x10^6 psi
ν	0.3	0.3

Using the data in Table 5.9, with Equation (5.7.5),

$$\frac{r}{t} = 330$$

$$\sigma_{x,cr} = 54.90\, ksi, \quad P_{cr} = (\sigma_{x,cr})(t)(2\pi r) = 1763\ lbs$$

Boundary Conditions

The STAGs FEA solution is based on fixed BCs. The average of fixed and simple BCs are used for the HyperSizer theoretical solution. The BCs for which the NASA solution is based are not specified in NASA SP-8007 report [5.1].

5.7.1.2 Computed Buckling Knockdown Factors and Allowable Loads

STAGS

The knockdown used by STAGs was not based on statistical data, but rather is a purely computed value based on the effect of imperfections. The knockdown is 0.44, giving an allowable load of (.44)(1778)=782 (lb). See Arbocz [5.4].

NASA SP-8007

The NASA buckling knockdown is intended to provide a constant 99% reliability. The empirical buckling knockdown factor, γ, is given by

$$\gamma = 1 - 0.901(1-e^{-\phi}) \qquad \phi = \frac{1}{16}\sqrt{\frac{r}{t}}, \quad for\frac{r}{t} \leq 1500 \tag{5.7.6}$$

Using the data in Table 5.9, with equation (5.7.6),

$$\frac{r}{t} = 330, \quad \phi = 1.1353 \qquad \gamma = 0.3885 \qquad P_{allowable} = (1763)(0.3885) = 685\ lbs$$

HyperSizer

Because the NASA knockdown is based on 99% reliability, we will set our HyperSizer knockdown also to a 99% reliability (K=2.33).

$$\gamma_{allowable} = \gamma_{\mu}\left(P_{ratio} - 2.33\eta\right) \tag{5.7.7}$$

The HyperSizer equivalent knockdown is computed two ways. The first way is by using the generally defined CFs (η=0.136 and μ_1 = 0.3956, μ_2 = -0.1144, and μ_3 = 0.8751; see section 5.5) from a larger collection of other test data, and does not include these 32 data points.

From above, the NASA knockdown is computed to be γ = 0.3885. Therefore the HyperSizer effective knockdown, γ_μ, is

$$\gamma_{\mu} = \frac{\mu_1 + \mu_2 \dfrac{|D_{13}| + |D_{23}|}{D_{11} + D_{22}} + \mu_3 \gamma_{nasa}}{0.8\left(1 + \dfrac{b}{\pi\, r}\right)} \qquad b \le \frac{\pi r}{2} \quad (\textit{quarter cylinder})$$

$$= \frac{0.3956 + 0 + .8751(.3885)}{0.8\left(1 + \dfrac{2.040}{\pi 1.2992}\right)} = 0.6130$$

where b=(πr/2)=2.04 is ¼ of the cylinder circumference. The combined effect of the three μ_i terms is γ_μ = 0.6130. Using equation (5.7.7).

$$\gamma_{allowable} = 0.6130\left(0.9847 - 2.33(.136)\right) = 0.4094$$

$$P_{allowable} = 1764\left(0.4094\right) = 722\ lb$$

The second way is by using specifically defined CFs (η=0.10 and γ_μ = 0.5119) based solely on these 32 data points and is included to show the statistics 'in-fact.' This is accomplished by performing statistics just on the 32 test data points, as summarized in Table 5.11.

η = 0.1

γ_μ = (average test) / (theoretical) = 903 / 1764 = 0.5119

using equation (5.7.7)

$$\gamma_{allowable} = 0.5119\left(1 - 2.33(.1)\right) = 0.3926$$

$$P_{allowable} = 1764\left(0.3926\right) = 693\ lb$$

5.7.1.3 Prediction Summary

Table 5.10, Beer Can Failure Allowables (crushing load)

Method	Theoretical buckling load (lbs)	Knockdown factor	Allowable buckling load (lbs)
STAGS [5.4] non linear FEA	1778	0.44 [3]	782
HyperSizer Raleigh Ritz CFs based on other data[1]	1764	0.409 [4]	722
HyperSizer Raleigh Ritz CFs based only on this data[2]	1764	0.3926 [4]	693
NASA SP-8007 closed form solutions	1763	0.3885 [5]	685

[1] The HyperSizer correlation factors are defined statistically for 109 other test data, and does not include these 32 cans. Intended for general use on any curved buckling analysis.

[2] The HyperSizer correlation factors are defined statistically for just these 32 cans. Specific to these tests.

[3] computed to account for panel imperfections [5.4]

[4] HyperSizer computed knockdown (for 99% reliability).

[5] empirical NASA SP-8007 knockdown (for 99% reliability).

Referring to Table 5.10, the NASA SP-8007 buckling knockdown is defined a-priori and not adjusted to include these 32 data points. Similarly, the HyperSizer computed knockdown (0.409) is also defined a-priori and not adjusted to include this these 32 data points. Therefore these 32 tests points represent a true verification for both. However, the second HyperSizer computed knockdown (0.3926) is based solely on these 32 data points and is included to show the statistics 'in-fact.' The Probability Density Function (PDF) of the beer can test data using the test average and standard deviation is plotted in Fig. 5.9.

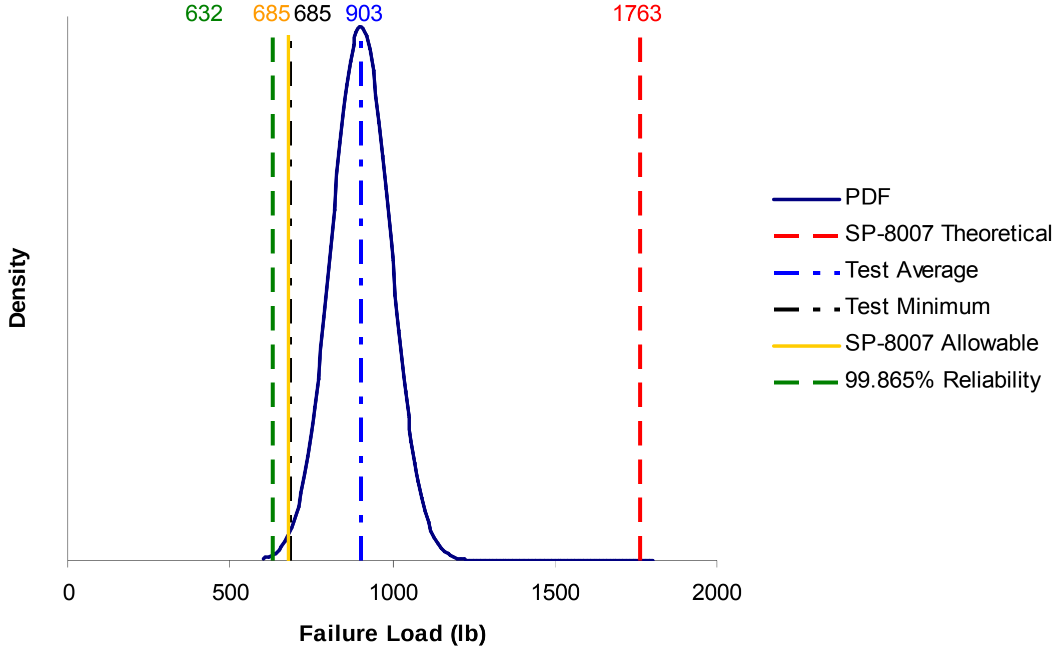

Fig. 5.9, PDF for 32 beer can buckling test articles. The NASA SP-8007 theoretical buckling load is shown as the vertical red line. The other plotted vertical lines are the test average (903) and minimum (685), and the SP-8007 buckling allowable load.

5.7.1.4 Test Data Failure Loads

Table 5.11 shows the complete listing of the experimentally measured beer can buckling loads. Table 5.12 shows the resulting statistical values from the data. Fig. 5.10 is a histogram of the 32 failure loads. Note the minimum value (685 lb) is more than 10% lower than the next lowest failure load, and in some cases might be considered to be an outliner. In the present analysis, however, this point was not considered and outliner and was included in all calculations.

The average failure load (statistical mean) of the 32 tests was 4.017 kN (903 lbs). Using a 3σ limit on the test data, that is three standard deviations from the mean to the lower left end of the bell curve, would put the load limit at 4.017 – 3*0.402 = 2.811 kn (632 lbs). The 3σ limit represents 99.865% confidence in the load carrying capability of a can.

Table 5.12, Beer Can Test Summary Failure Results

	Metric Units (kN)	English Units (lbs)
Average (mean)	4.02	903
Min	3.05	685
Max	4.68	1052
σ	0.402	90.4
$\eta (= \sigma / \mu)$	0.1	0.1
3σ (1 failure in 1000)	2.81	632

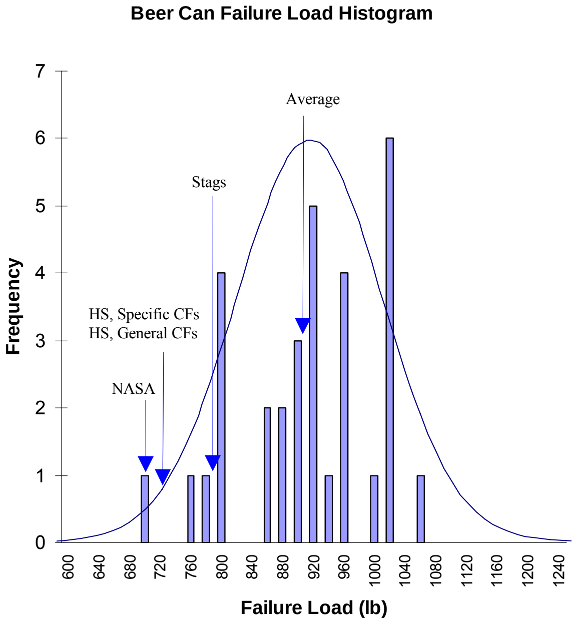

Fig. 5.10, Histogram of the 32 beer can buckling failure loads.

Table 5.11, 32 beer can buckling failure loads.

Failure Load (lb)	
685	
753	NASA HS, Specific CFs HS, General CFs
771	
782	Stags
789	
794	
798	
859	
859	
861	
875	
897	
897	
899	
901	
901	Average
906	
906	
917	
935	
944	
951	
953	
960	
996	
1003	
1005	
1009	
1012	
1012	
1014	
1052	

5.7.1.5 Correlation Summary

STAGS Allowable Load
It is interesting to note that the computed knockdown factor as presented in [5.4] was 0.44. This knockdown is not based on statistical data, but rather is a purely computed value based on the STAGs computed effect of imperfections. The buckling allowable based on this knockdown of 0.44 is 782 *lb*. Three of the 32 cans failed below this value.

HyperSizer Allowable Load
The HyperSizer allowable load =**693** based on the specifically defined CFs (η=0.10 and γ_μ = 0.5119) from these 32 data points.

The HyperSizer allowable load =**722** based on the generally defined CFs (η=0.136 and μ_1 = 0.3956, μ_2 = -0.1144, and μ_3 = 0.8751; see section 5.5) from a larger collection of other test data, that does not include these 32 data points.

The lowest failure load was 685. However, this minimum value is considered an outlier since it is more than 10% less than the next lowest failure load of 752. So only one can, a possible outlier, failed lower than either buckling allowable.

NASA SP-8007 Allowable Load
The NASA SP-8007 empirical buckling knockdown of 0.3885 along with a theoretical buckling prediction of 1763 provides a buckling allowable of 685, which coincidentally matches exactly the lowest failure load of the 32 cans.

The corresponding sigma level of confidence for a knockdown of 0.3885 can be backed out:

$$\gamma_{allowable} = \gamma_\mu(1 - K\eta)$$

with *NASA* $\gamma_{\text{allowable}}$ = 0.3885, γ_μ = (average test)/(theoretical) = 903/1763 = 0.512, and η = .1, this causes the NASA *K* factor to be ≈ 2.4 which translates to ≈99.2% reliability.

5.7.1.6 Final comments

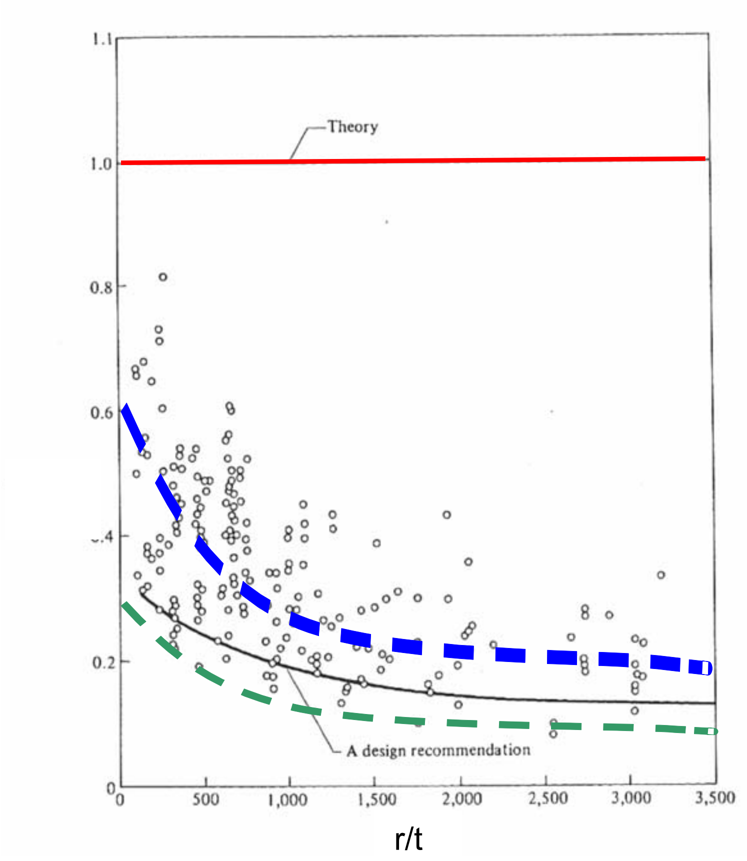

Fig. 5.11, Traditional one knockdown approach to cylindrical panel buckling, noted as a design recommendation. The black curve is the original NASA SP-8007 knockdown, the green curve, a possible more conservative knockdown, and the blue curve, the average (typical) failure. The original, one constant knockdown equation doesn't give insight into the average test data, nor does it allow the engineer to choose his level of reliability, such as the green curve.

Fig 5.11 shows cylindrical panel buckling test data as points. Each test data point is normalized against its theoretical value (vertical axis). The horizontal axis represents decreasing theoretical accuracy as the radius/shell thickness (r/t) ratio increases. Fig. 5.11 is related to the NASA SP8007 report. Note the large discrepancy between theory (red line) and test results, i.e. inaccuracy of theoretical. The design recommendation is an established knockdown defined as an equation that includes the r/t ratio. So regardless if the knockdown is expressed as a single value or as a curve fit equation, the NASA one knockdown approach defines a once-and–for-all acceptable limit of risk.

Other curve fit equations, such as the blue and green curves can be defined based on a function of selected parameters. Even though the knockdown (black curve) is somewhat dynamic based on changing variables, in this case the r/t ratio, the first shortcoming with this traditional approach is that the acceptable level of risk (black curve) is "cast-in-stone" when first defined, and for the most part unchanging as more test data becomes available. In fact, the actual comparison is rarely known by the practicing engineer.

A second shortcoming is the acceptable level of risk defined originally may not meet the reliability requirement of your particular design (shown as green dashed-curve). A program manager should be able to choose required knockdown/reliability for each design project. Furthermore, insight and flexibility should be provided to bring each analysis failure mode to a consistent value.

The third shortcoming, which also relates directly to the goal of efficient structural certification using analysis, is that with a single knockdown that takes the theoretical value (shown as red line) down to an allowable design-to value, does not provide nor expose any knowledge of an average or expected typical failure load, represented with a blue curve. So unlike being able to use “typical” material properties for test predictions, the user is left to perform test correlations using a “design-to” failure analysis allowable, which should for almost all cases significantly under predict, and be very conservative to test results.

5.8References

5.1 NASA SP-8007, Buckling of Thin-Walled Circular Cylinders, NASA Space Vehicle Design Criteria (Structures), August 1968.

5.2 Collier Research Corporation, "Consistent Structural Integrity and Efficient Certification with Analysis", SBIR Contract/PO # 7067581 Final Report, Volumes 1, 2, and 3, August 2004.

5.3 Wilkins, D.J., “Anisotropic Curved Panel Analysis,” General Dynamics, Fort Worth, TX, May 15, 1973, ADA309250.

5.4 Arbocz, J., Starnes, J., Nemeth, M., “On the Accuracy of Probabilistic Buckling Load Predictions”, AIAA-2001-1236.

5.5 Verduyn, W. D. “A Testing Machine for Statistical Analysis of Small Imperfect Shells” Report LR-357, Delft University of Technology, Sept 1982.

PART C: NEW ANALYSIS METHODS DEVELOPED

6 Composite Bonded Joint Stress Analysis and Failure

A powerful new analysis capability, now available in HyperSizer, extends its thermoelastic and failure analysis formulations to examine the detailed stress fields of composite bonded joints and determine their margins of safety. The goal of this new capability is to provide an efficient tool that is fast enough to be included in preliminary design, but still accurate enough to achieve near final design solutions. This new capability is called BondJo.

In current practice, the complexity of bonded joint behavior requires generation and analysis of detailed finite element models that are time consuming to develop, run, and post-process. Such detailed finite element analyses, which must include 3D solid elements, are seldom done in preliminary design, where the design dimensions, materials, layups and loads are constantly changing. Therefore, the joint analysis is many times left to final design where changes become much more problematic and costly to implement. More frequently, specialty type codes such as A4EI by Hart-Smith are used in industry as rapid analysis tools. BondJo falls within this class of tools but is more accurate and solves more general loadings than A4EI (see section 6.3.1).

BondJo captures the primary physics of the bonded joint problem in a very rapid procedure, (on the order of 1/40th of a second) meaning that bonded joint analysis not only can be performed in preliminary design, but actually becomes a part of the structural optimization procedure.

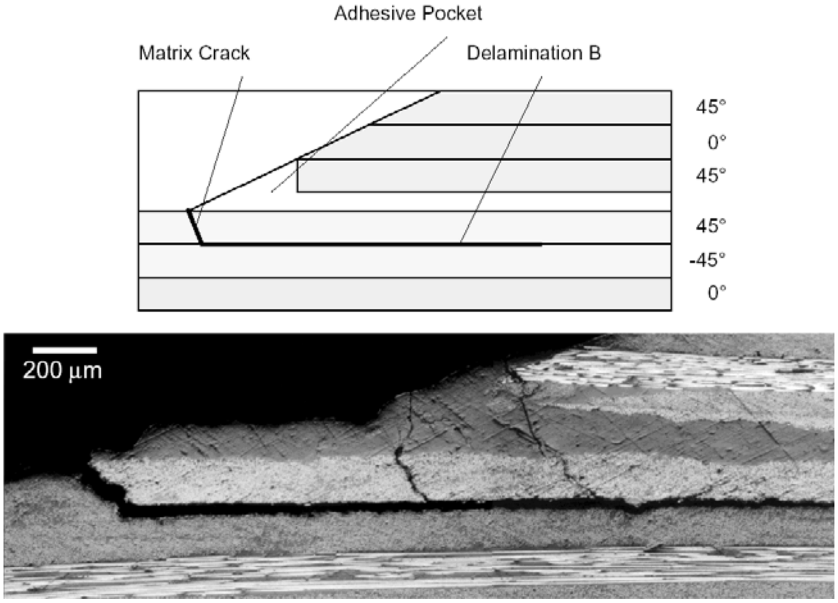

Fig. 6.1, HyperSizer now includes the ability to predict composite bonded joint failure to help avoid failure such as this.

BondJo resolves the full in-plane and interlaminar stress fields in the adherends and the shear and peel stresses in the adhesive layer. In most bonded joint failures, damage initiates close to the joint free edge, propagates into the first one or two plies of the adherends and causes either delamination or fracture of laminated adherends. This type of failure is shown in Fig. 6.1. In the failure of adherends, the out-of-plane stresses play an important role, particularly in delamination. BondJo's ability to predict these stresses, coupled with its speed, makes BondJo a powerful software tool for preliminary aircraft design.

6.1 Rapid, Accurate and Reliable Failure Prediction

The purpose for developing the new HyperSizer-BondJo analysis code is predicting failure for composite bonded joints. Fig. 6.1.1 shows a typical skin-stringer type of aircraft structure, which could represent for example a wing or fuselage. In previous versions, HyperSizer could isolate a section of this structure (b) for strength and panel stability analysis; however without the bonded joint analysis capability, it would miss failure modes of the type shown at (c). This type of delamination failure is very common in the 1st or 2nd facesheet ply close to the bonded stiffeners, therefore capturing this failure early in the design process is key.

In addition to delamination failures, several other failure modes have been identified as important for bonded joints. Heslehurst and Hart-Smith [6.1.1] identified 6 broad categories of failure for bonded joints as shown in Fig. 6.1.2. Categories 'a' and 'b' include failures that occur in the adherends while 'c' through 'f' include failures that occur in the adhesive layer.

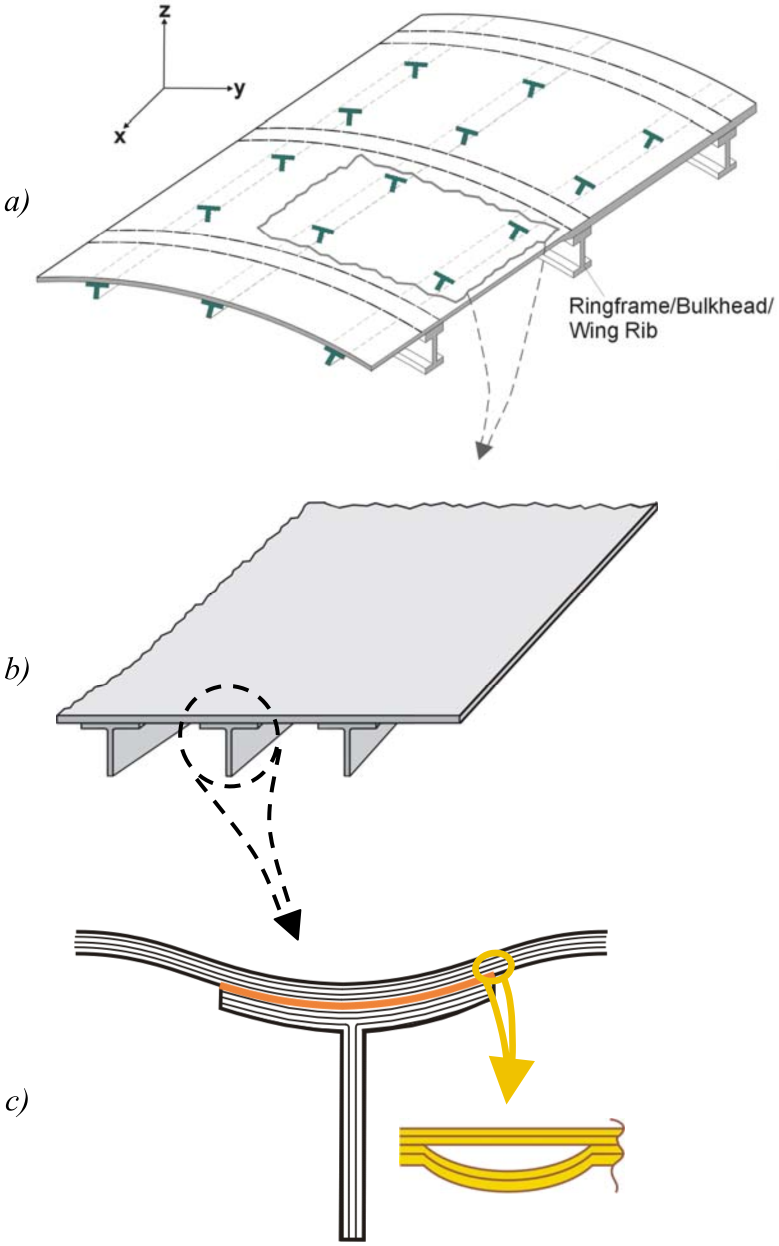

Fig. 6.1.1, A common composite failure mode for stiffened aircraft structure occurs at the reentrant corner of a bonded flange.

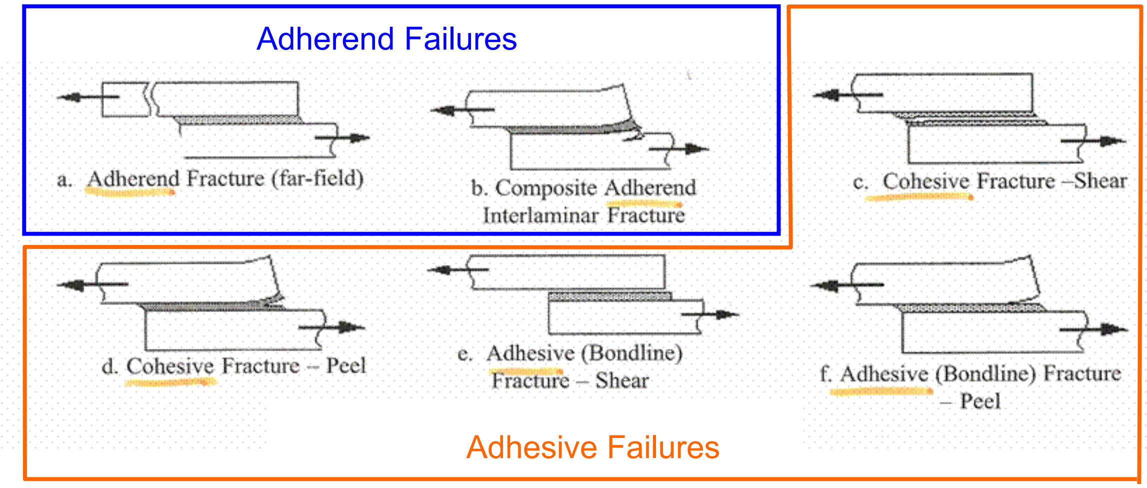
Adherend Failures
a. Adherend Fracture (far-field)
b. Composite Adherend Interlaminar Fracture
c. Cohesive Fracture –Shear
d. Cohesive Fracture – Peel
e. Adhesive (Bondline) Fracture – Shear
f. Adhesive (Bondline) Fracture – Peel
Adhesive Failures

Fig. 6.1.2, Failure modes in adhesively bonded joints identified by Heslehurst and Hart-Smith [6.1.1].

While these figures show failure modes for single lap joints, the issues and the failure modes are the same for all types of bonded joints, including bonded doubler joints that we use to represent the facesheet to stiffener joint of a stiffened panel.

Fig. 6.1.3 again illustrates one of the most common types of failure bonded joints at the stiffener along with a sample failure criterion that attempts to predict that failure. The important thing to note about joint failure criteria (detailed in Section 6.5), is that they rely completely on knowing the stress state in the joint. This particular criterion depends on the interlaminar shear and peel stresses of the adherends, which in the past have been difficult to obtain without detailed FEA. BondJo provides a very rapid method of determining these stresses.

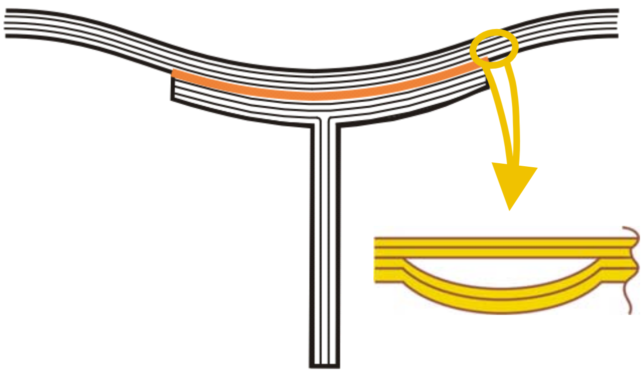

Sample Delamination Failure Criterion

$$\frac{\tau_{13}^2}{\tau_{13,allow}^2}+\frac{\tau_{23}^2}{\tau_{23,allow}^2}+\frac{\sigma_{33}^2}{\sigma_{33,allow}^2}=1$$

Fig. 6.1.3, Failure prediction methods require accurate prediction of out-of-plane interlaminar shear and peel stresses.

6.1.1 References

6.1.1 R. Heslehurst and J. Hart-Smith, The Science and Art of Structural Adhesive Bonding, SAMPE Journal, Vol. 38, No. 2, March/April 2002.

6.2 Accurate Interlaminar Stress Predictions

Deriving accurate stress and strain fields in the bonded joint begins with an understanding of the loading and boundary conditions of the assembled structure. In Fig. 6.2.1 the typical skin-stringer stiffened structure is once again shown, this time with general membrane, bending, out of plane shear and pressure loads. These loads could come from a finite element analysis, fuselage beam theory, or if determinate (such as pressurized tank hoop loads), typed by hand into the HyperSizer interface.

These general airframe loads are reduced by HyperSizer into local "point" loads at the stiffened panel level (b) and these panel loads are sent to BondJo to resolve detailed stresses and strains in the joint itself, such as the interlaminar shear and peel stresses shown (c). Note the generality of loads that are passed to the BondJo analysis including local deflections do to pressure, membrane forces, and bending moments in the direction transverse to the stiffener.

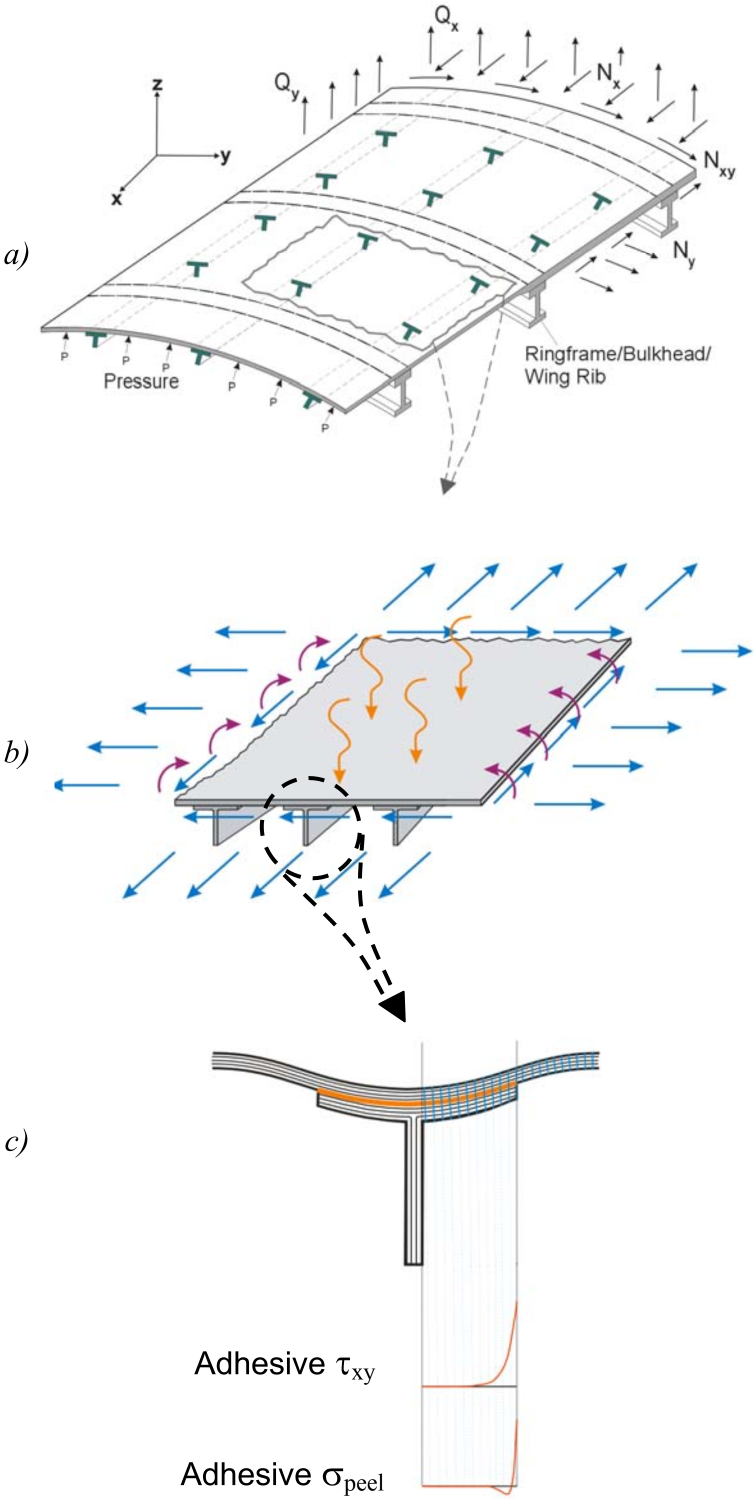

Fig. 6.2.1, HyperSizer rapidly and accurately resolves aircraft stiffened structure panel loads into interlaminar stresses of the adhesive and laminate adherends.

6.2.1 In-Service Structural Panels vs. Standalone Test Articles

In solving for the stresses and displacements, BondJo assumes that these joints deform in “cylindrical bending”, meaning deflections are a function of the panel y direction only. Deflections that vary in the x (or stiffener) direction caused by panel curvature in that direction, are disallowed. These assumptions make it possible to solve stresses and strains in the stiffener bond for in-service stiffened panels in a very efficient manner.

At first glance this might seem limiting; however, the cylindrical bending assumption in this use does not limit its applicability. **For most in-service applications, this assumption and therefore the BondJo methodology is sufficient and appropriate.**

Consider the typical skin-stringer structure shown in Fig. 6.2.2. In this situation, the stiffener to skin bonded joint is a piece of what is referred to as an “in-service” panel. The panel is not isolated from other structure in the same way that a standalone test article would be. A panel in this situation is supported between stiff ringframes, bulkheads or ribs, which causes two effects.

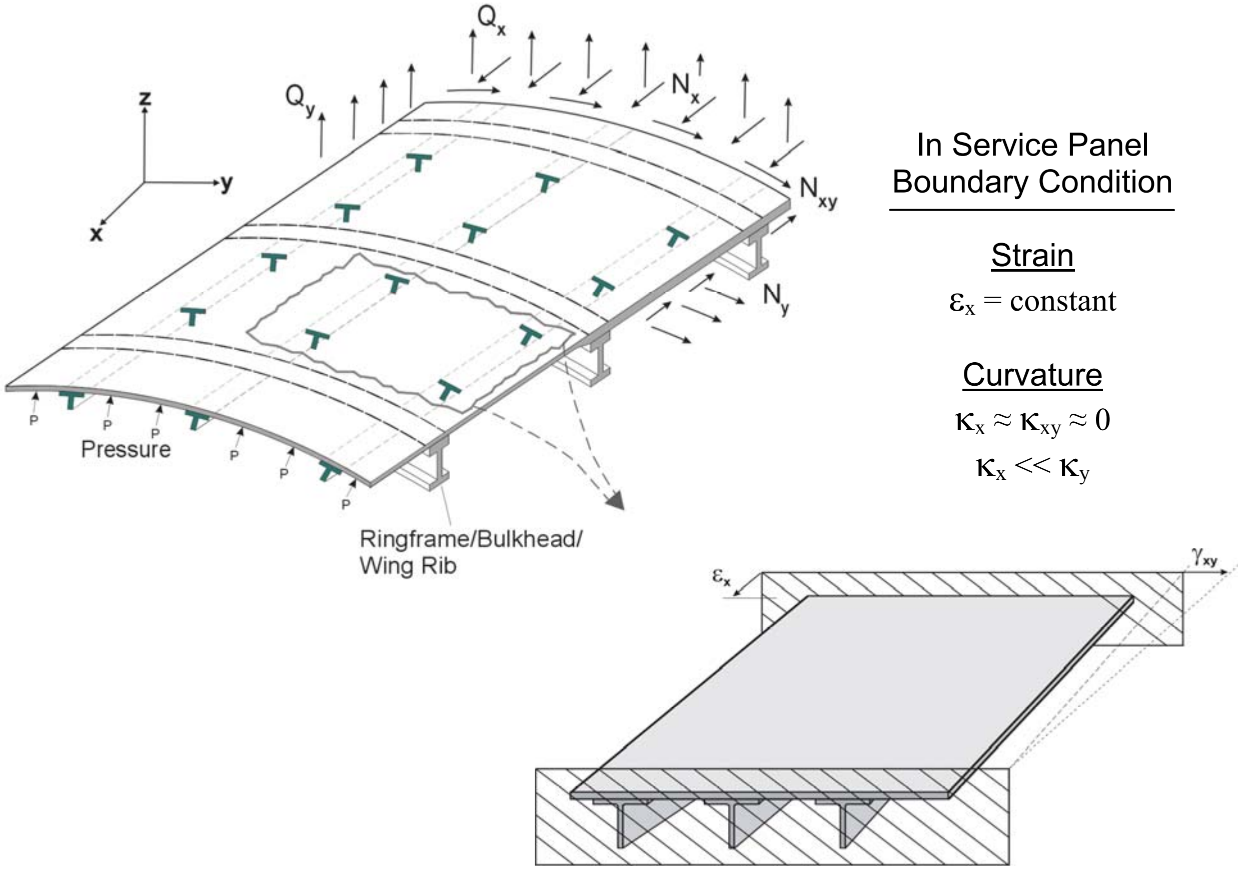
Q_x
Q_y
z
y
x
N_x
N_{xy}
N_y
P
Pressure
Ringframe/Bulkhead/ Wing Rib
In Service Panel Boundary Condition
Strain
ε_x = constant
Curvature
$\kappa_x \approx \kappa_{xy} \approx 0$
$\kappa_x << \kappa_y$
ε_x
γ_{xy}

Fig. 6.2.2, The effective boundary conditions on an “in-service panel” enforced uniform edge deformation.

First, the strain in the stiffener direction, ε_x, will be constant throughout the panel. This is in contrast to the transverse strain, ε_y, which will be different between the panel facesheet and stiffener flange region (which is properly accounted for in BondJo). Second, because the effective bending stiffness of the panel is several orders of magnitude greater in the stiffener direction than in the transverse direction (i.e. $D_{11} >> D_{22}$), the curvature in the stiffener direction will be much smaller than the curvature in the transverse direction. In fact, in most in-service loading conditions, the curvature in the stiffener direction is nearly zero.

In contrast to the in-service panel boundary condition is the case of a small, standalone test article that is free to deform in the stiffener direction. This situation is depicted in Fig. 6.2.3.

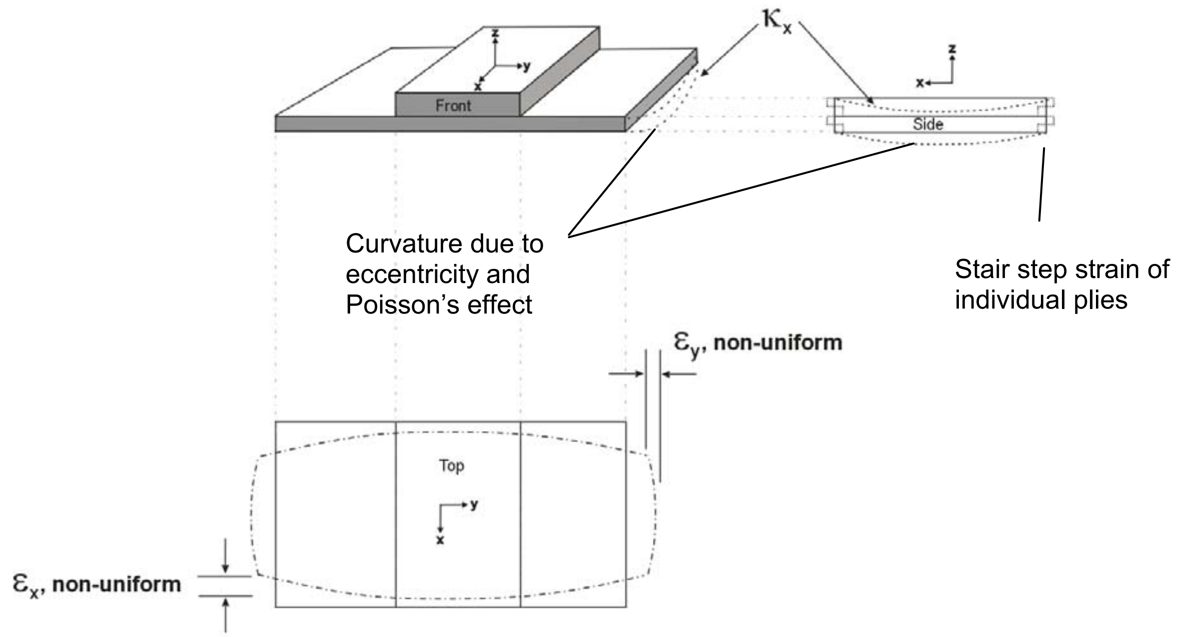
κ_x
z
y
x
Front
z
x
Side
Curvature due to eccentricity and Poisson's effect
Stair step strain of individual plies
ε_y, non-uniform
Top
y
x
ε_x, non-uniform

Fig. 6.2.3, Free boundary conditions on standalone test article permit non-uniform edge deformation and curvature in both axes.

In this situation, unlike the in-service panel boundary condition, the panel is free to do several things that do not occur in true aircraft panels. First, in the top view, it can be seen that the strain in both the x and y directions is non-uniform along the edges. Second, as seen in the side and front views, the panel may curve both perpendicular and parallel to the stiffener direction (this will cause the test article to deform in a saddle shape). Finally, because the individual plies each have primary stiffnesses in different directions, the edge may not remain planar, and in fact could take on a stair step deformation as shown in the side view.

Accurately modeling this type of stand-alone problem requires theory that does not assume cylindrical bending and models full 3-D elasticity for the individual plies. In general, this means going to 3-D solid model FEA. The BondJo methodology is really intended for acreage panel structural problems and would not yet be expected to do well in regions of panel closeouts or stiffener terminations. These types of problems would also require tests or detailed FEA.

Our conclusion then is that for standalone bonded test articles, we would not expect accurate results, however for the majority of in-service aircraft bonded structures, BondJo is appropriate and will generate accurate stress and strain fields.

6.2.2 In-Service Panel Deformations

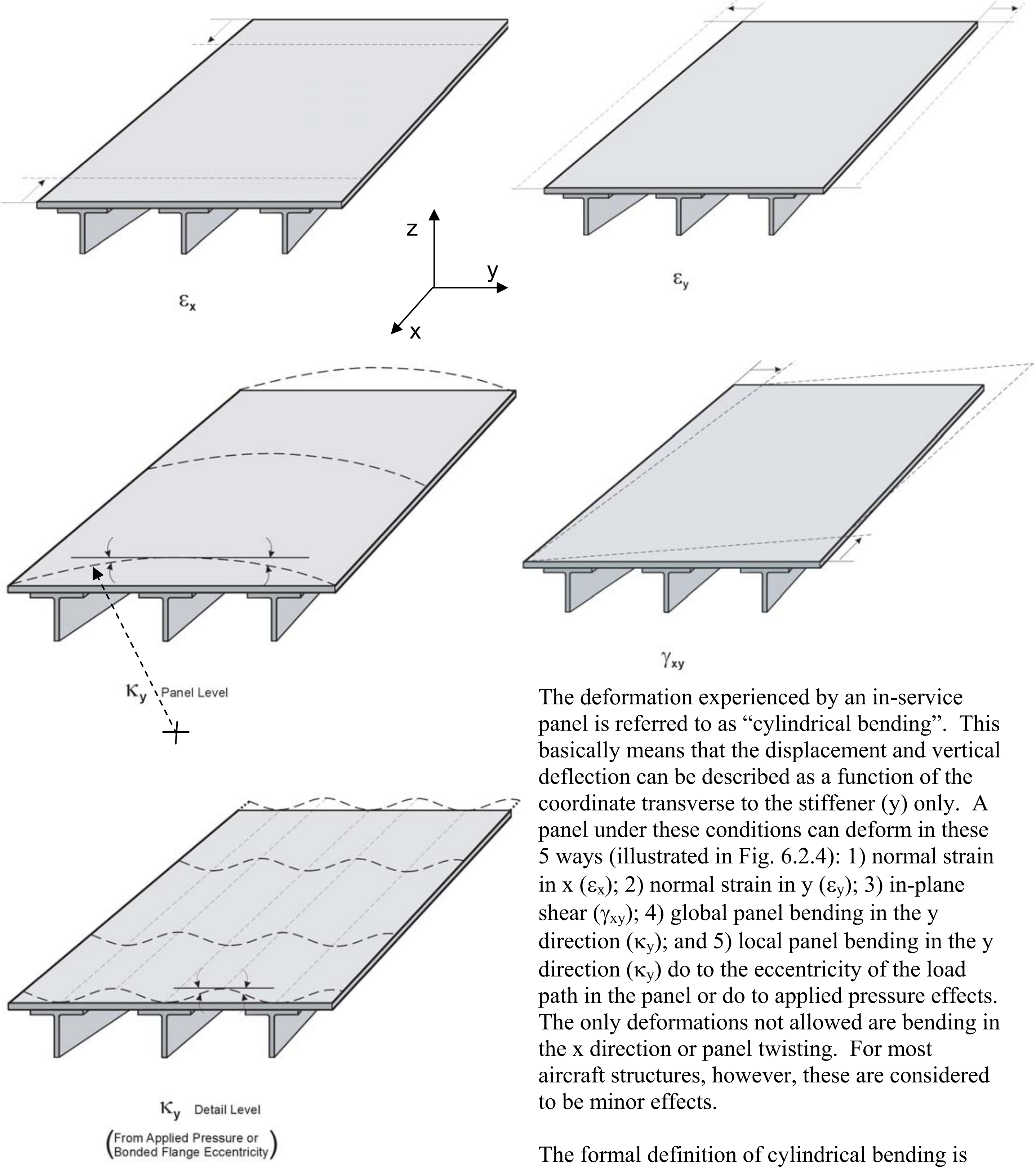
ε_x
z
y
x
ε_y
κ_y Panel Level
γ_{xy}
κ_y Detail Level
(From Applied Pressure or Bonded Flange Eccentricity)

The deformation experienced by an in-service panel is referred to as "cylindrical bending". This basically means that the displacement and vertical deflection can be described as a function of the coordinate transverse to the stiffener (y) only. A panel under these conditions can deform in these 5 ways (illustrated in Fig. 6.2.4): 1) normal strain in x (ε_x); 2) normal strain in y (ε_y); 3) in-plane shear (γ_{xy}); 4) global panel bending in the y direction (κ_y); and 5) local panel bending in the y direction (κ_y) do to the eccentricity of the load path in the panel or do to applied pressure effects. The only deformations not allowed are bending in the x direction or panel twisting. For most aircraft structures, however, these are considered to be minor effects.

The formal definition of cylindrical bending is discussed in detail in Section 6.4.5

Fig. 6.2.4, The five deformations of in-service panels are handled by BondJo

6.2.3 In-Plane and Through Thickness Stress Distributions

When HyperSizer-BondJo executes, its primary results are stress fields throughout the joint and margins of safety. First, plots of stresses and strains are generated in the plane of the joint at any number of user-chosen z locations as shown by the light blue, purple and green circles of Fig. 6.2.5. These plots are represented by a user-defined number of points along the joint (panel y direction) and the failure criteria described in Section 6.5 are applied at each of these points.

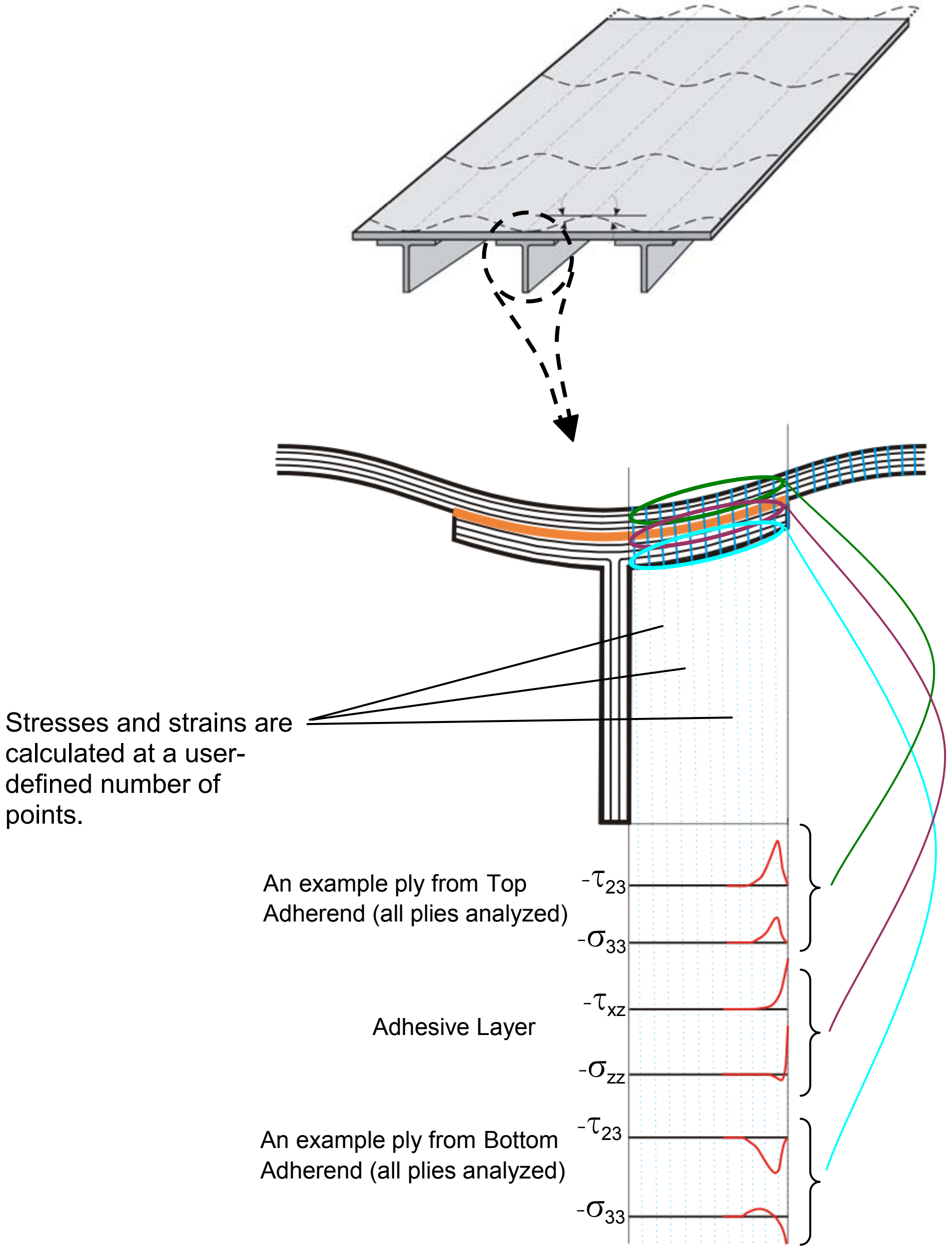
Stresses and strains are calculated at a user-defined number of points.
An example ply from Top Adherend (all plies analyzed)
$-\tau_{23}$
$-\sigma_{33}$
Adhesive Layer
$-\tau_{xz}$
$-\sigma_{zz}$
An example ply from Bottom Adherend (all plies analyzed)
$-\tau_{23}$
$-\sigma_{33}$

Fig. 6.2.5, Interlaminar stress calculations throughout depth of bonded joint, including adhesive and laminated adherends. Note that adhesive stresses are in the panel coordinating system (x, y, z), adherend stresses are in each ply coordinate (1, 2, 3).

In addition to plots in the plane of the joint, BondJo also generates through-thickness stress plots, again at user-prescribed y locations throughout the joint. Fig. 6.2.6 shows how interlaminar shear (red lines) and peel stresses (black lines) vary greatly as the free edge of the joint is approached. Not only are the magnitudes different, but the character of the curves completely change near the free edge as the peel stress goes from compressive to tensile.

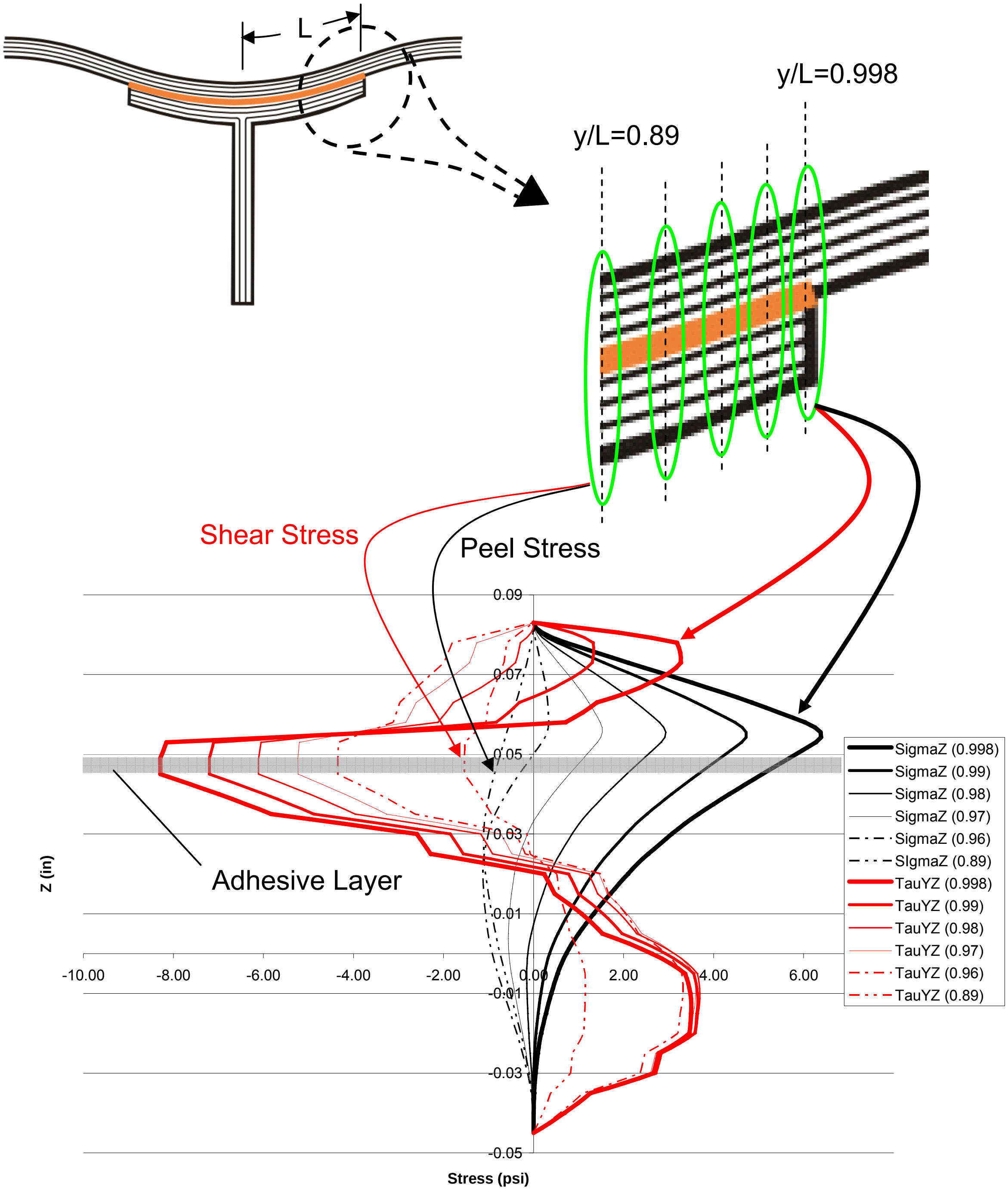

Fig. 6.2.6, Stress calculations performed by HyperSizer through the depth of the joint show how the interlaminar shear and peel stress vary greatly as the free edge of the joint is approached.

In Fig. 6.2.6, the thickest lines represent the through thickness stresses very close to the free edge (approximately ½ ply thickness away from the free edge, which is where the characteristic distance is assumed to be), while the lightest curves represent through thickness stresses approximately 20 ply thicknesses away. Notice that the peel stress plot completely reverses from compression to tension in this short distance. Without a tool like BondJo (or a detailed FEA), this effect would be completely missed. This type of plot illustrates the need for a tool like BondJo that can include these types of effects early in the preliminary design process.

A similar plot of in-plane stresses through the laminate, shown in Fig. 6.2.7, shows how they also vary like the interlaminar stresses near the joint free edge. The effects of the differing ply angles can be seen in the in-plane stress plots, where the slant represents the variation of stress through an individual ply caused from laminate curvature.

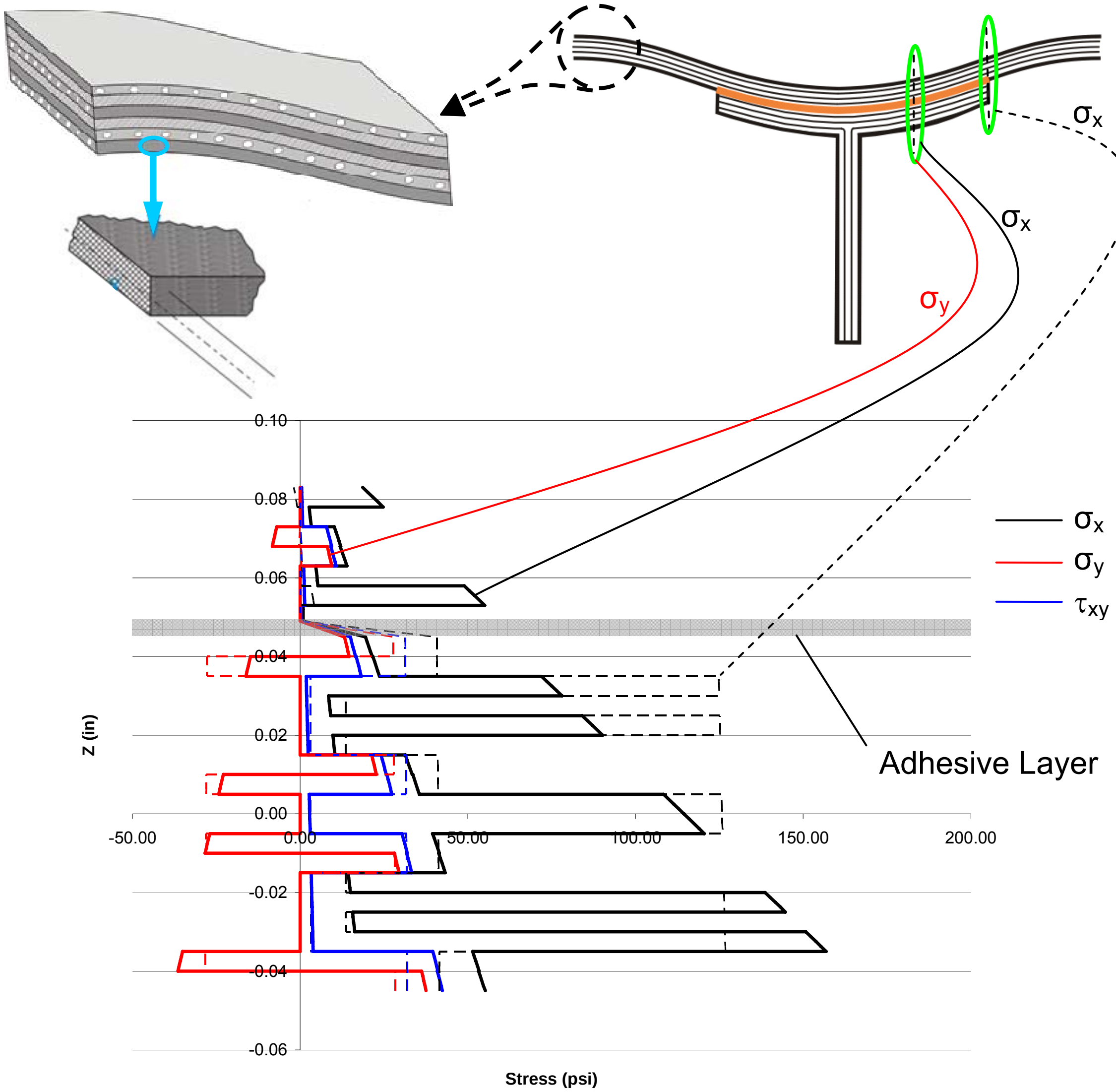

Fig. 6.2.7, In-plane stresses through the laminate and adhesive depth also vary near the joint free edge.

6.2.4 Non-linear Adhesives

Several other effects are applicable to bonded joint analyses that can have substantial effects on both the stress-strain fields and failure predictions. The first of these effects is the non-linear stress-strain relationship of the adhesive layer. Many adhesive materials used in composite bonded joints are known to exhibit non-linear behavior. Several non-linear material models have been developed and implemented in BondJo and are described in Section 6.4.

The net effect of the adhesive non-linear behavior is to lower the overall stresses, especially the peak interlaminar shear and peel stresses at the free edge of the joint, as shown in Fig. 6.2.8.

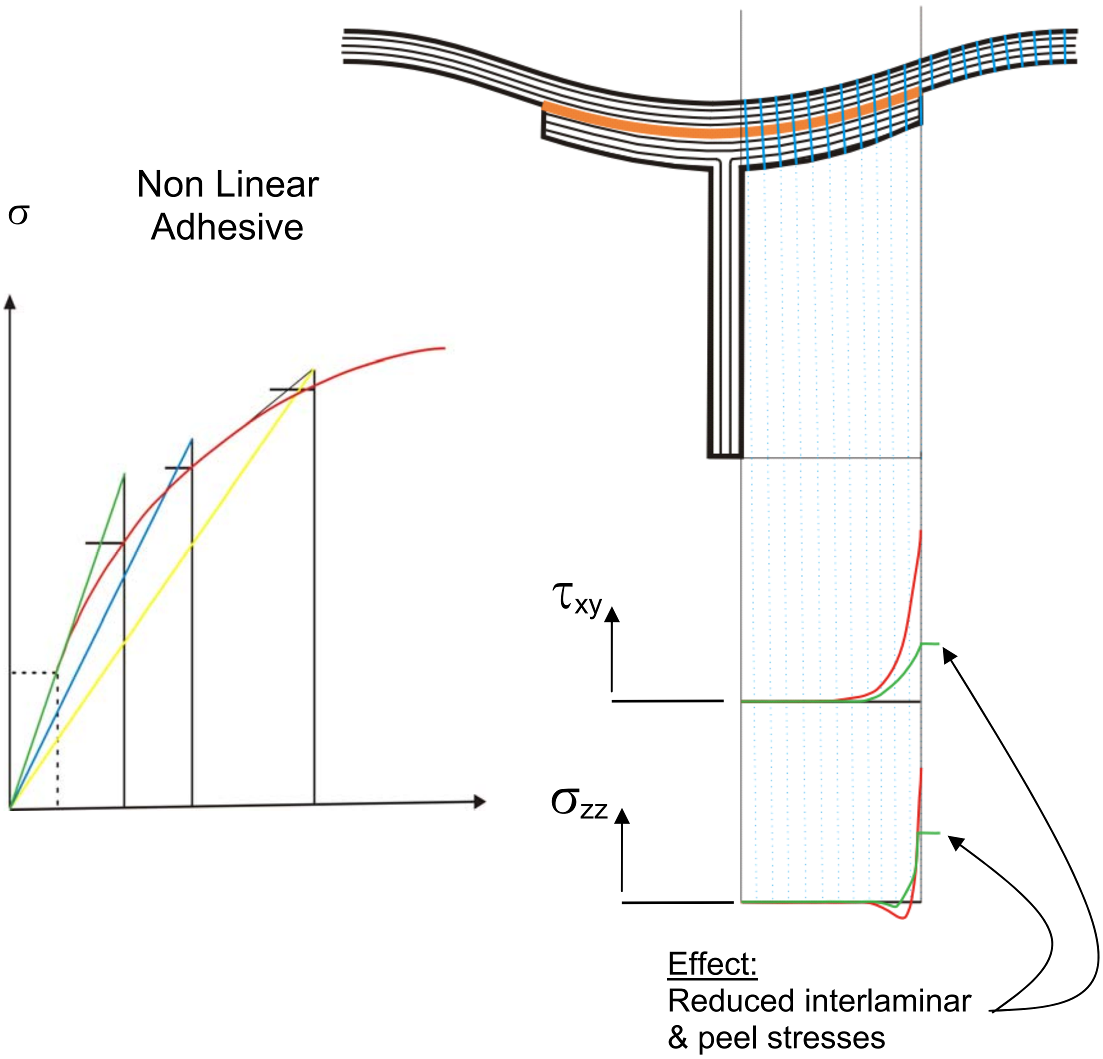

Effect:
Reduced interlaminar & peel stresses

Fig. 6.2.8, Non-linear adhesive effects can reduce peak interlaminar shear and peel stress near the free edge of a bonded joint. Analysis of non-linear adhesives is now available in HyperSizer-BondJo.

6.2.4.1 Bonded Joint Example with Non-Linear Adhesive

The following example problem was modeled with HyperSizer-BondJo's non-linear adhesive joint capability and the results for several non-linear material models are shown on the following pages. Notice how in all cases the peak interlaminar shear and peel stresses are reduced for the non-linear adhesive.

Note: This example uses the typical academic sign convention. See Section 6.11 for details.

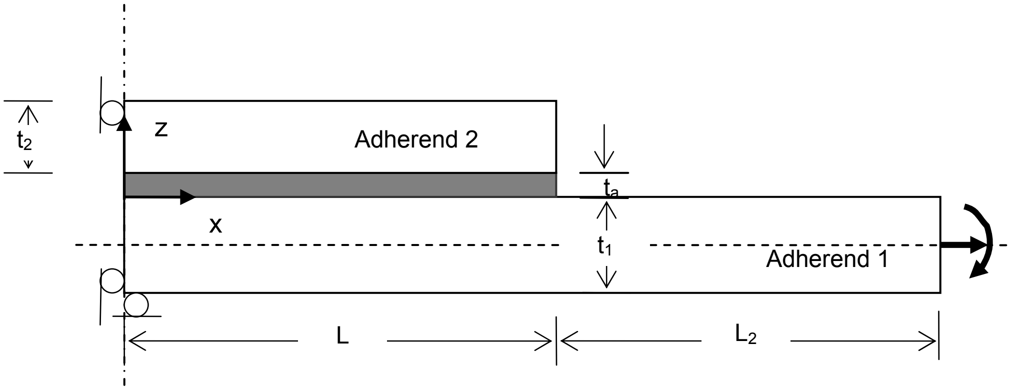

Fig. 6.2.9, Composite bonded doubler joint example configuration

Adherend 1: Graphite/Epoxy $E_1 = 164.0$GPa $E_2 = E_3 = 8.3$ GPa $G_{12} = 2.1$ GPa $\nu_{12} = 0.34$ lay-up: 12 plies (from bottom to top) $[60^o/30^o/0^o/60^o/30^o/0^o/60^o/30^o/0^o/60^o/30^o/0^o]$	Adherend 2: Graphite/Epoxy $E_1 = 164.0$GPa $E_2 = E_3 = 8.3$ GPa $G_{12} = 2.1$ GPa $\nu_{12} = 0.34$ lay-up: 12 plies (from bottom to top) $[0^o/30^o/60^o/0^o/30^o/60^o/0^o/30^o/60^o/0^o/30^o/60^o]$
Adhesive: (epoxy AY 103) Ea = 2.8 GPa $\nu_a = 0.4$ $\lambda = 1.3$ $S_{prop} = 27.0$ MPa $S_{ult} = 71.5$ MPa $e_{ult} = 0.049$ (See Fig. 6.2.X, Stress-strain curve of AY103)	Dimensions: L = 20 mm $L_2 = 30$ mm $t_1 = 1.5$ mm $t_2 = 1.5$ mm $t_{adhesive} = 0.05$ mm ply thickness = 0.125 mm

Loading and Boundary Conditions:

Right Face: $N_{xx} = 600$ N/mm; $Q_x = 0$; $N_{xy} = 0$; $\beta_x = 0$

Symmetry (left side): $\rightarrow u_0 = w = \beta = v_0 = 0$

Number of Segments:

Region 1 (M1) = 10, Region 2 (M2) = 5

Number of x-points within each region = 40

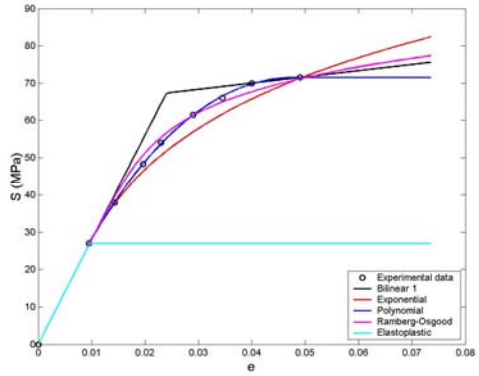

Fig. 6.2.10, Stress-strain curves of epoxy AY103 adhesive

Results

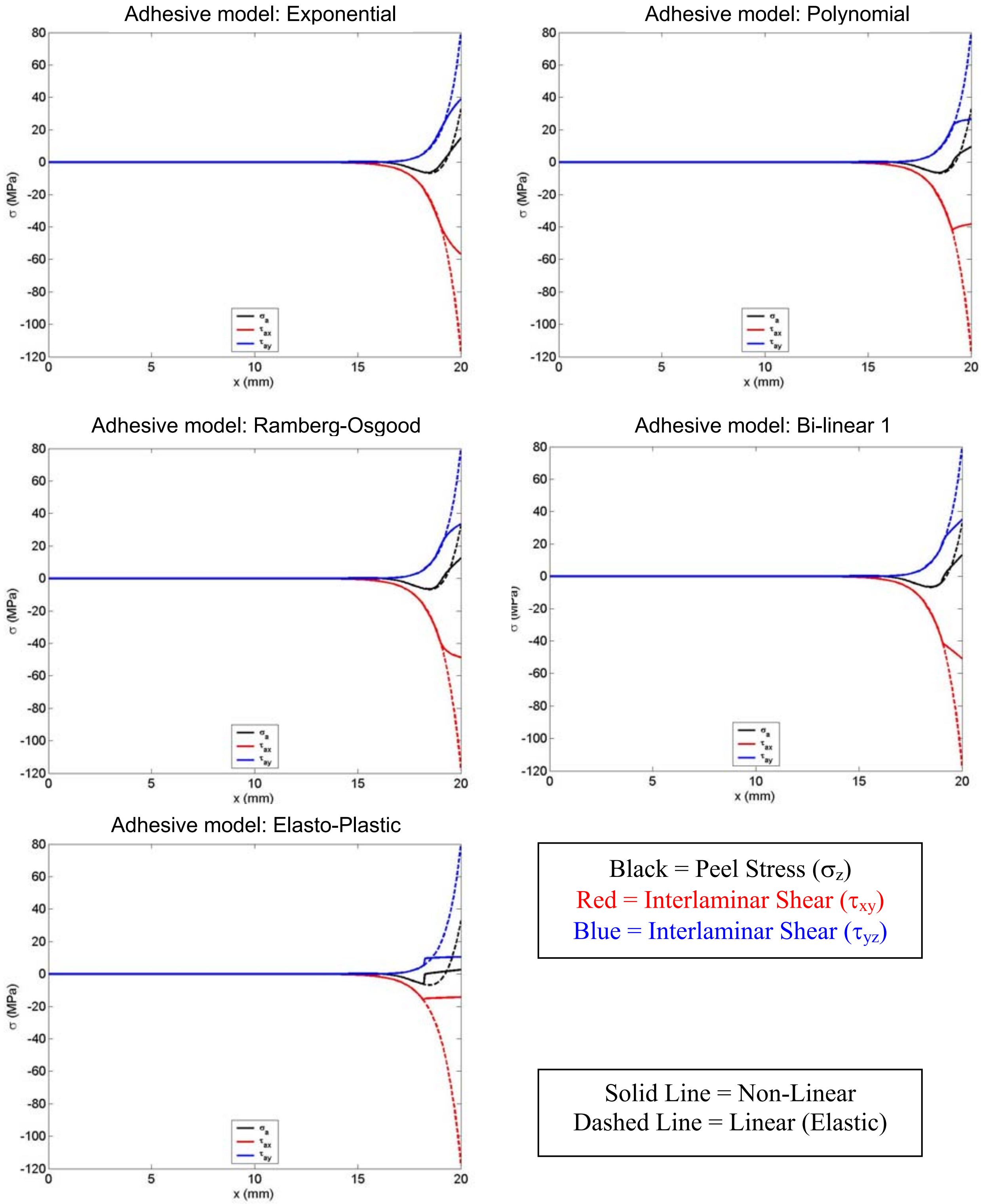

Black = Peel Stress (σ_z)
Red = Interlaminar Shear (τ_{xy})
Blue = Interlaminar Shear (τ_{yz})

Solid Line = Non-Linear
Dashed Line = Linear (Elastic)

Fig. 6.2.11, Linear versus non-linear results for a bonded doubler, five different material models compared

6.2.5 Scarfed and Stepped Joints

A second effect that is included in BondJo is that of a scarfed or stepped adherend as shown in Fig. 6.2.12. While a theoretical formulation for a true scarfed adherend exists, in the commercial HyperSizer software today, the scarfed joint is actually modeled approximately with many small steps. An example of this is shown in the NASA Validation Example (Section 6.10.3) where a 25° scarf was approximated with 9 steps.

Just as with the non-linear adhesive effect, the net effect of scarfing or stepping the adherend is to lower the overall stresses, especially the peak interlaminar shear and peel stresses at the free edge of the joint, as shown in Fig. 6.2.12.

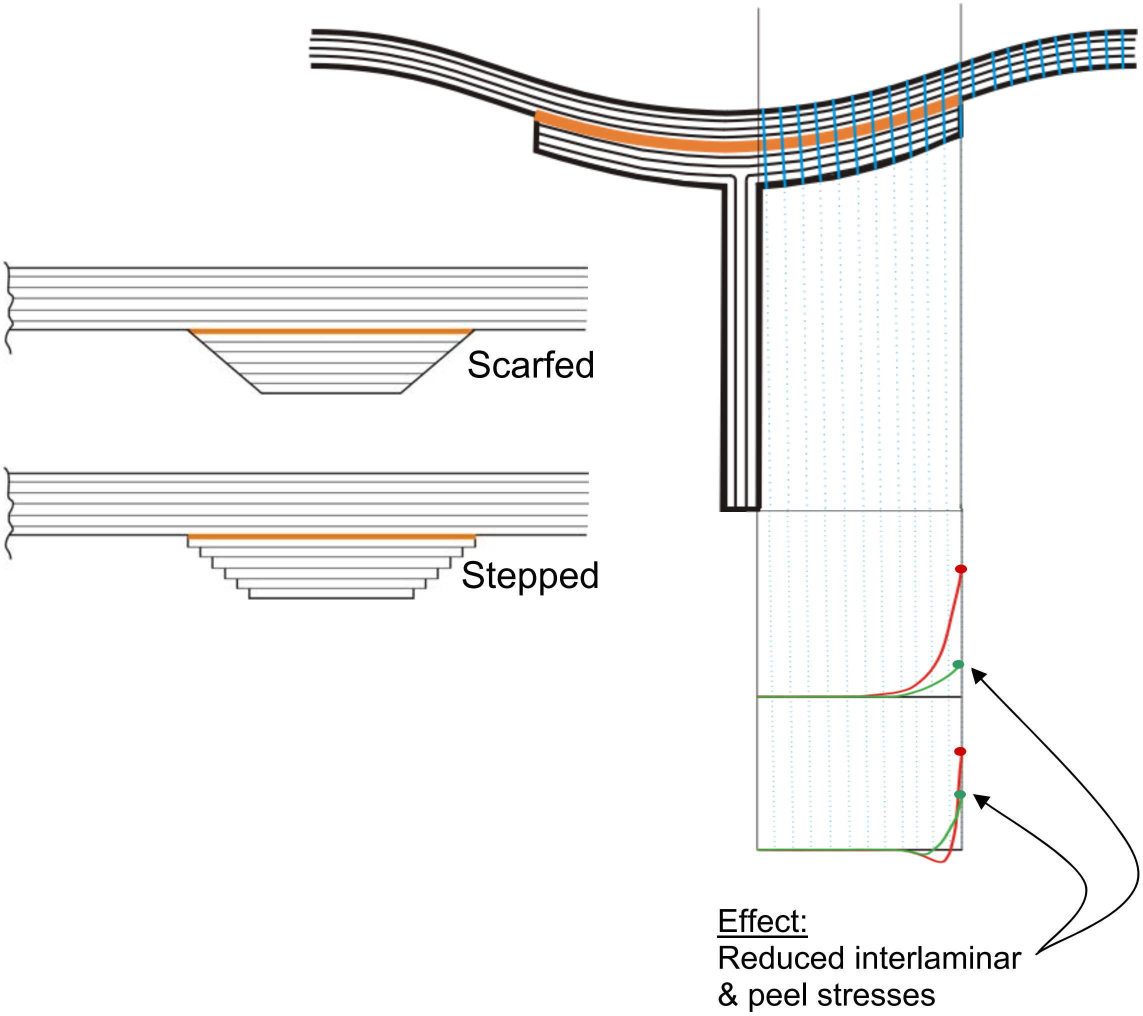

Effect:
Reduced interlaminar
& peel stresses

Fig. 6.2.12, Scarfed or stepped effects can reduce peak interlaminar shear and peel stress near the free edge of a bonded joint. Analysis of the stepped joint configuration is now available in HyperSizer-BondJo.

When BondJo solves the stepped or scarfed joint (just as with the non-stepped joint), the through thickness out-of-plane stresses are not constant or even linear through each ply but are actually a cubic function of z.

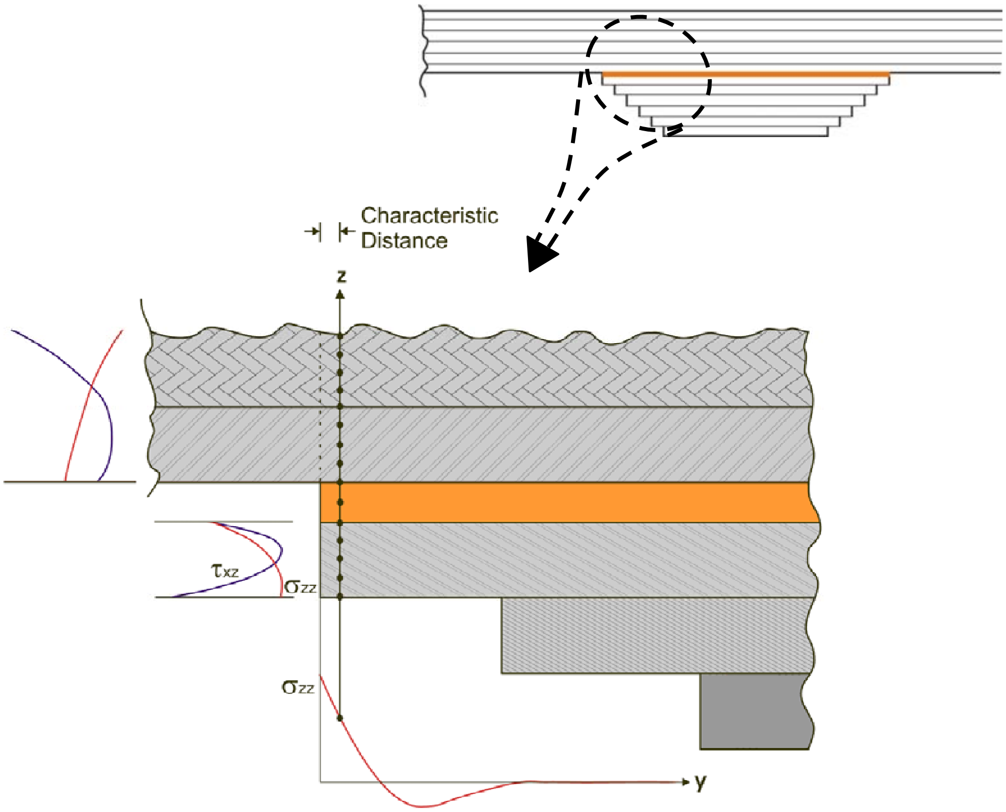

Fig. 6.2.13, HyperSizer BondJo computes stresses through the thickness of each ply. Note the variation of interlaminar stress in the last ply in contact with the adhesive.

6.2.5.1 Bonded Joint Example with Stepped Adherend

Note: This example assumes the typical academic sign convention. See Section 6.11 for details.

The following example problem of a stepped bonded doubler joint was modeled with HyperSizer-BondJo's non-linear adhesive joint capability and the results for several non-linear material models are shown on the following pages. These different non-linear models are described in detail in Section 6.4.

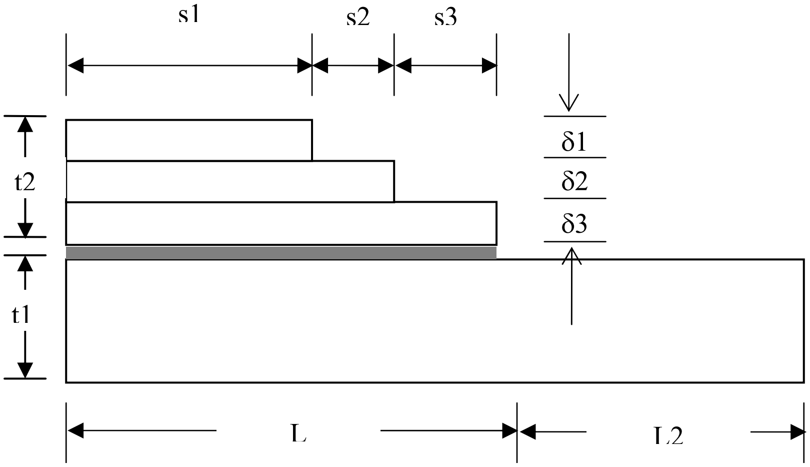

Fig. 6.2.14, Composite stepped bonded doubler joint example configuration

Adherend 1: Graphite/Epoxy $E_1 = 164.0$GPa $E_2 = E_3 = 8.3$ GPa $G_{12} = 2.1$ GPa $\nu_{12} = 0.34$ lay-up: 12 plies (from bottom to top) $[60^o/30^o/0^o/60^o/30^o/0^o/60^o/30^o/0^o/60^o/30^o/0^o]$	Adherend 2: Graphite/Epoxy $E_1 = 164.0$GPa $E_2 = E_3 = 8.3$ GPa $G_{12} = 2.1$ GPa $\nu_{12} = 0.34$ lay-up: 12 plies (from bottom to top) $[0^o/30^o/60^o/0^o/30^o/60^o/0^o/30^o/60^o/0^o/30^o/60^o]$
Adhesive: (epoxy AY 103) Ea = 2.8 GPa $\nu_a = 0.4$ $\lambda = 1.3$ $S_{prop} = 27.0$ MPa $S_{ult} = 71.5$ MPa $e_{ult} = 0.049$ See Fig. 6.2.X, (previous example) Stress-strain curve of AY103	Dimensions: L = 20 mm s1 = 14 mm $L_2 = 30$ mm s2 = 3 mm $t_1 = 1.5$ mm s3 = 3 mm $t_2 = 1.5$ mm δ1 = δ2 =δ3 = 4*ply thickness $t_{adhesive} = 0.05$ mm ply thickness = 0.125 mm

Loading and Boundary Conditions:

Right Face: $N_{xx} = 600$ N/mm; $Q_x = 0$; $N_{xy} = 0$; $\beta_x = 0$
Symmetry (left side): → $u_0 = w = \beta = v_0 = 0$

Number of Segments:

Region 1 (M1_step1, M1_step2, M1_step3) = [8 5 5], Region 2 (M2) = 5
Number of x-points within each region = 40

Results

Black = Peel Stress (σ_z)
Red = Interlaminar Shear (τ_{xy})
Blue = Interlaminar Shear (τ_{yz})

Solid Line = Non-Linear
Dashed Line = Linear (Elastic)

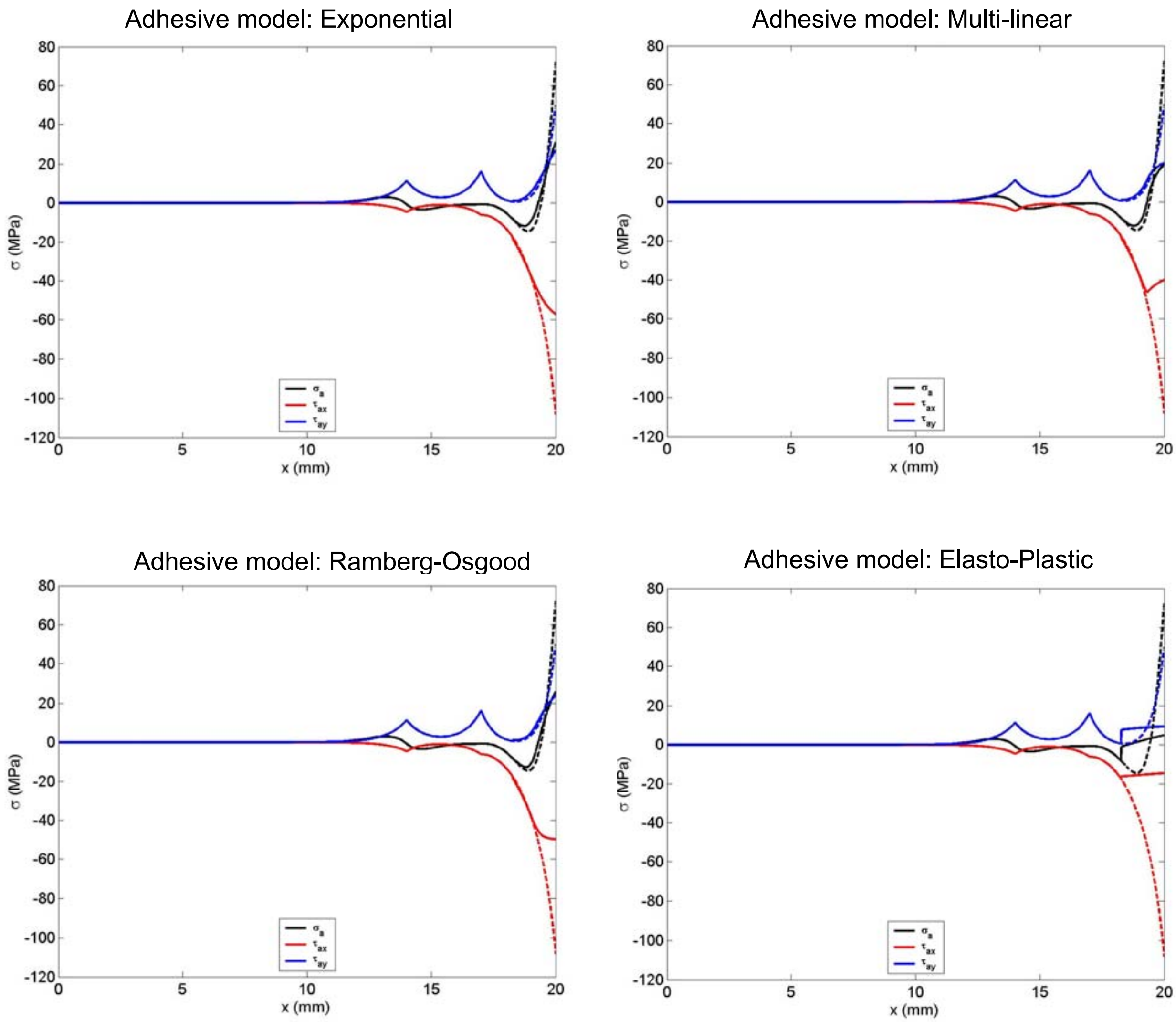
Adhesive model: Exponential

Adhesive model: Multi-linear

Adhesive model: Ramberg-Osgood

Adhesive model: Elasto-Plastic

Fig. 6.2.15, Linear versus non-linear results for a stepped bonded doubler, four different material models compared.

6.2.6 Spew Fillets

A third effect that can change the stresses in the bonded joint is that of including a spew fillet as shown in Fig. 6.2.16. In manufactured joints, this type of fillet develops naturally as a result of the manufacturing process. Since the inclusion of the fillet reduces the effect of the singularity at the reentrant corner and reduces the peak stresses at the free edge, this will be an important effect to consider. While we realize its importance, this effect is not yet included in the HyperSizer-BondJo code. Our plan is to develop the analysis theory and implement in a future release.

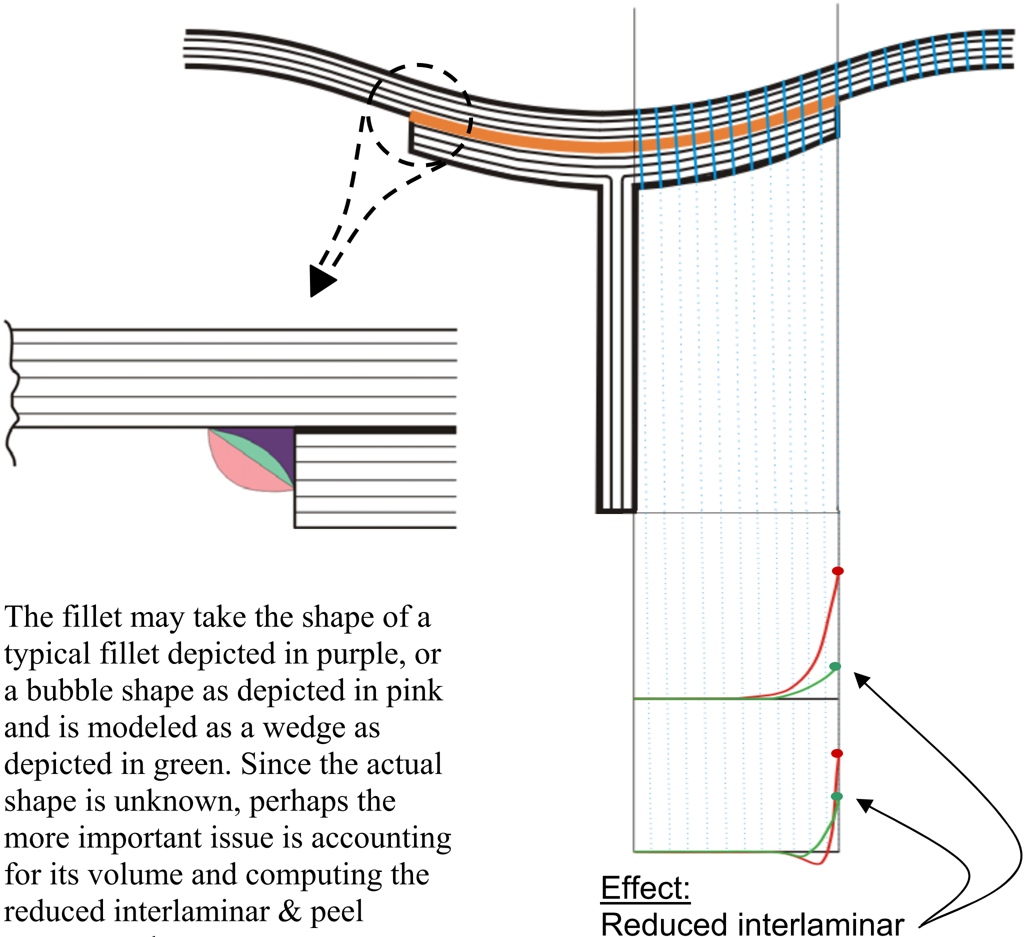

The fillet may take the shape of a typical fillet depicted in purple, or a bubble shape as depicted in pink and is modeled as a wedge as depicted in green. Since the actual shape is unknown, perhaps the more important issue is accounting for its volume and computing the reduced interlaminar & peel stresses at the reentrant corner.

Effect:
Reduced interlaminar
& peel stresses

Fig. 6.2.16, Spew fillets can reduce peak interlaminar shear and peel stress near the free edge of a bonded joint. This effect is not yet accounted for in Hyperizer BondJo.

6.3 *Why a New Capability was Developed*

Several methods for analysis of composite bonded joints existed prior to the development of HyperSizer-BondJo. These methods range from closed form analytical methods such as Hart-Smith A4EI to complex solid model FEA where all physics and general boundary conditions are included. HyperSizer-BondJo lies between by addressing some of the limitations of Hart-Smith, while at that same time providing an efficient analysis that can be included in preliminary design.

6.3.1 Contrasting HyperSizer with Hart-Smith (A4EI)

The cylindrical bending formulation of HyperSizer-BondJo allows for a more general problem solution than that allowed in Hart-Smith. This is illustrated in Fig. 6.3.1, where the additional loadings of Ny, Qy and Nxy are not considered with Hart-Smith (as well as most other non-FEA bonded joint analysis methods), yet are included in HyperSizer-BondJo.

A second consideration is that while Hart-Smith can calculate both shear and peel stress in the adhesive, the approach is not unified as it is with BondJo and peel stress is actually backed out of the analysis by applying a curvature, looking at the bending moments in the adherends, and calculating peel stress from those curvatures. This approach is less accurate and less general than the HyperSizer-BondJo unified approach.

Finally, Hart-Smith provides no out-of-plane stresses (interlaminar shear or peel) in the adherends, which are necessary for many bonded joint laminate failure modes.

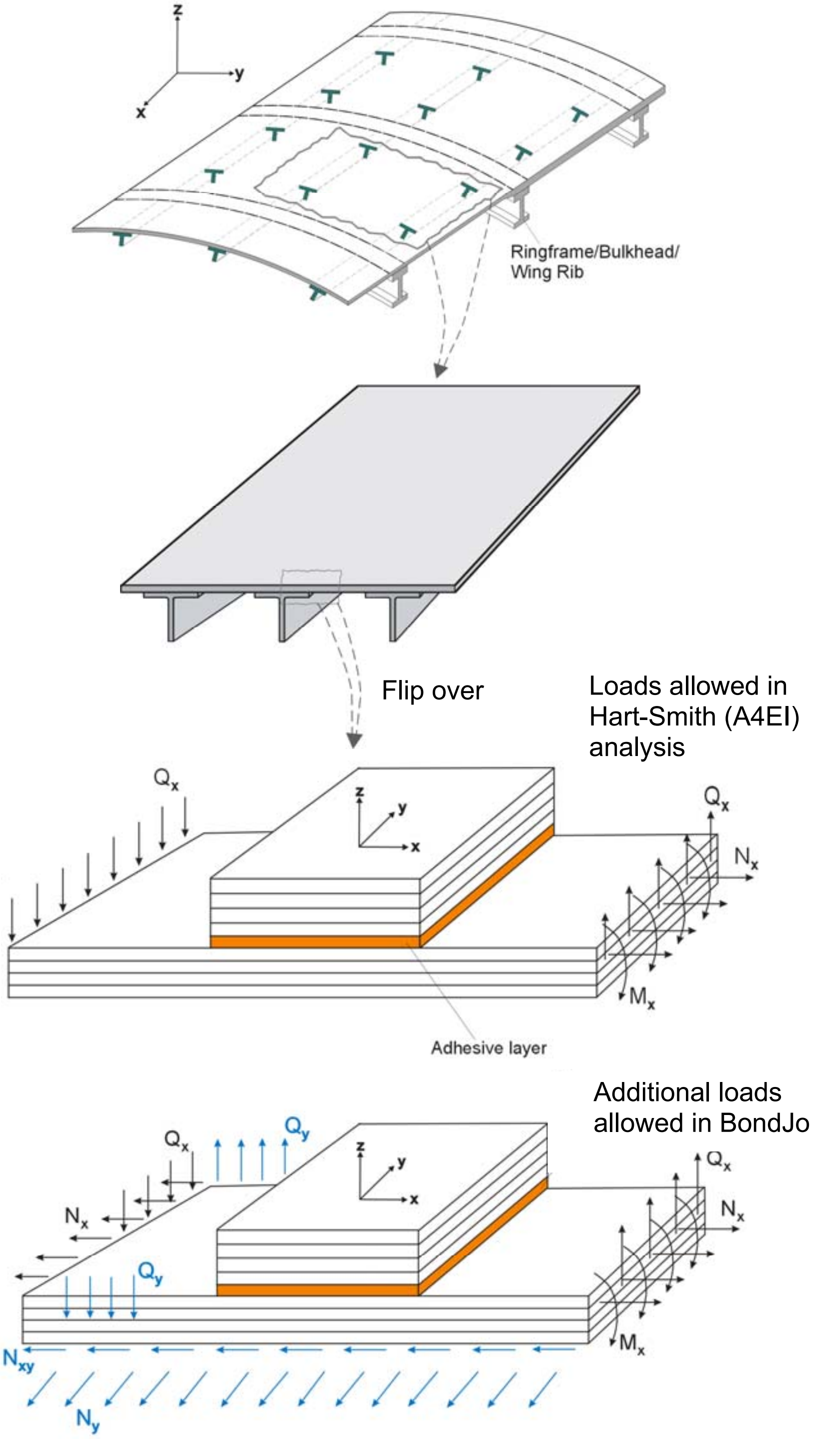

Fig. 6.3.1, Hart-Smith (A4EI) permitted loads, (shown in the typical academic coordinate system) in contrast to those loads accounted for in HyperSizer-BondJo, which are shown with blue arrows.

Contrast between HyperSizer-BondJo and Hart-Smith is provided in Table 6.3.1.

Table 6.3.1, Comparison of HyperSizer-BondJo to Hart-Smith A4EI (All coordinates listed using the typical academic sign convention)

		Bonded Joint Analysis By Hart-Smith (A4EI)	**Bonded Joint Analysis In HyperSizer®**
Solver		1-D closed-form stress analysis, no unified approach is used.	Mortensen's close-form solutions, a unified approach and modification. [6.3.1]
Joints		Conventional joints: Single-, double-lap, scarfed, stepped – joints (adherend can be straight or scarfed, see details in the section: joint type).	Conventional joints: Single-, double-lap, scarfed, stepped – joints (adherend can be straight or scarfed (ply-drop-off)).
Dimension		1D problem	2D – generalized cylindrical bending.
Loads and effects	Mechanical loads	N_x, Q_x, M_{xx}.	N_x, Q_x, M_{xx}, N_y, Q_y, and N_{xy} (M_{yy} and M_{xy} not supported). Also can enter strains and curvatures and in any combination with the forces and moments.
	Non-mechanical loads	1. Thermal stresses 2. defects in *bond layer*, such as moisture, porosity, thickness variation are considered, etc.	1. Thermal stresses 2. Moisture in laminates 3. Electromagnetic effects
Adherends	material	Linear elastic homogeneous isotropic beam (not composite), no transverse deformation is accommodated.	Linear elastic classical laminate (orthotropic, and represented by A, B, D matrices), no transverse deformation is yet accommodated but will be in a future release.
	output	1. Longitudinal normal stress and strain, as well as displacement (*u, w*). 2.Interlaminar stresses are not available	1. In-plane stresses, strains, and displacement (*u, v, w*). 2. Interlaminar shear and peel stresses are available.
Adhesive	material	1. Linear tension-shear spring. 2. Elasto-plastic material.	1.2D isotropic linear elastic spring. 2. High order theory (to be developed) 3. Elasto-plastic material 4. Spew fillet effect (to be developed)
	Output	Shear and peel stresses only, which are constants through the thickness by using the spring model.	Shear and peel stresses only, which are constants through the thickness by using the spring model, but may vary if using high order theory (HOT).
Failure analysis and design rule		1. select the joint design so as to ensure failure in the adherend rather than the adhesive; 2. ductility of adhesives is beneficial in reducing stress peaks in the adhesive; 3. Providing sufficient overlap length to ensure that some of the adhesive is so lightly loaded that creep cannot occur there.	1. Damage zone failure criterion is introduced – take the stress/strain values at the points certain distance away from the singular points or the average over a distance. 2. Composite adherend failure caused by in-plane and the interlaminar stresses. 3. Adhesive cohesive failure is based on the max. effective strain (for complaint adhesive). 4. Failure rule for brittle adhesive. 5. Failure rule for interfacial debonding (adhesive / adherends).

Convergence of solution		Has stability/convergence problems with stepped joints. (reported by NG, OAI, others)	Convergence is more robust. Can manually choose number of points per segment (More automation later)
Joint types [Fig. 6.4.1]	Single-lap with straight adherend	Solved adhesive shear stress from shear-lag model; introduced bending moment caused by eccentricity of loading path to solve peel stress.	Modified Mortensen's Unified approach (generalized plane strain)
	Single-lap with scarfed adherend	Not clear the exact procedure used. The solution is given in power series. Only the peak values of stresses are solved, no distribution along the bondline.	Modified Mortensen's Unified approach (generalized plane strain)
	double-lap with straight adherend	Solved adhesive shear stress from shear-lag model; Solved peel stress from beam-on-elastic foundation model.	Modified Mortensen's Unified approach (generalized plane strain)
	double-lap with scarfed adherend	Not clear the exact procedure used. The solution is given in power series. Only the peak values of stresses are solved, no distribution along the bondline.	Modified Mortensen's Unified approach (generalized plane strain)
	Single sided scarfed lap joint	Not clear the exact procedure used. The solution is given in power series. Only the peak values of stresses are solved, no distribution along the bondline.	Modified Mortensen's Unified approach (generalized plane strain)
	Double sided scarfed lap joint	Not clear the exact procedure used. The solution is given in power series. Only the peak values are solved, no distribution along the bondline.	Modified Mortensen's Unified approach (generalized plane strain)
	Single sided stepped lap joint	Shear-lag model, only shear stress is solved.	Modified Mortensen's Unified approach (generalized plane strain)
	Double sided stepped lap joint	Shear-lag model, only shear stress is solved.	Modified Mortensen's Unified approach (generalized plane strain)
	Bonded doubler with straight adherend	Solution could be obtained by modification of that of the single-lap joint with straight adherend.	Modified Mortensen's Unified approach (generalized plane strain)
	Bonded doubler with stepped adherend	Not available	Modified Mortensen's Unified approach (generalized plane strain)

Robustness	Not robust for scarfed or stepped joints.	The solution is very stable, good for conventional joints, some verification has been performed with FEA as detailed in section 6.9, but more is needed.
Run time	N/A	Around 0.1 sec. with 15 segments in the overlap region for linear analysis of double-lap joint with straight adherends. 1/40 sec for bonded doubler.

Note: conclusion on Hart-smith’s approach to analyzing bonded joints is based on limited publications, particularly MIL-HDBK-17-3E [6.3.2] and NASA report [6.3.3 - 6.3.5].

6.3.2 Contrasting HyperSizer with FEA

Table 6.3.2, Comparison of HyperSizer-BondJo with Stresscheck FEA

		Bonded Joint Analysis With FEA (StressCheck®)	**Bonded Joint Analysis By HyperSizer-BondJo®**
Solver		p-version finite element method [6.3.6].	Mortensen's close-form solution [6.3.1].
Joint type		Conventional joints and more general joint configuration.	Conventional joints: Single-, double-lap, scarfed, stepped – joints (adherend can be straight or scarfed (ply-drop-off)).
Dimension		2D – plane strain. 3D – thin solids (by extruding 2D mesh).	2D – cylindrical bending
Loads	Mechanical loads	2D plane strain: FX (DX), FZ (DZ), MX (θy), MZ(θy). 3D: Multi-axial loads. See Fig. 6.3.4 for details	N_x, Q_x, N_{xy}, M_{xx}, N_y, Q_y, N_{yx}, (ref. plane is the neutral axis of each adherend). See the sign convention in Section 6.11.
	Non-mechanical loads	Thermal	Thermal, moisture in laminates. Electromagnetic effect (future development).
Adherend	material	The adherend was meshed with several layers of single-plies usually adjacent to the bondlines and sub-laminates, to which homogenous linear elastic materials (orthotropic or isotropic) properties are calculated and assigned.	Linear elastic classical laminate (A, B, D matrices).
	output	All directional (3D) stresses, strains and displacements. Interlaminar stresses are available.	In-plane stress, strain components, and displacement (*u, v, w*). Interlaminar stresses are not available.
Adhesive	material	Continuum homogenous isotropic linear elastic / nonlinear materials	2D isotropic linear elastic spring High order theory (future development). Non-linear material models
	Output	All directional (3D) stresses, strains and displacements.	Shear and peel stresses only, which are constants through the thickness by using the spring model, but may vary if using high order theory.
Singularities at the free edges or bi-material interface corners		Not intend to capture singularities, zone around reentrant corner is considered to be "polluted" and not analyzed. Compared to *h*-method, it reaches convergence rapidly in the vicinity of singular points with relatively coarse mesh.	Can not capture the singularities. The solutions at the singular points are stable as geometry, material and external loads change.

Failure criterion	1. Damage zone failure criterion is introduced – take the stress/strain values at a certain distance away from the singular points. 2. Composite ply failure is based on the interlaminar stress interaction rule. 3. Adhesive cohesive failure is based on the max. effective strain (for compliant adhesive). 4. Not known if failure rule exists for brittle adhesive. 5. Not known if failure rule exists for interfacial debonding (adhesive / adherends). 6. Not known if failure rule exists for metallic adherends. 7. Continuously extracting stress/ strains at critical points or zone to check with failure criterion.	Suggested failure criteria include: 1. Damage zone failure criterion. 2. Composite ply failure caused by the interlaminar stresses. 3. Adhesive cohesive failure is based on the max. effective strain (for complaint adhesive). 4. Failure rule for brittle adhesive. 5. Failure rule for interfacial debonding (adhesive / adherends). 6. Failure rule for metallic adherends.
Process	1. Automated convergence reporting.	1. The convergence of results not an issue for a reasonable number of segments.
Pre-process	In the graphics user-interface, input 1. Geometry 2. Material properties (orthotropic/isotropic), laminate (ply property, angle, etc, but generate effective homogenous material properties), elastoplastic properties for adhesive. 3. Meshing parameter 4. External loads and B.C.	Input the followings through the HyperSizer interface (or through ASCII files in Matlab). 1. Geometry 2. Material properties for laminate (giving ply properties and angle), elastoplastic properties for adhesive. 3. External loads and B.C.
Post-process	1. Extract engineering information (stress/strain) in any user defined coordinate system, or in the lamina for both flat and cylindrical description of the laminate properties. 2. Compute average stress/strain along element edges, element faces, and arbitrary curves or element volume. 3. Color coding of laminate materials makes visualization easier. 4. Visualize the result output.	1. Could extract engineering information (stress/strain) in any user defined coordinate system, or in the lamina for both flat and cylindrical description of the laminate properties. 2. Could compute average stress/strain along certain curves or volume (not arbitrary).

Special features	1. Design load: First the design load is applied to the bonded joint and, after a material nonlinear analysis is performed, the margins of safety are computed for the different modes of failure identified for the joint. For each mode of failure a different expression for the margin of safety is required, which may be based on average quantities. 2. Failure load: After the design load analysis, the load is incremented by a specified amount and the solution is performed again. At the end of each load step a check is performed to determine whether any of the failure criteria has been exceeded. Once the first failure mode is reached, it is possible to stop the analysis or continue to increment the load until all margins are exceeded.	
Run time	Not sure.	Approx. 0.025 seconds for one analysis, not including pre or post processing
Robustness	Can solve more general joint configurations.	The solution is very stable, good for conventional joints.

6.3.2.1 When is 2D FEA Inadequate and 3D Solid Model FEA required

In general, when analyzing bonded composite joints with FEA, 3D solid finite elements are required to solve for the in-and out of plane stresses for the following reasons.

1. To capture the out-of-plane effects and to compute the full stress field in the adherends, where the output stress components include σ_{xx}, σ_{yy}, σ_{zz}, σ_{xy}, σ_{xz}, σ_{zy}. The out-of-plane stress components $\sigma_{xz,}$ $\sigma_{xy,}$ in particular can not be obtained by using 2D plane stress, plane strain, or shell element FE models.

2. To account for off-axis plies (such as +/-45°) in laminated adherends. Although generalized plane strain elements (such as Ansys PLANE183, PLANE 182 elements) allow for 3D material property inputs, the effects of these off-axis plies (such as in-plane shear, τ_{xy}) would not be seen without solid elements.

3. For a stand-alone test panel, as described in Fig. 6.2.3, non-uniform strain and curvature in each direction requires a full 3-D elasticity solution and hence would require 3-D solid elements in the FEA. This same argument applies to areas such as panel closeouts or stiffener terminations where the stress and strain fields are very general.

Because HyperSizer-BondJo is intended to solve problems involving in-plane shear and general off-axis plies, the finite element models that we used for verification use solid elements. Although our goal is not to solve problems such as the stand alone test article, points 1 and 2 above dictate that solid models are required.

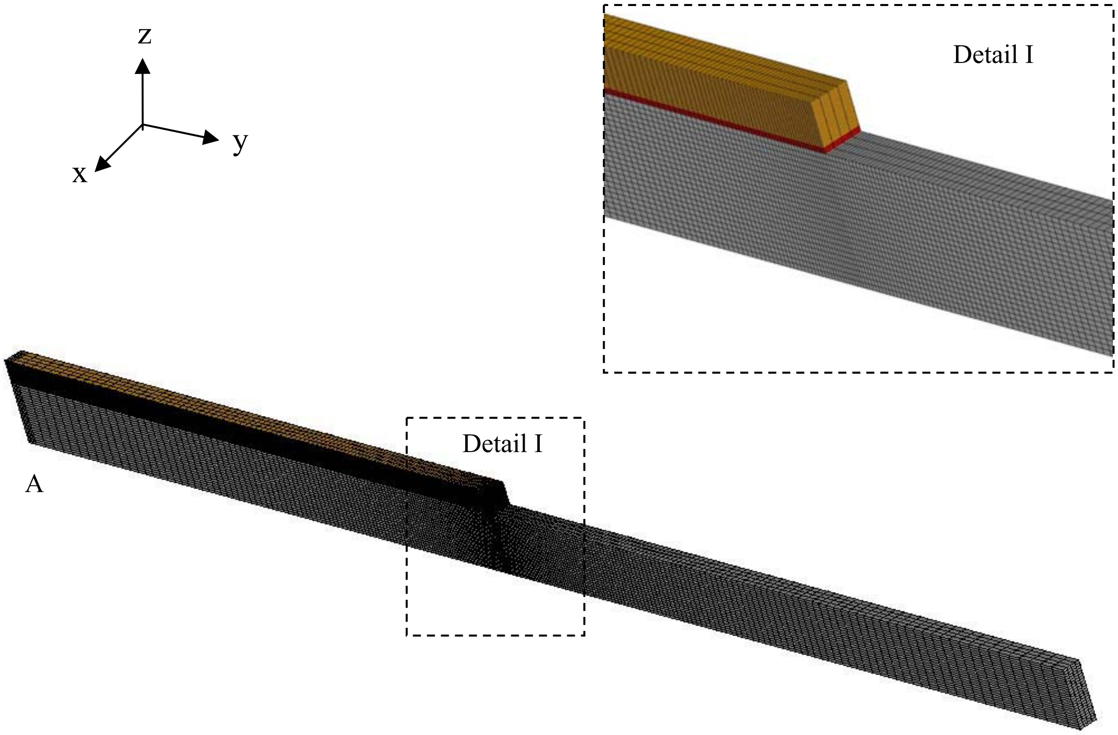

Fig. 6.3.4, Meshes of 3D finite element model for the bonded doubler (based on HyperSizer panel coordinate system).

The finite element model developed for the bonded doubler verifications to HyperSizer-BondJo were initially constructed using the commercial finite element package ANSYS using 37,312 eight-noded anisotropic solid elements (SOLID64). Mesh density along the longitudinal direction gradually increases toward the adhesive free edge from both symmetric plane and right end. The adhesive layer was modeled using four layers of elements to capture the through-the-thickness gradient of peel and shear stresses. To obtain accurate solution for out-of-plane (interlaminar) stresses in the adherends, 24 layers of elements were used in the through-the-thickness direction. Each ply of the laminated adherend thus can be explicitly modeled with one or more layers of elements. Four elements were used through the width. Fig. 6.3.4 shows the finite element mesh for the entire domain and the details at the adhesive free edge. The boundary conditions at the symmetric plane (y=0, left side) is $u_y = 0$ and $u_z = 0$ at bottom node A. The front and back planes are constrained in the x-direction, i.e. $u_x = 0$, to reflect in-service stiffened panel boundary conditions. The boundary conditions at the right end of plate depend on the problem of interest.

For the panel in-service boundary condition, there are no variations of stress or displacement in the x-direction, therefore the number of elements in this direction theoretically do not affect the results. However, fewer elements (for example, going to one element in this direction) may result in over-constrained boundaries and thus cause FEA numerical problems. In the ANSYS model, four elements were used through the width, although in future analyses, this number may be reduced to two.

6.3.2.2 Observations from HyperSizer – FEA comparisons

In one of our marquee verification examples, laminated, composite joint results from HyperSizer-BondJo are compared with those from the p-based finite element analysis code, Stresscheck. The problem chosen is complex enough to test out all of the features of the software. Because the adherends are laminates, finding the through-the-thickness stress distribution requires explicit modeling of each ply in the finite element model. The geometry and materials for this problem are described in Section 6.9.2 and in Volume 3, Section 7.

The FEM was initially built in-house using the commercial FEA analysis package, ANSYS. After many weeks of effort to obtain good solutions from this model, this effort was abandoned. Efforts to get good results were unsuccessful and we were never able to determine if the problems were related to our inexperience with this type of laminated solid element model, mesh refinement, or limitations with ANSYS. Our company contains no experts in solid FEA modeling, however in talking with others in industry, we determined that perhaps ANSYS was not the tool of choice for this type of problem. Two FEA packages have emerged as leaders for this type of detailed analysis, Stresscheck and Abaqus.

Using Stresscheck, with the help of Lockheed Martin, we were able to build a robust verification model for comparison with HyperSizer-BondJo. While the results between the two codes were not identical, there is in general a good match.

First, the trends in all stresses are very similar between the codes with in-plane stresses being virtually identical and out-of-plane stresses differing somewhat near the free edge. In most cases where the results differ, however, HyperSizer-BondJo tends to predict higher stresses, resulting in more conservative answers.

Second, in preliminary design, where geometry, materials, layups and loads can be constantly changing, it would be impractical to perform FEA for each design iteration. Our recommendation is to use a tool like HyperSizer-BondJo for preliminary design and then verify with FEA as required for final design.

6.3.3 References

6.3.1 F. Mortensen, “Development of tools for engineering analysis and design of high-performance FRP-composite structural elements”, Ph.D. thesis, 1998.
6.3.2 MIL-HDBK-17-E3, 1997.
6.3.3 Hart-Smith, L. J., "The key to designing durable adhesively bonded joints," Composites, Volume 25, Issue 9, Pages 895-898, 1994.
6.3.4 Hart-Smith, L.J., "Adhesive-Bonded Single-Lap Joints," NASA-CR-112236, NASA Langley Research Center, 1973b.
6.3.5 Hart-Smith, L.J., "Adhesive Bond Stresses and Strains at Discontinuities and Cracks in Bonded Structures," Journal of Engineering Materials and Technology, 100, 15-24, 1978.
6.3.6 S.P. Engelstad and R.L., Actis, “Development of p-version handbook solution for analysis of composite bonded joints,” internal report.

6.4 Theoretical Development of Bonded Joint Stress Analysis

6.4.1 Summary

Note: All theoretical development in Section 6.4 is presented assuming the typical academic sign convention. See Section 6.11 for details.

The method for stress analysis of **BondJo** is developed based on the Mortensen's [6.4.6] unified approach for bonded joints and is extended to: a) generalized plane strain to admit longitudinal mechanical loads; b) accommodate hygrothermal loads; and c) compute out-of-plane interlaminar shear and peel stresses in the adherends. The adherends are modeled as linear classical laminates in generalized cylindrical bending described by using 'Love-Kirchhoff' theory. Both linear and nonlinear behaviors of adhesive layer are admitted in the analysis. For linear analysis, the adhesive layer is modeled as continuously distributed linear tension/compression and shear springs. Inclusion of nonlinear behavior of adhesive in the analysis is by using a secant modulus approach for the nonlinear tensile stress–strain relationship in conjunction with yield criterion. Based on the constitutive and kinematic relations for the adherends, the constitutive relations for the adhesive layers are adopted. Finally, the equilibrium equations for the joints are derived, and by combination of these equations and relations, the set of governing equations is obtained. This results in a set of first order ordinary differential equations, called the governing system equations, describing the system behavior. The governing system equations are solved numerically using the 'multi-segment method of integration'. After the governing system equations are solved, the in-plane stress components of adherends can be calculated directly through laminate constitutive equations derived from the Classical Lamination Theory (CLT). Unlike the in-plane stress components, the interlaminar stress components of adherends are obtained through point-wise equilibrium equations.

6.4.2 Symbols

Table 6.4.1, Symbols used in BondJo theoretical development

u_0, v_0, w	Middle plane displacements in *x*, *y* and *z* directions respectively
β_x	Middle plane slope with respect to *x*-axis
$\boldsymbol{\kappa} = \{\kappa_x, \kappa_y, \kappa_{xy}\}$	Curvatures of middle plane of laminates
N_{xx}, N_{yy}, N_{xy}	In-plane stress resultants
M_{xx}, M_{yy}, M_{xy}	In-plane moment resultants
N^*_{xx}, N^*_{yy} and N^*_{xy}	Hygrothermal in-plane stress resultants
M^*_{xx}, M^*_{yy}, M^*_{xy}	Hygrothermal in-plane moment resultants
Q_x, Q_y	Shear out-of-plane forces acting on the planes with normal in *x* and *y* directions
A_{jk}, B_{jk} and D_{jk}	Laminate extensional, coupling and flexural rigidities
$\overline{Q}_{ij}^{(k)}$	In-plane stiffness matrix of the *k*th ply

$\{y^i\}$	Vector containing fundamental variables $\{y^i\} = \{u_0^i, w^i, \beta_x^i, v_0^i, N_{xx}^i, N_{xy}^i, M_{xx}^i, Q_x^i\}$
$[\mathbf{A}_{ij}^r(x^r)]$	A (*m, m*) sub-coefficient matrix for the system of governing equations
$\{\mathbf{B}_i^r(x^r)\}$	A (m,1) sub-matrix of non-homogeneous load terms in system of governing equations
$\boldsymbol{\varepsilon}^*$	Hygrothermal in-plane strain in laminates
τ_{ax}, τ_{ay}, σ_a	Adhesive longitudinal shear, transverse shear and peel stresses
γ_{ax}, γ_{ay}, ε_{az}	Adhesive longitudinal shear, transverse shear and peel strains
$\boldsymbol{\alpha}$ and $\boldsymbol{\beta}$	Thermal expansion coefficients and moisture expansion coefficients
σ_{xx}, σ_{yy}, σ_{xy}	In-plane stress components
τ_{xz}, τ_{yz}, σ_{zz}	Out-of-plane stress components
ε_{xx}, ε_{yy}, γ_{xy}	In-plane strain components
γ_{xz}, γ_{yz}, ε_{zz}	Out-of-plane strain components
σ_1, σ_2, σ_3	The principal stresses
ε_1, ε_2, ε_3	The principal strains
e_0	Constant strain in y-direction applied to joints
$\boldsymbol{\varepsilon}^0 = \{\varepsilon_x^0, \varepsilon_y^0, \varepsilon_z^0\}$	In-plane strain of the middle plane of laminates
E_a, G_a	Young's modulus and shear modulus of adhesive
s	Effective stress
J_{2D}	The second invariant of the deviatoric stress tensor
J_1	The first invariant of stress tensor
σ_e	Compressive yield stress
σ_s	Tensile yield stress
λ	Ratio of the compressive yield stress to the tensile yield stress
e	Effective strain
I_{2D}	The second invariant of the deviatoric strain tensor
I_1	The first invariant of strain tensor
t_1	Thickness of adherend 1
t_2	Thickness of adherend 2
t_a	Thickness of adhesive layer

6.4.3 Bonded Joint Concepts Analyzed By BondJo

The theory presented herein is applicable to the following joint concepts and analysis programs that were developed for each under this SBIR.

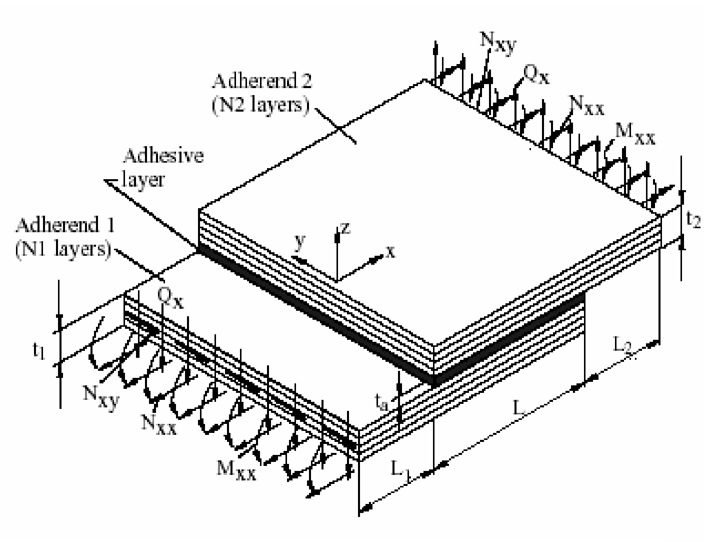

Nxy
Qx
Nxx
Mxx
Adherend 2
(N2 layers)
Adhesive
layer
Adherend 1
(N1 layers)
y
z
x
t2
Qx
t1
Nxy
Nxx
Mxx
ta
L2
L
L1

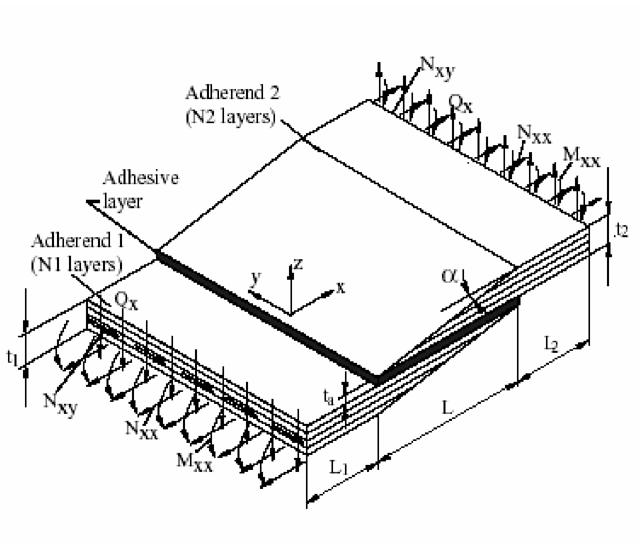

Nxy
Qx
Nxx
Mxx
Adherend 2
(N2 layers)
Adhesive
layer
Adherend 1
(N1 layers)
y
z
x
α
t2
Qx
t1
Nxy
Nxx
Mxx
ta
L2
L
L1

Single-lap joint with straight adherend

Single-lap joint with scarfed adherend

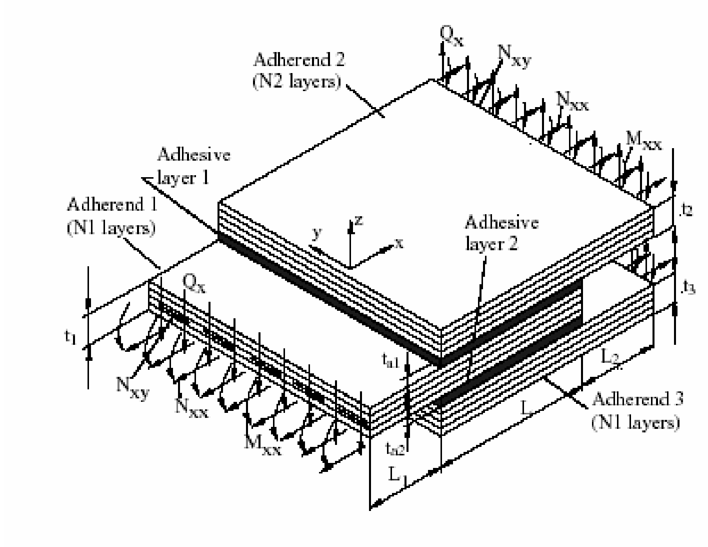

Qx
Nxy
Nxx
Mxx
Adherend 2
(N2 layers)
Adhesive
layer 1
Adherend 1
(N1 layers)
y
z
x
Adhesive
layer 2
t2
t3
Qx
t1
Nxy
Nxx
Mxx
ta1
ta2
L2
L
L1
Adherend 3
(N1 layers)

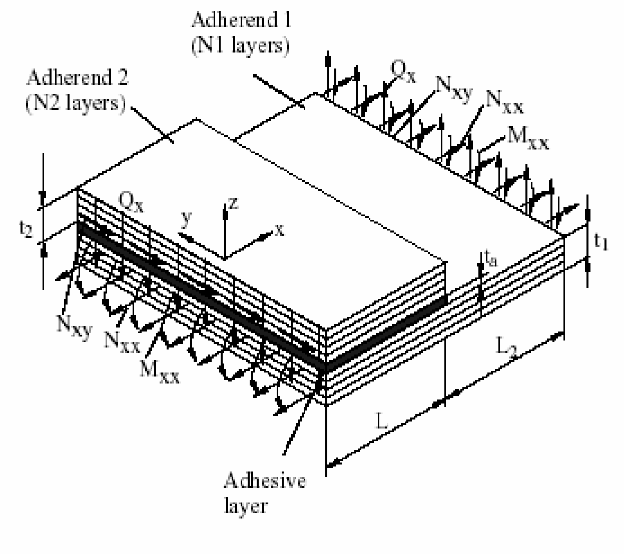

Adherend 1
(N1 layers)
Adherend 2
(N2 layers)
Qx
Nxy
Nxx
Mxx
Qx
y
z
x
t2
t1
ta
Nxy
Nxx
Mxx
L2
L
Adhesive
layer

Double-lap joint with straight adherend

Bonded doubler joint with straight, scarfed, or stepped adherend

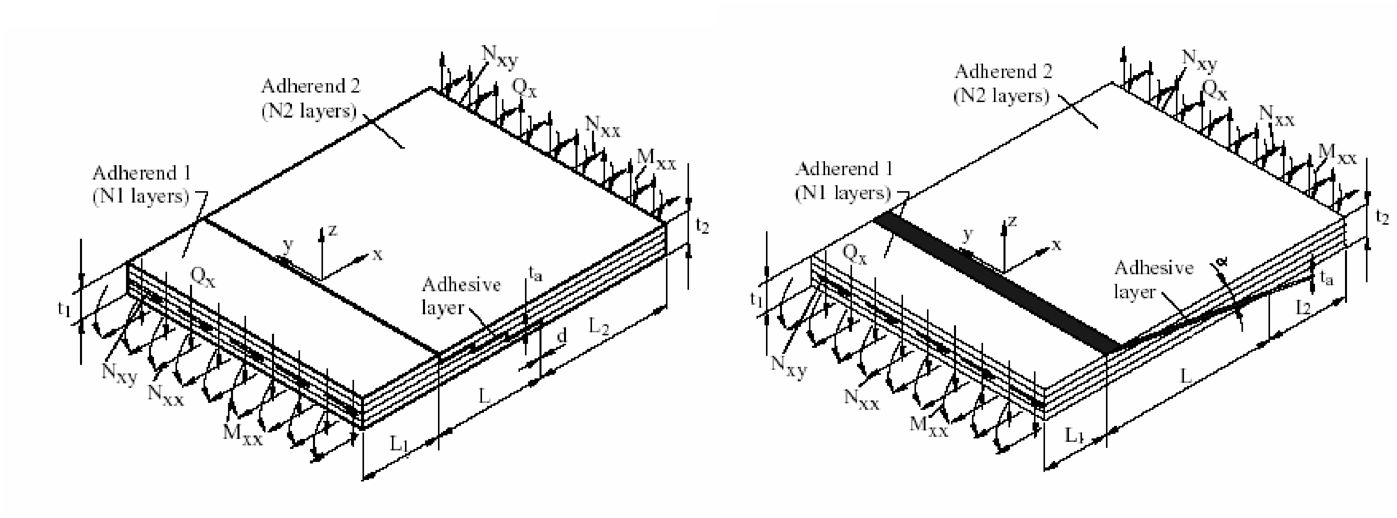
Adherend 2
(N2 layers)
Adherend 1
(N1 layers)
N_{xy}
Q_x
N_{xx}
M_{xx}
t_1
t_2
t_a
Adhesive
layer
d
L_1
L
L_2
x
y
z
α

Single sided stepped joint

Single sided scarfed joint

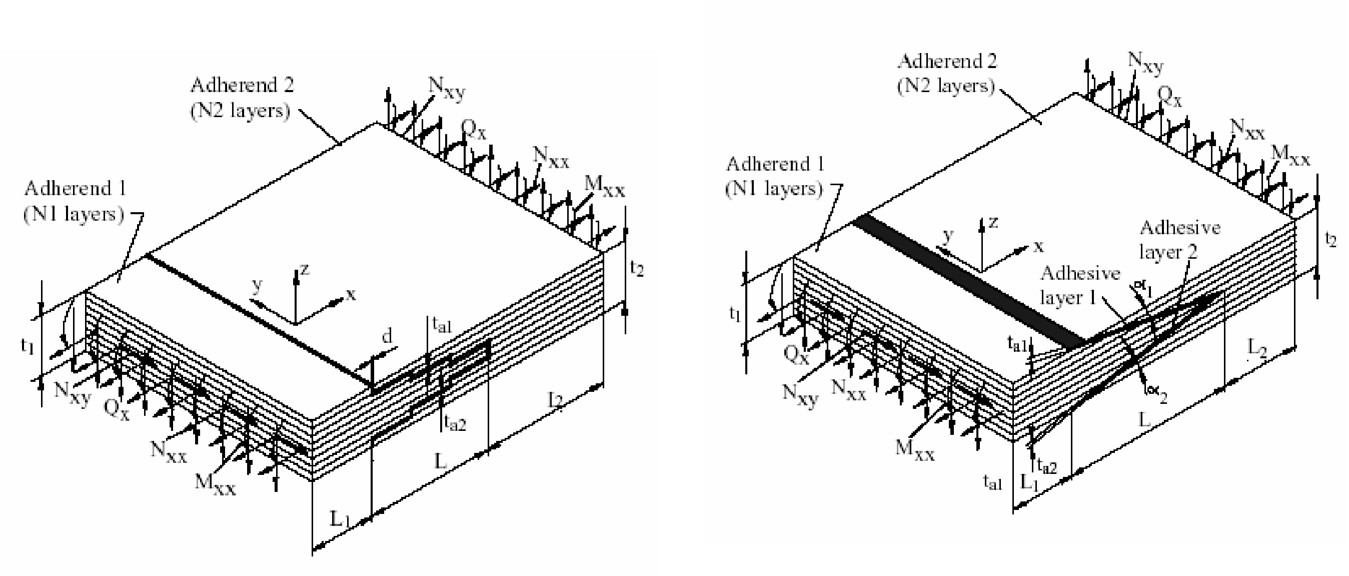
Adherend 2
(N2 layers)
Adherend 1
(N1 layers)
N_{xy}
Q_x
N_{xx}
M_{xx}
t_1
t_2
t_{a1}
t_{a2}
d
Adhesive
layer 1
Adhesive
layer 2
α_1
α_2
L_1
L
L_2
x
y
z

Double sided stepped joint

Double sided scarfed joint

Fig. 6.4.1, Composite bonded joint configurations implemented in BondJo versions. The bonded doubler (panel stiffener joint) and single lap joint are part of the commercial HyperSizer-BondJo release.

6.4.4 Basic assumptions for the structural modeling of bonded joints

The basic restrictive assumptions of the structural modeling are the following:
The adherends:

- Beams or plates in cylindrical bending, which are described by use of ordinary 'Kirchhoff'; plate theory ('Love–Kirchhoff' assumptions).
- Generally orthotropic laminates using classical lamination theory (e.g. asymmetric and unbalanced composite laminates can be included in the analysis).
- The laminates are assumed to obey linear elastic constitutive laws.
- The strains are small, and the rotations are very small.

The adhesive layer:

- Modeled as continuously distributed linear tension/compression and shear springs.
- Inclusion of non-linear adhesive properties, by using a secant modulus approach for the nonlinear tensile stress–strain relationship in conjunction with a modified von Mises yield criterion.

Load and boundary conditions (typical academic sign convention):

- General boundary and load conditions. One of each pair in the following can be applied: ($u_0 \sim N_{xx}$), ($v_0 \sim N_{xy}$), ($w \sim Q_x$), ($\beta_x \sim M_{xx}$)
- Thermal load: uniform temperature change ΔT
- In-plane transverse (y) direction, uniform strain $\varepsilon_{yy}{}^0$ can be applied (generalized plane strain), or the equivalent transverse force, N_{yy}.
- Can get reaction (moments) in y-direction: M_{yy}, M_{xy}.

The system of governing equations is set up for two different cases, i.e. the adherends are modeled as plates in cylindrical bending or as wide beams.

6.4.5 Adherends as Plates in Generalized Cylindrical Bending

The generalized cylindrical bending can be defined as a wide plate, where the longitudinal displacement and vertical deflection can be described as a function of the longitudinal coordinate only, while the in-plane transverse displacement can accommodate generalized plane strains. As a consequence of this, the longitudinal displacements and deflection in the width directions will be uniform, while the in-plane transverse displacement varies linearly. Thus, the displacement field can be described as:

$$u_0^i = u_0^i(x) \qquad v_0^i = e_0^i y + v_0^i(x) \qquad w^i = w^i(x) \tag{6.4.5.1}$$

where u_0 is the midplane displacement in the longitudinal direction (x-direction), v_0 is the midplane displacement in the width direction (y-direction), and w is the displacement in the out-of plane transverse direction (z-direction), e_0 is the uniform strain in y direction The displacement components u_0, v_0, w are all defined relative to the middle surfaces of the laminates, and i corresponds to the laminate/adherend number..

The boundary conditions at the boundaries in the width direction are not well defined within the concept of 'cylindrical bending''. However, it is assumed that there are some restrictive constraints on the boundaries, such that they not are capable of moving and rotating freely. It should be noted that the concept of ‘cylindrical bending’; is not unique, and that other definitions than the one used in the present formulation can be adopted, see Whitney [6.4.10].

Considering the adherends are subjected to both mechanical and non-mechanical (such as hygrothermal strains) loads together, the constitutive equations for the laminated adherends are given as:

$$\begin{aligned}
N^i_{xx} &= A^i_{11}u^i_{0,x} + A^i_{12}e^i_0 + A^i_{16}v^i_{0,x} - B^i_{11}w^i_{,xx} - N^{i*}_{xx} \\
N^i_{yy} &= A^i_{12}u^i_{0,x} + A^i_{22}e^i_0 + A^i_{26}v^i_{0,x} - B^i_{12}w^i_{,xx} - N^{i*}_{yy} \\
N^i_{xy} &= A^i_{16}u^i_{0,x} + A^i_{26}e^i_0 + A^i_{66}v^i_{0,x} - B^i_{16}w^i_{,xx} - N^{i*}_{xy} \\
M^i_{xx} &= B^i_{11}u^i_{0,x} + B^i_{12}e^i_0 + B^i_{16}v^i_{0,x} - D^i_{11}w^i_{,xx} - M^{i*}_{xx} \\
M^i_{yy} &= B^i_{12}u^i_{0,x} + B^i_{22}e^i_0 + B^i_{26}v^i_{0,x} - D^i_{12}w^i_{,xx} - M^{i*}_{yy} \\
M^i_{xy} &= B^i_{16}u^i_{0,x} + B^i_{26}e^i_0 + B^i_{66}v^i_{0,x} - D^i_{16}w^i_{,xx} - M^{i*}_{xy}
\end{aligned} \tag{6.4.5.2}$$

where A^i_{jk}, B^i_{jk} and D^i_{jk} (j, k = 1, 2, 6) are the extensional, coupling and the flexural rigidities. N^i_{xx}, N^i_{yy} and N^i_{xy} are the in-plane stress resultants and M^i_{xx}, M^i_{yy} and M^i_{xy} are the moment resultants. N^{i*}_{xx}, N^{i*}_{yy} and N^{i*}_{xy} are the in-plane hygrothermal stress resultants, while M^{i*}_{xx}, M^{i*}_{yy} and M^{i*}_{xy} are the hygrothermal moment resultants. The expression of the hygrothermal terms are given as

$$N^*_n = \sum_{k=1}^{N} \{\overline{Q}^{(k)}_{nm} \cdot \varepsilon^{(k)*}_m \cdot t_k\} \text{ and } M^*_n = \sum_{k=1}^{N} \{\overline{Q}^{(k)}_{nm} \cdot \varepsilon^{(k)*}_m \cdot (z^2_k - z^2_{k-1})/2\} \tag{6.4.5.3}$$

where $\varepsilon^{(k)*}_m$ is the in-plane hygrothermal strain vector in each ply, i.e., $\varepsilon^*_m = \alpha_m \Delta T + \beta_m \Delta c$ (see [6.4.4]).

For the advanced joint types such as a scarfed or stepped lap the rigidities A^i_{jk}, B^i_{jk} and D^i_{jk} (j, k = 1, 2, 6) are determined as functions of the longitudinal direction of the joint within the overlap zone, since the adherend thicknesses are variable within the overlap. From the ‘Love-Kirchhoff’; assumptions, the following kinematic relations for the laminates are derived:

$$u^i = u^i_0 + z\beta^i_x, \qquad \beta^i_x = -w^i_{,x}, \qquad \beta^i_y = 0 \tag{6.4.5.4}$$

where u^i is the longitudinal displacement, $u^i{}_0$ is the longitudinal displacement of the mid-plane, and w_i is the vertical displacement of the i-th laminate.

6.4.6 Constitutive Relations for the Adhesive Layer

6.4.6.1 Linear spring adhesive model

The coupling between the adherends is established through the constitutive relations for the adhesive layer, which as a first approximation is assumed to be homogeneous, isotropic and linear elastic. The constitutive relations for the adhesive layer are established by use of a two-parameter elastic foundation approach, where the adhesive layer is assumed to be composed of continuously distributed shear and tension/compression springs. The constitutive relations of the adhesive layer are suggested in accordance with Thomsen [6.4.7, 6.4.8] and Tong [6.4.9]:

$$\begin{aligned} \tau_{ax} &= G_a \cdot \gamma_{ax} = \frac{G_a}{t_a}(u^i - u^j) \\ \tau_{ay} &= G_a \cdot \gamma_{ay} = \frac{G_a}{t_a}(v^i - v^j) \\ \sigma_a &= E_a \cdot \varepsilon_{az} = \frac{E_a}{t_a}(w^i - w^j) \end{aligned} \tag{6.4.6.1}$$

where i and j are the numbers of the adherends, G_a is the shear modulus, and E_a is the elastic modulus of the adhesive layer.

6.4.6.2 Non-linear adhesive model

Most polymeric structural adhesives exhibit inelastic behavior, in the sense that plastic residual strains are induced even at low levels of external loading. Thus, the assumption of linear elasticity of the adhesive is an approximation. Analysis of non-linear adhesives and related solution procedures is described fully in Section 6.4.9.

6.4.6.3 Equilibrium equations

The equilibrium equations are derived based on equilibrium elements in- and outside the overlap zone for each of the considered joint types. The equilibrium equations are derived for plates in generalized cylindrical bending. The general equilibrium equations outside the overlap zone for each of the adherends (Fig. 6.4.2),

$$\left.\begin{aligned} N^i_{xx,x} &= 0 \\ N^i_{xy,x} &= 0 \\ Q^i_{x,x} &= 0 \\ M^i_{xx,x} &= Q^i_x \\ M^i_{xy,x} &= Q^i_y \end{aligned}\right\} \quad \text{outside the overlap zone} \tag{6.4.6.2}$$

where *i* corresponds to the adherends *i*=1, 2, 3.

In generalized cylindrical bending the stress and moment resultants are only a function of the longitudinal coordinate *x*, and the derivatives with respect to the width direction *y* are all equal to zero. The equilibrium equations derived inside the overlap zones can be divided into the following two groups:

- Joints with one adhesive layer inside the overlap zone.
- Joints with two adhesive layers inside the overlap zone.

These two groups are further divided into joints with straight or scarfed adherends within the overlap. However, in the following only the equilibrium equations for joints with two straight adherends within the over lap will be shown, i.e. single lap joint (see Fig. 6.4.2 and Fig. 6.4.4); bonded doubler and single sided stepped lap joint. For a full description of the derivation of the equilibrium equations for the rest of the joint types, see Mortensen [6.4.6].

$$\begin{array}{ll}
N^1_{xx,x} = -\tau_{ax}, & N^2_{xx,x} = \tau_{ax}, \\
N^1_{xy,x} = -\tau_{ay}, & N^2_{xy,x} = \tau_{ay}, \\
Q^1_{x,x} = -\sigma_a, & Q^2_{x,x} = \sigma_a, \\
M^1_{xx,x} = Q^1_x - \tau_{ax}\cdot\dfrac{t_1(x)+t_a}{2}, & M^2_{xx,x} = Q^2_x - \tau_{ax}\cdot\dfrac{t_2(x)+t_a}{2}, \\
M^1_{xy,x} = Q^1_y - \tau_{ay}\cdot\dfrac{t_1(x)+t_a}{2} & M^2_{xy,x} = Q^2_y - \tau_{ay}\cdot\dfrac{t_2(x)+t_a}{2}
\end{array} \qquad (6.4.6.3)$$

where $t_1(x)$ and $t_2(x)$ are the adherend thicknesses and t_a is the adhesive layer thickness. For the single lap joint and for the bonded doubler the adherend thicknesses will remain the same in the entire overlap zone. For the single sided stepped lap joint, the adherend thicknesses will change inside the overlap zone between each step.

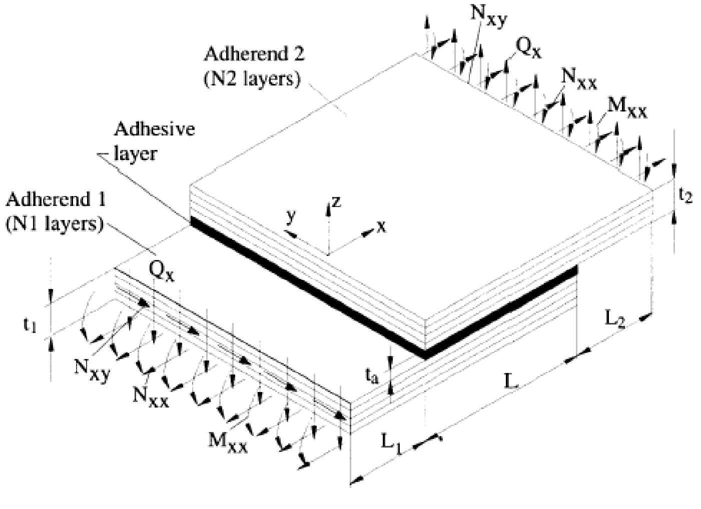

Fig. 6.4.2, Schematic illustration of adhesive single lap joint with straight adherends in the overlap zone subjected to general loading conditions.

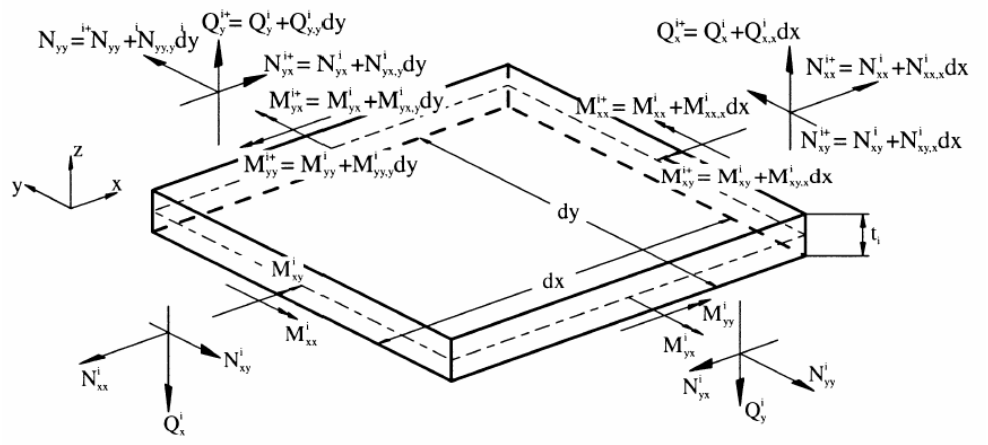
$N^{i+}_{yy}=N^{i}_{yy}+N^{i}_{yy,y}dy$
$Q^{i+}_{y}=Q^{i}_{y}+Q^{i}_{y,y}dy$
$N^{i+}_{yx}=N^{i}_{yx}+N^{i}_{yx,y}dy$
$M^{i+}_{yx}=M^{i}_{yx}+M^{i}_{yx,y}dy$
$M^{i+}_{yy}=M^{i}_{yy}+M^{i}_{yy,y}dy$
$Q^{i+}_{x}=Q^{i}_{x}+Q^{i}_{x,x}dx$
$N^{i+}_{xx}=N^{i}_{xx}+N^{i}_{xx,x}dx$
$M^{i+}_{xx}=M^{i}_{xx}+M^{i}_{xx,x}dx$
$N^{i+}_{xy}=N^{i}_{xy}+N^{i}_{xy,x}dx$
$M^{i+}_{xy}=M^{i}_{xy}+M^{i}_{xy,x}dx$
z
y
x
dy
dx
t_i
M^{i}_{xy}
M^{i}_{xx}
N^{i}_{xx}
N^{i}_{xy}
Q^{i}_{x}
M^{i}_{yy}
M^{i}_{yx}
N^{i}_{yx}
N^{i}_{yy}
Q^{i}_{y}

Fig. 6.4.3, Equilibrium elements of adherend outside the overlap zone.

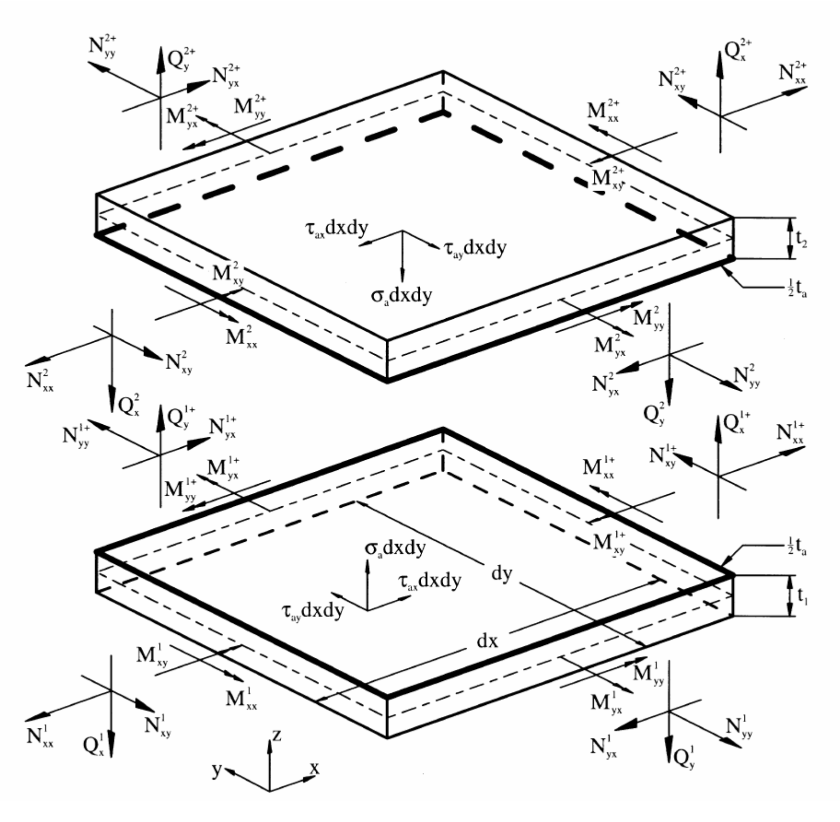
N^{2+}_{yy}
Q^{2+}_{y}
N^{2+}_{yx}
M^{2+}_{yx}
M^{2+}_{yy}
Q^{2+}_{x}
N^{2+}_{xy}
N^{2+}_{xx}
M^{2+}_{xx}
M^{2+}_{xy}
$\tau_{ax}dxdy$
$\tau_{ay}dxdy$
$\sigma_{a}dxdy$
t_2
$\frac{1}{2}t_a$
M^{2}_{xy}
M^{2}_{xx}
N^{2}_{xx}
N^{2}_{xy}
Q^{2}_{x}
M^{2}_{yy}
M^{2}_{yx}
N^{2}_{yx}
N^{2}_{yy}
Q^{2}_{y}
N^{1+}_{yy}
Q^{1+}_{y}
N^{1+}_{yx}
M^{1+}_{yx}
M^{1+}_{yy}
Q^{1+}_{x}
N^{1+}_{xx}
N^{1+}_{xy}
M^{1+}_{xx}
M^{1+}_{xy}
$\frac{1}{2}t_a$
$\sigma_{a}dxdy$
$\tau_{ax}dxdy$
$\tau_{ay}dxdy$
dy
dx
t_1
M^{1}_{xy}
M^{1}_{xx}
N^{1}_{xx}
Q^{1}_{x}
N^{1}_{xy}
M^{1}_{yy}
M^{1}_{yx}
N^{1}_{yx}
Q^{1}_{y}
N^{1}_{yy}
z
y
x

Fig. 6.4.4, Equilibrium element of adherends inside the overlap zone for joints with one adhesive layer and straight adherends.

6.4.6.4 The complete set of system equations

From the equations derived, it is possible to form the complete set of system equations for each of the bonded joint configurations. Thus, combination of the constitutive and kinematic relations, i.e. Eqns. (6.4.5.2) and (6.4.5.4), together with the constitutive relations for the adhesive layers, i.e. Eqn. (6.4.5.5), and the equilibrium equations lead to a set of 8 linear coupled first-order ordinary differential equations describing the system behavior of each of the adherends. The total set of coupled first-order ordinary differential equations within the overlap zone is therefore 16 for joints with two adherends inside the overlap zone, and 24 for the joints with 3 adherends inside the overlap zone. The actual derivations of the governing equations for the different bonded joint types are quite lengthy and described in Mortensen [6.4.6]. The governing equations can be expressed in the following general form within each region, i.e inside and outside the overlap zone:

$$\psi^n\{\{y^i(x^r)\}\},x = \begin{bmatrix} [\mathbf{A}^r_{11}(x^r)] & .. \; .. & [\mathbf{A}^r_{1n}(x^r)] \\ . & & . \\ . & & . \\ . & & . \\ . & & . \\ [\mathbf{A}^r_{n1}(x^r)] & .. \; .. & [\mathbf{A}^r_{nn}(x^r)] \end{bmatrix} \qquad (6.4.6.4)$$

$$\psi^n\{\{y^i(x^r)\}\} + \gamma^n\{\{\mathbf{B}^r_i(x^r)\}\}$$
$$\psi^n\{\{y^i(x^r)\}\} = \{\{y^1(x^r)\},\{y^i(x^r)\},\cdots,\{y^n(x^r)\}\}$$
$$\gamma^n\{\{\mathbf{B}^r_i(x^r)\}\} = \{\{\mathbf{B}^r_1(x^r)\},\{\mathbf{B}^r_2(x^r)\},\cdots,\{\mathbf{B}^r_n(x^r)\}\}$$

where n is the number of adherends within the region considered. The values of n are between 1 and 3 (both included) depending on the type of joint and the region considered. $[\mathbf{A}^r_{ij}(x^r)](i,j=1,...n)$ is a $(m,\ m)$ sub-coefficient matrix for the system of governing equations, and $\{\mathbf{B}^r_i(x^r)\}$ is a (m,1) sub-matrix of non-homogeneous load terms, where m is the number of equations for each adherend, i.e. 8 for the cylindrical bending case and 6 for the beam case. For the cylindrical bending case the vector $\{y^i\}$ is the vector containing the fundamental variables, which are those quantities that appear in the natural boundary conditions at an edge x = constant defined by:

$$\{y^i\} = \{u^i_0, w^i, \beta^i_x, v^i_0, N^i_{xx}, N^i_{xy}, M^i_{xx}, Q^i_x\} \;\; (i = 1, 2, 3) \qquad (6.4.6.5)$$

These variables will be determined through the analysis. In addition, the quantities can be determined from the equilibrium equations and the constitutive relations. These quantities can be considered as the stress and moment resultants necessary to keep the structure in a state of cylindrical bending. For the beam case the problem is reduced to a set of 6 coupled first-order ordinary differential equations for each adherend, and the solution vector containing the fundamental variables for each adherend for this problem is defined by:

$$\{y^i_{res^i}\} = \{N^i_{yy}, M^i_{yy}, M^i_{xy}, Q^i_y\} \;\; (i = 1, 2, 3) \qquad (6.4.6.6)$$

can be determined from the equilibrium equations and the constitutive relations. These quantities can be considered as the stress and moment resultants necessary to keep the structure in a state of cylindrical bending.

6.4.6.5 The boundary conditions

To solve the adhesive bonded joint problems (see Fig. 6.4.2) the boundary conditions and continuity conditions have to be stated. In the following the boundary conditions and continuity conditions are stated for a single lap joint, see Fig. 6.4.2:

$x = -L_1, L + L_2$: prescribed : u_0^i or N_{xx}^i , v_0^i or **Error! Objects cannot be created from editing field codes.**, β_x^i or M_{xx}^i , w^i or Q_x^i . $i = 1, 2$

$x = 0$, adherend 1, continuity cross junction
adherend 2, $N_{xx}^2 = N_{xy}^2 = Q_x^2 = M_{xx}^2 = 0$

$x = L$, adherend 1, $N_{xx}^1 = N_{xy}^1 = Q_x^1 = M_{xx}^1 = 0$
adherend 2, continuity cross junction

Non-mechanical loads: constant transverse strain e_0, temperature change ΔT, moisture content Δc

The boundary conditions for adherend 1 at $x = L$ and for adherend 2 at $x = 0$ are derived from the assumption that the adherend edge is free, see Fig. 6.4.2. The boundary conditions for other joint types can be prescribed similarly, please see details in Mortensen [6.4.6].

6.4.6.6 Multi-segment method of integration

The governing equations, together with the boundary conditions constitutes a multiple point boundary value problem to which no general closed-form solution is obtainable. The multiple-point boundary value problem is therefore solved using the ‘multi-segment method of integration’. The method is based on a transformation of the original ‘multiple point’ boundary value problem into a series of initial value problems. The principle behind the method is to divide the original problem into a finite number of segments, where the solution within each segment can be accomplished by means of direct integration. Fulfillment of the boundary conditions, as well as fulfillment of continuity requirements across the segment junctions, is assured by formulating and solving a set of linear algebraic equations. For a detailed description of the method, see Mortensen [6.4.6].

6.4.7 In-plane Stresses in the Adherends

The laminate lay-up and coordinate system is shown in Fig. 6.4.5. The in-plane stresses and strains of the laminated adherends can be obtained directly from CLT, in which Kirchhoff’s linear assumption is applied, i.e., $\gamma_{yz} = \gamma_{zx} = 0$ and $\varepsilon_z = 0$. This assumption leads to the linear relation between the displacement field of laminate and the middle-plane displacement

$\boldsymbol{u}^0 = \{u^0, v^0, w^0\}$, i.e.,

$$\begin{aligned} w(x,y,z) &= w^0 \\ u(x,y,z) &= u^0 - z\frac{\partial w}{\partial x} \\ v(x,y,z) &= v^0 - z\frac{\partial w}{\partial y} \end{aligned} \tag{6.4.7.1}$$

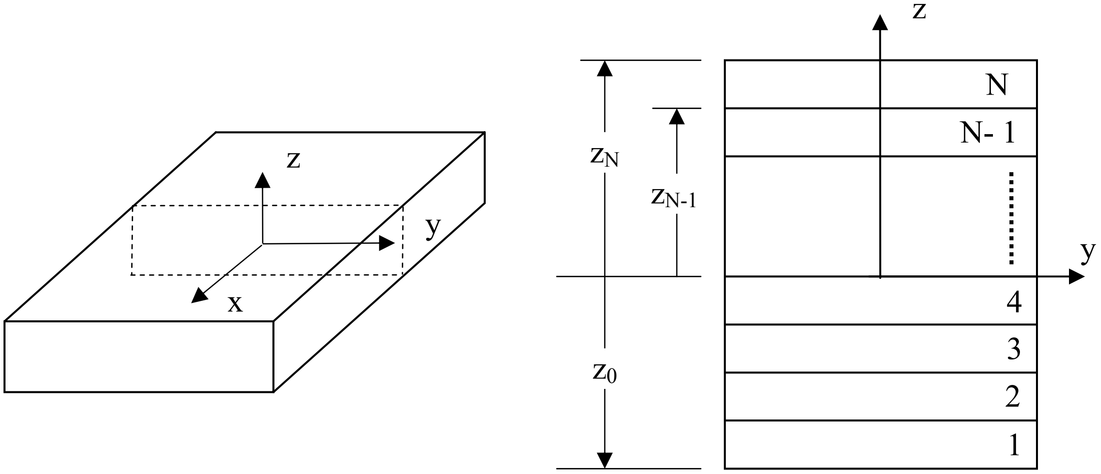

Fig. 6.4.5, Lay-up of a laminate and the coordinate system.

The in-plane strain fields in the laminate can thus be derived from the kinematics relation. They are

$$\begin{aligned} \varepsilon_x &= \frac{\partial u}{\partial x} = \frac{\partial u^0}{\partial x} + z(-\frac{\partial^2 w}{\partial x^2}) = \varepsilon_x^0 + z\kappa_x \\ \varepsilon_y &= \frac{\partial v}{\partial y} = \frac{\partial v^0}{\partial y} + z(-\frac{\partial^2 w}{\partial y^2}) = \varepsilon_y^0 + z\kappa_y \\ \gamma_{xy} &= \frac{\partial v}{\partial x} + \frac{\partial u}{\partial y} = \frac{\partial v^0}{\partial x} + \frac{\partial u^0}{\partial y} + z(-2\frac{\partial^2 w}{\partial x \partial y}) = \gamma_{xy}^0 + z\kappa_{xy} \end{aligned} \tag{6.4.7.2}$$

where $\boldsymbol{\varepsilon}^0 = \{\varepsilon_x^0, \varepsilon_y^0, \varepsilon_z^0\}$ is strain of middle plane and $\boldsymbol{\kappa} = \{\kappa_x, \kappa_y, \kappa_{xy}\}$ is the curvature of middle-plane. The in-plane deformation of an arbitrary point in the laminate can be obtained through (17) once the middle-plane deformation is known. The later can be solved from the overall equilibriums and constitutive equation of the laminate.

Under the assumption of cylindrical bending and generalized plane strain, the middle-plane displacement is given in the forms as following

$$u^0 = u^0(x) \qquad v^0 = e_0 y + v^0(x) \qquad w^0 = w^0(x) \tag{6.4.7.3}$$

Thus, Eqn. (6.4.7.2) can be reduced to

$$\begin{aligned}
\varepsilon_x &= \frac{\partial u^0}{\partial x} + z(-\frac{\partial^2 w}{\partial x^2}) = u^0_{x,x} + z\beta_{x,x} \\
\varepsilon_y &= \frac{\partial v^0}{\partial y} + z(-\frac{\partial^2 w}{\partial y^2}) = e_0 \\
\gamma_{xy} &= \frac{\partial v^0}{\partial x} + \frac{\partial u^0}{\partial y} + z(-2\frac{\partial^2 w}{\partial x \partial y}) = v^0_{x,x}
\end{aligned} \tag{6.4.7.4}$$

The in-plane stress components of the laminated adherends can be obtained through the constitutive equation for each ply. Considering the hygrothermal effect, the in-plane stresses of the *k*th ply are given by

$$\begin{bmatrix} \sigma_{xx} \\ \sigma_{yy} \\ \tau_{xy} \end{bmatrix}^{(k)} = \begin{bmatrix} \overline{Q}_{11} & \overline{Q}_{12} & \overline{Q}_{16} \\ \overline{Q}_{21} & \overline{Q}_{22} & \overline{Q}_{26} \\ \overline{Q}_{61} & \overline{Q}_{62} & \overline{Q}_{66} \end{bmatrix}^{(k)} \left\{ \begin{bmatrix} \varepsilon_{xx} \\ \varepsilon_{yy} \\ \gamma_{xy} \end{bmatrix} - \begin{bmatrix} \varepsilon^*_{xx} \\ \varepsilon^*_{yy} \\ \gamma^*_{xy} \end{bmatrix} \right\}^{(k)} \tag{6.4.7.5}$$

where $\boldsymbol{\varepsilon}^*$ is the hygrothermal strain, which is given by

$$\begin{bmatrix} \varepsilon^*_{xx} \\ \varepsilon^*_{yy} \\ \gamma^*_{xy} \end{bmatrix} = \Delta T \begin{bmatrix} \alpha_x \\ \alpha_y \\ \alpha_s \end{bmatrix} + \Delta c \begin{bmatrix} \beta_x \\ \beta_y \\ \beta_s \end{bmatrix} \tag{6.4.7.6}$$

where $\boldsymbol{\alpha}$ and $\boldsymbol{\beta}$ are the coefficients of thermal and moisture expansion, respectively.

6.4.8 Out-of-plane (Interlaminar) Stresses in the Adherends

Even though the Classical Laminate Theory does not account for the transverse deformation, the interlaminate stresses can also be calculated approximately through equilibrium equations. Without body force, the equilibrium equations are given as

$$\begin{aligned}
\frac{\partial \sigma_{xx}}{\partial x} + \frac{\partial \tau_{xy}}{\partial y} + \frac{\partial \tau_{xz}}{\partial z} &= 0 \\
\frac{\partial \tau_{xy}}{\partial x} + \frac{\partial \sigma_{yy}}{\partial y} + \frac{\partial \tau_{yz}}{\partial z} &= 0 \\
\frac{\partial \sigma_{zz}}{\partial z} + \frac{\partial \tau_{yz}}{\partial y} + \frac{\partial \tau_{xz}}{\partial x} &= 0
\end{aligned} \tag{6.4.8.1}$$

Under the assumption of cylindrical bending, $\frac{\partial \sigma_{yy}}{\partial y} = \frac{\partial \tau_{yz}}{\partial y} = \frac{\partial \tau_{xy}}{\partial y} = 0$. Thus, the interlaminar stress components can be obtained from the following relations,

$$\begin{aligned} \tau_{xz} &= -\int_{free\ \ surface}^{z} \left(\frac{\partial \sigma_{xx}}{\partial x}\right) \mathrm{d}\, z \\ \tau_{yz} &= -\int_{free\ \ surface}^{z} \left(\frac{\partial \tau_{xy}}{\partial x}\right) \mathrm{d}\, z \\ \sigma_{zz} &= -\int_{free\ \ surface}^{z} \left(\frac{\partial \tau_{xz}}{\partial x}\right) \mathrm{d}\, z \end{aligned} \tag{6.4.8.2}$$

by assuming that they vanish at the free surfaces. One simple way to calculate the interlaminar stresses is to numerically differentiate the solutions obtained by Mortensen's *multi-segment method*, which gives the numerical solutions of variables $\{u^0, v^0, w^0, \beta_x, N_{xx}, N_{xy}, M_{xx}, Q_x\}$ in the adherends and then integrate Eqn. (6.4.8.2) numerically. However, the large oscillation is found in the results due to lack of continuity of the derivatives of the variables at the interface between segments.

In order to overcome the oscillation problem, we have to do some algebra to avoid using numerical derivatives of the multi-segment solutions. First, expand Eqn. (6.4.7.5) and write the in-plane stress component σ_{xx} and τ_{xy} as

$$\begin{aligned} \sigma_{xx}^{(k)} &= \overline{Q}_{11}^{(k)}[\varepsilon_{xx}^{(k)} - \varepsilon_{xx}^{(k)*}] + \overline{Q}_{12}^{(k)}[\varepsilon_{yy}^{(k)} - \varepsilon_{yy}^{(k)*}] + \overline{Q}_{16}^{(k)}[\gamma_{xy}^{(k)} - \gamma_{xy}^{(k)*}] \\ &= \overline{Q}_{11}^{(k)}\{(u_{,x}^{0} + z^{(k)}\beta_{x,x}) - \varepsilon_{xx}^{(k)*}\} + \overline{Q}_{12}^{(k)}[e_0 - \varepsilon_{yy}^{(k)*}] + \overline{Q}_{16}^{(k)}[v_{,x}^{0} - \gamma_{xy}^{(k)*}] \end{aligned} \tag{6.4.8.3}$$

$$\begin{aligned} \tau_{xy}^{(k)} &= \overline{Q}_{16}^{(k)}[\varepsilon_{xx}^{(k)} - \varepsilon_{xx}^{(k)*}] + \overline{Q}_{26}^{(k)}[\varepsilon_{yy}^{(k)} - \varepsilon_{yy}^{(k)*}] + \overline{Q}_{66}^{(k)}[\gamma_{xy}^{(k)} - \gamma_{xy}^{(k)*}] \\ &= \overline{Q}_{16}^{(k)}\{(u_{,x}^{0} + z^{(k)}\beta_{x,x}) - \varepsilon_{xx}^{(k)*}\} + \overline{Q}_{26}^{(k)}[e_0 - \varepsilon_{yy}^{(k)*}] + \overline{Q}_{66}^{(k)}[v_{,x}^{0} - \gamma_{xy}^{(k)*}] \end{aligned} \tag{6.4.8.4}$$

Assuming the hygrothermal strains are constants in each ply, the derivatives of σ_{xx} and τ_{xy} are thus given as

$$\frac{\partial \sigma_{xx}^{(k)}}{\partial x} = \overline{Q}_{11}^{(k)}[u_{,xx}^{0} + z^{(k)}\beta_{x,xx}] + \overline{Q}_{16}^{(k)}[v_{,xx}^{0}] \tag{6.4.8.5}$$

$$\int_{free}^{z} \frac{\partial \sigma_{xx}^{(k)}}{\partial x} dz = \sum_{k=1}^{i} \overline{Q}_{11}^{(k)}[\left(z^{(k+1)} - z^{(k)}\right)u_{,xx}^{0} + \frac{1}{2}\left(z^{(k+1)^2} - z^{(k)^2}\right)\beta_{x,xx}] + \sum_{k=1}^{i} \overline{Q}_{16}^{(k)}[v_{,xx}^{0}\left(z^{(k+1)} - z^{(k)}\right)] \tag{6.4.8.6}$$

$$\frac{\partial \tau_{xy}^{(k)}}{\partial x} = \overline{Q}_{16}^{(k)}[u_{,xx}^{0} + z^{(k)}\beta_{x,xx}] + \overline{Q}_{66}^{(k)}[v_{,xx}^{0}] \tag{6.4.8.7}$$

$$\int_{free}^{z} \frac{\partial \tau_{xy}^{(k)}}{\partial x} dz = \sum_{k=1}^{i} \overline{Q}_{16}^{(k)}[\left(z^{(k+1)} - z^{(k)}\right)u_{,xx}^{0} + \frac{1}{2}\left(z^{(k+1)^2} - z^{(k)^2}\right)\beta_{x,xx}] + \sum_{k=1}^{i} \overline{Q}_{66}^{(k)}[v_{,xx}^{0}\left(z^{(k+1)} - z^{(k)}\right)] \tag{6.4.8.8}$$

Instead of taking numerical derivatives of u^0, β_x and v^0 to get $u^0_{,xx}$, $\beta_{x,xx}$ and $v^0_{,xx}$, we can obtain their expression from the equilibrium equations of joints. For example, for the single-lap and bonded doubler joints, we have the following relations

$$\begin{aligned} u^0_{,xx} &= k_{11}N_{xx,x} + k_{21}N_{xy,x} + k_{31}M_{xx,x} \\ \beta_{x,xx} &= k_{41}N_{xx,x} + k_{51}N_{xy,x} + k_{61}M_{xx,x} \\ v^0_{,xx} &= k_{71}N_{xx,x} + k_{81}N_{xy,x} + k_{91}M_{xx,x} \end{aligned} \tag{6.4.8.9}$$

where

$$\begin{aligned} N^1_{xx,x} &= \frac{G_a}{t_a}u^1_0 + \frac{G_a t_1}{2t_a}\beta^1_x - \frac{G_a}{t_a}u^2_0 + \frac{G_a t_2}{2t_a}\beta^2_x & \qquad N^2_{xx,x} &= -\frac{G_a}{t_a}u^1_0 - \frac{G_a t_1}{2t_a}\beta^1_x + \frac{G_a}{t_a}u^2_0 - \frac{G_a t_2}{2t_a}\beta^2_x \\ N^1_{xy,x} &= \frac{G_a}{t_a}v^1_0 - \frac{G_a}{t_a}v^2_0 & N^2_{xy,x} &= -\frac{G_a}{t_a}v^1_0 + \frac{G_a}{t_a}v^2_0 \\ M^1_{xx,x} &= Q^1_x + \frac{G_a(t_1+t_a)}{2t_a}u^1_0 + \frac{G_a t_1(t_1+t_a)}{4t_a}\beta^1_x & M^2_{xx,x} &= Q^2_x + \frac{G_a(t_2+t_a)}{2t_a}u^1_0 + \frac{G_a t_1(t_2+t_a)}{4t_a}\beta^1_x \\ &\quad - \frac{G_a(t_1+t_a)}{2t_a}u^2_0 + \frac{G_a t_2(t_1+t_a)}{4t_a}\beta^2_x & &\quad - \frac{G_a(t_2+t_a)}{2t_a}u^2_0 + \frac{G_a t_2(t_2+t_a)}{4t_a}\beta^2_x \\ Q^1_{x,x} &= \frac{E_a}{t_a}w^1 - \frac{E_a}{t_a}w^2 & Q^2_{x,x} &= -\frac{E_a}{t_a}w^1 + \frac{E_a}{t_a}w^2 \end{aligned} \tag{6.4.8.10}$$

on the overlap region and on the non-overlap region, they are

$$\begin{aligned} N^i_{xx,x} &= 0 \\ N^i_{xy,x} &= 0 \\ Q^i_{x,x} &= 0 \qquad\qquad (i = 1,2) \\ M^i_{xx,x} &= Q^i_x \end{aligned} \tag{6.4.8.11}$$

Note that eqns. (6.4.8.10) and (6.4.8.11) may have different forms for other joint types. As hygrothermal effect is considered, the system equations given by Mortensen's need to be modified, as Eqn. (6.4.5.2). Also note that the interlaminar stresses solved by the above approach are based on the equilibrium equations and the in-plane stresses obtained by Classical Lamination Theory. They do not satisfy the free edge boundary conditions, where the shear stresses should drop to zero.

6.4.9 Nonlinear Analysis of Adhesive

The method developed by Mortensen to analyze the adhesively bonded composite joints has been implemented recently in Collier Research Corp. This method assumes cylindrical bending of laminated adherends and spring-like response of the adhesive layer. Good agreement has been reached for the adhesive shear and peel stresses between Mortensen's elastic solution and FEA. We expect that good agreement will be reached between them for nonlinear solutions as the adhesive is treated as an elasto-plastic material. Mortensen has briefly explained the nonlinear formulation and solution procedure; however, it is rather difficult for engineers to implement it as many details have not been disclosed. This report will give the detailed procedure for implementation of the nonlinear analysis of bonded joints. Finally, numerical examples will be presented.

6.4.9.1 Non-linear Material Model of the Adhesive

Adhesives can be characterized using the updated standard test methods following two ways: one is the test of bulk adhesive, and the other is determination of *in-situ* adhesive properties in the bonded joints. The bulk adhesive properties are intrinsic and not influenced by the adherends. In the case of adhesive joints, adhesives are constraint between adherends and their properties are subjected to the influence of adherends and are thus more representative of real behavior. However, Jeandrau [6.4.12, 6.4.13] confirmed that difference between the adhesive shear modulus obtained in joint test is almost same as those obtained through tension-compression test for the bulk material ($G = E/2(1+v)$).

The nonlinear adhesive behavior can be modeled with a measured true stress-strain curve, either in pure tension or in pure shear and a mathematical model that takes all stress combination into account. The measured stress-strain curves can be characterized by a variety of mathematical models for the sake of analytical and numerical analysis. In the following, we briefly describe some most commonly used mathematical models.

6.4.9.1.1 Elastic-plastic model

This model contains two parts: one is linear elastic part; another is plastic part without hardening. The model can be expressed as

$$\sigma = \begin{cases} E\varepsilon & \text{as } |\varepsilon| \le \varepsilon_s \\ \sigma_s & \text{as } \varepsilon > \varepsilon_s \\ -\sigma_s & \text{as } \varepsilon < -\varepsilon_s \end{cases} \tag{6.4.9.1}$$

where σ_s is the yield stress and ε_s is the yield strain.

6.4.9.1.2 Bi-linear model

This model contains also two parts: one is linear elastic part; another is plastic part with linear hardening. The model can be expressed as

$$\sigma = \begin{cases} E\varepsilon & \text{as } |\varepsilon| \le \varepsilon_s \\ \sigma_s + E_p(\varepsilon - \varepsilon_s) & \text{as } \varepsilon > \varepsilon_s \\ -\sigma_s - E_p(\varepsilon - \varepsilon_s) & \text{as } \varepsilon < -\varepsilon_s \end{cases} \tag{6.4.9.2}$$

where E_p is the slope of the curve of the plastic part, as shown in Fig. 6.4.6.

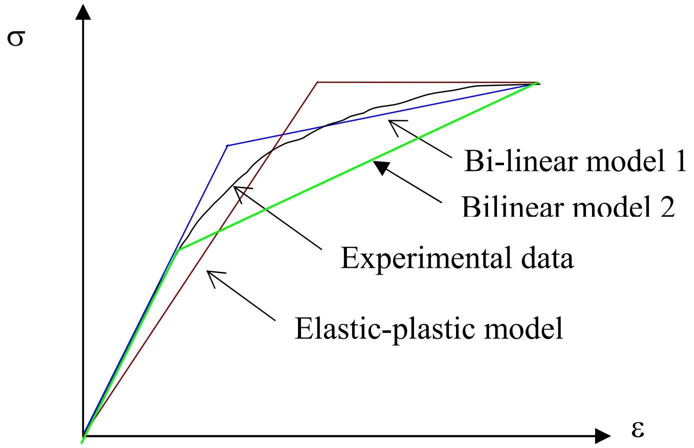

Fig. 6.4.6, Models for nonlinear adhesive stress-strain curves

6.4.9.1.3 Power law material model

This model represents a set of continuous curves that can be expressed as

$$\sigma = A\varepsilon^n + B \tag{6.4.9.3}$$

where *A, B* are constants. These constants are determined by forcing the continuity of slope and value at the yield point σ_s. The model can be handled easily in mathematics.

6.4.9.1.4 Ramberg-Osgood model

This model represents a set of continuous curves, with expression as

$$\varepsilon = \frac{\sigma}{E} + \frac{3}{7}\frac{\sigma_0}{E}\left(\frac{\sigma}{\sigma_0}\right)^n \tag{6.4.9.4}$$

where n is the material constant, and $n > 1$. As σ is very small, the model represents quasi-linear elastic material.

6.4.9.1.5 Multilinear (Polynomial) model

The stress-strain relation of adhesives shown in Fig. 6.4.6 can be fitted using polynomials.

6.4.9.2 Yielding of the Adhesive

For most ductile materials, such as metals, plastic, etc., their yield behaviors have been regarded to be related only to the deviatoric stress (s_{ij}). However, the yield behavior of polymeric structural adhesives is depended on both deviatoric and hydrostatic stress (σ_{ii}) components. This phenomena result in the difference between the yield stresses in uniaxial tension and compression. Based on the observation of experiments, Gali et al. (1981) found that the bulk polymeric adhesive properties obtained by a uni-axial test, such as tension, compression and torsion, can be related to the properties of an 'in-situ' adhesive layer in shear by a combined stress law that follows a modified Von Mises criterion, which is given as

$$s = C_S (J_{2D})^{1/2} + C_V J_1 \,,\ C_S = \frac{\sqrt{3}(1+\lambda)}{2\lambda} \,,\ C_V = \frac{\lambda - 1}{2\lambda} \,,\ \lambda = \frac{\sigma_c}{\sigma_t} \tag{6.4.9.5}$$

where s is the effective stress, J_{2D} is the second invariant of the deviatoric stress tensor, J_1 is the first invariant of stress tensor and n is the ratio of the compressive yield stress to the tensile yield stress. J_{2D} and J_1 are defined by:

$$J_{2D} = \frac{1}{6}[(\sigma_1 - \sigma_2)^2 + (\sigma_2 - \sigma_3)^2 + (\sigma_3 - \sigma_1)^2] \tag{6.4.9.6}$$

$$J_1 = \sigma_1 + \sigma_2 + \sigma_3 \tag{6.4.9.7}$$

For $\lambda = 1$, Eqn. (6.4.9.1) reduces to the well-known Von Mises criterion.

The effective strain e is given as

$$e = C_S \frac{1}{1+v}(I_{2D})^{1/2} + C_V \frac{1}{1-2v} I_1 \tag{6.4.9.8}$$

where v is Poisson's ratio, I_{2D} is the second invariant of the deviatoric strain tensor and I_1 is the first invariant of the strain tensor. I_{2D} and I_1 are defined by

$$I_{2D} = \frac{1}{6}[(\varepsilon_1 - \varepsilon_2)^2 + (\varepsilon_2 - \varepsilon_3)^2 + (\varepsilon_3 - \varepsilon_1)^2] \tag{6.4.9.9}$$

$$I_1 = \varepsilon_1 + \varepsilon_2 + \varepsilon_3 \tag{6.4.9.10}$$

6.4.9.3 Stresses of Elastic Adhesive Layer

In Mortensen's model, the adhesive is regarded as a tension-shear spring, by which the adhesive transverse normal strain and in-plane shear strain are simply derived from the difference of displacements of the surface plies of the upper and bottom adherends. We recall the Mortensen's formulation for the adhesive strains, which are given as

$$\gamma_{ax} = (u^i - u^j)/t_a \qquad \gamma_{ay} = (v^i - v^j)/t_a \qquad \varepsilon_{zz} = (w^i - w^j)/t_a \tag{6.4.9.11}$$

where i and j are the number of the adherends, apparently $i \neq j$. The stresses in adhesive are then given by Hooke's law,

$$\tau_{ax} = G_a \gamma_{ax} \qquad \tau_{ay} = G_a \gamma_{ay} \qquad \sigma_{zz} = E_a \varepsilon_{zz} \tag{6.4.9.12}$$

where G_a and E_a shear and Young's modulus of the adhesive. Thus, the stress and strain invariants defined in Eqns. (6.4.9.6), (6.4.9.7), (6.4.9.9), (6.4.9.10) can be expressed as

$$J_{2D} = \frac{1}{6}[2\sigma_{zz}^2 + 6(\tau_{ax}^2 + \tau_{ay}^2)] \qquad J_1 = \sigma_{zz} \tag{6.4.9.13}$$

$$I_{2D} = \frac{1}{6}[2\varepsilon_{zz}^2 + \frac{3}{2}(\gamma_{ax}^2 + \gamma_{ay}^2)] \qquad I_1 = \varepsilon_{zz} \tag{6.4.9.14}$$

6.4.9.4 Non-linear Solution Procedure

As was mentioned, the mechanical properties of the bulk adhesive are not only almost same in elastic range but also closely related in inelastic range to the in-situ structural adhesives. The non-linear adhesive properties are included by implementing an effective stress-strain relationship derived either experimentally from tests on bulk adhesives, or from mathematical models.

Based on the secant modulus approach by Mortensen for the nonlinear effective stress-strain relationship for the adhesive, as shown in Fig. 6.4.7, the solution procedure for determining the stress distribution in the adhesive layer can be described by the following steps.

1) Calculate the effective strains e_1 and stresses s_1^* according to Eqn. (6.4.9.5) and (6.4.9.8) for **each point** of the adhesive (See Fig.6.4.8), using the **linear elastic** solution procedure, assuming a uniform elastic modulus E_1 and for the adhesive. In this step you will get linear solutions for the given adhesive modulus.
2) If the calculated effective stress s_1^* at any point in the adhesive is above the elastic limit (s_{prop}), then determine the effective stress s_1 at **each point** according to the corresponding effective strain e_1 (calculated in step 1) using the experimental stress-strain relation in Fig. 6.4.7.
3) Calculate the difference $\Delta s_1 = s_1^* - s_1$ between the 'calculated' and the 'experimental' effective stresses, and determine the specific secant-modulus E_2 defined by:

$$E_2 = \{1 - \delta(\Delta s_1 / s_1)\} E_1 \tag{6.4.9.15}$$

   δ is a non-negative weight-factor, which determines the change of the modulus in each iteration. Note that in the Matlab code, instead of using a fix number through the iteration, δ is taken as 0.9/iteration empirically for each point. As iteration number increases δ becomes smaller, so that it ensures convergence.
4) Re-run the procedure (steps (1) – (2)) with the elastic modulus E_1, for **each adhesive point** modified as per step (3).
5) Compare the 'calculated' effective stresses s^* for each adhesive point with 'experimental' values s obtained from the effective stress-strain curve.
6) Repeat steps (4)-(5) until the difference between the 'calculated' and 'experimental' stresses (Δs) drops below (or less than) a specific fraction ($|\Delta s / s| < 2\%$) of the experimental stress values.

Note that in order to increase the computation efficiency; we don't calculate the effective stress and strain values at "each point", as described in Mortensen's thesis. Instead, we selected finite points along the adhesive layer. More points should be selected in the free edge regions where stress and strain gradients are expected to be large, as shown in Fig. 6.4.8.

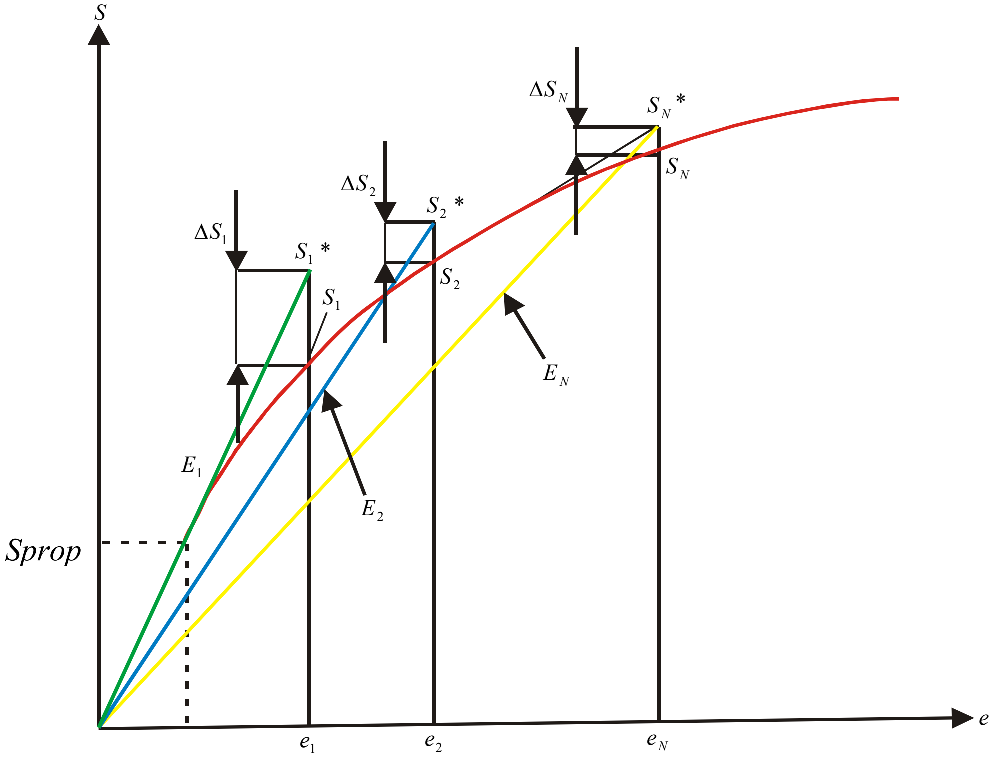

S
ΔS_N
S_N *
S_N
ΔS_2
S_2 *
S_2
ΔS_1
S_1 *
S_1
E_N
E_1
E_2
Sprop
e_1
e_2
e_N
e

Fig. 6.4.7, Illustration of the nonlinear solution procedure for adhesive joints.

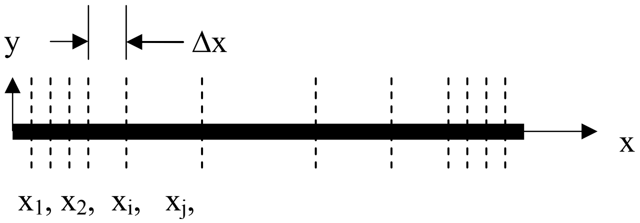

y
Δx
x
x_1, x_2, x_i, x_j,

Fig. 6.4.8, Points on the adhesive layer in nonlinear analysis.

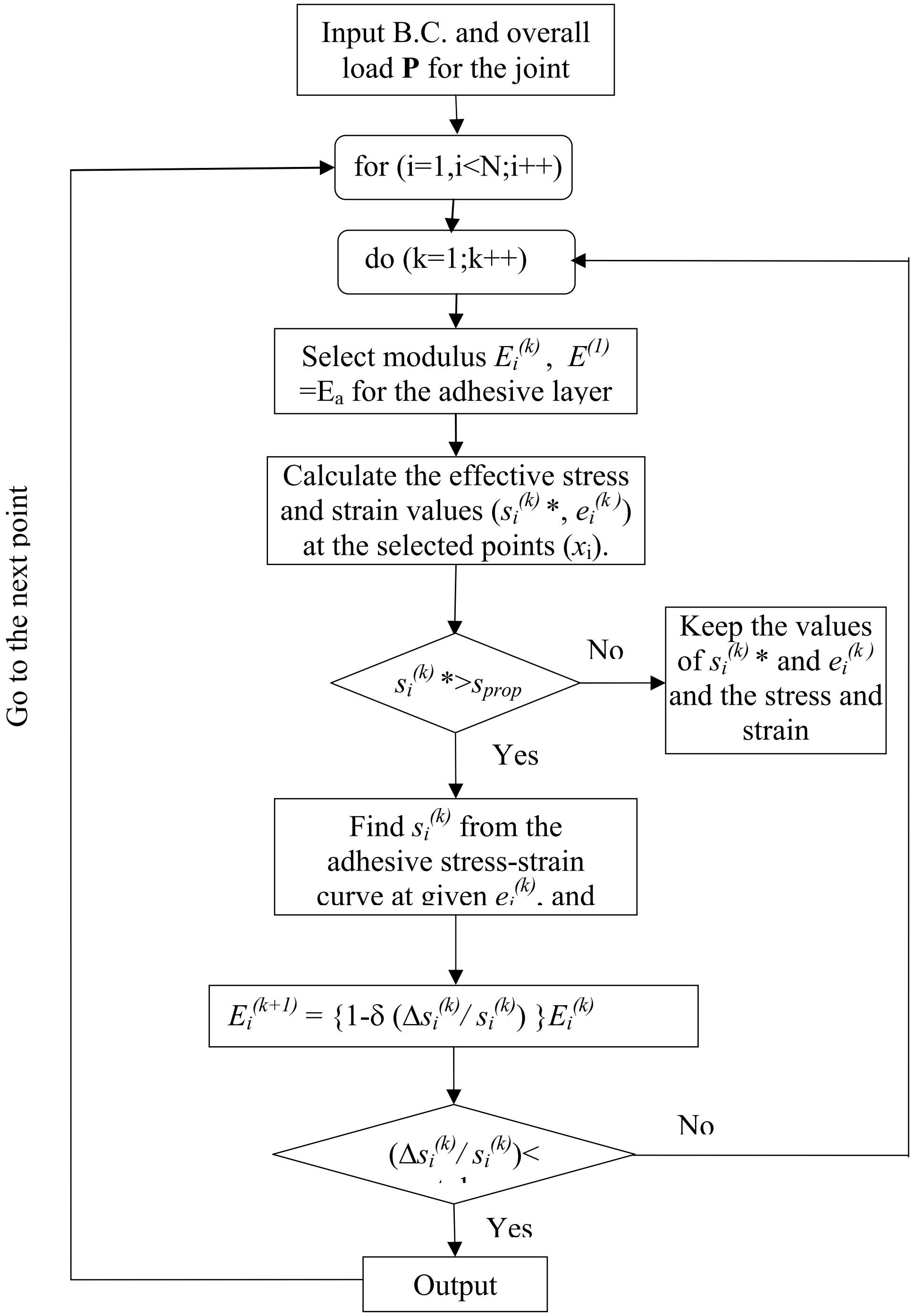
Input B.C. and overall load **P** for the joint
for (i=1,i<N;i++)
do (k=1;k++)
Select modulus $E_i^{(k)}$, $E^{(1)}$ =E_a for the adhesive layer
Calculate the effective stress and strain values ($s_i^{(k)}$ *, $e_i^{(k)}$) at the selected points (x_i).
$s_i^{(k)}$ *>s_{prop}
No
Keep the values of $s_i^{(k)}$ * and $e_i^{(k)}$ and the stress and strain
Yes
Find $s_i^{(k)}$ from the adhesive stress-strain curve at given $e_i^{(k)}$, and
$E_i^{(k+1)}$ = {1-δ ($\Delta s_i^{(k)}$/ $s_i^{(k)}$) }$E_i^{(k)}$
($\Delta s_i^{(k)}$/ $s_i^{(k)}$)<
No
Yes
Output
Go to the next point

Fig. 6.4.9, Flow chart for the nonlinear analysis for the adhesively bonded joints.

Fig. 6.4.9 shows the flow chart for the nonlinear analysis procedure, modifying the existing computer code.

6.4.9.5 Conclusions

The Elastic-plastic solutions look reasonable. The accuracy needs to be verified with FEA. The computation time is proportional to the number of yield points, i.e. the more yield points, the more time it takes. The solution may oscillate if the load becomes unreasonably large and far exceeds the ultimate strength of adhesives, however this becomes irrelevant as the assumption is that the adhesive would have failed long before reaching this load magnitude.

6.4.10 References

6.4.1 Adams, R. D., Coppendale J., Peppiatt N. A., “Failure analysis of aluminium – aluminium bonded joints,” Adhesion 1978, 2:105–19.

6.4.2 Gali S., Dolev G., Ishai O., “An effective stress/strain concept in mechanical characterization of structural adhesive bonding,” International Journal of Adhesion and Adhesives 1981, 1:135–40.

6.4.3 Harris, J. A., Adams R. D., “Strength prediction of bonded single lap joints by non-linear finite element methods,” International Journal of Adhesion and Adhesives 1984; 4:65–78.

6.4.4 Herakovich, C. T., “Mechanics of Fibrous Composites,” 1998, John Wiley & Sons, Inc.

6.4.5 Lilleheden, L., “Properties of adhesive in situ and in bulk,” International Journal of Adhesion and Adhesive 1994, 14(1):31–7.

6.4.6 Mortensen, F., (1998), “Development of Tools for Engineering Analysis and Design of High-Performance FRP-Composite Structural Elements,” Ph.D. Thesis, Institute of Mechanical Engineering, Aalborg University (Denmark), Special Report no. 37.

6.4.7 Thomsen, O. T., “Analysis of adhesive bonded generally orthotropic circular cylindrical shells,” PhD thesis. Institute of Mechanical Engineering. Aalborg University, Denmark, Special Report, 4, 1989.

6.4.8 Thomsen, O. T., “Elasto-static and elasto-plastic stress analysis of adhesive bonded tubular lap joints,” Composite Structures 1992, 21:249–59.

6.4.9 Tong, L. “Bond strength for adhesive-bonded single-lap joints,” Acta Mechanic 1996, 117:101–13 [Springer-Verlag].

6.4.10 Whitney, J. M., Structural analysis of laminated anisotropic plates. Lancaster: Technomic Publishing Company, 1987.

6.4.11 Aboudi, J., M.-J., Pindera and Arnold, S.M. (1999) “Higher-Order Theory for Functionally Graded Materials,” *Composites: Part B* 30, 777-832.

6.4.12 Jeandrau, J. P., (1986), “Intrinsic Mechanical Characterization of Structural Adhesives,” *International Journal of Adhesion and Adhesives*, Vol.6, pp.229-231.

6.4.13 Jeandrau, J. P., (1991), “Analysis and Design Data for Adhesively Bonded Joints,” *International Journal of Adhesion and Adhesives*, Vol.11, pp.71-79.

6.4.14 Gali, S., Dolev, G. and IshaiC, O., (1981), “An Effective Stress/Strain Concept in Mechanical Characterization of Structural Adhesive Bonding,” *International Journal of Adhesion and Adhesives*, Vol.1, pp.135-140.

6.5 Strength Failure Theories

6.5.1 Summary of Failure Modes and Equations

The failure theories that are implemented in HyperSizer are listed in more detail in Volume 3. These theories fall into two broad categories, those that apply to the adherends, such as matrix or fiber cracking or delamination, and those that apply to the adhesive.

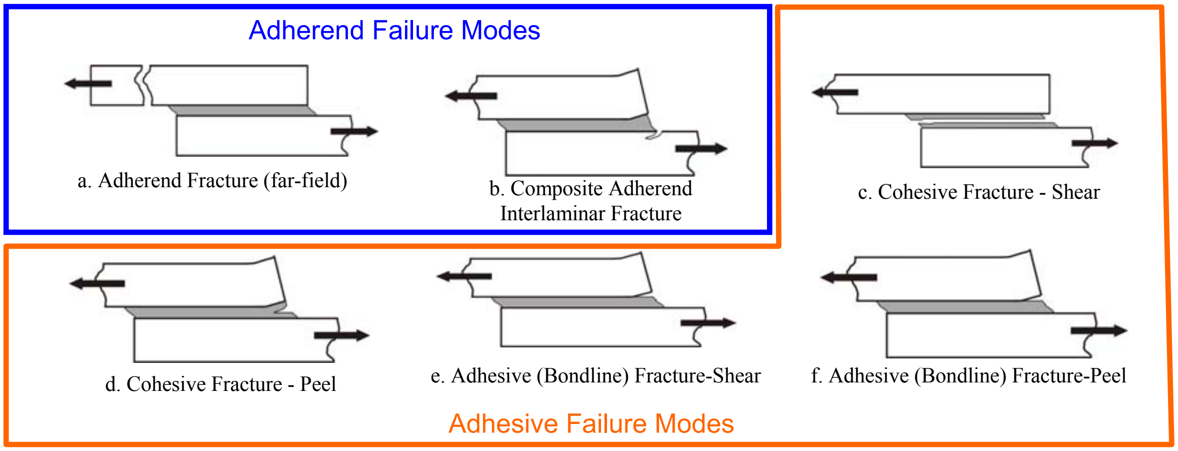

a. Adherend Fracture (far-field)

b. Composite Adherend Interlaminar Fracture

c. Cohesive Fracture - Shear

d. Cohesive Fracture - Peel

e. Adhesive (Bondline) Fracture-Shear

f. Adhesive (Bondline) Fracture-Peel

Fig. 6.5.1, Failure modes in adhesively bonded joints identified by Heslehurst and Hart-Smith

The failure modes depicted in Fig. 6.5.1 are represented by the following equations:

a. Equations (6.5.2.12), (6.5.2.13)
b. Equations (6.5.2.1)-(6.5.2.11)
c. Equations (6.5.3.1), (6.5.3.2), 6.5.3.6), (6.5.3.7)
d. Equations (6.5.3.1) - (6.5.3.5), (6.5.3.8).
e. Equations (6.5.3.6)
f. Equations (6.5.3.4), (6.5.3.8)

6.5.2 Adherend Failure

6.5.2.1 Interlaminar delamination

Interlaminar delamination is a typical failure mode for adhesive bonded joints. Most researchers believe it is caused by the weakness of composite adherends in the through thickness direction. There are a number of failure criteria proposed for predicting the failure of bonded joints due to interlaminar delamination.

Adams [6.5.1] proposed one simple Maximum Stress criterion, which assumed that interlaminar failure in a composite adherend occurs when the normal tensile stress at the interface exceeds its ultimate strength. It is given as

$$\frac{\sigma_3}{Z} = 1 \tag{6.5.2.1}$$

where Z is the through-the-thickness tensile strength of the composite adherends. This criterion regards the interfacial peel stress as the major contributor to the delamination failure.

Hoyt [6.5.4] used the following failure criterion to predict the damage initiation induced by interlaminar stresses in bonded doubler with [45/0/45/0/45/0/45/0/45] IM7/8552 Fabric for the flange and [45/-45/90/45/-45/0/-45/45/90/-45/45] for the skin. It is

$$\frac{\sigma_3}{Z} + \left(\frac{\tau_{13}}{R}\right)^2 = 1 \tag{6.5.2.2}$$

where *R* is the interlaminar shear strength in the 13-plane. In general, the laminate normal tensile strength is less than through-the-thickness shear strength, so that in Equation (6.5.2.2) the contribution from the normal stress is greater than shear stress. Thus this criterion can be regarded as a matrix-dominated interfacial criteria. This criterion has been studied by Long [6.5.6], who concluded that the observed failures within the prepreg layer can be accurately described using Equation (6.5.2.2) for adhesively bonded ARALL-1 single and double-lap joints. However, Tong [6.5.10] indicated that it is less accurate as fiber breakage contributes to interlaminar delamination within the 0-degree surface ply near the bondline. Thus, Tong proposed and tested 6 interactive failure criteria considering the contribution of axial stresses causing fiber breakage.

$$\frac{\sigma_1(\sigma_1 - \sigma_3)}{X_t^2} + \left(\frac{\sigma_3}{Z}\right)^2 + \left(\frac{\tau_{13}}{R}\right)^2 = 1 \tag{6.5.2.3}$$

$$\frac{\sigma_1(\sigma_1 - \sigma_3)}{X_t^2} + \left(\frac{\sigma_3}{Z}\right) + \left(\frac{\tau_{13}}{R}\right)^2 = 1 \tag{6.5.2.4}$$

$$\left(\frac{\sigma_1}{X_t}\right)^2 + \left(\frac{\sigma_3}{Z}\right)^2 + \left(\frac{\tau_{13}}{R}\right)^2 = 1 \tag{6.5.2.5}$$

$$\left(\frac{\sigma_1}{X_t}\right)^2 + \left(\frac{\sigma_3}{Z}\right) + \left(\frac{\tau_{13}}{R}\right)^2 = 1 \tag{6.5.2.6}$$

$$\left(\frac{\sigma_1^2 - \sigma_1\sigma_3}{X_t X_c}\right) + \left(\frac{\sigma_3}{Z}\right)^2 + \left(\frac{\tau_{13}}{R}\right)^2 = 1 \tag{6.5.2.7}$$

$$\left(\frac{\sigma_1^2 - \sigma_1\sigma_3}{X_t X_c}\right) + \left(\frac{\sigma_3}{Z}\right) + \left(\frac{\tau_{13}}{R}\right)^2 = 1 \tag{6.5.2.8}$$

where σ_1 is axial stress of ply, X_t and X_c are the ultimate tensile and compressive strength in the fiber direction for each ply. A 3-D extension to Equation (6.5.2.7) that accounts for transverse normal and in-plane shear stress has also been implemented. This equation is given as:

$$\left(\frac{\sigma_1^2-\sigma_1\sigma_3}{X_tX_c}\right)+\left(\frac{\sigma_2^2-\sigma_2\sigma_3}{Y_tY_c}\right)+\left(\frac{\sigma_3}{Z}\right)^2+\left(\frac{\tau_{23}}{Q}\right)^2+\left(\frac{\tau_{13}}{R}\right)^2+\left(\frac{\tau_{12}}{S}\right)^2=1 \qquad (6.5.2.9)$$

Camanho et al. [6.5.2] proposed the criteria for onset of delamination based on Hashin-Rotem work. It is given as

$$\left(\frac{\sigma_{33}}{Z}\right)^2+\left(\frac{\tau_{23}}{Q}\right)^2+\left(\frac{\tau_{13}}{R}\right)^2=1,\ \sigma_{33}>0 \qquad (6.5.2.10)$$

and

$$\left(\frac{\tau_{23}}{Q}\right)^2+\left(\frac{\tau_{13}}{R}\right)^2=1,\ \sigma_{33}<0 \qquad (6.5.2.11)$$

where Q is transverse shear strength of laminate in 23-plane.

6.5.2.2 Matrix cracking

In addition to delamination in the adherends, matrix cracking is also considered as one of major damage modes in laminated adherends. Minguet et al. [6.5.7, 6.5.8] investigated the composite Skin-stiffener debonding and believed that the maximum tensile stress in the matrix is the cause of the matrix cracking. Thus, the corresponding failure criterion is given by Krueger et al. [6.5.5] as

$$\frac{\sigma_{tt\_principal}}{Y_t}=1 \qquad (6.5.2.12)$$

where $\sigma_{tt\_principal}=\dfrac{\sigma_{22}+\sigma_{33}}{2}+\sqrt{(\dfrac{\sigma_{22}-\sigma_{33}}{2})^2+\tau_{23}^2}$ is the maximum principal stress in transverse plane. Y_t is the transverse tensile strength of the ply.

Sectional fracture

Sectional failure is also a common failure mode in composite bonded joints. Cheuk and Tong [6.5.3] reported this type of failure in a series experiments on bonded doublers with T300/934 plain woven prepregs. In general, maximum in-plane stress/strain criterion is used for this type of failure.

$$\frac{\sigma_{11}}{X_t} = 1 \text{ or } \frac{\varepsilon_{11}}{\varepsilon_1^{ult}} = 1 \tag{6.5.2.13}$$

where F_x^{ult} and ε_x^{ult} are the maximum tensile stress and strain of the adherend.

6.5.3 Adhesive Failure (cohesive and adhesive/adherend interface failure)

Adhesives are more susceptible to failure due to tensile strain than pure shear and compression. For some adhesives, the nonlinear behavior dominates and strain to failure can exceed 100%. Thus, for the cohesive failure of ductile adhesive, the maximum strain criterion is given as

$$\frac{\varepsilon_{eqv.}}{S_{eqv.}} = 1 \tag{6.5.3.1}$$

where $\varepsilon_{eqv.}$ is Von Mises equivalent strain in the adhesive. Alternatively, Tong [6.5.11] also proposed a simple formulation to calculate the strain energy density in the adhesive, and used it for the adhesive failure criteria. It is given as

$$\left(\frac{U_{II}}{U_{IIC}}\right)^{\alpha} + \left(\frac{U_I}{U_{IC}}\right)^{\beta} = 1 \tag{6.5.3.2}$$

where α and β are real constants, and U_{IC} and U_{IIC} are the critical bond strain energy density of pure peel and pure shear, respectively.

Another failure criterion for the adhesive layer considering adhesive spew fillet is the maximum principal stress. As shown by Adams [6.5.1], the initial damage in the adhesive spew fillet is caused by the maximum principal stress, thus

$$\frac{\sigma_{principal}}{F_{\max}} = 1 \tag{6.5.3.3}$$

where F_{max} is the tensile strength of the bulk adhesive.

For general decohesion and debonding failure, an empirical interactive failure criterion was proposed by Tong and Steven [6.5.12].

$$\left(\frac{\sigma_{33}}{F_{peel}}\right)^2 + \left(\frac{\tau_{13}}{F_{shear}}\right)^2 + \left(\frac{\tau_{23}}{F_{shear}}\right)^2 = 1 \qquad \text{as } \sigma_{33} > 0 \tag{6.5.3.4}$$

$$\left(\frac{\tau_{13}}{F_{shear}}\right)^2 + \left(\frac{\tau_{23}}{F_{shear}}\right)^2 = 1 \qquad \text{as } \sigma_{33} < 0 \tag{6.5.3.5}$$

where F_{peel} and F_{shear} are the bondline peel and shear strength, which can be measured in a tensile shear experiment.

The shear dominant failure criterion for adhesives includes maximum shear stress,

$$\left(\frac{\sqrt{\tau_{13}^2+\tau_{23}^2}}{F_{shear}}\right)=1 \qquad (6.5.3.6)$$

and maximum shear strain

$$\left(\frac{\sqrt{\varepsilon_{13}^2+\varepsilon_{23}^2}}{\gamma_{shear}^{ult}}\right)=1 \qquad (6.5.3.7)$$

where γ_{shear}^{ult} is the ultimate shear strain of the adhesive. Likewise, the peel dominant failure criterion for the adhesive is,

$$\left(\frac{\sigma_{33}}{F_{peel}}\right)=1 \qquad \text{as } \sigma_{33}>0 \qquad (6.5.3.8)$$

6.5.4 Fracture Mechanics Based Failure Criteria

The methods presented so far have dealt primarily with damage initiation, rather than with ultimate failure, which is much more difficult to predict. In order to predict ultimate failure, we propose to implement Fracture Mechanics based failure criteria. This approach recognizes that all materials contain flaws and that adhesive joints usually fail by the initiation (or sub critical growth) and propagation of flaws of a critical size within the adhesive layer. Fracture mechanics attempts to link these processes with predictions of the joint strength under various loading conditions by analyzing the stress state within the joint, particularly in the vicinity of the critical flaw and comparing this with material properties that describe the tendency of the cracks to propagate. The two main approaches are the energy method and the stress intensity factor method developed.

Prediction for damage growth is difficult because the initial crack size, location and growth path can not be determined by simple analysis. According to [6.5.4], the selection of an initial crack size is based on many factors, including manufacturing acceptance and/or damage tolerance criteria for the specific structure. The authors also indicated that in the analysis the location of the crack interface is specified a–priori based on the damage initiation site and experience with typical crack paths in composite structures. The crack interfaces are modeled along the direction of anticipated crack growth. The same strategy is also used by Cvitkovich, et al. [6.5.14]

Once the initial crack size, location, and path are determined, the analyses are relatively easy. The damage growth rate under the monotonic or cyclic loads can be calculated by using the energy criterion (strain energy release rate) and so the fatigue life can be determined. The technique used in the paper to calculate the Strain Energy Release Rate (SERR) is called Virtual Crack Closure Technique (VCCT), which can be easily implemented together with finite element analysis, but is not suitable for analytical methods.

Analytical methods calculating the SERR of cracks in bonded joints or at bi-material interfaces can be found in the literature [6.5.15-6.5.18]. These methods will be implemented into ***HS-BondJo*** in future development.

6.5.5 References

6.5.1 Adams, R. D. and Wake, W. C., 1984, Structural Adhesive Joints in engineering. London: Elsevier Applied Science Publishers.

6.5.2 Camanho, P.P. and Matthews, F. L., (1999), "Delamination Onset Prediction in Mechanically Fastened Joints in Composite Laminates," J. Composite Materials, Vol.33, No.10, pp906-927.

6.5.3 Cheuk, P. T. and Tong L., (2002), "Failure of adhesive bonded composite lap shear joints with embedded precrack," *Composites Science and Technology*, 62, 1079-1095.

6.5.4 Hoyt, D. M., Ward, S. H., Minguet, P. J., "Strength and Fatigue Life Modeling of Bonded Joints in Composite Structure," *American Society for Composites (ASC) 15th Technical Conference*, September 2000.

6.5.5 Krueger, R., Paris, I. L. and O'Brien, T. K., 2000, "Fatigue life methodology for bonded composite skin/stringer configurations," Proceedings of the American Society for Composites, 15th Technical Conference, pp.729-736.

6.5.6 Long R. S., (1991), "static strength of adhesively bonded ARALL-1 joints," *J. Composite Materials*, 25, 391-415.

6.5.7 Minguet, P. J. and O'Brien, T. K., "Analysis of Test Methods for Characterizing Skin/Stringer Debonding Failures in Reinforced Composite Panels," in *Composite Materials: Testing and Design* (Twelfth Volume), ASTM STP 1274, 1996, pp. 105--124.

6.5.8 Minguet, P. J. and O'Brien, T. K., "Analysis of Composite Skin/Stringer Bond Failures Using a Strain Energy Release Rate Approach," in *the Tenth International Conference on Composite Materials*, vol. I, A. Poursartip and K. Street, Eds., 1995, pp. 245--252.

6.5.9 Personal contact with Lockheed Martin

6.5.10 Tong, L. (1997), "An assessment of failure criteria to predict the strength of adhesively bonded composite double lap joints," *J. Reinforced Plastics and Composites*, 16,699-713.

6.5.11 Tong, L., (1997), "Strength of Adhesively Bonded Single-lap and Lap-shear Joints,"Int. J. Solids Structures, Vol.35, No.20, pp.2601-2616.

6.5.12 Tong, L. and Steven, G. P., Analysis and Design of Structural Bonded Joints, Kluwer Academic Publishers, 1999.

6.5.13 Jon Gosse, PowerPoint file "Strain Invariant Failure Theory".

6.5.14 Cvitkovich, M. K., O'Brien, T. K. and Minguet, P. J., (1997), "Fatigue Debonding Characterization in Composite Skin/Stringer Configurations," NASA Technical Memorandum 110331.

6.5.15 Cheuk, P. T. and Tong L., (2002), "Failure of adhesive bonded composite lap shear joints with embedded precrack," *Composites Science and Technology*, 62, 1079-1095.

6.5.16 Williams, J. G., (1998), "On the calculation of energy release rates for cracked laminates." *Int. J. Fracture*, 36, 101-119.

6.5.17 Charalambides, P. G., Lund, J., Evans, A. G., and McMeeking, R. M. (1989). "A test specimen for determining the fracture resistance of bimaterial interfaces." *J. of Applied Mechanics*, 56, 77-82.

6.5.18 Evans, A. G., Rühle, M., Dalgleish, B. J., and Charalambides, P. G. (1990). "The fracture energy of bimaterial interfaces." *Mater. Sci. Engng.*, A 126, 53-64.

6.6 Issues with Predicting Peak Bonded Joint Interlaminar Stresses

6.6.1 Disparity in Stress Results from Different Analysis Methods

At first glance, it appears that HyperSizer-BondJo over-predicts peak stresses relative to the finite element analysis in the area of the singularity at the reentrant corner (see Fig. 6.6.1). There are several reasons for this disparity and because failure prediction is only slightly dependent on the actual peak stress value, these differences may not be a concern.

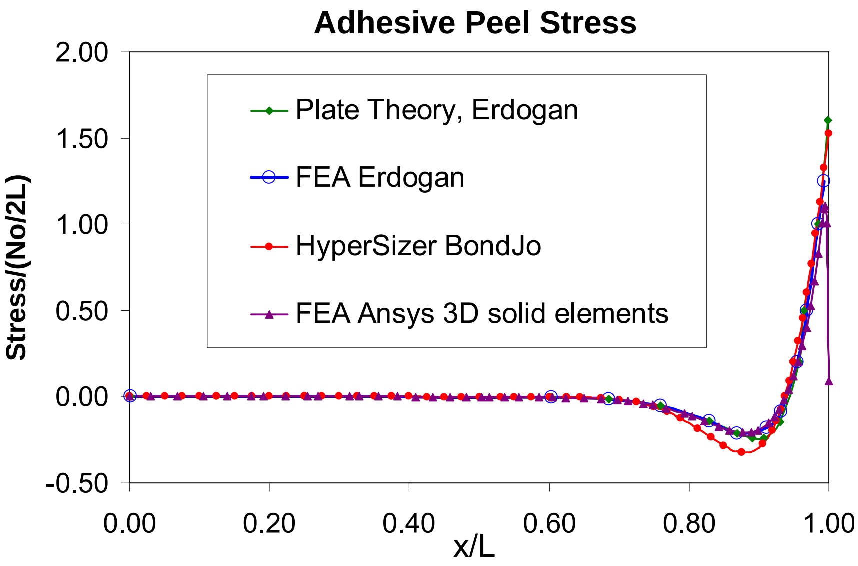

Fig. 6.6.1, Differences in peak interlaminar stress predictions at the reentrant corner.

First of all, most finite element analyses typically have trouble converging in the vicinity of singularities. In our comparison between BondJo and ANSYS solid model FEA, consistently higher peak stresses were seen in the BondJo results over the FEA peak stresses. This is thought to be a problem of mesh refinement around the reentrant corner. As the mesh is further refined, however, numerical problems can begin to occur. Obtaining good results at the singularity with "h" type FEA is difficult.

In the Stresscheck solid FEA model used for BondJo verification, instead of trying to resolve the singularity itself, a small circular region surrounding the reentrant corner was defined in which the results are completely ignored (see Fig. 6.6.2). This is done because it is assumed that results in this region are "polluted". In this case, the actual peak stress, which occurs exactly at the free edge, is not known.

Second, when post-processing the FEA results, there is a potential disparity among the FEA results themselves. The peak stress can depend on the number of points chosen for plotting. This is shown in Fig. 6.6.3. As the number of plotting points chosen from the Stresscheck FEA increases from 75 to 500 points, the

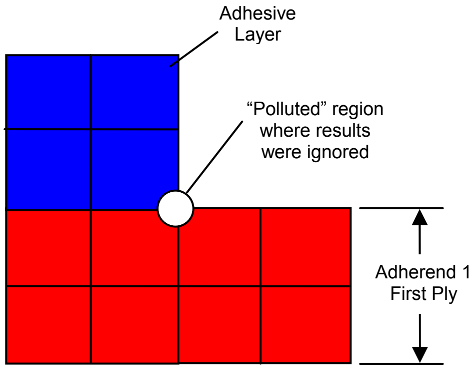

Fig. 6.6.2, In our Stresscheck verification example, a small area around the reentrant corner was defined inside of which the FEA results are ignored.

reported peak stress increases 60% from 2.76 to 4.37 psi. Based on this trend, perhaps even 500 points is not enough and adding more points would result in an even higher peak stress. For this same case BondJo reports a peak stress of 5.76 psi and a stress of 5.29 psi at only ½ ply thickness away (the assumed characteristic distance), both of which are higher than those values returned by the FEA. In reality, the peak stress most likely lies somewhere in between the BondJo results and those of the FEA.

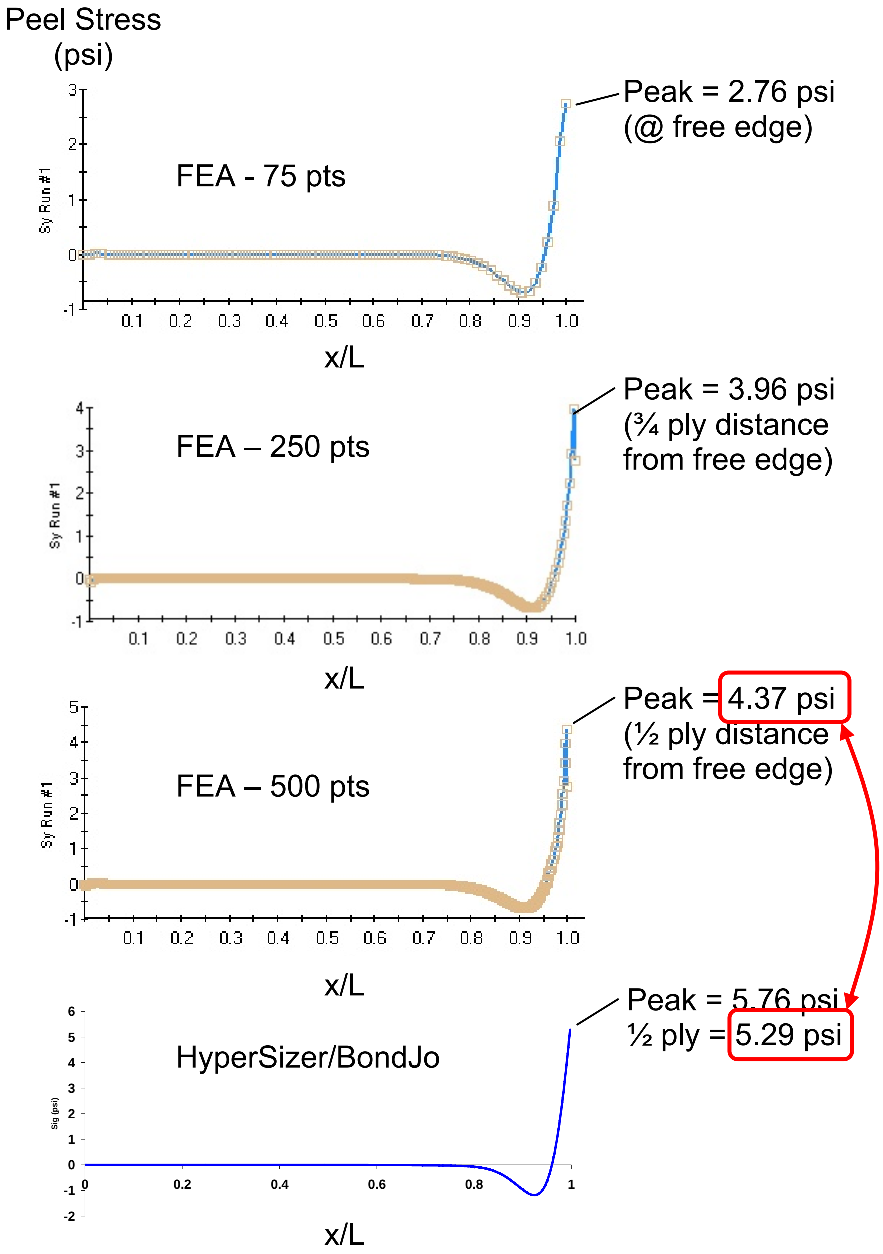

Fig. 6.6.3, As the number of points chosen from the Stresscheck FEA increases from 75 to 500 points, the shape of the curve remains the same, however the peak stress increases. The proper comparison is at the ½ ply distance away from the edge.

Although the peak stresses reported by the two methods can be different, the shape of the stress curve and the integrated effect of those stresses are very similar. In the next section, several different methods of predicting failure are discussed and it is put forth that the actual value of the peak stress may not be critical.

6.6.2 Uncertainty in Predicting Failure at the Reentrant Corner

It was established in the previous section that the peak interlaminar and peel stresses for bonded joints, which generally occur at the singularity of the reentrant corner, are hard to predict and different tools and approaches will generally give different values for these peak stresses. In real-world applications, however, this peak stress is not what will drive a joint to ultimate failure. Imperfections, spew fillets, non-linear material properties, etc. will all drive the solution away from the extreme stress concentration, and even if a failure such as a small crack does occur exactly at the free edge, that crack may be stable and not experience growth that would lead to ultimate failure of the joint.

In practice, there are several methods of using predicted stress fields to predict ultimate failure of the joint. Four of these are shown in Fig. 6.6.4. The first of these (Fig. 6.6.4a) simply evaluates a set of failure criteria using the stress field at some prescribed or 'characteristic' distance away from the reentrant corner. This method is simple, however, determining the appropriate distance to use is not straightforward and may be dependent on the material, the ply angle sequence, and the joint geometry. To be valid, this distance must correlated to test data.

Methods b) and c) are similar in that they look at the integrated effect of the stress field, rather than the stress exactly at the free edge. Using methods such as these would presumably yield similar failure predictions regardless of which tool was used for stress prediction because they depend on the shape of

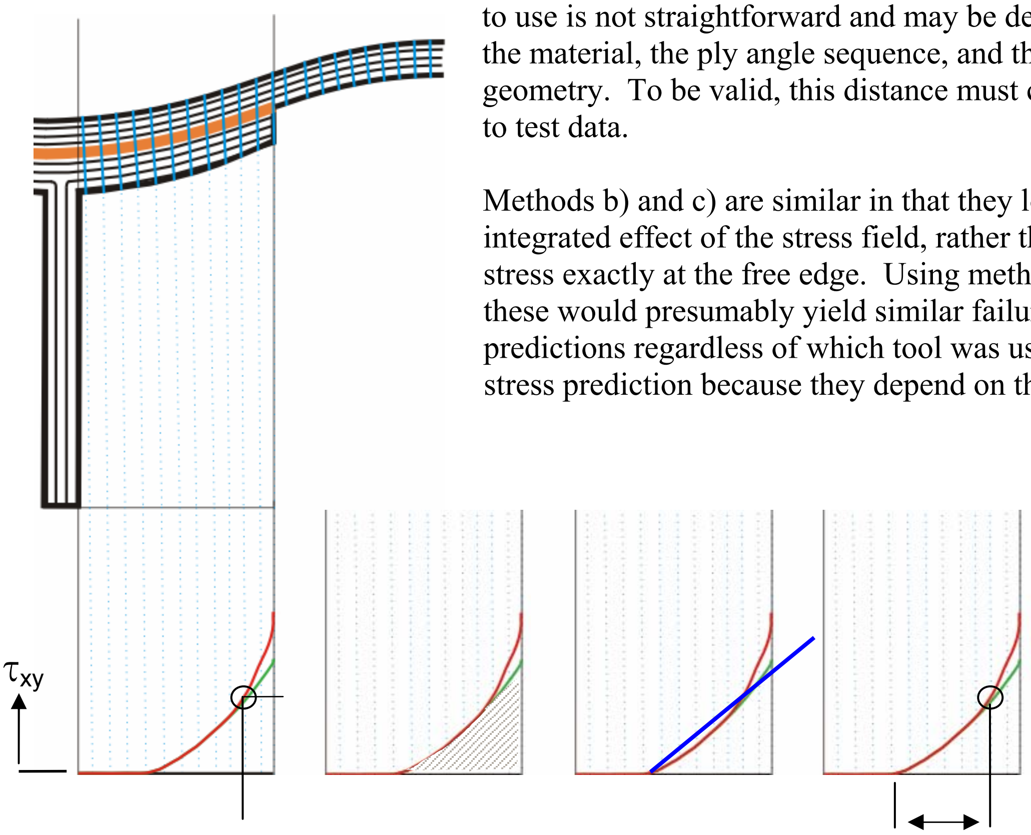

a) characteristic distance

b) area under the curve

c) slope of the curve

d) bond line length

Fig. 6.6.4, Rather than relying solely on the peak stresses for failure prediction, four methods are identified for predicting failure in bonded joints based on stresses near the reentrant corner. HyperSizer-BondJo uses the bond-line length method, which evaluates failure criteria using stresses at all points near the free edge outside of a characteristic distance. The recommended "rule-of-thumb" distance is ½ ply thickness or 0.0025".

the stress curve rather than stress at a single location. Just as with the characteristic distance method, however, failure methods that are based on either of these methods must be calibrated to test data to be useful.

The “bond line length” method evaluates stress at all points within a certain distance of the reentrant corner, but still outside some characteristic distance. This method is very similar to the characteristic distance method. The difference is that instead of evaluating failure criteria at a single point, the failure criteria are evaluated throughout the adherends and adhesive at many points to be sure that the critical stress combination is found. Just as with the other methods, however, the value of the characteristic distance is not easy to determine, and must be tied to test data for a particular material system, layup and geometry. This is the method that we have implemented for failure prediction in HyperSizer-BondJo and our recommended characteristic distance, in the abscense of any comprehensive test data, is approximately ½ ply thickness, or about 0.0025".

6.7 HyperSizer Example: Composite Bonded Joint

The developed Bonded Joint Analysis software is now an integral part of both the HyperSizer Basic and Pro software packages and will be commercially available with the production release of HyperSizer Version 4.4 (expected in summer of 2005).

6.7.1 Software Operation

Wherever possible, the incorporation of BondJo into HyperSizer made use of the existing infrastructure for material properties, laminates, dimensions, optimization parameters, etc. In most cases, experienced HyperSizer users will see few differences between the way structural materials and dimensions are specified today and those that are required for BondJo analysis.

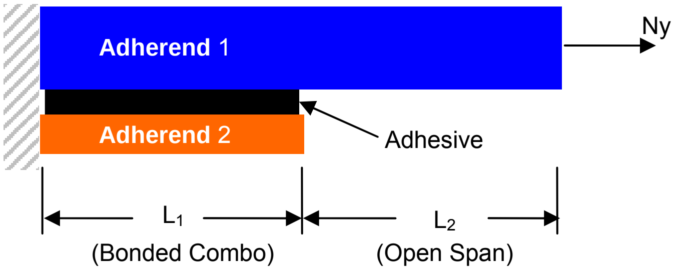

Note: All geometry, load specifications, and results for this example are reported in the HyperSizer panel coordinate system. See Section 6.11 for details.

Fig. 6.7.1, Configuration for bonded joint example

The example described below demonstrates setting up a problem for BondJo analysis. First the laminate and material properties are specified for the top facesheet (in BondJo, Adherend 1).

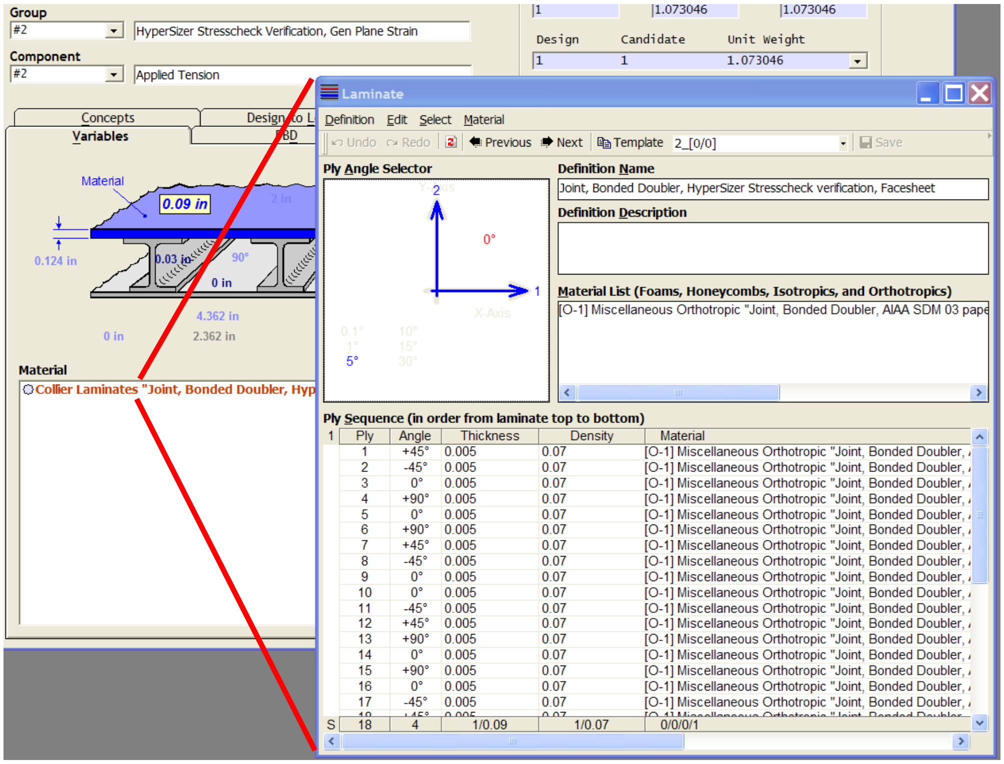

Group: #2 HyperSizer Stresscheck Verification, Gen Plane Strain

Component: #2 Applied Tension

1	1.073046	1.073046

Design	Candidate	Unit Weight
1	1	1.073046

Material: ○ Collier Laminates "Joint, Bonded Doubler, Hyp

Template: 2_[0/0]

Definition Name: Joint, Bonded Doubler, HyperSizer Stresscheck verification, Facesheet

Definition Description:

Material List (Foams, Honeycombs, Isotropics, and Orthotropics)

[O-1] Miscellaneous Orthotropic "Joint, Bonded Doubler, AIAA SDM 03 pape

Ply Sequence (in order from laminate top to bottom)

1	Ply	Angle	Thickness	Density	Material
	1	+45°	0.005	0.07	[O-1] Miscellaneous Orthotropic "Joint, Bonded Doubler,
	2	-45°	0.005	0.07	[O-1] Miscellaneous Orthotropic "Joint, Bonded Doubler,
	3	0°	0.005	0.07	[O-1] Miscellaneous Orthotropic "Joint, Bonded Doubler,
	4	+90°	0.005	0.07	[O-1] Miscellaneous Orthotropic "Joint, Bonded Doubler,
	5	0°	0.005	0.07	[O-1] Miscellaneous Orthotropic "Joint, Bonded Doubler,
	6	+90°	0.005	0.07	[O-1] Miscellaneous Orthotropic "Joint, Bonded Doubler,
	7	+45°	0.005	0.07	[O-1] Miscellaneous Orthotropic "Joint, Bonded Doubler,
	8	-45°	0.005	0.07	[O-1] Miscellaneous Orthotropic "Joint, Bonded Doubler,
	9	0°	0.005	0.07	[O-1] Miscellaneous Orthotropic "Joint, Bonded Doubler,
	10	0°	0.005	0.07	[O-1] Miscellaneous Orthotropic "Joint, Bonded Doubler,
	11	-45°	0.005	0.07	[O-1] Miscellaneous Orthotropic "Joint, Bonded Doubler,
	12	+45°	0.005	0.07	[O-1] Miscellaneous Orthotropic "Joint, Bonded Doubler,
	13	+90°	0.005	0.07	[O-1] Miscellaneous Orthotropic "Joint, Bonded Doubler,
	14	0°	0.005	0.07	[O-1] Miscellaneous Orthotropic "Joint, Bonded Doubler,
	15	+90°	0.005	0.07	[O-1] Miscellaneous Orthotropic "Joint, Bonded Doubler,
	16	0°	0.005	0.07	[O-1] Miscellaneous Orthotropic "Joint, Bonded Doubler,
	17	-45°	0.005	0.07	[O-1] Miscellaneous Orthotropic "Joint, Bonded Doubler,
	18	+45°	0.005	0.07	[O-1] Miscellaneous Orthotropic "Joint, Bonded Doubler,
S	18	4	1/0.09	1/0.07	0/0/0/1

Fig. 6.7.2, Adherend 1 (top facesheet) laminate specification

The next step is to specify a laminate for the stiffener flange (BondJo: Adherend 2). In the current version of HyperSizer, the adhesive material and adhesive thickness for the bonded joint are considered to be part of the flange (as shown as the "blue" isotropic ply in Figure 2). This means that optimum combinations of adherends and adhesive are determined by creating many unique laminates. Therefore there there is no convenient way to optimize the adhesive material or thickness separately from the flange material and thickness at this time. In a future version of HyperSizer, the adhesive material and thickness will become separate variables and the optimization will be more general and convenient.

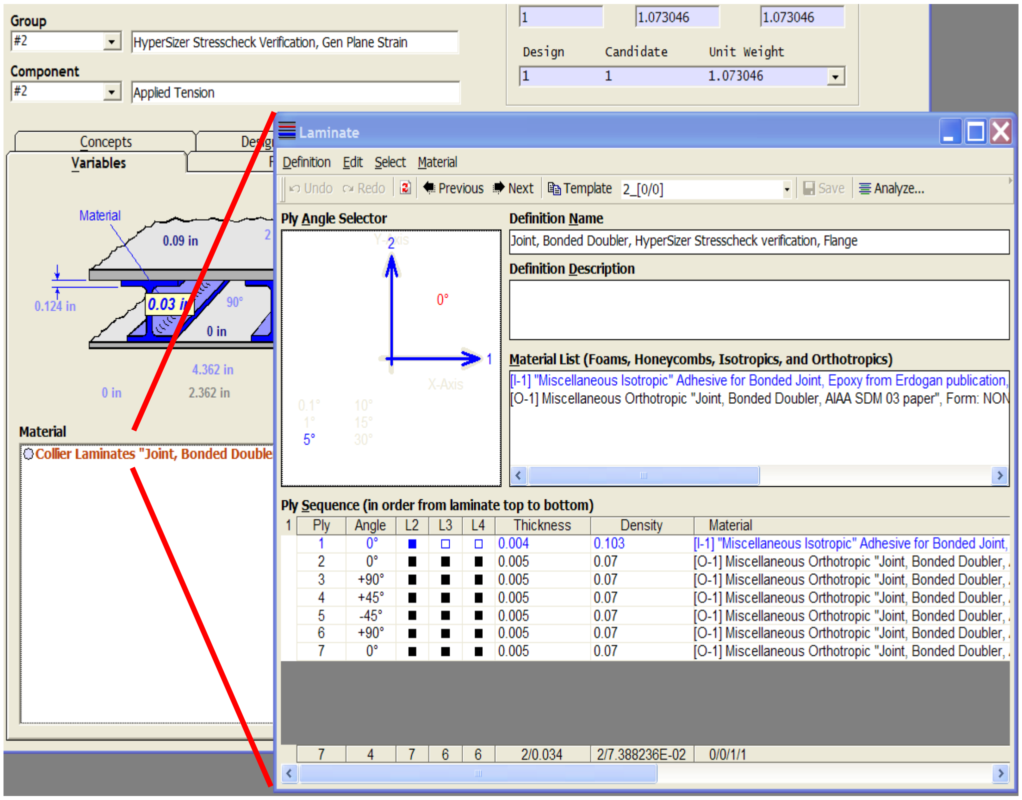

Group: #2 HyperSizer Stresscheck Verification, Gen Plane Strain

Component: #2 Applied Tension

1 1.073046 1.073046

Design Candidate Unit Weight
1 1 1.073046

Template 2_[0/0]

Ply Angle Selector

Definition Name: Joint, Bonded Doubler, HyperSizer Stresscheck verification, Flange

Definition Description

Material List (Foams, Honeycombs, Isotropics, and Orthotropics)
[I-1] "Miscellaneous Isotropic" Adhesive for Bonded Joint, Epoxy from Erdogan publication,
[O-1] Miscellaneous Orthotropic "Joint, Bonded Doubler, AIAA SDM 03 paper", Form: NON

Material
○ Collier Laminates "Joint, Bonded Double

Ply Sequence (in order from laminate top to bottom)

1	Ply	Angle	L2	L3	L4	Thickness	Density	Material
	1	0°	■	□	□	0.004	0.103	[I-1] "Miscellaneous Isotropic" Adhesive for Bonded Joint,
	2	0°	■	■	■	0.005	0.07	[O-1] Miscellaneous Orthotropic "Joint, Bonded Doubler,
	3	+90°	■	■	■	0.005	0.07	[O-1] Miscellaneous Orthotropic "Joint, Bonded Doubler,
	4	+45°	■	■	■	0.005	0.07	[O-1] Miscellaneous Orthotropic "Joint, Bonded Doubler,
	5	-45°	■	■	■	0.005	0.07	[O-1] Miscellaneous Orthotropic "Joint, Bonded Doubler,
	6	+90°	■	■	■	0.005	0.07	[O-1] Miscellaneous Orthotropic "Joint, Bonded Doubler,
	7	0°	■	■	■	0.005	0.07	[O-1] Miscellaneous Orthotropic "Joint, Bonded Doubler,
	7	4	7	6	6	2/0.034	2/7.388236E-02	0/0/1/1

Fig. 6.7.3, Flange laminate (adherend 2) and adhesive specification

After specifying materials and geometry, the joint can be viewed to-scale through HyperSizer's graphics form.

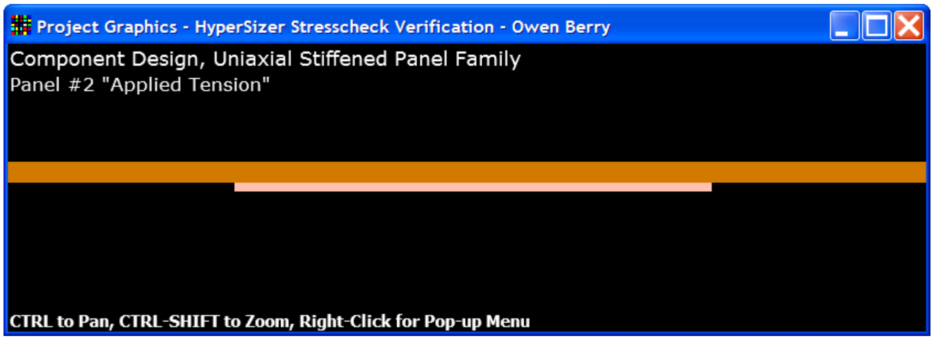

Project Graphics - HyperSizer Stresscheck Verification - Owen Berry

Component Design, Uniaxial Stiffened Panel Family
Panel #2 "Applied Tension"

CTRL to Pan, CTRL-SHIFT to Zoom, Right-Click for Pop-up Menu

Fig. 6.7.4, Bonded joint geometry shown in HyperSizer graphics

General uniaxial or biaxial forces and moments with or without shear are then applied to the joint through the HyperSizer FBD tab. Loads can be entered either as typed-in forces or moments (lb/in or lb-in/in), specified strains or curvatures, or if this joint is part of a global FEM, the forces will be imported automatically from the finite element analysis. In addition to general loading, general constrained boundary conditions can be applied.

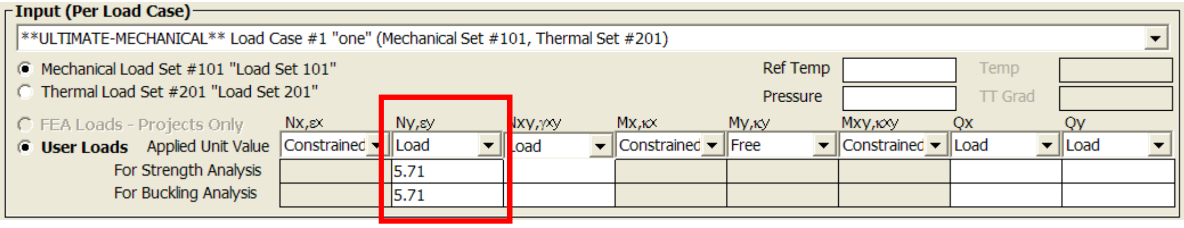

Input (Per Load Case)

ULTIMATE-MECHANICAL Load Case #1 "one" (Mechanical Set #101, Thermal Set #201)

● Mechanical Load Set #101 "Load Set 101"
○ Thermal Load Set #201 "Load Set 201"

Ref Temp
Pressure
Temp
TT Grad

○ FEA Loads - Projects Only
● **User Loads**

	Nx,εx	Ny,εy	Nxy,γxy	Mx,κx	My,κy	Mxy,κxy	Qx	Qy
Applied Unit Value	Constrained	Load	Load	Constrained	Free	Constrained	Load	Load
For Strength Analysis		5.71						
For Buckling Analysis		5.71						

Fig. 6.7.5, Joint loads entered on HyperSizer's FBD tab

Several joint specific options have not yet been included into the main HyperSizer GUI and are handled through a special set of data called "backdoor data" which are entered through a temporary HyperSizer interface. Backdoor data is that data which is required for a HyperSizer capability that has not yet been implemented through the main GUI, but is stored and maintained in the database.

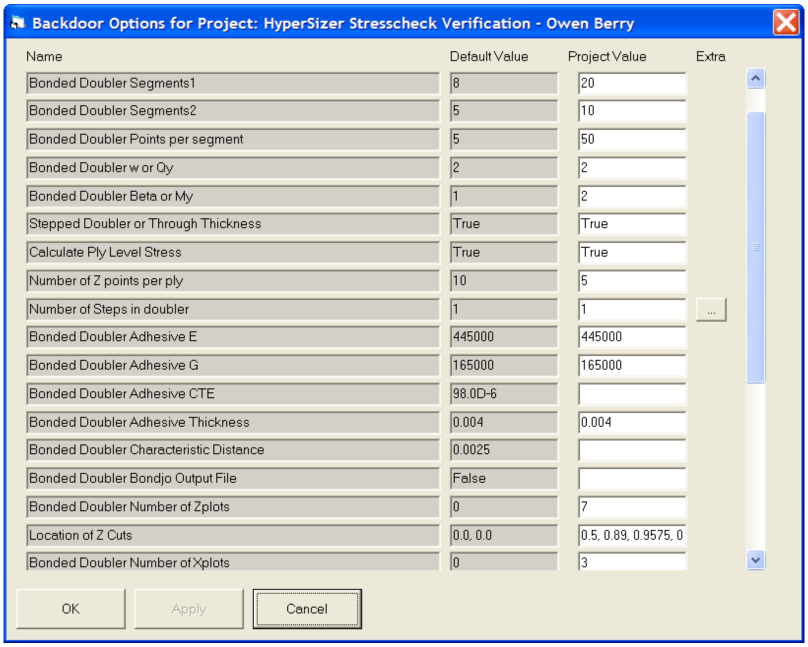

Backdoor Options for Project: HyperSizer Stresscheck Verification - Owen Berry

Name	Default Value	Project Value	Extra
Bonded Doubler Segments1	8	20	
Bonded Doubler Segments2	5	10	
Bonded Doubler Points per segment	5	50	
Bonded Doubler w or Qy	2	2	
Bonded Doubler Beta or My	1	2	
Stepped Doubler or Through Thickness	True	True	
Calculate Ply Level Stress	True	True	
Number of Z points per ply	10	5	
Number of Steps in doubler	1	1	...
Bonded Doubler Adhesive E	445000	445000	
Bonded Doubler Adhesive G	165000	165000	
Bonded Doubler Adhesive CTE	98.0D-6		
Bonded Doubler Adhesive Thickness	0.004	0.004	
Bonded Doubler Characteristic Distance	0.0025		
Bonded Doubler Bondjo Output File	False		
Bonded Doubler Number of Zplots	0	7	
Location of Z Cuts	0.0, 0.0	0.5, 0.89, 0.9575, 0	
Bonded Doubler Number of Xplots	0	3	

Fig. 6.7.6, Joint parameters entered as "backdoor data"

The backdoor data includes items like the number of "segments" into which each domain is divided for analysis, the number of y and z points through each segment and through each ply respectively at which stresses are calculated, the characteristic distance for margin of safety calculation, the y locations at which through-thickness stress plots are to be generated, and the z locations at which stress plots along y are calculated.

After the problem has been fully defined, the user simply presses the analyze button and after a few seconds the software will automatically generate over 40 plots (depending on the plots specified in the backdoor data) that fully describe the displacement, forces, in- and out-of-plane stresses in the bonded joint. The run-time depends on the number of segments and y and z points specified in the backdoor, but are usually on the order of 1 second or less on a typical 2.8 GHz workstation. With most of the time spent initializing the plots. The numerical runtime is on the order of 1/40th second and this is what is relevant for optimizing. This means that this analysis will lend itself very well to rapid optimization that considers many different joint configurations.

6.7.2 Analysis Result Screenshots

Adherend Global Results

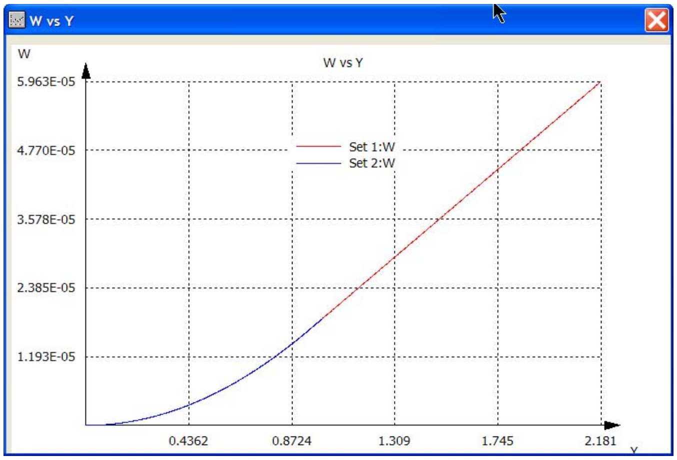
W vs Y
W
W vs Y
5.963E-05
4.770E-05
3.578E-05
2.385E-05
1.193E-05
Set 1:W
Set 2:W
0.4362
0.8724
1.309
1.745
2.181
Y

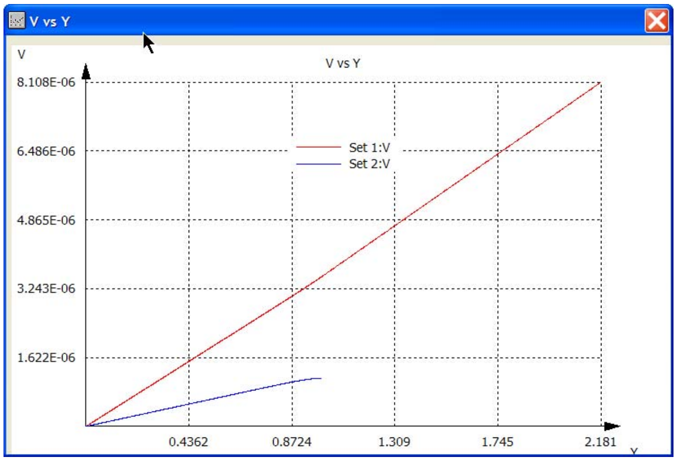
V vs Y
V
V vs Y
8.108E-06
6.486E-06
4.865E-06
3.243E-06
1.622E-06
Set 1:V
Set 2:V
0.4362
0.8724
1.309
1.745
2.181
Y

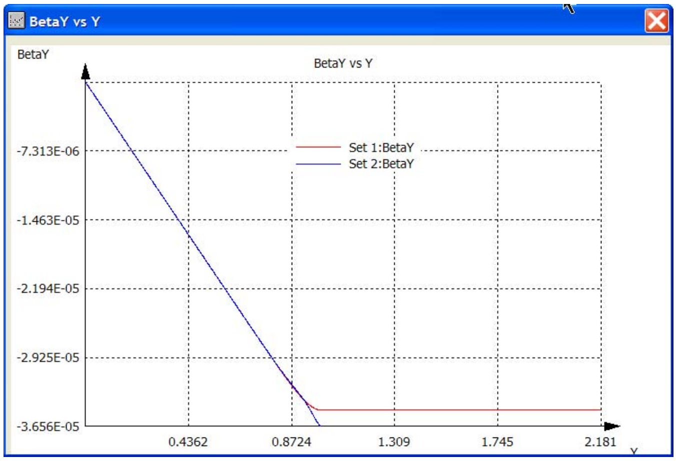
BetaY vs Y
BetaY
BetaY vs Y
-7.313E-06
-1.463E-05
-2.194E-05
-2.925E-05
-3.656E-05
Set 1:BetaY
Set 2:BetaY
0.4362
0.8724
1.309
1.745
2.181
Y

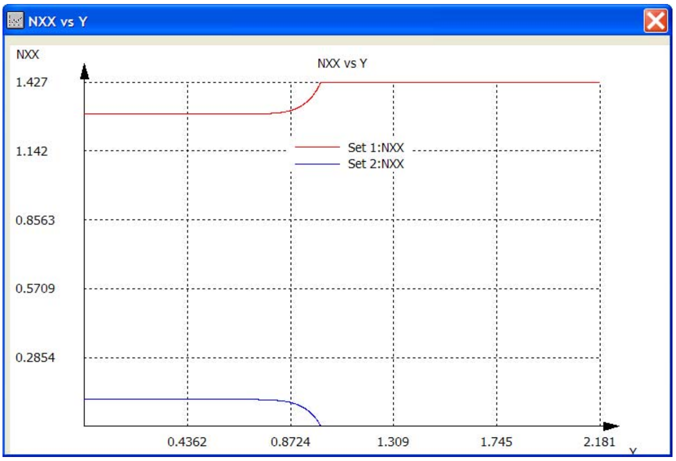
NXX vs Y
NXX
NXX vs Y
1.427
1.142
0.8563
0.5709
0.2854
Set 1:NXX
Set 2:NXX
0.4362
0.8724
1.309
1.745
2.181
Y

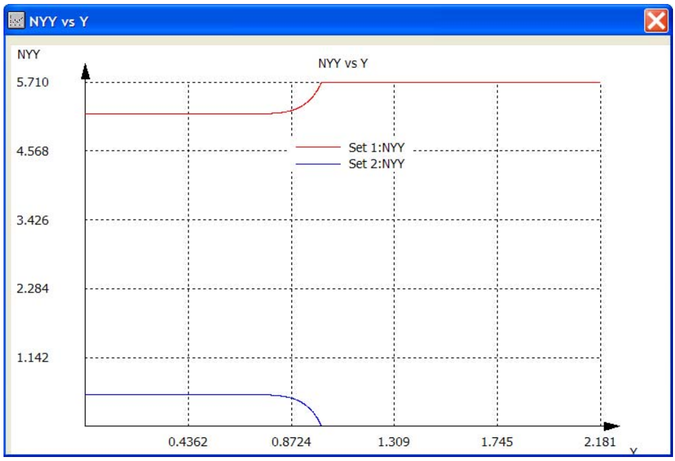
NYY vs Y
NYY
NYY vs Y
5.710
4.568
3.426
2.284
1.142
Set 1:NYY
Set 2:NYY
0.4362
0.8724
1.309
1.745
2.181
Y

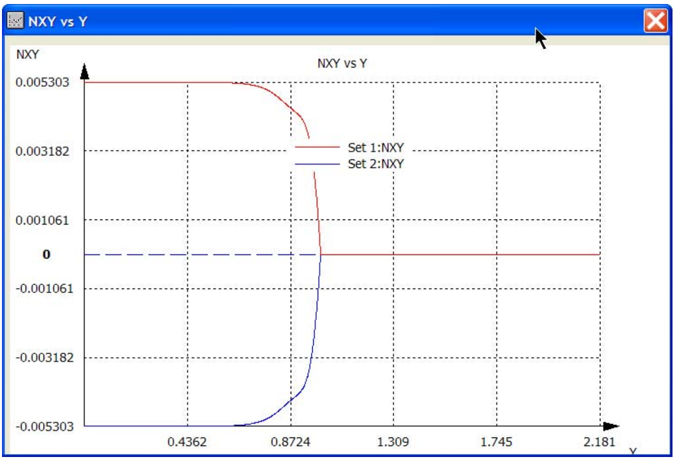
NXY vs Y
NXY
NXY vs Y
0.005303
0.003182
0.001061
0
-0.001061
-0.003182
-0.005303
Set 1:NXY
Set 2:NXY
0.4362
0.8724
1.309
1.745
2.181
Y

Note: Red Lines are Centerline Adherend 1, Blue Lines are Centerline Adherend 2

Adherend Global Results (cont.)

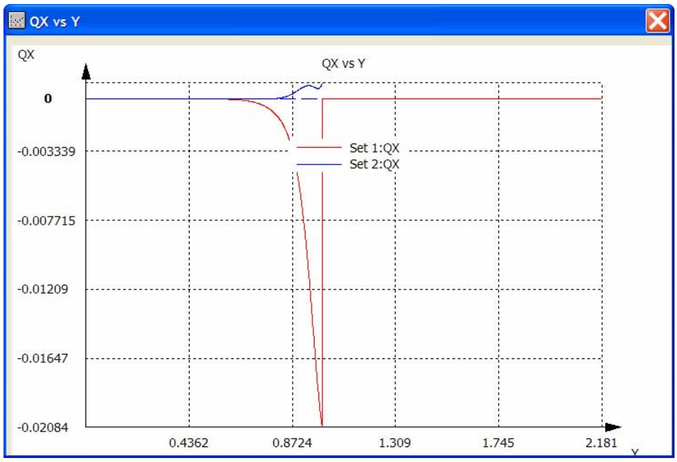

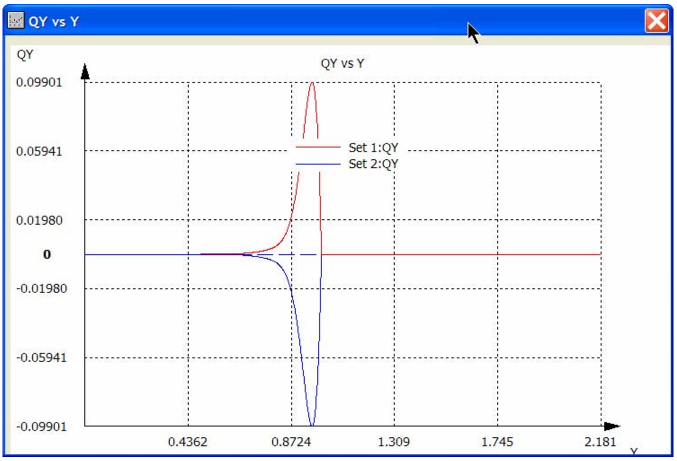

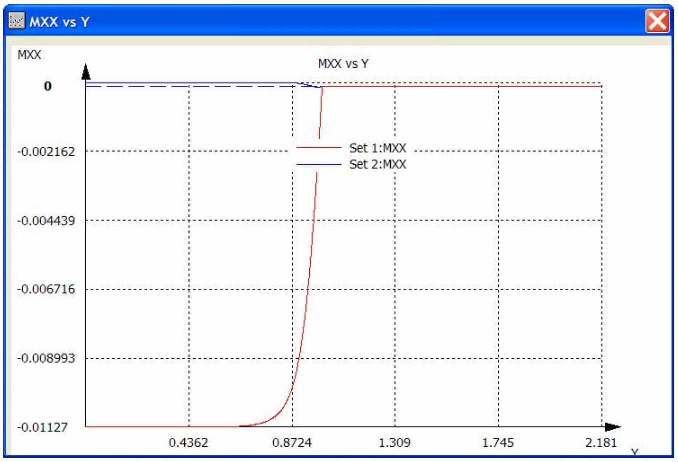

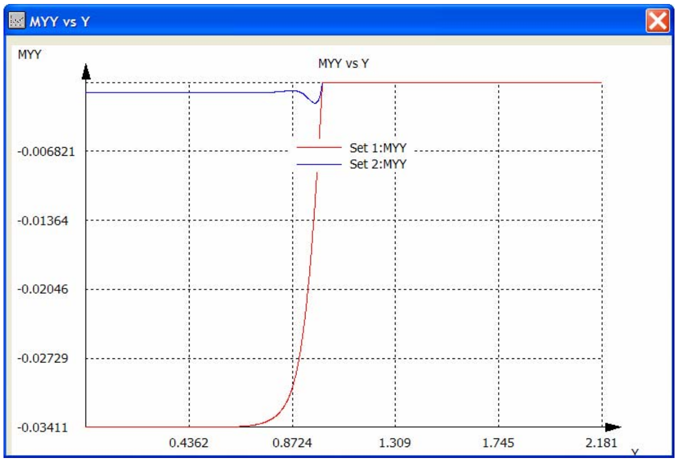

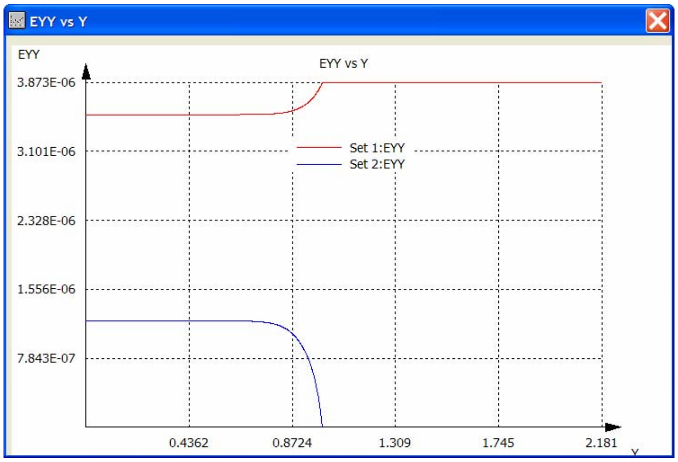

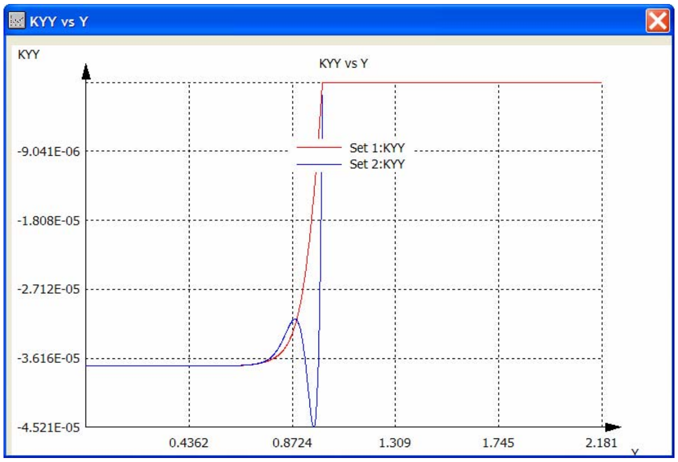

Adhesive Midplane Stresses

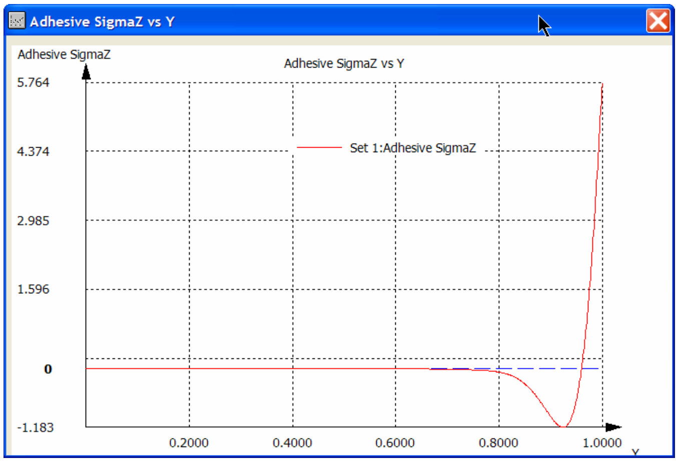

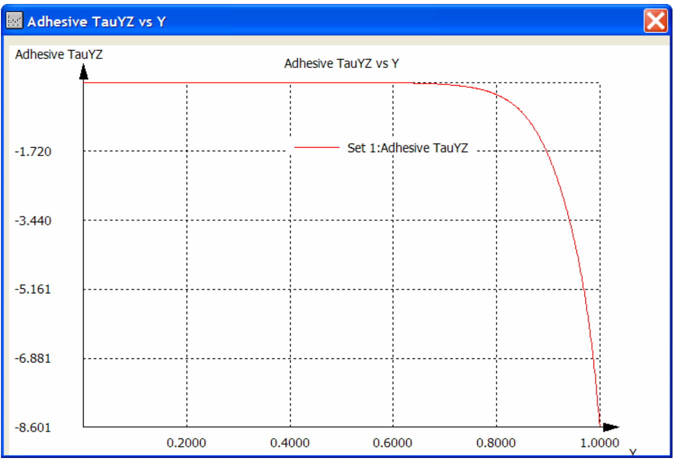

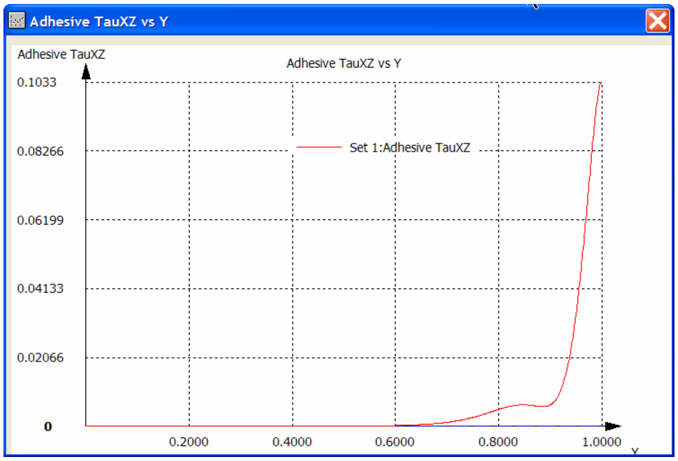

Adherend Through-Thickness Stress Plots (X = 0.5")

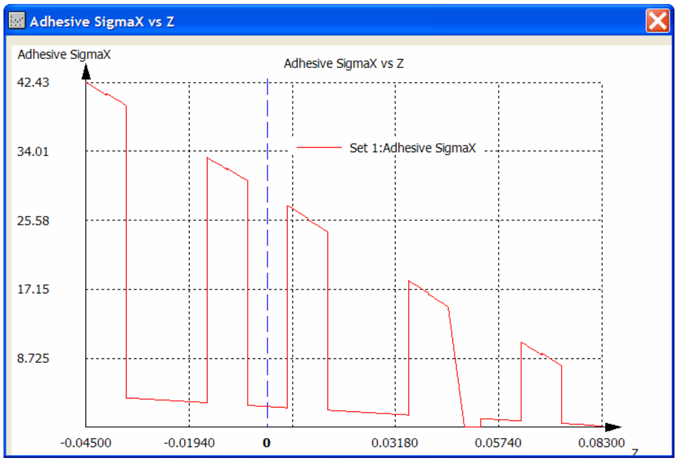

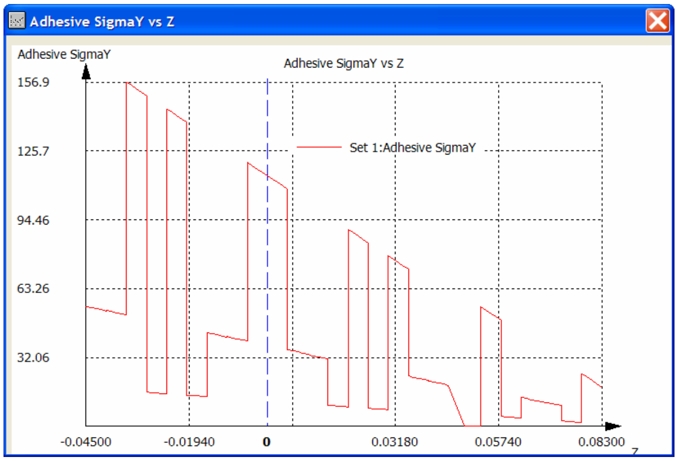

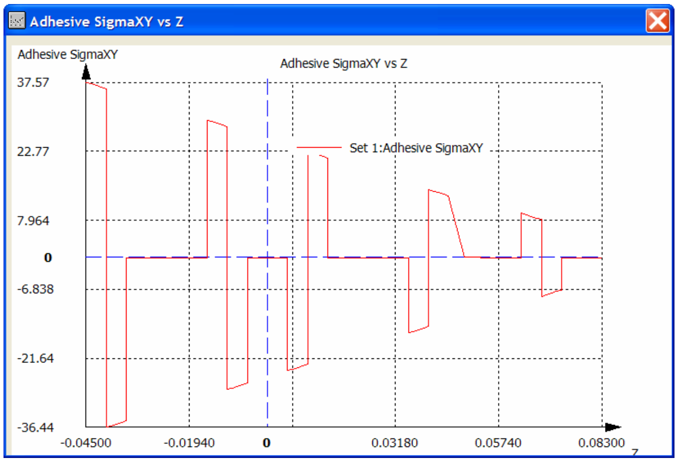

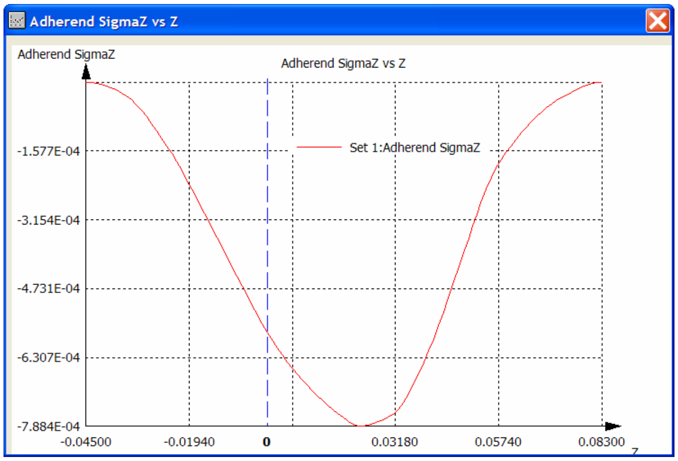

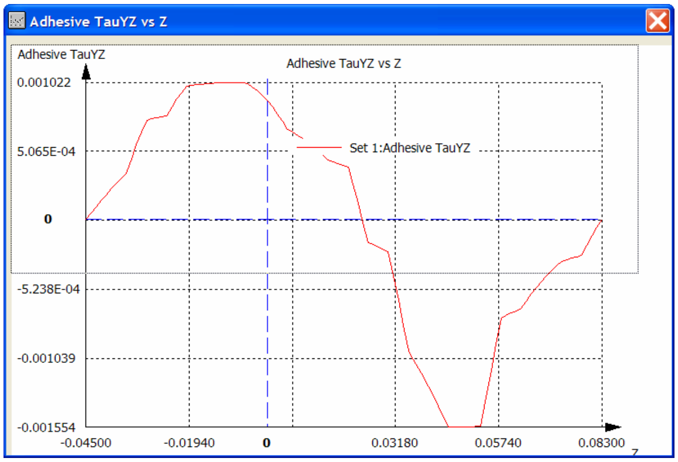

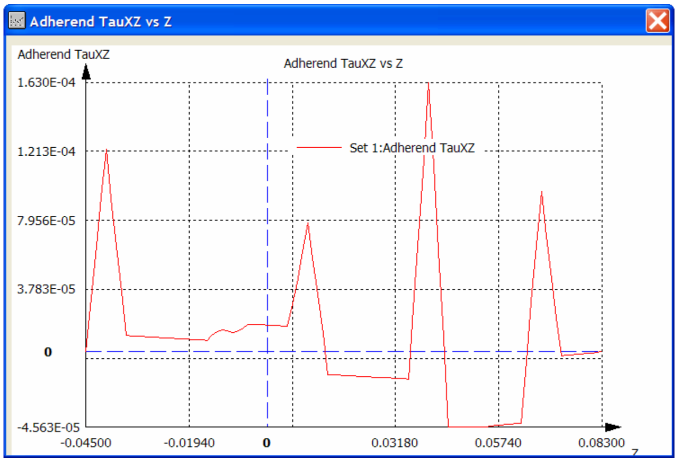

Adherend Through-Thickness Stress Plots (X = 0.89”)

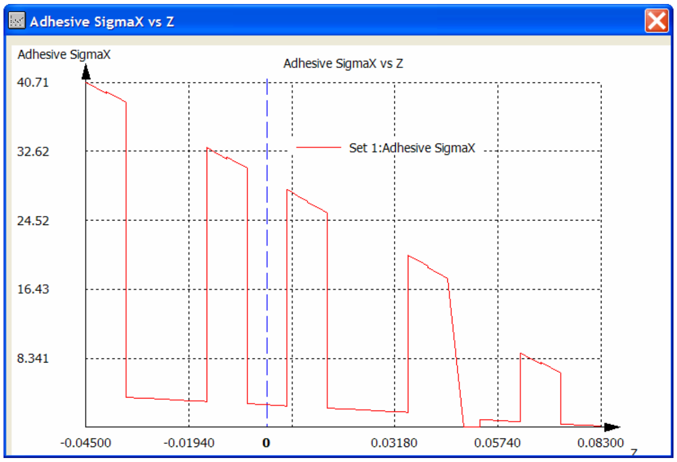

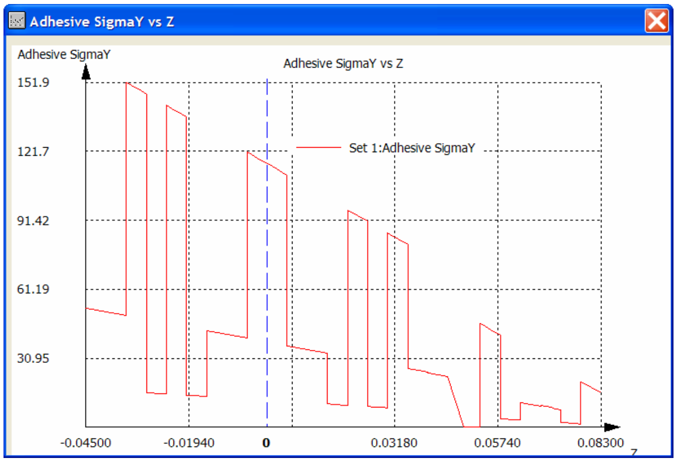

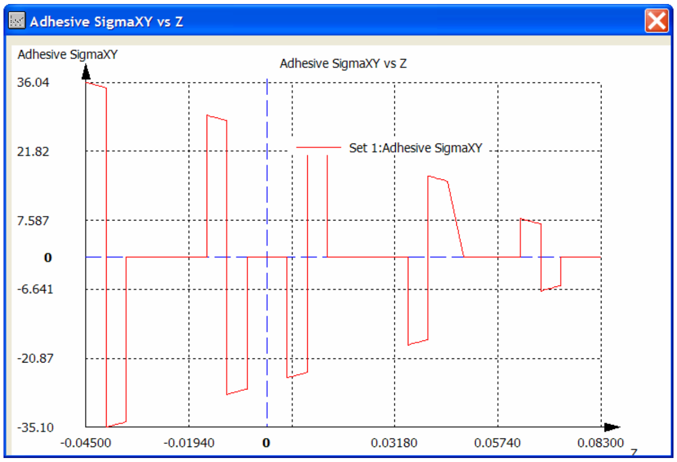

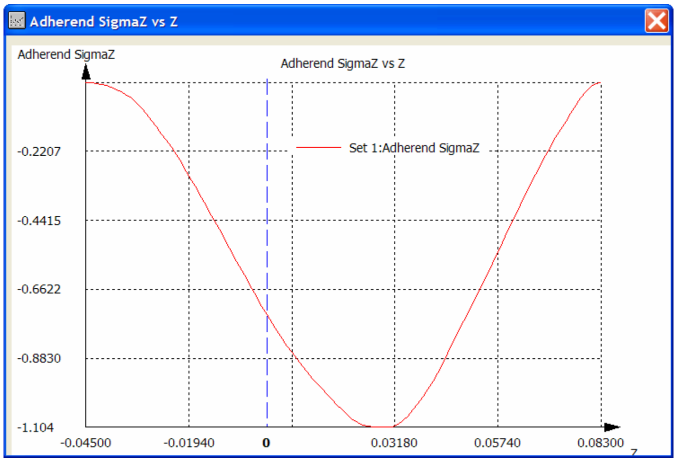

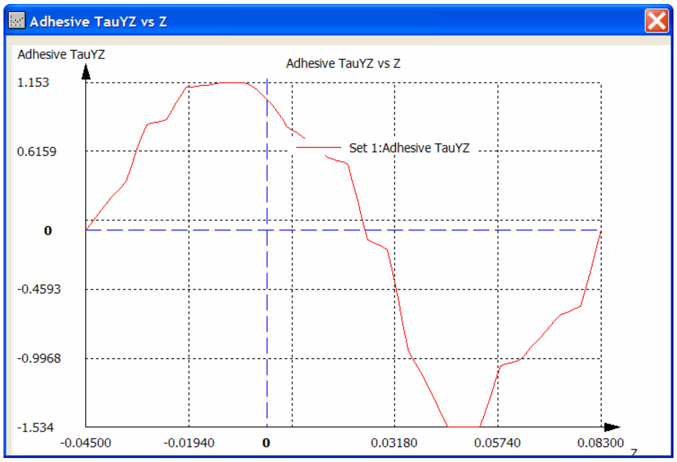

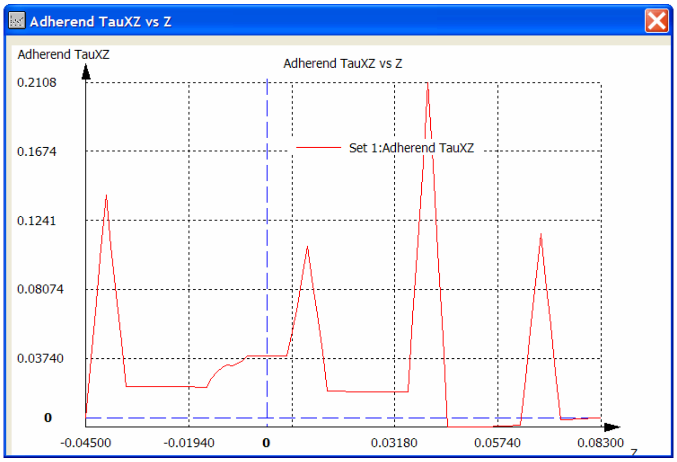

Adherend Through-Thickness Stress Plots (X = 0.9575”)

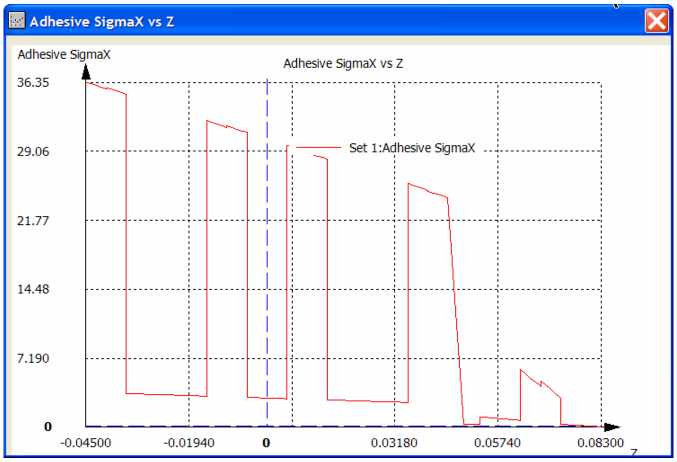

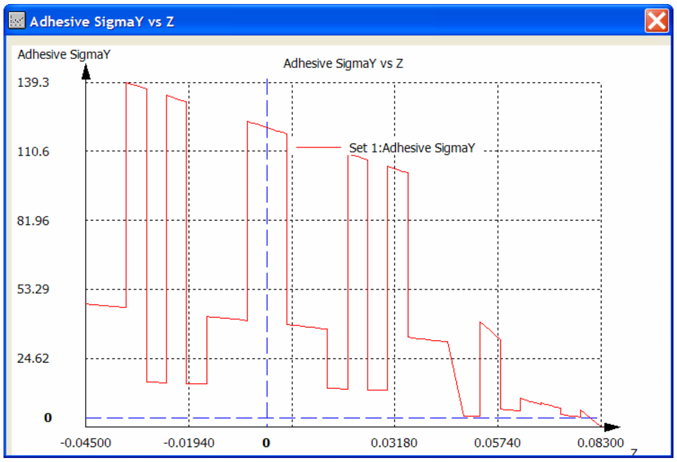

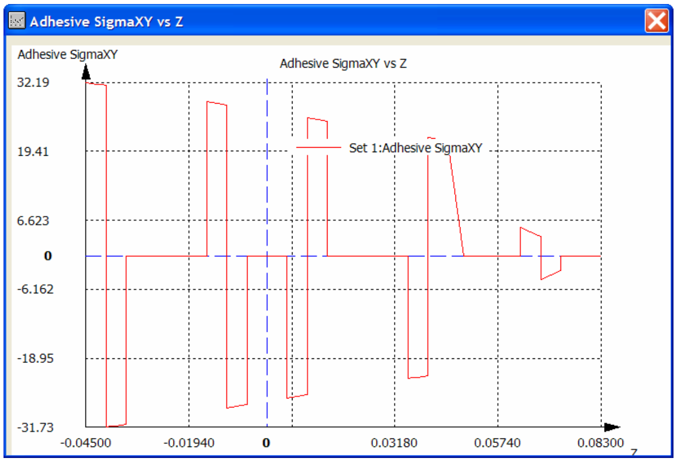

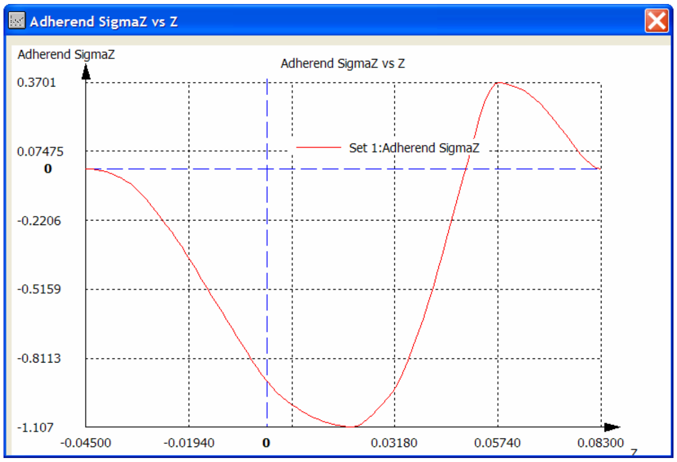

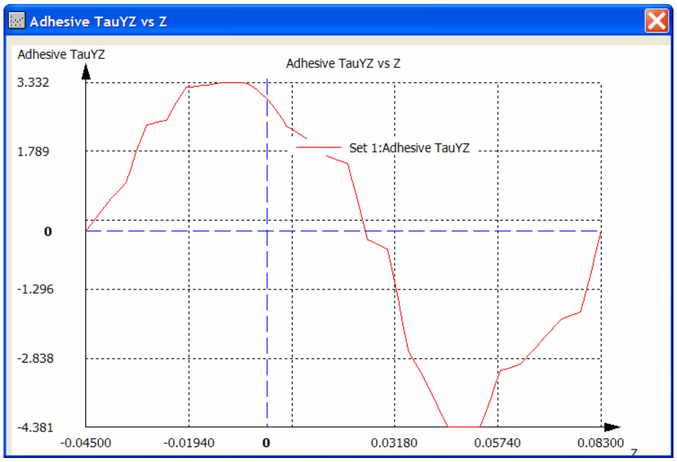

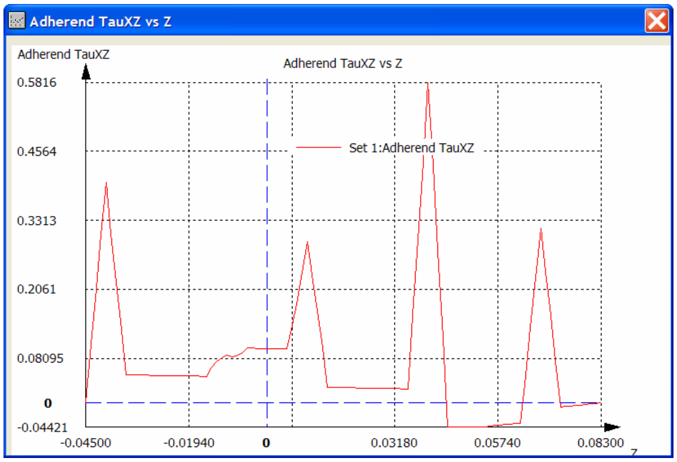

Adherend 1 Midplane Stress Plots

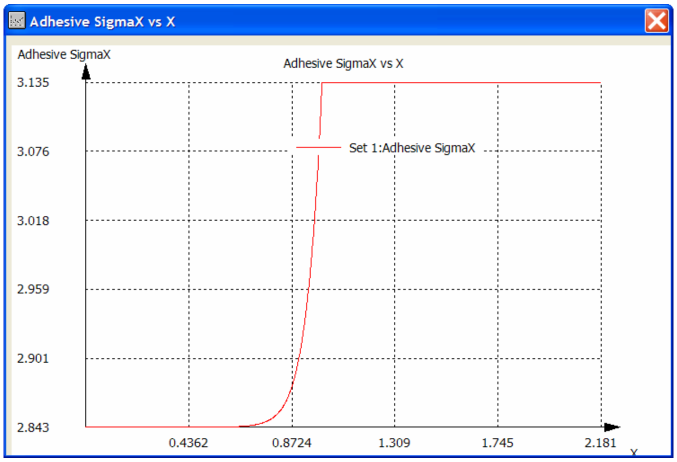

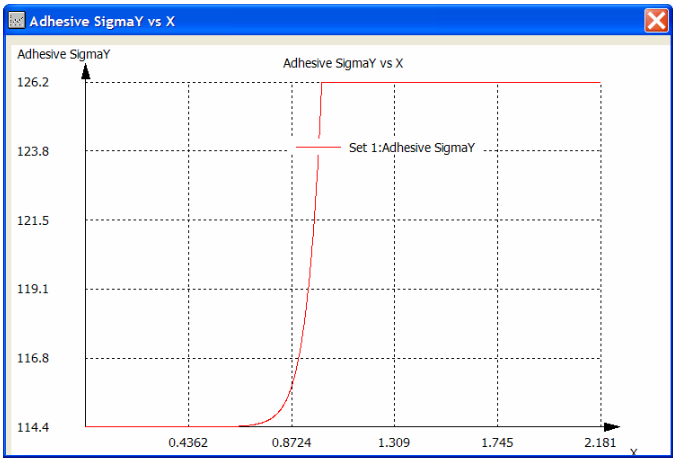

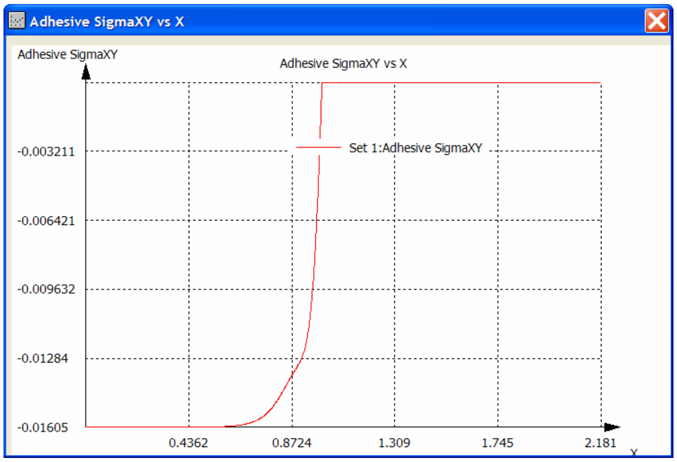

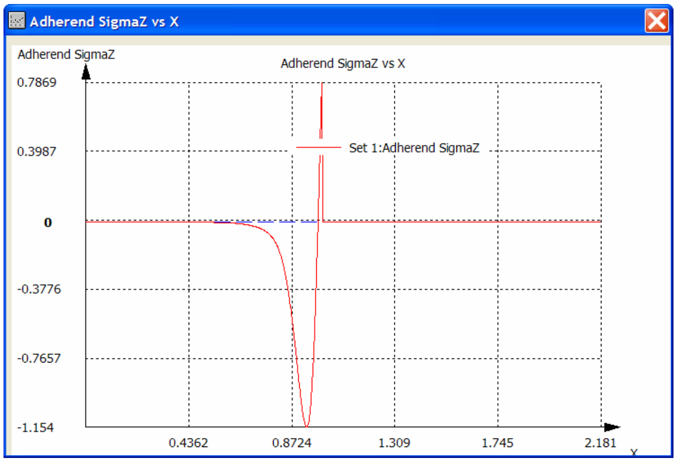

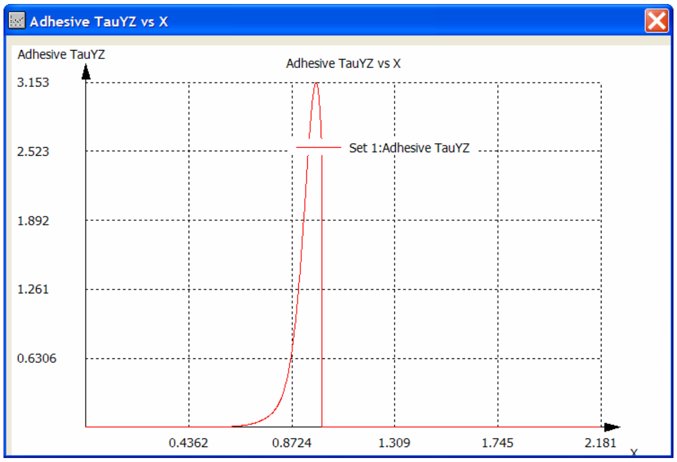

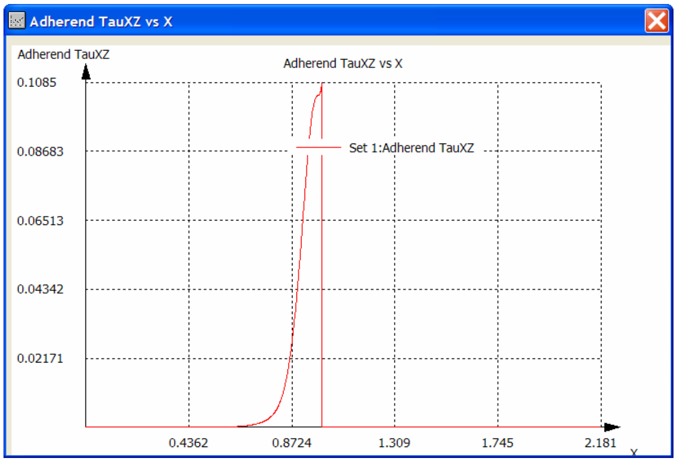

Adherend 2 Midplane Stress Plots

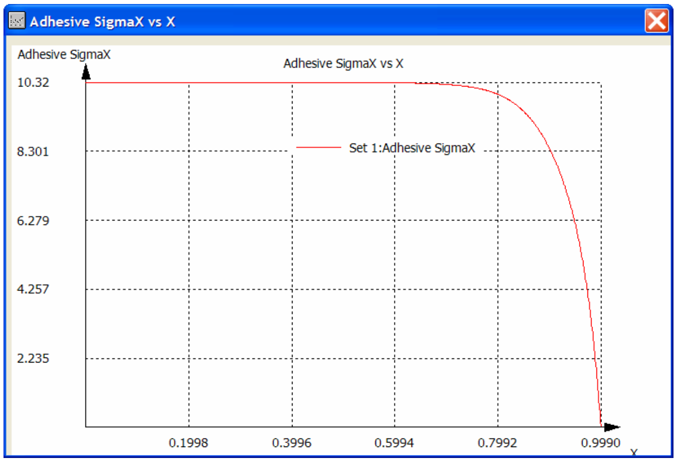

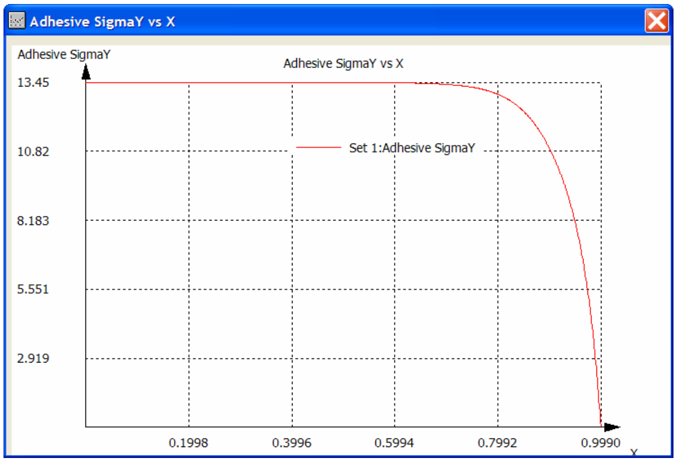

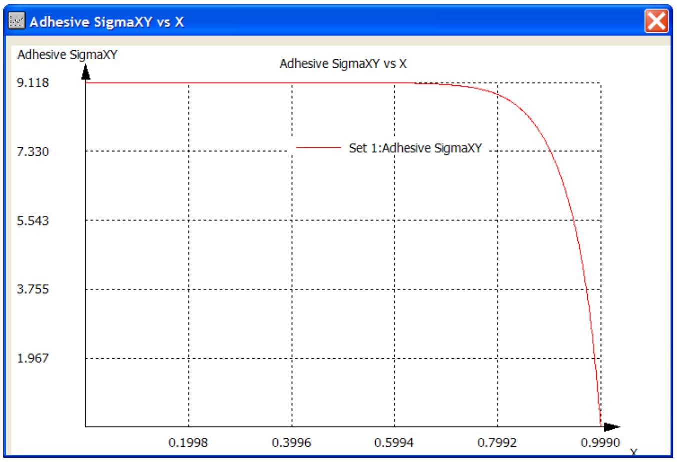

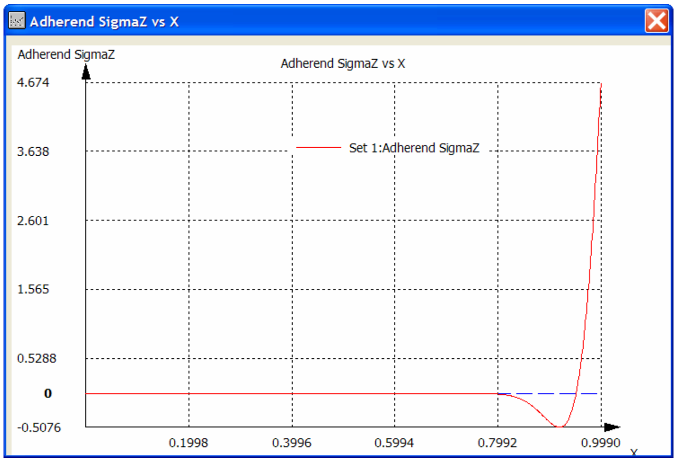

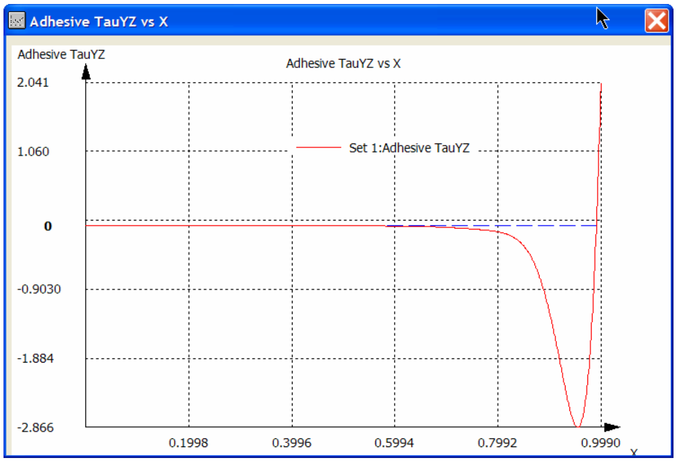

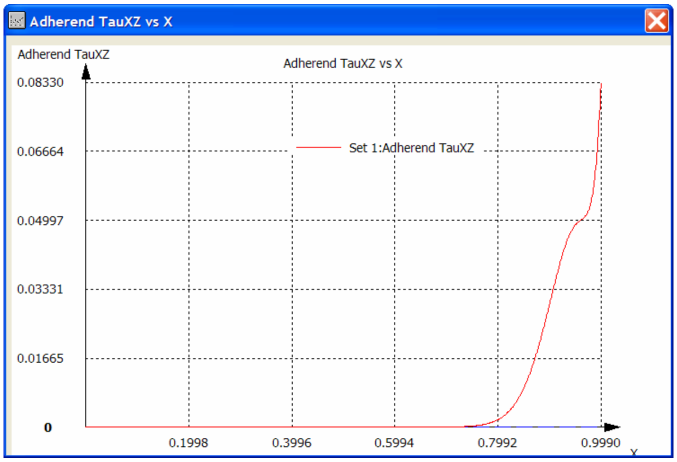

The data describing each of these plots are easily exported from HyperSizer into comma delimited files for plotting in Microsoft Excel or any other plotting package.

In addition to the detailed displacement, force and stress plots available, HyperSizer also automatically calculates margins of safety and reports these on the Failure tab as shown in Fig. 6.7.7. (Note, this screenshot does not correspond to the same problem as the above screenshots) As described in Volume 3, HyperSizer automatically calculates 13 different margins (fracture and delamination) for the adherends and 6 margins for the adhesive.

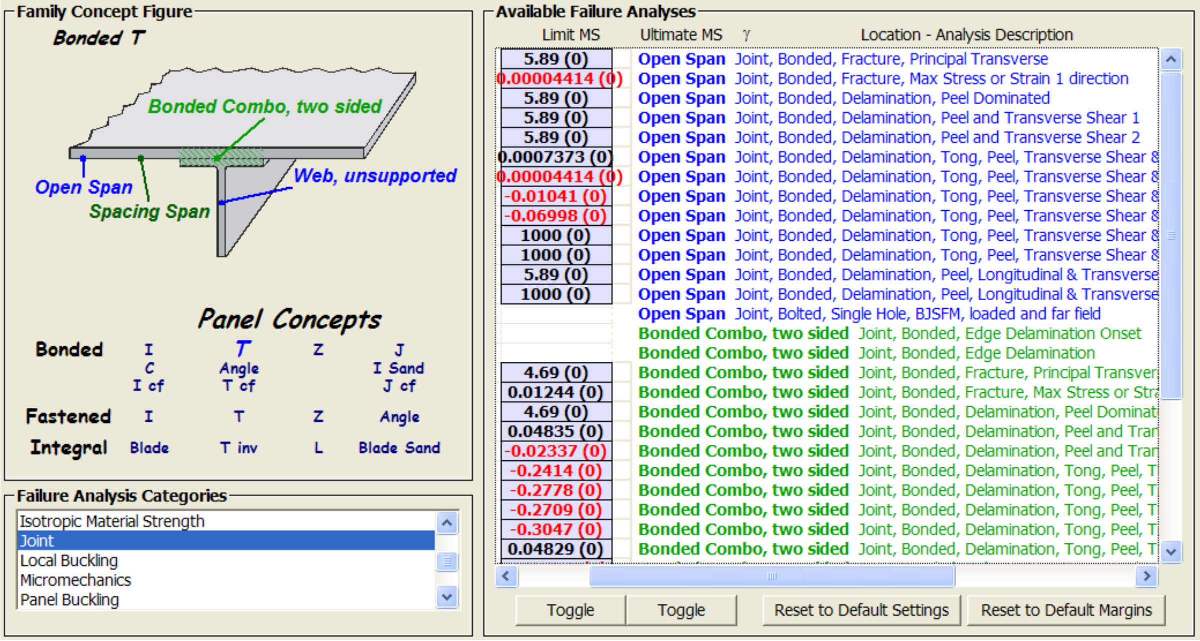

Limit MS	Ultimate MS	γ	Location - Analysis Description
5.89 (0)			**Open Span** Joint, Bonded, Fracture, Principal Transverse
0.00004414 (0)			**Open Span** Joint, Bonded, Fracture, Max Stress or Strain 1 direction
5.89 (0)			**Open Span** Joint, Bonded, Delamination, Peel Dominated
5.89 (0)			**Open Span** Joint, Bonded, Delamination, Peel and Transverse Shear 1
5.89 (0)			**Open Span** Joint, Bonded, Delamination, Peel and Transverse Shear 2
0.0007373 (0)			**Open Span** Joint, Bonded, Delamination, Tong, Peel, Transverse Shear
0.00004414 (0)			**Open Span** Joint, Bonded, Delamination, Tong, Peel, Transverse Shear
-0.01041 (0)			**Open Span** Joint, Bonded, Delamination, Tong, Peel, Transverse Shear
-0.06998 (0)			**Open Span** Joint, Bonded, Delamination, Tong, Peel, Transverse Shear
1000 (0)			**Open Span** Joint, Bonded, Delamination, Tong, Peel, Transverse Shear
1000 (0)			**Open Span** Joint, Bonded, Delamination, Tong, Peel, Transverse Shear
5.89 (0)			**Open Span** Joint, Bonded, Delamination, Peel, Longitudinal & Transverse
1000 (0)			**Open Span** Joint, Bonded, Delamination, Peel, Longitudinal & Transverse
			Open Span Joint, Bolted, Single Hole, BJSFM, loaded and far field
			Bonded Combo, two sided Joint, Bonded, Edge Delamination Onset
			Bonded Combo, two sided Joint, Bonded, Edge Delamination
4.69 (0)			**Bonded Combo, two sided** Joint, Bonded, Fracture, Principal Transver
0.01244 (0)			**Bonded Combo, two sided** Joint, Bonded, Fracture, Max Stress or Str
4.69 (0)			**Bonded Combo, two sided** Joint, Bonded, Delamination, Peel Dominat
0.04835 (0)			**Bonded Combo, two sided** Joint, Bonded, Delamination, Peel and Tran
-0.02337 (0)			**Bonded Combo, two sided** Joint, Bonded, Delamination, Peel and Tran
-0.2414 (0)			**Bonded Combo, two sided** Joint, Bonded, Delamination, Tong, Peel, T
-0.2778 (0)			**Bonded Combo, two sided** Joint, Bonded, Delamination, Tong, Peel, T
-0.2709 (0)			**Bonded Combo, two sided** Joint, Bonded, Delamination, Tong, Peel, T
-0.3047 (0)			**Bonded Combo, two sided** Joint, Bonded, Delamination, Tong, Peel, T
0.04829 (0)			**Bonded Combo, two sided** Joint, Bonded, Delamination, Tong, Peel, T

Fig. 6.7.7, Composite Joint Margins of safety reported on the failure tab

6.7.3 Limitations of Capability

The primary limitation of the current implementation of HyperSizer-BondJo, as mentioned earlier, is the adhesive material and thickness are currently tied to the material and thickness of adherend 2. This makes automatic optimization of the adhesive inconvient, however this is considered to be a temporary limitation. In a future HyperSizer release, a database and interface will be provided that will allow for continuous variable optimization of the bonded joint geometry (i.e. overlap length, adhesive thickness) and adhesive material.

The second limitation is that only the bonded doubler joint type is commercially available. There is no single lap joint or any other type of lap joint represented in the commercial software at this time. An internal single lap joint code has been completed and V&V and the next step is to integrate it into the commercial HyperSizer. Another future development will be to identify these joints on a full airframe finite element model and automatically pull loads from the FEA in order to analyze and size them.

A third limitation that is believed to be minor is that, while HyperSizer will accept any general combination of loadings and deformations on a stiffened panel, the cylindrical formulation of Bondjo does not accept prescribed applied moments or curvatures in the stiffener direction or in the bending-twisting axis.

6.8 Future Development

6.8.1 Inclusion of deformable shear theory in the adherend

Classical lamination theory, which is currently used in BondJo, does not account for the actual transverse deformation of adherends, which is pronounced in laminates with low transverse shear moduli. Neglecting transverse shear of adherends will induce errors to interlaminar stresses calculation and even for the adhesive stresses. This is the only major potential weakness of BondJo's current methodology. First order shear deformable theory would be a relatively easy extension to BondJo that could address this shortcoming.

First order shear deformable theory for the joints, including the kinematics and constitutive equations are given in Whitney [6.8.1]. This theory postulates that the displacement field of the adherend is a linear function of the z coordinate, as shown by the following equations:

Error! Objects cannot be created from editing field codes.

and the transverse strains are then found by:

Error! Objects cannot be created from editing field codes.

where it can be seen that the transverse strains are linear functions of the z coordinate. Including these effects in BondJo would mean incorporating these equations into the adherend constitutive equations.

Although CLT also assumes the displacements (mainly *u* and *v*) are linear functions of z coordinates, it postulates that planar cross sections of the plate remain plane (Kirchoff-Love Hypothesis) and perpendicular to the neutral axis after deformation. Thus, it leads the deflection *w* to be constant through the z direction and γ_{yz}, γ_{zx} and ε_{zz} to be zeros. However, the First-Order Shear Deformable Theory does not guarantee that the cross section remains perpendicular to the neutral axis after deformation, but assumes that *w* is a linear function of z such that out-of-plane strains could develop, as can be seen from above equations.

$$[z\psi_x\,(x, y),\ z\psi_y\,(x, y),\ z\phi_x\,(x, y)] + [u_0,\ v_0,\ w_0] = [u,\ v,\ w]$$

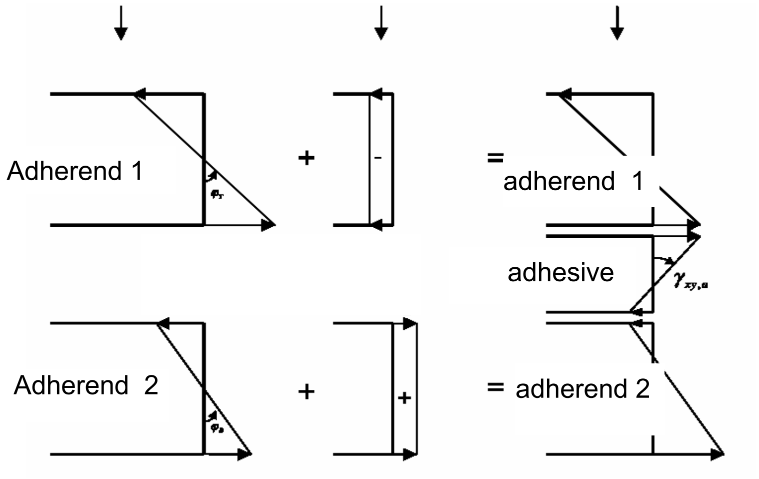
Adherend 1
+
-
=
adherend 1
adhesive
$\gamma_{xy,a}$
Adherend 2
+
+
=
adherend 2

Fig. 6.8.1, Introducing first-order shear deformable theory into bonded joint analysis

Fig. 6.8.1 illustrates the strategy of including the first-order shear deformable theory for the adherends. The displacements shown in the figure include *u*, *v* and *w*, which are all linear functions of *z* direction. It should be noted that displacement of adherends varies in *x*-*z* plane.

6.8.2 Inclusion of geometric non-linearity in joint analysis.

One effect that must be considered whenever analyzing bonded joints is that of geometric non-linearity. This effect is not presently considered in the BondJo formulation, however, **for bonded doubler joints, with normal material/geometry configurations, predicted failure loads in the joint occur at much lower strain/curvature levels than where the panel becomes geometrically non-linear.**

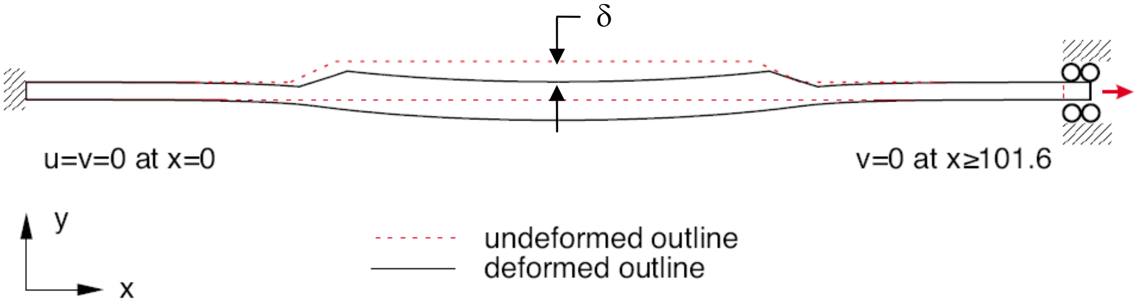
δ
u=v=0 at x=0
v=0 at x≥101.6
y
x
undeformed outline
deformed outline

Fig. 6.8.2, This is typical linear deformation of a bonded doubler joint. HyperSizer BondJo captures this response very accurately. Because the linear deformation is small, non-linear geometric deformation at loads levels where failure can occur is not a significant effect.

As an example, consider the validation case presented in Section 6.10.2 that compares HyperSizer-BondJo failure predictions to a series of tests from Cheuk and Tong. In this configuration, the total length of the joint is 140 mm. The total vertical deformation (δ) of the joint at the predicted failure load of 13 kN is only about 1.2 mm. This only amounts to a deflection of only 0.8%, which is well within the acceptable 2% limit for linear “small deflection “analysis”.

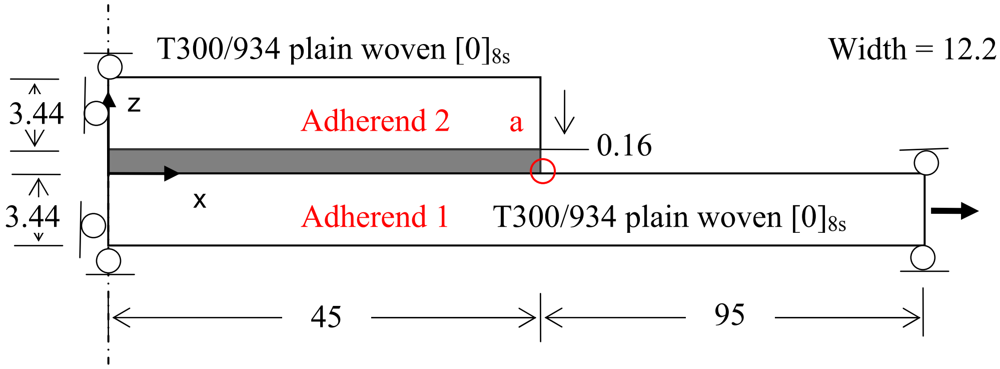
T300/934 plain woven $[0]_{8s}$
Width = 12.2
3.44
z
Adherend 2
a
0.16
3.44
x
Adherend 1
T300/934 plain woven $[0]_{8s}$
45
95

All dimensions in mm.

Fig. 6.8.3, Schematic of bonded doubler test specimens examined by Cheuk and Tong.

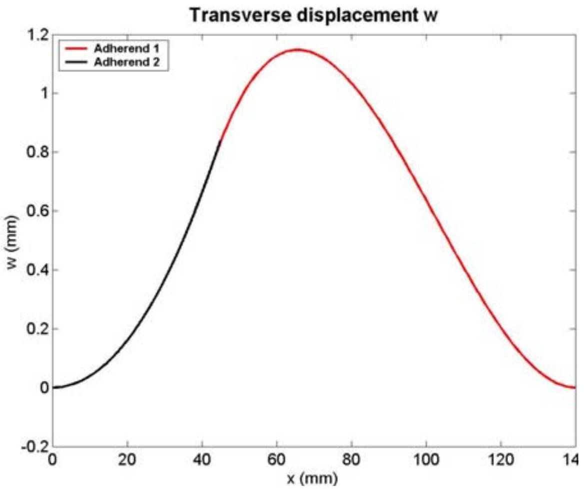

Fig. 6.8.4, Vertical deflection, w, of the Cheuk and Tong validation problem at the predicted failure load. The maximum deflection of about 1.2 mm is only 0.8% of the total bond length, well within the limits of linear analysis.

As another example, Fig. 6.8.5, from reference [6.8.5, Fig. 8], shows that for a bonded doubler joint non-linear geometric effects are not significant.

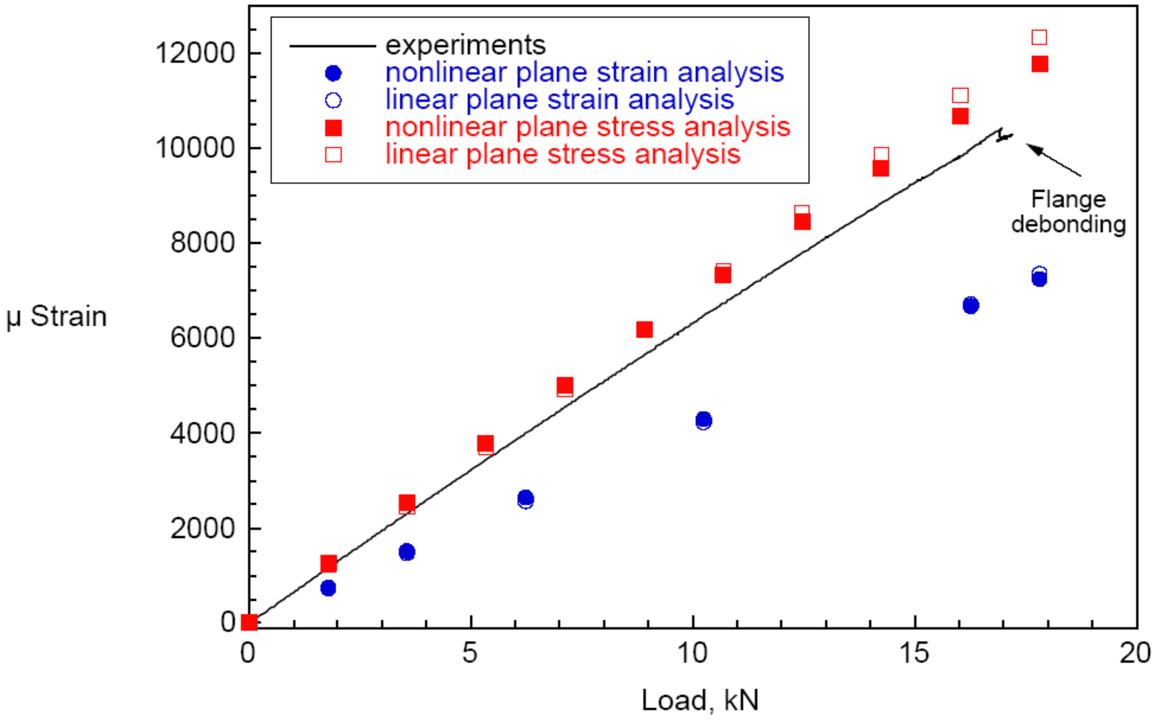

Fig. 6.8.5, This is a comparison of finite element analysis results to the experimental result of axial strain vs load for bonded doubler specimens. It shows that for both plane stress and plane strain, geometric nonlinearity does not generate significant differences in response.

While for a bonded doubler joint, non-linear geometry effects may not be substantial, in the single lap joint this may not be true and geometric non-linear may become more important

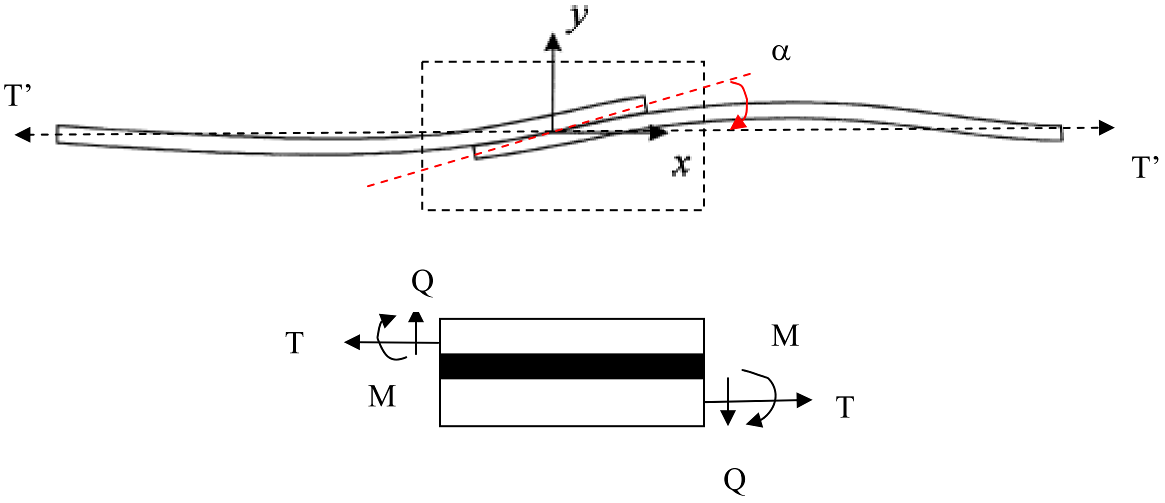

Fig. 6.8.6, An engineering method to model the geometric nonlinearity in the single lap joint. The core idea is to solve the fields in the over-lap region under the equivalent forces (moment) from the deformed body.

To model the geometric nonlinearity in the adherends, one needs to modify the kinematics equation with infinitesimal strain to account for large rotation. The strain in the adherends with large rotation is given by

$$\varepsilon_{ij} = \frac{1}{2}\left[\frac{\partial u_j}{\partial X_i} + \frac{\partial u_i}{\partial X_j} + \frac{\partial u_k}{\partial X_i}\frac{\partial u_k}{\partial X_j}\right] \tag{6.8.2.1}$$

An alternative to modeling geometric nonlinearity in the single-lap joints is to use a simplified engineering based approach. The core idea is to solve the fields in the over-lap region under the equivalent forces (moment) from the deformed body, as shown in Fig. 6.8.6. The moment at the edge of overlap region can be obtained with the formula $M = k \bullet 1/2T't$ [6.8.4] where *k* is called the moment reduction factor and is related to the adherend flexibility. Hart-smith [6.8.2], Goland and Reissner [6.8.3] provide empirical relationships for *k*.

The shear force Q can also be expressed as

$$Q = \frac{1}{2c}[(t+\eta)T - 2M] \tag{6.8.2.2}$$

where *c* is the overlap length, *t* is adherend thickness and η is the adhesive thickness. Once the edge loads are determined, the solution can be obtained in the over-lap region. Even though the above formulae were developed for isotropic adherends with equal thicknesses, the method could be easily extended to more general cases. The key of this engineering method is to find the relationship of the overlap region edge load to the flexibility of the adherend.

6.8.3 Replace Spring Model with Higher Order Theory Continuum Model

HyperSizer-BondJo uses a spring model for the adhesive layer. This model could capture the stress concentration near the free edge, but could not satisfy the boundary condition at the free edge exactly (that is, shear stress drops to zero), nor give the through-the-thickness variation of adhesive stresses.

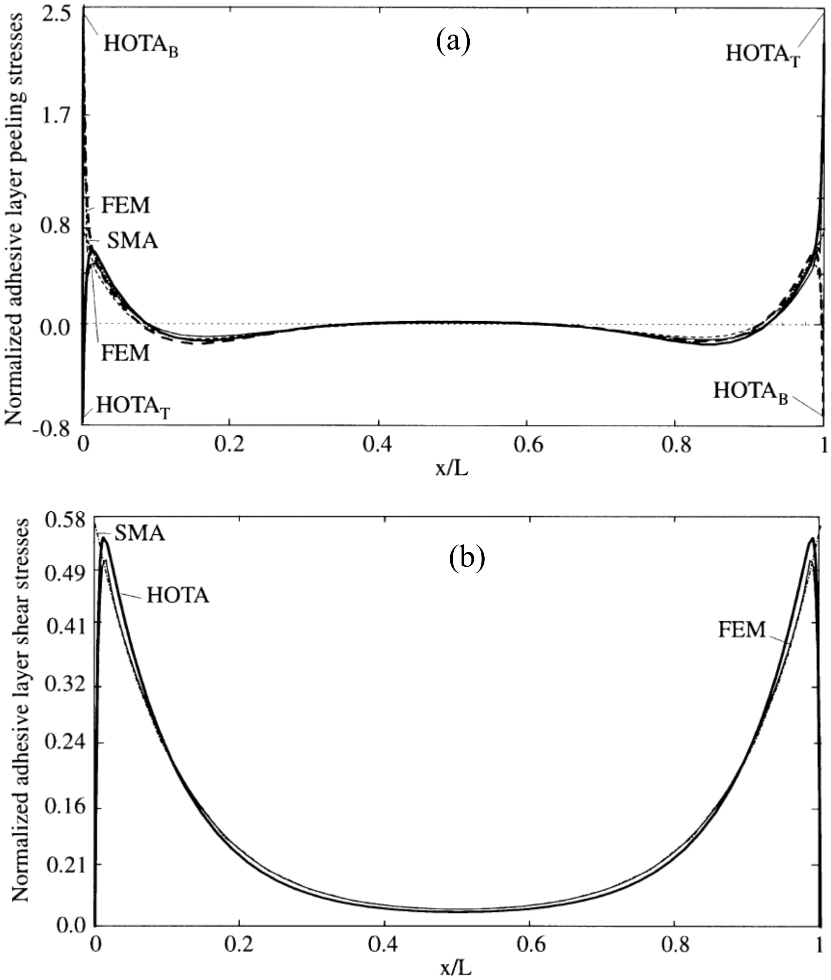

SMA – Spring Model Approach

HOTA – High-order theory Approach

FEA – Finite element Analysis

Note: Note that in the symbol HOTA$_T$, the subscript “T” represents “upper interface” of adhesive layer, “B” represents “lower interface” of adhesive layer.

Fig. 6.8.7, Normalized adhesive layer (a) peel stresses, (b)interlaminar shear stress, using the spring model approach (SMA), the high-order theory approach (HOTA, $\tau_{ax}=0$ at x=0, L) and the finite element method (FEM) for a single lap joint with no spew-fillet.

In contrast, a high-order theory approach (HOTA) could satisfy the free edge boundary condition and give the through-the-thickness variation of adhesive stresses, as shown in Fig. *6.8.7(a)* and *(b)*.

Though “academically” appealing to show that peel and transverse shear stresses reduce to zero after reaching a peak value, this is expected to be a relatively insignificant effect to capture. The key reason is described in Section 6.6 in that the failure prediction is generally performed using peel or transverse stress fields not exactly at the free edge, but some characteristic distance away from the free edge.

6.8.4 Micromechanics Analysis of Bonded Joints

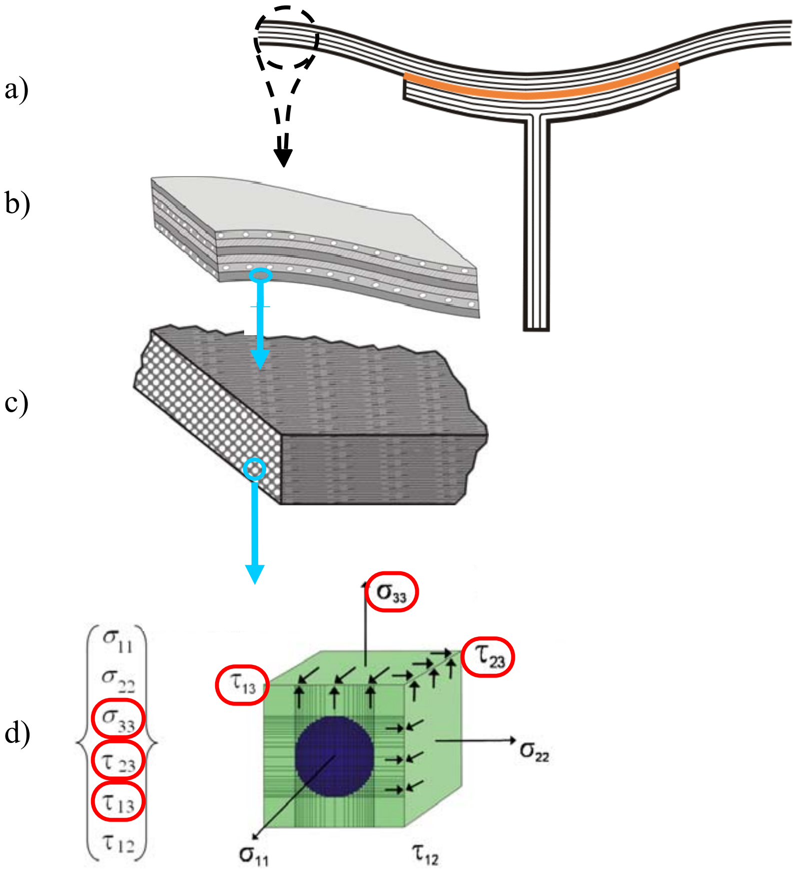

Fig. 6.8.8, Forces on the stiffened panel (a) are resolved into laminate level forces (b) which are in-turn resolved into individual ply stresses (c) using lamination theory imbedded in HyperSizer-BondJo. With BondJo, HyperSizer can now send not only in-plane stresses, but also out-of-plane stresses (shown in red circles) to a micromechanics analysis ('d') of a single fiber/matrix subcell.

A recent addition to the commercial HyperSizer software is the integration of a NASA developed micromechanics code called MAC/GMC (Micro Analysis Code/General Method of Cells). MAC/GMC has the ability to analyze a “repeating unit cell” that can represent a single fiber/matrix volume (or multiple fiber/matrix volumes), which is assumed to continuously repeat in all directions to make up the composite laminate. The process is illustrated in Fig. 6.8.8 where stiffened panel forces are resolved into laminate forces and then into individual ply stresses. Without BondJo, HyperSizer is able to resolve the in-plane stresses (σ_{11}, σ_{22}, τ_{12}) and pass them to the micromechanics analysis, however with the addition of BondJo, HyperSizer can now resolve not only the in-plane stresses, but also the out-of-plane stresses (shown with red circles) and send them along with in-plane stresses to MAC/GMC so that a full fiber/matrix analysis can be performed.

6.8.5 References

6.8.1 Whitney, J. M., Structural Analysis of Laminated Anisotropic Plates, Chapter 11, Technomic Publishing Co., Inc, 1987.

6.8.2 Hart-Smith, L. J., “Adhesive-Bonded Single-lap Joints,” NASA CR-112236, 1973.

6.8.3 Goland, M., and Reissner, E., “The Stress in Cemented Joints,” ASME journal of Applied Mechanics, Vol.11, 1944, pp.A17-A22.

6.8.4 Chen, D. and Cheng, S., 1983, “An analysis of Adhesive-Bonded Single-lap Joints,” J. Appl. Mech., Vol.50, pp.109.

6.8.5 Krueger, R. et al., “Fatigue Life Methodology for Bonded Composite Skin/Stringer Configurations” NASA/TM-20010-210842; ARL-TR-2432, April 2001.

6.9 *Verification Examples*

6.9.1 Bonded Doubler Verification – Delale and Erdogan, monolithic

Note: This example uses the typical academic sign convention. See Section 6.11 for details.

The first set of verification examples compare results from HyperSizer-BondJo with a series of results from Delale and Erdogan [6.9.1]. On the left side of configuration, symmetric boundary conditions are prescribed. Two loadings and two material systems were studied. Results for the first of these material systems using aluminum adherends, are presented here. Results for the second material system, which includes a homogeneous orthotropic material, are presented in Volume 3, Section 6. The first loading condition applies uniaxial tension and the second applies a moment to the right edge. A full description of this problem and the results for all loading/material combinations is given in Volume 3, Section 6.

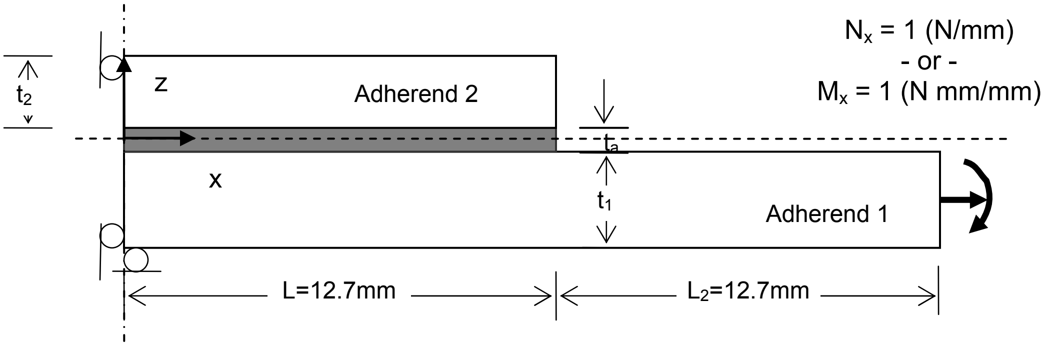

Adherend 1: Aluminum, monolithic, t_1 = 1.524 mm
Adherend 2: Aluminum, monolithic, t_2 = 0.762 mm
Adhesive: Epoxy, t_a = 0.1016 mm

Fig. 6.9.1, Configuration of bonded doubler joint example

Note that the Delale and Erdogan plate solution, shown in Fig. 6.9.2 and 6.9.3, is not general (cannot handle composite materials nor general loadings and boundary conditions) as does the implemented approach in HyperSizer. Also note that the method implemented in HyperSizer tends to over predict the dip at $0.8 < X/L < 0.9$. Though this appears to be a concern, so far, it has been insignificant in both the prediction of free edge peel and interlaminar stresses that are used in adhesive failure predictions and for failure predictions of delamination and fracture for laminates. It has also been determined that this dip does not effect strain energy release rates calculations using the virtual crack closure technique.

Results

A sampling of the results comparing HyperSizer-BondJo results to those from a solid model FEA for the aluminum-aluminum joint configuration is shown in the following Figs. 6.9.2 and 6.9.3. More comprehensive results for these problems are shown in Volume 3, Section 6.

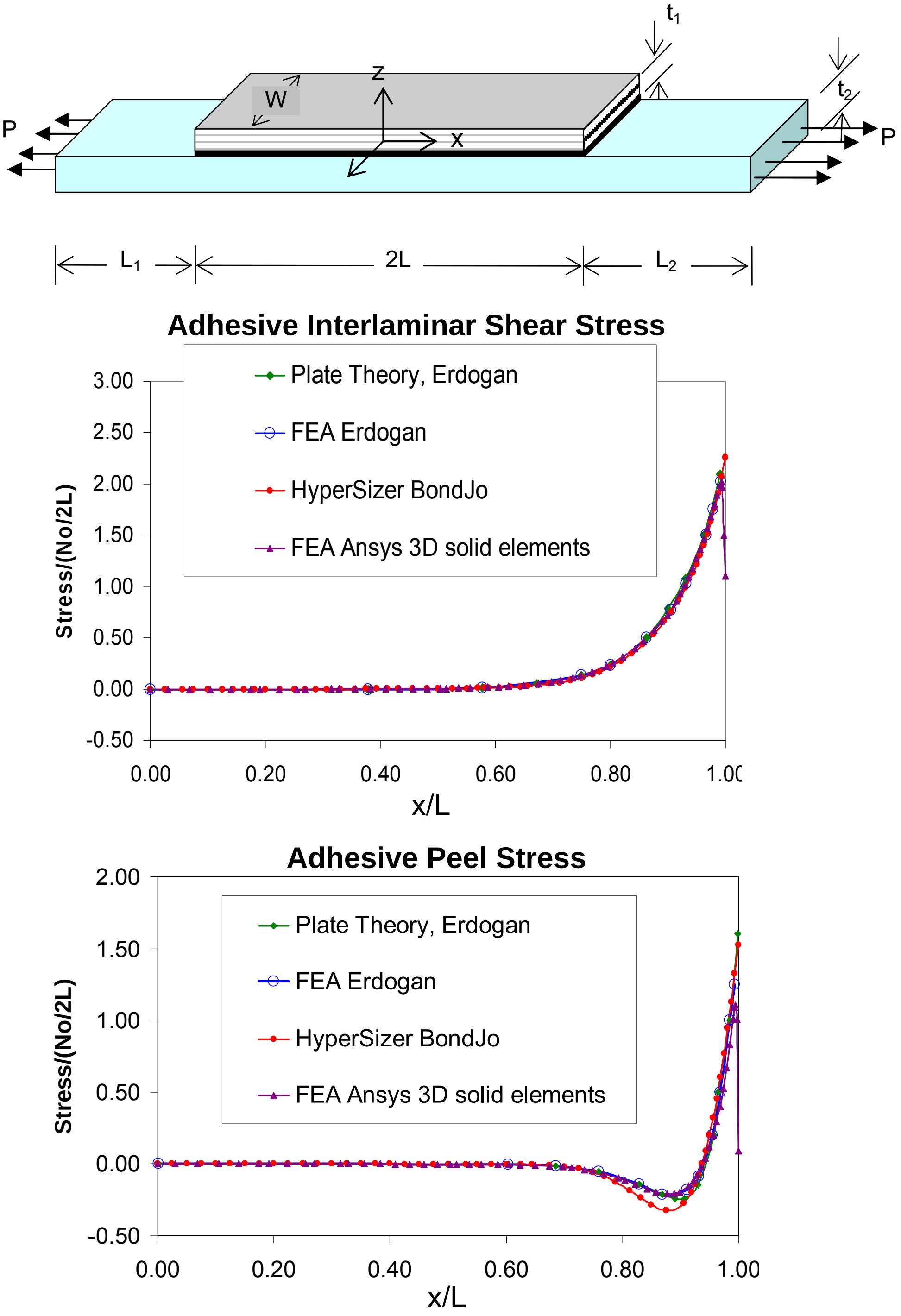

Fig. 6.9.2, Comparisons for the applied tensile load case between BondJo, Ansys 3D solid FEA, Delale and Erdogan's analytical plate theory and independent FEA performed by Delale and Erdogan.

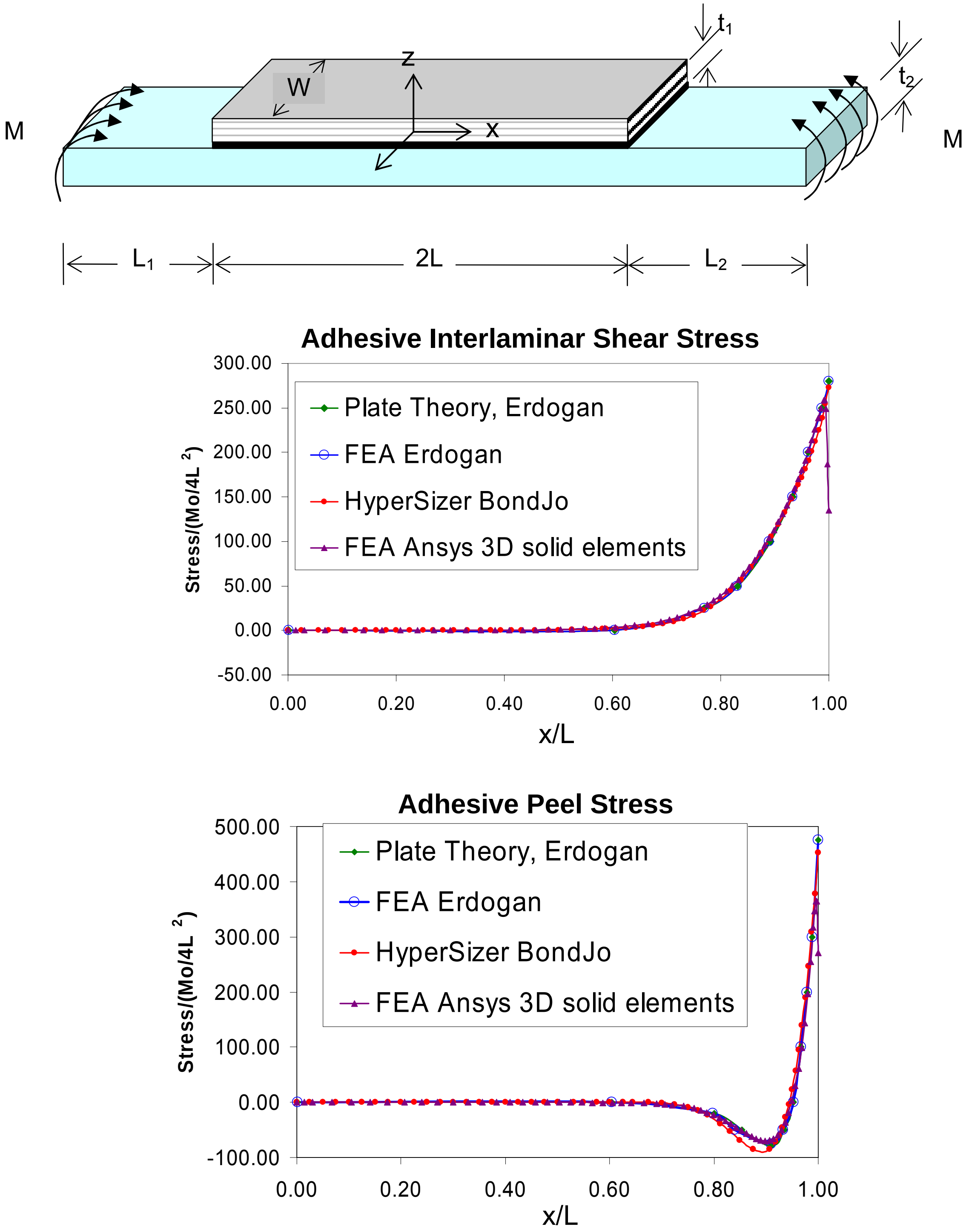

Fig. 6.9.3, Comparisons for the applied moment case between BondJo, Ansys 3D solid FEA, Delale and Erdogan's analytical plate theory and independent FEA performed by Delale and Erdogan.

Black = Peel Stress (σ_z)
Red = Interlaminar Shear (τ_{xy})
Blue = Interlaminar Shear (τ_{yz})

Solid Line = HyperSizer-BondJo
Dashed Line = ANSYS Solid FEA

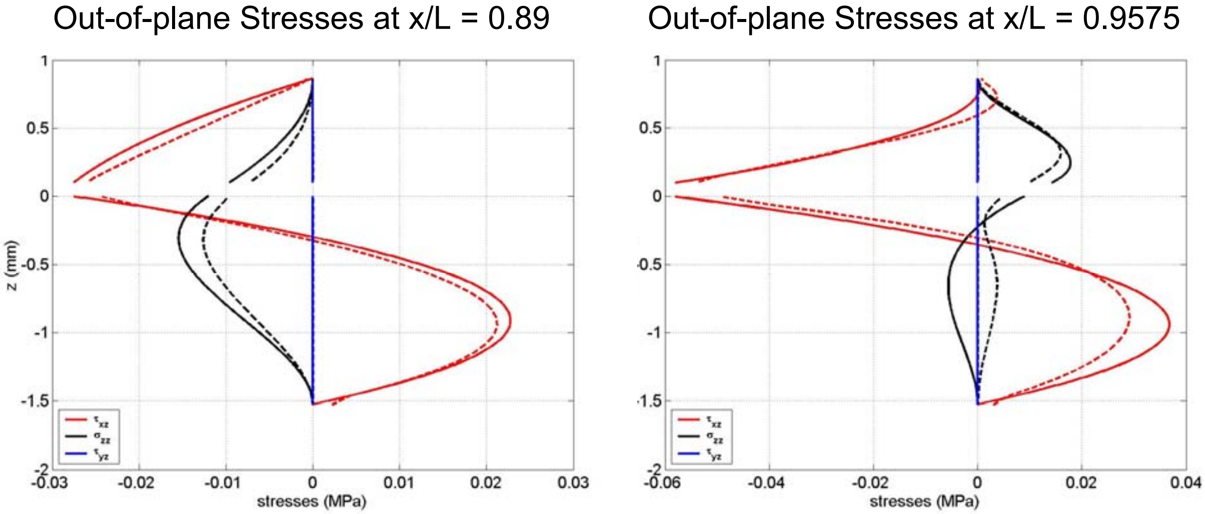
Out-of-plane Stresses at x/L = 0.89

Out-of-plane Stresses at x/L = 0.9575

Fig. 6.9.4, Through-the-thickness distribution of out-of-plane (interlaminar) stresses in the adherends of bonded doubler (aluminum-aluminum) subjected to uniaxial tension (N_{xx} = 1 N/mm)

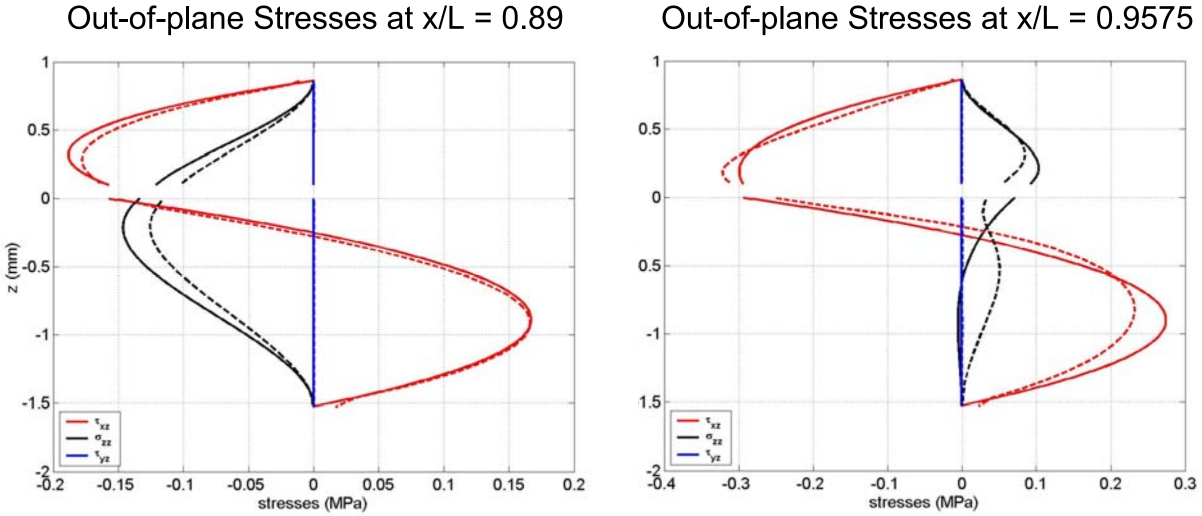
Out-of-plane Stresses at x/L = 0.89

Out-of-plane Stresses at x/L = 0.9575

Fig. 6.9.5, Through-the-thickness distribution of out-of-plane (interlaminar) stresses in the adherends of bonded doubler (aluminum-aluminum) subjected to unixaial tension (M_{xx} = 1 N-mm/mm)

6.9.2 Bonded Doubler Verification – StressCheck FEA, [0/±45/90] Laminate

Note: This example assumes the typical academic sign convention. See Section 6.11 for details.

The problem that was run in HyperSizer-BondJo and compared to Stresscheck uses laminated adherends with off axis plies subjected first to tensile and then to bending moment loading. To determine through-the-thickness distribution of stresses in the FEA required explicit modeling of each ply in the FEA. The schematic representation of the bonded doubler problem is shown in Fig. 6.9.6. Adherend 1 was made of boron/epoxy prepreg tape and has a [45/-45/0/90/0/90/45/-45/0]s lay-up with nominal thickness of 0.005 in. Adherend 2 was also made of boron/epoxy prepreg tape, with lay-up of [0/90/45/-45/90/0], and nominal thickness of 0.005 in. The thickness of the adhesive layer is 0.004 in. These results are discussed more fully in Volume 3, Section 7.

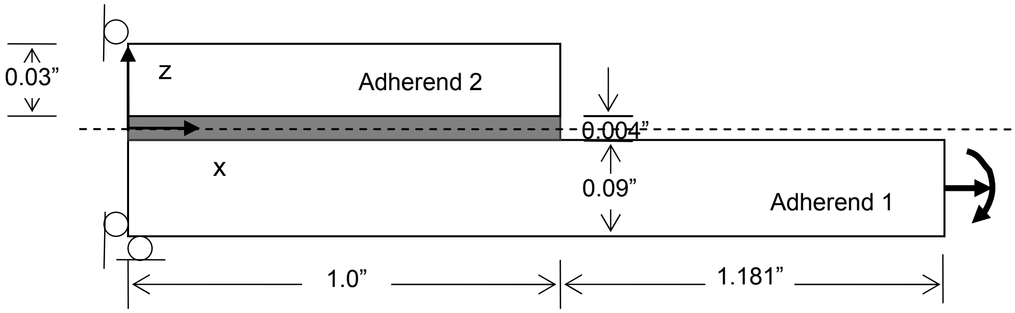

Adherend 1: Boron/epoxy [45/-45/0/90/0/90/45/-45/0]$_{s,}$ 18 plies of prepreg tape, t=0.005"
Adherend 2: Boron/epoxy [0/90/45/-45/90/0], 6 plies of prepreg tape, t=0.005"
Adhesive: Epoxy, $t_a = 0.004$ in.

Fig. 6.9.6, HyperSizer-BondJo to Stresscheck verification problem

The comparison between HyperSizer-BondJo and StressCheck shows that most of the results match very well, including adhesive interlaminar shear and peel stresses, adherend middle-plane displacement, and stresses in the adherends. Adhesive peel stress match generally well between BondJo and StressCheck, except in the non-critical “trough” region, where peel stress becomes negative and HyperSizer-BondJo tends to overpredict the stress. The adherend out-of-plane stresses components match well also, except again in the peel stress at the “trough” region.

Black = Peel Stress (σ_z)
Red = Interlaminar Shear (τ_{yz})
Blue = Interlaminar Shear (τ_{xz})

Solid Line = HyperSizer-BondJo
Dashed Line = Stresscheck FEA

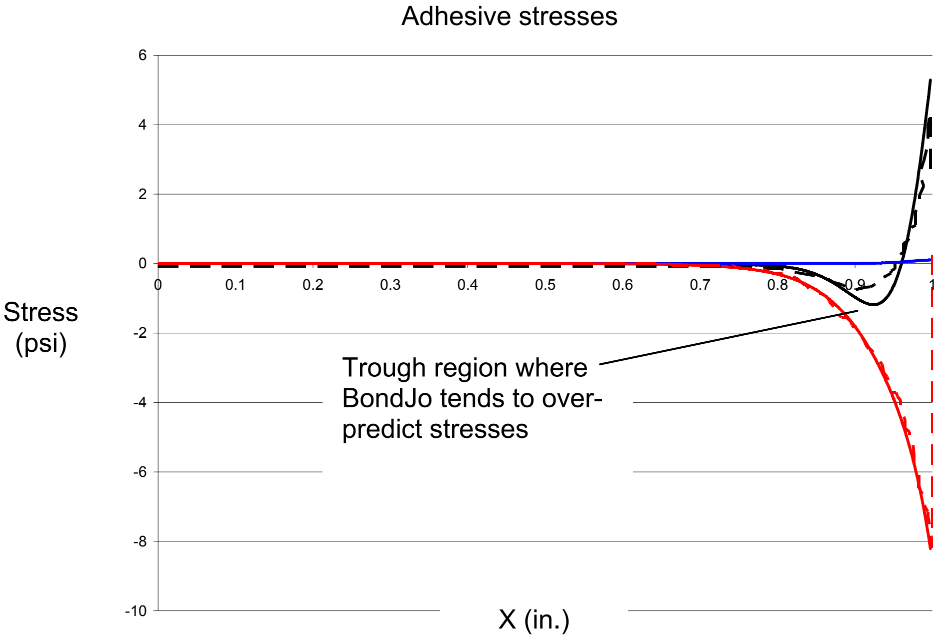

Fig. 6.9.7, Adhesive stress validation results between HyperSizer-BondJo and Stresscheck for panel applied axial force

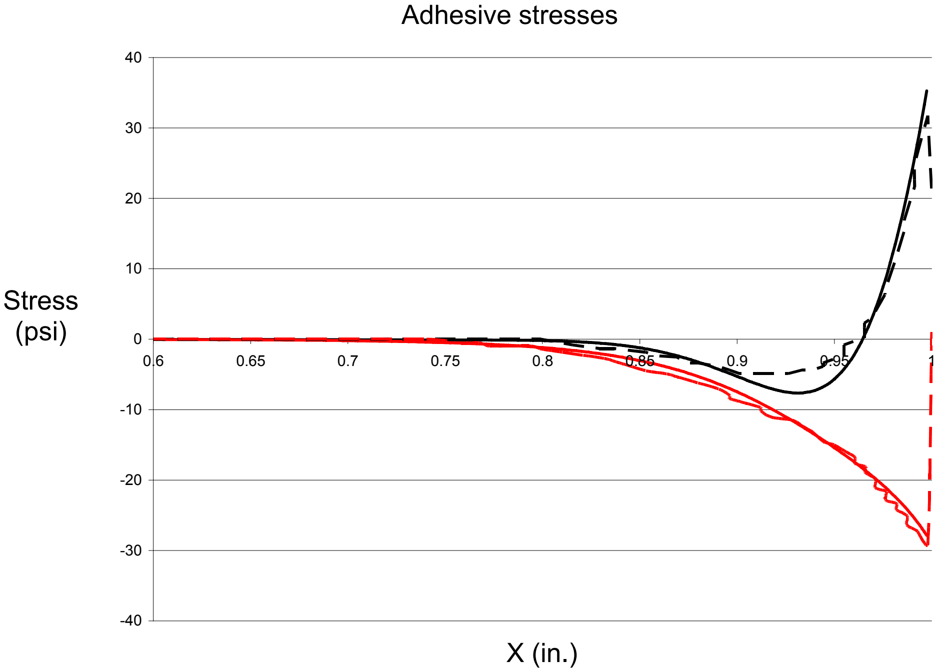

Fig. 6.9.8, Adhesive stress validation results between HyperSizer-BondJo and Stresscheck for panel applied moment.

Black = Peel Stress (σ_z)
Red = Interlaminar Shear (τ_{yz})
Blue = Interlaminar Shear (τ_{xz})

Solid Line = HyperSizer-BondJo
Dashed Line = Stresscheck FEA

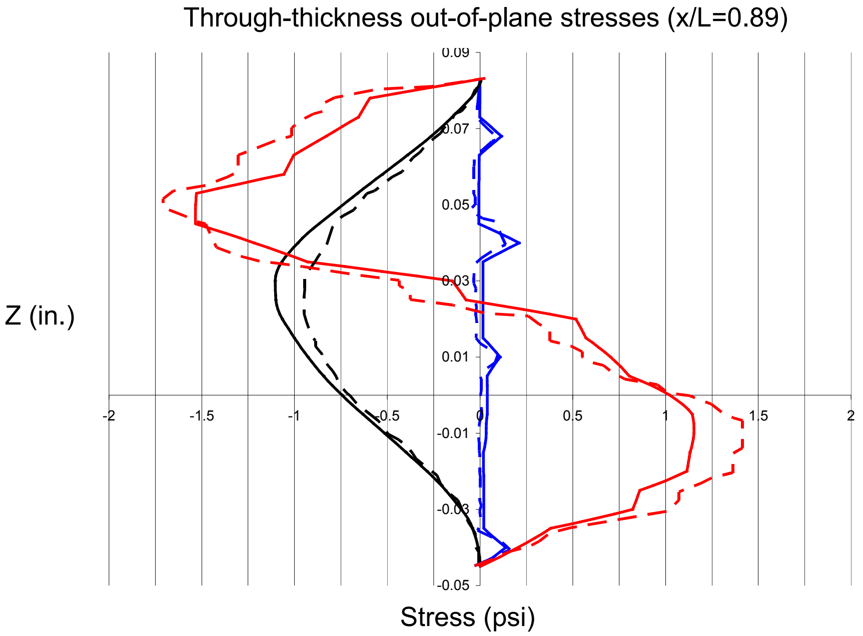

Fig. 6.9.9, Through-thickness stress result comparison between HyperSizer-BondJo and Stresscheck for panel applied axial force

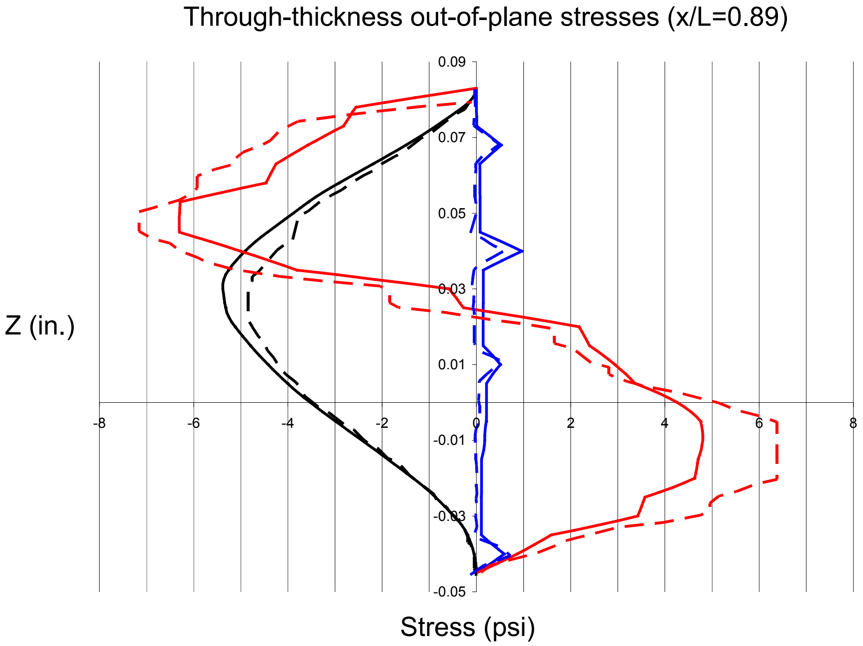

Fig. 6.9.10, Through-thickness stress result comparison between HyperSizer-BondJo and Stresscheck for panel applied moment

6.9.3 Bonded Doubler Verification – Mortensen [0/30/60] Laminate

Note: This example assumes the typical academic sign convention. See Section 6.11 for details.

The next problem is a pure verification that the theory described in Section 6.4 was implemented correctly and consistently. The problem was presented in Mortensen [6.9.2] and because BondJo's theoretical development originated from that work, it is not surprising that our results match those in [6.9.2] exactly. A full description of this problem is given in Volume 3, Section 6.

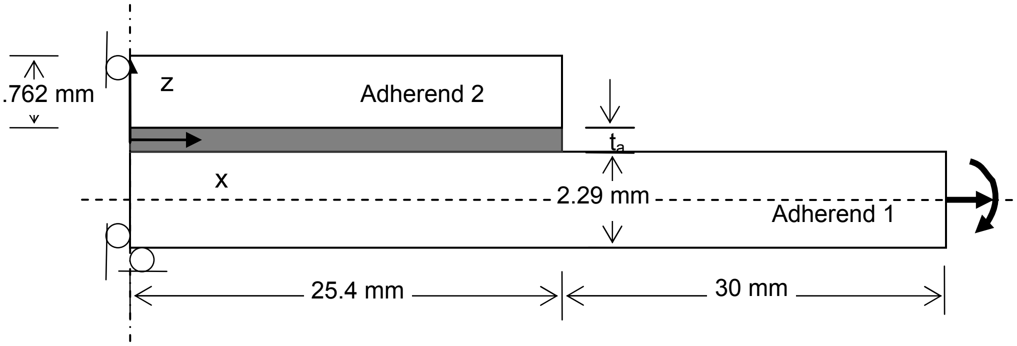

Adherend 1: Graphite/epoxy, $[60/30/0/60/30/0/60/30/0]_2$, 18 plies
Adherend 2: Graphite/Epoxy, $[0^o/30^o/60^o/0^o/30^o/60^o]$, 6 plies
Adhesive: Epoxy, $t_a = 0.1016$ mm

Fig. 6.9.11, Configuration of Mortenson's composite bonded doubler joint example example

Results

A sampling of the results comparing HyperSizer-BondJo results to those of Mortensen are shown below. More comprehensive results for this problem are shown in Volume 3.

Red = Adherend 1
Black = Adherend 2

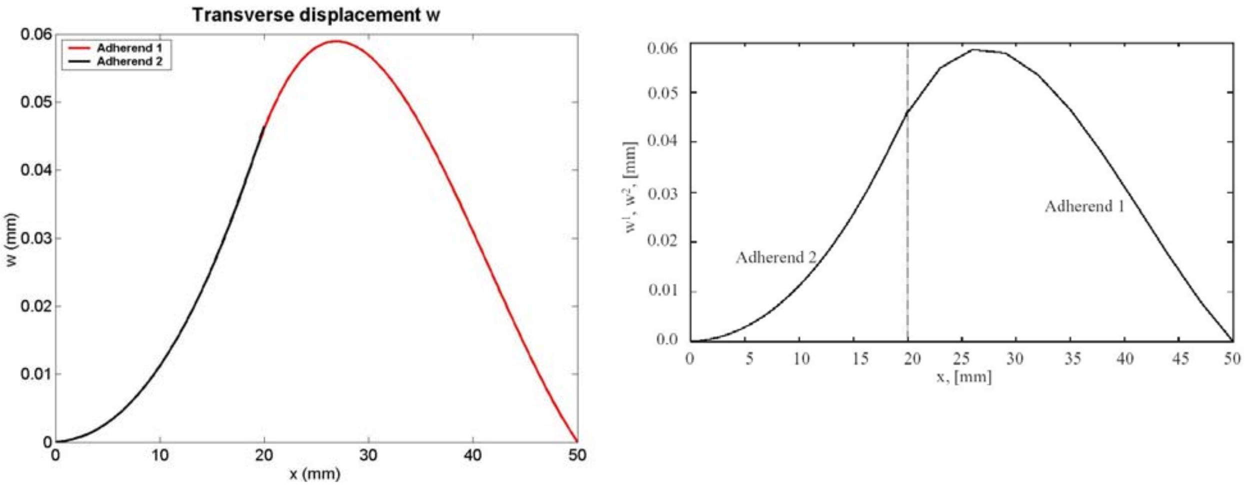

a) HyperSizer-BondJo Result *b) Mortensen Result*

Fig. 6.9.12, Adherend transverse displacement comparison between HyperSizer-BondJo and Mortensen

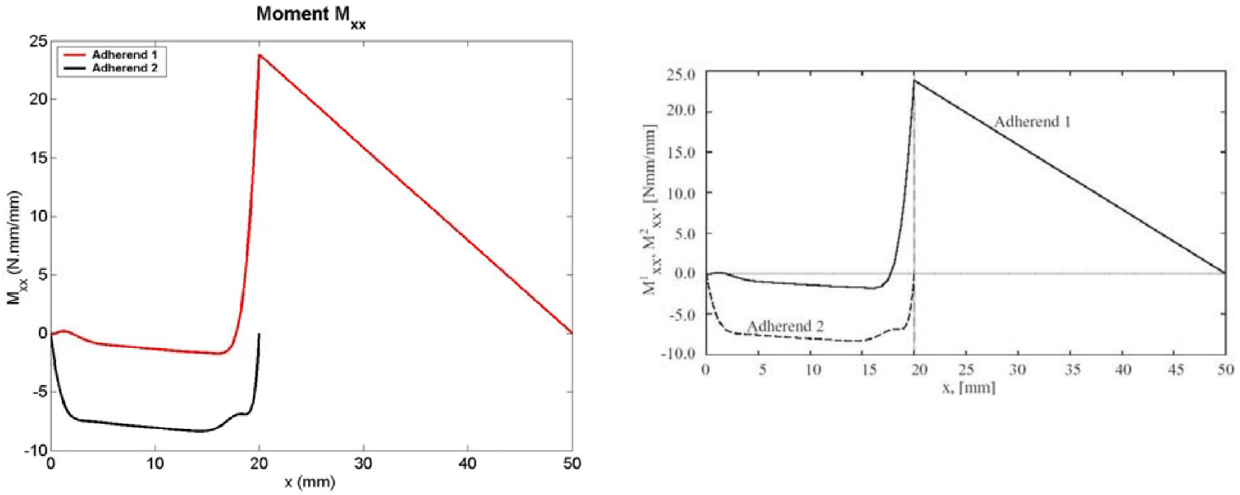

a) HyperSizer-BondJo Result *b) Mortensen Result*

Fig. 6.9.13, Adherend bending moment comparison between HyperSizer-BondJo and Mortensen

Black = Peel Stress (σ_z)
Red = Interlaminar Shear (τ_{xy})
Blue = Interlaminar Shear (τ_{yz})

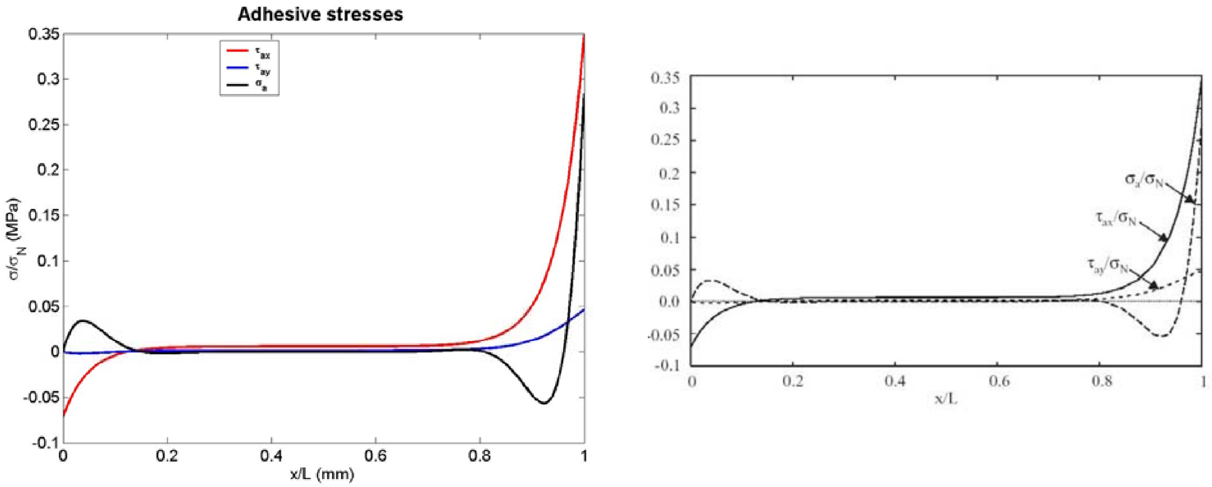

a) HyperSizer-BondJo Result *b) Mortensen Result*

Fig. 6.9.14, Out-of-plane adhesive stress comparison between HyperSizer-BondJo and Mortensen

6.9.4 Single Lap Verification – Mortenson, [0/30/60] Laminate

Note: This example assumes the typical academic sign convention. See Section 6.11 for details.

A second verification problem, this one for a single lap joint, was chosen from Mortensen [6.9.2] to verify the theory described in Section 6.4 was implemented correctly and consistently. Most of the HyperSizer-BondJo results matched exactly with Mortensen's, however, some initially showed large discrepancies with the author's results. Upon contacting the author, we learned that there were errors in the author's original code and the HyperSizer-BondJo results are correct [6.9.3]. The corrected result supplied by the author match HyperSizer-BondJo's results exactly. The configuration of the single-lap joint is illustrated in Fig. 6.9.15.

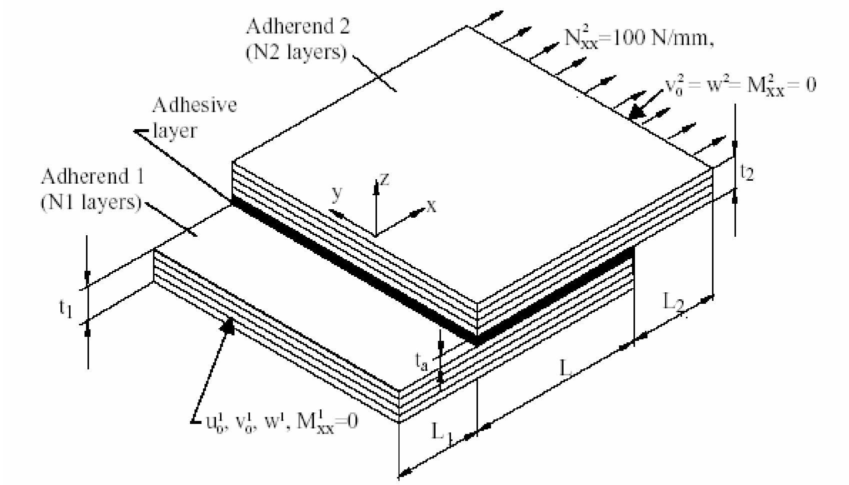

Adherend 1: Graphite/Epoxy, $[0/30/60]_4$, 12 plies, t_1 = 1.5mm
Adherend 2: Graphite/Epoxy, $[60/30/0]_4$, 12 plies, t_2 = 1.5mm
Adhesive: Epoxy AY103, t_a = 0.05 mm
Lengths: $L_1 = L_2$ = 30 mm; L = 20 mm

Fig. 6.9.15, Mortensen's example for single lap joints. The joint is simply supported at both ends (clamped in the width direction) $t_1 = t_2 = 1.5$ mm, $t_a = 0.05$ mm, $L_1=L_2=30$ mm, $L = 20$ mm.

BondJo | Mortenson [6.9.2]

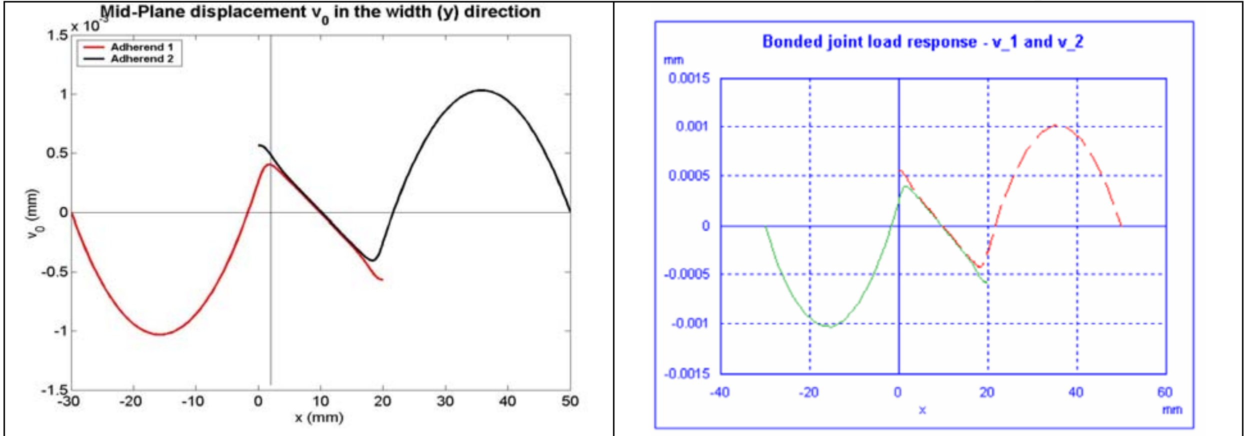

a)

b) *this corrected plot was obtained from the author of [6.4.6] and is different from results in the original source [6.9.3]*

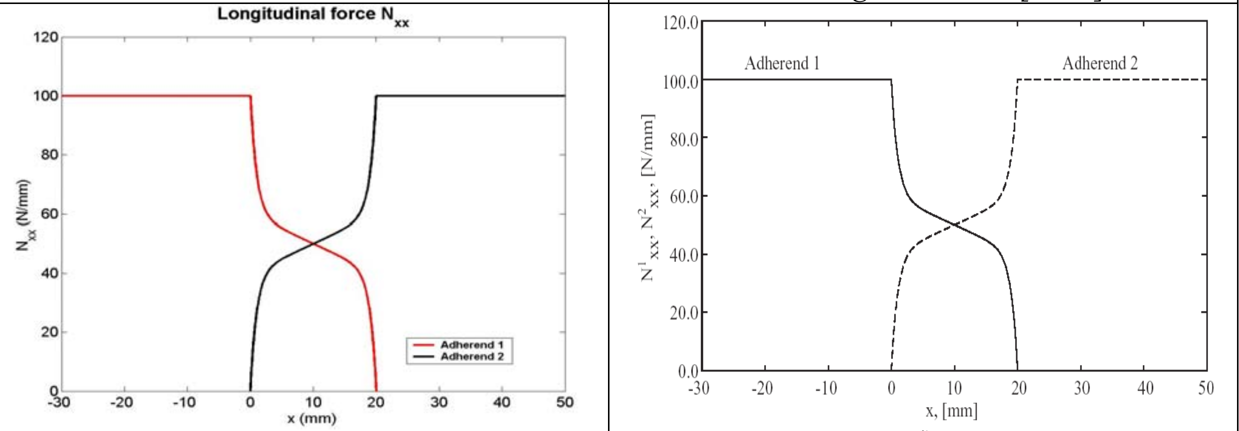

c) | d)

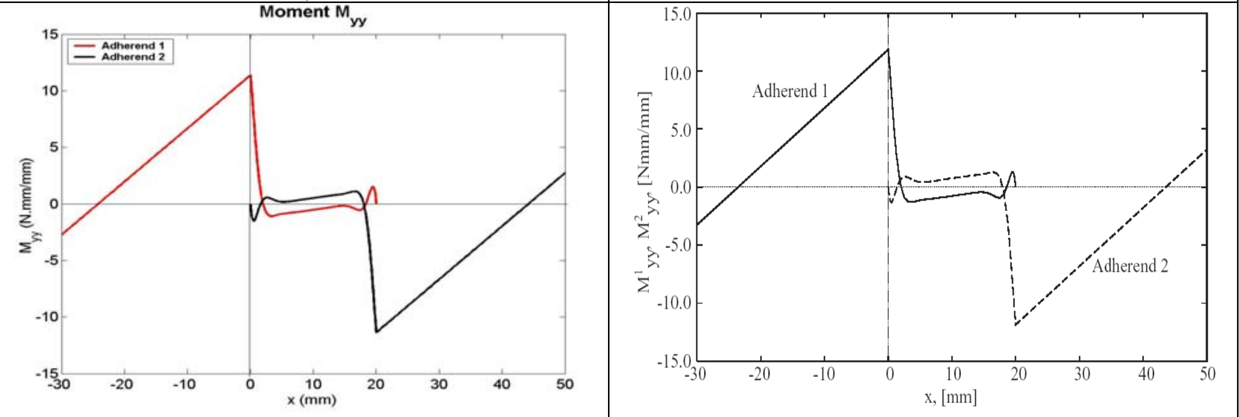

e) | f)

Fig. 6.9.16, Single-lap joint results comparison between HyperSizer-BondJo and Mortensen

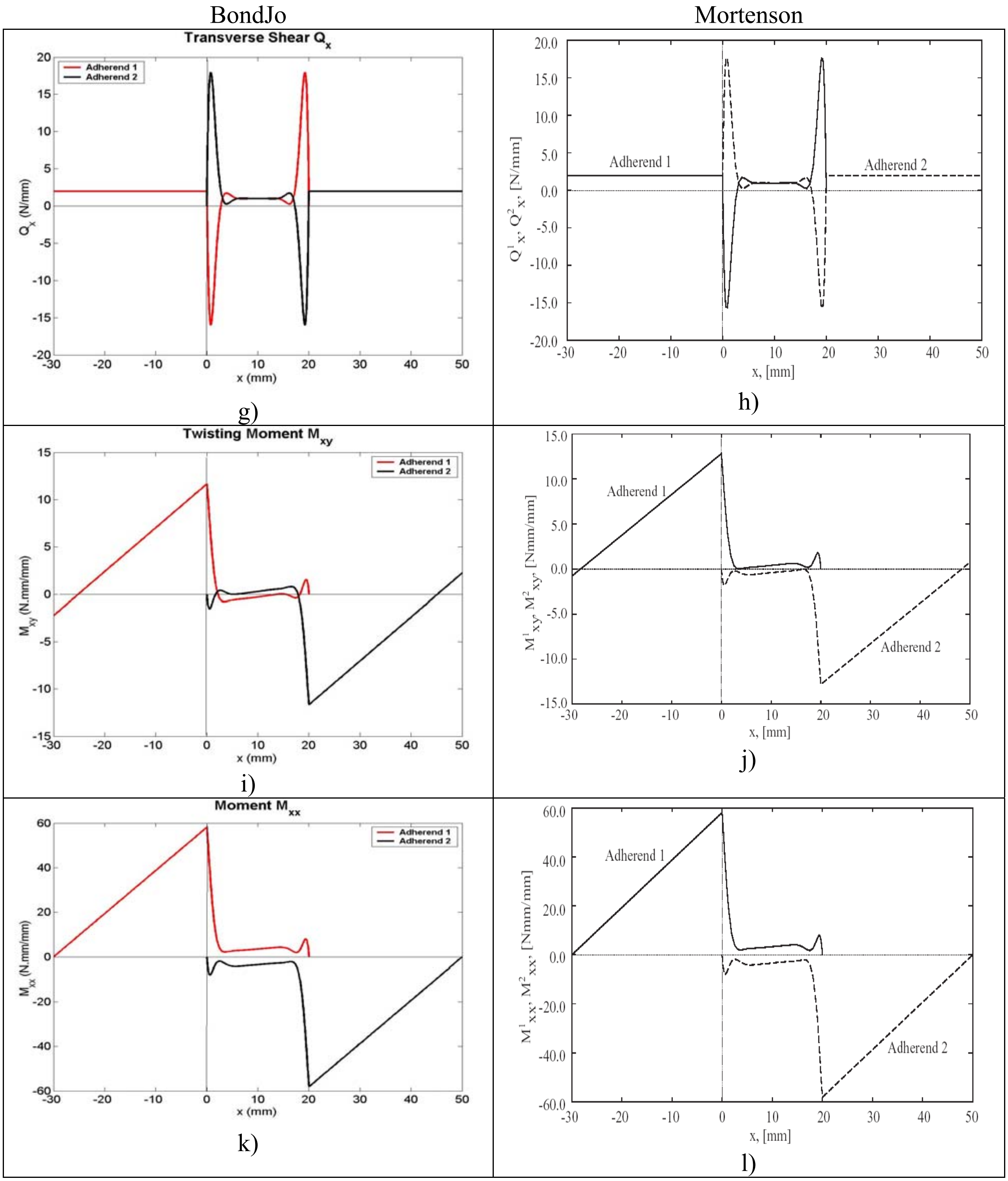

Fig. 6.9.16, Single-lap joint results comparison between HyperSizer-BondJo and Mortensen

6.9.5 References

6.9.1 F. Delale, F., Erdogan, M. N., Aydinoglu, , "Stress in Adhesively Bonded Joints: A Closed – Form solution," J. composite Materials, 15, 1981, pp 249.

6.9.2 Mortensen, F., "Development of Tools for Engineering Analysis and Design of High-Performance FRP-Composite Structural Elements," Ph.D. Thesis, Institute of Mechanical Engineering, Aalborg University (Denmark), Special Report no. 37, 1998.

6.9.3 ESAComp 2.0 software, personal contact.

6.10 Validation examples

6.10.1 Approach Summary

For bonded doublers, only two examples were found in the literature that contained sufficient problem setup and test details to allow meaningful comparisons. These two examples are from Tong [6.10.1] and NASA [6.10.2]. A validation of the HyperSizer-BondJo single lap joint implementation is also presented based on a series of tests from Tong [6.10.3].

These validation cases are modeled using HyperSizer-BondJo and the predicted failure loads are compared to the published test data. Neither test data strain gage readings nor computed stress values were disclosed in the literature, so HyperSizer-Bondjo computed interlaminar shear and peel stress values could not be compared to outside sources.

Table 6.10.1, Summary of bonded doubler validation examples

	Tong problem [6.10.1]	**NASA problem** [6.10.2]
Joint type	Bonded doubler without steps	Stepped (tapered) bonded doubler
Adherends	T300/934 plain woven fabric	Facesheet: IM7/8552 Prepreg tape [45/-45/0/-45/45/90/90/-45/45/0/45/-45] Doubler: IM7/8552 plain woven fabric, [45/0/45/0/45/0/45/0/45]
Adhesive	Linear elastic (FM300k) and non-linear material properties	Linear elastic (Grade 5 FM300) and non-linear material properties
Failure modes	Sectional fracture (ultimate failure), (failure modes are usually associated with the character of adherend material, in this case matrix cracking is NA)	Matrix cracking in the facesheet prepreg tape (damage initiation) (failure modes are usually associated with the character of adherend material, in this case a tape would exhibit matrix cracking)
Tested failure load	18.62 kN (ultimate longitudinal tensile load)	Values scatters, the average is 17.8 kN. (longitudinal tensile load for damage initiation)
Predicted failure load	14 kN (damage initiation load), based on non-linear adhesive and zero characteristic distance.	24.4 kN (damage initiation load) based on linear elastic adhesive and zero characteristic distance.
Failure criterion	Max principal stress (σ_{11} is dominant)	Max principal stress in the transverse plane to the fiber direction, σ_{22} AND σ_{33}
Possible methods for improvement	1. characteristic distance is not likely to make a difference we believe because the dominant σ_{11} does not vary sharply.	1. Characteristic distance is likely to make a difference we believe because the failure criteria includes σ_{33} which varies sharply near the free edge. 2. Use different failure criteria, such as delamination, to improve prediction of initial failure

6.10.2 Bonded Doubler Validation – Tong Example

A schematic for the geometric configuration of bonded doubler specimens used by Cheuk and Tong [6.10.1] is shown in Fig. 6.10.1. The material used for manufacturing the composite adherends was T300/934 carbon/epoxy plain-woven, with orientation of 0°. Both linear and nonlinear analyses were performed to predict the failure load of the specimen subjected to longitudinal tension. The maximum principal stress criterion was used to predict sectional fracture of the adherends. The results were compared to ultimate failure experimental data provided by Tong. It shows that the failure location predicted by *HS-BondJo* matches well with experimental observation, however the predicted failure load for both linear and non-linear adhesives was fairly conservative compared to the average test observed failure load, as shown in Table 6.10.1. The discrepancy may be due to the progressive damage involved in the experiment, whereas ***HS-BondJo*** accounts only for damage initiation. Refer to the Volume 3 for a more detailed description of the problem and results.

Note: This example assumes the typical academic sign convention. See Section 6.11 for details.

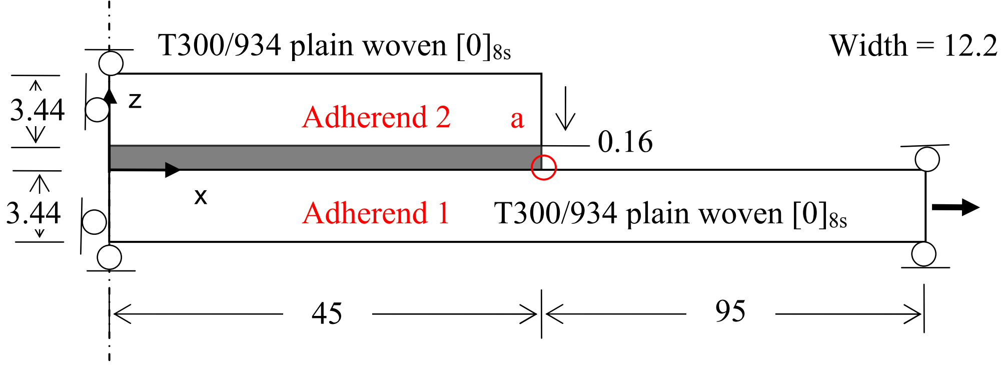
T300/934 plain woven $[0]_{8s}$
Width = 12.2
3.44
z
Adherend 2
a
0.16
x
3.44
Adherend 1
T300/934 plain woven $[0]_{8s}$
45
95

All dimensions in mm.

Fig. 6.10.1, Schematic of bonded doubler test specimens examined by Cheuk and Tong. Six specimens were tested and the results are summarized in Table 6.10.2.

Table 6.10.1, Comparison of HyperSizer-BondJo predicted to average test failure load

	Average Test	**HS-BondJo Linear Adhesive**	**HS-BondJo Non-Linear Adhesive**
Failure Load	18.6 kN (4180 lb)	13 kN (3147 lb)	14 kN (3147 lb)

Table 6.10.2, Individual test data summary for bonded doubler specimens.

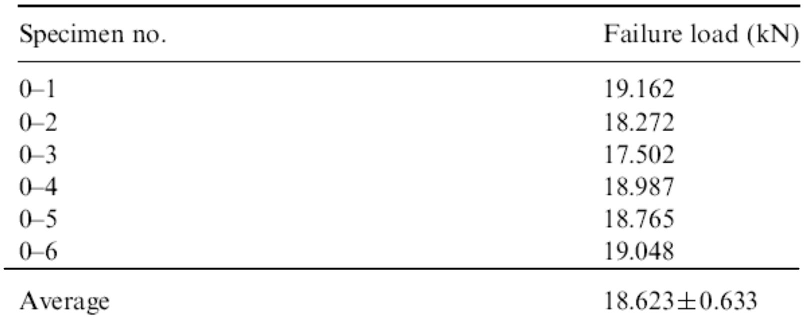

Specimen no.	Failure load (kN)
0–1	19.162
0–2	18.272
0–3	17.502
0–4	18.987
0–5	18.765
0–6	19.048
Average	18.623±0.633

Results

Typical results from the HS-BondJo analysis of this problem are shown below. The margin of safety was calculated along the length of the joint and through its thickness as shown in Figs. 6.10.2 and 6.10.3. Because no strain gage or other data was provided by the author, the only validation metric for HS-BondJo was the failure load as listed in Table 6.10.1.

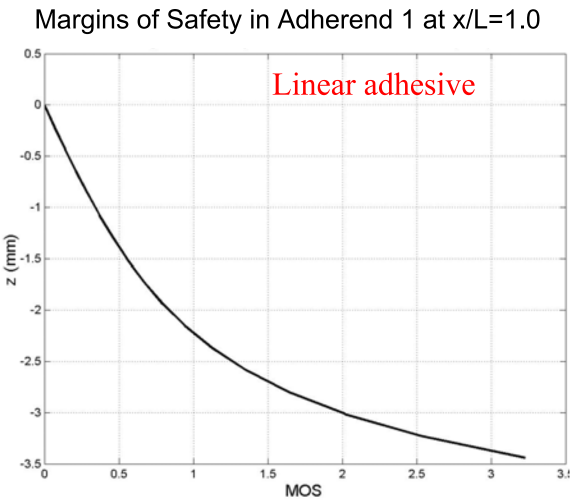

Fig. 6.10.2, Through-the-thickness distribution of margin of safety of adherend 1 at point a with linear adhesive under P =13 kN.

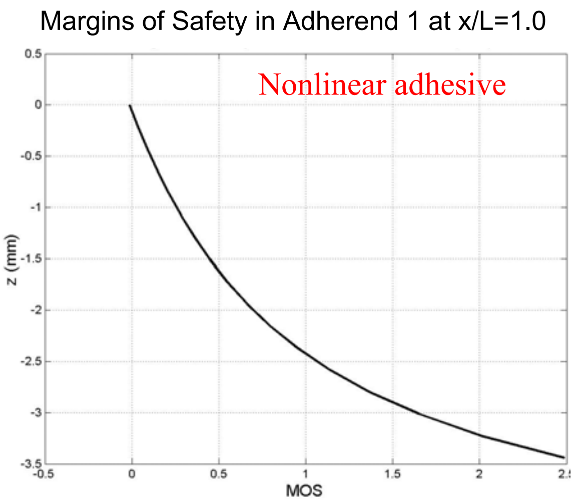

Fig. 6.10.3, Through-the-thickness distribution of margin of safety of adherend 1 at point a with nonlinear adhesive under P =14 kN.

6.10.3 Bonded Doubler Validation – NASA Example

A second validation problem involved skin/flange specimens that were studied by NASA [6.10.2]. The configuration is shown schematically in Fig. 6.10.4. The specimen consists of a tapered flange bonded to the skin. The skin was made of IM7/8552 graphite/epoxy prepreg tape with nominal ply thickness of 0.148 mm with the layup shown below. The flange was IM7/8552 plain woven fabric, with a nominal thickness of 0.212 mm. The flange was pre-cured, cut to size, machined with a 25° taper along the edges and co-bonded with uncured skin using one ply (0.178 mm) of grade 5, FM 300 adhesive film. The panel then was cut into 1.0 in. wide by 7 in. long specimens.

Note: Results for this Validation Example have been updated in [6.10.5]

Note: This example uses the typical academic sign convention. See Section 6.11 for details.

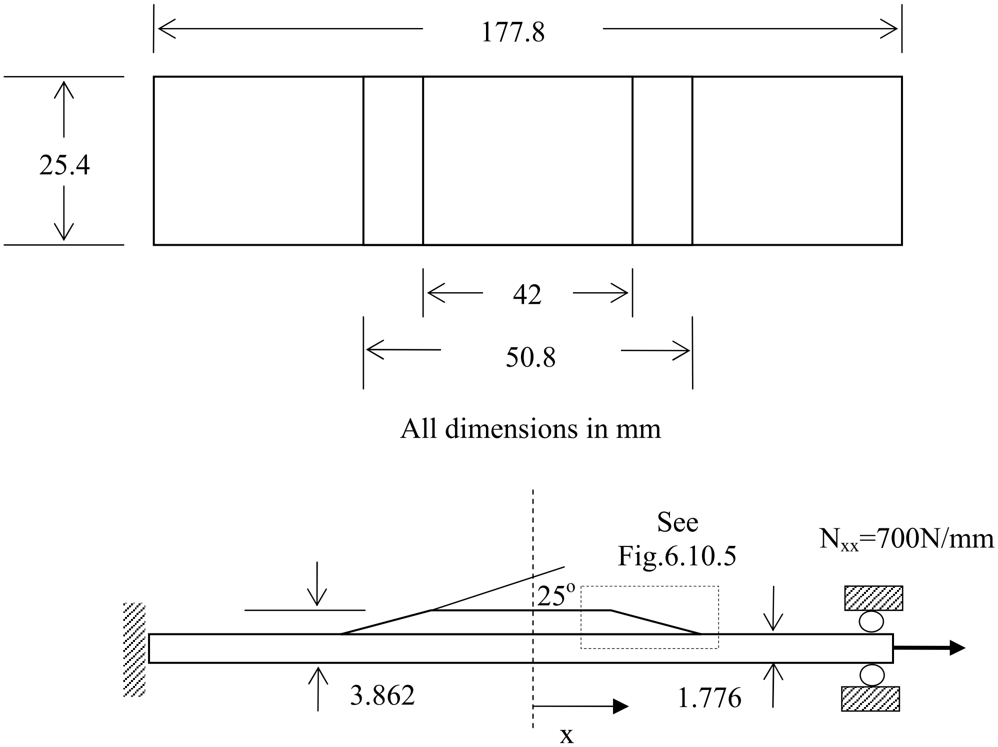

Skin: [45/-45/0/-45/45/90/90/-45/45/0/45/-45] IM7/8552 Prepreg, $t_{ply} = 0.148$
Stiffener: [45/0/45/0/45/0/45/0/45] IM7/8552 plain woven fabric, $t_{ply} = 0.212$
Adhesive: Grade 5 FM300, thickness = 0. 178 mm

Fig. 6.10.4, Schematics of a skin/flange specimen

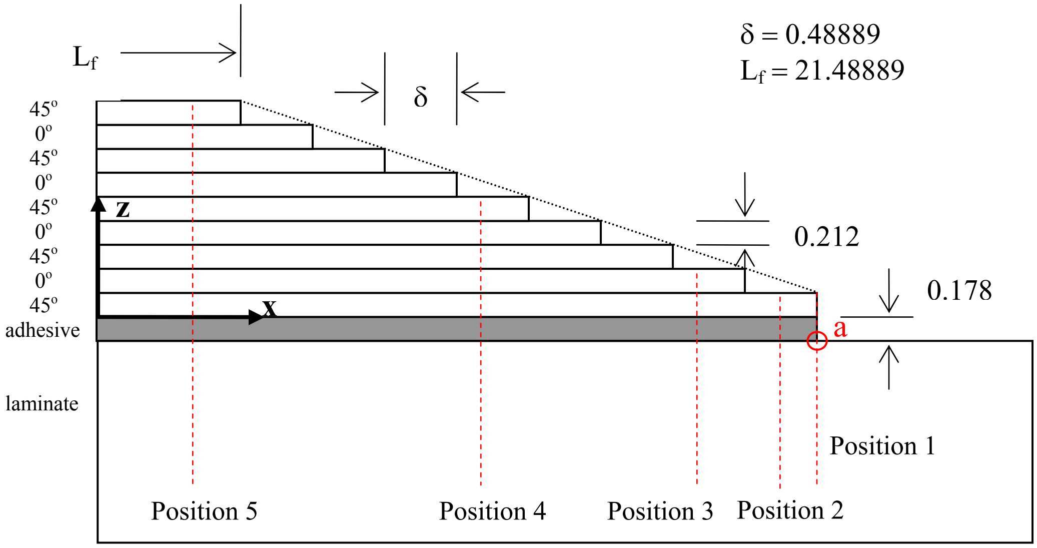

Fig. 6.10.5, Modeling of the flange scarf

Both linear and nonlinear adhesive properties are used in the analysis. The failure criterion of maximum transverse principal stress is used to predict the onset of matrix cracking and the corresponding margin of safety is checked at every point in the adherends. The experimental data, which includes both quasi-static and fatigue failure data, is shown in Fig. 6.10.6. The BondJo results are compared only to the average quasi-static test failure load of 17.8 kN. The predicted location of damage onset by linear analysis is consistent with experimental observation, however the predicted damage initiation load is 24.4 kN, about 1.4 times the test average result. In the analysis using nonlinear adhesive properties, yielding of the adhesive prevented matrix cracking failure from occurring, even at 27.6 kN. Davila [6.10.3] also studied this problem and pointed out that matrix cracking should not be used to predict damage initiation because the initial matrix cracking is very minor and leads very quickly to delamination. His suggestion was to use a delamination failure criterion to predict damage initiation. Please refer to the Volume 3 for detailed description of validation of this problem.

Table 6.10.3, Comparison of HyperSizer-BondJo predicted to average test failure load

	Average Test (static failure only)	**HS-BondJo Linear Adhesive**	**HS-BondJo Non-Linear Adhesive**
Failure Load	17.8 kN (4000 lb)	24.4 kN (5480 lb)	> 27.6 kN (6200 lb)

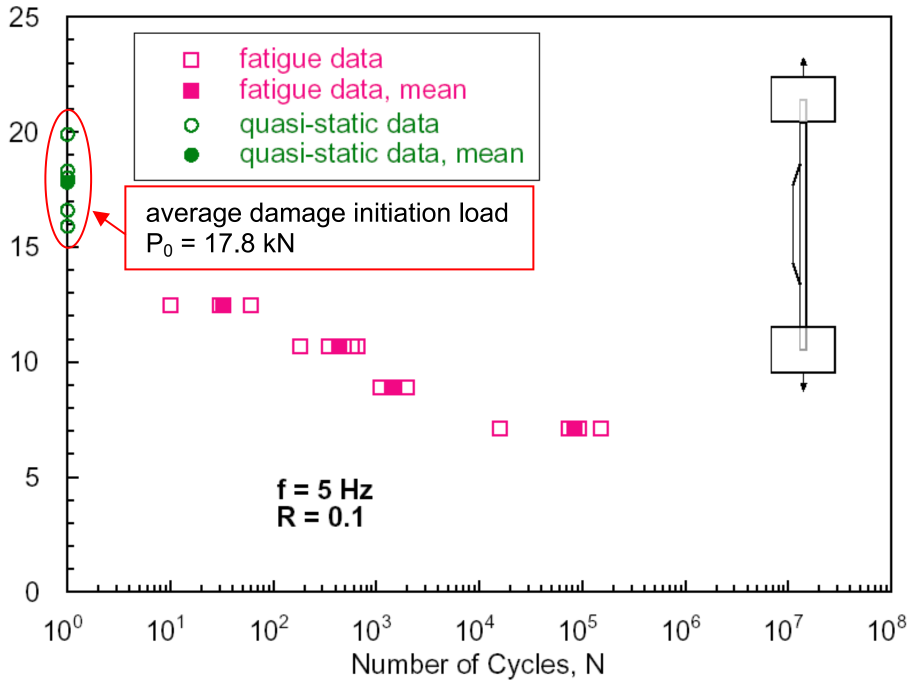

Fig. 6.10.6, Quasi-static and fatigue failure loads for the NASA tested skin/flange specimens. HyperSizer-BondJo results were compared only to the quasi-static data.

Results

A sampling of the results from HyperSizer-BondJo results for the NASA scarfed flange validation example. More comprehensive results for this problem are shown in Volume 3.

Black = Peel Stress (σ_z); Red = Interlaminar Shear (τ_{xy}); Blue = Interlaminar Shear (τ_{yz})

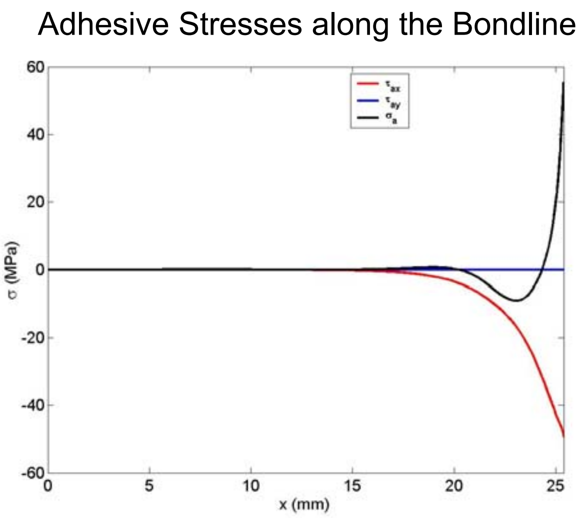
Adhesive Stresses along the Bondline

Fig. 6.10.7, Adhesive peel and interlaminar shear stresses along the bondline of the NASA skin/flange specimens.

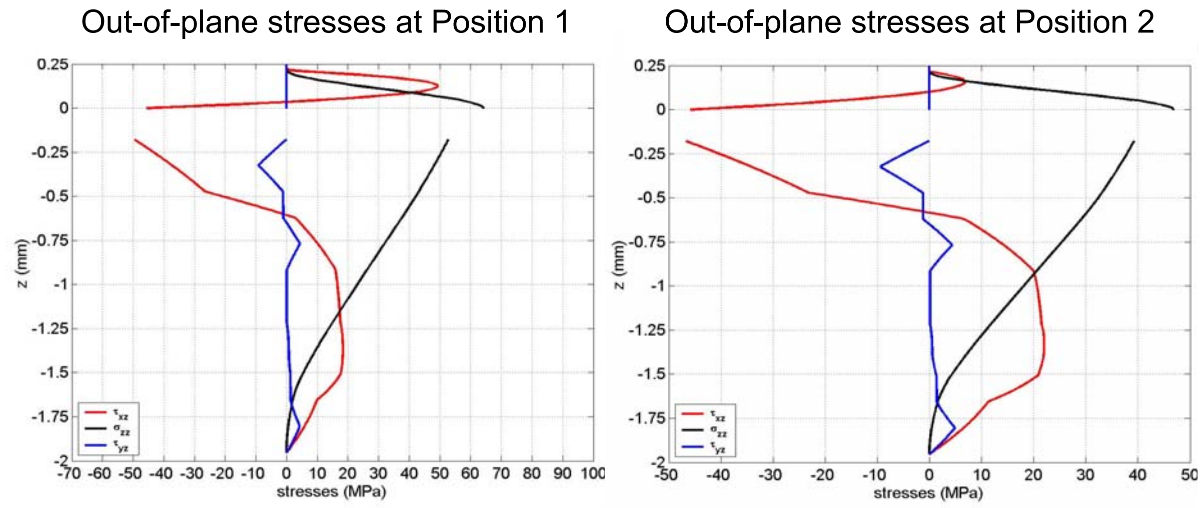
Out-of-plane stresses at Position 1

Out-of-plane stresses at Position 2

Fig. 6.10.8, Through-the-thickness distribution of interlaminar stresses at positions 1 and 2, as shown in Fig. 6.10.5

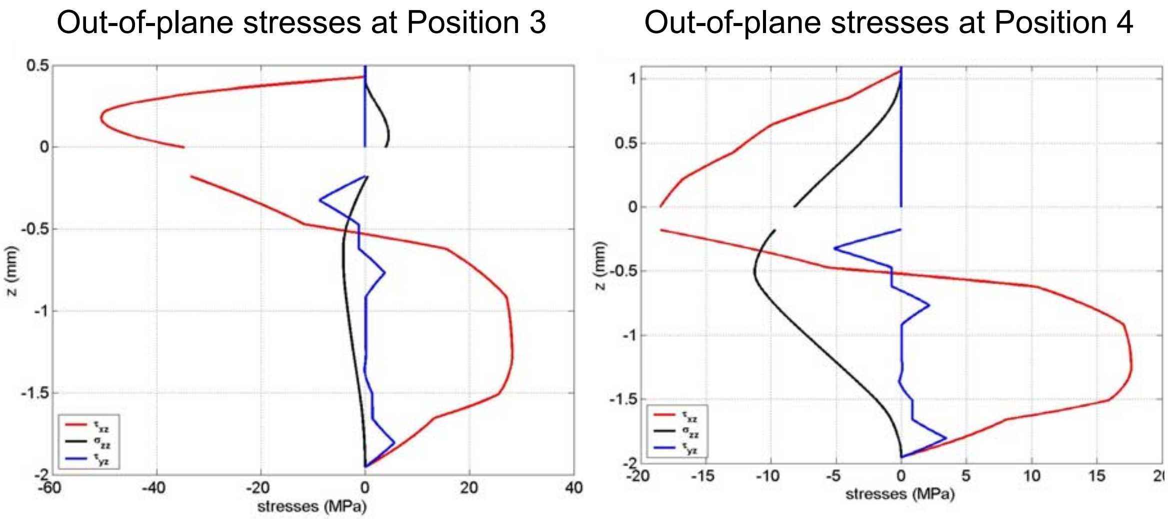

Fig. 6.10.9, Through-the-thickness distribution of interlaminar stresses at positions 3 and 4, as shown in Fig. 6.10.5

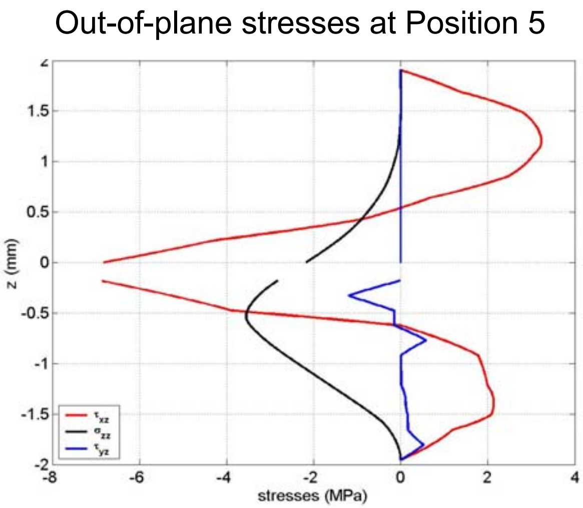

Fig. 6.10.11, Through-the-thickness distribution of interlaminar stresses at positions 5, as shown in Fig. 6.10.5

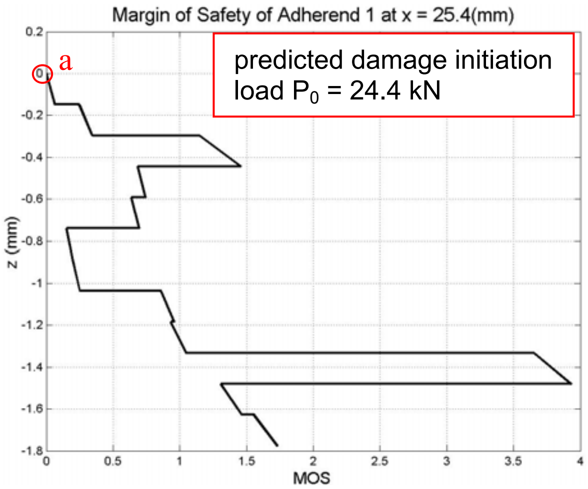

Fig. 6.10.12, Through-the-thickness distribution of the margin of safety of skin at the bondline corner(position 1), under longitudinal tension of 24.4 kN. Note this is adherend 1 only, therefore z=0 is at the bondline.

6.10.4 Single Lap Validation – Tong Example

Note: This example uses the typical academic sign convention. See Section 6.11 for details.

Tong's single-lap joint specimen [6.10.4] without pre-cracks was selected as a validation case for HyperSizer-BondJo's single-lap joint capability. The specimen is schematically illustrated in Fig. 6.10.13. The joint adherends are manufactured by laminating eight plies of T300/934 plain woven prepreg in the 0° direction. The adherends were bonded together using FM300-K film adhesive with uniform thickness of 0.16 mm. Both linear and nonlinear analyses were performed to predict the failure load of the specimen subjected to longitudinal tension, although the linear and non-linear results show very little difference. Max stress criterion is used to predict initial failure. The tested load-displacement curves of the joint specimens show very pronounced initial damage and damage evolution prior to the ultimate failure, as shown in Fig. 6.10.14. The failure location predicted by HS-BondJo matches well with experimental observation. The predicted failure load with linear analysis is 6.85 kN, which correlates well with the measured initial failure load of 7.2 kN. The predicted initial failure load using nonlinear adhesive is only slightly different, which is 6.82 kN. This is due to that the in-plane tensile stress is less affected by yield of adhesive layer than the out-of-plane stresses. Please refer to the Volume 3 for detailed description of validation of Tong's problem for single-lap joints.

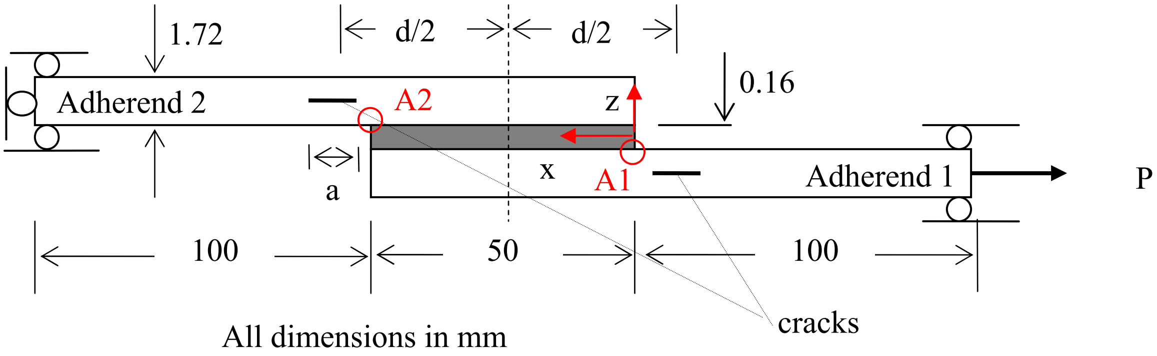

Fig. 6.10.13, Single lap joint configuration in Tong's problem.

Table 6.10.3, Comparison of HyperSizer-BondJo predicted to average test failure load

	Average Damage Initiation Load for 20 Specimens	HS-BondJo Linear Adhesive	HS-BondJo Non-Linear Adhesive
Failure Load	7.2 kN	6.85 kN	6.82 kN

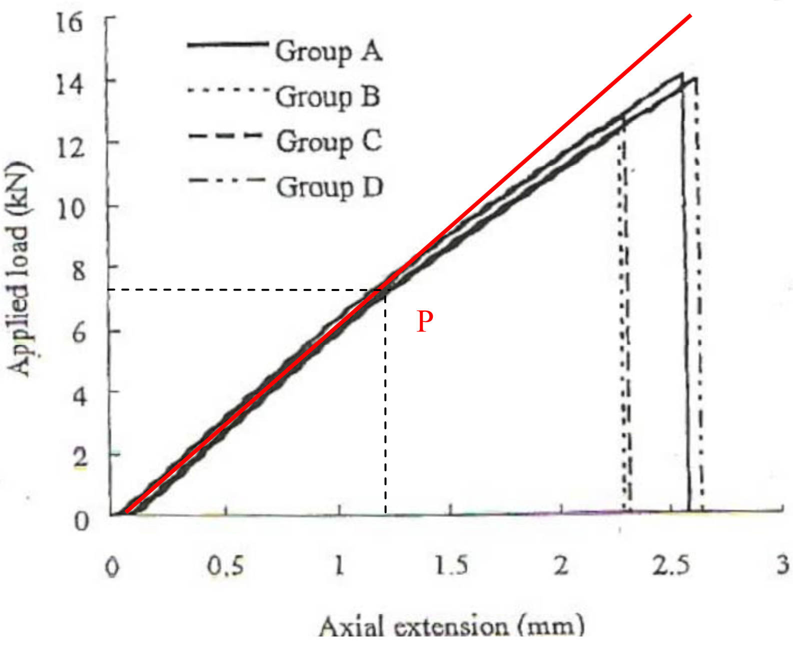

Fig. 6.10.14, All of the load-displacement curves from the experimental results deviate from linear at the almost the same point 'P', where initial failure occurs. Thus, the initial failure load can be estimated as F_{ini} = 7.2 kN. As the load continues to increase, the damage (delamination) evolves to their respective ultimate failure loads.

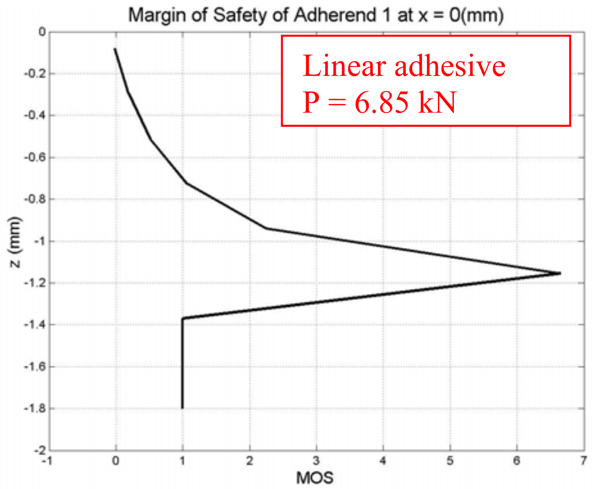

Fig. 6.10.15, Through-the-thickness margin of safety of adherend 1 at point 'A1' with linear adhesive (P =6.85 kN). Note this is adherend 1 only, therefore z=0 is at the bondline.

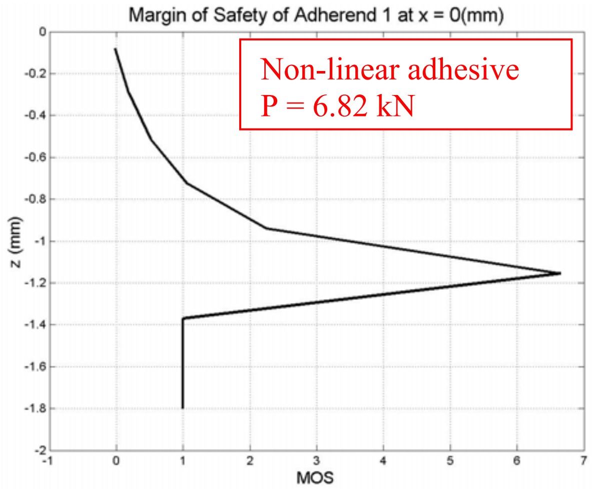

Fig. 6.10.16, Through-the-thickness margin of safety of adherend 1 at point 'A1' with nonlinear adhesive (P =6.82 kN). Note this is adherend 1 only, therefore z=0 is at the bondline.

6.10.5 References

6.10.1 Cheuk, P. T. and Tong L., (2002), "Failure of adhesive bonded composite lap shear joints with embedded precrack," *Composites Science and Technology*, 62, 1079-1095.

6.10.2 Krueger, R., Paris, I. L., O'Brien T. K., and Minguet, P. J., 2001, "Fatigue life methodology for bonded composite skin/stringer configurations," NASA/TM-2001-210842, ARL-TR-2432

6.10.3 Davila, C., Personal Correspondence, March, 2004.

6.10.4 Tong, L., (1998), "Failure of adhesive-Bonded Composite Single Lap Joints with Embedded Cracks," AIAA journal, Vol.36, No.3, pp.448.

6.10.5 Yarrington, P., Zhang, J., Collier, C., and Bednarcyk, B., "Failure Analysis of Adhesively Bonded Composite Joints" AIAA SDM Conference, April 2005.

6.11 Sign Conventions and Reference Planes

6.11.1 Sign Convention

Equations, loads, geometry specifications and results in this document are reported in either of two sign conventions, depending on whether the discussion involves a full aircraft panel application or a standalone test article. These two coordinate systems are referred to as the "HyperSizer Panel" sign convention or the "Typical Academic" sign convention.

The first of these, the HyperSizer Panel sign convention, is shown in Fig. 6.11.1. This sign convention follows that of a typical skin-stringer type of airframe construction. The x-direction of the panel is parallel to the direction of the panel stiffeners and for composite laminates, this is also the 0° ply direction. The positive z-direction in this case is in the opposite direction of the stiffener. All loads, results and geometry specifications in the HyperSizer software are always reported using this sign convention.

The second sign convention, called the "Typical Academic" sign convention is shown in Fig. 6.11.2. This is the coordinate system that is most likely to be encountered in the literature for either test specimens or new analytical techniques for bonded joints. In this case, the x direction is perpendicular to the stiffener and the positive z-direction is in the same direction as the stiffener. All of the theoretical development as well as the verification and validation examples in this document are reported using the typical academic sign convention.

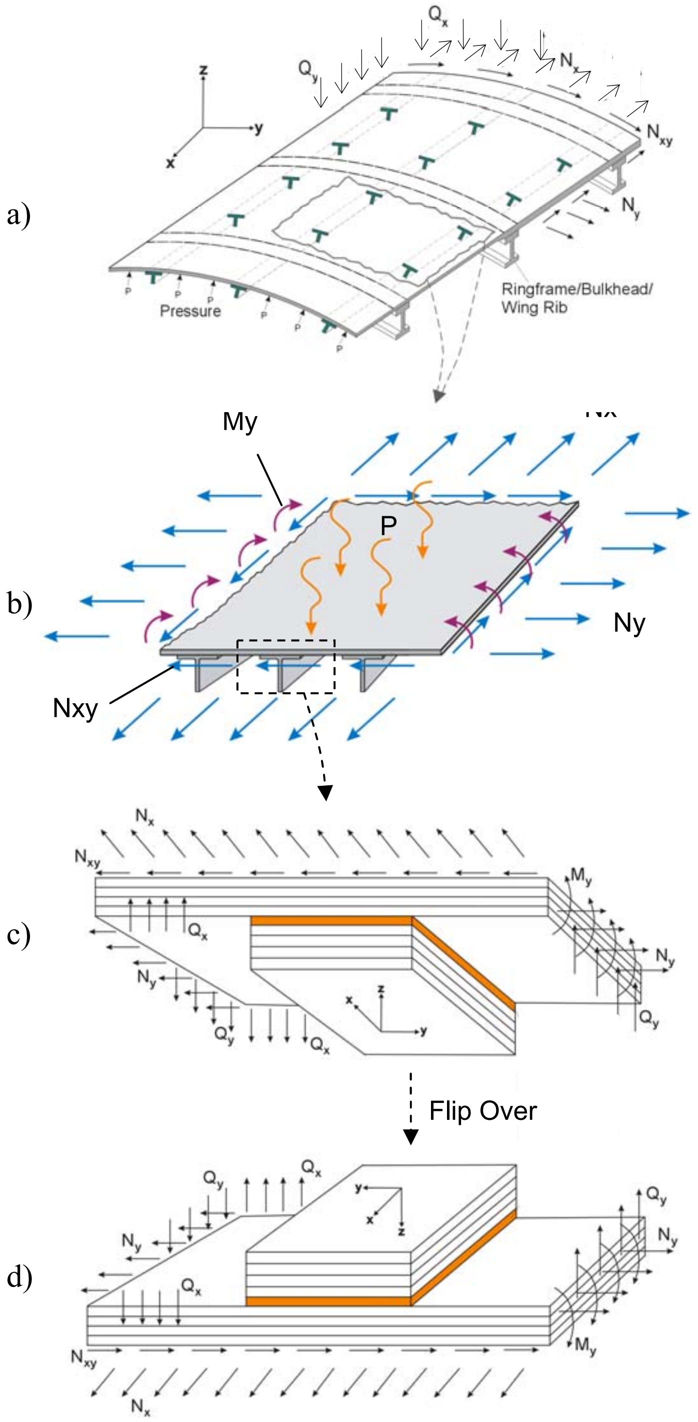

Fig. 6.11.1, The "HyperSizer panel" sign convention follows that of a typical aircraft skin-stringer type structure where the x-direction lines up with the stiffeners or the 0° direction of composite laminates. HyperSizer loads and results are reported in this coordinate system.

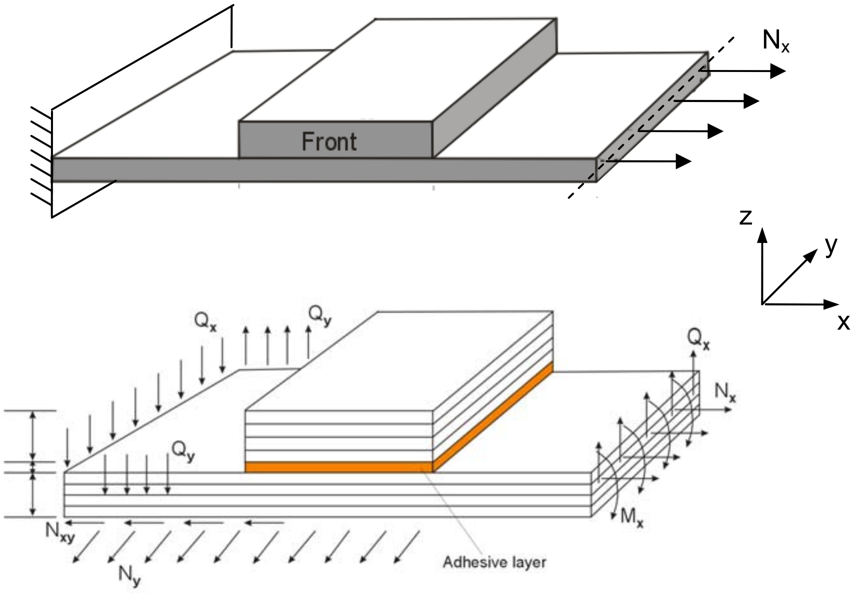
N_x
Front
z
y
x
Q_x
Q_y
Q_x
N_x
t_2
t_a
t_1
Q_y
M_x
N_{xy}
N_y
Adhesive layer

Fig. 6.11.2, The "typical academic" sign convention follows that of a standalone test article. In general, this is the sign convention that appears in technical articles that describe test data or analysis methods specific to joint analysis. Most of the HyperSizer-BondJo verification and validation results are reported using this sign convention.

6.11.2 Reference Planes

6.11.2.1 Reference Planes for Reporting of Results

In all of the result plots shown for the bonded joint examples, it is important to understand not only the sign conventions but also the reference at which these results are plotted. In the HyperSizer panel coordinate system, the reference plane is always the midplane of the panel facesheet as shown in Fig. 6.11.3. This is true for the force, displacement, moment and curvature plots as well as for results such as the panel effective ABD matrices and neutral axis offsets.

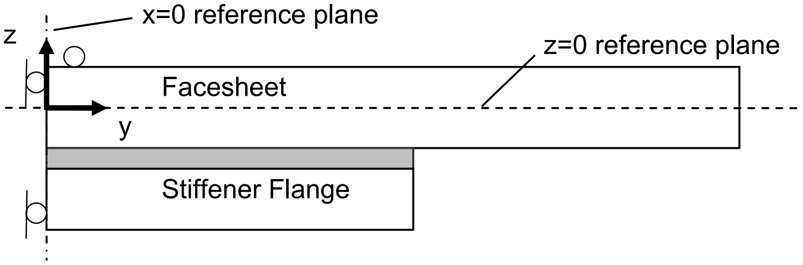

Fig. 6.11.3, Reference plane for reporting of results in the HyperSizer panel coordinate system. HyperSizer reports all results such as forces, moments, displacements, curvatures, etc. as well as ABD matrices and neutral axis offsets at the midplane of the upper facesheet. The x coordinate originates at the center of the joint.

The reference plane for results in the typical, academic coordinate system is shown in Figs. 6.11.4 and 6.11.5. In each of these cases, the z=0 reference plane is located at the midplane of the adhesive layer. In the case of a bonded doubler, the x=0 reference plane is located at the centerline of the overlap region such that the joint is symmetric about the z axis. In the case of a single lap joint, as shown in Fig. 6.11.5, the x=0 reference plane is located at one end of the overlap region.

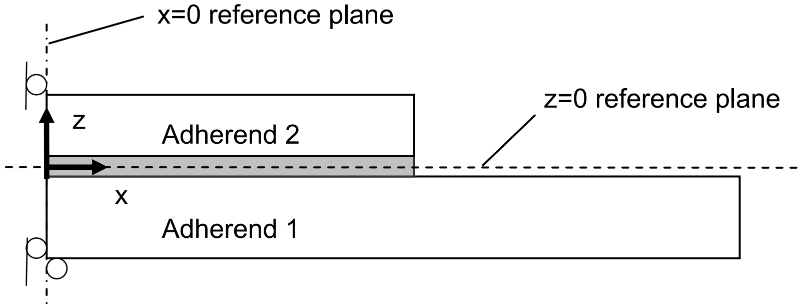

Fig. 6.11.4, Reference plane for reporting results in the typical academic sign convention. Plots of stresses and strains under this sign convention always assume that the z=0 reference plane is at the center of the adhesive layer such that adherend 2 is positive z and adherend 1 is negative z. The x coordinate originates at the center of the joint.

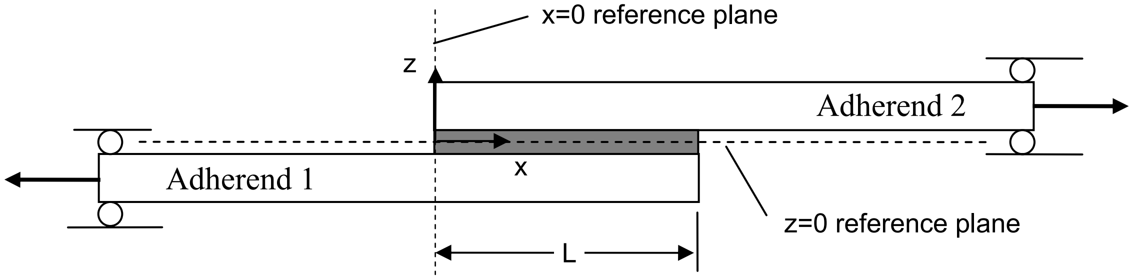

Fig. 6.11.4, Reference plane for reporting results in the typical academic sign convention for single lap joints. Plots of stresses and strains under this sign convention always assume that the z=0 reference plane is at the center of the adhesive layer. The x coordinate originates at the beginning of the overlap region.

6.11.2.2 Reference Planes for Introduction of Loads

The reference plane for introduction of loads in each coordinate system is not necessarily the same as that for reporting of results. In the HyperSizer coordinate system, shown in Fig. 6.11.4, the two reference planes are one and the same. That is, loads are always introduced at the midplane of the stiffener facesheet.

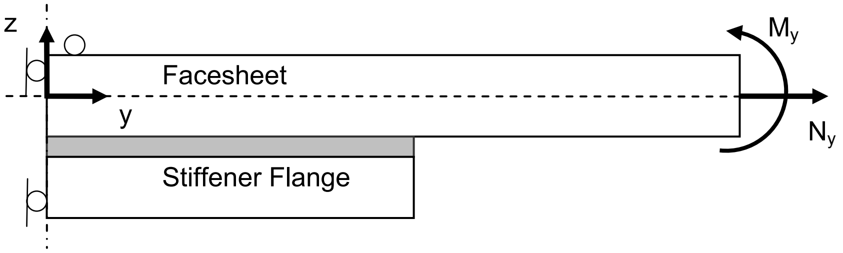

Fig. 6.11.4, In the HyperSizer panel coordinate system, loads are always introduced at the same reference location as the reporting of results, that is the midplane of the stiffened panel facesheet.

In the typical academic coordinate system, the formulation of BondJo allows for introduction of loads in either adherend, as shown in Fig. 6.11.5. These loads are applied at the neutral axis of that adherend. Note that if the laminate is unsymmetric, this reference location will not be the same as the laminate midplane. In all bonded doubler verification and validation example cases presented here, loads are applied only for adherend 1 and the loads for adherend 2 are set to zero (this is the realistic case of a loaded bonded doubler joint).

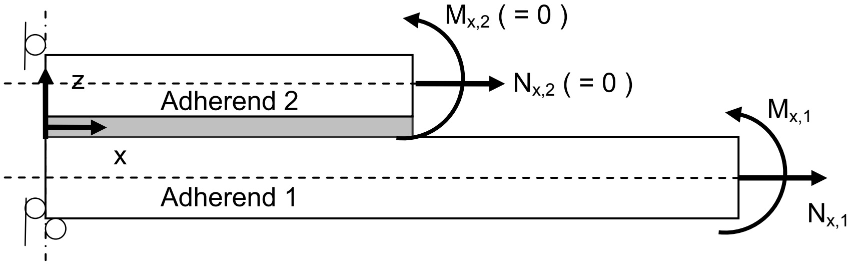
$M_{x,2}$ (= 0)
$N_{x,2}$ (= 0)
z
Adherend 2
$M_{x,1}$
x
Adherend 1
$N_{x,1}$

Fig. 6.11.5, In the BondJo formulation, each adherend of the joint is treated as a separate piece for introduction of loads and they are introduced at the adherend neutral axis. In all cases presented here, the loads at the free edge of adherend 2 ($M_{x,2}$ and $N_{x,2}$) are set to zero and loads are only applied to adherend 1.

7 Composite Material Stress Analysis and Failure

This chapter covers certification issues with composite material laminate strength. The primary purpose of this chapter is to document failure theories and how to design composite laminates for required level of conservatism.

Contents

Design criteria are first discussed then an extensive review of the most current strength failure theories is provided, following with detailed description of the following three new theories implemented in HyperSizer:

- Hashin fiber and matrix failure criteria (section 7.5.3 and 7.8)
- LaRC03 fiber and matrix failure criteria. This is an actively developed criteria from NASA Langley's Carlos Davila (section 7.5.6 and 7.7)
- Strain Invariant Failure Theory (SIFT) on the micromechanics level using the Generalized Method of Cells (GMC), not FEA. This is an actively developed criteria from Boeing's Jon Gosse. (section 7.5.7 and 7.9)

The strength of composite laminates has been an area of active research for several decades. There are many failure criteria that range from the simplistic such as max strain and max stress to more complicated ones such as Puck and the newer emerging LaRC03 [7.1, Davila] and the Strain Invariant Failure Theory (SIFT) proposed by Gosse [7.2 and 7.3, Gosse] that includes some aspects of micromechanics that investigates failure at the ply and matrix constituent level. For all of these criteria, including others such as Tsai-Hill, Tsai-Wu, Tsai-Hahn, and Hashin we have included in the composite material strength correlation examples in Vol 3. The World Wide Failure Exercises (WWFE), [7.4, 7.5 and 7.6 WWFE], reports the failure criteria that best matches their test data is Puck. The Puck failure theory was researched and is described in Section 7.5.5. However, we decided to not implement it in HyperSizer because it is deemed un-robust and impractical to use by industry due to the need for specialized material data. LaRC03, also a physically based approach appears to perform comparable to Puck, without the need for identifying complex fitting parameters which Puck requires [7.7, 7.24, Puck]. Data types identified by MIL-HDBK-17 are all that is needed for LaRC03.

Though HyperSizer implements sophisticated theories such as the promising LaRC03 and the micromechanics based Boeing Strain Invariant Failure Theory (SIFT), as developers of a commercial tool, we are attempting to strike a proper balance between these physically based approaches and simpler ones that effectively capture behavior on the macroscopic level. The best new research along with traditional methods is investigated to find the right balance of theory and practicality. With this in mind, based on the World Wide Failure Exercises (WWFE) published data and other published data, the **Tsai-Hahn failure criteria best matched our larger set of test data and required the least amount of CF fitting**, i.e. is tentatively deemed most accurate. Note that the Tsai-Hahn failure criterion is not included in the WWFE reports. The complete listing of our determined correlation factors for each failure criteria is reported in Volume 3, Chapter 1.

Summarized in Volume 3 are important findings from the correlation to 130 test data points, including those from the World Wide Failure Exercises (WWFE). Statistically relevant amounts of correlation data are provided in Volume 3, chapters 3 & 4. Chapter 3 contains failure envelopes generated by HyperSizer for failure theories: Max Strain, Max Stress, Tsai-Hill, Tsai-Wu, Tsai-Hahn, Hoffman, Hashin Matrix Cracking, Hashin Fiber Failure, LaRC03 Matrix Cracking, and LaRC03 Fiber Failure. Overlaid on the HyperSizer predicted failure envelopes are test data from WWFE and other published data. Next to the HyperSizer failure envelopes are the published failure envelopes produced by the invited research contributors of the WWFE. This layout provides a convenient visualization comparison. Chapter 4 provides the CFs and histograms for each failure theory to all of the 130 test data points. Issues related to Material & Processing (M&P) and in-situ strengths are addressed in Volume 2, Chapter 4.

7.1 Background

Practicality, an appropriate engineering cost of applying a theory successfully, is the key to acceptance of any failure theory. Acceptable costs vary with the criticality of a part and the volume of the end product. Costs of applying failure criteria are:

- programming tool automation
- verification and validation of the delivered method/tool
- deployment and training cost of the tool.

These costs are substantial, especially for more advanced theories that are physically based (as defined later in this chapter) and challenging to correctly implement and verify. HyperSizer, as a result of this SBIR, provides one means of reducing the implementation cost of deploying many different failure criteria by

- automating their use in a verified tool
- validating all of them with significant test data
- providing a way for the end user to correlate to in-house tests the effects of their specific material processing (M&P)
- reducing Information Systems (IS) deployment effort and reducing the amount of engineering end-user training time.

7.1.1 The Physics of Composite Failure

Failure of composites occurs physically at the fiber/matrix constituent level. The fiber, matrix, or the interface that bonds the fiber to the matrix fails. Polymer matrix composites (PMC), are typically brittle even with ductile matrix materials because the material system as a whole is limited by fiber strain.

Pure tension fiber failure is straightforward to characterize. Compression fiber failure is likely not limited by the strength of the fiber, but rather by the fiber/matrix interaction during fiber buckling or during kink banding. As such, fiber waviness and misalignment during processing (M&P) is an important effect and gives rise to the notion of “apparent compression strength.” Less stiff fibers such as fiberglass may actually fail in pure compression strength. Observed nonlinear in-plane shear behavior may be due to fiber rotation instead of matrix material nonlinearity.

Some of the included test data from the World Wide Failure Exercises (WWFE) include both graphite and glass fibers. The failure envelope for a glass fiber composite, shown in Fig. 7.1.1, depicts six unique physical failures identified by the LaRC03 theory, two of which are for fiber compression.

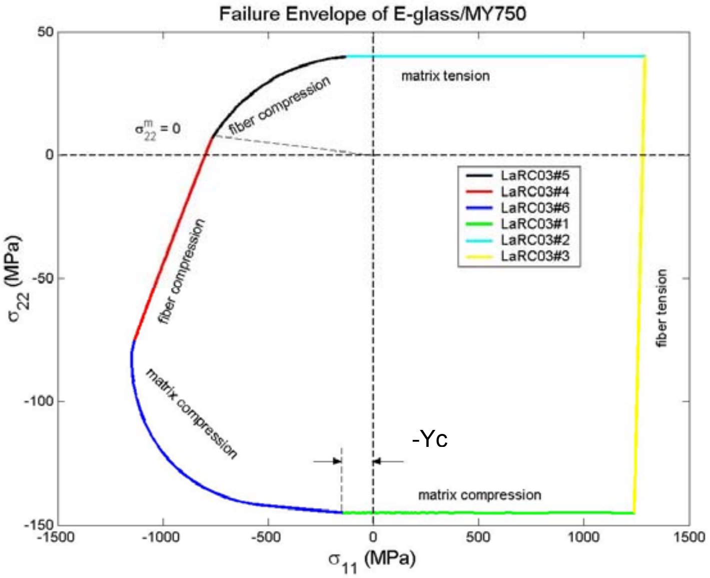

Fig. 7.1.1, LaRC03 failure criteria distinguishes between six different possible physical failures, and so, unlike interaction criteria such as Tsai-Wu or Tsai-Hahn, is deemed more promising in the long term, especially for progressive failure.

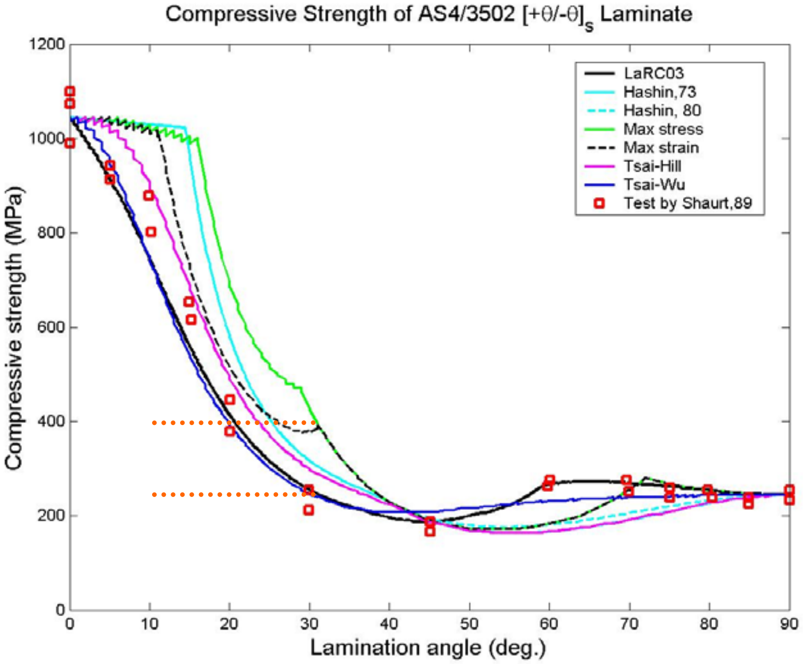

Fig. 7.1.2, Compressive strength of [+/-θ]s AS4/3502 predicted by different failure theories. For the 0, 90, and 45 angles, the criteria pass through the test data since these angles are test data given anchor points. At different angles the predictions vary. As an example of error, the orange horizontal lines indicate the large difference in test and prediction at 30° for max strain. In this plot LaRC03 matches best. Tsai-Hahn is not included.

7.1.2 V&V of Failure Criteria

All failure criteria must be backed up with statistically relevant test data before use on a production vehicle. Proper verification and validation for failure criteria must be given to the industrial end user before its use. To address this need, we have collected 130 test data points and have correlated this data to almost all of the currently used failure criteria. Failure theories can be classified as either being physically based (ie. able to distinguish between type of failure: matrix vs. fiber) and those that do not distinguish but can still handle general loadings via interaction terms. It will be shown that although current research and future improvement is likely with the physically based criteria, such as NASA Langley's LaRC03; to date, without specific M&P correlation, the Tsia-Hahn interaction criteria, from our data, is most reliable and accurate. Fig. 7.1.2 compares tests to failure theory predictions for a specific M&P.

The composite strengths included in this report are for pristine laminates, meaning without damage. For an airframe design, damage tolerance and survivability allowables would be determined and used as additional limiting strength requirements. Furthermore, the strength allowables presented here are based on damage initiation and not ultimate laminate strength which can be predicted using progressive failure techniques. The presented CFs are based on 130 tests of either unidirectional ply or [+/-θ] laminates which do not possess post damage initiation strength. In essence, the effects of off axis loading on a unidirectional tape material of single ply, or [+/-θ] laminate are correlated. Note, that the anchor points for nearly all failure criteria are the 0°, 90°, and 45° (i.e. pure shear) ply orientations. So at these angles the material allowable strengths are “a given” and all failure criteria pass through these points, such as shown in Fig. 7.1.2.

7.1.3 Uncertainty at the Ply Level

Even if a failure theory is physically based and able to discern the actual constituent failure, the practical focus is to identify the form and process dependent properties on the macroscopic (ply) level, which by definition includes many of the built-in uncertainties and variability that exist in a laminate [7.8]. This is particularly true when moisture and temperature play a significant role in the stress/strain when failure occurs. Presented in Chapter 4.7 is a method for including specific M&P effects into all failure criteria correlations, including physically based theories that may not natively capture such macroscopic uncertainties.

Vol 3, Ch 3 illustrates significant variation in observed test data. Even the most straightforward strength properties are difficult to measure accurately due to panel processing, specimen machining, test techniques, and intra vs. inter lab variability. Combined stress states are nearly impossible to characterize in a repeatable manner for general use with any failure criteria [7.8]. Clearly, the need is to view composite strength not in a deterministic fashion, but rather in a probabilistic manner that is founded on establishing these variabilities to derive the required confidence in design.

The traditional manner to include variability in composite materials is to statistically characterize each individual property on the ply level as being either an “A” or “B” Basis design-to value. This design criteria approach is discussed next.

7.2 *Design Criteria*

7.2.1 Typical material properties vs. Design-to allowables

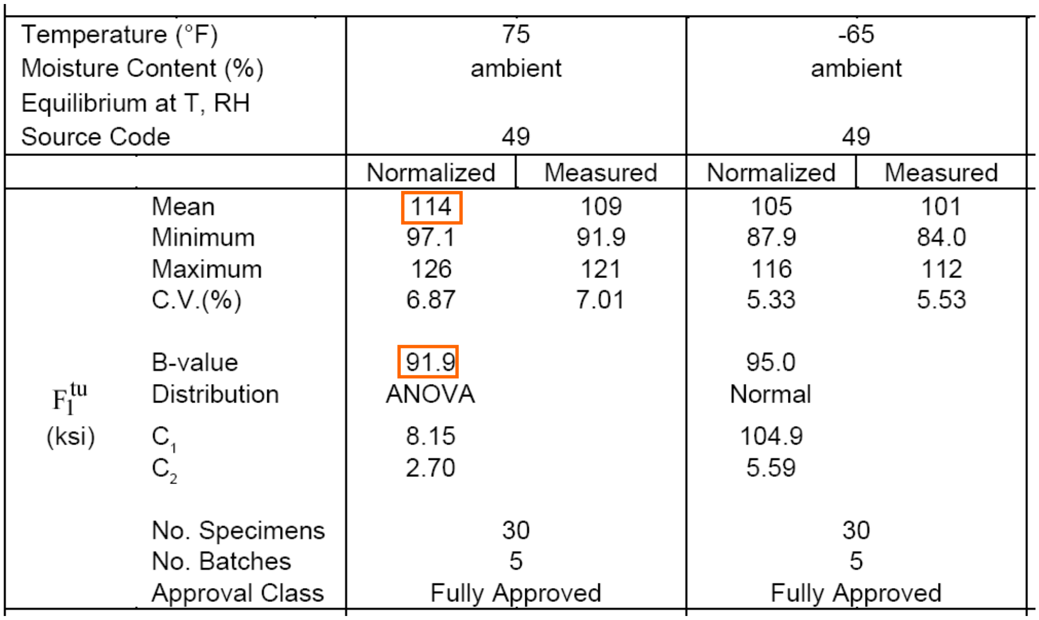

Temperature (°F)		75		-65	
Moisture Content (%)		ambient		ambient	
Equilibrium at T, RH					
Source Code		49		49	
		Normalized	Measured	Normalized	Measured
	Mean	114	109	105	101
	Minimum	97.1	91.9	87.9	84.0
	Maximum	126	121	116	112
	C.V.(%)	6.87	7.01	5.33	5.53
	B-value	91.9		95.0	
F_1^{tu}	Distribution	ANOVA		Normal	
(ksi)	C_1	8.15		104.9	
	C_2	2.70		5.59	
	No. Specimens	30		30	
	No. Batches	5		5	
	Approval Class	Fully Approved		Fully Approved	

Fig. 7.2.1, An example table from Mil Hnbk 17 showing typical (mean) and design-to (B-value) material properties. For, F_1^{tu}, the typical value is 114 ksi, and the B-basis is 91.9 ksi, a 20% reduction in allowable stress.

There are two distinct types of material properties. Typical which are derived from average experimental measurements, and design-to allowables, which are conservative values that represent a statistical confidence. When performing test predictions, typical properties are used. When designing or analyzing margin-of-safeties, design-to allowables are used, either "A" or "B" basis. [7.9, 7.10]

"A" basis – At least 99% of the population of values is expected to equal or exceed the A basis mechanical property allowable, with a confidence of 95%.

"B" basis – At least 90% of the population of values is expected to equal or exceed the B basis mechanical property allowable, with a confidence of 95%.

7.2.2 Design-to allowables

There are many real world structural integrity and design issues that must be considered when establishing design-to allowables. In this report, pristine laminates (un-notched) are addressed. Other important in-service conditions reduce pristine allowables to lower strain/stress values noted as ***Notched*** values [7.8, Rousseau's book]. These additional in-service allowables are for:

- Damage Tolerance
- Durability
- Survivability

7.2.3 Ply vs. laminate allowables

Some companies in industry define final design strength allowables for composites on the laminate level. Others in industry define final deign-to allowables on the ply level. Primarily all of the data and methods presented in this report are based on ply level approach. It is likely that either approach, which at first glance may seem vastly different, in essence provide nearly equivalent resulting load allowables.

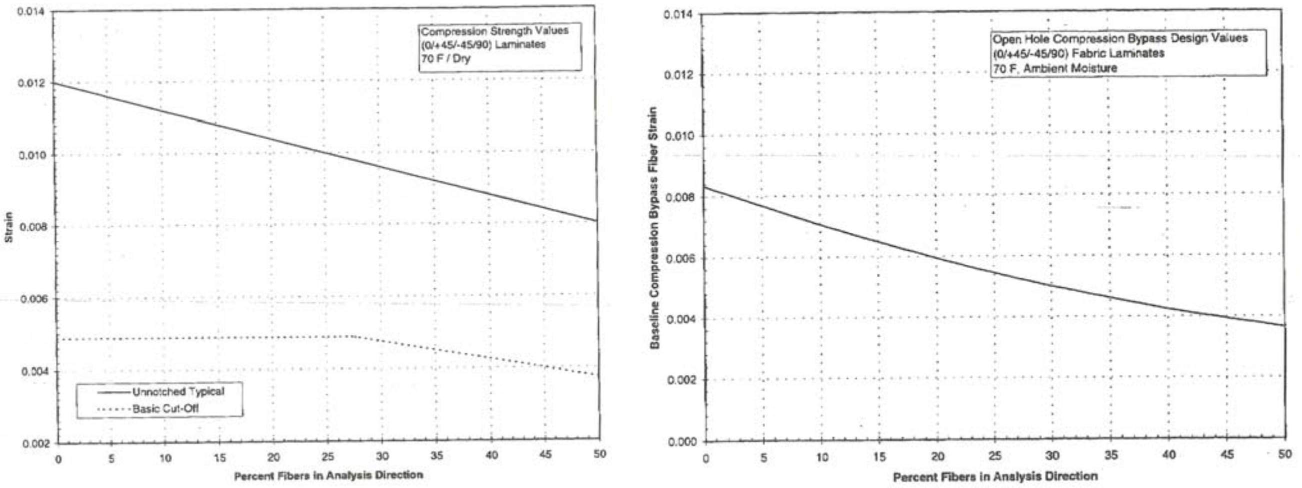

Fig. 7.2.2, An example "carpet pot" laminate based strain allowable for a (0/±45/90) layup graphed as a function of % fibers in the analysis direction. Note in the left figure that the design-to strain is ≈½ the typical un-notched measured allowable strain.

A benefit of laminate testing is the ability to capture in-situ macromechanic effects. However, in-situ effects can also be captured and quantified on the ply level as described in section Ch 4.7 and accurately used to quantify laminate strength. As a side note, this approach to identifying laminate design to values is similar to the NASA SP-8007 buckling curve, in that the curve includes both data scatter and a defined reliability with no data insight as to how to adjust an allowable for different reliabilities.

7.2.4 1st ply damage initiation vs. progressive failure

Composite laminated material may continue to carry additional loading after a ply fails. Post damage initiation strength can be analyzed and is often referred to as progressive failure. Traditional aerospace design margins-of-safety for laminate strength are based on first ply failure. This may change in the future with the availability of reliable progressive failure methods. When performing test article ultimate failure prediction, progressive failure analyses, in conjunction with typical material properties, are needed.

Progressive damage can be modeled iteratively with any failure criteria to; identify a damage initiation, increment a load increase until another failing event, and continue until eventual final collapse. A benefit may be that physically based failure criteria, due to distinguishing between fiber/matrix constituent failures, may prove to be better suited than interaction type failure criteria such as Tsai series.

Progressive failure may also be modeled on the ply (macro) and fiber/matrix constituent (micro) levels.

7.2.4.1 Macro ply level progressive failure

If on the ply level, because LaRC03, Hashin, and Puck are all phenomenological based in that they identify failure as being in the matrix or fiber, this may lend them well to progressive failure techniques. An interaction type failure like Tsai-Wu or Tsai-Hahn may not be appropriate for progressive failure. For this reason, LaRC03 may prove to be the better failure criteria for a typical laminate that will undergo progressive failure to achieve ultimate loading.

7.2.4.2 Micro fiber/matrix level progressive failure

Fig. 7.2.3 shows computed failure envelopes for the WWFE AS4/3501-6 (Case 7) based on the micromechanics approach. Shown in the legend, is a HyperSizer micromechanics module called MAC/GMC, which stands for Micromechanics Analysis Code based on the General Methods of

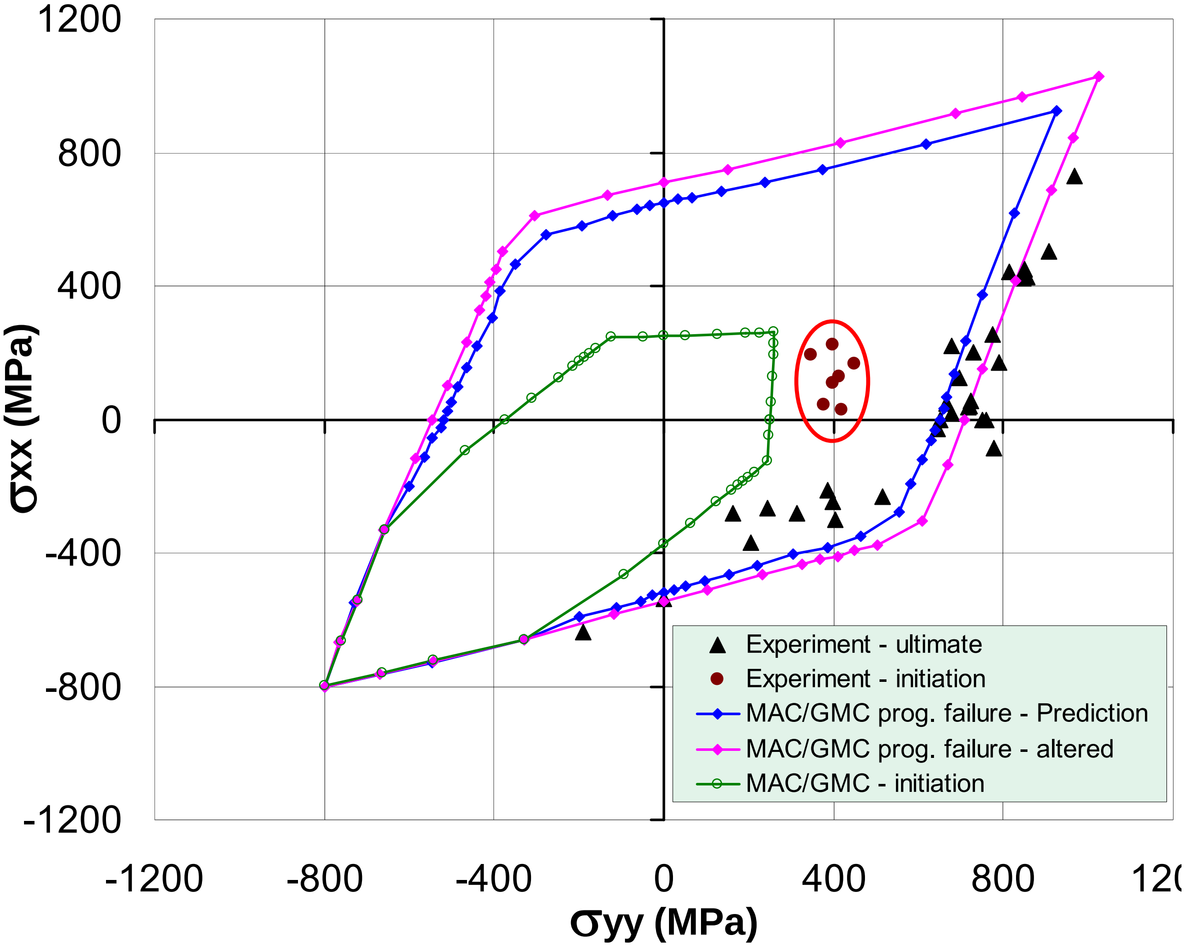

Fig. 7.2.3, Failure envelope of progressive failure modeled on the fiber/matrix constituent (micro) level. Failure data from the WWFE AS4/3501-6 [0/±45/90]s (Case 7). MAC/GMC is a HyperSizer micromechanics module.

Cells method. Since this is a [0/±45/90]s laminate, unlike a unidirectional or a ±θ layup, it will exhibit additional load carrying capability after first ply, damage initiation.

In Fig. 7.2.3, the red circle dots are damage initiation failures, and the black triangles are the ultimate, progressive failures. Large differences in load magnitudes exist between damage initiation and final failure, hence the value in benefiting from progressive failure. Two different attempts at predicting progressive failure at the micromechanics level are shown. The first in blue was performed by fully removing a micromechanics subcell when its stress level goes beyond its material allowable. Because this first implementation of micro progressive failure was performed without shear coupling, then when one cell was removed, in effect all of the subcells in that row were zeroed out as well. It is believed that a shear lag effect would cause a portion of the load to be redistributed back into the row, and until the HFGMC (higher theory of the general method of cells) is implemented in a progressive failure manner, the expedient solution was deemed to only remove 50% of the subcells stiffness. In this manner, a much better comparison to test ultimate failure was achieved as shown in magenta. The micromechanics analysis module nd progressive failure will be released in future production releases of HyperSizer.

7.3 Characteristic Dimension

One principal shortcoming in state-of-the-art composite material strength prediction is not the ability to predict in-service stresses, but rather predicting failure once the stresses are computed. There are many publications available on methods to accomplish stress computation in the vicinity of concentrated load gradients – but there are only a few publications that address failure prediction. A key difficulty in predicting failure is selecting how far from the bearing surface for a bolted hole, or how far away from the reentrant corner for a bonded joint, to "pull" the stresses. This location is known as the ***characteristic distance*** [7.11, 7.12] and is a function of many variables but is usually quantified as a constant value within a small range depending on the specific material system. The characteristic distance for a bonded joint (See mil-hdbk-17-3e, pp 5-24 to 5-25, in particular, see Fig. 5.3.2.2(b)) is usually about ½ ply thickness to the reentrant corner, and for a bolt loaded hole, about 3 ply thicknesses from the bearing surface (noted in red color).

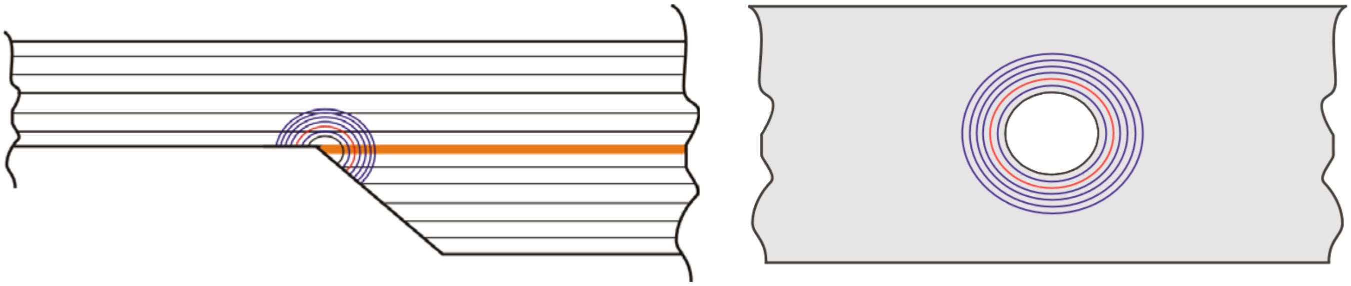

Fig. 7.3.1, Illustration of different radial distances used as appropriate characteristic distances for: left, bonded joint reentrant corner; and right, bolted hole bearing surface.

More advanced research defines the characteristic distance for a loaded hole, not as a constant, but as a characteristic equation which is a function of layup, and biaxial with shear loading interaction effects [7.13]. Though fundamentally any failure criteria is applicable once the stress/strain field prediction is made of a given geometric detail, the choice of failure criteria is inherently related to the characteristic distance defined during the test validation and correlation process. That is, a proper characteristic distance/equation is specific to a specific failure criteria.

For bonded joints, over 16 different failure criteria that include 3D stresses of interlaminar shear and peel are summarized and validated to tests in Volume 3.

7.4 Failure analyses for preliminary and final design

Design criteria for composite material strength are different based on the criticality of a structural part, and on the stage of design. Where as in preliminary design, design criteria are geared more to expedience, and for final design, more aligned to higher accuracy and test validation. The reader is referred to [7.8, Rousseau], for more insight.

7.5 Review of Best Failure Theories To Date

7.5.1 Max Strain, Max Stress, Tsai-Hill, Tsai-Wu, and Tsai-Hahn failure theories

7.5.1.1 Maximum Stress Criterion

The maximum stress criterion indicates failure when any stress component exceeds its uniaxial strength, with no interaction of the components. That is, failure occurs when,

$$\sigma_{11} \geq X_t, \qquad \sigma_{22} \geq Y_t, \qquad |\sigma_{12}| \geq S, \qquad \sigma_{11} \leq X_c, \qquad \sigma_{22} \leq Y_c, \tag{7.5.1.1}$$

where, X_t, Y_t, X_c, Y_c, and S, are the ply tensile strength in the fiber direction, the ply tensile strength in the transverse direction, the ply compressive strength in the fiber direction, the ply compressive strength in the transverse direction, and the ply in-plane (1-2) shear strength, respectively. Note that the compressive strengths (X_c and Y_c) take on negative values.

For a given ply (or point in a ply) the margin of safety based on the maximum stress criterion is

$$\mathrm{MOS}_{\max\,\sigma_{11}} = \begin{cases} \dfrac{X_t}{\sigma_{11}} - 1 & \sigma_{11} > 0 \\ \dfrac{X_c}{\sigma_{11}} - 1 & \sigma_{11} < 0 \end{cases} \tag{7.5.1.2}$$

$$\mathrm{MOS}_{\max\,\sigma_{22}} = \begin{cases} \dfrac{Y_t}{\sigma_{22}} - 1 & \sigma_{22} > 0 \\ \dfrac{Y_c}{\sigma_{22}} - 1 & \sigma_{22} < 0 \end{cases} \tag{7.5.1.3}$$

$$\mathrm{MOS}_{\max\,\sigma_{12}} = \frac{S}{|\sigma_{12}|} - 1 \tag{7.5.1.4}$$

and the margin of safety for the ply or (or point in the ply) based on the maximum stress criterion is the minimum of the three margins of safety given above.

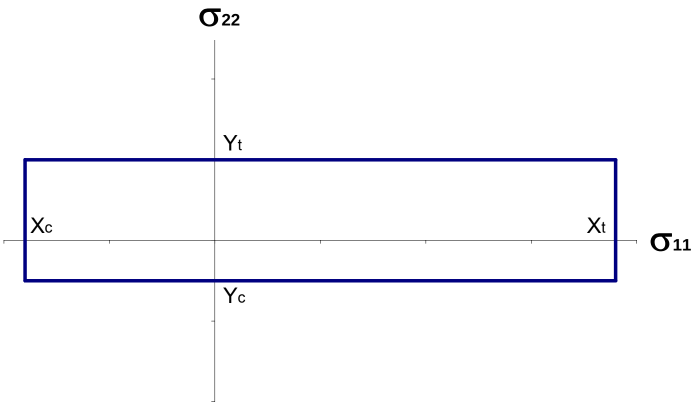

Fig. 7.5.1, Maximum Stress Failure Envelope

A major advantage of the maximum stress criterion is its simplicity. It is also based solely on uniaxial ply level test data, so it is easy to characterize for a given ply. A major disadvantage of the maximum stress criterion involves its lack of interaction among the stress components. For example, it predicts failure of a ply (or point in a ply) at the same stress in the fiber direction (X_t) regardless of whether a sizeable transverse stress (σ_{22}) and shear stress (σ_{12}) are also present. Obviously, this is incorrect as it is well documented that in many cases strong stress component interactions affect failure of many types of materials. As such, the maximum stress criterion is often inaccurate, particularly under highly multiaxial stress fields. In addition, the corners present in the failure envelope (Fig. 7.5.1) are not typically observed experimentally.

7.5.1.2 Maximum Strain Criterion

The maximum strain criterion is identical in form to the maximum stress criterion, but employs the strain components rather than stress components. That is, failure is predicted when,

$$\varepsilon_{11} \ge X_{\varepsilon t}, \quad \varepsilon_{22} \ge Y_{\varepsilon t}, \quad |\gamma_{12}| \ge S_{\varepsilon}, \quad \varepsilon_{11} \le X_{\varepsilon c}, \quad \varepsilon_{22} \le Y_{\varepsilon c}, \tag{7.5.1.5}$$

where, $X_{\varepsilon t}$, $Y_{\varepsilon t}$, $X_{\varepsilon c}$, $Y_{\varepsilon c}$, and S_{ε} are the ply tensile failure strain in the fiber direction, the ply tensile failure strain in the transverse direction, the ply compressive failure strain in the fiber direction, the ply compressive failure strain in the transverse direction, and the ply in-plane (1-2) engineering shear strength, respectively. Note that the compressive failure strains ($X_{\varepsilon c}$ and $Y_{\varepsilon c}$) take on negative values. A normal strain failure envelope (in strain space) appears identical to the rectangle shown in Fig. 7.5.1. If an orthotropic linearly elastic constitutive relationship is assumed,

$$\varepsilon_{11} = \frac{1}{E_{11}}\left(\sigma_{11} - \nu_{12}\sigma_{22}\right), \quad \varepsilon_{22} = \frac{1}{E_{22}}\left(\sigma_{22} - \nu_{21}\sigma_{11}\right), \quad \gamma_{12} = \frac{\sigma_{12}}{G_{12}} \tag{7.5.1.6}$$

and

$$X_{\varepsilon t} = \frac{X_t}{E_{11}}, \quad Y_{\varepsilon t} = \frac{Y_t}{E_{22}}, \quad S_{\varepsilon} = \frac{S}{G_{12}}, \quad X_{\varepsilon c} = \frac{X_c}{E_{11}}, \quad Y_{\varepsilon c} = \frac{Y_c}{E_{22}}, \tag{7.5.1.7}$$

the maximum strain criterion can be expressed in terms of stresses as,

$$\sigma_{11} - \nu_{12}\,\sigma_{22} \ge X_t, \quad \sigma_{22} - \nu_{21}\sigma_{11} \ge Y_t, \quad |\sigma_{12}| \ge S, \quad \sigma_{11} - \nu_{12}\,\sigma_{22} \le X_c, \quad \sigma_{22} - \nu_{21}\sigma_{11} \le Y_c, \tag{7.5.1.8}$$

which results in a quadrilateral failure envelope in normal stress space, as shown in Fig. 7.5.2. The margins of safety associated with the maximum strain criterion are given by,

$$\mathrm{MOS}_{\max\,\varepsilon_{11}} = \begin{cases} \dfrac{X_{\varepsilon t}}{\varepsilon_{11}} - 1 & \varepsilon_{11} > 0 \\ \dfrac{X_{\varepsilon c}}{\varepsilon_{11}} - 1 & \varepsilon_{11} < 0 \end{cases} \tag{7.5.1.9}$$

$$\mathrm{MOS}_{\max\,\varepsilon_{22}} = \begin{cases} \dfrac{Y_{\varepsilon t}}{\varepsilon_{22}} - 1 & \varepsilon_{22} > 0 \\ \dfrac{Y_{\varepsilon c}}{\varepsilon_{22}} - 1 & \varepsilon_{22} < 0 \end{cases} \tag{7.5.1.10}$$

$$\mathrm{MOS}_{\max \gamma_{12}} = \frac{S_\varepsilon}{|\gamma_{12}|} - 1 \tag{7.5.1.11}$$

and the margin of safety for the ply (or point in the ply) based on the maximum strain criterion is the minimum of the three margins of safety given above. Assuming an orthotropic linearly elastic constitutive relationship, these margins of safety can be expressed in terms of stress components by substitution using Eq. (7.5.1.6) and Eq. (7.5.1.7).

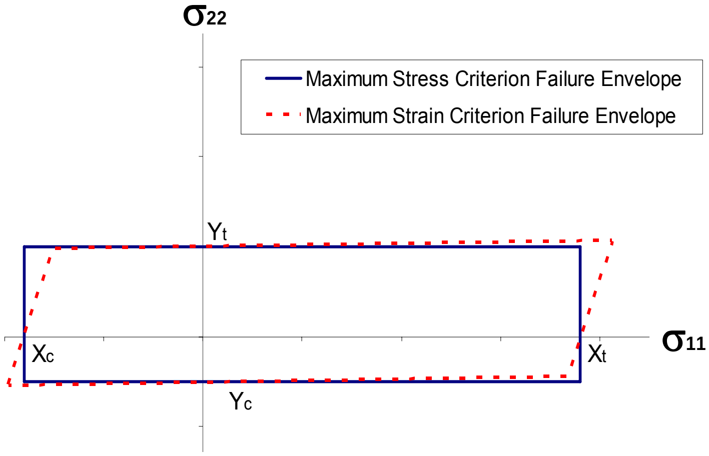

Fig. 7.5.2, Comparison, max stress to max strain

The advantages and disadvantages of the maximum strain criterion are generally similar to those of the maximum stress criterion. Which of these two criteria is more accurate and more conservative is dependent on the composite material under consideration. Care should be used when employing the maximum strain criterion with a highly ductile, nonlinear composite material (e.g., some metal matrix composites in the direction transverse to the fibers). In such an instance, where the stress-strain response becomes nearly flat (i.e., perfectly plastic) prior to failure, while the failure stress may be well known and quite repeatable, the failure strain may vary by 50% or more between tests. The failure strain is then a poor measure of failure due to its large variability. Obviously, in such a case, the elastic relations embodied by Eqs. (7.5.1.6) and (7.5.1.7) are not applicable, nor is Eq. (7.5.1.8).

7.5.1.3 Tsai-Hill Criterion

The Tsai-Hill criterion is based on an anisotropic extension of the von Mises yield criterion proposed by Hill [7.8] and applied to ply level failure by Tsai [7.14]. Unlike the maximum stress and maximum strain criteria, it involves a single relationship that includes all plane stress components acting on the ply, so the components are able to interact. Under plane stress conditions, for a unidirectional ply, the Tsai-Hill criterion predicts failure when,

$$\frac{\sigma_{11}^2}{X^2} - \frac{\sigma_{11}\sigma_{22}}{X^2} + \frac{\sigma_{22}^2}{Y^2} + \frac{\sigma_{12}^2}{S^2} \geq 1 \tag{7.5.1.12}$$

where, X, Y, and S, are, respectively, the ply strength in the fiber direction, the ply strength in the transverse direction, and the ply in-plane (1-2) shear strength. Under uniaxial loading conditions (i.e., only one of σ_{11}, σ_{22}, or σ_{12} applied) the Tsai-Hill criterion simplifies to the maximum stress criterion. However, in the presence of a multi-axial stress field, all three in-plane stress components affect the failure of the ply. The normal stress failure envelope represented by the Tsai-Hill criterion is shown in Fig. 7.5.3. Like a von Mises yield surface, the Tsai-Hill failure envelope is elliptical, however, the effects of anisotropy are obvious. Note that, in the presence of a superimposed in-plane shear stress ($\sigma_{12} > S$), the Tsai-Hill normal failure envelope shrinks.

The basic form of the Tsai-Hill criterion given in Eq. (7.5.1.12) does not distinguish between tension and compression. However, by employing X_t or X_c and Y_t or Y_c based on the signs of σ_{11} and σ_{22} , it is possible to include the effects of tension vs. compression in the Tsai-Hill criterion. This basically amounts to utilizing a different elliptical failure criterion in each of the four coordinates of the normal component stress space. Such a Tsai-Hill failure envelope is depicted in Fig. 7.5.4. Of course, this presupposes that the signs of the in-plane normal stress components are known a priori.

The Tsai-Hill criterion margin of safety of a ply (or a point in a ply) is given by,

$$\mathrm{MOS}_{\text{Tsai-Hill}} = \frac{1}{\sqrt{\dfrac{\sigma_{11}^2}{X^2} - \dfrac{\sigma_{11}\,\sigma_{22}}{X^2} + \dfrac{\sigma_{22}^2}{Y^2} + \dfrac{\sigma_{12}^2}{S^2}}} - 1 \qquad (7.5.1.13)$$

For details on the derivation of the margin of safety for various failure criteria, see Chapter 15 of Volume 3. The negative term appearing in the square root in the denominator of Eq. (7.5.1.13) implies that it is possible for the Tsai-Hill criterion to provide an infinite or undefined (i.e., a complex number) margin of safety. However, under normal circumstances where the transverse strength, Y, is less than the fiber direction strength, X, it is not possible for the term within the square root to become negative, therefore the margin of safety is well-behaved.

A significant advantage of the Tsai-Hill criterion, compared to the simpler maximum stress and strain criteria, is its improved accuracy [7.14]. The interaction of the stress components allows the Tsai-Hill criterion to correlate significantly better with experimental composite ply level failure data. In addition, the fact that the failure envelope is smooth is more realistic, and the fact that it entails one equation rather than three (in the case of identical tensile and compressive normal strengths) is also advantageous. These advantages come while the Tsai-Hill criterion is no more difficult to characterize than the maximum stress criterion (only the uniaxial composite strengths are required). A disadvantage is that it is more difficult to include distinct tensile and compressive normal strengths within the Tsai-Hill theory compared to the maximum stress and strain criteria. However, as discussed above, it can be done.

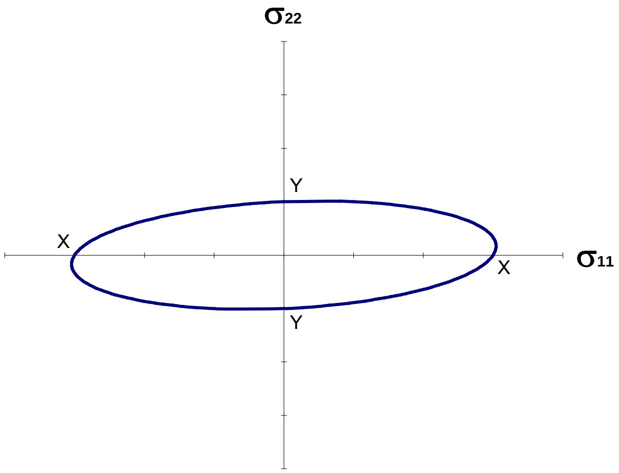

Fig. 7.5.3, Tsai Hill

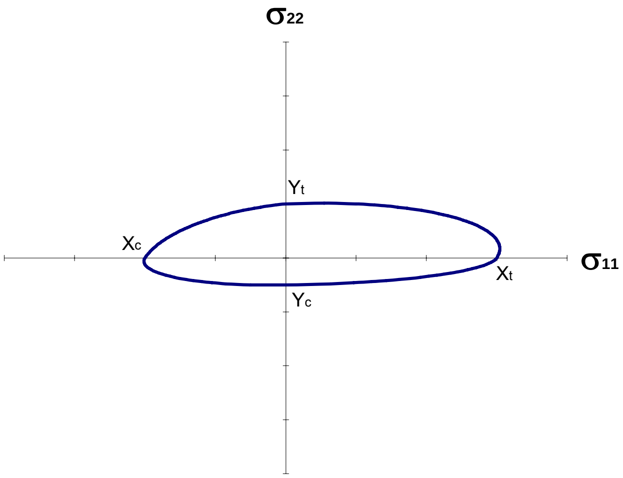

Fig. 7.5.4, Tsai-Hill with different compression/tension allowables

7.5.1.4 Tsai-Wu Criterion

The Tsai-Wu [7.15] criterion, like the Tsai-Hill criterion, is based on a single relationship. However, the Tsai-Wu criterion inherently includes distinct normal tensile and compressive strengths, clearly an advantage over the ad-hoc methodology required to include this feature within the Tsai-Hill criterion. Under plane stress conditions, for a unidirectional ply, and accounting for the fact that the shear strength (*S*) is independent of the sign of the shear stress (σ_{12}) the Tsai-Wu criterion predicts failure when,

$$\left(\frac{1}{X_t}+\frac{1}{X_c}\right)\sigma_{11}+\left(\frac{1}{Y_t}+\frac{1}{Y_c}\right)\sigma_{22}-\frac{\sigma_{11}^2}{X_tX_c}-\frac{\sigma_{22}^2}{Y_tY_c}+\frac{\sigma_{12}^2}{S^2}+2F_{12}\,\sigma_{11}\,\sigma_{22}\geq 1 \qquad (7.5.1.14)$$

where a new interaction term involving σ_{11} and σ_{22} and an accompanying interaction coefficient, F_{12}, are present. Thus, in addition to the five uniaxial ply level composite strengths (*X_t*, *Y_t*, *X_c*, *Y_c*, and *S*) present in the maximum stress (and Tsai-Hill) criterion, the Tsai-Wu criterion has introduced an additional coefficient that must be determined (or possibly discarded). Unfortunately, the F_{12} coefficient cannot be determined via a uniaxial ply level test, rather, a biaxial test is required. For example, if an in plane biaxial test is performed on a ply such that $\sigma_{11}=\sigma_{22}$ until failure at a stress level of $\sigma_{11}=\sigma_{22}=\sigma$, then the F_{12} coefficient is related to the biaxial strength, σ, by,

$$F_{12}=\frac{1}{2\sigma^2}\left[1-\left(\frac{1}{X_t}+\frac{1}{X_c}+\frac{1}{Y_t}+\frac{1}{Y_c}\right)\sigma+\left(\frac{1}{X_tX_c}+\frac{1}{Y_tY_c}\right)\sigma^2\right] \qquad (7.5.1.15)$$

Because of the difficulty of experimentally determining the F_{12} coefficient coupled with the fact that it typically has only a minor effect on the criterion's predictions, it is often simply set to zero. Alternatively, F_{12} may be selected to allow better correlation of the Tsai-Wu theory with available experimental failure data.

The normal stress failure envelope represented by the Tsai-Wu criterion is shown in Fig. 7.5.5, where the F_{12} coefficient has been set to zero. Like the Tsai-Hill failure envelope, the Tsai-Wu failure envelope is elliptical, and the effects of anisotropy are obvious. Also, in the presence of a superimposed in-plane shear stress ($\sigma_{12} > S$), the Tsai-Wu normal failure envelope shrinks.

The margin of safety of a ply (or a point in a ply), excluding the interaction term involving σ_{11} and σ_{22}, is given by,

$$\mathrm{MOS}_{\text{Tsai-Wu}} = \frac{2}{\left(\frac{1}{X_t}+\frac{1}{X_c}\right)\sigma_{11}+\left(\frac{1}{Y_t}+\frac{1}{Y_c}\right)\sigma_{22}+\sqrt{\left[\left(\frac{1}{X_t}+\frac{1}{X_c}\right)\sigma_{11}+\left(\frac{1}{Y_t}+\frac{1}{Y_c}\right)\sigma_{22}\right]^2+4\left[-\frac{\sigma_{11}^2}{X_t X_c}-\frac{\sigma_{22}^2}{Y_t Y_c}+\frac{\sigma_{12}^2}{S^2}\right]}}-1 \tag{7.5.1.16}$$

For details on the derivation of the margin of safety for various failure criteria (and how the additional interaction term may be included), see Chapter 15 of Volume 3. Note that the term within the square root of the denominator in Eq. (7.5.1.16) will always be positive as the normal tensile strengths (X_t and Y_t) are always positive and the normal compressive strengths (X_c and Y_c) are always negative. Further, while the terms in the denominator outside the square root may be negative, they will always sum to a smaller magnitude than the evaluated square root in the denominator. As such, the Tsai-Wu margin of safety will always be finite and real.

In addition to the advantage of included distinct tensile and compressive normal strengths, the Tsai-Wu criterion has the advantage over the Tsai-Hill criterion of being more mathematically consistent [7.16]. While it is somewhat more complex than the Tsai-Hill criterion, the Tsai-Wu criterion is generally considered to be more accurate than the Tsai-Hill criterion. In many cases, however, the failure predictions of these two theories are quite similar.

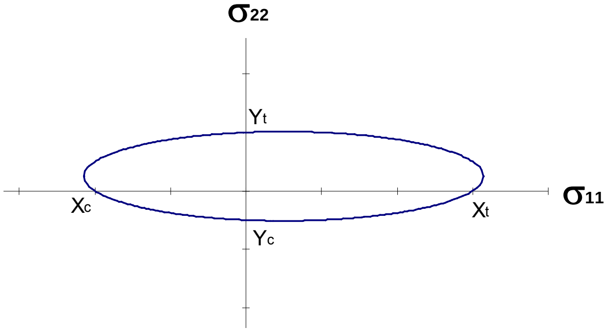

Fig. 7.5.5, Tsai Wu Failure Envelope.

7.5.1.5 Tsai-Hahn Criterion

A modification to the Tsai-Wu theory was proposed by Tsai and Hahn [7.17], which amounts to estimating the F_{12} coefficient as,

$$F_{12} \approx -\frac{1}{2\sqrt{X_t X_c Y_t Y_c}} \tag{7.5.1.17}$$

The Tsai-Wu criterion in which the F_{12} coefficient is calculated based on Eq. (7.5.1.17) is sometimes referred to as the Tsai-Hahn criterion.

7.5.1.6 Summary of Tsai Theories

Tsai interaction theories consider the anisotropy of composite materials but do not capture the physics of various failure mechanisms. In WWFE [7.5, 7.6], Tsai theory has described the available experimental results better than other theories for unidirectional laminae. However, it has been noted that the theory predicts enhancement of strength under a compression-compression biaxial loading case. The predicted shapes by Tsai theory of the final failure envelopes for the multi-directional laminates agreed quite well with available experimental results. As expected, the predicted initial failure envelopes for the multi-directional laminates that continue into progressive failure, are in poor agreement with test data and the revised theory by the WWFE contributors that introduce a post-initial failure model significantly improved the results. In addition, Tsai theory is linear elastic and can not predict the large non-linear strains observed in the test cases where high lamina shear was involved. Overall, Tsai theory proved to be in the leading group of those tested in WWFE, with Tsai-Hahn the best overall.

7.5.2 Zinoviev failure theory

Zinoviev used a development of the maximum stress failure theory, which embodies a very simple, but carefully structured, set of non-interactive criteria to identify failure mechanisms and to take appropriate post-initial failure action. There is less of an attempt (compared to Puck, for example) to provide physically based failure models.

The theory gave reasonably good descriptions of the unidirectional lamina failure envelopes though, as expected for a non-interactive failure theory, it overestimated the measured lamina strengths at certain loading combinations. The theory was one of the best at predicting initial failure events for multi-directional laminates, though none of the theories were particularly robust in this area.

The theory gave a reasonably good fit to the experimental final failure envelopes for all of the multi-directional laminates, by giving careful attention to effective lamina property degradation and unloading after initial failure, and by allowing for fiber orientation during loading.
Although the theory assumed linear-elastic material properties, it also gave reasonably good descriptions of nearly all of the stress/strain curves. The Zinoviev theory was not considered for integration into the HyperSizer software and the details of the method can be found in [7.18].

7.5.3 Hashin failure theory (2D and 3D)

Hashin did not participate in WWFE, but he has been recognized as a pioneer for distinguishing failure modes in composite failure criteria. Based on his observation of failure of fibrous composite laminates with different orientations, he originally proposed a set of failure criteria [7.19] in 1973, which are known as the Hashin-Rotem criteria. Two different failure modes were identified for unidirectional lamina: fiber failure and matrix failure. The 1973 version of Hashin criteria assumed a quadratic interaction between the tractions on the failure plane. In 1980, Hashin [7.20] revised the criteria by introducing the contribution of in-plane shear stress to the criterion for fiber tensile failure mode and adding a linear term in the criterion for compressive matrix failure mode. The 1980 version of the Hashin failure criteria has been referred to as the 2D version of Hashin's failure criteria, which is given by:

Tensile fiber mode ($\sigma_{11} > 0$)

$$\left(\frac{\sigma_{11}}{X_T}\right)^2 + \left(\frac{\sigma_{12}}{S}\right)^2 = 1 \tag{7.5.3.1}$$

Compressive fiber mode ($\sigma_{11} < 0$)

$$|\sigma_{11}| = X_C \tag{7.5.3.3}$$

Tensile matrix mode ($\sigma_{22} > 0$)

$$\left(\frac{\sigma_{22}}{Y_T}\right)^2 + \left(\frac{\sigma_{12}}{S}\right)^2 = 1 \tag{7.5.3.4}$$

Compressive matrix mode ($\sigma_{22} < 0$)

$$\left(\frac{\sigma_{22}}{2S_T}\right)^2 + \left[\left(\frac{Y_C}{2S_T}\right)^2 - 1\right]\frac{\sigma_{22}}{Y_C} + \left(\frac{\sigma_{12}}{S}\right)^2 = 1 \tag{7.5.3.5}$$

where

X_T is the longitudinal tensile strength of Uni-Directional (UD) lamina
X_C is the longitudinal compressive strength of UD lamina
Y_T is the transverse tensile strength of UD lamina
Y_C is the transverse compressive strength of UD lamina
S is the in-plane shear strength of UD lamina
S_T is the out-of-plane transverse shear strength of UD lamina

With reference to the fiber failure mode, the only difference in the 1980 version is the contribution of in-plane shear stress to the failure in tension, a modification with no clear physical basis. Although the deduction procedure of the final version of the criterion is cumbersome, the modification comes from the quadratic interaction Hashin assumes between the components of the stress vector associated with the plane of failure. It is important to note that the Hashin's emphasis was to avoid any connection with energy concepts. Instead, his proposal is the simplest way to approximate an assumed interaction between different effects once a simple linear interaction is discarded. It is noticeable, in any case, that in his paper, Hashin considered the possibility of discarding the contribution of the in-plane shear to the tensile failure of the fiber. An explanation of the physical basis of the contribution of the shear to the failure of the fibers has not been found in the literature, although a specific search has not been conducted for this topic. It may be possible to clarify this question by means of a micromechanics analysis, followed by the appropriate tests.

With reference to the matrix failure mode, the approach followed by Hashin is different due to the impossibility of determining the plane of failure. He assigned the failure to a quadratic interaction between stress invariants, canceling the contribution of σ_{11} based on the assumption that any possible plane of failure is parallel to the fibers and that the components of the stress vector of any of these planes do not depend on σ_{11}.

Hashin also developed a 3D failure criteria by adding the contribution of out-of-plane stress and their allowables in a similar way. They are given as

Tensile fiber mode

$$\left(\frac{\sigma_{11}}{X_T}\right)^2 + \frac{1}{S^2}\left(\sigma_{12}^2 + \sigma_{13}^2\right) = 1 \tag{7.5.3.6}$$

Compressive fiber mode

$$\left|\sigma_{11}\right| = X_C \tag{7.5.3.7}$$

Tensile matrix mode ($\sigma_{22} + \sigma_{33} > 0$)

$$\frac{1}{Y_T^2}(\sigma_{22} + \sigma_{33})^2 + \frac{1}{S_T^2}\left(\sigma_{23}^2 - \sigma_{22}\sigma_{33}\right) + \frac{1}{S^2}(\sigma_{12}^2 + \sigma_{13}^2) = 1 \tag{7.5.3.8}$$

Compressive matrix mode ($\sigma_{22} + \sigma_{33} < 0$)

$$\frac{1}{Y_C}\left[\left(\frac{Y_C}{2S_T}\right)^2 - 1\right](\sigma_{22} + \sigma_{33}) + \frac{1}{4S_T^2}(\sigma_{22} + \sigma_{33})^2 + \frac{1}{S_T^2}\left(\sigma_{23}^2 - \sigma_{22}\sigma_{33}\right) + \frac{1}{S^2}\left(\sigma_{12}^2 + \sigma_{13}^2\right) = 1 \tag{7.5.3.9}$$

In the tensile matrix mode, discarding the linear term in the 2D case leads to an expression identical to his 1973 proposal. In the compressive matrix mode, the linear term is not discarded, and the expression is forced to satisfy the fact that if the material fails in the presence of transversely isotropic pressure ($\sigma_{22} = \sigma_{33} = -\sigma$), this pressure can reach values much larger than the compressive uniaxial failure stress Y_C. The implication of this idea, which is supported by available experimental results, on other failures is not clear. In any case, the most serious doubts about the criterion come from the interaction between stresses and allowables derived from the interaction between invariants. It is surprising to find that an out-of-plane allowable S_T appears in matrix compression mode, i.e. Eq. (7.5.3.5). Paris [7.21] performed a parametric study of the influence of the value of S_T in the predictions for different 2D cases. He showed that this inconsistency in Hashin's 1980 proposal leads to unconservative predictions of matrix compression failure with increasing values of S_T.

It is also noted that in both the 2D and 3D formulations, the failure criterion for fiber compressive mode is simply the maximum stress criteria in the longitudinal direction. However, experimental results show that the compressive strength X_C can be significantly reduced when in addition to $\sigma_{11} < 0$, a significant in-plane shear σ_{12} is superimposed. Obviously, Hashin's failure theory does not account for this effect. In addition, Hashin's failure criterion for compressive matrix mode can not explain the experimental observation that moderate transverse compression increases shear strength of a UD lamina.

7.5.4 Sun failure theory

Sun [7.22] took the same form of Hashin-Rotem failure criteria, but he replaced the ply strength with the 'in-situ' strength. Sun's modification is shown below

$$\left(\frac{\sigma_{11}}{X_{is}}\right) = 1 \tag{7.5.4.1}$$

$$\left(\frac{\sigma_{22}}{Y_{is}}\right)^2 + \left(\frac{\sigma_{12}}{S_{is}}\right)^2 = 1 \tag{7.5.4.2}$$

in which X_{is}, Y_{is} and S_{is} are the 'in-situ' longitudinal strength, transverse strength and shear strength, respectively. This criterion is generalized for either tensile or compressive stresses; the corresponding (tensile or compressive) strengths must be chosen based on the sign of the applied stresses. Failure is assumed when one of the two equations is satisfied. If Eqn. (7.5.4.1) is satisfied, then fiber breakage occurs. Eqn. (7.5.4.2) represents the condition for matrix failure. The mode of matrix failure is determined by comparing the ratios σ_{22}/Y and σ_{12}/S. Compared to Hashin criteria, introduction of the concept of 'in-situ' strength gave more flexibility in selecting the allowables so as to make the failure criteria match experiments better phenomenologically.

Sun's renovation using 'in-situ' strength of lamina has experimental basis. It was found that transverse matrix cracking initiation stress (or strain) of a lamina in a laminate is usually larger than the transverse strength of the unidirectional laminate. This so-called 'in situ transverse strength' in some cases could be as high as 2.5 times the unidirectional transverse strength [7.23]. The 'in situ' strength is dependent on the lamina thickness and the constraints from the adjacent layers. Sun believed that the same phenomenon exists for shear strength, although it has not been reported in the literature.

In WWFE [7.5, 7.6], initial failure envelopes for the multidirectional laminates predicted by Sun Linear failure theory (L) were in moderate agreement with the measured ones (ranked 8th). However, the predicted final failure envelopes for the multi-directional laminates were better (ranked 5th). The predicted stress/strain curves were rather mixed. If the response was heavily fiber dominated, the strength predictions using Sun's theory were in good agreement with experiment. However, if shearing of the laminae was a dominant feature, this linear-elastic based theory underestimated the large non-linear deformations observed in the experiments. The Sun theory performed better than the Hashin-Rotem theory in modeling the post-initial failure response. Overall the Sun (L) theory had few fundamental weaknesses and performed sufficiently well to be in the leading group of theories. The Sun failure theory was not considered for integration into the HyperSizer software.

The key of Sun's failure theory is to determine the 'in-situ' strength of lamina. But this appears not a simple task. In WWFE, Sun took the 'in situ' tensile transverse and shear strength to be 1.5 times those measured from unidirectional laminates base on his experience. Sun has also tried to give some physical explanation of 'in-situ' strength of laminate under transverse compression. The failure criterion given by Sun for matrix compression is

$$\left(\frac{\sigma_{22}}{Y_C}\right)^2 + \left(\frac{\sigma_{12}}{S-\eta\sigma_{22}}\right)^2 = 1 \qquad (7.5.4.3)$$

where η is an experimentally determined constant which can be regarded as the internal material friction parameter. The ‘in-situ’ shear strength $S-\eta\sigma_{22}$ increases with transverse compression σ_{22} (negative sign) so that it takes into account of the beneficial role of that compressive stress σ_{22}. Even though Sun’s failure theory for compressive matrix mode is a big step forward from Hashin’s, it has not given the physics basis of all the in-situ strengths used in the theory, instead the theory used many empirical relations. For instance, Eqn. (7.5.4.3) assumes that the failure plane is always parallel to the fiber direction, however, many test cases show that with increase of transverse compressive stress, the failure plane varies from 0° to 53°. Therefore, to give the insight of the failure mechanisms of matrix compressive failure requires more refined theories.

7.5.5 Puck failure theory

Evolving from extensive experimental studies, Puck’s failure theory [7.24] attempts to correlate the experimental results with micromechanical failure mechanism of composite material. Puck’s phenomenological model not only distinguishes failure modes of fiber breakage and inter fiber failure (matrix cracking), but also gives more realistic mechanics basis for the failure. In the following, we discuss Puck’s Fiber Failure (FF) Criteria and Inter Fiber Failure (IFF) Criteria.

7.5.5.1 Fiber failure (FF)

Puck assumed that fiber failure in a UD composite under a combined state of stress (σ_{11}, σ_{22}, σ_{33}, τ_{12}, τ_{13}, τ_{23}) will occur at the same fiber stress as that which is acting in the fibers at failure under a uniaxial stress σ_{11}, as shown in Figure 7.5.6. The fiber failure criterion is given as

$$\begin{aligned} \sigma_{f1} &= X_{fT} \quad for \quad \sigma_{f1} \geq 0 \\ \sigma_{f1} &= X_{fC} \quad for \quad \sigma_{f1} < 0 \end{aligned} \qquad (7.5.5.1)$$

By this it is assumed that for the fiber, the failure condition of the maximum normal stress in the fiber direction holds. It should be pointed out that X_{fT} and X_{fC} are the tensile stress or the compressive stress in the fiber which are reached under uniaxial tensile or compressive load with σ_{11} at fracture of the unidirectional composite material but not in single fibers or fiber bundles. Assuming linear elastic material behavior, these are given by

$$X_{fT} = \frac{X_T}{E_1} E_{f1} = \varepsilon_{1T} E_{f1} \text{ and } X_{fC} = \frac{X_C}{E_1} E_{f1} = \varepsilon_{1C} E_{f1} \qquad (7.5.5.2)$$

While X_{fT} can be regarded as the ‘true’ tensile strength of the fiber (embedded in the composite), X_{fC} is usually not the ‘true’ compressive strength of the fiber, because at $\sigma_{f1} < 0$, failure mostly occurs through elastic instability (so-called kinking) of the fibers embedded elastically in the matrix. However, it can be assumed that the buckling is not influenced by an additional stress σ_{22}, at most by an additional stress τ_{12}. Thus, X_{fc} can be regarded as a constant.

Thus, Puck's fiber failure criterion is actually established on the basis of the maximum true fiber stress, which needs to be calculated from micromechanics models. However, unlike traditional micromechanical analysis, Puck developed an empirical model to calculate the fiber stress. Under bi-axial loading (σ_{f1}, σ_{f2}), Puck gave the fiber longitudinal strain as

$$\varepsilon_{f1} = \frac{\sigma_{f1}}{E_{f1}} - \frac{v_{f12}}{E_{f1}} m_{\sigma f} \sigma_{22} \tag{7.5.5.3}$$

where the term $m_{\sigma f}\sigma_{22}$ is the fiber stress σ_{f2}, the factor $m_{\sigma f}$ accounts for a 'stress magnification effect' caused by the different moduli of fibers and matrix (in the transverse direction), which leads to an uneven distribution of the stress σ_{22} . From the micromechanics point of view, $m_{\sigma f}$ is equivalent to a "stress concentration factor". Puck gave the values of $m_{\sigma f}$ based on his experience. For glass fiber composites, $m_{\sigma f} \approx 1.3$; for carbon fiber composites, $m_{\sigma f} \approx 1.1$.

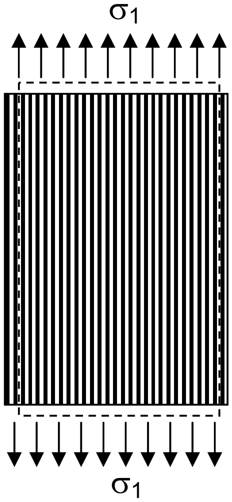

Fig. 7.5.6, lamina subjected to longitudinal stress

Assuming perfect bond between fiber and matrix, the fiber failure criterion under combined (σ_{f1}, σ_{f2}), loading is given as

$$\begin{aligned} f_E(FF) &= \frac{1}{\varepsilon_{1T}}\left(\varepsilon_1 + \frac{v_{f12}}{E_{f1}} m_{\sigma f}\sigma_2\right) = 1 \qquad \text{for}(...) \geq 0 \\ f_E(FF) &= \frac{1}{\varepsilon_{1C}}\left(\varepsilon_1 + \frac{v_{f12}}{E_{f1}} m_{\sigma f}\sigma_2\right) = -1 \qquad \text{for}(...) < 0 \end{aligned} \tag{7.5.5.4}$$

after some algebra. To account for the strength reduction by fiber kinking induced by in-plane shear load as fibers are subjected to compressive loading, Puck added an empirical shear correction in Eqn.(7.5.5.4). Then the failure criterion for fiber compression becomes

$$f_E(FF) = \frac{1}{\varepsilon_{1C}}\left|\left(\varepsilon_1 + \frac{v_{f12}}{E_{f1}} m_{\sigma f}\sigma_2\right)\right| = 1 - (10\gamma_{21})^2 \qquad \text{for } (...) < 0 \tag{7.5.5.5}$$

where $(10\gamma_{21})^2$ is a purely empirical factor. Note that γ_{21} is used in this shear correction, instead of τ_{21}. Puck explained that the value of τ_{21} is uncertain after crack initiation while the value of γ_{21} is not.

7.5.5.2 Inter-Fiber Failure (matrix cracking)

Based on extensive experimental studies on carbon-fiber/epoxy and glass-fiber/epoxy laminates subjected to transverse compression or tension, Puck found that unidirectional layers usually fracture on planes parallel to the fiber direction, with various angles as the loads change. Similar to the Mohr-Coulomb criterion for rock and soil, Puck believed the fracture in the lamina is exclusively created by the stresses which act on the fracture plane. In the case of inter-fiber fracture on an inclined plane parallel to the fibers these are a normal stress, σ_n, and two shear stresses, τ_{nt} and τ_{n1} (Fig. 7.5.7). The stress σ_n represents a transverse stressing ($\sigma_\perp$), the shear stress τ_{nt} a transverse-transverse shear stressing $\tau_{\perp\perp}$ and the shear stress τ_{n1} a transverse-longitudinal shear stressing ($\tau_{\perp\parallel}$). The term `stressing' has been introduced by Puck in order to distinguish between stress conditions of different character, e.g. $\sigma_\parallel$, $\sigma_\perp$, $\tau_{\perp\perp}$, $\tau_{\perp\parallel}$.

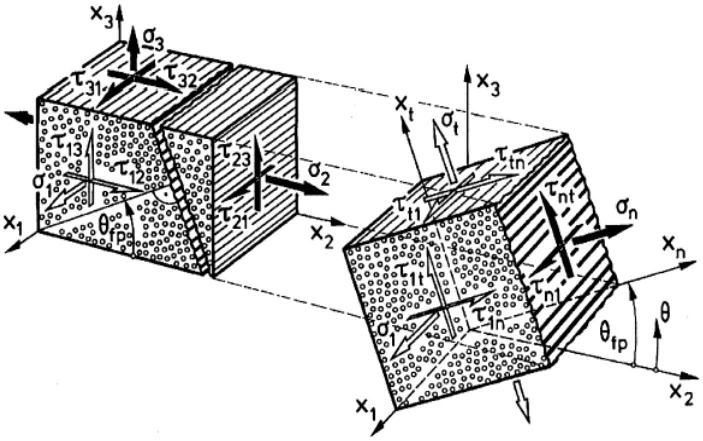

Figure 7.5.7, The concept of fracture plane in UD lamina

When $\sigma_n > 0$, i.e. transverse tensile stressing, it causes fracture together with τ_{nt} and τ_{n1}. Because of the existing symmetry, the direction of the shear stresses cannot influence fracture. The failure criterion for $\sigma_n > 0$ is given by Puck as

$$f_{E(IFF)} = \left(\frac{\sigma_n}{R_\perp^{(+)A}}\right)^2 + \left(\frac{\tau_{nt}}{R_{\perp\perp}^A}\right)^2 + \left(\frac{\tau_{nl}}{R_{\perp\parallel}^A}\right)^2 = 1 \tag{7.5.5.6}$$

where

$R_\perp^{(+)A}$ is the fracture resistance of the action plane due to transverse-tensile stressing
$R_{\perp\perp}^A$ is the fracture resistance of the action plane due to transverse-transverse stressing
$R_{\perp\parallel}^A$ is the fracture resistance of the action plane due to transverse/parallel shear stressing

The strength allowables used in the equation (7.5.5.6) are consistent with Puck's hypothesis: fracture of the plane in which the stresses act which cause fracture is exclusively created by the stresses which act in this plane. Consequently, the three stresses σ_n, τ_{nt}, τ_{n1}, which must necessarily have a common stress action plane, must be compared to the fracture resistances R^A of their action plane, and not just to some strength which might belong to any other fracture plane.

It is well-known that a tensile stress $\sigma_n > 0$ promotes fracture, while a compressive stress $\sigma_n < 0$ impedes shear fracture. For $\sigma_n < 0$, the shear stresses τ_{nt} and τ_{n1} (or just one of them) have to cause fracture against an additional fracture resistance, which increases with increasing $|\sigma_n|$ like an internal friction. Puck proposed a simple equation describing this effect, which resembles the fracture hypothesis by Mohr-Coulomb,

$$f_{E(IFF)} = \left(\frac{\tau_{nt}}{R^A_{\perp\perp} - p^{(-)}_{\perp\perp}\sigma_n} \right)^2 + \left(\frac{\tau_{nl}}{R^A_{\perp\parallel} - p^{(-)}_{\perp\parallel}\sigma_n} \right)^2 = 1 \tag{7.5.5.7}$$

where $p^{(-)}_{\perp\parallel}$ is the slope of the (σ_n, τ_{nl}) on the fracture envelope for $\sigma_n \leq 0$, at $\sigma_n = 0$; $p^{(-)}_{\perp\perp}$ is the slope of the (σ_n, τ_{nt}) on the fracture envelope for $\sigma_n \leq 0$, at $\sigma_n = 0$. The two *p* parameters are equivalent to the coefficients of friction (η) used by Sun's criterion (Eqn. 7.5.4.3).

(i) *Fracture resistances*

Eq. (7.5.5.6) and (7.5.5.7) are the failure criteria for the inter-fiber fracture (or so-called matrix cracking) under tensile and compressive normal stress on the fracture plane. Nevertheless, these two failure criteria are not convenient to use directly due to the difficulty in obtaining the strength allowables on the fracture plane and the *p* parameters. If a stress $\sigma_n > 0$ is acting alone and fracture occurs in its stress action plane, the fracture resistance $R^{(+)A}_{\perp}$ equals the tensile strength Y_T. This is the case with the UD materials of laminates examined here, which does not mean that it is so in general. However, a $\tau_{\perp\parallel}$ shear stressing always causes fracture only in its action plane; thus, we can write $R^A_{\perp\parallel} = S_{21}$. With $R^A_{\perp\perp}$, the situation is totally different for the materials to be analyzed. A shear stressing $\tau_{\perp\perp}$ which acts alone does not lead to shear fracture in its action plane, but to tensile fracture in a plane which is inclined by 45° to the action plane of the shear stress. Up to now, no experiment is known which would allow a direct measurement of the fracture resistance $R^A_{\perp\perp}$ against fracture caused by a $\tau_{\perp\parallel}$ stressing. Hence, $R^A_{\perp\perp}$ must be derived from the transverse compressive strength, Y_C, assuming a mathematically formulated master fracture surface. For the friction parameters, *p,* in Eqn (7.5.5.7), in general, $p^{(-)}_{\perp\parallel}$ is fitted to the experimentally deduced slope of the (σ_{22}, τ_{12}) fracture envelope for $\sigma_{22} \leq 0$ at the point $\sigma_{22} = 0$, and $p^{(-)}_{\perp\perp}$ can be calculated from Puck's empirical relation $p^{(-)}_{\perp\perp} = p^{(-)}_{\perp\parallel} R^A_{\perp\perp} / R^A_{\perp\parallel}$.

(ii) *Fracture planes*

Another issue needs to be solved before the failure criteria are used is determining the angle of fracture plane. In general the angle of the fracture plane parallel to the fiber is not known in advance which one of the infinite number of possible fiber parallel planes will become the fracture plane, when the load reaches the fracture load. It certainly is the one with the highest numerical value of the angle dependent failure index $f_{E(IFF)}$. That means that one has to search for $[f_{E(IFF)}(\theta)]_{max} = f_{E(IFF)}(\theta_{fp})$, where θ_{fp} is the angle for fracture plane. To identify it, one has to compare the numerical values of the computed $f_{E(IFF)}(\theta)$ for a sufficiently high number of values for θ between -90° and +90°. But for a plane state of stress (σ_{11}, σ_{22}, τ_{12}), Puck developed an analytical solution for θ_{fp}.

(iii) *Degradation models*

Puck also took into account the effect of progressive damage occurring in laminates and consequently developed degradation models for the failure criteria. One of the degradation models assumes equal degradation of all fracture resistances in the inter-fiber fracture conditions due to single fiber failure. Puck used a weakening factor f_w to account for this effect and proposed an empirical relation for f_w, which is given as

$$f_w = 1 - \left|\frac{\sigma_1}{\sigma_{1D}}\right| = 1 - (0{,}9 f_{E(FF)})^n \tag{7.5.5.8}$$

where n is the empirical degradation exponent; Puck uses n = 8 for relatively high fracture strain matrix, otherwise, uses n = 6.

In addition to the degradation model for fracture resistance, Puck also proposed a degradation model to realistically cover the progressive reduction of certain transverse stiffnesses of the unidirectional ply as a result of increasing crack density. Opening cracks are regarded as if they were 'smeared', and their global effect on the secant moduli E_{2s} and G_{12s} as well as the major Poisson's ratio v_{12} are described by diminishing all three quantities with a reduction factor η, which is determined experimentally.

(iv) *List of IFF failure criteria in 2D and 3D stress states*

To facilitate the failure criteria, Puck simplified Eqns. (7.5.5.6) and (7.5.5.7) and also took into account for all of the issues mentioned above with sophisticated mathematical treatment and many empirical relations. Table 7.5.1 summarizes the simplified failure criteria together with relations for the parameters for the inter-fiber failure under the plane stress state (σ_{11}, σ_{22}, τ_{21}) and three-dimensional stress state (σ_{11}, σ_{22}, σ_{33}, τ_{12}, τ_{13}, τ_{23}), respectively.

Table 7.5.1, Summary of Puck IFF criteria for plane stress case

IFF failure modes and criteria	Parameters
IFF on (σ_{22},τ_{12}) plane as $\boldsymbol{\sigma_{22} \geq 0}$ (**Mode A, $\boldsymbol{\theta_{fp} = 0}$**) $\sqrt{\left(\frac{\tau_{12}}{S_{12}}\right)^2 + \left(1 - p_{\perp\parallel}^{(+)}\frac{Y_T}{S_{12}}\right)^2\left(\frac{\sigma_{22}}{Y_T}\right)^2} + p_{\perp\parallel}^{(+)}\frac{\sigma_{22}}{S_{12}} = 1 - \left\|\frac{\sigma_{11}}{\sigma_{1D}}\right\|$	$p_{\perp\parallel}^{(+)} = -\left(\frac{d\tau_{12}}{d\sigma_{22}}\right)_{\sigma_{22}=0}$ of (σ_{22},τ_{12}) curve, $\sigma_{22} \geq 0$
IFF on (σ_{22},τ_{12}) plane as $\boldsymbol{\sigma_{22} < 0}$ **and** $\boldsymbol{0 \leq \left\|\frac{\sigma_{22}}{\tau_{12}}\right\| \leq \frac{R_{\perp\perp}^{A}}{\|\tau_{12C}\|}}$ for (**Mode B, $\boldsymbol{\theta_{fp} = 0}$**) $\frac{1}{S_{12}}\left(\sqrt{\tau_{12}^2 + \left(p_{\perp\parallel}^{(-)}\sigma_{22}\right)^2} + \left(p_{\perp\parallel}^{(-)}\sigma_{22}\right)\right) = 1 - \left\|\frac{\sigma_{11}}{\sigma_{1D}}\right\|$	$p_{\perp\parallel}^{(-)} = -\left(\frac{d\tau_{12}}{d\sigma_{22}}\right)_{\sigma_{22}=0}$ of (σ_{22},τ_{12}) curve, $\sigma_{22} \leq 0$

	$R^A_{\perp\perp} = \dfrac{Y_C}{2(1+p^{(-)}_{\perp\perp})} = \dfrac{S_{12}}{2p^{(-)}_{\perp\parallel}}\left(\sqrt{1+2p^{(-)}_{\perp\parallel}\dfrac{Y_C}{S_{12}}}-1\right)$ $p^{(-)}_{\perp\perp} = p^{(-)}_{\perp\parallel}\dfrac{R^A_{\perp\perp}}{S_{12}}$ $\tau_{12C} = S_{12}\sqrt{1+2p^{(-)}_{\perp\perp}}$
IFF on (σ22,τ12) plane **(Mode C,** $\boldsymbol{\cos\theta_{fp} = \sqrt{\dfrac{f_w R^A_{\perp\perp}}{(-\sigma_{22})}}}$ **)** **as** $\boldsymbol{\sigma_{22} < 0}$ **and** $\boldsymbol{0 \le \left\lvert\dfrac{\tau_{12}}{\sigma_{22}}\right\rvert \le \dfrac{\lvert\tau_{12C}\rvert}{R^A_{\perp\perp}}}$ $\left[\left(\dfrac{\tau_{21}}{2(1+p^{(-)}_{\perp\perp})S_{21}}\right)^2+\left(\dfrac{\sigma_2}{Y_C}\right)^2\right]\dfrac{Y_C}{(-\sigma_2)} = 1-\left\lvert\dfrac{\sigma_1}{\sigma_{1D}}\right\rvert$	$p^{(-)}_{\perp\parallel} = -\left(\dfrac{d\tau_{12}}{d\sigma_{22}}\right)_{\sigma_{22}=0}$ of (σ_2,τ_{12}) curve, $\sigma_{22} \le 0$ $R^A_{\perp\perp} = \dfrac{Y_C}{2(1+p^{(-)}_{\perp\perp})} = \dfrac{S_{12}}{2p^{(-)}_{\perp\parallel}}\left(\sqrt{1+2p^{(-)}_{\perp\parallel}\dfrac{Y_C}{S_{12}}}-1\right)$ $p^{(-)}_{\perp\perp} = p^{(-)}_{\perp\parallel}\dfrac{R^A_{\perp\perp}}{S_{12}}$ $\tau_{12C} = S_{12}\sqrt{1+2p^{(-)}_{\perp\perp}}$

Table 7.5.2, Summary of Puck IFF criteria for 3D stress case

IFF failure modes and criteria	Parameters
For $\sigma_n(\theta) \ge 0$ $f_E(\theta) = \sqrt{\left[\left(\dfrac{1}{R^{(+)A}_{\perp}}-\dfrac{p^{(+)}_{\perp\psi}}{R^A_{\perp\psi}}\right)\sigma_n(\theta)\right]^2+\left(\dfrac{\tau_{nt}(\theta)}{R^A_{\perp\perp}}\right)^2+\left(\dfrac{\tau_{nl}(\theta)}{R^A_{\perp\parallel}}\right)^2}+\dfrac{p^{(+)}_{\perp\psi}}{R^A_{\perp\psi}}\sigma_n(\theta)$	$\dfrac{p^{(+)}_{\perp\psi}}{R^A_{\perp\psi}} = \dfrac{p^{(+)}_{\perp\perp}}{R^A_{\perp\perp}}\cos^2\psi+\dfrac{p^{(+)}_{\perp\parallel}}{R^A_{\perp\parallel}}\sin^2\psi$ $\dfrac{p^{(-)}_{\perp\psi}}{R^A_{\perp\psi}} = \dfrac{p^{(-)}_{\perp\perp}}{R^A_{\perp\perp}}\cos^2\psi+\dfrac{p^{(-)}_{\perp\parallel}}{R^A_{\perp\parallel}}\sin^2\psi$ $\cos^2\psi = \dfrac{\tau^2_{nt}}{\tau^2_{nt}+\tau^2_{nl}}$ $\sin^2\psi = \dfrac{\tau^2_{nl}}{\tau^2_{nt}+\tau^2_{nl}}$
For $\sigma_n(\theta) < 0$ $f_E(\theta) = \sqrt{\left[\left(\dfrac{p^{(-)}_{\perp\psi}}{R^A_{\perp\psi}}\right)\sigma_n(\theta)\right]^2+\left(\dfrac{\tau_{nt}(\theta)}{R^A_{\perp\perp}}\right)^2+\left(\dfrac{\tau_{nl}(\theta)}{R^A_{\perp\parallel}}\right)^2}+\dfrac{p^{(-)}_{\perp\psi}}{R^A_{\perp\psi}}\sigma_n(\theta)$	$R^{(+)A}_{\perp} = Y_T$ $R^A_{\perp\parallel} = S_{12}$ $R^A_{\perp\perp} = \dfrac{Y_C}{2(1+p^{(-)}_{\perp\perp})}$

7.5.5.3 Parameters in Puck's failure criteria

There are seven independent parameters that must be determined before Puck's inter-fiber failure criteria are used. Those parameters include three strength parameters, $R^{(+)}_{\perp}, R_{\perp\parallel}, R^{(-)}_{\perp}$ of the UD ply, and four inclination parameters $p^{(-)}_{\perp\parallel}, p^{(+)}_{\perp\parallel}, p^{(-)}_{\perp\perp}, p^{(+)}_{\perp\perp}$, which are the slopes at $\sigma_n = 0$ of some contour lines of the master fracture body. In [7.7] Puck describes the details of how to find those parameters for a particular material system. The procedure of determining those parameters is rather complicated and relies on the author's personal experience and preference. The relations used for determining those parameters are given in the Table 7.5.1 and 7.5.2. In particular, the inclination parameters must be obtained by taking slopes from experiment curves. Table 7.5.3, copied here from [7.7], summarizes these parameters for the Glass-fiber/epoxy (GRP) and Carbon-fiber/epoxy (CFRP) material systems.

Table 7.5.3, Strength values and inclination parameters for typical FRP in Puck failure criteria

	$R_{\perp}^{(+)}$ [N/mm^2]	$R_{\perp}$ [N/mm^2]	$R_{\perp}^{(-)}$ [N/mm^2]	$p_{\perp\parallel}^{(+)}$ [-]	$p_{\perp\parallel}^{(-)}$ [-]	$p_{\perp\perp}^{(-)}$ [-]	$p_{\perp\perp}^{(+)}$ [-]
GRP	45	65	145	0.3	0.25	0.20~0.25	0.20~0.25
GFRP	50	100	230	0.35	0.30	0.20~0.30	0.20~0.30

The parameters for other material system however must be determined by following Puck's procedure and referring to his experience and experimental results.

7.5.5.4 Overall performance of Puck failure criteria and its adaptability to industry

In the WWFE, Puck theoretical failure envelopes for the unidirectional laminae were in very good agreement with the experimental results. The predicted final failure envelopes and stress/strain curves for the multi-directional laminates were also generally in good agreement. Discrepancies between theory and experiment emerged in the test cases where large non-linear deformations were present. In these instances, predictions of final failure strain were much smaller than the observed values and the failure envelope was not closed. Overall, the results show that the Puck theory captures most features of the experimental results and therefore appears to be one of the best currently available.

However, Puck's failure theory is not easily implemented or used. First of all, Puck's failure theory contains a very sophisticated treatment of failure phenomenon. Some of those treatments are based on empirical relations and personal experience, instead of physically based phenomena, making the theory difficult to understand. Secondly, the material parameters for Puck's failure theory are not derived from standard material tests. Therefore they are difficult to quantify with a particular material system without considerable experience and testing that is not currently done in industry. While the failure theory has good predictive capability, these factors will make it hard to gain industry acceptance.

7.5.6 LaRC03 failure theory

The LaRC03 failure theory was proposed by Davila and Camanho [7.25] at NASA Langley Research Center to describe the failure phenomena of fibrous composite materials. A typical failure envelope from this method is shown in Fig. 7.1.1 where six unique failure mechanisms are identified. The theory was developed using micromechanical analysis combined with the concepts of Hashin's failure modes, Sun's 'in-situ' strength, Mohr-Coulomb's internal compressive friction and Puck's action plane. Most importantly, LaRC03 theory uses standard (MIL-HDBK) test data, which are readily available to industry. The current version of the

LaRC03 failure theory is applicable to FRP in-plane stress, a more advanced version for FRP in 3D stress state is in under development [7.26].

7.5.6.1 Matrix failure

LaRC03 introduces a new set of criteria for matrix fracture (called Inter-Fiber Failure by Puck). In the case of matrix tension, the fracture planes are normal to the plane of the plies and parallel to the fiber direction. For matrix compression, however, the plane of fracture may not be normal to the ply and the angle of the fracture plane that is calculated using Mohr-Coulomb theory.

7.5.6.1.1 Criterion for matrix failure under transverse compression ($\sigma_{22} < 0$)

Puck's failure theory proposes that the shear strength increases on the fracture plane of the matrix due to internal friction under compression. In LaRC03, the effective shear stress on the fracture plane increases instead of the shear strength due to the internal friction. The effective stress $\tau_{eff,}$ which is the actual shear stress on the fracture plane, is related to the stresses τ^T and σ_n acting on the fracture plane by the expression $\tau_{eff} = \tau^T + \eta\sigma_n$, where σ_n is the normal stress on the fracture plane, η is called the coefficient of internal friction and it is assumed to be a material constant.

In general, the fracture plane is subjected to transverse as well as in-plane stresses, in which case the effective stresses must be defined in both orthogonal directions.

$$\begin{aligned} \tau^T_{eff} &= \left\langle \left|\tau^T\right| + \eta^T\sigma_n \right\rangle \\ \tau^L_{eff} &= \left\langle \left|\tau^L\right| + \eta^L\sigma_n \right\rangle \end{aligned} \tag{7.5.6.1}$$

where the terms η^T and η^L are referred to as coefficients of transverse and longitudinal influence, respectively, and the operand <x> = x if x ≥ 0; otherwise <x> = 0. Matrix failure under compression loading is assumed to result from a quadratic interaction between the effective shear stresses acting on the fracture plane. The failure index for a failure mode is written as an equality stating that stress states that violate the inequality are not physically admissible. The matrix failure index (FI_M) is

LaRC03 #1

$$FI_M = \left(\frac{\tau^T_{eff}}{S^T}\right)^2 + \left(\frac{\tau^L_{eff}}{S^L_{is}}\right)^2 \le 1 \tag{7.5.6.2}$$

where S^T and $S^L{}_{is}$ are the transverse and longitudinal shear strengths, respectively. The subscript "*is"* indicates that for general laminates, the *in-situ* longitudinal shear strength rather than the strength of a unidirectional laminate should be used. The constraining effect of adjacent plies substantially increases the effective strength of a ply. It is assumed here that the transverse shear strength S^T is not subjected to 'in-situ' effects. The effective stresses for an angle of fracture plane between 0° and 90° can be written in terms of the plane stress components and fracture angle, as

$$\begin{aligned} \tau^T_{eff} &= \left\langle -\sigma_{22}\cos\alpha(\sin\alpha - \eta^T\cos\alpha) \right\rangle \\ \tau^L_{eff} &= \left\langle \cos\alpha(\left|\tau_{12}\right| + \eta^T\sigma_{22}\cos\alpha) \right\rangle \end{aligned} \tag{7.5.6.3}$$

The coefficients of influence η^T and η^L can be obtained from the case of uniaxial transverse compression ($\sigma_{22} < 0$, $\tau_{12} = 0$). At failure, the in-plane compressive stress is equal to the matrix compressive strength, so η^T can be solved from

$$\tau_{eff}^T = S^T = Y^C \cos\alpha(\sin\alpha - \eta^T \cos\alpha) \tag{7.5.6.4}$$

as

$$\eta^T = \frac{-1}{\tan(2\alpha_0)} \tag{7.5.6.5}$$

where α_0 is the fracture angle that maximizes the effective transverse shear stress. Puck determined that when loaded in transverse compression, most unidirectional graphite/epoxy composites fail by transverse shear along a fracture plane oriented at α_0=53°±2°. Therefore, the coefficient of transverse influence is in the range $0.21 \leq \eta^T \leq 0.36$. Note that if the fracture plane were oriented at α_0=45°, the coefficient of transverse influence would be equal to zero.

The transverse shear strength S^T is a material property that is difficult to measure experimentally. However, S^T can be obtained from Eq. (7.5.6.4) by substituting Eq. (7.5.6.5).

$$S^T = Y^C \cos\alpha_0 (\sin\alpha_0 + \frac{\cos\alpha_0}{\tan 2\alpha_0}) \tag{7.5.6.6}$$

For a typical fracture angle of α_0=53° gives S^T=0.378Y^C. The coefficient of longitudinal influence, η^L, can be determined from shear tests with varying degrees of transverse compression. In the absence of biaxial test data, η^L can be estimated from empirical coupling of the longitudinal and transverse shear strengths, similar to that proposed by Puck. The expression for η^L used in the LaRC03 formulation is:

$$\frac{\eta^L}{S^L} = \frac{\eta^T}{S^T} \Rightarrow \eta^L = -\frac{S_{is}^L \cos 2\alpha_0}{Y^C \cos^2 \alpha_0} \tag{7.5.6.7}$$

The key to predicting matrix compressive failure is to determine the fracture plane angle, α. Under combined loads, the angle of the fracture plane is the one that maximizes the failure index, *FI*, in Eqn. (7.5.6.2). In LaRC03, the fracture angle is obtained by searching for the maximum of the failure index numerically (Similar strategy used by Puck for 3D IFF criterion) over the range of possible fracture angles: $0 < \alpha < \alpha_0$. Fig. 7.5.8 shows the matrix failure envelopes at various fracture angles for a unidirectional E-Glass/LY556 composite in the plane of transverse compression and in-plane shear. As is seen in the figure, the fracture angle that maximizes the *FI* for small transverse stresses is α=0°. When the applied transverse stress σ_{22} has a magnitude equal to approximately 2/3 of the transverse compressive strength, Y^C, the angle of the critical fracture plane switches from α=0° to α=40°, and then rapidly increases to α= 53°, the angle of fracture for uniaxial transverse compression.

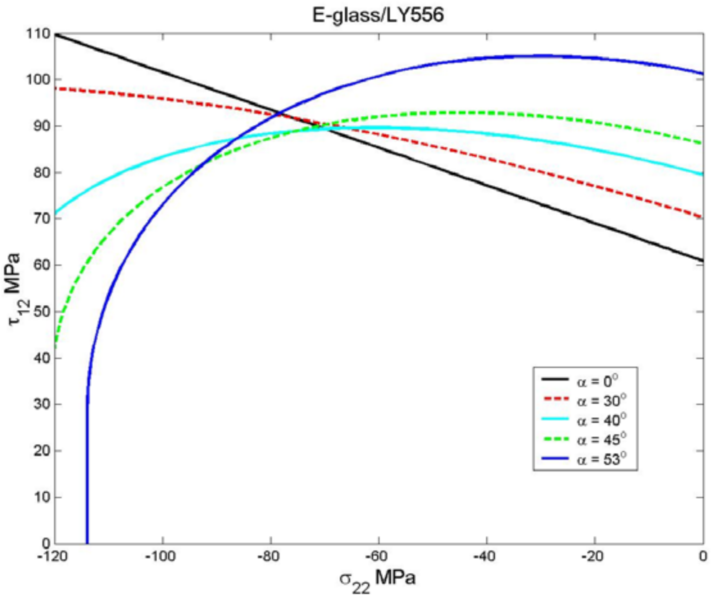

Fig. 7.5.8, Matrix failure envelopes for a typical unidirectional E-glass/epoxy lamina subjected to in-plane transverse compression and shear loading.

7.5.6.1.2 Criterion for matrix failure under transverse tension ($\sigma_{22} > 0$)

The matrix failure of composites under transverse tension is believed to result from catastrophic propagation of matrix cracks, which may originate from manufacturing defects. Many failure criteria only provide phenomenological models to describe this failure event, but do not probe into the micromechanism of the failure, such as Tsai, Hashin and even Puck. LaRC03 proposes an approach based on fracture mechanics to analyze the critical condition for crack propagation in a UD ply, which is either embedded in a laminate or unconstrained.

In-situ strength

Like Sun's linear failure theory, LaRC03 considered the 'in-situ' effect occurring in laminated composites as it predicts matrix cracking under the presence of both in-plane shear and transverse tensile stresses. The 'in-situ' effect, originally observed in tensile tests of cross-ply glass fiber reinforced plastics, is characterized by higher transverse tensile and shear strengths of a ply when it is constrained by plies with different fiber orientations in a laminate, when compared with the strength of the same ply in a unidirectional laminate. The 'in-situ' strength also depends on the number of plies clustered together, and on the fiber orientation of the constraining plies.

In-situ strengths can be obtained from experimental [7.23, 7.25, 7.27] and analytical methods [7.28, 7.29, 7.30]. As we recall, Sun has used the 'in-situ' tensile transverse and shear strength to be 1.5 times those measured from unidirectional laminates for the entire test case based on his experience. In LaRC03, the 'in-situ' strengths are calculated using Dvorak's model [7.28] for the propagation of cracks in a constrained ply. The results are given in the following.

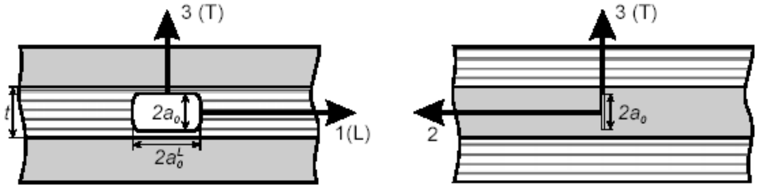

Fig. 7.5.9, A crack embedded in a constrained UD ply (Dvorak's model)

Based on the Dvorak's model, the mixed-mode energy release rate (ERR) for a crack growth in a constrained UD ply under in-plane shear and transverse tensile stresses, as shown in Fig. 7.5.9, are given by

$$\begin{aligned} G(T) &= \frac{\pi a_0}{2}(\eta_I^2 \Lambda_{22}^0 \sigma_{22}^2 + \eta_{II}^2 \Lambda_{44}^0 \sigma_{12}^2) \\ G(L) &= \frac{\pi a_0}{4}(\xi_I^2 \Lambda_{22}^0 \sigma_{22}^2 + \xi_{II}^2 \Lambda_{44}^0 \sigma_{12}^2) \end{aligned} \tag{7.5.6.8}$$

where *T* denotes transverse direction and *L* denotes longitudinal direction, as shown in Fig. 7.5.9. The parameters η_i and ξ_i i=I, II are the stress intensity reduction coefficients for propagation in the transverse and longitudinal directions, respectively. These coefficients account for the constraining effects of the adjoining layers on crack propagation: the coefficients are nearly equal to 1.0 when $2a_0 \ll t$, and are less than 1.0 when $a_0 \approx t$. Considering that a transverse crack can promote delamination between the plies, Dvorak et al. suggested that the effective value of η_i can be larger than obtained from the analysis of cracks terminating at the interface, and suggested the use of $\eta_i = \xi_i = 1$. The parameters Λ^0_{jj} are given as:

$$\Lambda_{22}^0 = 2\left(\frac{1}{E_2} - \frac{v_{12}^2}{E_1}\right) \qquad \Lambda_{44}^0 = \frac{1}{G_{12}} \tag{7.5.6.9}$$

Further, the ERR in Eq. (7.5.6.8) can be decomposed into mode I and mode II, as

$$G_I(T) = \frac{\pi a_0}{2}\Lambda_{22}^0 \sigma_{22}^2 \qquad G_{II}(T) = \frac{\pi a_0}{2}\Lambda_{44}^0 \sigma_{12}^2 \tag{7.5.6.10}$$

$$G_I(L) = \frac{\pi a_0}{4}\Lambda_{22}^0 \sigma_{22}^2 \qquad G_{II}(L) = \frac{\pi a_0}{4}\Lambda_{44}^0 \sigma_{12}^2 \tag{7.5.6.11}$$

The corresponding fracture toughnesses are given as

$$G_{IC}(T) = \frac{\pi a_0}{2}\Lambda_{22}^0 \left(Y_{is}^T\right)^2 \qquad G_{IIC}(T) = \frac{\pi a_0}{2}\Lambda_{44}^0 \left(S_{is}^T\right)^2 \tag{7.5.6.12}$$

$$G_{IC}(L) = \frac{\pi a_0}{4}\Lambda_{22}^0 \left(Y_{is}^T\right)^2 \qquad G_{IIC}(L) = \frac{\pi a_0}{4}\Lambda_{44}^0 \left(S_{is}^T\right)^2 \tag{7.5.6.13}$$

LaRC03 failure criterion for matrix cracking under transverse tension is established based on Hahn's mix-mode criterion [7.31] for crack propagation. It is given as

LaRC03 #2
$$FI_M = (1-g)\frac{\sigma_{22}}{Y_{is}^T} + g\left(\frac{\sigma_{22}}{Y_{is}^T}\right)^2 + \frac{\sigma_{12}}{S_{is}^L} = 1 \tag{7.5.6.14}$$

where g is the ratio of fracture toughness of mode I to mode II, $g = \frac{G_{IC}}{G_{IIC}} = \frac{\Lambda_{22}^0}{\Lambda_{44}^0}\left(\frac{Y_{is}^T}{S_{is}^L}\right)^2$. Similar to Puck, the criterion presented in Eqn. (7.5.6.14) contains both linear and quadratic terms of the transverse normal stress and a quadratic term of the in-plane shear stress. In addition, if g =1 Eqn. (7.5.6.14) reverts to Sun's criterion for transverse matrix cracking under both in-plane shear and transverse tension, where the ply strengths are the 'in-situ' strengths.

The 'in-situ' strength used in LaRC03 #2 can be obtained from either experiments or analytical solutions. The analytical solution can be derived from Eqns. (7.5.6.12)-(7.5.6.13). For thick embedded plies, (e.g. the ply thickness is approximately 0.7 mm [7.28]), cracks will grow unstably in the transverse direction because the energy release rate for the crack slit is twice as large in the transverse direction as it is in the longitudinal direction, which can be seen in Eqs. (7.5.6.10) and (7.5.6.11). Therefore, the 'in-situ' strength for thick embedded plies can be solved from Eqn. (7.5.6.12), as

$$Y_{is}^T = \sqrt{\frac{2G_{IC}(T)}{\pi a_0 \Lambda_{22}^0}} \qquad S_{is}^T = \sqrt{\frac{2G_{IIC}(T)}{\pi a_0 \Lambda_{44}^0}} \tag{7.5.6.15}$$

In case of thin plies, which are usually referred to as one having a thickness smaller than the typical defect, t < 2a$_0$, crack defects can only grow in the longitudinal (L) direction, or trigger a delamination between the plies. The 'in-situ' strengths can be calculated from the components of the fracture toughness as:

$$Y_{is}^T = \sqrt{\frac{8G_{IC}(T)}{\pi t \Lambda_{22}^0}} \qquad S_{is}^T = \sqrt{\frac{8G_{IIC}(T)}{\pi t \Lambda_{44}^0}} \tag{7.5.6.16}$$

where it can be observed that the 'in-situ' strengths are inversely proportional to $t^{1/2}$. The toughness G_{Ic} (L) and G_{IIc}(L) can be assumed to be the values measured by standard Fracture Mechanics tests, such as the DCB for mode I and the ENF test for mode II.

In the case of unidirectional laminates, which is a particular case of thick plies, the 'in-situ' strength is given in terms of tensile and shear strengths measured from unidirectional laminate tests.

$$\begin{aligned} Y_{is}^T &= 1.12\sqrt{2}Y^T \\ S_{is}^T &= \sqrt{2}S^L \end{aligned} \tag{7.5.6.17}$$

7.5.6.2 Fiber failure

7.5.6.2.1 Criterion for fiber tension failure

Fiber breakage under longitudinal tension has been regarded to occur when the longitudinal fiber stress or the strain reach the limit. Puck has made an attempt to distinguish the true fiber stress and lamina stress, using an approximate micromechanical analysis. As a result, Puck's model defined an "effective" strain acting along the fibers as the criterion judging fiber failure. Similarly, the LaRC03 criterion for fiber tension failure used a non-interacting maximum allowable strain criterion that is simple to measure and is independent of fiber volume fraction and Young's moduli. The LaRC03 failure index for fiber tensile failure is given as:

LaRC03 #3
$$FI_F = \frac{\varepsilon_{11}}{\varepsilon_1^T} = 1 \tag{7.5.6.18}$$

7.5.6.2.2 Criterion for fiber compression failure

The real difficulty in prediction of fiber failure has been encountered when the fibers were subjected to longitudinal compression. Sun and Hashin used the maximum stresses in fiber direction for the criterion of fiber failure, but their theories did not take into account the effect of in-plane shear which could considerably reduce the compressive strength of lamina due to the fiber kinking induced. Puck tried to solve this problem by adding an empirical term of shear strain in the original form of fiber compressive failure criterion, but that empirical term does not provide a micromechanics basis for the failure mechanism.

LaRC03 established the failure criterion for fiber compression based on recent development of micromechanical theories of fiber compressive failure. Those studies showed that compressive failure of aligned fiber composites results from collapse of the fibers due to shear kinking and damage of the supporting matrix (see the representative works of Fleck [7.32], Soutis [7.33], and Shultheisz [7.34]). Fiber kinking occurs as shear deformation leads to the formation of a kink band. Argon [7.35] found that the fiber misalignment leads to shearing stresses between fibers that rotate the fibers, increasing the shearing stress and leading to instability. Several authors [7.36, 7.37] have considered that misaligned fibers fail by the formation of a kink band when local matrix cracking occurs. Potter et al. [7.38] assumed that additional failure mechanisms that may occur under uniaxial longitudinal compression, such as crushing, brooming, and delaminations, are essentially triggered by matrix failure.

It turns out that matrix failure around misaligned fibers is the major reason for fiber compressive failure. Thus, LaRC03 attempted to establish a matrix failure criterion in misaligned fiber frames when fibers are in compression. As shown in Fig. 7.5.10, the imperfection in fiber alignment is idealized as a local region of waviness. The misaligned fiber frames are characterized by misalignment angle φ.

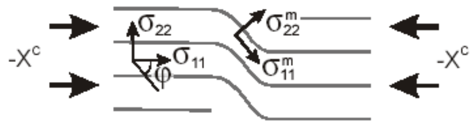

Fig. 7.5.10, misaligned fibers under compression

The ply stresses in the misalignment coordinate frame *m* shown in Fig. 7.5.10 are

$$\begin{aligned}
\sigma_{11}^{m} &= \cos^2\varphi\sigma_{11} + \sin^2\varphi\sigma_{22} + 2\cos\varphi\sin\varphi\sigma_{12} \\
\sigma_{22}^{m} &= \sin^2\varphi\sigma_{11} + \cos^2\varphi\sigma_{22} - 2\cos\varphi\sin\varphi\sigma_{12} \\
\sigma_{12}^{m} &= -\frac{1}{2}(\sin 2\varphi\sigma_{11} - \sin 2\varphi\sigma_{22}) + \cos 2\varphi\sigma_{12}
\end{aligned} \qquad (7.5.6.19)$$

The total misalignment angle φ can be decomposed into an initial (constant) misalignment angle φ^0 that represents a manufacturing imperfection, and an additional rotational component φ^R that results from shear loading. The angles φ^0 and φ^R can be calculated using small angle approximations and Eqn. (7.5.6.19).

$$\begin{aligned}
\varphi^{R} &= \frac{\tau_{12}^{m}}{G_{12}} = \frac{-\varphi\sigma_{11} + \varphi\sigma_{22} + |\sigma_{12}|}{G_{12}} \\
\varphi^{0} &= \varphi^{C} - \varphi^{R}\Big|_{X^C} \Rightarrow \varphi^{0} = \varphi^{C}\left(1 - \frac{X^C}{G_{12}}\right)
\end{aligned} \qquad (7.5.6.20)$$

where φ^C is the total misalignment angle for the case of axial compression loading only ($\sigma_{11} = -X^C$ and $\sigma_{22} = \sigma_{12} = 0$), which is given as

$$\varphi^{C} = \tan^{-1}\left(\frac{1 - \sqrt{1 - 4\left(\frac{S_{is}^{L}}{X^{C}} + \eta^{L}\right)\left(\frac{S_{is}^{L}}{X^{C}}\right)}}{2\left(\frac{S_{is}^{L}}{X^{C}} + \eta^{L}\right)} \right) \qquad (7.5.6.21)$$

The total misalignment angle φ then becomes

$$\varphi = \frac{|\sigma_{12}| + (G_{12} - X^{C})\varphi^{C}}{G_{12} + \sigma_{11} - \sigma_{22}} \qquad (7.5.6.22)$$

Finally, fiber compression failure by formation of a kink band is predicted using the stresses from Eqn. (7.5.6.19) and the failure criterion for matrix tension or matrix compression. For matrix compression ($\sigma_{22}^{m} < 0$), the criterion is the Mohr-Coulomb criterion given in Eqn. (7.5.6.2), with $\alpha=0°$ and $\tau^{T}_{eff} = 0$. The criterion for kinking becomes:

LaRC03 #4
$$FI_F = \left\langle \frac{\left|\tau_{12}^m\right| + \eta^L \sigma_{22}^m}{S_{is}^L} \right\rangle = 1 \tag{7.5.6.23}$$

For fiber compression with matrix tension ($\sigma_{22}^m > 0$), the transformed stresses of Eqn. (7.5.6.19) are substituted into the matrix tensile failure criterion given in Eqn. (7.5.6.14) to yield the following criterion for fiber kinking:

LaRC03 #5
$$FI_F = (1-g)\frac{\sigma_{22}^m}{Y_{is}^T} + g\left(\frac{\sigma_{22}^m}{Y_{is}^T}\right)^2 + \frac{\sigma_{12}^m}{S_{is}^L} = 1 \tag{7.5.6.24}$$

This criterion has a good correlation with those proposed by Edge, Sun and others. For example, in the case of $\sigma_{22} = 0$, the fiber failure criterion for Eq. (7.5.6.24) becomes

$$FI_F = -\frac{\sigma_{11}}{X^C} + \frac{\left|\sigma_{12}\right|}{kS^L} = 1 \text{ with } k = \frac{1}{1-\varphi^2 - 2\eta^L\varphi} > 1 \tag{7.5.6.25}$$

The linear interaction between σ_{11} and σ_{12} in Eq. (7.5.6.16) is identical to the form used by Edge [7.39] for the WWFE. For T300/914C, Edge suggests using an empirical value of $k = 1.5$. However, Edge also indicates that other researchers have shown excellent correlation with experimental results with $k = 1$. Using the WWFE strength values of X^C=900 MPa, S^L=80 MPa, Y^C=200 MPa, an assumed fracture angle in transverse compression of 53°, we get: $\eta^L = 0.304$, $\varphi^C = 5.3°$. With the approximation $\varphi \cong \varphi^C$, Eq. (7.5.6.25) gives $k = 1.07$.

7.5.6.3 Matrix Damage in Biaxial compression

In the presence of high transverse compression combined with moderate fiber compression, matrix damage can occur without the formation of kink bands or damage to the fibers. The matrix fracture plane has different angles with variation of ratio of transverse compression to fiber compression. Thus, the matrix damage criterion can be calculated using the same matrix cracking criterion but in the misaligned frame, as shown in Fig. 7.5.10. It can be written as

LaRC03 #6
$$FI_M = \left(\frac{\tau_{eff}^{mT}}{S^T}\right)^2 + \left(\frac{\tau_{eff}^{mL}}{S_{is}^L}\right)^2 = 1 \tag{7.5.6.26}$$

where the effective shear stresses in the misaligned frame are defined as

$$\begin{aligned} \tau_{eff}^{mT} &= \left\langle -\sigma_{22}^m \cos\alpha(\sin\alpha - \eta^T \cos\alpha)\right\rangle \\ \tau_{eff}^{mL} &= \left\langle \cos\alpha(\left|\tau_{12}^m\right| + \eta^L \sigma_{22}^m \cos\alpha)\right\rangle \end{aligned} \tag{7.5.6.27}$$

7.5.7 Strain Invariant Failure Theory (SIFT)

Recently, Gosse [7.2, 7.3, 7.40] has proposed a new failure theory called Strain Invariant Failure Theory (SIFT) for damage initiation in polymer composites. Based on the experimental investigation, SIFT attributes the damage initiation to be either dilatational or distortional deformation in the matrix or in the fiber. Implementation of SIFT requires resolution of stresses at the micromechanics level between the matrix and fiber phases. With respect to unidirectional tape composite product forms, there are two critical strain invariants that dictate damage (or failure) initiation within the matrix phase,

$$J_1 \geq J_1^{critical} \text{ and } \varepsilon_{equivalent} \geq \varepsilon_{equivalent}^{critical} \tag{7.5.6.28}$$

and one critical strain invariant that dictates damage (or failure) initiation within the fiber phase,

$$\varepsilon_{equivalent}^{fiber} \geq \varepsilon_{equivalent}^{fiber \quad critical} \tag{7.5.6.29}$$

The strain invariants are:

$$J_1 = \varepsilon_1 + \varepsilon_2 + \varepsilon_3$$

and

$$\varepsilon_{equivalent} = \sqrt{0.5[(\varepsilon_1 - \varepsilon_2)^2 + (\varepsilon_1 - \varepsilon_3)^2 + (\varepsilon_2 - \varepsilon_3)^2]}$$

where ε_1, ε_2, and ε_3 are the principal strains.

Using stresses at the micromechanics level, SIFT attempts to predict ply strength for different load combinations of biaxial and shear. At this time, it does not provide a superior method of computing transverse allowables for 90° tension loads. It also does not address the problem of determining the 90° tension allowable when the ply is embedded between different layups, that is, dilational matrix cracking. Finally, it provides no progressive failure capability. So when there is good test data for the combination of loads on a ply, then should use that. Therefore, if reliable and complete test data is available at the ply level, other failure methods as described above may provide more accuracy. However, of only fiber or matrix allowable data is available, SIFT can provide useful results.

7.5.8 Summary Conclusions

This report reviews the up-to-date best failure theories for FRP, including Hashin, Sun, Tsai, Zinoviev, Puck and LaRC03. In the following, we summarize the features of LaRC03 and compared it with Hashin, Sun, Tsai, Zinoviev, Puck, max stress and max strain failure theories.

Table 7.5.4, Comparison of up-to-date best failure theories for FRP

		Hashin	Sun (L)	Tsai	Zinoviev	Puck	LaRC03	Max stress	Max strain
Features	Physically based	yes	yes	no	no	yes	yes	no**	no**
	Input parameters	standard	Non-standard	standard	standard	Non-standard	standard	standard	standard
	Damage model	N/A	available	available	Available	Available (Empirical)	N/A	N/A	N/A
Predicative capability	Fiber tension	fair	fair	N/D*	N/D	Very good	Very good	N/D	N/D
	Fiber compression	poor	poor	N/D	N/D	good	good	N/D	N/D
	Matrix tension	Very good	Very good	N/D	N/D	Very good	Very good	N/D	N/D
	Matrix compression	poor	poor	N/D	N/D	good	good	N/D	N/D
WWFE cases	UD lamina	fair	good	good	good	good	good	fair	fair
	Multi-directional laminates	N/A	fair	poor-IF^A good-FF^A	good	good	N/A	poor	poor
	Cross-ply laminate	fair^B	good	Good after revised	good	good	good^B	fair^B	fair^B

A. IF stands for initial failure; FF stands for final failure
B. The assessment is based on prediction for Shuart's experiment
* N/D stands for "not distinguished".
** Max stress and max strain theories are considered non-physically based because they do not indicate the actual failure mechanism. That is, these theories give no indication if a failure is due to fiber breakage, matrix crack propogation, fracture plane shear, etc.

It can be seen that Puck and LaRC03 show good predictive capability due to its physically based model for different failure modes and good accuracy. However, LaRC03 shows better adaptability to industry because of its readily available input parameters. As such, LaRC03 was implemented into HyperSizer and the detailed procedure is addressed in this report. The Newton-Raphson method was used to solve the nonlinear equations in LaRC03 and thus to generate the failure envelopes. This method proves to be much more efficient and accurate as more data points are taken. LaRC03 is expected to be continuously modified by NASA and the new updates will also be verified and implemented into HyperSizer.

7.6 *Blank Section*

7.7 Implementation of LaRC03 Failure Theory

Two issues have to be solved before LaRC03 failure criteria are implemented: 1) the availability and credibility of input parameters; 2) numerical methods for generation of LaRC03 failure envelopes. These two issues will be discussed below.

7.7.1 Input parameters for LaRC03 failure criterion

Eleven unidirectional material parameters are required for input to the six LaRC03 failure criteria, identified in Fig. 7.1.1 and described in Section 7.5. These parameters are listed in Table 7.7.1.

Table 7.7.1, Required UD material properties for LaRC03

E_1	Longitudinal Young's modulus
E_2	Transverse Young's modulus
G_{12}	In-plane shear modulus
ν_{12}	In-plane Poisson ratio
X^T	Longitudinal tensile strength
X^C	Longitudinal compressive strength
Y^T	Transverse tensile strength
Y^C	Transverse compressive strength
S^L	In-plane shear strength
$G_{IC}(L)$	Mode I fracture toughness
$G_{IIC}(L)$	Mode II fracture toughness

Two other material parameters are optional. They are

Table 7.7.2, Optional UD material parameters for LaRC03

α_0	Fracture angle of matrix compressive failure
η^L	Longitudinal coefficient of influence of internal friction

where α_0 can be entered as 53° or extracted from test data; η^L can be calculated from Eqn. (7.5.6.7) or from test data.

The material parameters in Table 7.7.1 are the common unidirectional lamina data, which can be obtained from standard tests. Most of the data are also available in various composite design handbooks, such as MIL-HDBK-17. Among all the material data listed in Table 7.7.1, only the fracture toughness can be obtained from standard fracture mechanics tests. For example, G_{IC} can be measured from DCB test, and G_{IIC} can be measured from ENF test. However, compared to other material strength of UD ply, the fracture toughness are not well collected in composite design handbooks. In many cases, only G_{IC} is provided, but no data is released for G_{IIC}. In such situations, G_{IIC} can be calculated from certain mixed-mode crack propagation criterion. NASA [7.41] has recently reviewed currently used mixed-mode delamination failure criteria and compared those to experimental data, including power law, exponential Hackle, exponential K_I/K_{II}, linear interaction, bilinear criteria, etc. Those delamination criteria can be used to calculate G_{IIC} once G_{IC} is known, or vice versa. In particular, Davila [7.1] recommended using power law and B-K criteria. They are given as

$$\left(\frac{G_I}{G_{IC}}\right)^{\alpha} + \left(\frac{G_I}{G_{IC}}\right)^{\beta} = 1 \tag{7.7.1.1}$$

where the exponent α and β in the power law are usually selected to be either 1 or 2. And the B-K criterion is established in terms of the single-mode fracture toughness G_{IC} and G_{IIC} and parameter γ.

$$G_T = G_{IC} + (G_{IIC} - G_{IC})\left(\frac{G_{II}}{G_T}\right)^{\gamma} \tag{7.7.1.2}$$

where G_T is the total energy release rate.

Another concern is about the 'in-situ' strength of the embedded lamina. There are two 'in-situ' strengths used in LaRC03, one is the in-plane shear strength S_{is}^{L}, another is transverse tensile strength Y_{is}^{T}. The ideal way of obtaining the 'in-situ' strengths is to measure them in the tests directly. However, this kind of information is rare for a particular material system. As a result, LaRC03 provides analytical formulae to estimate the S_{is}^{L} and Y_{is}^{T} by using the fracture toughness of material in Eqns. (7.5.6.8-7.5.6.17).

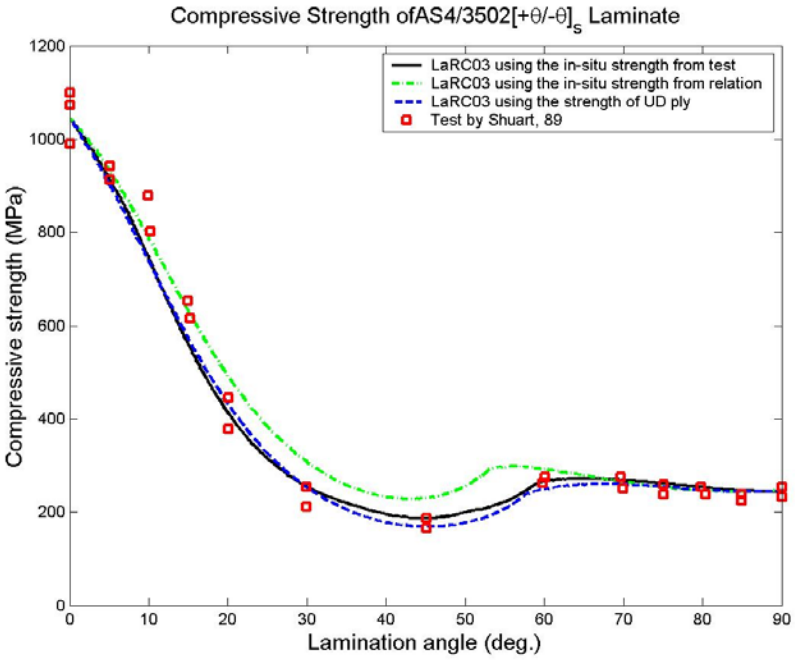

Fig. 7.7.1, Compressive strength of [+/-θ]s AS4/3502 predicted by LaRC03 using different values of in-situ strength .

In LaRC03, choosing different values of in-situ strengths has a great impact on the predicted failure stresses. Fig.7.7.1 shows predicted strength by LaRC03 for the cross-ply [±θ]s AS4/3502 laminate, using the in-situ shear strengths obtained from three different resources: the test, the formulae given by LaRC03 and the data of the UD ply strength given in Mil-Hdbk-17-2E. The in-situ shear strength from test is 95.1 MPa, as reported by Shuart [7.42]. The data of the UD ply strength is found in Mil-Hdbk-17-2E, as 102 MPa, and the in-situ strength derived from the LaRC03 formulae is S_{is} = 114.8 MPa (G_{Ic}= 82 J/m^2, G_{IIc} = 120.5 J/m^2). The results in Fig.7.7.1 show that the predicted strengths using the test S_{is} = 95.1 MPa correlate the best with the experimental results, while the one from LaRC03 formulae generates relatively larger error.

The above example shows that the in-situ strengths estimated by LaRC03 formula are less accurate, so that they cause errors in strength prediction of the laminate. This may result from the following reasons: 1) the strength predicted by fracture mechanics was developed accounting for residual thermal stresses, which have not yet been implemented in the code; 2) In the data, it is not clear if the G_{IIc} given is G_{IIc}(L) or G_{IIc}(T); 3) The nonlinearity of shear may play an important role. To count for those difficulties, some empirical relations have been proposed. For example, Sun has suggested taking 'in-situ' tensile transverse and shear strength to be 1.5 times those measured from unidirectional laminates for the WWFE test cases base on his experience. Davila [7.26] also suggested that for internal plies with typical ply thicknesses of 0.13 mm, one can use the following empirical relations: $S_{is}^L = 1.5S^L$ and $Y_{is}^T = 2Y^T$. If the plies are thicker, the 'in-situ' strength decreases by the square root of the thickness. The research on how to improve the prediction of the 'in-situ' strength is still ongoing at NASA. The implementation of LaRC03 in HyperSizer uses the user input values for UD plies as the in-situ strength.

7.7.2 Methods of generation of LaRC03 failure envelops

LaRC03 failure theory contains six failure criteria for different failure modes. The methods for generating failure envelopes for these six failure criteria are very different. Particularly, the method for LaRC03#1, #2 and #3 is quite straightforward, while the method for LaRC03 #4, #5 and #6 is rather complicated. In the following, we will address the details of the method for LaRC03 #4, #5 and #6 in particular.

7.7.2.1 Newton-Raphson method

The equations for generating the failure envelopes of LaRC03 criteria #4, #5 and #6 are nonlinear in nature (See section 7.5.6). As such, the nonlinear solution procedure could be used to solve these equations. Newton-Raphson method proves to be an effective and efficient method for this type of problem. In the following, we briefly describe Newton-Raphson method for the one-dimensional case.

Suppose we have a non-linear equation f(x) with one unknown x,

$$f(x) = 0 \tag{7.7.2.1}$$

If an initial approximation is given, i.e., x_0 = starting value, then the solution of the equation can be found through the following iteration

$$x_j = x_{j-1} - f(x_{j-1}) / f'(x_{j-1}) \quad j = 1,2,3\ldots n \tag{7.7.2.2}$$

The process is iterated until it converges, usually until $|x_j - x_{j-1}|$ is smaller than the accuracy wanted in the solution, or until the $f(x_j)$ is sufficiently close to 0 (general criteria are difficult to define). Convergence may, of course, not be obtained if the first approximation was poor (again this is difficult to define in general).

Newton-Raphson method for the scalar case has a very simple geometrical interpretation: it is the extrapolation to 0 along the tangent to the graph of *f*(*x*). The error after iterations is proportional to the square of the error before iterations, as shown in Eqn. (7.7.2.3). Once the relationship between e_{n+1} and e_n is known then the *order of the iterative scheme* (which is basically the speed of convergence) is the power of e_n. Thus, Newton-Raphson is a *second order scheme* and we have very fast convergence.

$$e_{n+1} \approx -\frac{e_n^2 f''(x)}{2f'(x)} \tag{7.7.2.3}$$

7.7.2.2 Equations for generation of failure envelopes

The methods for generating failure envelopes of criteria #4, #5 and #6 are basically the same. As a result, we choose LaRC03 #5 as an example to describe the method. In the σ_{11}-σ_{22} plane (same for other planes), the points (σ_{11}, σ_{22}) can be also expressed in the polar coordinate system, as shown in Fig. 7.7.2.

$$\sigma_{22} = r\sin t \quad \text{and} \quad \sigma_{11} = r\cos t \tag{7.7.2.4}$$

where *r* is the module of projection from the origin to the point on the failure envelope; *t* is the angle of the projection. Thus, if the angle is given, the point on the envelope can be defined only when the *r* is known.

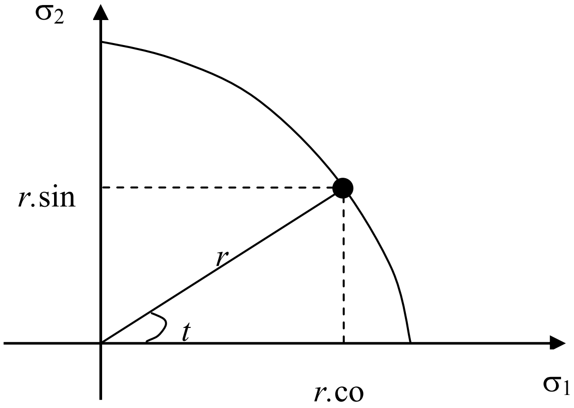

Fig. 7.7.2, Polar coordinates of a point in the failure envelope

Eqns. (7.7.2.5)-(7.7.2.9) are the complete system equations for generating failure envelopes of LaRC03 #5 in the σ_{11}-σ_{22} plane.

$$\sigma_{22}(r,t) = r\sin t \quad \text{and} \quad \sigma_{11}(r,t) = r\cos t \tag{7.7.2.5}$$

$$f(r,t) = (1-g)\frac{\sigma_{22}^m}{Y_{is}^T} + g\left(\frac{\sigma_{22}^m}{Y_{is}^T}\right)^2 + \frac{\sigma_{12}^m}{S_{is}^L} - 1 \tag{7.7.2.6}$$

$$\begin{aligned}
\sigma_{11}^{m} &= \cos^2\varphi\sigma_{11} + \sin^2\varphi\sigma_{22} + 2\cos\varphi\sin\varphi\sigma_{12} \\
\sigma_{22}^{m} &= \sin^2\varphi\sigma_{11} + \cos^2\varphi\sigma_{22} - 2\cos\varphi\sin\varphi\sigma_{12} \\
\sigma_{12}^{m} &= -\frac{1}{2}(\sin 2\varphi\sigma_{11} - \sin 2\varphi\sigma_{22}) + \cos 2\varphi\sigma_{12}
\end{aligned} \tag{7.7.2.7}$$

$$\varphi = \frac{|\sigma_{12}| + (G_{12} - X^C)\varphi^C}{G_{12} + \sigma_{11} - \sigma_{22}} \tag{7.7.2.8}$$

$$\varphi^C = \tan^{-1}\left(\frac{1 - \sqrt{1 - 4\left(\frac{S_{is}^L}{X^C} + \eta^L\right)\left(\frac{S_{is}^L}{X^C}\right)}}{2\left(\frac{S_{is}^L}{X^C} + \eta^L\right)} \right) \tag{7.7.2.9}$$

If the projection angle *t* is given, apparently, these equations, which are one-dimensional nonlinear equations about the unknown *r*, can be solved by using Newton-Raphson method, as described by Eqn. (7.7.2.1-7.7.2.2). Noted that the Newton-Raphson procedure needs to calculate the derivatives of all the variables involved in the criteria with respect to the unknowns. In the following, the expressions of the derivatives with respect to unknown *r* are given.

$$\frac{df}{dr} = (1-g)\frac{d\sigma_{22}^{m}/dr}{Y_{is}^{T}} + 2g\left(\frac{\sigma_{22}^{m}}{Y_{is}^{T}}\right)\frac{d\sigma_{22}^{m}}{dr} + \frac{d\sigma_{12}^{m}/dr}{S_{is}^{L}} \tag{7.7.2.10}$$

$$\frac{d\tau_{12}^{m}}{dr} = -\cos 2\varphi \cdot \varphi' \cdot (\sigma_{11} - \sigma_{22}) - \frac{1}{2}\sin 2\varphi \cdot (\sigma_{11}' - \sigma_{22}') - 2\sin 2\varphi \cdot \varphi' \cdot \tau_{12} + \cos 2\varphi \cdot \tau_{12}' \tag{7.7.2.11}$$

$$\frac{d\sigma_{22}^{m}}{dr} = \sin 2\varphi \cdot \varphi' \cdot (\sigma_{11} - \sigma_{22}) + \sin^2\varphi \cdot \sigma_{11}' + \cos^2\varphi \cdot \sigma_{11}' - 2\cos 2\varphi \cdot \varphi' \cdot \tau_{12} - \sin 2\varphi \cdot \tau_{12}' \tag{7.7.2.12}$$

$$\frac{d\sigma_{11}^{m}}{dr} = -\sin 2\varphi \cdot \varphi' \cdot (\sigma_{11} - \sigma_{22}) + \cos^2\varphi \cdot \sigma_{11}' + \sin^2\varphi \cdot \sigma_{22}' + 2\cos 2\varphi \cdot \varphi' \cdot \tau_{12} + \sin 2\varphi \cdot \tau_{12}' \tag{7.7.2.13}$$

$$\frac{d\varphi}{dr} = \frac{[|\tau_{12}| + (G_{12} - X^C)\varphi^C]}{(G_{12} + \sigma_{11} - \sigma_{22})^2}(\sigma_{11}' - \sigma_{22}') \text{ (assume } \tau_{12} \text{ is constant here)} \tag{7.7.2.14}$$

$$\frac{d\sigma_{11}}{dr} = \cos t \quad \text{and} \quad \frac{d\sigma_{22}}{dr} = \sin t \tag{7.7.2.15}$$

The Newton-Raphson method proved to be very efficient solving the above nonlinear equations, particularly when a lot of points in the failure envelopes need to be calculated.

7.8 Implementation of Hashin Failure Theory

Two issues have to be solved before Hashin failure criteria (2D and 3D versions) are implemented: 1) the availability and credibility of input parameters; 2) numerical methods for generation of failure envelopes and calculation of margins of safety (MS). These two issues will be discussed below.

7.8.1 Input parameters for Hashin failure criterion

Six unidirectional material parameters are required for the input of Hashin failure criteria. They are listed in Table 7.8.1.

Table 7.8.1, Required UD material properties for Hashin failure criteria

X_T	Longitudinal tensile strength of UD lamina
X_C	Longitudinal compressive strength of UD lamina
Y_T	Transverse tensile strength of UD lamina
Y_C	Transverse compressive strength of UD lamina
S	In-plane shear strength of UD lamina
S_T	the interlaminar shear strength of UD lamina

The material parameters in Table 7.8.1 are common unidirectional lamina data, which can be obtained from either standard tests or various composite design handbooks, such as MIL-HDBK-17. It is noticed that in both 2D and 3D versions of Hashin criteria, there are two shear strengths used: in-plane shear strength S and interlaminar shear strength S_T. In practical design, S and S_T are sometimes not distinguished for UD fibrous lamina since the two shear strengths mainly result from the same failure mechanism, i.e., the failure of resin between fibers. However, it can be seen that the error will be introduced with respect to Hashin 3D failure criterion, if $S = S_T$. Thus, there is a concern about the relation between the actual values of S and S_T. Of course, this is not a problem if the value of S_T is known for a particular composite. Paris [7.21] did a parametric study in terms of the relative values of S_T with respect to S, taking S as the value corresponding to a particular material, AS/3501. In the study, Paris took different values of *k* in the relation: $S_T = k\,S$, where *k* has been taken, for the purpose of covering the whole range of possible situations, with values greater and smaller than 1. It was found that if S_T is smaller than S, it leads to conservative predictions. In addition, for a given value of *k*, the error is a function of the stress state. The error is greater when σ_{12} is not dominant versus σ_{22} and starts to decrease rapidly when σ_{12} starts to become dominant.

7.8.2 Generation of failure envelopes and calculation of margin of safety

Generating failure envelopes for Hashin failure criteria in a given plane is not difficult since all the variables (stress components) in the equations are explicit. In the following, we will describe the procedure of failure envelope generation by taking an example of Hashin 2D failure criterion for the tensile fiber failure mode ($\sigma_{11} > 0$). Let's look at the equation,

$$\left(\frac{\sigma_{11}}{X_T}\right)^2+\left(\frac{\sigma_{12}}{S}\right)^2=1 \tag{7.8.2.1}$$

In the σ11-σ12 plane, the points (σ11, σ12) can be also expressed in polar coordinate system, as

$$\sigma_{12}=r\sin t \quad \text{and} \quad \sigma_{11}=r\cos t \tag{7.8.2.2}$$

where *r* is the module of projection from the origin to the point on the failure envelope; *t* is the angle of the projection. Thus, if the angle is given, the point on the envelope can be determined when the *r* is known. Substituting Eqn. (7.8.2.2) into (7.8.2.1) yields

$$\left(\frac{r}{X_T}\right)^2\cos^2 t+\left(\frac{r}{S}\right)^2\sin^2 t=1 \tag{7.8.2.3}$$

thus, *r* can be easily solved for a given angle *t*, that is

$$r=\frac{1}{\sqrt{\left(\frac{\cos t}{X_T}\right)^2+\left(\frac{\sin t}{S}\right)^2}} \tag{7.8.2.4}$$

Then, substitution of the solved variable *r* and given angle *t* into Eqn. (7.8.2.2) would give the values of σ11 and σ12. This procedure can be applied to generate the failure envelopes of any Hashin failure criterion at any given plane.

Another method commonly used for generating failure envelopes is a purely numerical approach based on the same principle described above. Instead of a solving the variable explicitly from the equations, the numerical method takes "trial-and-correct" procedure to approach the solution iteratively. For example, when solving Eqn. (7.8.2.3), one could give an initial value for r arbitrarily, and then calculate the difference between the result of the left hand-side of equation and the value of 1 at the right-hand side. Then use the difference to adjust the initial value for r and repeat the procedure till the difference falls into tolerable range. The advantage of this method is that it can be applied to almost any form of failure criteria regardless of the expressions of the equations. However, this method proves to be inefficient when many points need to be calculated.

The margin of safety of Hashin failure criteria can be calculated using the procedure described in Vol.3, Chapter 15.

7.9 Implementation of Strain Invariant Failure Theory (SIFT)

7.9.1 Conditions of using SIFT for matrix failure

SIFT provides two failure criteria for matrix failure, the dilatational strain invariant, J_1 and the equivalent strain invariant, $\varepsilon_{equivalent}$. From tests of off-axis unidirectional IM7/epoxy composite lamina, Gosse [7.2] observed that when the ply angle is less than 30 degrees, $\varepsilon_{equivalent}$ controls; while between 30 and 90 degrees, J_1 controls, as shown in Fig. 7.9.1. However, this treatment does not account for matrix failure under compression. The dilational strain, J_1, basically accounts for void growth and it is reasonable to be used as the criterion for matrix cracking under tension. It seems unsound to apply J_1 to address the matrix failure under compression. Gosse has not addressed this issue in his recent publication [7.1]. Instead, Kelly [7.40] believes that the J_1 criterion is suited only to interlaminar failure of composite structures subjected to tension–tension load cases where failure is dominated by volume increase of the matrix. In all other load cases, it is more appropriate to use criteria such as von Mises strain criterion to predict the matrix failure dominated by distortion. As such, we used the following form of SIFT in our implementation.

The SIFT method as described in [7.2] and [7.3] was implemented using HyperSizer Micromechanics. The initial attempts to verify against Gosse's results have been unsuccessful. From our observations and communications with other industry method developers, the consensus is there are missing key pieces of information that have not been released in the publicly available documentation. We believe this is the reason we are not yet successfully implementing the full SIFT method.

For matrix:	For fiber
If $J_1 \geq 0$, $J_1 \geq J_1^{critical}$ If $J_1 < 0$, $\varepsilon_{equivalent} \geq \varepsilon_{equivalent}^{critical}$	$\varepsilon_{equivalent} \geq \varepsilon_{equivalent}^{critical}$

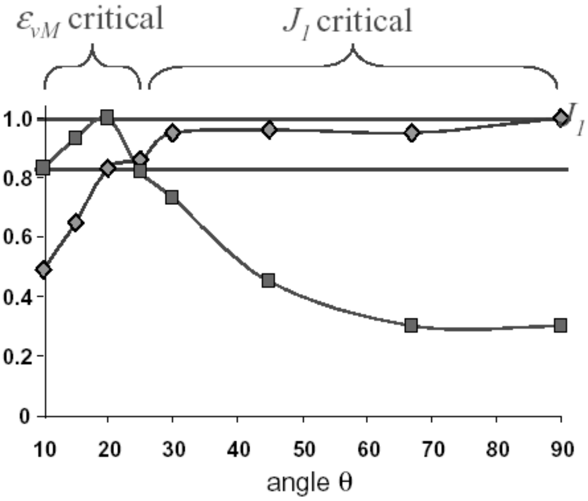

Fig. 7.9.1, Measurement of critical strain invariants in the matrix of IM7/epoxy composites.

7.9.2 Critical values of the strain invariants

Obtaining the critical values of J_1 and $e_{\text{equivalent}}$ has two different choices. The first method was used by Gosse, who backed out these values from global–to-micro FE models of specimens under the actual failure loads. The second method uses the bulk constituent material strength data to calculate the J_1 and $\varepsilon_{\text{equivalent.}}$ For example, in uni-axial tension or compression tests, the yield strain, $\varepsilon_{\text{yield}}$, is available and can be used to find $J_1^{critical}$.

$$J_1^{critical} = \varepsilon_1 + \varepsilon_2 + \varepsilon_3 = \varepsilon_{yield} + (-2v)\varepsilon_{yield} = (1-2v)\varepsilon_{yield} \tag{7.9.1.1}$$

or if we know $J_1^{critical}$, the yield strain $\varepsilon_{\text{yield}}$ can also be backed out from Eqn. (7.9.1.1). This relation is quite useful, particularly when the experimental value of $J_1^{critical}$ is not available. Likewise, the equivalent strain $\varepsilon_{eq}{}^{critical}$ can be obtained from the relation,

$$\varepsilon_{equivalent}^{critical} = \sqrt{0.5[(\varepsilon_{yield} + v_{12}\varepsilon_{yield})^2 + (\varepsilon_{yield} + v_{13}\varepsilon_{yield})^2 + (-v_{12}\varepsilon_{yield} + v_{13}\varepsilon_{yield})^2]} \tag{7.9.1.2}$$

For fibers, $v_{12} = v_{13}$, so Eqn. (7.9.1.2) reduces to

$$\varepsilon_{equivalent}^{critical} = (1 + v_{12})\varepsilon_{yield} \tag{7.9.1.3}$$

7.9.3 Margin of Safety

The margin of safety for SIFT can be obtained by using the procedure described in Vol.3, Chapter 15. The result is given as

$$MOS_{J1} = \frac{J_1^{critical}}{\varepsilon_1 + \varepsilon_2 + \varepsilon_3} - 1 \tag{7.9.1.4}$$

$$MOS_{\varepsilon e} = \frac{\varepsilon_{equivalent}^{critical}}{\sqrt{\frac{1}{2}\left[(\varepsilon_1 - \varepsilon_2)^2 + (\varepsilon_2 - \varepsilon_3)^2 + (\varepsilon_1 - \varepsilon_3)^2\right]}} - 1 \tag{7.9.1.5}$$

7.9.4 Multi-scale analysis exploring the fields in fiber and matrix phases

Multi-scale analysis was performed by using HyperSizer to find the fields from laminate level to constituent (micro) level, as shown in Fig. 7.9.2. In particular, the micro-level analysis was performed using *HyperSizer Micromechanics*, a computationally efficient, user-friendly, micromechanics analysis code designed for accurately predicting the elastic and inelastic thermomechanical response of multiphased materials including polymer-, ceramic-, and metal-matrix composites. The underlying analytical engine of HyperSizer Micromechanics is the NASA developed Micromechanics Analysis Code/Generalized Method of Cells (MAC/GMC) [7.42, 7.43].

MAC/GMC can predict the elastic and inelastic thermomechanical response of both continuous and discontinuous multiphased composite materials with an arbitrary internal microstructure and reinforcement shape. It computes this response based on closed-form expressions for the macroscopic composite response in terms of the properties, size, shape, distribution, and response of the individual constituents or phases that make up the material. GMC allows the use of any inelastic (e.g., viscoplastic) deformation and/or life (e.g., fatigue) constitutive models to describe each constituent phases' (e.g., fiber, interface, matrix, etc.) behavior. Thus, *HyperSizer Micromechanics* is ideally suited for conducting sensitivity/parametric studies, enabling engineers and material scientists to easily and accurately design a composite material for a given application.

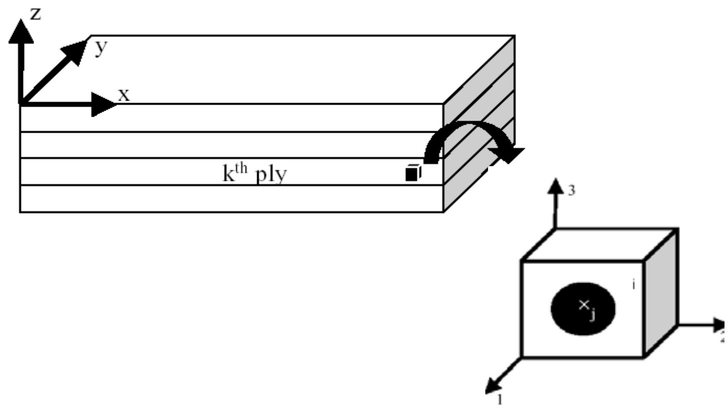

Fig. 7.9.2, Multi-scale analysis from laminates to constituents.

The implementation of SIFT determines the maximum strain invariants for the fiber/matrix constituents based on Eqn. (7.9.1.5) and returns the minimum margin of safety.

7.9.5 Verification

The verification cases were selected from Gosses's examples [7.2] of UD un-notched uniformly strained IM7/977-3 lamina (fiber orientation varied between 15° and 90°, relative to the loading axis). Table 7.9.1 summarizes the failure loads from these examples

Table 7.9.1, Failure loads for matrix dominated lamina (IM7/977-3 tape)

case	Fiber angle (degree)	Fracture strain (in/in)	Fracture stress (ksi)	Failure load (lb)
1	15	0.01203	57.67	11.534×10^3
2	20	0.01483	41.50	8.300×10^3
3	25	0.01412	33.35	6.670×10^3
4	30	0.01454	27.92	5.584×10^3
5	45	0.01263	16.74	3.348×10^3
6	67	0.00996	12.76	2.552×10^3
7	90	0.01013	12.38	2.476×10^3

Figure 7.9.3 shows stress-strain curves for the tested lamina of 15 20 25 30, 45, 67 and 90 -degrees. It can be seen that 15, 20 25 and 30 –degree lamina show very strong nonlinearity.

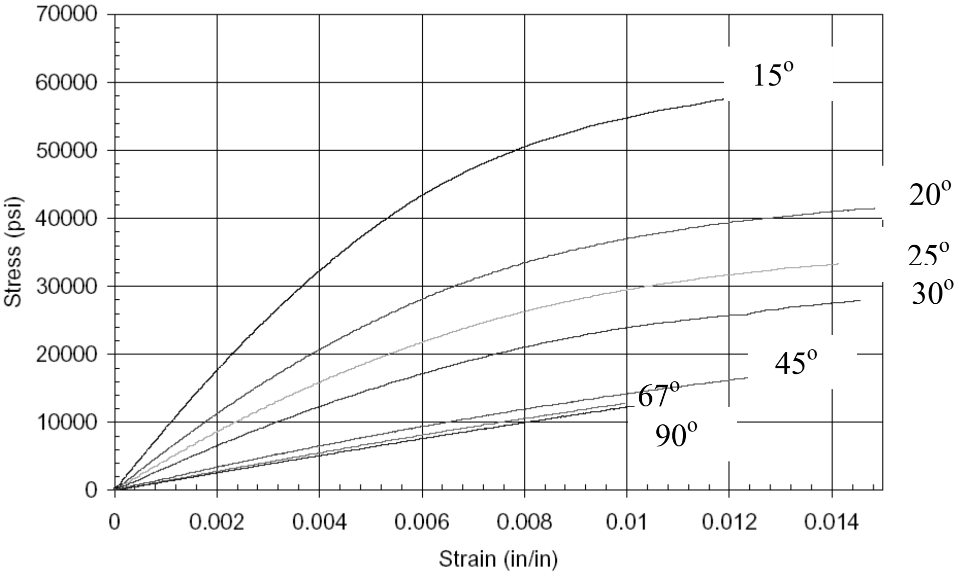

Fig. 7.9.3, Experimental stress-strain curves for IM7/977-3 lamina under tension.

The material properties of constituents are given below by Gosse.

Table 7.9.2, material properties of IM7 fiber and 977-3 resin

	E_{11} (msi)	E_{22} (msi)	G_{12} (msi)	G_{23} (msi)	ν_{12}	ν_{23}	a_1	a_2
IM7 fiber	39.30	2.50	4.00	1.20	0.32	0.20	-0.60	4.60
977-3 Resin	0.55	0.55	0.202	0.202	0.36	0.36	32.00	32.00

The effective critical matrix strain invariants were derived for IM7/977-3 using Gosses's FE micromechanics model. The results are copied below for reference.

Table 7.9.3, Maximum point, phase average, and homogenized lamina effective strain invariants within the matrix phase of the matrix dominated UNT data

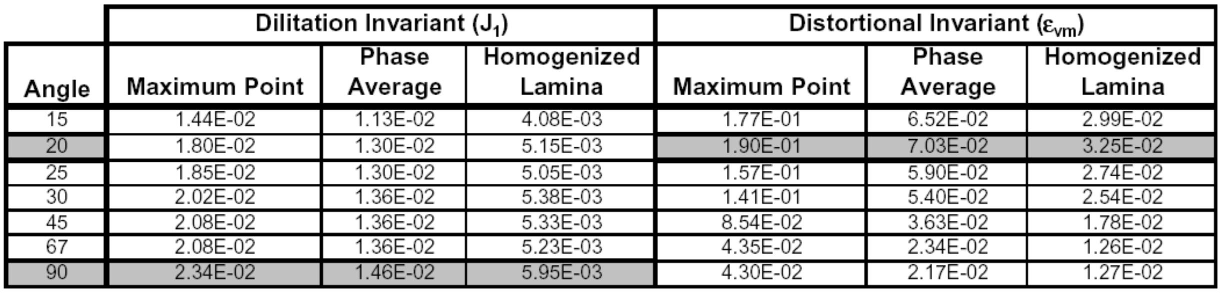

	Dilitation Invariant (J_1)			Distortional Invariant (ε_{vm})		
Angle	Maximum Point	Phase Average	Homogenized Lamina	Maximum Point	Phase Average	Homogenized Lamina
15	1.44E-02	1.13E-02	4.08E-03	1.77E-01	6.52E-02	2.99E-02
20	1.80E-02	1.30E-02	5.15E-03	1.90E-01	7.03E-02	3.25E-02
25	1.85E-02	1.30E-02	5.05E-03	1.57E-01	5.90E-02	2.74E-02
30	2.02E-02	1.36E-02	5.38E-03	1.41E-01	5.40E-02	2.54E-02
45	2.08E-02	1.36E-02	5.33E-03	8.54E-02	3.63E-02	1.78E-02
67	2.08E-02	1.36E-02	5.23E-03	4.35E-02	2.34E-02	1.26E-02
90	2.34E-02	1.46E-02	5.95E-03	4.30E-02	2.17E-02	1.27E-02

The strain invariant failure theory states that composite materials exhibit the onset of irreversible events for one of two deformation modes, dilatation as measured by J_1, and distortion as measured by e_{vm}. As shown in Table 7.9.3, the homogenous, phase -averaged and maximum point enhanced representations of the lamina critical strain invariants all demonstrate the same trends. That is, as the fiber orientation of the lamina decreases the failure mechanism shifts from dilatational -dominant to distortional dominant. The trends are gradual where the deformation mode describing failure is dominant. The data in Table 7.9.3 shows that there are two failure modes that compete and that these two failure modes mirror the two deformation modes. Therefore, if there are two deformation modes, then there should be two critical deformation modes describing failure. One will always dominate except where both are coincident (from Fig. 7.9.3 this would be somewhere around 25° for the material system IM7/977-3). Table 7.9.3 gives experimental verification of the existence of two effective critical deformation mechanisms (dilatation (J_1) and distortion (e_{vm}) with respect to the matrix constituent within the composite material IM7/977-3.

Efforts of verification

HyperSizer Micromechanics uses rectangular subcells to represent the matrix and fiber phases, as shown in Fig. 7.9.4. The region in blue color represents fiber and the grey region represents matrix. The initial effort was made to compare the effective properties of composites using different unit cell configurations with those predicted by Gosse using FEA. The results are listed in Table 7.9.4. It can be seen that the values of v_{23} and G_{23} predicted by HS micromechanics are substantially different (>30) from the FEA results.

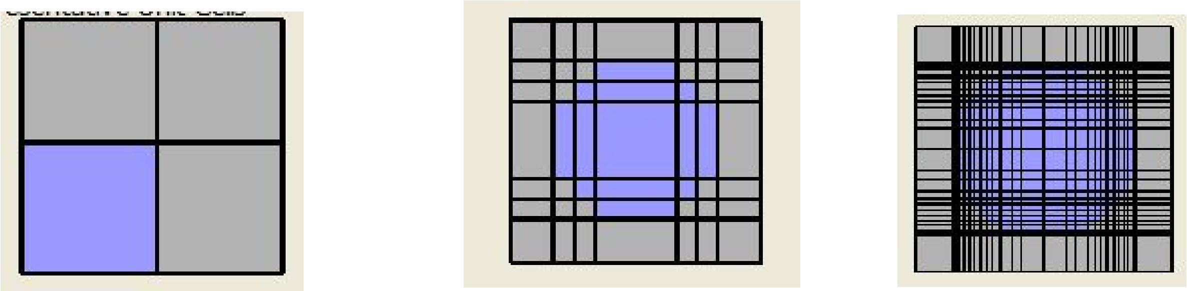
(a) (b) (c)

Fig. 7.9.4, configurations of unit cells a) 2 by 2 subcells b) 7 by 7 subcells c) 26 by 26

Table 7.9.4, Comparison of predicted effective properties of IM7/977-3 ($V_f = 0.60$)

	E_1 (Msi)	**E_2 (Msi)**	**E_3 (Msi)**	**v_{12}**	**v_{23}**	**G_{12} (Msi)**	**G_{13} (Msi)**	**G_{23} (Msi)**
MAC 2x2	23.8	1.446	1.446	0.34	0.27	0.64	0.64	0.40
MAC 7x7	23.8	1.418	1.418	0.34	0.28	0.69	0.69	0.40
MAC 26x26	23.8	1.409	1.409	0.34	0.29	0.66	0.66	0.40
FEA	23.8	1.31	1.31	0.36	0.394	0.707	0.707	0.498

Next, the margin of safety was calculated using SIFT with MAC/GMC for the different angled laminae using the three different subcell configurations. It should be mentioned that in this effort, the critical value of J_1 for the matrix is derived from Gosse's calculation for 90-degree lamina, i.e., $J_1 = 2.34e-2$. The yield strain is then backed out from Eq. (7.9.2.1), $\varepsilon_{yield} = 8.36e-2$ in/in for matrix and $\varepsilon_{yield} = 3.38e-2$ in/in for fiber. Table 7.9.5 summarizes the predicted values of J_1 and margins of safety at the reported failure loads. If the method is obtaining accurate results, the margins of safety should be zero for each case.

Table 7.9.5, MOS ($J_1^{critical} = 2.34e-2$) and predicted J_1 in the matrix phase under failure loads

	Nx = 2476 (N/mm) for [90°]		Nx = 2552 (N/mm) for [67°]		Nx = 3348 (N/mm) for [45°]		Nx = 5584 (N/mm) for [30°]		Nx = 6670 (N/mm) for [25°]	
	MOS	J_1 x10^{-2}	MOS	J_1 x10^{-2}	MOS	J_1 x10^{-2}	MOS	J_1 x10^{-2}	MOS	J_1 x10^{-2}
MAC 2x2	1.904	0.8058	2.315	0.7059	3.217	0.2371	3.878	0.4797	4.304	0.5437
MAC 7x7	1.932	0.7981	2.346	0.6993	3.257	0.7184	3.921	0.4755	4.240	0.4466
MAC 26x26	1.530	0.9249	-1	inf	-1	inf	-1	inf	-1	inf

It can be seen that large errors occur in all of the situations listed in Table 7.9.5. This may result from the difference between FEA and MAC/GMC. Fig. 7.9.5 shows those errors more clearly. Table 7.9.6 shows the local strain fields calculated by *HyperSizer micromechanics*.

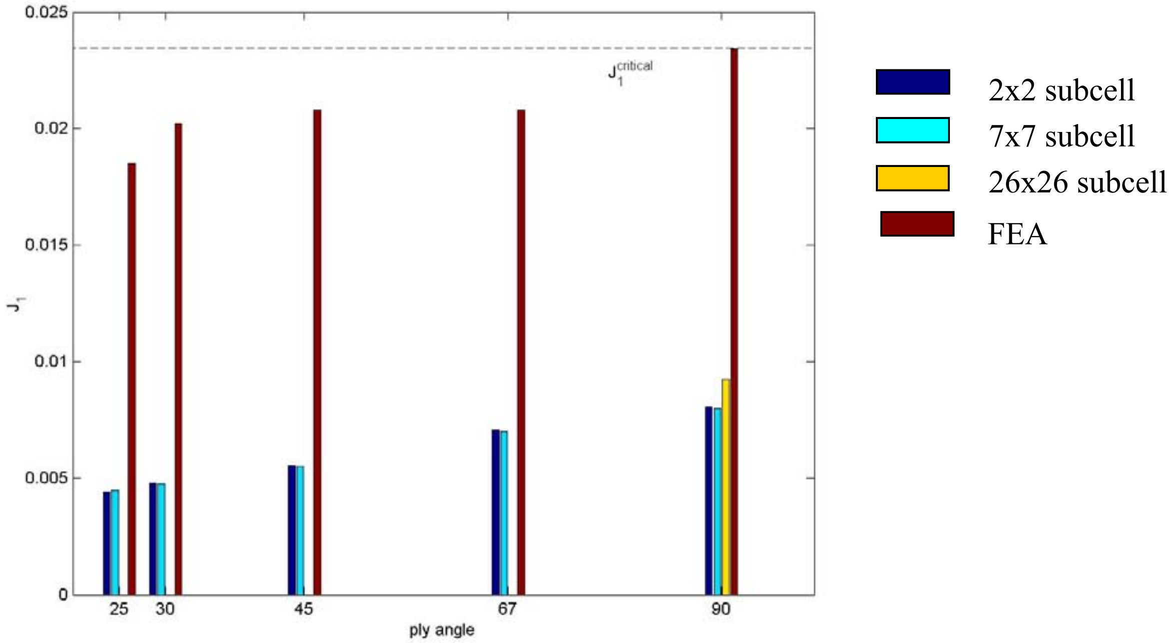

Fig. 7.9.5, Comparison of matrix phase J_1 predicted by Gosse and HyperSizer under failure loads

Table 7.9.6, local strain fields (26 by 26 subcells) in the angle-ply lamina using $J_1^{critical} = 2.34e\text{-}2$

	ε_{11}	ε_{22}	ε_{33}
90°	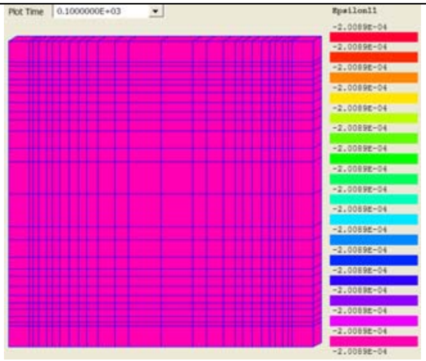	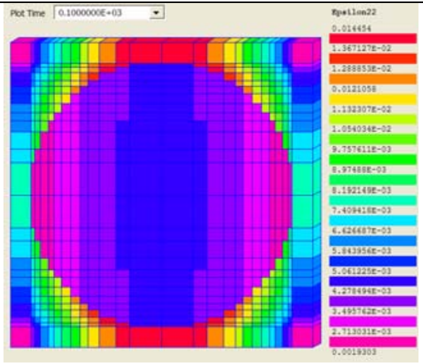	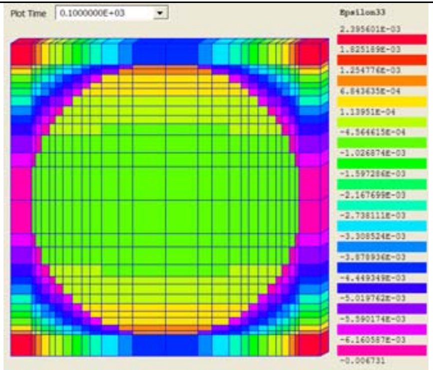
67°	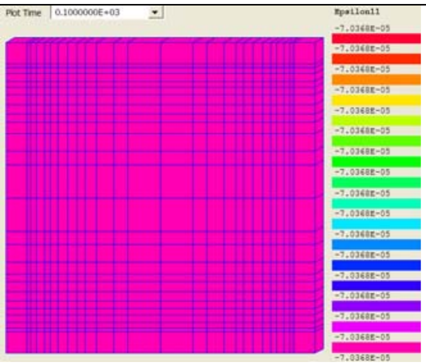	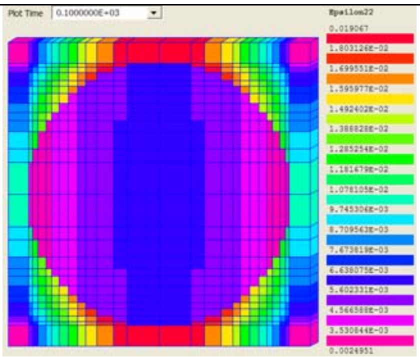	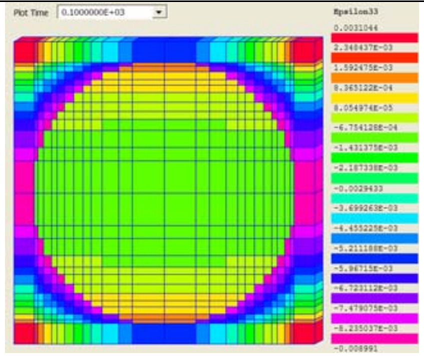
45°	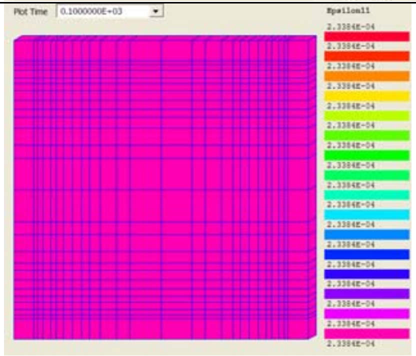	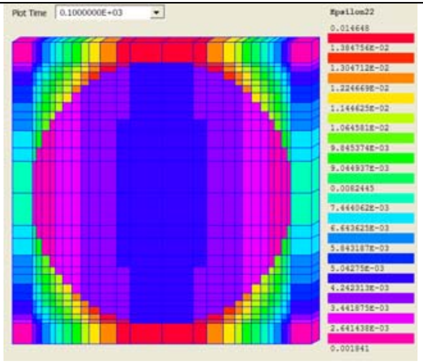	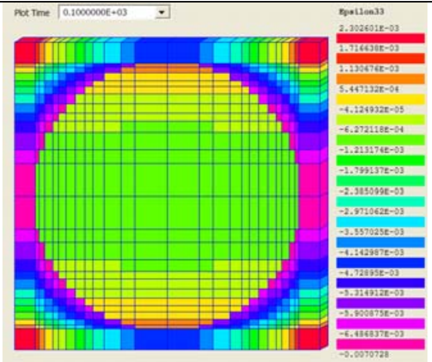
30°	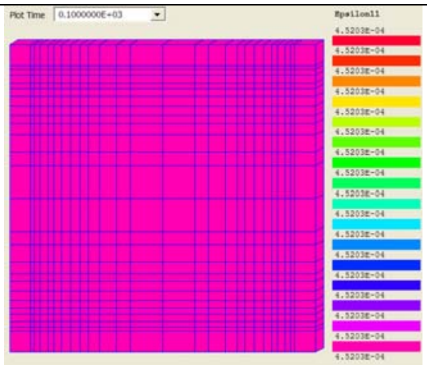	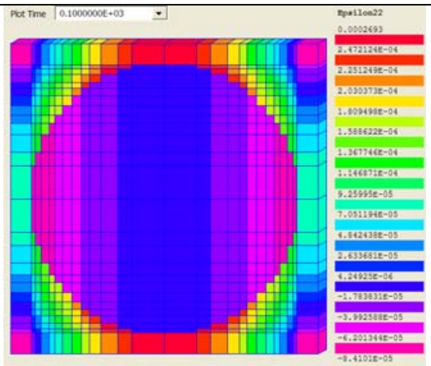	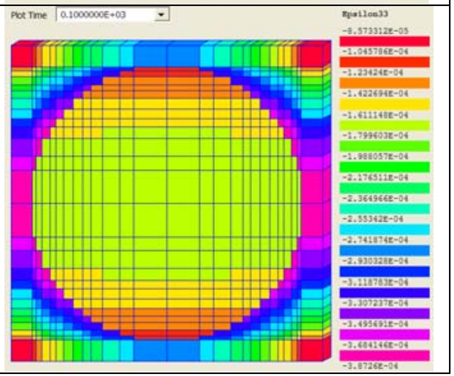

25°	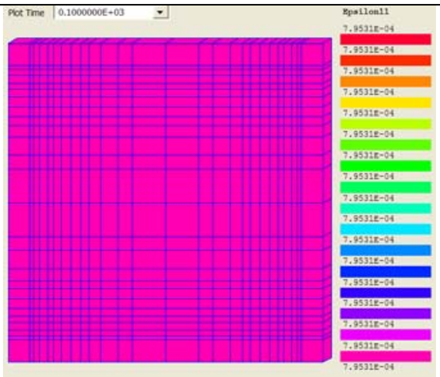	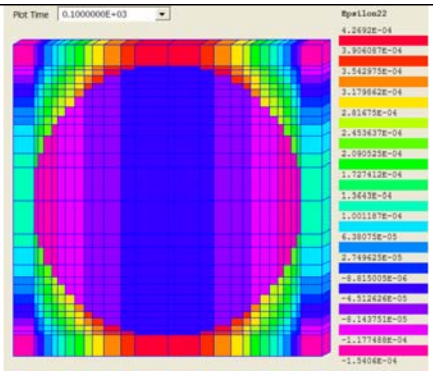	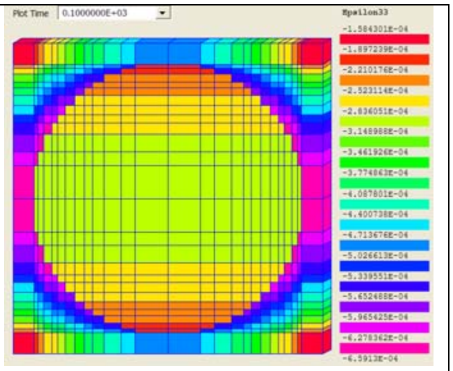

The large differences shown above may result from the discrepancy of accuracy of HyperSizer micromechanics and FEA. We could get the clue from the results of effective properties predicted by FEA and HyperSizer, as shown in Table 7.9.7. Note that comparing HyperSizer with FEA is not the purpose of this study, but rather verifying HyperSizer's implementation of SIFT. Thus, the critical values of strain invariants should be from HyperSizer, not from FEA if we try to verify SIFT using HyperSizer in all the cases.

The following effort was made to verify SIFT using $J_1^{critical}$ derived from HyperSizer. First, we selected 90-degree lamina and make a parametric study of ε_{yield} to find the critical value of J_1. The $J_1^{critical}$ in the matrix found by HyperSizer is 0.798e-2 (ε_{yield} = 2.85e-2). Table 7.9.7 summarizes the predicted values of J_1 in the matrix phase and MOS. It can be seen that the J_1 values predicted are not constants at the failure loads. The variation of J_1 is still large, as shown clearly in Fig. 7.9.6.

Table 7.9.7, MOS ($J_1^{critical}$ = 0.798 e-2) and predicted J_1 in the matrix phase under failure loads

	Nx = 2476 (N/mm) for [90]		Nx = 2552 (N/mm) for [67]		Nx = 3348 (N/mm) for [45]		Nx = 5584 (N/mm) for [30]		Nx = 6670 (N/mm) for [25]	
	MOS	J_1 x10^{-2}	MOS	J_1 x10^{-2}	MOS	J_1 x10^{-2}	MOS	J_1 x10^{-2}	MOS	J_1 x10^{-2}
MAC 2x2	0	0.798	0.1300	0.7062	0.4377	0.5550	0.6630	0.4798	0.8915	0.4210
MAC 7x7	0	0.798	0.1408	0.6995	0.4511	0.5499	0.6776	0.4757	0.9110	0.4176
MAC 26x26	0	0.798	0.1344	0.7034	0.4432	0.5529	0.6690	0.4798	0.9017	0.4196

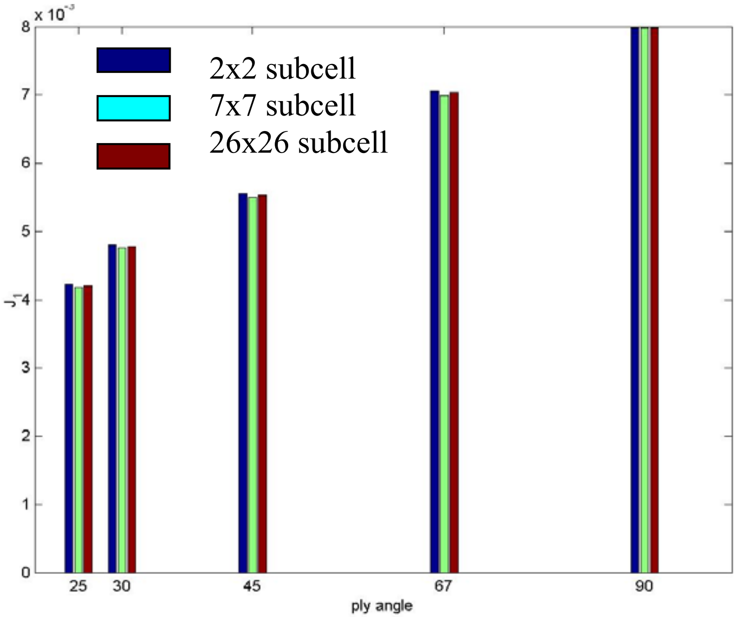

Fig. 7.9.6, J_1 in the matrix phase predicted by HyperSizer under failure loads

Another possible factor which may contribute to the large variation of J_1 is material nonlinearity. In Fig.7.9.3, it clearly shows that the laminae exhibit nonlinearity under uniaxial tension, particularly the 15, 20, 25, 35 –degree laminates. Thus, using linear elastic analysis is inappropriate, particularly using the failure stress as the input failure load for HyperSizer micromechanics. Instead, we tried to use failure strain as the failure load input. Again, we need to find out the critical value of J_1 with HyperSizer. The critical J_1 was found as 0.9548e-2 (ε_{yield} = 3.41e-2) through parametrical study. Table 7.9.8 summarizes the results of MOS and J_1 in the matrix predicted using $J_1^{critical}$ = 0.9548e-2 and under failure strain instead of failure stresses. Fig. 7.9.7 shows the variation of J_1 predicted. It can be seen that in this effort the variation of J_1 decreases compared to previous two efforts.

Table 7.9.8, MOS ($J_1^{critical}$ = 0.9548e-2) and predicted J_1 in the matrix phase under failure loads

	ε_{xx} = 0.01013 for [90]		ε_{xx} = 0.00996 for [67]		ε_{xx} = 0.01263 for [45]		ε_{xx} = 0.01454 for [30]		ε_{xx} = 0.01412 for [25]	
	MOS	J_1 x10^{-2}	MOS	J_1 x10^{-2}	MOS	J_1 x10^{-2}	MOS	J_1 x10^{-2}	MOS	J_1 x10^{-2}
MAC 2x2	0	0.9548	0.2071	0.7910	0.2962	0.7366	0.3589	0.7026	0.4802	0.6450
MAC 7x7	0	0.9548	0.2105	0.7888	0.2527	0.7622	0.2946	0.7375	0.4078	0.6782
MAC 26x26	0	0.9548	0.2213	0.7818	0.2780	0.7471	0.3260	0.7200	0.4422	0.6620

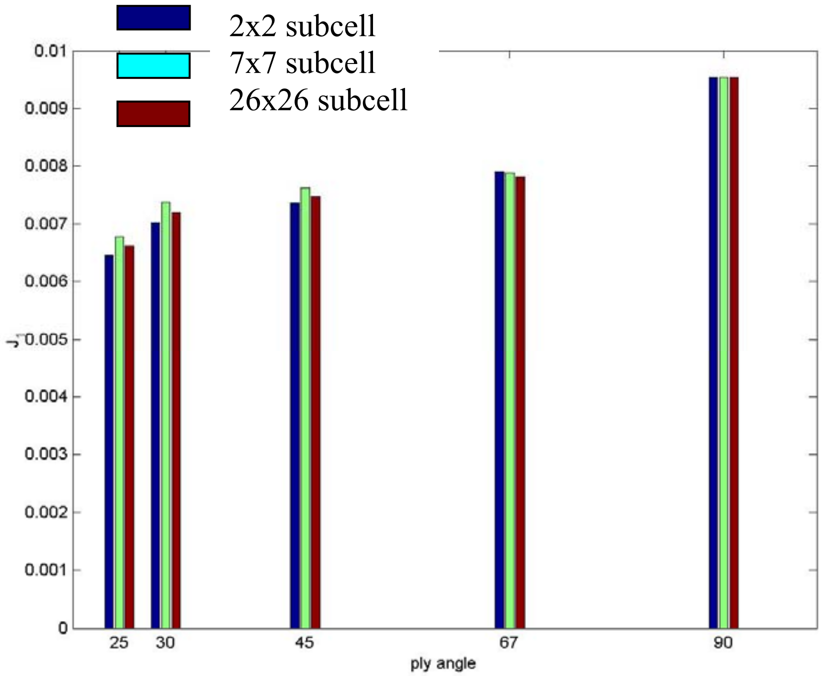

Fig. 7.9.7, J_1 in the matrix phase predicted by HyperSizer under failure loads

7.9.6 Discussion

SIFT has been implemented into HyperSizer through the MAC/GMC load margin capability, but the verification has been challenging and obviously more work needs to be done.

1. The verification cases were selected from the tension tests by Gosse of 25, 30, 45, 67 and 90 –degree UD lamina. Fig. 7.9.3 clearly shows the non-linear behavior of the material as the ply angle decreases. Gosse's finite element based micromechanics model did not take into account nonlinearity, so it is unclear to us how it was able to overcome this limitation and match the test data.

    a. Gosse explains that "The nonlinear behavior is mainly precipitated by the changing Poisson's ratio with increasing strain up to the yield point. At the yield point the Poisson's ratio of the neat polymer in tension is approximately 1/2 and consequently behaves as an incompressible material from the yield point to ultimate failure. Incompressible behavior equates to a stable J_1 strain with an increasing equivalent strain from the yield point to ultimate failure and consequently the equivalent distortional mechanism dominates. It is for the same reasons that nonlinear behavior is exclusively exhibited by the distortional dominated lamina. The effect of increasing Poisson's ratio causes an increase in the equivalent strains and a decrease in the J1 strains from the linear elastic strain. The present analysis is not currently accounting for the increase in equivalent or the decrease in J1 due to a lack of definition of the change in Poisson's ratio with increasing strain." So it seems that, despite not taking the nonlinearity into account, even through an alteration of the Poisson ratio as he suggests, Gosse somehow manages to achieve reasonable results.

2. The local strain fields predicted by MAC/GMC and those predicted by FEA are expected to be different. We should not attempt to compare MAC/GMC results to FEA because first, it is not our purpose (our purpose is to verify our SIFT implementation). Secondly, MAC/GMC and FEA both are approximate methods, which are hardly verified by each other. For the current problem, many details of the FEA models used by Gosses are not clear, such as boundary conditions on the laminate level to match up with the test conditions, and convergence test of the meshes used for the micromechanics model. We suspect that Gosse's results are dependent on the level of FE mesh refinement, as this would effect the J_1 concentration in the FE results.

3. A better evaluation of the effectiveness of SIFT would be to enter "good" fiber-matrix constitutive properties for laminae from the WFE and then use SIFT to try to predict initial failure (which is all SIFT can do for cases where the laminate exhibits progressive failure) and final failure in the cases where there is no progressive damage.

4. We also question whether SIFT can significantly improve the accuracy of micromechanics-based failure prediction compared to some simple criteria, such as max strain/stress, etc. Although SIFT is physically based, it cannot fully explain the matrix compression failure mechanism.

5. It may be that SIFT tends to work well in the context of FEA micromechanics. Has it been shown that SIFT is better than max stress, for instance, employed on the micro-level in FEA? If so, this could be related to the mesh-dependent concentrations that arise in FEA micromechanics. (In the context of trying to compare to Gosse's problem, this might be difficult to determine. This is because of the problem becomes non-linear, we can compare either to a strain based criteria, or a stress based criteria, but not both simultaneously, see 11 below) Perhaps SIFT overcomes some of the difficulties associated with comparing a maximum value from a concentration with an allowable (we have seen this problem with Bondjo and BJSFM, where it seems that a characteristic distance must be used rather than the absolute peak value). In MAC/GMC, on the other hand, the concentrations are muted (i.e., averaged out) by the GMC formulation. As such, this problem related to the high concentration are less of an issue.

6. A relatively new addition to MAC/GMC called the High Fidelity Generalized Method of Cells (HFGMC) is more like FEA and would be expected to behave somewhere between FEA and GMC with respect to SIFT and other micro-scale failure criteria. This method will be implemented in a future release of HyperSizer Micromechanics.

7. As shown in Figure 7.9.8, we are attempting to correctly capture the local strains (actually local J_1) in the composite by applying the global stress or strain based on elastic analysis. Thus, while we are applying the correct global failure stress in case 1, the strain is completely wrong. Conversely, in case 2, we are applying the correct global failure strain, but the wrong stress. Without getting both of these correct, it is difficult to see how we will be able to extract a reasonable local J1 to compare to the allowable J1. It is also difficult to see how the Gosse FEA micromechanics analysis was able to accomplish this.

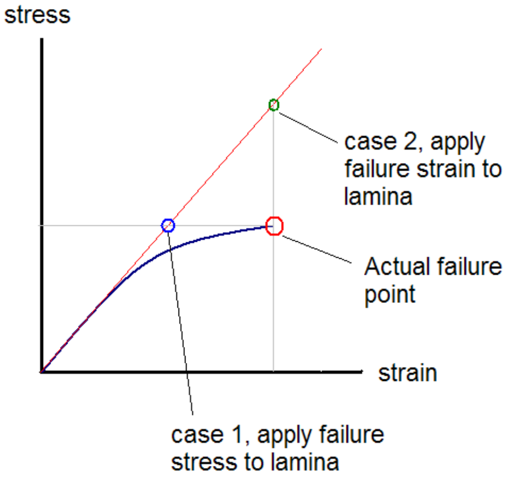

Fig. 7.9.8, Dealing with nonlinearity when implantation of SIFT.

7.10 References

7.1 Davila, C. G. and Camanho, P. P., “Analysis of the effects of residual strains and defects on skin/stiffener debonding using decohesion elements,” 44th AIAA/ASME/ASCE/AHS, SDM conference, 2003, Norfolk, VA.

7.2 Gosse, J. H., Christensen S., Wollschlager, J. A., Llanos A., 2004, “A Strain Invariant Failure Theory (SIFT) for Composite Materials,” submitted to Journal of Composite Materials.

7.3 Gosse, J. H., 2001, “Strain Invariant Failure Criteria for Polymers in Composite Materials,” 42nd AIAA SDM conference, Seattle, WA.

7.4 Hinton M. J., Soden P. D., “Predicting failure in composite laminates: the background to the exercise,” Compos. Sci. Tech, Vol.58, 1998, pp.1001–10.

7.5 Soden, P.D., Hinton, M.J., and Kaddour, A.S., "A Comparison of the Predictive Capabilities of Current Failure Theories for Composite Laminates," Composites Science and Technology, Vol. 58, No. 7, 1998, pp.1225-1254.

7.6 Hinton, M.J., Kaddour, A.S., and Soden, P.D., "A Comparison of the Predictive Capabilities of Current Failure Theories for Composite Laminates, Judged against Experimental Evidence," Composites Science and Technology, Vol. 62, No. 12-13, 2002, pp. 1725-1797.

7.7 Puck, A., Kopp, J., and Knops, M., “Guidelines for the determination of the parameters in Puck’s action plane strength criterion,” *Compos. Sci. Tech*, Vol.62, 2002, pp.371–378.

7.8 Rousseau, C. Q., 2003 “A Range of Practical Failure Criteria for Laminated Composites”, Composite Materials: Testing and Design, Fourteenth Volume, ASTM STP 1436, C.E. Bakis, Ed., ASTM International, West Conshohocken, PA.

7.9 MIL-HDBK-5J, Metallics

7.10 Jackson Jana and Rice Richard, PRELIMINARY MATERIAL PROPERTIES HANDBOOK, Materials & Manufacturing Directorate, Air Force Research Laboratory AFRL-ML-WP-TR-2001-4027, July 2000, Chapter 9 - Statistical and Data Presentation Guidelines

7.11 Whitney, J., and Nuismer, R., “Stress Fracture Criteria for Laminated Composites Containing Stress Concentrations,” Journal of Compostie Materials, V8, July 1974, pp253-265

7.12 Nuismer, R. and Whitney, J., “Uniaxial Failure of Composite Laminates Containing Stress Concentrations”, Fracture Mechanics of Composites, ASTM STP 593, ASTM, 1975, pp. 117-142.

7.13 Bau, Hui and Hoyt D.M., “Characterizing Notched Composites Strength with Empirical and Analytical Methods”, STTR AF96T009 – Phase II Final Report, 24April00

7.14 Tsai, S.W. (1968) “Strength Theories of Filamentary Structures” in R.T. Schwartz and H.S. Schwartz (Eds.), *Fundamental Aspects of Fiber Reinforced Composites*, Wiley Interscience, New York, 3-11.

7.15 Tsai, S.W. and Wu, E.M. (1971) “A General Theory of Strength for Anisotropic Materials” *Journal of Composite Materials*, 58-80.

7.16 Jones, R.M. (1975) *Mechanics of Composite Materials*, Hemisphere Publishing Corp., New York.

7.17 Tsai, S.W. and Hahn, H.T. (1980) *Introduction to Composite Materials*, Technomic Pub. Co., 1980.

7.18 Zinoviev P., Grigoriev S. V., Labedeva O. V., and Tairova L. R., “Strength of multilayered composites under plane stress state,” Compos Sci. Tech., Vol.58, 1998, pp.1209–24.

7.19 Hashin, Z., and Rotem, A., "A Fatigue Criterion for Fiber-Reinforced Materials," Journal of Composite Materials, Vol. 7, 1973, pp. 448-464.

7.20 Hashin, Z., "Failure Criteria for Unidirectional Fiber Composites," Journal of Applied Mechanics, Vol. 47, 1980, pp. 329-334.

7.21 Paris, F., “A study of failure criteria of fibrous composite materials,” NASA/CR-2001-210661.

7.22 Sun, C. T., Tao, J. X., “Prediction of failure envelopes and stress strain behaviors of composite laminates,” Compos Sci Tech., Vol.58, 1998, pp.1125–36.

7.23 Flaggs, D. L. and Kural, M. H., “Experimental determination of the in-situ transverse strength in graphite/epoxy laminates,” J. Composite Materials, Vol.16, 1982, pp.103-116.

7.24 Puck, A., and Schurmann, H., “Failure analysis of FRP laminates by means of physically based phenomenological models,” *Compos. Sci. Tech*, Vol.58, 1998, pp.1045–68.

7.25 Davila, C. G. and Camanho, P. P., “Failure criteria for FRP laminates in plane stress,” NASA/TM-2003-212663.

7.26 Davila, C., Personal communication.

7.27 Wang, A.S.D., "Fracture Mechanics of Sublaminate Cracks in Composite Materials," Composites Technology Review, Vol. 6, No. 2, 1984, pp. 45-62.

7.28 Dvorak, G. J., and Laws, N., "Analysis of Progressive Matrix Cracking in Composite Laminates II. First Ply Failure," Journal of Composite Materials, Vol. 21, 1987, pp. 309-329.

7.29 Laws, N., and Dvorak, G.J., "Progressive Transverse Cracking in Composite Laminates," Journal of Composite Materials, Vol. 22, 1988, pp. 900-919.

7.30 Tan, S.C., and Nuismer, R.J., “A Theory for Progressive Matrix Cracking in Composite Laminates,” Journal of Composite Materials, Vol. 23, 1989, pp. 1029-1047.

7.31 Hahn, H.T., and Johannesson, T., "Fracture of Unidirectional Composites: Theory and Applications," Mechanics of Composite Materials, G.J. Dvorak ed., AMD, 1983, pp. 135-142.

7.32 Fleck, N.A., and Liu, D., “Microbuckle Initiation from a Patch of Large Amplitude Fibre Waviness in a Composite under Compression and Bending,” European Journal of Mechanics -A/Solids, Vol. 20, No. 1, 2001, pp. 23-37.

7.33 Soutis, C., Smith, F.C., and Matthews, F.L., “Predicting the Compressive Engineering Performance of Carbon Fibre-Reinforced Plastics,” Composites Part A: Applied Science and Manufacturing, Vol. 31, No.6, 2000, pp. 531-536.

7.34 Schultheisz, C.R., and Waas, A.M., "Compressive Failure of Composites, Part 1: Testing and Micromechanical Theories," Progress in Aerospace Sciences, Vol. 32, 1996, pp. 1-42.

7.35 Argon, A.S., Fracture of Composites, Treatise of Materials Science and Technology, Vol. 1, Academic Press, New York, 1972.

7.36 Berg, C.A., and Salama, M., “Fatigue of Graphite Fibre-Reinforced Epoxy in Compression,” Fibre Science and Technology, Vol. 6, No. 2, 1973, pp. 79-118.

7.37 Schapery, R.A., “Prediction of Compressive Strength and Kink Bands in Composites Using a Work Potential,” International Journal of Solids and Structures, Vol. 32, No. 6-7, 1995, pp. 739-765.

7.38 Potter, D.S., Gupta, V., and Hauert, S., “Effects of Specimen Size and Sample Aspect Ratio on the Compressive Strength of Graphite/Epoxy Laminates,” Composites Science and Technology, Vol. 60, No.12-13, 2000, pp. 2525-2538.

7.39 Edge, E.C., "Stress-Based Grant-Sanders Method for Predicting Failure of Composite Laminates," Composites Science and Technology, Vol. 58, No. 7, 1998, pp. 1033-1041.

7.40 Li, R., Kelly, D. and Ness, R., 2003, “Application of a First Invariant Strain Criterion for Matrix Failure in Composite Materials,” Journal of Composite Materials, vol.37, No.22.

7.41 Reeder, J. R. “An Evaluation of Mixed-Mode Delamination Failure Criteria,” NASA technical memorandum 104210, 1992.

7.42 Shuart, M.J., "Failure of Compression-Loaded Multidirectional Composite Laminates," AIAA Journal, Vol.27, No. 9, 1989, pp. 1274-1279.

7.43 Bednarcyk, B.A. and Arnold, S.M., “MAC/GMC 4.0 User’s Manual Volumes 1-3” NASA TM 212077/Vol. 1-3, 2002.

7.44 Tay, T.E., Tan, S.H.N., Tan, V.B.C. and Gosse, J. H., “Damage Progression by the Element-Failure Method (EFM) and Strain Invariant Failure Theory (SIFT),” personal communication.

7.45 Chang, F.-K., and Chen, M.-H., "The In Situ Ply Shear Strength Distributions in Graphite/Epoxy Laminated Composites," Journal of Composite Materials, Vol. 21, 1987, pp. 708-733.

7.46 Swanson, S.R., Messick, M. J. and Tian, Z., J. Composite Materials, 1987, 21, 619-630.

7.47 Swanson, S.R. and Qian, Y., Composite Science and Technology, 1992, 43, 197-203.

7.48 A Voloshin and M. Arcan, Experimental Mechanics, 1980, 20, 280-284

7.49 Waas, A.M., and Schultheisz, C.R., “Compressive Failure of Composites, Part II: Experimental Studies,” Progress in Aerospace Sciences, Vol. 32, No. 1, 1996, pp. 43-78.

7.50 Wronski, A.S., and Parry, T.V., “Compressive Failure and Kinking in Uniaxially Aligned Glass-Resin Composite under Superposed Hydrostatic Pressure,” Journal of Material Science, Vol. 17, 1982, pp. 3656-3662.

7.51 Sigley, R.H., Wronski, A.S., and Parry, T.V., “Axial Compressive Failure of Glass-Fibre Polyester Composites under Superposed Hydrostatic Pressure: Influence of Fibre Bundle Size,” Composite Science and Technology, Vol. 43, 1992, pp. 171-183.

7.52 Gosse, J. H., 2004, “A Damage Functional Methodology for Assessing Post-Damage Initiation Environments in Composite Structure,” 45th AIAA SDM conference, Palm spring, California.

7.53 Paley, M. and Aboudi, J., 1992, “Micromechanical Analysis of Composites by the Generalized Cells Model,” Mechanics of Materials, Vol. 14, pp. 127-139.

7.54 Krueger, R., Paris, I. L., O’Brien T. K., and Minguet, P. J., 2001, “Fatigue Life Methodology for Bonded Composite Skin/Stringer Configurations,” NASA/TM-2001-210842, ARL-TR-2432.

7.55 MIL-HDBK-17, Material: “IM7 12k/8552 unidirectional tape”.

7.56 MIL-HDBK-17, Material: “IM7G 12k/8552 unidirectional tape (Hexcel)”.

7.57 Hoyt, D. M., Ward, S. H., Minguet, P. J., "Strength and Fatigue Life Modeling of Bonded Joints in Composite Structure," American Society for Composites (ASC) 15th Technical Conference, September 2000.

7.58 Collier, C., Yarrington, P., Van West, B., “Composite, Grid-Stiffened Panel Design for Post Buckling Using HyperSizer” AIAA-2002-1222, AIAA SDM Conference, April 2002.

7.59 Zhang, J. and Collier, C.S. (2004) “Calculation of Margin of Safety (MOS)” CRC-12-Feb-2004, Collier Research Corporation, Hampton, VA. Also submitted to *Composites Science and Technology*.

7.60 Hill, R. (1950) *The Mathematical Theory of Plasticity*, Oxford University Press, London.